Study of DNA behavior in solution and at interfaces and the role of micellar dynamics and rheology in drug controlled release

Lourdes Monica Bravo Anaya

▶ To cite this version:

THÈSE

Pour obtenir le grade de

DOCTEUR DE L'UNIVERSITÉ GRENOBLE ALPES

préparée dans le cadre d'une cotutelle entre l'*Université Grenoble Alpes* et la *Universidad de Guadalajara*

Spécialité : **Doctorat IMEP2/ Mécanique des fluides, procédés, énergétique**

Arrêté ministériel : le 6 janvier 2005 - 7 août 2006

Présentée par

Lourdes Mónica BRAVO ANAYA

Thèse dirigée par **Yahya RHARBI**
codirigée par **J.F. Armando SOLTERO MARTÍNEZ et Erika Roxana LARIOS DURÁN**

préparée au sein des : **Laboratoire Rhéologie et Procédes (Grenoble)**
Laboratorio de Reología (Guadalajara)
Laboratorio de Electroquímica y Corrosión (Guadalajara)

dans **l'École Doctorale Grenoble INP** et le **Posgrado en Ciencias en Ingeniería Química U.de G.**

Étude du comportement d'ADN en solution et aux interfaces et le rôle de la dynamique micellaire et la rhéologie dans la libération contrôlée de médicaments.

Thèse soutenue publiquement le **02/12/2015**, devant le jury composé de :

M.Yahya RHARBI
DR HDR Université Grenoble Alpes (Directeur de thèse)
M. J.F. Armando SOLTERO MARTÍNEZ
Professeur à l'Université de Guadalajara (Co-directeur de thèse)
Mme. Erika Roxana LARIOS DURÁN
Professeure à l'Université de Guadalajara (Co-encadrante de thèse)
M. Christophe CHASSENIEUX
Professeur à l'Université du Maine (Rapporteur)
M. Pablo TABOADA
Professeur à l'Université de Santiago de Compostela (Rapporteur)
M. Mohamed NACEUR BELGACEM
Professeur / Directeur de Grenoble INP-Pagora et de l'Agefpi (Président du Jury)
Mme. Laurence NOIREZ
DR au Laboratoire Leon Brillouin (Examinateur)
M. José Luis HERNÁNDEZ LÓPEZ
Professeur au Centro de Investigación y Desarrollo en Electroquímica (Examinateur)
Mme. Marguerite RINAUDO
Professeure Honoraire de l'Université Joseph-Fourier (Invitée)
M. Martín Rigoberto ARELLANO MARTÍNEZ
Professeur à l'Université de Guadalajara (Invité)

This document presents the work that was developed as a cotutelle thesis between the "Universidad de Guadalajara", México, and the "Université Grenoble Alpes", France. Gene and drug delivery applications are reached through the understanding and the knowledge of the behavior of different polymer systems.

The following research topics are included in this thesis:

→ *Study of DNA behavior in solution and at interfaces.*

→ *The role of micellar dynamics and rheology in drug controlled release.*

ABSTRACTS

Study of DNA behavior in solution and at interfaces

Nowadays, the target for reaching a greater efficiency in DNA compaction processes, the innovation of DNA sensors development and the study of changes in the interfacial properties generated between metal surfaces and DNA molecules has become an area of great interest in bioengineering. This section of the thesis proposes the coupling of rheological, electrochemical and optical techniques to perform a detailed study of DNA molecules behavior in the bulk state of the solution and at the interface with two different metallic surfaces, as a function of parameters such as temperature, DNA concentration and electric potential. Firstly, the rheological behavior of DNA/buffer solutions, as well as the evidence of the critical concentrations (C^* and C_e) is discussed from simple steady state and oscillatory dynamic shear experiments. After studying DNA solutions properties, electrochemical and optical techniques are used to identify structural changes in Au/DNA and Pt/DNA interfaces and to describe the arrangement of DNA chains in the electrochemical double-layer as a function of concentration and within each characteristic regime, i.e. dilute and semi-dilute regimes. The obtained response trough Electrochemical Impedance Spectroscopy (EIS), Modulation Interfacial of the Capacitance (MIC) and Surface Plasmon Resonance (SPR) techniques reflects an adsorption process of DNA molecules taking place onto the metal surfaces. Finally, by selecting DNA concentrations in the dilute regime, we studied the formation of chitosan-DNA nanoparticles with defined stoichiometry for gene transfer.

The role of micellar dynamics and rheology in drug controlled release

The specific delivery of active ingredients, known as vectorization, has actually become a great challenge in therapeutic research. This process has been used to control the distribution of active ingredients such as proteins, genes for gene therapy and drugs, to a target by associating it with a vector. Molecules for chemotherapy are frequently hydrophobic and require vectorization to be transported to the target cell. In this section of the thesis, we look up to understand the collective exchange dynamics (fusion and fission) between amphiphilic block copolymer micelles at the equilibrium and out of the equilibrium, and the exchange dynamics between these micelles (representing vectors) and the simplest model of cells (liposomes). We used a fluorescent technique with hydrophobic pyrene derivative to probe the fusion and fission of micelles at equilibrium. After characterizing amphiphilic block copolymers structure and studying their dynamics in and out of equilibrium, we proposed a time scan fluorescence technique to quantify the collective vectorization dynamics between amphiphilic block copolymer micelles and liposomes. The effect of the variation of several parameters such as liposome concentration and a chitosan adsorption were investigated in order to control the vectorization dynamics between these vectors and cells models.

Acknowledgments

Thanks to Dr. Armando Soltero, for his unconditional support, for being a great supervisor, a guide throughout all this time on research, for his advices, his teachings and for giving to me the opportunity of sharing an international project with France.

Thanks to Dr. Roxana Larios, for the time-shared during this PhD thesis, for all her teachings in the field of electrochemistry, for the shared conferences all around the world and for all the scientific discussions. Thanks also for sharing with me, at the beginning of this path, the sparkle of passion to science, the first sparkle I noticed in Mexico.

Thanks to Dr. Marguerite Rinaudo, for all her unconditional support during the closure of this project, for sharing an amazing year full of fantastic work, for all her teaching and all her patience. Thanks also for changing my life through all the learning experiences in the field of polymers, specifically polyelectrolytes. Thanks for the time-shared…in France, in México, even virtually at any hour of the day.

Thanks to Dr. Frédéric Pignon for all his support, for all his teaching in the field of rheology and for all the time-shared during the experiments and conferences. Thanks also for all his help while finishing the thesis and for all the good moments shared.

Thanks to Dr. Yahya Rharbi, for sharing this cotutelle project with Dr. Armando Soltero and selecting me as the appropriate candidate for the work. Thanks for all the interesting moments spend together and for the trust placed in me to perform the project.

Thanks to Dr. Nadia ElKissi for all her valuable support, for giving to me the wonderful opportunity to work in the Laboratoire Rhéologie et Procédés. Thanks for the good moments and talks shared.

Thanks to Dr. Enrique Michel, for his unconditional support, help and trust. Thanks for being such a good friend and advisor, thanks for everything.

To Dr. Emma Macías, Dr. Juan Humberto Pérez, Dr. Norberto Casillas, Dr. Eduardo Mendizabal, thanks for all the teachings in the different science fields, thanks for all your support, while being in Mexico and even virtually when I was in France.

Thanks to everyone in the Laboratoire Rhéologie et Procédés. Thanks to Dr. Hélène Galliard, for all valuable help while performing the experiments, for all her teaching in the field of rheology and mechanics, thanks also for all the good moments spent each day and even for sharing with me kitchen recipes for being in good health. Thanks to Eric Faivre for all his valuable technical support in the laboratory, thanks also for the lunches shared with me and for all the fantastic discussions about music, dance, French culture, trips and literature. Thanks to the group composed by Didier Bléses, Frédéric Hugenell and Mohamed Karrouch for making everything possible and try to work in the best conditions, thanks also for all the good talks shared in the cafeteria. Thanks to Sylvie Garofalo, Claudine Ly-Lap, Manon Bautista and François Bergerot for all their support, their efficiency and for all the talks and good moments shared. Thanks to all for always receiving my with a smile, thanks for turning this hard work period in an incredible science-life experience.

Thanks to my officemates, Xabel García, Fanny Rasschaert, Maxime Rosello and Nagalaskshmaiah Malladi, for their patience to her tornado officemate and for the good moments shared during hard work time.

To my friends…Chourouk Mathlouthi, an incredible warrior and strong women, who showed to me that everything is possible, and that it is worth to work and fight for a goal with all the strength of the world, thanks for being such a wonderful friend and a great example

Study of DNA behavior in solution and at interfaces

PART I
CONTENT

Introduction

Deoxyribonucleic acid, referred as DNA, is a very long linear polymer containing the hereditary genetic information of living organisms and is able to transmit it from one generation to another [1,2]. Several physicochemical studies of DNA aqueous solutions have shown that it is a high molecular weight polymer ($3x10^5$-$8x10^{10}$) [3] and can present a semi-rigid and relaxed configuration. Genetic information is stored in the sequence of bases along the strands of the nucleic acid. The binding between these base pairs results in the formation of a double helix, a helical structure consisting of two strands stabilized by hydrogen bonds between bases and wearing negative charges due to phosphate groups [2,4,5].

Nucleotides are the monomers of DNA and have a variety of roles in cell metabolism. They represent the chemical bonds in the response of cells to hormones and the structural components of an array of enzyme cofactors and metabolic intermediates [2]. The structure of each protein and each molecular and cellular component results from the information programmed by the nucleotide sequence in the nucleic acids of a cell. DNA owns the ability to store and transmit the genetic information across generations, which is a fundamental condition for life [6]. Genetic information is never lost and can be transmitted to new generations through replication phenomenon, since the structure of DNA allows its duplication in two identical molecules between them and identical to the original molecule. DNA transcription's ability is the basis of gene therapy, which consists in providing a functional gene to the cells that don't have it, in order to correct a genetic defect or an acquired disease. The essential step of gene therapy, called genetic transfection, consists in the introduction of DNA into cells through a specific agent called vector, and largely determines the efficiency of the technique [7, 8]. Looking for a greater efficiency in this process, it is necessary a vast knowledge and understanding of DNA conformational transitions, DNA chains interactions with cationic molecules and a thorough characterization of DNA solutions as a function of parameters such as DNA concentration, pH, ionic strength and temperature, for an optimal design of vectors [9, 10].

Different techniques have been used to study DNA solutions in order to understand the interactions between DNA chains. DNA molecule has also been considered as a model for the study of polymeric fluids in the area of rheology, so part of their molecular dynamics and macroscopic properties have been previously reported [11-14]. In the field of study of polymers, there is an important distinction between dilute polymers solutions, where the coils are separated from one to another, and more concentrated solutions, where the coils overlap [15]. This threshold is known as the overlap concentration (C*), also considered as the overlap onset and a transition region between the dilute regime and the semi-dilute regime [15]. At higher concentrations, it has been reported a second critical concentration, C_e, defined as the entanglement concentration, at which the coils begin to become entangled. The dynamic properties in the unentangled regime for polymer solutions with concentrations between C* and C_e, are described by the Rouse model [16]. *Mason et al.* reported that

for aqueous solutions of calf thymus DNA, C_e is identified around a DNA concentration of 2 mg/mL at 25°C, when experimental data agree with the model of flexible polymers dissolved in a good solvent [17].

On the other side, part of the microscopic information of DNA solutions has been obtained and analyzed through techniques such as Dielectric Relaxation Spectroscopy (DRS), which has contributed to a deeper analysis of the dynamics of DNA solutions in a wide range of temperatures and frequencies (10^6 -10^2 Hz) [18-20]. With this method, two relaxation processes were identified at temperatures below 273 K and a better understanding of conformational changes of DNA molecules in solution was accomplished. The study of the response of DNA molecules under the effect of electric fields is of great scientific interest due to its applicability in the development of biosensors, the analysis of the interactions DNA-DNA, DNA-RNA, DNA-protein, among others, and it has been evolving during the last years [21-23]. The electrochemical techniques provide also microscopic information of the physicochemical and electrical properties of the interface DNA/metal surfaces. Chronoamperometry, voltammetry and chronopotentiometry have been used as tools for detecting different electrochemical processes observed in DNA solutions, however, the technique of Electrochemical Impedance Spectroscopy (EIS) has been regarded as a more sensitive and favorable technique than the others [24]. DNA sensors, which transduce changes in the interfacial properties between the electrode and the electrolyte induced by DNA hybridization, DNA conformational changes and DNA damage by an electrical signal, have been investigated through the electrochemical techniques mentioned above in order to improve its sensitivity. However, when the current differences are not significant in a range of low concentrations, the technique EIS is more favorable than other electrochemical techniques since the differences are usually obtained by the inverse of the impedance with current, i.e. $\Delta R(Z) = \Delta V / \Delta I$ [24].

Currently, a more precisely and detailed understanding of the behavior of DNA molecules in solution, based on different parameters such as temperature, DNA concentration, ionic strength and pH, among others, has raised the interest in studying this system by coupling rheological, electrochemical and optical techniques. In this work, a conjunction between rheometry and several electrochemical techniques is proposed in order to perform a detailed study of DNA molecules behavior in the bulk state of the solution and at the interface with two different metal surfaces, i.e. gold and platinum. The electrochemical techniques chosen for their high sensitivity to adsorption processes on metal surfaces are the Electrochemical Impedance Spectroscopy [24] and the Modulation of the Interfacial Capacitance (MIC) [25]. Structural and conformational changes observed in DNA molecules, according to the parameter variation mentioned before, are also studied with Surface Plasmon Resonance (SPR) [26] and Circular Dichroism [27]. Finally, with the selection of DNA concentrations in the dilute regime, we studied the formation of chitosan-DNA nanoparticles for gene transfer. Different techniques are used to determine the role of chitosan amount on the formed complex: the obtained data from conductivity, ζ-potential, dynamic light scattering, circular dichroism and UV-Vis measurements are combined to determine the complex stoichiometry, the net charge, the dimensions, the conformation

and the thermal stability of the complex, respectively.

Justification

Studies of DNA molecules in aqueous solutions performed through different approaches allow to assess the solute-solvent interactions and to examine the strong influence of the molecule nature and its physicochemical properties while interacting with other kind of molecules in solution or with metal surfaces. The results allow us to aspire to a better understanding of the molecular interactions and to seek an increase in the efficiency of their applications. Actually, the ability to detect DNA and RNA by using DNA hybridization sensors is used in genomics and the expectations in electrochemical methods increase day to day [28], as well as the development of DNA biosensors [29, 30], the evaluation of DNA-protein interactions [31] and gene therapy studies [32].

Currently, the research to achieve a greater efficiency in the processes of DNA compaction [33, 34] and the study of the changes generated in the interfacial properties between DNA molecules and metal surfaces of different natures [28] represent areas of great scientific interest. It is noteworthy that, for a large group of biopolymers such as DNA, proteins, lipids and polysaccharides, the combination of their chemical structure and molecular dynamics govern numerous vital functions in living organisms [35].

Assumptions

The possibility to take some concepts of the theory of polymer solutions used in physicochemical and rheological studies can open new opportunities in the research field of systems, such as DNA in solution, by using different techniques like electrochemical and optical ones. Electrochemical techniques such as Electrochemical Impedance Spectroscopy (EIS) and Modulation of the Interfacial Capacitance (MIC) are proposed to determine characteristic parameters that will allow identifying and studying the transitions of DNA molecules in solutions adsorbed onto metal surfaces in a detailed way. Therefore, the obtained information will show a great overview of the system.

Through the study of DNA solutions by using the aforementioned techniques it will be possible to identify the critical concentrations C* and C_e and to analyze and discuss the behavior of the system within each regime, i.e. dilute and semi-dilute regimes. It is expected to have a detailed outline of the variations of each monitored parameter as a function of the analyzed variables (temperature, DNA concentration, ionic strength, electric potential). The knowledge of DNA molecules behavior in the dilute regime and their electrostatic interactions with cationic polymers will allow an optimal design of non-viral vectors for gene therapy.

Objectives

General objective

The general objective of this thesis is to analyze and to discuss the physicochemical properties and the interactions of DNA chains in the bulk state of the solution and to study the structural behavior of electrochemical double-layer formed by DNA molecules at two metal interfaces, as a function of temperature and DNA concentration by applying rheological, electrochemical, and optical techniques.

Specific objectives

- Quantify the transitions of DNA/TE buffer system by Rheometry, Electrochemical Impedance Spectroscopy (EIS), Modulation of the Interfacial Capacitance (MIC).

- Determine the behavior of DNA/TE buffer system in the dilute and semi-dilute regimes as a function of DNA concentration and temperature using different techniques and novel approaches.

- Quantify the basic stages of the adsorption-desorption process of DNA molecules onto platinum and gold electrodes.

References

[1] J. D. Watson, F.H.C. Crick, The structure of DNA, *Cold Spring Harb. Symp. Quant. Biol.* **18**, 123-131 (1953).

[2] J. M-Berg, J. L. Tymoczko, L. Stry, *Biochemestry 5th Edition*, New York: W H Freeman, (2002).

[3] A. Tsortos, G. Papadakis, E. Gizeli, The intrinsic viscosity of DNA, *Biopolymers* **95**, 826 (2011).

[4] M. Sun, S. Pejanovic, J. Mijovic, Dynamics of deoxyribonucleic acid solutions as studied by dielectric relaxation spectroscopy and dynamic mechanical spectroscopy *Macromolecules* **38**, 9854 (2005).

[5] G.S. Manning, A procedure for extracting persistence lengths from light scattering data on intermediate molecular weight DNA, *Biopolymers* **20**, 1751 (1981).

[6] R. Hodge, *The molecules of life: DNA, RNA and proteins*, Facts On File, Inc. (2009).

[7] J.-P. Behr, Gene transfer with synthetic cationic amphiphiles: Prospects for gene therapy, *Bioconjugate Chem* **5**, 382 (1994).

[8] A. Dugaiczyk, S.L.C. Woo, B.W. O'Malley, *Genes in pieces.* In: *Ontogeny of Receptors and Mode of Action of Reproductive Hormones* (Hamilton, Clark, and Sadler, eds) Raven Press, p. 1 (1979).

[9] M. Cárdenas, A. Braem, T. Nylander, B. Lindman, DNA compaction at hydrophobic surfaces induced by a cationic amphiphile, *Langmuir* **19**, 7712 (2003).

[10] E. Serres, P. Vicendo, E. Pérez, T. Noel, I. Rico-Lattes, DNA Condensation and transfection of cells in culture by a new polynorbornane polycationic polymer, *Langmuir* **15**, 6956 (1999).

[11] R. E. Teixeira, A. K. Dambal, D. H. Richter, E. S. G. Shaqfeh and S. Chu, The individualistic dynamics of entangled DNA in solution, *Macromolecules* **40**, 2461-2476 (2007).

[12] M. Doi , S.F. Edwards, *The Theory of Polymer Dynamics*; Clarendon: Oxford, (1986).

[13] R.G. Larson, *The Structure and Rheology of Complex Fluids*; Oxford University Press: New York, (1998).

[14] S. Laib, R.M. Robertson, D.G. Smith, Preparation and characterization of a set of linear DNA molecules for polymer physics and rheology studies, *Macromolecules* **39**, 4115 (2006).

[15] P.G. de Gennes, *Scaling concepts in polymer physics.* Ithaca, NY: Cornell University Press, (1979).

[16] Y. Heo, R.G. Larson, The scaling of zero-shear viscosities of semidilute polymer solutions with concentration, *J. Rheol.* **49**, 1117 (2005).

[17] T.G. Mason, A. Dhople and D. Wirtz, Linear viscoelastic moduli of concentrated DNA Solutions, *Macromolecules* **31**, 3600 (1998).

[18] S. Tomić, S. Dolanski Babić, T. Vuletić, S. Krča, D. Ivanković, L. Griparić and R. Podgornik, Dielectric relaxation of DNA aqueous Solutions, *Phys. Rev. E* **75**, (2007).

[19] S. Mashimo, T. Umehara, S. Kuwabara and S. Yagihara, Dielectric study on dynamics and structure of water bound to DNA using a frequency range 10M-10GHz, *J. Phys. Chem.* **93**, 4963 (1989).

[20] J. Baker-Jarvis, C. A. Jones, B. Riddle, Properties and dielectric relaxation of DNA in solution, in NIST Technical Note, p. 1 (1998).

[21] E. Paleček, Polarographic behaviour of native and denatured deoxyribonucleic acids, *J. Mol. Biol.* **20**, 431 (1966).

[22] J. Flemmig, The adsorption of DNA in the mercury-electrolyte interface, *Biopolymers* **6**, 1697 (1968).

[23] W. Sun, M. Yang, K. Jiao, Electrochemical behaviors of neutral red on single and double stranded DNA modified electrode, *Int. J. Electrochem. Sci.* **2**, 93-101 (2007).

[24] J.-Y. Park and S.-M. Park, DNA hybridization Sensors based on electrochemical impedance Sspectroscopy as a detection tool, *Sensors* **9**, 9513-9532 (2009).

[25] E.R. Larios-Durán, R. Antaño-López, M. Keddam, Y. Meas, H. Takenouti, V. Vivier, Dynamics of double-layer by AC modulation of the interfacial capacitance and associated transfer functions *Electrochimica Acta* 55, 6292- 6298 (2010).

[26] K. Tamada, F. Nakamura, M. Ito, X. Li, A. Baba, SPR-based DNA detection with metal nanoparticles, *Plasmonics* **2**, 185-191 (2007).

[27] J. Kypr, I. Kejnovská, D. Renčiuk and M Vorlíčková, Circular dichroism and conformational polymorphism of DNA, Nucleic Acids Research **37** (6), (2009).

[28] E. Paleček, F. Scheller and J. Wang, Electrochemistry of nucleic acids and proteins – Towards electrochemical sensors for genomics and proteomics, *Perspective in Bioanalysis* **1**, 73 (2005).

[29] M. Yi, K.-H. Jeong, L. P. Lee, Theoretical and experimental study towards a nanogap dielectric biosensor, *Biosensors and Bioelectronics* **20**, 1320-1326 (2005).

[30] E. Paleček, M. Fojta, M. Tomschik, J. Wang, Electrochemical biosensors for DNA hybridization and DNA damage, *Bionsens. Bio-electron.* **13**, 621-628 (1998).

[31] E. M. Boon and J.K. Barton, Charge transport in DNA, *Curr. Opin. Struct. Biol.* **12**, 320 (2002).

[32] J. Wang, G. Rivas, M. Jiang, and X. Zhang, Electrochemically induced release of DNA from gold ultramicroelectrodes, *Langmuir* **15**, 6541 (1999).

[33] M. Cárdenas, K. Schillén, T. Nylander, J. Jansson and B. Lindman, DNA compaction by cationic surfactant in solution and at polystyrene particle solution interfaces: a dynamic light scattering study, *Phys . Chem . Chem. Phys.*, **6**, 1603–1607 (2004).

[34] S. K. Filippov, C. Koňák, P. Kopečková, L. Starovoytova, M. Spírková and P.Stěpánek, Effect of hydrophobic interactions on properties and stability of DNA-polyelectrolyte complexes, *Langmuir* **26**(7), 4999–5006 (2010).

[35] C. A. Sprecher, W. A. Baase and W. Curtis Johnson Jr., Conformation and circular dichroism of DNA, *Biopolymers* **18**, 1009-1019 (1979).

CHAPTER 1

DNA, the molecule of life

1. DNA, the molecule of life

1.1. Physics and chemistry of life

For several decades now, science has shown that life is possible due to the interactions between organic molecules, particularly DNA, RNA (ribonucleic acid) and proteins. The behavior of these molecules changes due to the different structures they can have, resulting in the union of atoms that form three-dimensional blocks, which are combined into increasingly larger structures. Up to 1950, very few information was known about the structures and functions of these molecules. Then, a series of major discoveries in physics and chemistry presented the functions and mechanisms within the cells, changing drastically the course of biology and suggesting a new field of study actually known as molecular biology [1].

In 1953, a geneticist called James Watson and his British colleague Francis Crick proposed a construction scheme of DNA, showing that the molecule contains the genetic material of cells and organisms. They revealed the mechanism of DNA replication and they showed that evolution is possible due to mutations that may suffer DNA molecule [2]. The model proposed by Watson and Crick describes DNA as a pair of strands that bind helically around a common axis. However, DNA generally acquires more complex spatial configurations in order to get packed enough for being as effective as possible, since the length of the molecule is sometimes up to one million times the size of the nucleus containing it. Therefore, the great discoveries of the twentieth century are led by studies of the chemical nature and three-dimensional structure of genetic material, DNA. The sequence of the monomers, i.e. the nucleotides, encodes the instructions to form all the cell components and provides a template for the production of identical DNA molecules to be distributed at the moment of cell division. The effective storage and reproduction of the genetic material define each species, distinguishing from each other and ensuring its continuity through successive generations [3].

1.2. DNA structure

1.2.1. Double helix structure

DNA is a long, thin organic polymer, a molecule that is built on an atomic scale. The basic unit of DNA is a linear polymer composed of four different subunits of monomers called deoxyribonucleotides, arranged in a precise linear sequence. Each deoxyribonucleotide is composed by a nitrogenous base, a deoxyribose sugar and a phosphate group. The nitrogenous bases that can build the deoxyribonucleotides are: adenine (A) and guanine (G), classified as a purines; thymine (T) and cytosine (C), classified as pyrimidines.

DNA linear sequence is the one that encodes the genetic information as mentioned before. Two of these polymeric strands are wound together to form the double helix of DNA. Before cell division, the two DNA strands are separated, so they operate as a template for the synthesis of a new complementary strand, immediately generating two identical double-helical molecules, as shown in *Figure 1.1*. If one strand is damaged, the continuity of the information is secured with the information in the other strand.
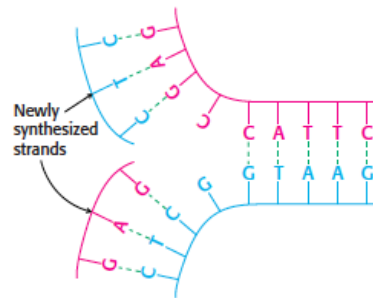
Figure 1.1. *DNA replication, as suggested by Watson and Crick [4].*

The two chains of deoxyribonucleotide constituting a DNA molecule remain linked together because of the bonds formed between the nitrogenous bases of both strands. The binding of the bases is due to hydrogen bonding, so adenine can only be attached with thymine and guanine with cytosine (*Figure 1.2.*) [1,3].
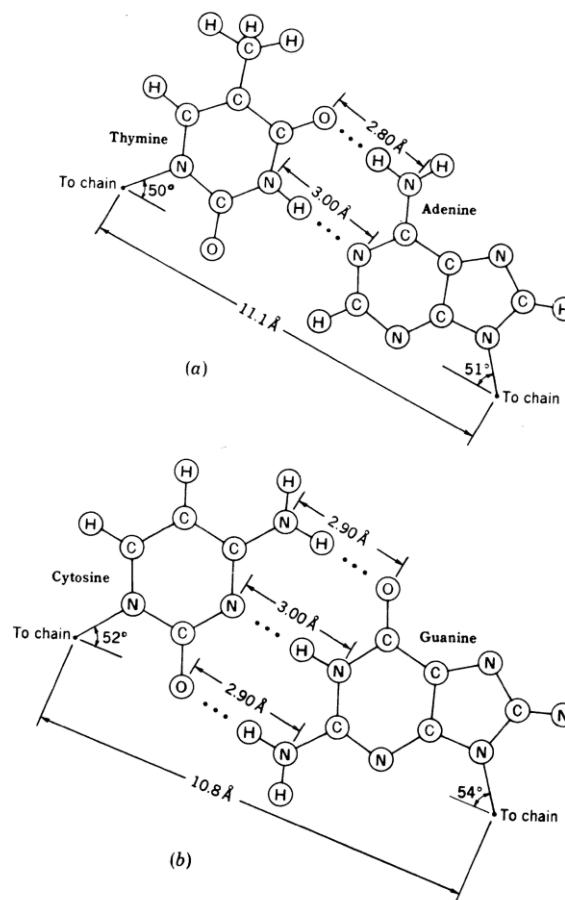
Figure 1.2. *Hydrogen bonds formation between a) A-T and b) G-C [5].*

A-T pairs form two hydrogen bonds: one between the amino groups of the purine and the carbonyl of the pyrimidine, and another one between nitrogen atoms of the respective rings. G-C pairs form three hydrogen bonds: two between the amino and carbonyl groups of each base and a third between nitrogen atoms of the rings. The pairing between purines, pyrimidines or non-complementary bases, A-C or G-T is not favored since they can't form suitable hydrogen bonds, the formation could present steric hindrance or the geometry of the helix could break.

An important source of information about DNA structure came from the work of Erwin Chargaff and his colleagues during the 1940s [6]. They found that the four nucleotides are presented in different ratios in DNA molecules from different organisms and that the amount of certain bases is closely related between them. This information was obtained from DNA molecules of a variety of species, such as calf-thymus, rye germ and wheat germ, so it was possible to reach the following conclusions:

1. The composition of the bases present in DNA molecules varies from species to species.

2. DNA samples isolated from different tissues of the same species have the same base composition.

3. The composition of the bases in DNA molecules of a given species does not change with the age of the organism, nutritional status or changes in the environment.

4. The number of adenosine residues is equal to the number of thymidine residues (A=T). The number of guanosine residues equals the number of cytidine residues (G=C). Finally, the sum of purine residues equals to the sum of pyrimidine residues, i.e.: A+G=T+C.

Unlike proteins, whose two-dimensional or three-dimensional structures depend mainly on the composition and order of their amino acids, DNA has, under normal conditions, a regular structure, regardless of the frequency or the order of the four bases.

In the common form of the DNA molecule (B-DNA), purine and pyrimidine rings of each chain are stacked inside de helix each 0.34 nm, with the plane of the rings almost perpendicular to the axis. Since the length between each consecutive base pair is equal to 0.34nm, the helix makes one complete turn every 3.4 nm, or each ten base pairs. The double helical structure has two external grooves, one wide (major groove) and another one narrow (minor groove) (*Figure 1.3*).
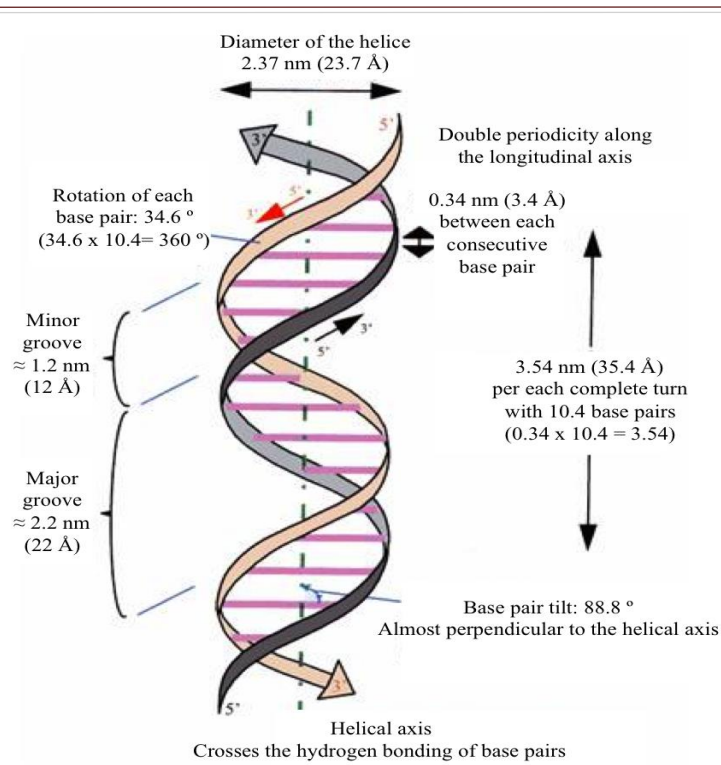
Figure 1.3. *Double helix structure [7].*

1.2.2. Alternative forms of the double helix

DNA is a considerably flexible molecule having a significant rotation around a certain number of links in the sugar-phosphate backbone. Temperature changes can cause bending, stretching and decoupling of the strands of the molecule. Several significant deviations from the structure proposed by Watson and Crick have been found in cellular DNA, but they generally don't affect the key properties of DNA, this is, complementarity of the strands.

The structure proposed by Watson and Crick is also known as the B form (B-DNA) and it is the most stable structure for a random sequence of DNA molecules, which are under physiological conditions. B-DNA is the standard reference point for any study about DNA properties. However, two alternative forms of DNA double helix are also known and are possible due to the elasticity of the deoxyribose-phosphate backbone, which allows alternative configurations (*Figure 1.4*). These structural variations are known as A-form and Z-form. The A-form (A-DNA) is rare, it only exists in a dehydrated state and it differs from the B-form in a deviation of 20° with respect to the double helix axis. This difference reduces the distance between pairs in approximately 0.29 nm and increases the number of base pairs per turn in 11 or 12 pairs. Any biological function has been attributed to A-form until now. The Z-form (Z-DNA) is considered as a more radical variation of B-form, which its clearest distinction is the helical rotation to the left. This form owns 12 pairs per helical turn, its structure is thinner and more elongated than B-DNA structure and it acquires a zigzag shaped appearance. *Table 1.1* presents a comparative of some structural properties between A-DNA, B-DNA and Z-DNA.
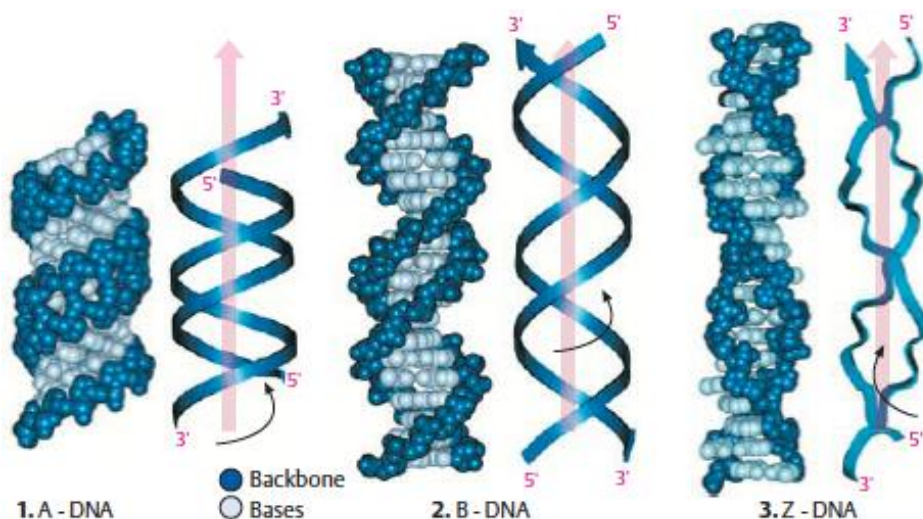
Figure 1.4. *A-DNA, B-DNA and Z-DNA representations [3].*

Table 1.1.- *Structural properties of A, B and Z DNA forms [3].*

Properties	A – form	B – form	Z – form
Helical sense	Dextrorotatory	Dextrorotatory	Levorotary
Diameter	≈ 2.6 nm	≈ 2.0 nm	≈ 1.8 nm
Base pairs per helical turn	11	10.5	12
Helical increase per base pair	0.26 nm	0.34 nm	0.7 nm
Base inclination normal to the helix axis	20º	6º	7º
Sugar conformation	C-3' endo	C-2' endo	C-2' endo for pyrimidines C-3' endo for purines

1.2.3. Variation in the arrangement of DNA strands

DNA exists in both linear and circular molecule forms [8,9]. Bacterial plasmids, some bacterial chromosomes and many genomes of mammalian viruses consist of a single circular DNA molecule, covalently closed and double stranded. Although it is known that the nuclear DNA of eukaryotic cells is organized in large units of linear chains, numerous investigations are modifying this concept. At the nucleus, during the period of cell division, a considerable part of the fibril chromatin is organized as multiple loops. The two ends of each loop are attached to the nuclear membrane structures and acquire the behavior of a circular unit. Therefore, the nucleus of the eukaryotic cell contains multiple units of circular DNA.

Usually, the DNA inside the cell is associated with different proteins attached there to DNA molecules, which unwind the helix and cause a decrease in the number of turns per unit compared to B-

form. By separating the proteins attached to DNA, the total number of turns is established. This is a quick process for linear DNA because the two strands have the ability to rotate freely around each other. However, if the DNA is in a closed circular shape, the total number of turns of a strand over the other can't be changed without producing compensating torsions [10].

1.2.4. Denaturation and renaturation

DNA solutions tend to present high viscosities at room temperature (25 ºC) and pH 7.0 that decrease if the solutions are brought to extremes of pH or to temperatures above 70 ºC, which depend on the external salt concentration of the solutions. This change indicates that DNA has undergone a physical change. High temperatures and extremes of pH cause denaturation (or melting) of double-helical DNA. DNA denaturation is the process where double-stranded DNA unwinds and separates into single-stranded strands throughout the breaking of hydrogen bonds between bases (*Figure 1.5*).

Renaturation of DNA is a rapid one-step process if a double-helical fragment of at least twelve residues remains in the double-stranded configuration. When the temperature or the pH is returned to it's initial state or to the range in which most organisms live, the unwound segments of the two strands rewind spontaneously. Though, if the two strands of DNA are totally separated, renaturation takes place in two steps. The first step is moderately slow and consists on the formation of a segment of complementary double helix by the matching of two strands by random collisions forming. The second step is faster than first one, so the unpaired bases bind successively as base pairs and the two strands close themselves to form the double helix [3]. A decreasing in the absorption of UV light compared to a solution with the same concentration of free nucleotides is obtained due to single nucleotides chain of DNA after denaturation. The absorption is further decreased when two complementary nucleic acids strands are paired, known as the hypochromic effect. Denaturation of a double-stranded DNA produces an increase of the absorption. In this manner, by monitoring the absorption of UV light at a wavelength of usually 260 nm it is possible to identify the transition from double-stranded helical DNA to single-stranded DNA.
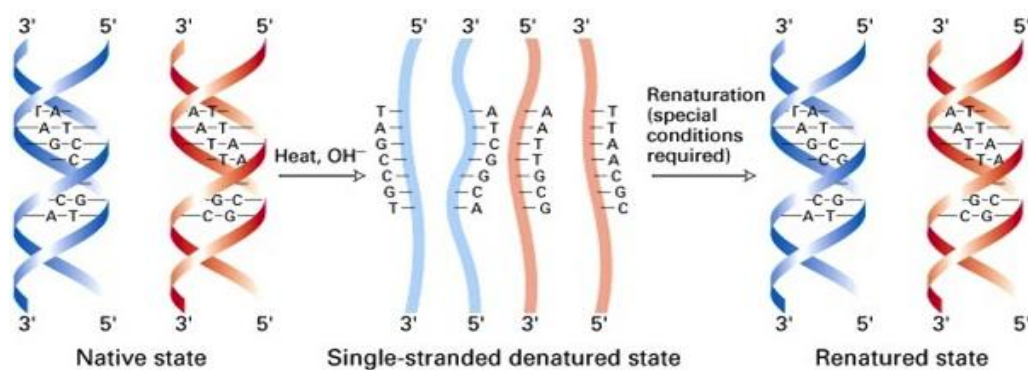
Figure 1.5. *Reversible denaturation of DNA [3].*

Each species of DNA have a characteristic denaturation temperature, also referred as melting point (T_m). DNA melting point increases while increasing the content of G-C base, since they possess three hydrogen bonds that require more heat energy to dissociate than A-T base pairs. In this manner, with the determination of the T_m of a DNA specimen, under fixed conditions of pH and ionic strength, it is possible to estimate its base composition.

1.3. DNA in solution

1.3.1. Hydration

Water is considered as a structural component of great importance in DNA molecule, in which its effect in performance is remarkable, especially in cellular environments where high solute concentration limits the amount of water contained therein [11]. Hydration is one type of interaction responsible of the secondary structure of nucleic acids and other physicochemical properties of these molecules [12]. During strand separation, the water molecules linked closely to the double helix play an important role in the formation and stability of DNA structures. Thus, any conditions that may impair water activity have an effect on the stability of a particular DNA conformation [13].

Changes in the hydration and in the reorganization of water molecules can be characterized and properly studied through density and sound velocity methods as they provide essential data on the hydration of the solute. Such techniques have been used to characterize the hydration properties of DNA duplex [14] and complexes formed between DNA and drugs [15], proving that the G-C bases are hydrated at higher rates than A-T base pairs. The physicochemical properties obtained using these techniques have also been useful to assess the structure of the complexes formed between DNA molecules and cationic surfactants [16,17].

1.3.2. Properties of DNA as a polyelectrolyte

One of the most interesting features of DNA molecule is that each base pair owns two elementary negative charges. This way, DNA molecule is characterized by having an exceptionally high linear charge density. The negative charges attract small cations in the solution, usually Na^+, which create a positively charged cloud around DNA chain [18]. Several important properties of DNA are strongly dependent on DNA concentration and on the salt content, usually NaCl, due to the electrostatic interactions between negatively charged DNA molecule and the cloud of counterions. The theoretical approaches will be discussed in detail in *Chapter 2* of this thesis.

1.3.3. DNA as a polymer solution in good solvent

1.3.3.1. Dilute and semi-dilute regimes

Various techniques have contributed to understand the macroscopic [19,20] and/or microscopic [25] behavior of DNA molecules in solution. In the field of study of polymers, there is an important distinction between dilute polymers solutions, where the coiled chains are separated from one another, and more concentrated solutions, where the coils overlap. This threshold is known as the overlap concentration (C*), also considered as a transition region between the dilute regime and the semi-dilute regime [20] (*Figure 1.6*). At higher concentrations, it has been reported a second critical concentration, C_e or C**, (depending on the authors) defined as the limit for semi-dilute entangled regime [19]. These concentrations macroscopically identify conditions to which interactions and entanglement between DNA molecules in solution are presented. This behavior will also be discussed in *Chapter 2* of this thesis.

$$C < C \star \qquad C = C \star \qquad C > C \star$$

(a)   (b)   (c)
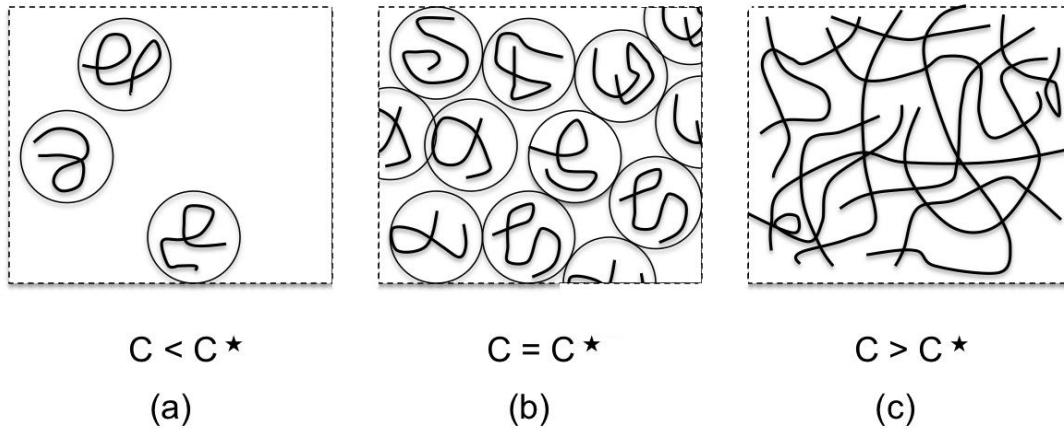
Figure 1.6. *Crossover between dilute and semi-dilute solutions: a) dilute, b) overlap concentration, and c) semi-dilute [21, 22].*

1.3.3.2. Dynamics of DNA solutions

There are some rheological studies of aqueous solutions of DNA that have provided information about the dynamics of DNA chains in solution. The viscosity, η, and the relaxation time, τ_c, of diluted solutions of T2 and T7 bacteriophage DNA in glycerol were studied by "creep recovery" measurements and were reported by *Klotz et al.* [23]. The rheological behavior of T2 DNA saline solutions was studied by *Musti et al.* at high concentrations within the entangled regime [24]. These results validate the postulated hypotheses by *Raspaud et al.* [22], who proposed that the value of the entanglement concentration, C_e, is greater than the value of the overlap concentration, C*, for DNA strands. Among the contributions in the study of the viscoelastic behavior of salt solutions of calf thymus DNA, *Mason et al.* reported the dependence of the G modulus plateau (G_p) and the crossover frequency (ω_c) with DNA

concentration using a power law as follows: $G_p \sim C^{2.3}$ and $\omega_c \sim C^{-2.4}$. The values were found to be consistent with the model of flexible polymers dissolved in a good solvent [22]. Furthermore, the nonlinear rheological behavior of semi-diluted solution of T4 bacteriophage DNA was studied by *Jary et. al* [25], who reported three characteristic areas for shear stress as a function of the shear rate. They related this behavior to the one observed in worm-like micelles systems. Recent investigations performed by *Boukany et al.* [26] discuss the consequences of entanglements in concentrated solutions of DNA through linear and nonlinear rheological studies. Due to entanglements, polymeric fluids undergo a very high elastic deformation before transforming and reach a state of flux under continuous external deformation. Therefore, when the external deformation is faster than the relaxation rates of the chain, the entangled network disentangles progressively so that flow can take place.

Currently, research has also focused in a more detailed study of the mechanical and dynamical properties of biopolymers study since they directly affect many biological processes, including protein folding and DNA transcription. The rigidity of the actin and myosin in muscles provides the structure that maintains the shape of the cell [27], while flexibility of DNA allows to the molecule to undergo a drastic change of state, from an elongated state to a very compact state during the compaction process [28]. Dynamics of biopolymer fluids have greatly attracted the attention, particularly the flow of DNA suspensions in devices "lab-on-chip", whose applications include the mapping of the genome [29, 30], DNA separation and the study of polymers physics [31]. The study of rheological and flow properties of DNA solutions has much practical importance and can lead to a better understanding of the dynamics of macromolecules [32].

1.4. DNA compaction

1.4.1. Compaction process

Compaction is the process where a long DNA molecule undergoes a transition between an elongated conformation into a very compact form. In nature, DNA compaction process occurs for packaging genomic material in small spaces such as the viral capsid and cell nuclei of eukaryotic cells [33]. In living cells, DNA strands are long, highly loaded and semi-rigid, so it is necessary to subject them to a strong compaction process in order to fill the available space. This process is also known as DNA condensation and may be reproduced and studied in vitro. *Bloomfield et al.* have summarized several studies that describe the physical and biochemical aspects of DNA compaction [34]. The application of DNA compaction in gene delivery is of great importance for the success of the protocols in gene therapy [35]. Other applications of this process are gene regulation, DNA manipulation and fabrication of nanostructures.

There are different forms of DNA compaction; three of them are mentioned here. In aqueous

solutions, DNA adopts an elongated spiral conformation due to the high repulsions between the negatively charged phosphate groups. After the addition of the compaction agent, DNA undergoes a strong compaction process. The identification of these forms has been possible with the contributions of the group of *Zinchenko et al.* [36], who carried out DNA compaction studies for individual molecules. *Figure 1.7* shows three possible ways of compaction of DNA elongated strands. The first type of compaction is a process called "all-or-nothing", where there isn't an intermediate state but the elongated spiral state and the compact coexist [37]. This process is frequently observed when the attraction is generated between DNA molecules throughout the chain, either by adding small amounts of multivalent counterions or inducing unfavorable contacts between DNA monomers and the solvent, i.e. by adding a poor solvent, like ethanol, or neutral polymers. The second compaction process corresponds to a progressive transition from the elongated state to the compacted state. This usually happens when a strong attraction between consecutive DNA monomers is induced with polycations that have more than 10 monomers [38]. The highly packed structure of DNA molecules located inside viruses is most likely a combination of the two models recently mentioned. The third type is a possibly assisted compaction process, carried out through the adsorption of DNA molecules and of its packaging around nanoscale objects. This type of compaction has been observed in the chromatin of eukaryotic cells and can be generated *in vitro* when DNA is compacted with cationic nanoparticles or dendrimers [39, 40].
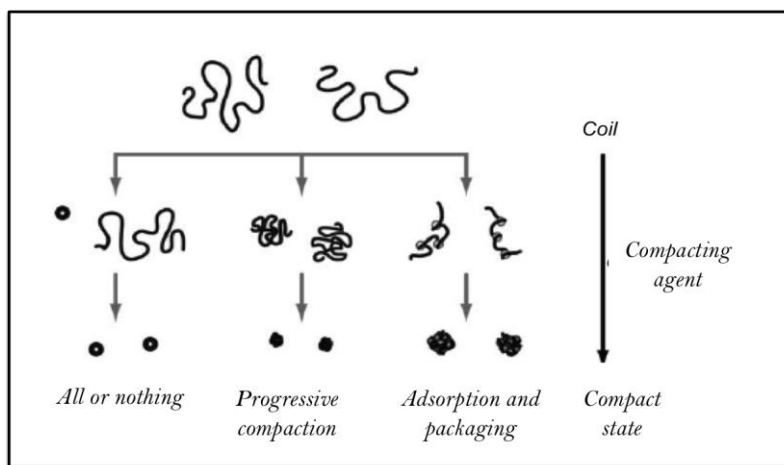
Figure 1.7. *Schematic representation of the three main methods of compaction in vitro* [38].

The form of compacted DNA results from a balance between surface energy and the rigidity of the DNA molecule, which can be modified by the addition of monovalent salts that produce larger DNA condensed molecules [41]. The most common form is a toroidal shape with a diameter equivalent to twice the persistence length (l_p) of DNA molecule [42], where double helical l_p is around 50 nm, however, there are also other common shapes: spherical beads [43] rods [44], flowers [45] and condensed rackets [46].

1.4.2. Gene therapy

Gene therapy is a technique by which genetically modified material (DNA) is handled and introduced into the patient's cells with the aim of achieving a therapeutic benefit. This technique consists in providing a functioning gene into the cells that lack this feature, in order to correct a genetic defect or an acquired disease. Although the primary use of this technique occurs in the fields of medicine and pharmacy, the application of genetic alteration protocols of living organisms is not limited only to these areas [47,48].

Gene therapy main protocol is called transfection, which is the process of deliberately introducing nucleic acids into cells [49]. Direct transfection of DNA chains into cells by endocytosis can't take place due to two reasons: on one hand, DNA negative charges and membranes repel each other, so it is necessary to neutralize DNA charge. On the other hand, since DNA size is too large to spontaneously cross the cell membrane, it is necessary to add a ligand that will form a neutral or positively charged complex in the nanoscale size, capable to introduce DNA into cell. This way, electrostatic repulsions with the membrane are discarded and the small size of the complex could have a similar size to that of a virus able to enter the cell. The agent that performs DNA neutralization, compaction and subsequently its introduction into the cell is called a vector. The efficiency on the transport of the genetically modified material into the target cells, especially at the stage of transfection, depends on the use and the characteristics of these vectors.

The ideal vector must accomplish several features to perform its function optimally [50]. They should allow the incorporation during the appropriate time of one or more required agents for the clinical application required, they must be specific for the target cell, they should not cause an inflammatory response and they must be stable and easy to obtain. Vectors also must adequately protect the genetic material on its way to the cell nucleus since several enzymes (DNase, restriction endonucleases and exonucleases) degrade DNA by hydrolyzing phosphodiester linkages of the molecule. Finally, they should promote interactions with the cell membrane and the efficient transfection of DNA chains genetically modified to cytoplasm, essential step of the gene therapy protocol.

Depending on the nature of the vectors they can be classified into two groups: viral and non-viral vectors [51]. Viruses have been naturally evolved over thousands of years by the evolution in order to perform an efficient transfection of genetic material into the cells of the body, so they are extremely efficient during the transfection process. In the past, most used vectors in gene therapy were the recombinant viruses. These vectors have an undeniable effectiveness in the transfer of DNA, but they also have associated limitations, such as the induction of the immune response, insertional mutagenesis, and infections, among others. Sometimes the virus doesn't enter into the cells of the desired tissue or doesn't have sufficient capacity to replicate in a given cell. In 2002 the Food and Drug Administration (FDA), agency responsible for health in the USA, banned the use of viral vectors in gene therapy [52].

Non-viral vectors are synthetic charged particles that bind to DNA genetically modified facilitating DNA transport and its entry into target cells under stable conditions. Non-viral gene transfer techniques represent a safer alternative than techniques using viral vectors. The main advantage of these agents is that they have an unlimited capacity for cloning; generally they have low toxicity and immunogenicity and allow repeated applications. However, the main disadvantage of such vectors is the low transfection efficiency, i.e.: orders of magnitude below that the efficiency obtained with viral vectors. Recently, three types of compounds have been used as non-viral vectors in gene therapy protocols: cationic surfactants [53], lipids and polycations [54].

1.5. Interfaces: DNA/substrates

1.5.1. DNA adsorption onto metal surfaces

The study of the interactions between DNA molecules and metal surfaces such as copper, silver, platinum and gold [55] has become a research topic of great interest since a detailed understanding of the adsorption and desorption processes is required for the optimization of "DNA chips", the development of biosensors and the functionalization of nanoparticles [56]. Currently, one of most studied surfaces due to their unique optical and electrical properties is gold [57]. However, several reports in the literature also revealed information about the irreversible DNA adsorption process at mercury and carbon electrodes [58]. DNA and RNA molecules adsorption studies on mercury electrodes have shown that such molecules can remain adsorbed at highly negative potentials, i.e. close to -1.2 V vs SCE [59]. *Miller* [60] was the first to study the adsorption of nucleic acids on a surface of polarized mercury, showing that the DNA preserves its double-helical structure when it is adsorbed onto the negatively charged mercury surface, while it unfolds at positive potentials. Their results also showed that the differential capacitance reached a constant value after the surface was covered in its entirety.

According to the theory of polymers adsorption at interfaces [61], the adsorption process of flexible linear polymers results in a conformational change in the topology of the polymer. *Brabec et al.* [62] found that all monomeric constituents of DNA, i.e. nucleobases, sugars and/or phosphoric acid residues, can participate in the adsorption of DNA molecules onto mercury electrodes. At neutral pH, the degree of participation of each constituent in the adsorption depends on the ionic strength, the electrode potential and the conformation of the polynucleotide in solution. At low ionic strengths, such as 0.1 M, double-stranded DNA is electrostatically adsorbed on a positively charged surface due to the negative charges of the phosphate groups. At negative potentials, DNA was only weakly adsorbed through sporadic bases due to the repulsion of unscreened phosphate charges from the electrode. Furthermore, single-stranded polynucleotides are mainly adsorbed through the nitrogen bases [62].

The adsorption and desorption processes of nucleic acids onto electrodes have been extensively studied by several conventional methods such as polarography and voltammetry [56, 63], and by other methods described by *Paleček et al.* [58]. However, measurements in the frequency domain performed by Electrochemical Impedance Spectroscopy (EIS) have generated great interest due to the advantages that offers this technique among other electrochemical techniques [64-68]. Several studies have focus on the adsorption kinetics and the mobility of DNA chains adsorbed by EIS and some mechanisms have been proposed for processes that are carried out at the electrode surface [55]. Recently, the adsorption and immobilization of DNA have been considered as fundamental methods for the construction of logic circuits, the assembly of DNA with other electronic components and for designing surfaces that exhibit a greater biological activity. Therefore, the adsorption of DNA molecules on solid surfaces is of great interest because of the various possible applications in modern molecular biology [69-71].

It is worth mentioning that since the first report on the differential capacitance of the double layer of nucleic acid solutions in mercury electrodes [67], the impedance of polarized interfaces has been widely used in measurement and research of the activities of biomolecules and the interactions of proteins, nucleic acids and bases with electrodes surfaces [72,73]. The Electrochemical Impedance Spectroscopy has the advantage of being a non-destructive technique that allows studying qualitatively and quantitatively the electrochemical oxidation-reduction processes and the adsorption processes. Similarly, it offers the possibility to separate the basic steps of the overall studied process based on the time constant of each step and to obtain their information at different time scales, as well as their characteristic times.

1.5.2. DNA conformational changes on surfaces, denaturation and renaturation

Investigations of the electric field effect in DNA conformation on metal surfaces started around the 1960s. In 1961, *Miller* [60] studied the differential capacitance of the double layer of adsorbed DNA double-stranded molecules and denatured DNA, concluding that at positive potentials, double stranded DNA begins to partially unroll on the electrode surface, whereas at negative potentials, DNA preserves its double helical structure. These results suggest that the DNA strands may be unwound at specific potentials on mercury electrodes and some other metal surfaces. The first studies on conformational changes of double-stranded DNA were carried out mostly by polarography and voltammetry [74].

The abilities that different surfaces acquire to stimulate renaturation/hybridization or denaturation/unfolding of DNA according to the applied polarization and the nature of the substrate are of great interest for the development of new biotechnologies. Additionally, the functionality of DNA is also relevant because the interactions within cells have a large number of surfaces electrically charged and biomacromolecules [75]. The reversible denaturation and renaturation of double stranded DNA form the basis of many methods and based diagnostic applications such as biosensors development and

nucleic acid amplification methods (i.e. polymerase chain reaction or the ligase chain reaction) [76].

It is expected that the spatial arrangement of adsorbed double-stranded DNA differs to that of single-stranded DNA, depending on the nature and the charge of the surface, as well as the ionic conditions near to the surface. The combination of electrochemical and optical methods, such as EIS, Voltammetry and Surface Plasmon Resonance (SPR), among others, is necessary for a better understanding of the spatial arrangement and the behavior of DNA molecules on electrically charged surfaces.

1.6. References

[1] R. Hodge, *The molecules of life: DNA, RNA and proteins*, Facts On File, Inc. (2009).

[2] F.H.C. Crick and J.D. Watson, Molecular structure of nucleic acids; a structure for deoxyribose nucleic acid, *Nature* **171**, 737-738 (1953).

[3] D.L. Nelson, M.M. Cox, *Lehninger Principles of Biochemistry*, 5th Edition, (2008).

[4] J. M. Berg, J. L. Tymoczko, G. J. Gatto Jr. and L. Stryer, *Biochemistry*, 8th Edition, (2015).

[5] R. Steiner and D.B.S. Millar, The nucleic acids in *Biological Polyelectrolytes*, edited A. Veis, Marcel Dekker Inc., New York (1970).

[6] N. Kresge, R. D. Simoni and R. L. Hill, Otto Fritz Meyerhof and the elucidation of the glycolytic pathway, *J. Biol. Chem.* **280**, e21 (2005).

[7] J. Luque, A. Herráez, *Texto Ilustrado de Biología Molecular e Ingeniería Genética, Conceptos, Técnicas y Aplicaciones en Ciencias de la Salud*, Harcourt, España, (2012).

[8] K. Klenin, H. Merlitz, J. Langowski, A Brownian dynamics program for the simulation of linear and circular DNA and other wormlike chain polyelectrolytes, *Biophysical Journal* **74**, 780-788 (1998).

[9] T. Garbella, P. Medveczky, T. Sairenji and C. Mulder, Detection of circular and linear herpesvirus DNA molecules in mammalian cells by gel electrophoresis, *Journal of Virology* **50**, 248-254 (1984).

[10] J. Vinograd and J. Lebowitz, Physical and topological properties of circular DNA, *The Journal of General Physiology*, 103-125 (1966).

[11] N.N. Degtyareva, B.D. Wallace, A.R. Bryant, K.M. Loo, J.T. Petty, Hydration changes accompanying the binding of minor groove ligands with DNA, *Biophysical Journal* **92**, 959-965 (2007).

[12] V.A. Buckin, B.I. Kankiya, R.L. Kazaryan, Hydration of nucleosides in dilute aqueous solutions. Ultrasonic velocity and density measurements, *Biophysical Chemistry* **34**, 211-223 (1989).

[13] C.H. Spink and J.B. Chaires, Effects of hydration, ion release, and excluded volume on the melting of triplex and duplex DNA, *Effects of Hydration, Biochemistry* **38**, 496-508 (1999).

[14] E. Liepinsh, G. Otting and K. Wüthrich, NMR observation of individual molecules of hydration water bound to DNA duplexes: direct evidence for a spine of hydration water present in aqueous solution, *Nucl. Acid. Res.* **20**(24), 6549-6553 (1992).

[15] T.V. Chalikian, G.E. Plum, A.P. Sarvazyan, and K.J. Breslauer, Influence of base composition, base sequence, and duplex structure on DNA hydration: apparent molar volumes and apparent molar adiabatic compressibilities of synthetic and natural DNA duplexes at 25 degrees C, *J. Biochemistry* **33**, 2394-2401 (1994).

[16] V. Buckin, E. Kudryashow, S. Morrisey, T. Kapustina, and K. Dawson, Do surfactants form micelles on the surface of DNA?, *Prog. Coll. Polym. Sci.* **110**, 214 (1998).

[17] S. Morrisey, E.D. Kudryashow, K. Dawson, and V.A. Buckin, Surfactant-DNA complexes in low ionic strength dilute Solutions, *Prog. Colloid and Polym. Sci.* **112**, 71-75 (1999).

[18] M. D. Frank-Kamenetskii, Biophysics of the DNA molecule, *Physics Reports* **288**, 13-60 (1997).

[19] T.G. Mason, A. Dhople and D. Wirtz, Linear viscoelastic moduli of concentrated DNA solutions, *Macromolecules* **31**, 3600-3601 (1998).

[20] Y. Heo, R.G. Larson, The scaling of zero-shear viscosities of semidilute polymer solutions with concentration, *J. Rheol.* **49**, 1117 (2005).

[21] P.G. de Gennes, *Scaling concepts in polymer physics.* Ithaca, NY: Cornell University Press, (1979).

[22] E. Raspaud, D. Lairez and M. Adam, On the Lumber of blobs per entanglement in semidilute and good solvent solution: melt influence, *Macromolecules* **28**, 927-933 (1995).

[23] L.C. Klotz and B.H. Zimm, Size of DNA determined by viscoelastic measurements: results on bacteriophages, Bacillus subtilis and Escherichia coli, *J. Mol. Biol.* **72**, 779-800 (1972).

[24] R. Musti, J.L. Sikorav, D. Laires, G. Jannink, and M. Adam, Viscoelastic properties of entangled DNA solutions, *C.R. Acad. Sci. II* **320**, 599-605 (1995).

[25] D. Jary, J. L. Sikorav and D. Lairez, Nonlinear viscoelasticity of entangled DNA molecules, *Europhys. Lett.* **46**, 251-255 (1999).

[26] P. E. Boukany and S-Q. Wang, Shear banding or not in entangled DNA solutions, *Macromolecules* **43**, 6950-6952 (2010).

[27] N. Wang, Mechanical interactions among cytoskeletal filaments, *Hypertension* **32**, 162–165 (1998).

[28] V.A. Bloomfield, DNA condensation by multivalent cations, *Biopolymers* **44**, 269–282 (1997).

[29] E.Y. Chan, N.M. Goncalves, R.A. Haeusler, A.J. Hatch, J.W. Larson, A.M. Maletta, G.R. Yantz, E.D. Carstea, M. Fuchs, G.C. Wong, S.R. Gullas and R. Gilmanshin, DNA mapping using microfluidic stretching and single-molecule detection of fluorescent site-specific tags, *Genome Res.* **14**, 1137–1146 (2004).

[30] J. S. Bader, R.W. Hammond, S.A. Henck, M.W. Demm, G.A. McDermott, J.M. Bustillo, J.W. Simpson, G.T. Mulhern and J.M. Rothberg, DNA transport by a micromachined Brownian ratchet device, *Proc. Natl. Acad. Sci. U. S. A.* **96**, 13165–13169 (1999).

[31] E. D. T. Aktins and M. A. Taylor, Elongational flow studies on DNA in aqueous solution and stress-induced scission of the double helix, *Biopolymers*, **32**, 911–923 (1992).

[32] G. Juarez and P. E. Arratia, Extensional rheology of DNA suspensions in microfluidic devices, *Soft Matter*, **7**, 9444 (2011).

[33] A. Estévez-Torres and D. Baigl, DNA compaction: fundamentals and applications, *Soft Matter* **7**, 6746 (2011).

[34] V. A. Bloomfield, DNA condensation, *Curr. Opin. Struct. Biol.* **6**, 334–341 (1996).

[35] B. Demeneix, Z. Hassani and J.-P. Behr, Towards multifunctional synthetic vectors, *Curr. Gene Ther.* **4**, 445–455 (2004).

[36] A. Zinchenko, D. Baigl and K. Yoshikawa, Nanostructures and organizations of compacted single chains of polyelectrolytes, *in Polymeric Nanostructures and Their Applications*, ed. H. S. Nalwa, American Scientific Publishers, Stevenson Ranch (CA), USA, (2007).

[37] M. Takahashi, K. Yoshikawa, V. V. Vasilevskaya and A. R. Khokhlov, Discrete coil-globule transition of single duplex DNAs induced by polyamines, *J. Phys. Chem. B* **101**, 9396–9401 (1997).

[38] T. Akitaya, A. Seno, T. Nakai, N. Hazemoto, S. Murata and K. Yoshikawa, Weak interaction induces an ON/OFF switch, whereas strong interaction causes gradual change: folding transition of a long duplex DNA chain by poly-L-lysine, *Biomacromolecules* **8**, 273–278 (2007).

[39] A. A. Zinchenko, K. Yoshikawa and D. Baigl, Compaction of single-chain DNA by histone-inspired nanoparticles, *Phys. Rev. Lett.* **95**, 22810 (2005).

[40] W. Chen, N. J. Turro and D. A. Tomalia, Using ethidium bromide to probe the interactions between DNA and dendrimers, *Langmuir* **16**, 15–19 (2000).

[41] C. C. Conwell, I. D. Vilfan and N. V. Hud, Controlling the size of nanoscale toroidal DNA condensates with static curvature and ionic strength, *Proc. Natl. Acad. Sci. U. S. A.* **100**, 9296–9301 (2003).

[42] N. V. Hud and K. H. Downing, Cryoelectron microscopy of lambda phage DNA condensates in vitreous ice: the fine structure of DNA toroids, *Proc. Natl. Acad. Sci. U. S. A.* **98**, 14925–14930 (2001).

[43] V. V. Vasilevskaya, A. R. Khokhlov, S. Kidoaki and K. Yoshikawa, Structure of collapsed persistent macromolecule: Toroid vs. spherical globule, *Biopolymers* **41**, 51–60 (1997).

[44] P. G. Arscott, A. Z. Li and V. A. Bloomfield, Condensation of DNA by trivalent cations. 1. Effects of DNA length and topology on the size and shape of condensed particles, *Biopolymers* **30**, 619–630 (1990).

[45] H. G. Hansma, Surface biology of DNA by atomic force microscopy, *Annu. Rev. Phys. Chem.* **52**, 71–92 (2001).

[46] K. Yoshikawa, Y. Yoshikawa and T. Kanbe, All-or-none folding transition in giant mamalian DNA, *Chem. Phys. Lett.* **354**, 354–359 (2002).

[47] V. Vijayanathan, T. Thomas and T. J. Thomas, DNA Nanoparticles and Development of DNA Delivery Vehicles for Gene Therapy, *Biochemistry*, **41**, 14086 (2002).

[48] D. Luo and W.M. Saltzman, Synthetic DNA delivery Systems, *Nat. Biotechnol.* **18**, 33-37 (2000).

[49] Y. Yaron, R.L. Kramer, M.P. Johnson, M.I. Evans, Gene therapy: Is the Future Here Yet?, *Fetal Diagnosis and Therapy* **24**, 179-197 (1997).

[50] N. Miller and R. Vile, Targeted vectors for gene therapy, *The FASEB Journal* **9**, 190-199 (1995).

[51] F. Liu and L. Huang, Development of non-viral vectors for systemic gene delivery, *Journal of Controlled Release* **78**, 259-266 (2002).

[52] X. Chen, J. Wang, N. Shen, Y. Luo, L. Li, M. Liu and R.K. Thomas, Gemini surfactant/DNA complex monolayers at the air-water interface: Effect of surfactant structure on the assembly, stability and topography of monolayers, *Langmuir* 18, 6222 (2002).

[53] J.-P. Behr, Gene transfer with synthetic cationic amphiphiles: prospects for gene therapy, *Bioconjugate Chem.* **5**, 382-389 (1994).

[54] W. Liu, S. Sun, Z. Cao, X. Zhang, K. Yao, W. W. Lu and K.D.K. Luk, An investigation on the

physicochemical properties of chitosan/DNA polyelectrolyte complexes, *Biomaterials* **26**, 2705–2711 (2005).

[55] E. Paleček, F. Scheller and J. Wang, Electrochemistry of nucleic acids and proteins – Towards electrochemical sensors for genomics and proteomics, *Perspective in Bioanalysis* **1**, 73 (2005).

[56] J. Liu, Adsorption of DNA onto gold nanoparticles and graphene oxide: surface science and applications, *Phys. Chem. Chem. Phys.* **14**, 10485-10496 (2012).

[57] J. Wang, From DNA biosensors to gene chips, *Nucleic Acids Research* **28**, 3011-3016 (2000).

[58] E. Paleček, M. Fojta, F. Jelen and V. Vetterl, Electrochemical analysis of nucleic acids, The Encyclopedia of Electrochemistry, *Bioelectrochemistry* **9**, Eds. A.J. Bard and M. Stratsmann, Wiley-VCH, Weinheim, 365 (2002).

[59] M. Fojta, V. Vetterl, M. Tomschik, F. Jelen, P. Nielsen, J. Wang and E. Paleček, Adsorption of peptide nucleic acid and DNA decamers at electrically charged surfaces, *Biophys. J.* **72**, 2285 (1997).

[60] I.R. Miller, The structure of DNA and RNA in the water-mercury interface, *J. Mol. Biol.* **3,** 229 (1961).

[61] C.A.J. Hoeve, Theory of polymer adsorption at interfaces, *J. Polymer Sci: Part C* **34**, 1-10 (1971).

[62] V. Brabec and E. Palecek, Adsorption of single-stranded and double-helical polynucleotides on the mercury electrode, *Biopolymers* **11**, 2577 (1972).

[63] P. Valenta and P. Grahmann, Electrochemical behavior of natural and biosynthetic polynucleotides at the mercury electrode. Part 1. The adsorption of denatured deoxyrribonucleic acid at the hanging mercury drop electrode. *J. Electroanal. Chem.* **49**, 41 (1974).

[64] C.M.A. Brett, and A.M.O. Brett, *Electrochemistry, Principles, Methods, and Applications*, Oxford University Press, Oxford (1993).

[65] Y.Z. Fu, R. Yuan, L. Xu, Y.Q. Chai, Y. Liu, D.P. Tang and Y. Zhang, Electrochemical impedance behavior of DNA biosensor based on colloidal Ag and bilayer two-dimensional sol-gel as matrices, *J. Biochem. Biophys. Methods* **62**, 163 (2005).

[66] S. Hason, J. Dvořák, F. Jelen and V. Vetterl, Interaction of DNA with echinomycin at the mercury electrode surface as detected by impedance and chronopotentiometric measurements, *Talanta* **56**, 905 (2002).

[67] M. Sluyters-Rehbach and J.H. Sluyters, The investigation of the adsorptive behaviour of electroactive species by means of admittance analysis: Part I. Theory of the case of reversible charge

transfer, *J. Electroanal. Chem.* **136**, 39 (1982).

[68] H. Kimura-Suda, D.Y. Petrovykh, M.J. Tarlov and L.J. Whitman, Base-dependent competitive adsorption of single-stranded DNA on gold, *J. Am. Chem. Soc.* **125**, 9014 (2003).

[69] G.M. Zhang, S.P. Surwade, F. Zhou and H.T. Liu, DNA nanostructure meets nanofabrication, *Chem. Soc. Rev.* **42**, 2488 (2013).

[70] D.K. Chattoraj and A. Mitra, Adsorption of DNA at solid-water interfaces and DNA-Surfactant binding interaction in aqueous media, *Curr. Sci.* **97**, 1430 (2009).

[71] H. Heli, A study of double stranded DNA adsorption on aluminum surface by means of electrochemical impedance spectroscopy, *Colloids and Surfaces B: Biointerfaces* **116**, 526-530 (2014).

[72] F.R.R. Teles and L.R. Fonseca, Trends in DNA biosensors, *Talanta* **77,** 606 (2008).

[73] N. Sattarahmady, A. Parsa and H. Heli, Albumin nanoparticle-coated carbon composite electrode for electrical double-layer biosupercapacitor applications, *J. Mater. Sci.* **48**, 2346 (2013).

[74] H. Berg, *Polarographic possibilities in protein and nucleic acid research, Top. Bioelectrochem. Bioenerg.*, Vol. **1**, 39 Ed. G. Milazzo, Wiley, London, (1976).

[75] E. Paleček and F. Jelen, Electrochemistry of nucleic acids and development of DNA sensors, *Critical Reviews in Analytical Chemistry*, **32**(3), 261-270 (2002).

[76] R. P. Johnson, N. Gale, J. A. Richardson, T. Brown and P. N. Bartlett, Denaturation of dsDNA immobilised at a negatively charged gold electrode is not caused by electrostatic repulsion, *Chem. Sci.*, **4**, 1625-1632 (2013).

CHAPTER 2

Characterization and rheological properties of DNA in solutions

2. Characterization and rheological properties of DNA in solution

The results of this chapter are the object of the following publication:

Conformation and rheological properties of calf-thymus DNA in solution.

L. M. Bravo-Anaya, M. Rinaudo and J. F. A. Soltero.

In press: Polymers, 2016

2.1. Introduction

2.1.1. Polyelectrolytes background

Polyelectrolytes are polymers, usually water soluble, carrying either positively or negatively charged ionizable groups. They can be either natural molecules, such as nucleic acids, proteins or certain polysaccharides, among others; they can be obtained by synthesis, such as polyacrylic acid and sodium polystyrene sulfonate, or they can be produced by chemical modification, such as carboxymethylcellulose [1]. Several biological molecules are polyelectrolytes, as DNA, polypeptides and glycosaminoglycans. Because of their fundamental importance in biology and biochemistry, and because of their hydrosolubility, polyelectrolytes have been subject of a continued interest in polymer science.

Depending on the charge of their dissociable groups, polyelectrolytes can be classified as cationic polyelectrolytes (polycations), anionic polyelectrolytes (polyanions) or amphoteric polyelectrolytes (able to act as an acid or a base) [2]. Polycations and polianions are accompanied by an equivalent amount of compensating ions (counterions), which distribution depends in the electrostatic potential created by the polyion. In the presence of an external electrolyte dissociated in aqueous media, it appears a new amount of counterions (exchangeable ions with those of the polyelectrolyte) and co-ions (ions of the same charge as the polyelectrolyte) [1].

A richer behavior of polyelectrolyte solutions with respect to uncharged polymer solutions is obtained due to the electrostatic interactions between charges [3-5]. For example, for polyelectrolytes, the crossover from dilute to semi-dilute regime takes place at lower polymer concentrations than in solutions of neutral chains. The original viscosity behavior of polyelectrolyte solutions at low polymer concentration in absence of external salt is a large reduced viscosity increase when concentration decreases due to electroviscous effects [7]. As first approach, in excess of external salt, i.e. 10^{-1} M in NaCl, polyelectrolytes behave as uncharged polymers able to be characterized with the usual techniques of polymer physical chemistry.

2.1.1.1. Polyelectrolytes characterization

Macromolecules constituting a polyelectrolyte are characterized by their average molecular weight related to their molecular weight distribution and also by their charge density or their charge parameter [1]. The optimum conditions to highlight the characteristics of a polyelectrolyte are to work in dilute solution, in the absence of external salt and in the absence of multivalent counterions. The molecule is similar to a charged wire containing υ charges over a length L (countour length) connected to the molecular weight (*Figure 2.1*) [1].
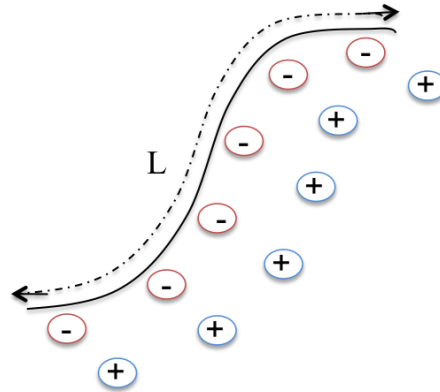
Figure 2.1 *Schematic representation of a polyanion surrounded by its counterions.*

The charge parameter was introduced by *Katchalsky* and allows an adequate characterization of polyelectrolytes [8]. The following equation is used to obtain the value of this parameter:

$$\lambda = \frac{u e^2}{e L k_B T}$$ (2.1)

where υ is the number of ionic sites on the chain of the polyelectrolyte, *e* the electron charge, ε the dielectric constant of the solvent, $k_B T$ corresponds to the Boltzmann term and L the contour length.

λ controls the behavior of electrostatic polyelectrolytes and describes the distribution of the potential around the polyion. The charge parameter λ equals to 1 in water ($\varepsilon \sim 80$) at room temperature, i.e. 25 °C, for an average distance between two ionized sites of 0.7 nm. This is also known as the Bjerrum length, l_B, (*Equation 2.2*), representing the distance between two identical elementary charges for which the electrostatic repulsion energy equals to $k_B T$.

$$l_B = \frac{e^2}{e k_B T}$$ (2.2)

Therefore, $\lambda = l_B/b_i$, were b_i represents the distance between two ionized sites for a polyelectrolyte. The distance between the projections of two successive charged groups in the axis of the polyelectrolyte is fixed by the chemical structure, the dissociation degree in the case of a weak polyelectrolyte (-NH₂, -COOH) and the conformation of the polyeletrolyte [9].

The Bjerrum length is related to the Debye length, κ^{-1}, and to the concentration of ions, C_i. The Debye length represents the distance between the elementary charges beyond which the electrostatic interactions are screened. In this way, the counterions interfere to screen the charges in addition of external salts. By analogy to the simple electrolytes theory, the Debye-Hückel length can be given by the following equation:

$$k^{-1} = \left(4\rho N_A l_B \sum C_i z_i^2 \right)^{-1/2} \tag{2.3}$$

where N_A is the Avogadro number, C_i the concentration of the ions presents in the solution and z_i their valence for small ions and not polyelectrolytes.

In order to study the role of the dimensions of the polyelectrolyte itself in a solution at low ionic concentration, it is necessary to work with an isoionic dilution, which allows determining and analyzing the viscosimetric behavior of a polyelectrolyte by setting up a constant range of electrostatic interactions (κ^{-1}= constant). Then it is shown that the polyelectrolyte acts as a simple electrolyte with a concentration C_m (in equiv/L) for $\lambda < 1$ or C_m/λ for $\lambda > 1$, were C_m corresponds to the concentration of ionized groups (counterions) and λ to the charge parameter of the polyelectrolyte. The following expressions for the total electrolyte concentration (C_T in equiv/L) are then established [1,9]:

For $\lambda < 1$: $C_T = C_m + Cs$ (2.4)

For $\lambda > 1$: $C_T = C_m/\lambda + Cs$ (2.5)

And κ^{-1} (nm) ~ 0.3 $C_T^{-1/2}$ (2.6)

where C_m is the concentration of the polyeletrolyte and C_s corresponds to the concentration of monovalent salt added to the solution, also given in equiv/L.

2.1.1.2. Theoretical models

Many theories have been developed in order to quantify and study the interactions polyelectrolyte - compensating ions. The study of charged macromolecules, which is related to its compensating ions in a polar solvent, with or without addition of salts, is very complex. Indeed, this study is influenced by many factors such as the asymmetry between small compensating ions and the large chains of the

polyion, the different conformations that the polymer can acquire and the intra-molecular and intermolecular interactions, including small ions and the solvent molecules [10].

The most appropriate model for this kind of studies is the linear model. When the Debye length (κ^{-1}) is sufficiently large compared with the average distance between two consecutive charges (b), the molecule becomes locally rigid, justifying a cylinder model as proposed by Katchalsky [8]. In this model, the effects of the end of the chains are neglected (experimentally, it was shown that it is necessary that the chain contains more than 15 or 20 ionic groups); it only imposes the radial variation of the electrostatic potential. It is assumed that the charges are uniformly distributed on the surface of the cylinder, or infinite long charged line, giving a constant charge density.

Three main theoretical approaches describe the distribution of compensating ions in polyelectrolyte solutions.

2.1.1.2.1. Oosawa's model

Oosawa's model is the simplest theoretical approach for polyelectrolytes. This model is composed by two phases separated by a potential difference $\delta\psi$, the macromolecular phase is characterized by its radius "a_0" and it's volume $V=\pi a_0^2 h$ containing the chain and condensed counterions. In the second phase, which volume equals to $\pi h(R^2-a_0^2)$, the ions are free. The cylinder of the molecule with radius "a_0" is placed inside this cylindrical coaxial cell, electrically neutral, with the same length "h" and radius "R_a" [11].

For the monovalent ions, the activity coefficient of the counterions (γ_a) is given by:

$$\ln(\frac{1-g_a}{g_a}) = \ln(\frac{j}{1-j}) + a_i / \ln(\frac{1}{j})$$

(2.7)

where φ is the volume fraction (*Equation 2.8*) occupied by the polyelectrolyte and α_i is the ionization degree.

$$\varphi = a_0^2/R_a^2$$

(2.8)

For infinite dilutions ($\varphi \rightarrow 0$), the expression given by *Equation 2.7* present the following limits

$$0 < \lambda < 1 \quad ; \gamma_a \rightarrow 1$$

(2.9)

$$\lambda > 1 \quad ; \gamma_a \rightarrow 1/\lambda$$

(2.10)

As long as the average distance between two consecutive charges, b, is greater to the Bjerrum length, l_B, (*Equation 2.2*), if $\lambda < 1$, any counterion is in the macromolecular phase with radius "a".

However, if $\lambda > 1$, an average fraction of compensating ions $(1- \lambda^{-1})$ will be inside the apparent macromolecular phase, which will decrease the macromolecule charge. The calculation model can be expanded in the case of several species of compensating ions [12]. However, the comparison between experimental values obtained with this theoretical prediction is imprecise with respect to the estimation of "a_0" and consecutively φ.

2.1.1.2.2. Katchalsky's model [8]

This approach leads to solve the Poisson-Boltzmann equation [13-16] for cylindrical geometry and high electrostatic potential (i.e. no linearization). It takes into account of the concentration of polymer firstly in absence of external salt and describes the distribution of the electrostatic potential around the polyion, as shown in *Figure 2.2* [1]. In this model, it is possible calculating the electrostatic potential in the cell volume (with radius R_a) and particularly at the surface of the polyion, $\Psi_{(a)}$, being "a" the minimum radius of the approach distance.
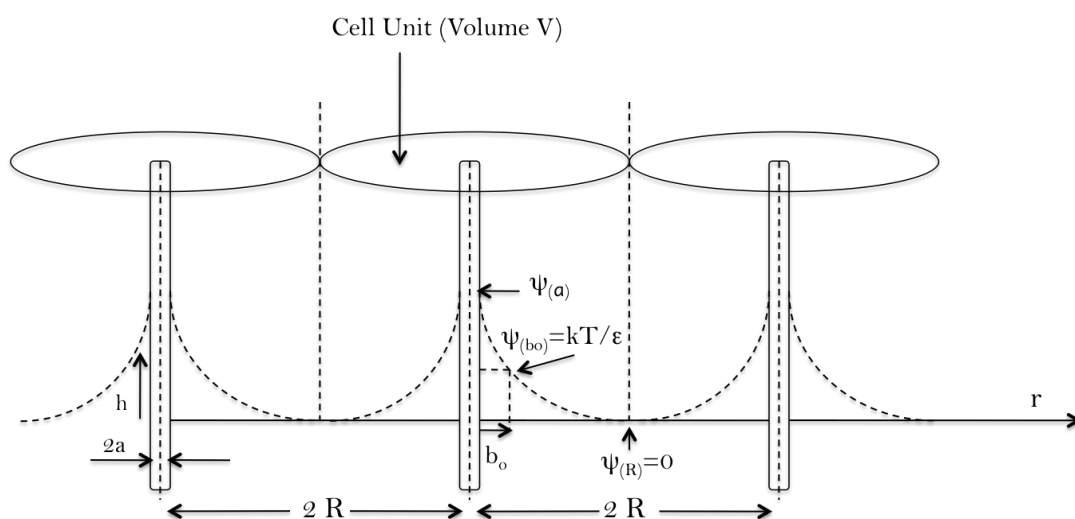
Figure 2.2. *Cell model proposed by Katchalsky et al. [1,17].*

In Katchalsky's model, the nature of the solvent is taken into account by using the dielectric constant and the compensating ions can't go through the cylindrical space with radius "a", defined as the minimum radius of approach (a$\leq$ r $\leq R_a$).

For monovalent counterions, the counterions distribution is imposed by $\Psi_{(r)}$ and the Poisson-Boltzmann equation is the following:

$$\nabla^2 \psi(r) = \frac{-4\rho r_o}{e} \exp(-e\psi/k_B T) \qquad r \geq a \qquad (2.11)$$

where ρ_o is the charge density corresponding to the condition $\psi = 0$, ε the dielectric constant, e the electron charge and $k_B T$ the Boltzmann term.

From the values of $\psi(r)$, *Lifson* and *Katchaslky* [8] calculated the electrostatic free energy and deduced the osmotic coefficient, ϕ, which in this case is equal to the activity coefficient, γ. In this manner, the following expressions were established for the monovalent counterions at infinite dilution:

$$\phi = \gamma_a = 1 - \lambda/2 \quad ; \quad \lambda < 1 \qquad (2.12)$$

$$\phi = \gamma_a = 1/2 \qquad ; \quad \lambda = 1 \qquad (2.13)$$

$$\phi = \gamma_a = 1/2\,\lambda \qquad ; \quad \lambda > 1 \qquad (2.14)$$

In addition, $\psi(r=a)$ allows determining the pKa variation of the ionic sites as a function of their dissociation by potentiometric titration.

2.1.1.2.3. Manning's model [18]

Manning's approach allows obtaining simple analytical expressions for electrostatic parameters and in a great range of conditions. The polyelectrolyte is considered as a uniformly charged wire, with infinite length and for infinite dilution. A critical value of the charge parameter is defined as $\lambda_{eff} = 1$ and corresponds to the value when a fraction of monovalent ions are "condensed".

This model allows a potential calculation of the Debye Hückel type, with a linearization of the potential when λ is ≤ 1. If $\lambda \geq 1$, a fraction $(1-1/\lambda)$ of the compensating ions is condensed along the chain, so $\lambda_{eff} = 1$. The other fraction, $1/\lambda$, of the counterions is distributed to the residual potential of the polyelectrolyte with the linearized Debye-Hückel potential.

At infinite dilution, the following predictions are proposed:

For movalent ions	*For divalent ions*
For $\lambda < 1$ $\qquad \phi = 1 - \lambda/2$ $\qquad \ln \gamma_a = -\lambda/2$	For $\lambda < 0.5$ $\qquad \phi = 1 - \lambda$ $\qquad \ln \gamma_a = -\lambda$
For $\lambda > 1$ $\qquad \phi = \frac{1}{2}\,\lambda$ $\qquad \gamma_a = 1.21\,\phi$ $\qquad f = 0.87\,\lambda^{-1}$	For $\lambda > 0.5$ $\qquad \phi = \frac{1}{4}\,\lambda$ $\qquad \ln \gamma_a = -\frac{1}{2} - \ln 2\,\lambda$ $\qquad f = 0.435\,\lambda^{-1}$

With this model it is possible to determine the characteristic parameters of the polyelectrolytes, such as the osmotic coefficient, ϕ, by osmotic pressure, the activity coefficient of the counterions, γ_a, by potentiometry and the transport coefficient, f, by conductivity.

2.1.2. Properties of polyelectrolytes

The properties of polyelectrolytes in solutions and at charged surfaces depend on the fraction of dissociated ionic groups, solvent quality for polymer backbone, dielectric constant of the solvent, salt concentration, and electrostatic interactions.

2.1.2.1. Conformation in diluted solution

In a diluted solution of a polyelectrolyte in water, the electrostatic interactions are important, as it is shown in *Figure 2.3.*
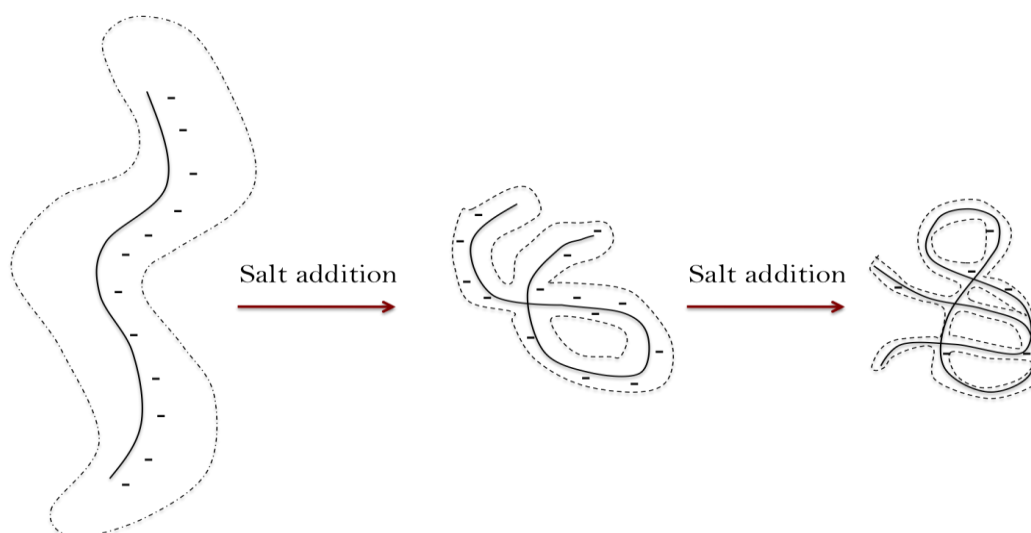
Figure 2.3. *Influence of the addition of salt, or a dilution (since the polyelectrolyte is an electrolyte) on the conformation of a polyelectrolyte [1].*

The electrostatic interchains and intrachains interactions have to be considered in the study of polyelectrolytes in diluted solutions [1]. Interchain electrostatic interactions, also known as long-range electrostatic interactions, are effective over a distance larger than the Debye length, and lead to structuring the solution. The electrostatic repulsions are screened in the presence of a simple electrolyte allowing studying isolated polyelectrolytes by using conventional polymers techniques as viscosity, light scattering, among others. On the other side, remaining intrachain electrostatic interactions correspond to interactions between charged neighbor sites on the same chain. These interactions lead to a moderate extension of the chain in presence of simple electrolyte at a low concentration. Therefore,

the dimensions of the chains depend on the ionic concentration of the solution. In large excess of external salt, the dimensions tend to the unperturbed conditions and the behavior looks like that of an uncharged polymer.

2.1.2.2. Persistence length

The persistence length, l_p, is a measure of the degree of structural stiffness of a polymer chain [19]. *Odijk* [20] and, independently, *Skolnick* and *Fixman* [21] studied the persistence length for polyelectrolytes, in particularly DNA. The persistence length measures the correlations along the polymer chain and represents the effective local stiffness of the polyelectrolyte as the sum of two contributions: the intrinsic persistence length, l_o, and the electrostatic persistence length, l_p, which depends in the ionic strength due to the ions concentration in the solution. This parameter can be calculated through the following equation:

$$l_p = l_o + l_e \tag{2.15}$$

Odijk proposed different possible scaling relations for semi-dilute polyeletrolyte solutions, in the presence of added salt and for salt-free polyelectrolyte solutions. He postulated several power laws for the correlation length, the radius of a single chain, scattering functions and osmotic pressure [20].

Therefore, Odijk's model makes possible to assess the electrostatic contribution, denoted as l_e, as follows:

$$l_e = \lambda^2 / (4 l_B \kappa^2) \; ; \; \lambda < 1 \tag{2.16}$$

$$l_e = 1 / (4 l_B \kappa^2) \; ; \; \lambda > 1 \text{ and } l_e \text{ (nm)} \sim 0.03 \, C_T^{-1} \tag{2.1}$$

Odijk [22] studied DNA as a wormlike chain of contour length L and persistence length l_p, bearing charges that interact via Debye-Hückel potential. The electrostatic persistence length for DNA molecule is given by *Equation 2.17*, which is correct only if the total persistence length is larger than the Debye length [23]. For ionic strengths lower than 0.1M NaCl, where it is necessary to neglect nonelectrostatic excluded-volume effects, he found a good agreement with the experiments of Harrington [24], who obtained the electrostatic persistence length of DNA as a function of ionic strength from intrinsic-viscosity and flow-birefringence data. In a separate treatment, *Reed et al.* [25] calculated the total persistence length and the radius of gyration for polyelectrolytes at different ionic concentrations and molar masses.

As well, many authors have extensively study the effect of electrostatics on the rigidity of the double helix of DNA and its persistence length in dependence of the ionic strength [19,22-24,]. DNA is one the stiffest polymers, with a persistence length of around 50 nm for a chain with 150 bp in 0.1 M aqueous NaCl [19]. *Maret et al.* [27] reported an ionic-strength dependence of DNA persistence length through magnetic birefringence experiments for DNA concentrations as low as 80 μg/mL and NaCl concentrations between 2.5 x 10^{-4} M and 2 M. They reported an intrinsic persistence length equal to 67 nm that is in relatively good agreement with the theoretical predictions of *Odijk* [22] and *Skolnick* and *Fixman* [21], when the counterion condensation is included following the concept of Manning. In salt excess, the unperturbed dimension of the gyration radius, $<S^2>$ allows determining the intrinsic persistence length from the Benoit-Doty relationship in the limit of large MW (*Equation 2.18*) [28].

$$<S^2_\theta> = l_p l_0 / 3 \tag{2.18}$$

2.1.3. Polymer characterization: relation [η](M)

Viscometry is a characterization method directly related to the hydrodynamic properties of macromolecules in solution, which depend of their molecular weight and the dimensions of the chains. In this way, it is possible to characterize the viscosity, η, of a polymer solution with a concentration C in a solvent with viscosity $η_s$, and to determine the intrinsic viscosity [η] of the polymer.

From viscosity measurements, it is possible to calculate the following parameters:

Relative viscosity:

$$h_{rel} = \frac{h}{h_s} \tag{2.19}$$

Specific viscosity:

$$h_{sp} = \frac{h - h_s}{h_s} \tag{2.20}$$

Reduced viscosity:

$$h_{red} = \frac{h_{sp}}{C} \tag{2.21}$$

Intrinsic viscosity:

$$[h](mL / g) = \lim_{C \to 0} h_{red} \tag{2.22}$$

where η_s is the solvent viscosity, η is the solution viscosity and C is the polymer concentration in g/mL.

According to the theory of macromolecule solution, the viscosity is given by the Huggins equation (*Equation 2.23*).

$$\frac{\eta_{sp}}{C} = [\eta] + K_H [\eta]^2 C \tag{2.23}$$

The intrinsic viscosity may also be obtained using the Kramer relation as follows:

$$\frac{\ln \eta_{rel}}{C} = [\eta] + K_K [\eta]^2 C \tag{2.24}$$

where K_H and K_K correspond to the Huggins and the Kraemer coefficients ($K_K + K_H = 0.5$). The Huggins constant depends of the solute-solvent given system and is most probably the same for several members of a polymer-homologous series [29, 30]. The intrinsic viscosity $[\eta]$ leads to the effective hydrodynamic volume of polymers in solution, which depend on the size and the shape of the molecule, influenced by polymer-solvent interactions.

For polyelectrolyte in salt excess ($C_s > 5 \times 10^{-2}$ M in NaCl), the intrinsic viscosity is also obtained by linear extrapolation of the reduced viscosity. The value of $[\eta]$ slightly decreases when the external salt concentration increases going to the unperturbed value obtained in a first approximation by extrapolation to infinite salt concentration. At low ionic concentration ($C_T < 10^{-3}$ M NaCl), the reduced viscosity varies strongly with polymer dilution, corresponding to an increase of the Debye length and consequently of the interchain electrostatic interactions (electroviscous effect).

The hydrodynamic and conformational properties of biological macromolecules such as DNA, proteins and polysaccharides have been widely studied by different groups [29, 31-33]. Intrinsic viscosity, which is a measure of the solute contribution to the viscosity of a solution, has been studied for linear and double-stranded DNA. Through intrinsic viscosity values it is possible to access to the molecular weight of the studied DNA by using the Mark-Houwink relation (*Equation 2.25*) [29].

$$[\eta] = K' M^a \tag{2.25}$$

where M is the molecular weight and α and K are the Mark-Houwink parameters, which depend on the particular polymer-solvent system and the particular temperature.

Tsortos et al. measured the intrinsic viscosity of small synthetic DNA molecules, with a number of pair bases between 20 and 395 and molecular weights between 1×10^4 and 2.4×10^5 [29]. They incorporated their results with the information reported in the literature for DNA molecules with

different molecular weights [34,35]. *Table 2.1* summarizes several Mark-Houwink type equations for double-stranded DNA molecules with different molecular weights.

Table 2.1.- *Mark-Houwink type equations for double-stranded DNA molecules [29].*

Equation ([η] in mL/g)	Molecular weight range
$[\eta] = 1.05 \times 10^{-5} M^{1.32}$	$3 \times 10^5 < M < 2 \times 10^6$
$[\eta] = 6.9 \times 10^{-2} M^{0.70}$	$2 \times 10^6 < M < 1.3 \times 10^8$
$[\eta] = 1.371 \times 10^{-1} M^{0.665} - 5$	$3 \times 10^5 £ M £ 1.3 \times 10^8$
$[\eta] = (3.5 \pm 0.6) \times 10^{-4} M^{1.05 \pm 0.01}$	$7 \times 10^3 £ M £ 2 \times 10^6$
$[\eta] = (8.0 \pm 0.7) \times 10^{-2} M^{0.69 \pm 0.005}$	$2 \times 10^6 £ M £ 8 \times 10^{10}$

2.1.4. Polymer chain dimensions and their viscoelastic properties

The size of the random coil polymers depends on the solvent and the polymer concentration. As presented in *Chapter 1* of this thesis, there is an important distinction between dilute and semi-dilute polymers solutions. *P.G. de Gennes* [5] discussed the overlap threshold (C=C*), where to swollen polymer coils fill the space. This concentration is the crossover between the dilute regime and the semi-dilute regime (*Figure 1.6*). *Yamakawa* [36] stated that for dilute solutions in good solvents the coils are expanded by the excluded volume effect, therefore, dimensions of polymer chains might vary depending on the used solvent. Therefore, the effects of solvent and concentration on chain dimensions are reflected on the viscoelastic behavior of the solutions.

Graessley [37] discussed the influence of polymer concentration on the chain dimension (R^2, the mean-square end-to-end chain distance) in a good solvent. At concentrations lower than C*, $R^2(C)$ is independent from C and corresponds to the dilute regime (*Figure 2.4*). The overlap concentration is not precisely defined, but it was proposed to correspond to a concentration at which the average spacing is 2S(0), where S(0) is the radius of gyration at zero concentration (*Equation 2.26*), with $S^2=R^2/6$ for random coils.

$$C^* = \frac{6^{3/2} M}{8 N_A R^3(0)}$$

(2.26)

where N_A is Avogadro's number.

Considering Flory-Fox equation, with the Flory constant equal to 2.5×10^{23}, the previous equation may be written as:

$$C^* = 0.77/ [\eta] \tag{2.27}$$

In a first approximation, C^* may also be estimated as $C^* \sim [\eta]^{-1}$.
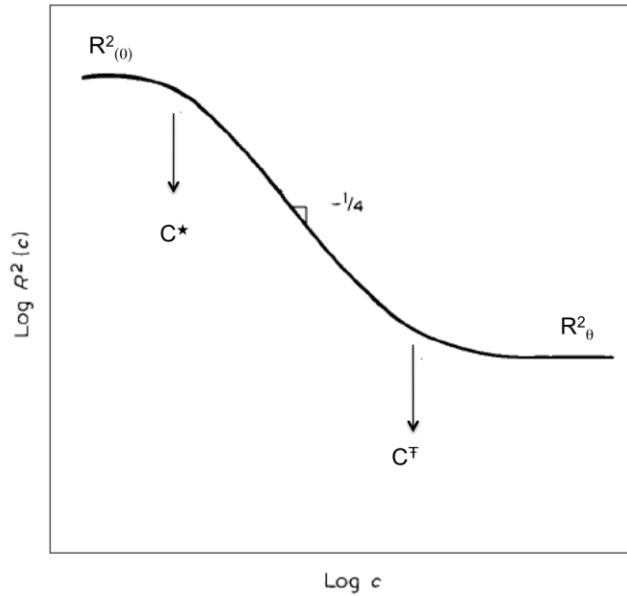
Figure 2.4. *Mean-average end-to-end distance R^2 as a function of polymer concentration [34].*

At concentrations higher than C^*, when C increases in the semi-dilute domain, the interactions between the neighbor molecules increase and the effect of the excluded volume of the molecule decreases due to the screening of the segments of the other molecules, so the dimensions decrease following a scaling relation:

$$R^2(c)= R^2(0) (C^*/C)^{1/4} \tag{2.28}$$

A second characteristic concentration was introduced by *Graessley* as C^{**} and indicates the transition between the semi-dilute region and the concentrated region, corresponding to the region where chain dimensions become independent of the concentration and in the unperturbed state (R^2_θ). He calculated C^{**} from the previous relation as:

$$C^{**}= C^*(R^2(0)/ R^2_\theta)^4 \tag{2.29}$$

$$\text{or } C^{**}= C^*([\alpha(0)]^8 \tag{2.30}$$

where $\alpha(0)$ is the expansion ratio of the chains at infinite dilution.

Graessley also introduced a concentration-polymer molecular weight diagram of viscoelastic regimes in a good solvent (*Figure 2.5*). In this diagram, he identified entangled and non-entangled semi-

dilute and concentrated regimes to analyse viscoelastic properties. Considering the molecular weight M_c for chain entanglement in undiluted state, the viscosity behavior can distinguish two C–M regimes:

$$C\,M < \rho M_c \quad \text{(not entangled)} \tag{2.31}$$

$$C\,M > \rho M_c \quad \text{(entangled)} \tag{2.32}$$
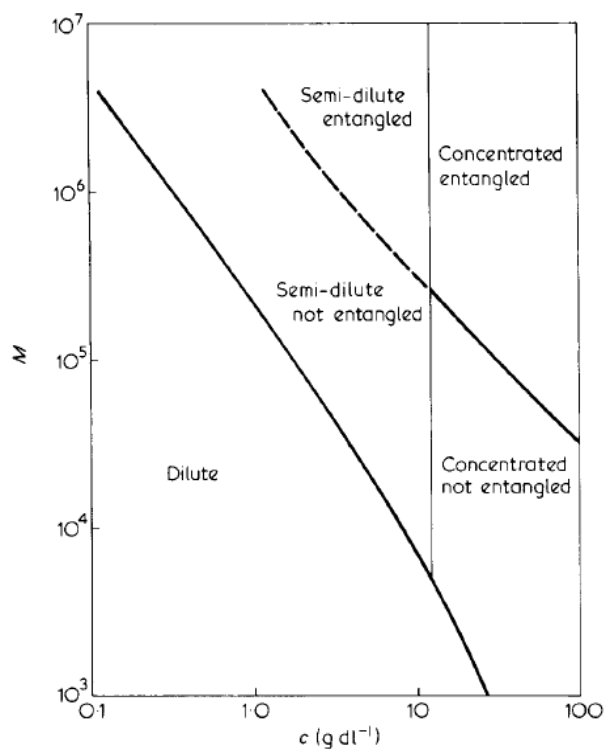
Figure 2.5. *Concentration-molecular weight diagram of viscoelastic regimes for polystyrene in a good solvent [37].*

2.2. Overview of the techniques

2.2.1. Viscosity measurements

The main methods to measure the viscosity are flow measurements in a single capillary, but in which the shear rate is not constant, or to shear experiments between two coaxial cylinders, for which the gradient is precisely defined and where the imposed stress can also be sinusoidal for measuring the dynamic viscosity.

2.2.1.1. Capillary viscometry

In capillary measurements, the studied fluid flows through a narrow tube as a result of hydrostatic or applied pressure. Inside the capillary viscometers, the velocity drop required for viscosity measurement is built up in the form of a laminar tube flow. The liquid flows in coaxial layers towards

the pressure drop through the capillary and a parabolic velocity flow occurs (*Figure 2.6*). The shear rate is null in the axis of the tube and maximum on the wall. These measurements are considered the most precise way of determining the viscosity of Newtonian and some Non-Newtonian viscous fluids and to get their intrinsic viscosity. Ubbelohde type viscometers or suspended-level viscometers use a capillary-based method of measuring viscosity. Poiseuille's law (*Equation 2.33*) is the basis for the capillary method and relates the rate of flow through a capillary to the viscosity of the liquid [38].

$$\frac{dV}{dt} = v\rho R^2 = \frac{\rho R^4}{8h}\left(\frac{-DP}{Dx}\right) = \frac{\rho R^4}{8h}\frac{|DP|}{L} \tag{2.33}$$

where t is the time that takes a volume V to flow. The ratio $\dfrac{dV}{dt}$ depends on the capillary radius, R, on the average applied pressure, P (*Equation 2.34*), on its length, L and the dynamic viscosity η. In this case:

$$DP = rgDH \tag{2.34}$$

where ρ is the density of the liquid, g the gravity and H is the average high of the liquid.

The relative viscosity is the given by the following expression:

$$h_{rel} = \frac{h}{h_s} = \frac{tr}{t_s r_s} \tag{2.35}$$

where t_s and ρ correspond to the flow time and the density of the solvent, respectively.

Then, the specific viscosity for dilute solutions is calculated as follows:

$$h_{sp} = h_{rel} - 1 = \frac{t - t_s}{t_s} \tag{2.36}$$
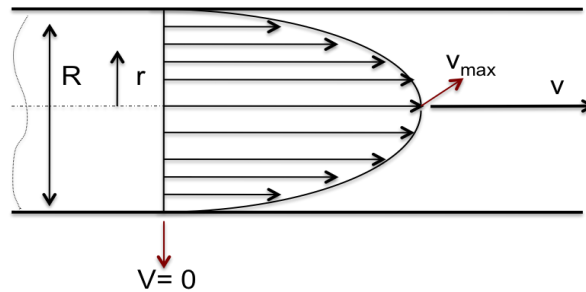
Figure 2.6. *Velocity profile with laminar tube flow.*

The Ubbelohde viscometer is related to the Ostwald viscometer since they are both made of glassware with a U shape, having a reservoir on one tube and a measuring bulb on the other tube. The studied liquid is introduced into the reservoir of the first tube and the sucked through the capillary in the other tube. This way, the liquid flows back through the measuring bulb and the measure of the time that the liquid takes to pass through two calibrated marks (A, B) is then related to the viscosity. The Ubbelohde device has a third glass arm at the end of the capillary and is open to the atmosphere, so the pressure head only depends on a fixed height and not on the total volume of the liquid (*Figure 2.7*).
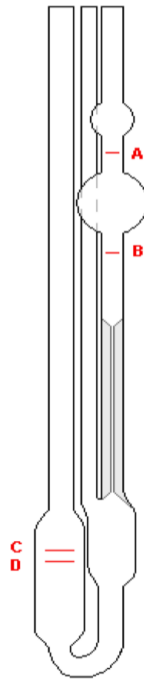
Figure 2.7. *Ubbelohde viscometer [39].*

2.2.1.2. Viscoelaticity by rheometry

Rheology focuses on the study of the relation between stress and strain that take place in materials subject to stress fields. The ability of a material to store strain energy is known as elasticity and can be considered as the capacity that this material has to return into its original shape after being deformed. On the other side, viscosity is a measure of the material's ability to resist the flow and reflects how the material can dissipate energy deformation through flow. The material may respond to the applied force with an elastic or viscous behavior, or usually a combination of both, which is called a viscoelastic behavior.

Two important laws describe the behavior of ideal solids and fluids: Hooke's law and Newton's law.

In 1678, Robert Hooke developed his "True Theory of Elasticity". He proposed that "the power of any spring is in the same proportion with the tension thereof". Hooke's law describes the behavior of an ideal elastic solid subject to an applied strain. This law states that if some strain is applied to a solid, the obtained stress (σ) in the material is directly proportional to the strain (γ):

$$\sigma = G\gamma \tag{2.37}$$

where G is the proportionality constant, also known as the rigidity modulus [40]. This modulus is a measure of the stiffness or the material's ability to resist any stress. The region where the modulus remains constant while the stress changes is called linear region, also referred as the Hookean area of the material.

Newton's law describes the behavior of an ideal viscous fluid. This states that the applied stress is proportional to the rate of shear strain, $\dot{\gamma}$, of the material (*Equation 2.38*).

$$\sigma = \eta\dot{\gamma} \tag{2.38}$$

where η is the proportionality constant called shear viscosity, which can be interpreted as the resistance of a fluid to move when it is subjected to stress. A fluid is considered as Newtonian if its viscosity doesn't depend on the shear rate.

From energy considerations, the elastic behavior represents complete recovery of energy expended during deformation, while the viscous flow represents a complete loss of energy as all the energy supplied during deformation is dissipated as heat. Most polymer solutions exhibit non-Newtonian behavior since their viscosities decrease with increasing shear rate. This behavior is called a pseudoplastic behavior [41]. A large number of the materials (from which polymers) have characteristics intermediate between elastic solids and viscous fluids, which are known as viscoelastic materials. Different geometries have been developed in order to determine the flow and viscoelastic properties of polymers. In this thesis, the studied liquid is trapped between a plate and a cone with radius R, whose axis is perpendicular to the plane of the plate and the truncated apex is located on the tray (*Figure 2.8*).
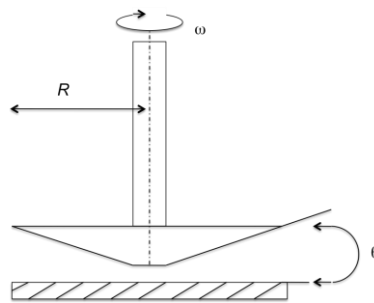
Figure 2.8. *Cone plane schema*

2.2.1.2.1. Dynamic measurements

Through dynamic measurements it is possible to determine the viscoelastic properties of the solutions. These measurements are performed applying a small sinusoidal strain (or stress) and measuring the resulting stress (or strain). The maximum amplitude of the strain and the stress, and the phase shift allow obtaining the complex modulus known as G(ω), (*Equation 2.39*).

$$G(w) = G'(w) + jG''(w) \tag{2.39}$$

The frequency dependent functions G'(ω) and G''(ω) correspond to the shear elastic modulus (or storage modulus) and to the shear viscous modulus (or loss modulus), respectively. G' is a measure of the stored energy and then released per cycle of deformation and G'' is a measure of the dissipated energy as heat per cycle of deformation per unit volume.

For a perfect elastic solid, G'(ω)=G and G''(ω)=0. Whereas for a viscous liquid, G'(ω)=0 and G''(ω)=ηω.

The loss tangent is another dynamic viscoelastic characteristic that links the relative effects of viscous and elastic components in a viscoelastic behavior (*Equation 2.40*).

$$\tan \delta(w) = G''/G' \tag{2.40}$$

Sometimes, the complex modulus |G*|, given by *Equation 2.41*, is also used to describe dynamic measurements.

$$\left|G*\right| = \sqrt{G'^2 + G''^2} \tag{2.41}$$

It is worth mentioning that polymeric fluids have memory, which means that when a force that forces them to flow is removed, the fluid tends to "go back" to its original position, nevertheless, it doesn't return completely. This is caused since a part of the fluid tends to be permanently deformed, but it has also an elastic portion that tends to recover its original shape. Maxwell equation includes viscous and elastic properties from Newton and Hooke laws, respectively, for gases that exhibit this behavior (*Equation 2.42* and *2.43*). However, actually this equation is used to successfully predict the behavior of a viscoelastic fluid with a single relaxation time.

$$G'(w) = G_p \frac{w^2 t_R^2}{1 + w^2 t_R^2} \tag{2.42}$$

$$G''(w) = G_p \frac{w t_R}{1 + w^2 t_R^2} \tag{2.43}$$

where G_p is the plateau modulus and τ_R the relaxation time.

2.2.1.2.2. Flow measurements

The rheological properties of materials at large strains are obtained through nonlinear measurements. Such experiments provide information on the rheological behavior of materials as they flow, either because shear or pressure gradients. In some cases, the structure of the materials is destroyed and other cases new structures are generated. A comparison between the obtained results from linear and nonlinear experiments can provide valuable information on the extent and type of structure that the material possesses.
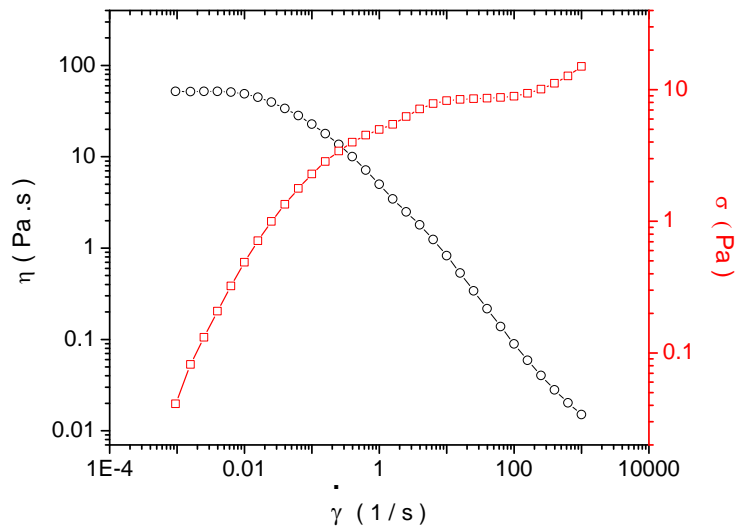
Figure 2.9. *Influence of shear rate on the viscosity (circles) and shear stress (squares) of a DNA concentration of 7.0 mg/mL at a temperature of 20 °C.*

Flow measurements can be performed in steady state or transient state. Steady state flow measurements provide information about shear stress (σ) and viscosity (η) of the polymer solution as a function of shear rate ($\dot{\gamma}$), as shown in *Figure 2.9* for a DNA solution, which behavior will be discussed in the experimental section.

2.2.1.2.3. Cox-Merz rule

The Cox-Merz rule is an empirical relationship in which a correspondence is observed between the steady state shear viscosity, η, plotted against shear rate, $\dot{g}$, and the magnitude of the complex viscosity, $|\eta^*|$, plotted against angular frequency, ω. The complex viscosity is defined by $\eta^*=G^*/j\omega$.

The Cox-Merz rule has been found to be applicable for many polymer melts and concentrated and semi-dilute solutions. However, some deviations from the rule occur at high frequencies, and the oscillatory data can either over or under estimate the steady state data. Some polymeric systems for which Cox-Merz rule do not apply are dilute solutions, cross-linked or gelled systems and most particulate dispersions.

2.3. Experimental conditions

2.3.1. Reagents

DNA/Buffer solutions were prepared from samples of calf thymus DNA with 13,000 base pairs (bp). Trizma, $C_4H_{12}ClNO_3$, (Tris-HCl) was used with a purity of 99.0%. This solution has a pKa of 8.06 and provides effective buffering capacity in a pH range between 7.0 and 9.2. Ethylenediaminetetraacetic acid (EDTA), $C_{10}H_{16}N_2O_8$, was also used with a purity of 99.0%. A solution of sodium hydroxide, NaOH, 3M was used for buffer solution elaboration. All solutions and dilutions were made with HPLC grade water. Sigma-Aldrich Company supplied all reagents.

2.3.2. Buffer Tris-HCl/EDTA preparation

A buffer solution was prepared in order to obtain and maintain a pH of 7.3. Appropriated amounts of Tris-HCl, 100 mM and EDTA, 10 mM were used to prepare the solution. Subsequently, this solution was placed on a magnetic stirrer, the pH was checked (2.75) and then adjusted to a value of 7.3 by adding NaOH solution (3 M).

2.3.3. Preparation of DNA/Buffer solutions

DNA solutions were prepared using appropriate amounts of DNA and a 9:1 ratio of HPLC water and Tris-HCl/EDTA buffer for each concentration. The vials were closed and sealed with parafilm to prevent water evaporation and changes in the concentration. All solutions were stored in a refrigerator at a temperature of 4 °C in order to prevent degradation.

2.3.4. UV-Vis measurements

DNA melting temperatures (T_m) were measured by recording the absorbance A_{260} as a function of temperature (T) using a Cary 400 Scan UV-Vis Spectrophotometer. The T_m cell block contains six cells for samples and six cells for the solvent. We used quartz cuvettes for all measurements. The solvent cuvettes were filled with the Tris-HCl/EDTA buffer solution and were used as the blank. The controlled instrument can be programmed to increase and decrease temperature with variable increments. The temperature was raised at a rate of 1 °C/min, from 25 to 90 °C. Then the temperature was decrease from 90 to 25 °C at a rate of 5 °C/min.

2.3.5. Ubbelohde viscometer

Viscosity measurements of DNA solutions between 0.01 and 0.4 mg/mL were carried out with an Ubbelohde viscometer from Schott Instruments GmbH. The selected capillary is a No. 501 01 capillary with a diameter of 0.53 ± 0.01 mm and a constant K equal to 0.005.

2.3.6. Geometries for rheological measurements

The rheological behavior of DNA/Buffer system was studied in the rheometers DHR-3, AR-G2 and ARES-G2 from the TA Instruments Company. Four different geometries were used depending on DNA concentration and the experiment carried on.

1.- Steel cone with a 60 mm diameter and an angle of 2° was used for DNA solutions with concentrations between 0.01 mg/mL to 0.4 mg/mL (DHR-3 rheometer).

2.- Steel cone with a 60 mm diameter and an angle of 1° was used for DNA solutions with concentrations between 0.5 mg/mL to 2 mg/mL (AR-G2 rheometer).

3.- Steel cone with a 40 mm diameter and an angle of 2° was used for DNA solutions with concentrations between 2 mg/mL to 30 mg/mL (AR-G2 rheometer).

4.- Steel cone with a 49 mm diameter and an angle of 4.469° was used for DNA solutions with concentrations between 2 mg/mL to 10 mg/mL to perform visualizations (ARES-G2 rheometer).

2.3.7. Dynamic and flow measurements

2.3.7.1. Strain sweeps

In order to define the linear viscoelastic regimes, the oscillation strain sweeps were carried out at an angular frequency of 10 rad/s in strain range between 0.01% and 100% and using 10 points per decade. For each DNA sample, each sweep was performed at the following temperatures 10, 20, 30 and 40 ºC.

2.3.7.2. Frequency sweeps

Frequency sweeps were carried out at a selected strain in the linear viscoelastic region in a frequency range between 0.01 and 100 rad/s and using 5 points per decade. For each DNA sample, each sweep was performed at the following temperatures 10, 20, 30 and 40 ºC.

2.3.7.3. Steady state flow measurements

Simple steady state measurements were performed in a shear rate between 1×10^{-3} and 1000 1/s and using 5 points per decade. For each DNA sample, each sweep was performed at the following temperatures 10, 20, 30 and 40 ºC. The experimental conditions allow calculating the Reynolds number, limit of validity for laminar flow.

2.3.8. Visualizations

Shear instabilities during rheological measurements were studied with a visualization device of the strain field inside the sample [42,43]. The cone (49 mm diameter and 4.469º) was pierced at a distance of 3 mm from the edge. A preparation with a DNA solution, identical to the one tested was colored with a white powder (TiO_2). Once the studied DNA sample was placed between the tools, a small quantity of white colored DNA solution was injected with a syringe through the bulk of the sample, forming a vertical filament. *Figure 2.10* shows the schematic diagram of the setup for the rheological measurements combined with visualization of the strain field inside the sample.

The deformation of the colored filament can be monitored with a video camera since the plane begins to rotate. *Figure 2.11* shows the initial mark of DNA colored solution in the bulk of the sample, which deformation is recorded by the camera during the rotation of the plate, then the homogeneous deformation recorded under shear rate and finally, the representation of localization, recorded under shear rate variation. To avoid evaporation from the sample during the test, a transparent cover was placed around the geometry.
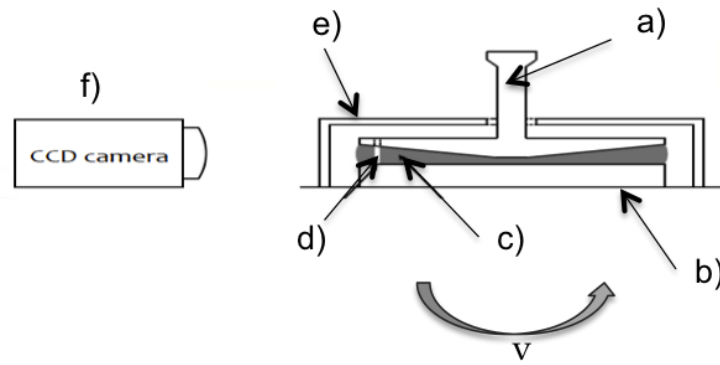
Figure 2.10. *Schematic diagram of the setup for the rheological measurements combined with visualization of the strain field inside the sample: a) truncated cone, b) plate, c) DNA solution, d) filament of DNA solution colored with TiO2, e) transparent cover to prevent water evaporation and f) CCD camera [42].*

FRONT VIEW
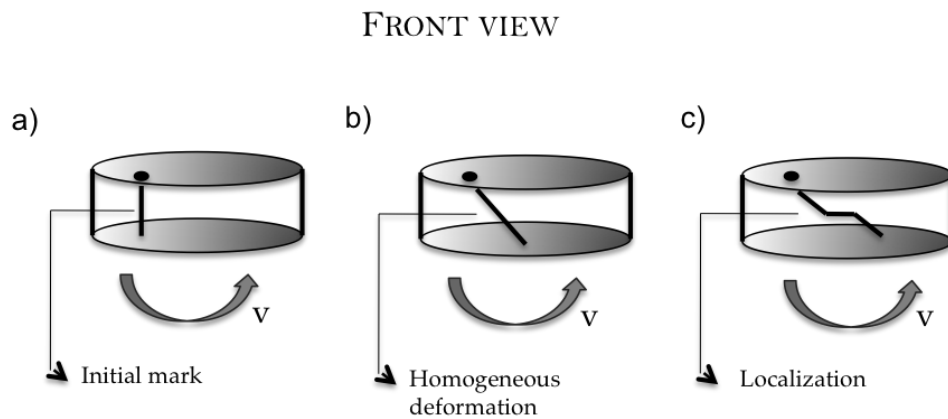
Figure 2.11 *a) Initial mark of DNA colored solution in the bulk of the sample, which deformation is recorded by the camera during the rotation of the plate. The angle of the camera is normal to the axis of the apparatus, b) homogeneous deformation recorded under shear rate and c) localization, also known as shear banding, recorded under shear rate variation [43].*

2.4. Experimental results and discussion

Calf-thymus DNA solutions in Tris-HCl/EDTA buffer (TE buffer) were firstly characterized by their polyelectrolytes properties in order to know DNA charge parameter and the contribution of the ionic strength of the buffer solution on DNA properties. DNA concentration and purity of the samples were validated through spectrophotometric measurements. Then, intrinsic viscosity was determined

through capillary and rheometry measurements to determine molecular weight. Finally, flow and viscoelastic properties were studied in a wide range of DNA concentrations and temperatures.

2.4.1. DNA charge parameter

DNA charge parameter plays an important role in thermodynamic properties of DNA solutions, i.e. the differences in Gibbs free energy, enthalpy and entropy between the coil and helix forms of DNA at any temperature and salt concentration. According to Manning's theory, only the non-condensed fraction of the compensating ions contributes to solution ionic strength and to the Debye length κ^{-1}. For DNA, the value of b_{helix} for the helical form is equal to 0.17 nm and the value of b_{coil} for the coil form is equal to 0.68 nm [44]. Considering that $\lambda = l_B/b$, as demonstrated before, then $\lambda_{helix} = 4.2$ and $\lambda_{coil} = 1.0$. It is worth to mention that λ is almost independent of temperature since for water, the product εT present only slightly variations with temperature.

Following the predictions proposed at infinite dilution, the subsequent parameters where calculated for each DNA form:

Double stranded DNA double-helix	Single stranded DNA
$\lambda_{helix} = 4.2$ For $\lambda > 1$ $\quad\quad \phi = 1/2\lambda = 0.12$ $\quad\quad \gamma_a = 1.21\ \phi = 0.14$ $\quad\quad f = 0.87\ \lambda^{-1} = 0.21$	$\lambda_{coil} = 1.0$ For $\lambda > 1$ $\quad\quad \phi = 1/2\lambda = 0.5$ $\quad\quad \gamma_a = 1.21\ \phi = 0.6$ $\quad\quad f = 0.87\ \lambda^{-1} = 0.87$

Therefore, according to the theory, the fraction 1-(1/4.2), equal to 0.76, corresponds to the phosphate groups neutralized by condensed counterions when DNA is in its double-helix form [44].

These values allow determining the contribution of DNA under Na salt form to the ionic concentration at a given weight concentration. Considering that the average molar mass of a nucleotide is equal to 379 g/mol, for a double stranded DNA weight concentration of 1 g/L, it comes that the effective ionic concentration is:

$C = (1/379) \times 0.12 = 3.17 \times 10^{-4}$ equiv/L

For a single stranded DNA weight concentration of 1 g/L, the effective ionic concentration is:

$C = (1/379) \times 0.5 = 13.19 \times 10^{-4}$ equiv/L

2.4.2. Ionic strength of TE buffer solution

TE buffer was selected since it is usually used in molecular biology, particularly in procedures concerning DNA or RNA. EDTA is used as a chelating agent of divalent counterion that can create metal complexes having an octahedral coordination structure. The ionic strength of TE buffer was determined through conductivity measurements, relating its conductivity to the concentration of a NaCl solution with the same conductivity. It was then determined that a corresponding NaCl concentration of 9.8 mM (very near to 10 mM, TrisHCl concentration) is equivalent to a conductivity of 1.64 mS measured for the TE buffer at a ratio 9:1 (Water: Buffer).

When DNA is solubilized in the buffer 9:1, the total ionic concentration for a DNA weight concentration of 1 g/L is:

$C_T = C_s + C = 10.32$ mM and the Debye length is $\kappa^{-1} \sim 2.95$ nm

These characteristics of DNA play an essential role on its conformation in solution as well as its contribution to conductivity, chain-chain interactions in concentrated solutions and on polycation associations.

2.4.3. Spectrophotometric measurement of DNA concentration and purity

DNA concentration of the studied samples was determined by measuring the absorbance at 260 nm (A_{260}), where DNA absorbs light most strongly, in a spectrophotometer [45]. The spectrophotometric conversions for one absorbance unit at 260 nm to concentration in µg/mL, depending on the nature of the chain, are presented in *Table 2.2*. Double-stranded DNA conversion was selected for our samples. It is worth to mention that these conversions are only valid for measurements performed at neutral pH.

Table 2.2.- *Spectrophotometric conversions for one A_{260} equals 1 unit to concentration [46]*

$A_{260} = 1$	Concentration (µg/mL)
Double-stranded DNA	50
Single-stranded DNA	33
RNA	40
Oligonucleotides	20-30

Absorbance measurements allow determining DNA concentration. In addition, DNA purity was evaluated by measuring the absorbance from 230 nm to 320 nm to detect other potential contaminants. The ratio A_{260}/A_{280} was found to be 1.87 ± 0.11, which is in good agreement with pure DNA ratio reported before (between 1.8 and 2.0) [47].

2.4.4. DNA melting temperature

2.4.4.1 DNA composition determination

Starting from the fact that DNA is a polyelectrolyte bearing a series of phosphate groups along its backbone and that it can exist in solution in its helical or randomly coiled form [44], it is important to determine the melting temperature, T_m, of DNA used at the specific conditions in this research. *Figure 2.12* shows the temperature dependence of the absorbance of calf-thymus DNA at a concentration of 0.042 mg/mL, from which is possible to identify the midpoint of the absorbance rise, corresponding to the T_m, at a temperature of 70 ± 0.6 °C.

Denaturing agents such as increase of temperature, increase or decrease of pH and decrease in Na^+ ion concentration, disrupt double helix DNA structure, unstuck the bases and produce the increase in absorbance [48]. The helix-coil transition is considered as the result of the tendency of the system to go from high-energy states to low-energy states and the tendency to go from low entropy states to high entropy states.
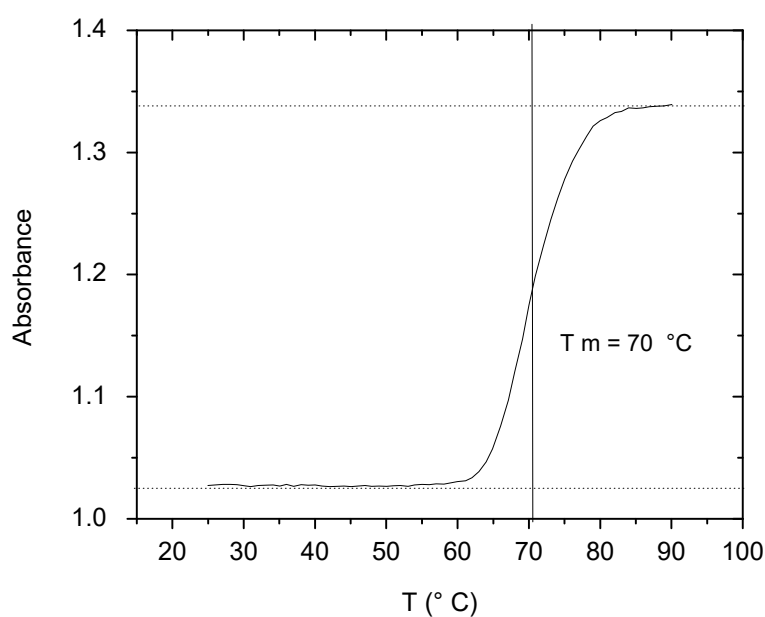
Figure 2.12. *Degree of denaturation at 260 nm of calf-thymus DNA (0.042 mg/mL) of in TE buffer at a pH of 7.3.*

According to the empirical relationship between T_m, G-C (Guanine-Cytosine) content and concentration of sodium ions in solution ([Na^+]) proposed by *Owen et al.* [49] it is possible to determinate the G-C content through *Equation 2.44*.

$$T_m = 176.0 - (2.60 - x_0)(36.0 - 7.04 \log[Na^+]) \qquad (2.44)$$

where x_0 corresponds to the fraction of G-C pairs in DNA.

In this manner, the calculated value for x_0 was found to be around 0.48, i.e. 48%, which is in good agreement with the reported G-C composition of preparations of Euchromatin DNA and Heterochromatin DNA from calf-thymus, determined by thin-layer chromatography, i.e. 44.5 ± 0.3% and 46.4 ± 0.5%, respectively, by *Gawrońska et al.* [50].

2.4.4.2. Influence of DNA and salt concentrations on the T_m

Salt concentration influence on melting temperature is presented on *Figure 2.13*. The temperature dependence of the absorbance of calf-thymus DNA at a concentration of 0.03 mg/mL was determined for a salt concentration range between 0 M and 3 x 10^{-2} M NaCl. Here it is possible to identify that DNA in water as a solvent, is partially denatured and that the addition of salt to the solution leads to an increase of DNA melting temperature, as expected. The observed decrease in T_m at low salt concentrations is caused by the increased electrostatic repulsion between the negative phosphate ions of DNA strands.
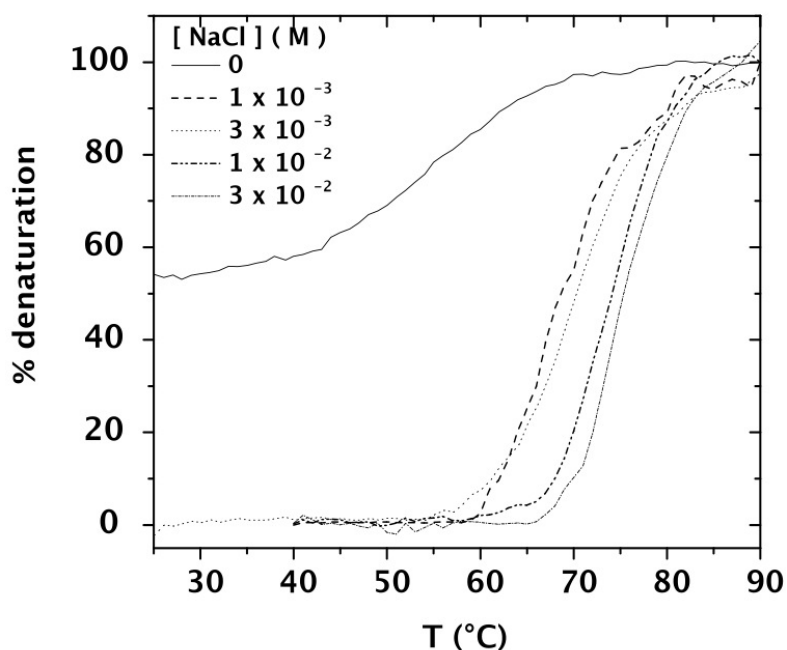
Figure 2.13. *Temperature dependence of the % denaturation of calf-thymus DNA 0.03 mg/mL at salt concentration between 0 M to 3x10⁻²M NaCl. The percent of denaturation is relative to the absorbancy at 25 °C.*

Figure 2.14 shows the variation of DNA melting temperature for different DNA and salt concentrations in a semi-log plot. A linear behavior is observed, as well as the T_m decrease at low salt

concentrations (as described before) and a slightly variation of T_m for different DNA concentrations at a same salt concentration [31].
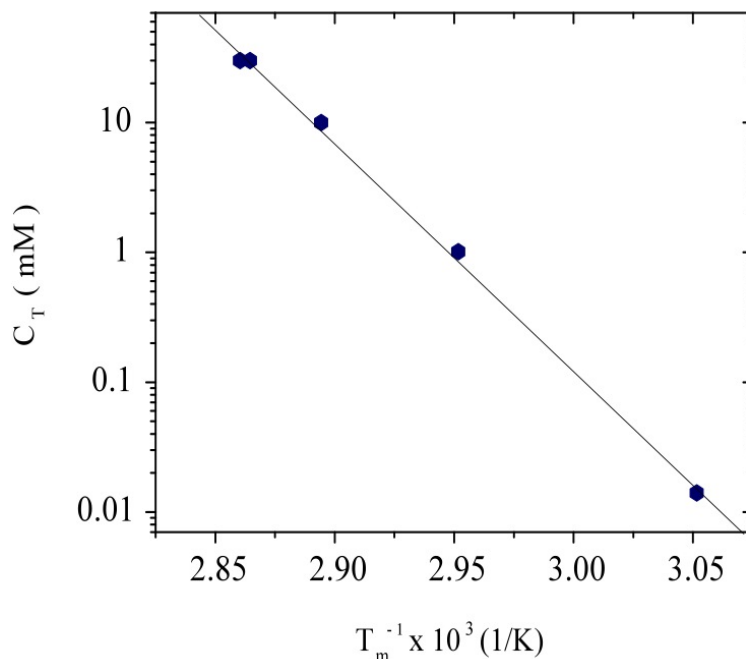
Figure 2.14. *Variation of the T_m with the salt concentration for different DNA concentrations.*

We can conclude that double helix DNA conformation is preserved in the TE buffer and in DNA solutions with salt concentrations higher than 10^{-3} M NaCl in the temperature range from 25 to 60 °C.

2.4.5. DNA intrinsic viscosity [η] and molecular weight determination

2.4.5.1. Capillary measurements in dilute solutions

Since DNA has one formal negative charge per nucleotide, the conformation of this molecule is certainly sensitive to changes in the ionic strength, in the amount of base pairs and in the molecular weight (in the low molecular weight domain). In this manner, the information about intrinsic viscosity of DNA in TE buffer solutions may lead to determine and understand the hydrodynamic and conformational properties of the molecule under specific conditions. At first instance, viscosity capillary measurements were performed in order to determine DNA intrinsic viscosity in TE buffer at a pH of 7.3 and at the temperatures of 10, 20, 30 and 40 °C. DNA dilutions were made by adding solvent of the same composition, i.e. TE buffer at a 9:1 ratio.

In order to remove the solvent contributions, the relative viscosity was calculated for each DNA concentration at each temperature by using *Equation 2.19*. As expected, DNA relative viscosity increases while increasing DNA concentration and, as we can observe, the temperature effect is negligible (*Figure 2.15*). All curves are nearly superposed. Specific and reduced viscosities were then calculated according the *Equations 2.20* and *2.21* in order to determinate DNA intrinsic viscosity at each temperature by extrapolation of the reduced viscosity to zero concentration.
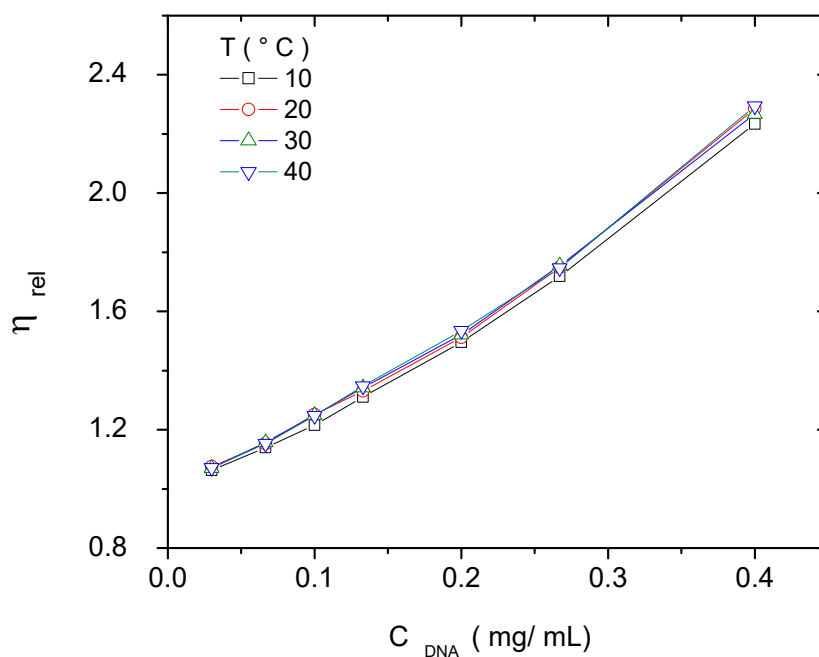
Figure 2.15. *Relative viscosity dependence with DNA concentration measured at several temperatures.*

The resulting values for the intrinsic viscosities are resumed in *Table 2.3*, but they are almost half of the expected values according to the Mark-Houwink type equation for double-stranded DNA (*Table 2.1*) reported by *Tsortos et al.* [29]. This is, for a reported average molecular weight for calf-thymus DNA, recently obtained by size-exclusion chromatography with dual low-angle light scattering/ refractometric detection, corresponding to 8 418 000 [51], the calculated intrinsic viscosity is equal to 4 858 mL/g. Therefore, we assume that the imposed shear rate in the capillary is too high to obtain the viscosity value equivalent to the zero shear viscosity of our DNA samples; for this reason, the intrinsic viscosities found are much lower than the expected. However, from these values it is possible to conclude that the hydrodynamic volume of DNA varies only slightly with temperature.

Table 2.3.- *Intrinsic viscosity determined through capillary measurements*

Temperature (ºC)	[η] (mL/g)
10	1975
20	2231
30	2245
40	2259

2.4.5.2. Cone-plate measurements in dilute solution

To allow getting the intrinsic viscosity at low shear rate, we selected the cone-plate rheometer. DNA shear viscosity was determined for a DNA concentration range between 0.010 and 0.367 mg/mL. A constant viscosity over a range of at least one decade of shear rate was obtained in order to determine with accuracy the zero shear viscosity of each sample tested. *Figure 2.16* shows the measured viscosities at a temperature of 20 ºC.
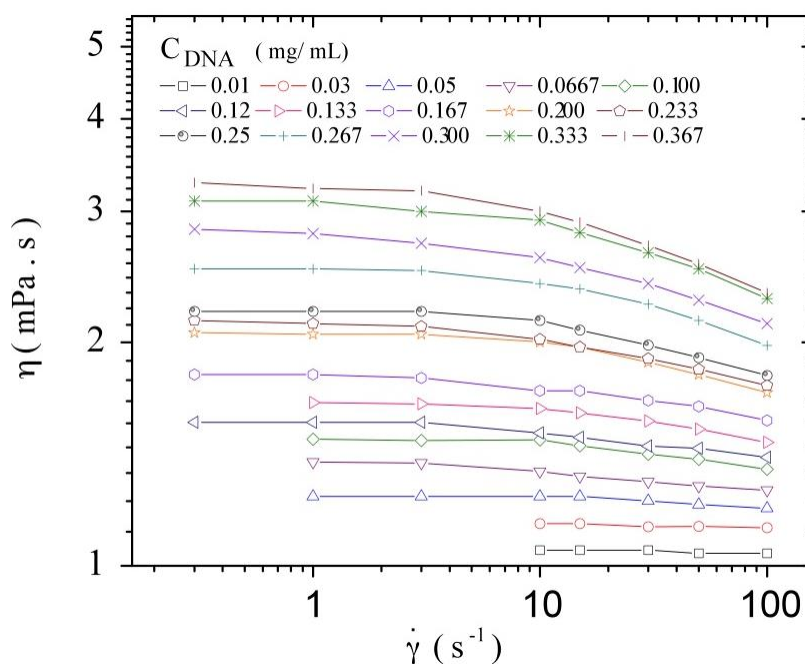
Figure 2.16. *Dependence of shear viscosity on shear rate for several DNA concentrations at 20 ºC.*

This figure shows the sensitivity of the solution viscosity with shear rate and justifies the low values obtained by capillary measurements. This viscosity dependence on shear rate can be treated with the Cross model, given by *Equation 2.45* [41].

$$\frac{h - h_{\text{¥}}}{h_0 - h_{\text{¥}}} = \frac{1}{1 + (K\dot{g})^m} \qquad (2.45)$$

where η_0 is the zero shear-rate viscosity from the Newtonian plateau, η_∞ is the infinite shear-rate viscosity, m is a dimensionless parameter related to the degree of shear thinning and K_c has the dimensions of time.

Reduced viscosities were calculated according *Equation 2.21* using the zero shear-rate viscosity from the Newtonian plateau and were plotted as a function of DNA concentration (*Figure 2.17*). A deviation from the linear behavior in the dilute regime, following Huggins relation, is clearly observed at the concentration of 0.23 mg/mL, which could be related to the overlap concentration of the system, C*. The entanglements in the semidilute regime make the system more complicated and lead to viscoelastic properties that need to be studied by shear flow and dynamic measurements [52]. The extrapolation to zero concentration gives the intrinsic viscosity, i.e. 4 850 mL/g, which is a closer value to the calculated intrinsic viscosity from the Mark-Houwink theoretical equation [29].
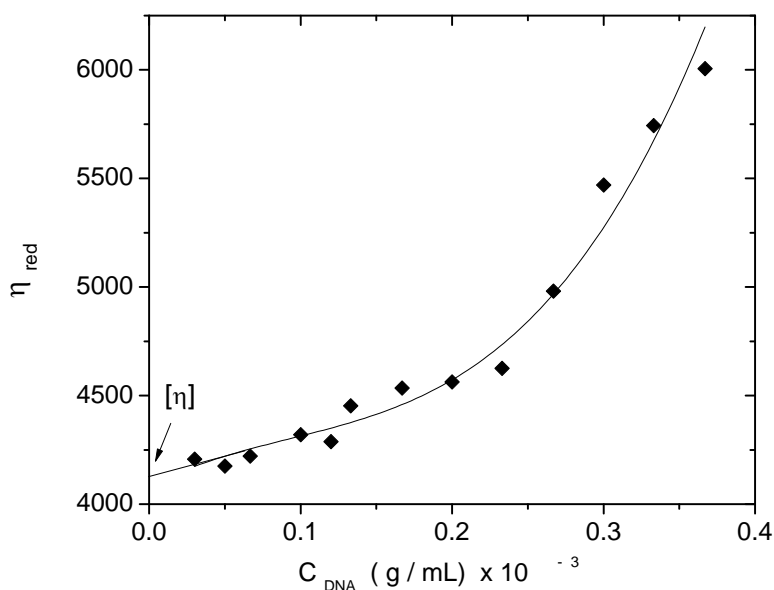
Figure 2.17. *η_{red} dependence with DNA concentration at a temperature of 20 ℃. The solid line represents only a visual aid.*

The viscosimetric average molecular weight of our DNA sample can be estimated using the Mark-Houwink relation (*Equation 2.26*), taking α as 0.69 for high molecular DNA chains and K as 6.9 x 10^{-4} [29]. Therefore, the molecular weight is equal to 6 559 500, between 6 000 000 and 8 000 000 (ultrahigh molecular weight range), in good agreement with the literature [51]. The obtained value for the Huggins constant, K_H, equals to 0.15, although is considerably low, is also in fairly agreement with values previously reported by *Tsortos et. al* [29] for different molecular weight DNA.

As discussed previously, $<S^2>$ and $[\eta]$ are two useful characteristics of polymers in dilute solution, i.e. where the concentration is lower than C*. This critical concentration can be estimated as a first approach by using the relation C*~ $[\eta]^{-1}$. In this manner, the calculated value for C* is equal to 0.245 mg/mL, which corresponds to the observed deviation point from the linear dependence of the reduced viscosity with DNA concentration (*Figure 2.17*). The first estimation of the radius of gyration may be calculated using C* according to *Equation 2.46* [52].

$$C^* = \left[\frac{\frac{4}{3} \rho \langle S \rangle^3 N_A}{M} \right]^{-1} \tag{2.46}$$

It comes that S^2 is equal to 237 nm, the average radius of gyration in TE buffer.

2.4.6. Rheological behavior as a function of DNA concentration and temperature

Taking into account the obtained results on DNA conformation in the buffer solution used in all the rheological study, as well as its stability upon temperature in the range covered (10 to 40°C) and the reduced viscosity that is nearly independent on the temperature; in the treatment of our experimental data, we adopted the value of the intrinsic viscosity determined at 20 °C for all the temperatures, as well as for the establishment of the master curves. In addition, the influence of ionic concentration may be considered as the increase in DNA concentration means also an increase of the total ionic concentration. At 1 mg/mL, $\kappa^{-1} \approx 2.95$ nm and for 10 mg/mL it comes that $\kappa^{-1} \approx 2.7$ nm, i.e. relatively small influence of the DNA concentration.

In order to describe the effects of DNA concentration on viscosity and to define the limits between the semi-dilute non entangled and entangled regimes of DNA/buffer solutions, we carried on flow and dynamic measurements. Both series of experiments were performed for a wide DNA concentration range in buffer 9:1 solution at the temperatures of 10, 20, 30 and 40 ºC. For dynamic experiments in the linear regime, we applied a strain of defined amplitude and frequency, from which it is possible to obtain the two components G'(ω) and G''(ω) and calculate the complex dynamic viscosity, given by *Equation 2.47*.

$$|\eta^*|(\omega) = (G'^2 + G''^2)^{1/2} \omega^{-1} \tag{2.47}$$

2.4.6.1. Steady state measurements

In the case of Newtonian fluids, the viscosity depends on temperature and pressure, however, for

polymeric fluids as DNA solutions, it also depends on shear rate, which is very sensitive to the molecular structure, as seen before. To complete our measurements, the influence of shear rate on the viscosity of DNA samples was studied in a large DNA concentration range at the temperatures of 10, 20, 30 and 40 ºC. Data obtained at a temperature of 20 ºC are presented in *Figure 2.18*. The observed flow curves are characterized by having three important characteristics: the viscosity η_0, in the Newtonian plateau, the critical shear rate $\dot{g}_c$ and the slope, *s* [52-54]. The critical shear rate is related to the characteristic time when the shear rate becomes lower than the relaxation time of DNA in solution, leading to the manifestation of structural changes such disentanglements, alignments of the molecules in the flow, among others, or to conformational modifications of the molecule. The viscosity in the Newtonian plateau corresponds to the viscosity when $\dot{g} < \dot{g}_c$. It is possible to observe that $\dot{g}_c$ decreases with the increase of DNA concentration.
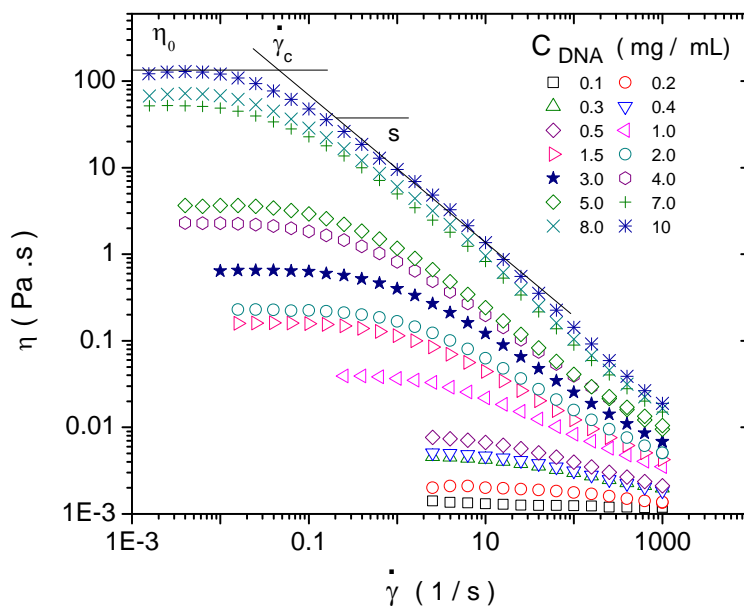
Figure 2.18. *Influence of shear rate on the viscosity of calf-thymus DNA at different DNA concentrations at a temperature of 20 ºC.*

Figure 2.19 shows the dependence of the specific viscosity on shear rate for a constant DNA concentration at the studied temperatures, i.e. 10, 20, 30 and 40 ºC. We can observe only very little influence of temperature on the rheological behavior of DNA solutions in the studied temperature range, i.e. low influence on the hydrodynamic volume of DNA (reflected by the intrinsic viscosity).
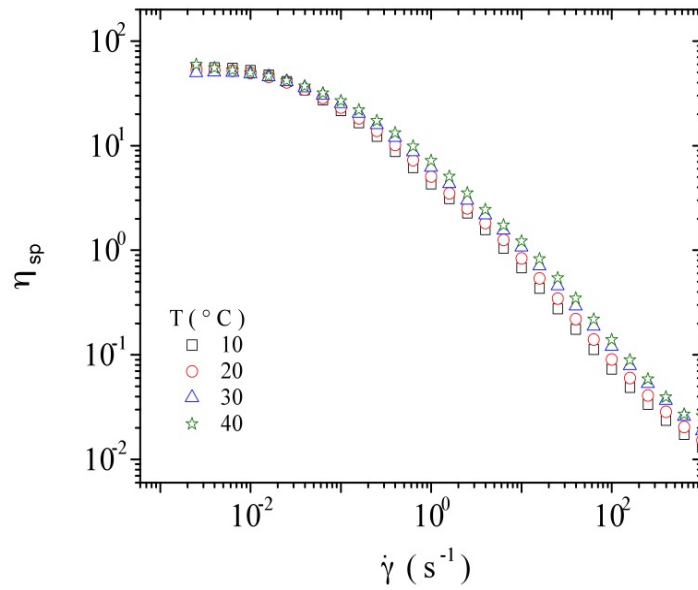
Figure 2.19. *Influence of shear rate on the specific viscosity of calf-thymus DNA at a concentration of 7 mg/mL at the temperatures of 10, 20, 30 and 40 ºC.*

By increasing DNA concentration it is possible to define the dilute, semi-dilute with entanglements and semi-dilute without entanglements regimes, delimited by the overlap concentration, C*, which first approach was given by C*~[η]$^{-1}$ and C**, also defined by *Mason et al.* [55] as the entanglement concentration, C_e, taking into account the references of *Raspaud et al.* [56].
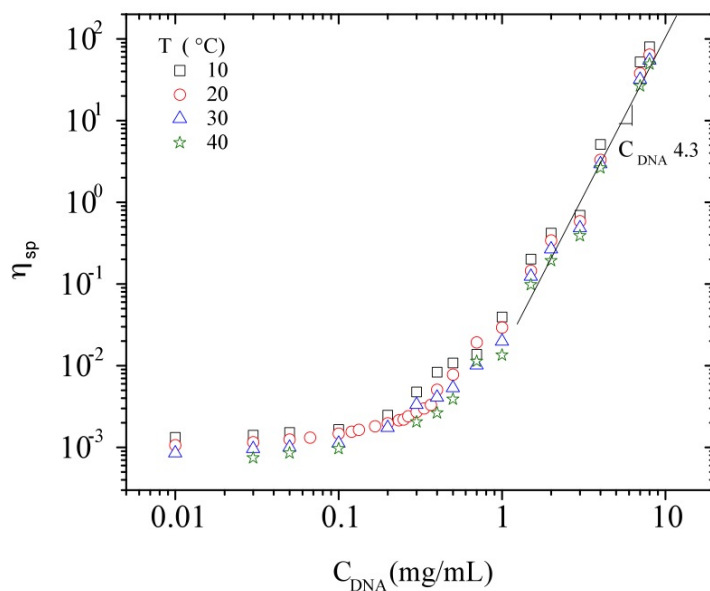
Figure 2.20. *Dependence of the specific viscosity, η_{sp}, at zero shear rate with DNA concentration at the temperatures for 10, 20, 30 and 40 ºC.*

DNA zero shear viscosity was firstly inspected in terms of the specific viscosity, η_{sp}, as a function of DNA concentration at the four studied temperatures (*Figure 2.20*). The obtained behavior in the DNA concentration range $2.0 < C_{DNA} < 10$ mg/mL was found to be consistent with previous results obtained for polymers dissolved in a good solvent [57]. The variation of η_{sp} with concentration, $\eta_{sp} \sim C_{DNA}$, was quantified with an average slope is equal to 4.2, i.e. $\eta_{sp} \sim C^{4.2}$. To analyse the data in terms of the overlap concentration the specific viscosity at zero shear rate was plotted in log-log as a function of $C_{DNA}[\eta]$ (*Figure 2.21*). This representation allows predicting the viscosity for different concentrations and molecular weights, as shown by *Berriaud et al.* [58], *Milas et al.* [59] and *Fouissac et al.* [60] for hyaluronans, a wormlike chain. $C^*[\eta] \approx 1$ can be identified and at larger concentration polymeric chains get progressively entangled. *Equation 2.48* can be used to estimate η_{sp} for a polymeric solution at a given concentration when the intrinsic viscosity is known. This equation was first used for hyaluronans with various molecular weights [61], from which it was possible to predict any viscosity of polymer solution by replacing $C[\eta]$ on the expression.

$$\eta_{sp} = C[\eta] + K_H(C[\eta])^2 + B(C[\eta])^n \tag{2.48}$$

where K_H is the Huggins constant and the values B and n are equal to 7.77×10^{-3} and 4.18, respectively.

Additionally, a new representation was proposed by *Cowman et al.* [62] (*Equation 2.49*), on the same hyaluronans [61,63] and now is tested successfully for calf-thymus DNA solutions at the DNA concentration range between 0.01 and 10 mg/mL, using a Huggins constant (identified as k_1) of 0.4, as found for perfectly soluble polymers.

$$\eta_{sp} = C[\eta]\left\{1 + k_1(C[\eta]) + k_2(C[\eta])^2 + k_3(C[\eta])^3\right\} \tag{2.49}$$

where the constant k_1, k_2 and k_3 can be calculated as follows:

$$k_1 = 0.4 \tag{2.50}$$

$$k_2 = (k_1)^2/2! = 0.08 \tag{2.51}$$

$$k_3 = (k_1)^3/3! = 7.1 \times 10^{-3} \tag{2.52}$$

For DNA at the highest concentrations, the concentration C^{**} is obtained when the linear behavior in this curve starts, also defined as the entanglement concentration, C_e. For the linear domain, the calculated slope is 4.3 ($\eta_{sp} \sim C^{4.3}$), which presents a slight deviation from the master curve having a maximum slope of 4. This kind of deviation was also detected for the reported experimental values for hyaluronan in 0.1N NaCl (with a slope of 4.18) and xanthan in 0.1 N NaCl (with a slope of 4.24) [64]. The limit for linear behavior in this curve is around $C[\eta] \sim 10$, the starting point of semi-diluted

entangled domain, i.e. 2.45 mg/mL for DNA. The obtained behavior in the DNA concentration range $2.0 < C_{DNA} < 10$ mg/mL was found to be consistent with previous results reported by Mason et al. obtained at 25°C [28]. The width of the semi-dilute domain (unentangled and entangled) is such as $C_e \sim 10 \ C^{**}$. The slope in the semi-dilute entangled regime deviates from the master curve representation, which fits very well at lower polymer concentrations. In fact, this may be connected with the reptation regime admitted over C^{**} (or C_e) for which η / η_{Rouse} varies as $(C/C_e)^{3.4}$. In these conditions, it comes that η varies as $(C/C_e)^{4.42}$. This power law fits well with our data where the slope is 4.3.
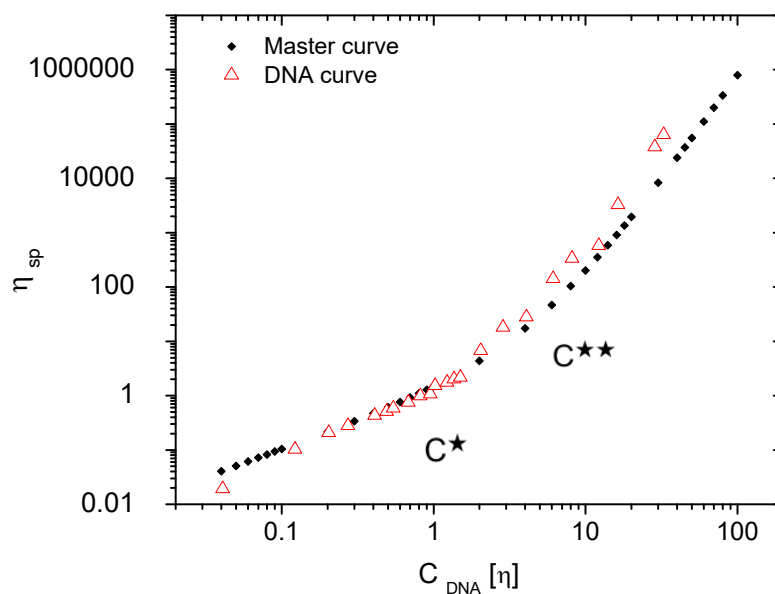
Figure 2.21. *Dependence of specific viscosity at zero shear rate as a function of the overlap parameter $C_{DNA}[\eta]$ for calf-thymus DNA solutions in TE buffer pH 7.3 at a temperature of 20 °C.*

The temperature effect on the specific viscosities of calf-thymus DNA solutions is shown in *Figure 2.22*, plotting the specific viscosity at zero shear rate as a function of $C_{DNA}[\eta]$, adopting the value of the intrinsic viscosity determined at 20 °C, as explained before. We can observe that all the temperatures present the same trend and that the viscosity of the solutions can be predicted with good accuracy at a specific DNA concentration.
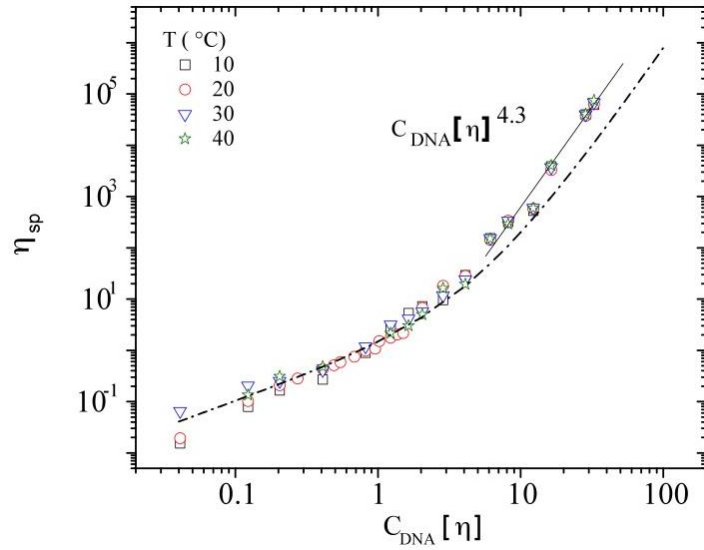
Figure 2.22. *Dependence of specific viscosity at zero shear rate as a function of the overlap parameter $C_{DNA}[\eta]$ for calf-thymus DNA solutions in TE buffer pH 7.3 at the temperatures 10, 20, 30 and 40 °C.*

The second important parameter characterizing DNA behavior is the critical shear rate, $\dot{g}_c$, obtained at the onset of the non-Newtonian flow.
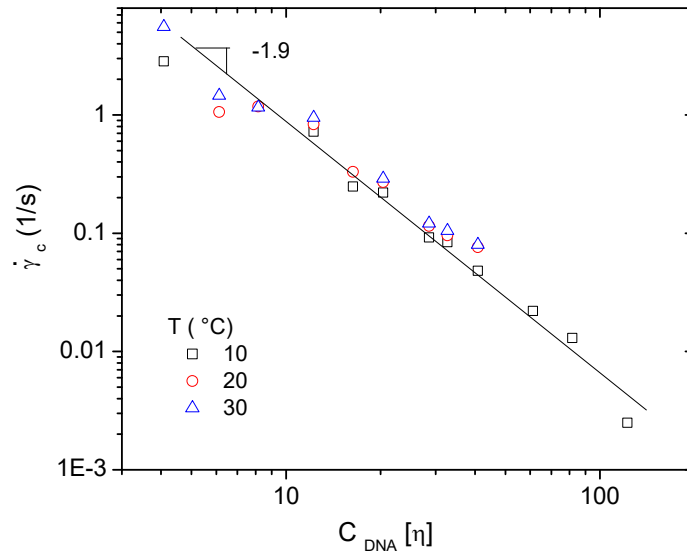
Figure 2.23. *Dependence of the critical shear rate, $\dot{g}_c$, of the onset of the Non-Newtonian viscosity with $C_{DNA}[\eta]$ for the temperatures 10, 20 and 30 °C.*

Figure 2.23 shows a log-log plot of $\dot{g}_c$ versus $C_{DNA}[\eta]$ for DNA concentrations in the semi-dilute regime. Due to lack of sensitivity, only the semi-dilute domain is covered from 2 mg/mL up to

10mg/mL. Considering that there is only a very small influence of the temperature on the critical shear rate values, a single curve is obtained in which all concentrations and temperatures are plotted. When the shear rate increases, the viscosity decrease was attributed to structural changes in the solution such as disentanglements, alignments of the molecules in the flow or to conformational modifications of the molecules among others. With this curve it is possible to obtain the relation $\dot{g}_c \sim C_{DNA}[\eta]^{-2.0\pm0.1}$, also reported for different molecular weight hyaluronans [59]. This exponent is in agreement with the scaling parameter from Rouse theory (9/4) corresponding to the longest relation time for an entanglement strand as mentioned by Colby et al. [65]. The calculated values for the critical shear rate with the Rouse model are in good agreement with the experimental values but only for higher concentration ($C_{DNA} \geq 7$ mg/mL). The scaling law relating the temperature influence, with an exponent of 7/12 in a good solvent (considerably low), is smaller in our case, probably due to the semi-rigid character of DNA [65].

The last important parameter is the slope relating the viscosity and the shear rate. In the power law region of η as a function of $\dot{g}_c$, the slope s depends on the overlap parameter $C[\eta]$, as discussed by *Graessley et. al* [66]. For $C_{DNA}[\eta] > 35$, the slope tends toward a limit, as predicted in the entanglement theory of *Graessley*, and is equal to -0.818.

Our results are presented in *Figure 2.24* and show that the limit value for calf-thymus DNA in TE buffer at a pH of 7.3 has an average slope of -0.82, which corresponds to the behavior described by *Graessley* and that has also been reported for a wide range of molecular weight hyaluronan samples.
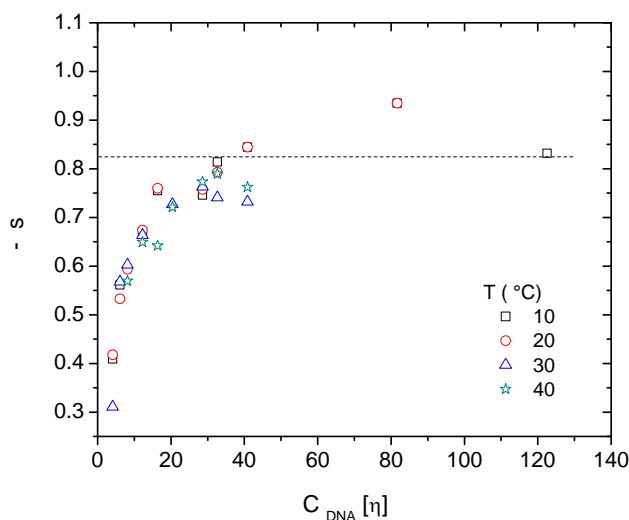
Figure 2.24. *Slope s in the power law region determined on flow curves of calf-thymus DNA in TE buffer at the temperatures of 10, 20, 30 and 40 ºC. (Dashed line represents the prediction of Graessley [65]).*

2.4.6.2. Dynamic measurements

The linear viscoelastic region (LVR) was first determined for calf-thymus DNA solutions in TE buffer at a pH of 7.3 through strain sweeps. This region is defined as the regime in which G' and G" are independent of the strain γ. All samples at the four studied temperatures exhibited a broad linear viscoelastic region, which extends to strain values around 30 %. *Mason et al.* previously described this behavior for calf-thymus DNA solutions at a pH of 8.0 and reported that for strains less than the 30%, G' and G" were independent of γ [55].
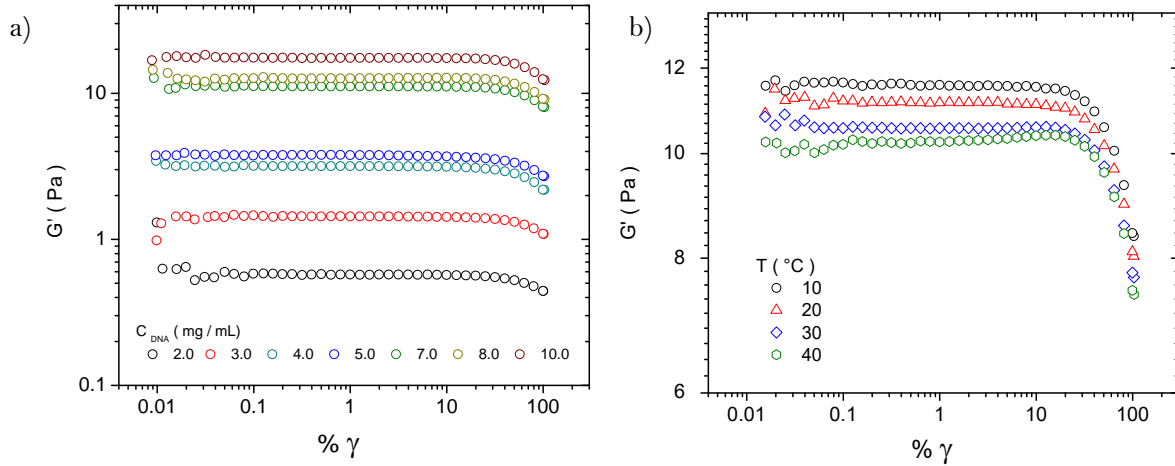
Figure 2.25. *Strain dependence of the storage modulus, G' for a) several DNA concentrations at the temperature of 10 °C and for b) a DNA concentration of 7 mg/mL at the temperatures of 10, 20, 30 and 40 °C.*

Figures 2.25a and *2.25b* show the storage modulus (G') versus strain percent (% γ) for several DNA concentrations at the temperature of 10 °C and for a constant DNA concentration with the temperature variation, respectively. By fixing γ= 0.02, inside of the linear regime, the spectra for the storage and the loss moduli in the same range of DNA concentrations at the four temperatures were measured subsequently. *Figures 2.26a* and *2.26 b* show the dependence of G' and G" with frequency for the DNA concentration range between 2.0 and 10.0 mg/mL at the temperature of 10 °C and for the DNA concentration 7.0 mg/mL at the temperatures of 10, 20, 30 and 40 °C, respectively.

The loss and storage moduli intersect in a characteristic frequency (ω_C), at which its reciprocal corresponds to the main relaxation time of the system, τ_c. This crossover frequency is related to a low-frequency viscosity, since at very low frequencies, the entanglements of the DNA solution can relax. The crossover frequency (ω_C) decreases with increasing DNA concentration and temperature. For solutions at which $C_{DNA} \leq 0.5$ mg/mL, the rheological behavior is predominantly viscous at all frequencies, however, at higher concentrations, the coils begin to overlap and become entangled, so an elastic behavior is observed.
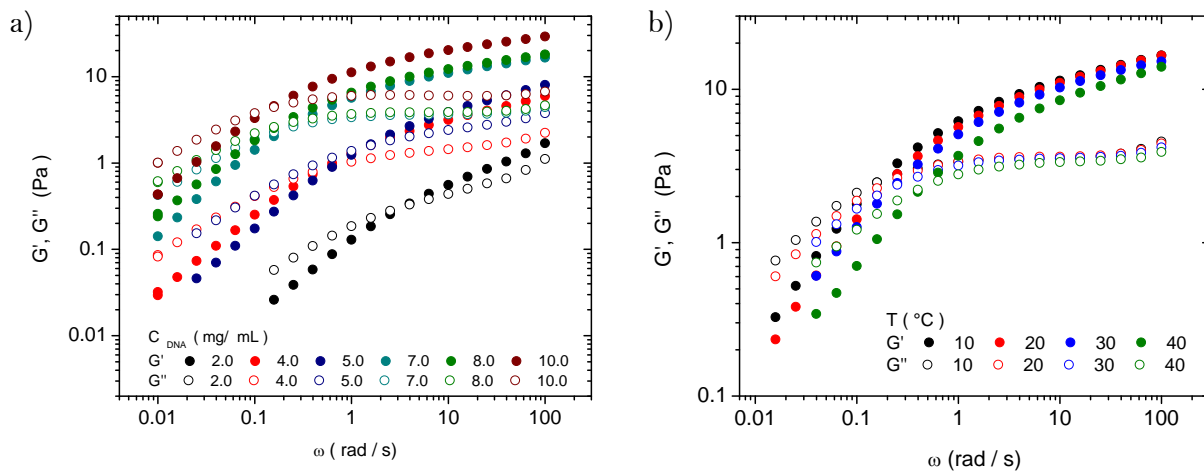
Figure 2.26. *Frequency dependence of the storage modulus, G', and the loss modulus, G'' for a) several DNA concentrations at the temperature of 10 °C and for b) a DNA concentration of 7 mg/mL at 10, 20, 30 and 40 °C.*

In the same way as DNA zero shear viscosity in terms of η_p was inspected as a function of DNA concentration between 2.0 and 10 mg/mL at the four studied temperatures (*Figure 2.20*), the crossover frequency, ω_c, was also analyzed as shown in *Figure 2.27*. As for η_p, the obtained behavior was found to be consistent with previous results obtained for polymers dissolved in a good solvent [57]. The variation of ω_c with concentration, was quantified with an average slope is equal to -2.17±0.12, i.e. $\omega_c \sim C^{-2.17}$. A reduced form of the characteristic relaxation time, τ_c, corresponding to ω_c^{-1}, can be obtained through the relation τ_c/η_s and is presented in *Figure 2.28*, where it is possible to observe the contribution of solvent viscosity to the relaxation time of DNA solutions at each studied temperature.
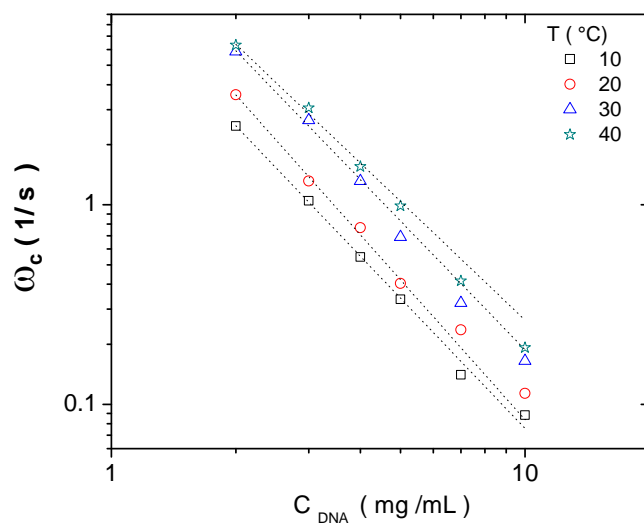
Figure 2.27. *Dependence of the crossover frequency (ω_c) with DNA concentration at 10, 20, 30 and 40 °C.*
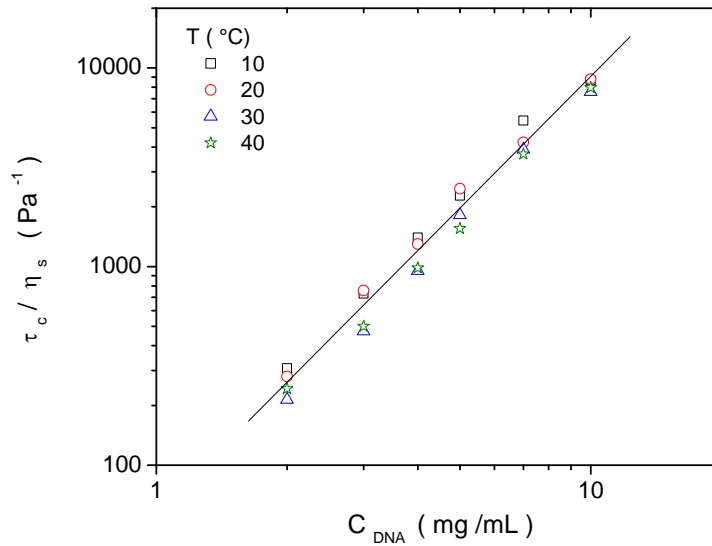
Figure 2.28. *Dependence of τ_c/η_s with DNA concentration at 10, 20, 30 and 40 ºC.*

Taking G'(ω) and G"(ω) at a given DNA concentration as reference makes possible obtaining a master curve as a function of DNA concentration from a horizontal (ax) and a vertical (ay) translation. First one represents the coefficient of translation of the frequencies and second one the coefficient of translation of the modulus. *Figure 2.29* shows the master curve obtained for the DNA concentration range between 1.5 and 10 mg/ml at the temperature of 20 ºC, by using as reference 4 mg/mL. The same procedure is used for the analysis of the temperature for each DNA concentration. *Figure 2.30* shows the master curve for a constant DNA concentration at the temperatures of 10, 20, 30 and 40 ºC.
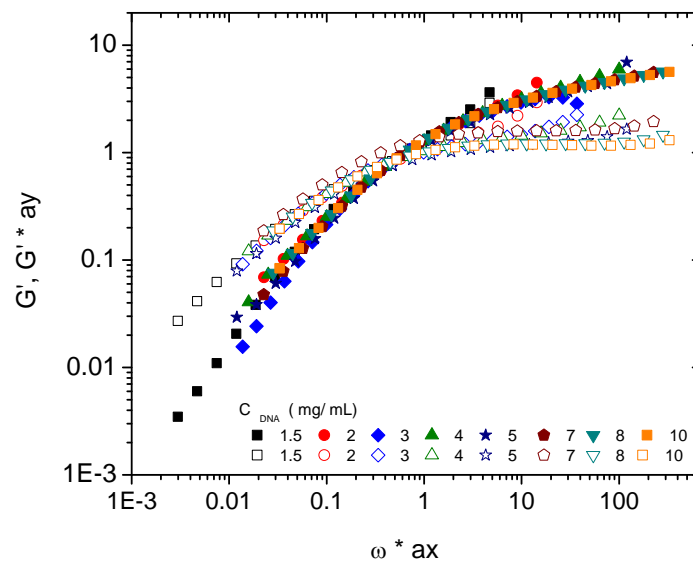
Figure 2.29. *Master curve for the reduced elastic (G') and viscous (G") moduli as a function of the reduced frequency for the concentration variation of calf-thymus DNA in TE buffer at a temperature of 20 ºC.*

81
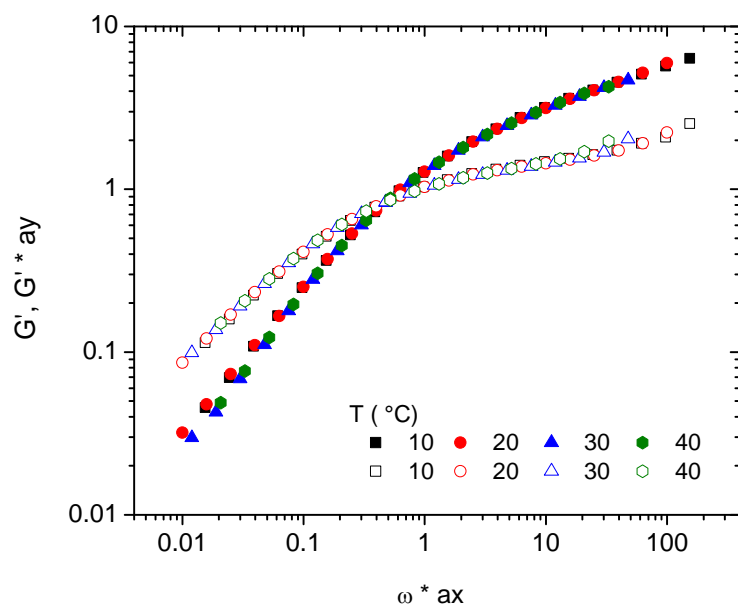
Figure 2.30. *Master curve for the reduced elastic (G') and viscous (G'') moduli as a function of the reduced frequency for the DNA concentration of 4 mg/mL at the temperatures of 10, 20, 30 and 40 ºC.*

Figure 2.31 shows that all DNA concentrations at the temperatures of 10, 20, 30 and 40 ºC collapse in a general master curve using the horizontal (ax) and the vertical (ay) translation obtained from the same DNA concentration as reference, i.e. 4.0 mg/mL, at a temperature of 20 ºC. We can determine from the superposition of the curves in one master curve that the main relaxation time of the system is only modified by the variation of DNA concentration.
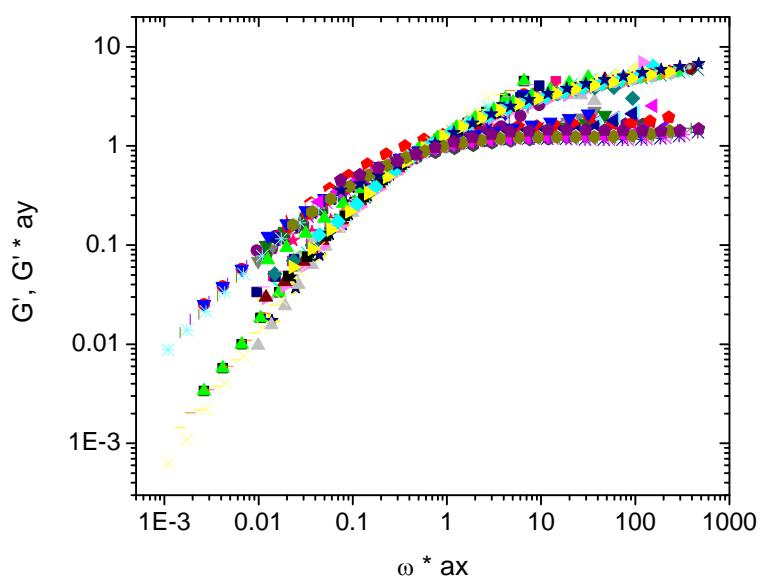
Figure 2.31. *Master curve for the reduced elastic (G') and viscous (G'') moduli as a function of the reduced frequency for the concentration variation of calf-thymus DNA in TE buffer at 10, 20, 30 and 40 ºC.*

The horizontal (ax) and vertical (ay) translation coefficients were plotted as a function of DNA concentration for all temperatures (*Figures 2.33* and *2.34*) and were subsequently analyzed by fitting the results with a power law that gives the following slope values: $ax \sim C^{2.32 \pm 0.16}$ and $ay \sim C^{-1.5 \pm 0.05}$. These exponents are in good agreement with those previously found on hyaluronan. The two series of shifts indicate that the moduli as a function of frequency is mainly imposed by concentration, i.e. density of entanglements [67].
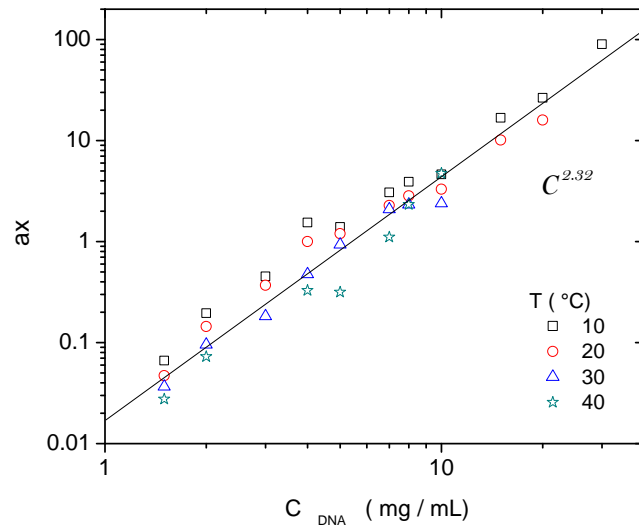
Figure 2.33. *Concentration shift factor (ax) applied to the moduli for obtaining the master curves at all temperatures.*
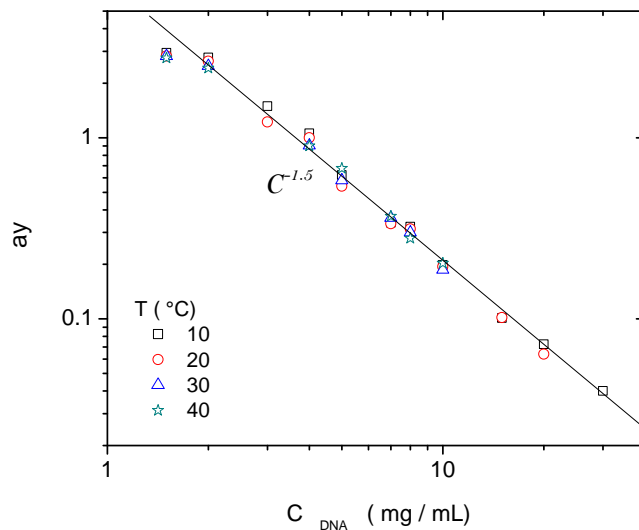
Figure 2.34. *Concentration shift factor (ay) applied to the moduli for obtaining the master curves at all temperatures.*

The Rouse relaxation time for an entanglement strand in the entangled semi-dilute concentration regime varies as $C^{9/4}$, which exponent is in good agreement with the ax shift. Nevertheless, the influence of temperature is lower than predicted by the scaling relation, as observed also on the critical shear rate. This temperature influence is related to the network relaxation. It is noted that the temperature dependence is smaller than for ax values and than in the scaling relationships proposed for ay. In this way, ay is mainly imposed by polymer concentration and density of entanglements as ax.

In order to compare our results from flow measurements with those from dynamic measurements, we calculated the complex dynamic viscosity, |η*|, from G'(ω) and G''(ω), as shown by *Equation 2.39*. According to the Cox-Merz rule [68], the steady state viscosity, η, can be compared with the complex dynamic viscosity, |η*|, by plotting both against shear rate and radial frequency, respectively. *Figure 2.35* shows, as an example of a constant DNA concentration at a constant temperature, a good superposition of |η*| (ω) and η ($\dot{γ}$) as a function of shear rate and radial frequency, respectively.
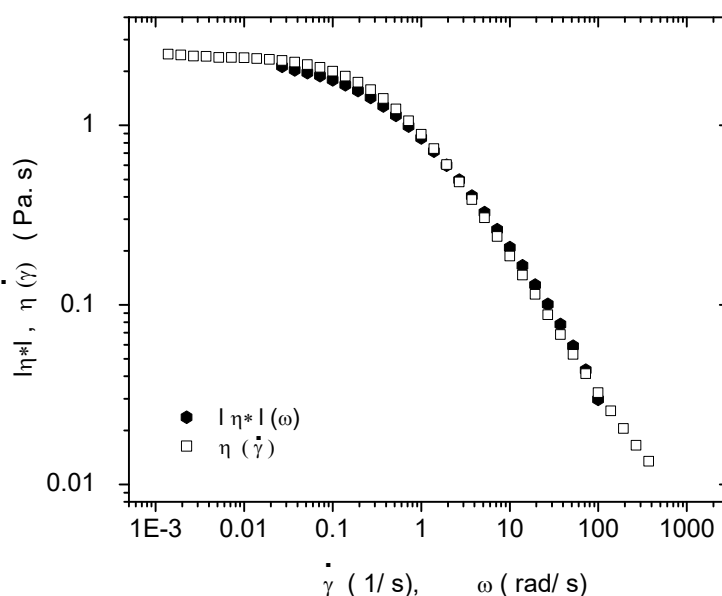
Figure 2.35. *|η*| (ω) and η ($\dot{γ}$) as a function of shear rate and radial frequency for a DNA concentration of 3.0 mg/mL at a temperature of 20 ºC.*

These data allow concluding that there are no strong interchain interactions at least until the DNA concentration of 10 mg/mL at all the studied temperatures. As well as we did for flow measurements, the slope *s* from the power law region of |η*| (ω) as a function of the radial frequency, was determined for each DNA concentration at each temperature. The obtained results are presented in *Figure 2.36*, in

comparison with the results from flow measurements. The same trend is obtained, with the limit value average slope around -0.82.
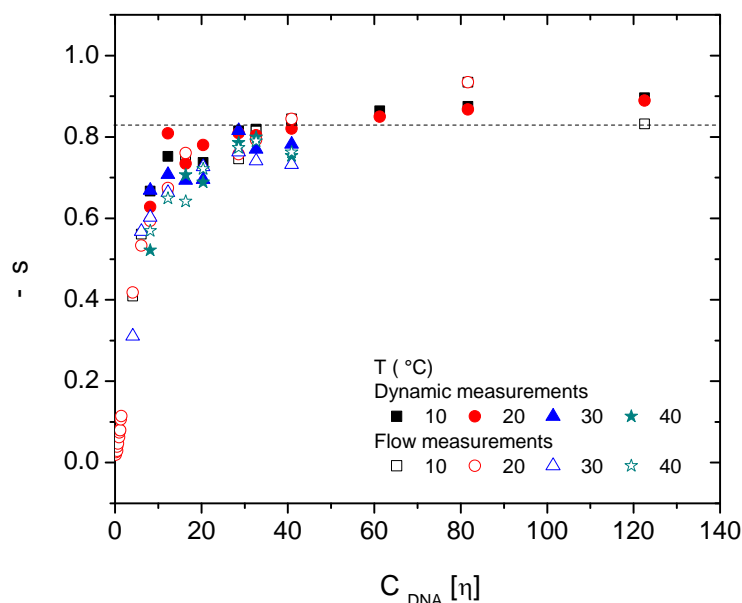
Figure 2.36. *Slope s in the power law region determined on flow and dynamic curves of calf-thymus DNA in TE buffer at the temperatures of 10, 20, 30 and 40 ºC. (Dashed line represents the prediction of Graessley [65]).*

2.4.7. Modeling of flow and dynamic response of DNA solutions in the semi-dilute regime with entanglements

2.4.7.1. Maxwell model

To better understand the dynamic curves, the Maxwell model was tested allowing interpreting the rheological behavior in the semidilute entangled regime. The entanglements may lead to an elastic behavior that could prevent DNA partition after replication during cell division. The lower frequency linear response is described by the elastic plateau modulus, G_p, and the terminal relaxation time of the Maxwell fluid, τ_R ($\approx\tau_c$). Since DNA solutions are considered as polydisperse in their molecular weight distribution [69], the relation $1/\omega_c = \tau_R \approx \tau_c$ has been used as an estimated approach to characterize the relaxation dynamics.

Figure 2.37 presents the moduli response for DNA concentrations of 2.0, 4.0, 7.0 and 10.0 mg/mL at the temperature of 20 ºC. The Maxwell generalized model [69] presented in *Equations 2.42* and *2.43* was used to fit calf-thymus DNA solutions dynamic response in the selected frequency range, for the DNA concentration range between 2.0 and 10.0 mg/mL. The best fit for experimental data was carried on using a six time-constants approach. As mentioned before, the main relaxation time, corresponding

to the reciprocal of the crossover frequency, is related to DNA entanglements main relaxation in the low-frequency viscosity region.
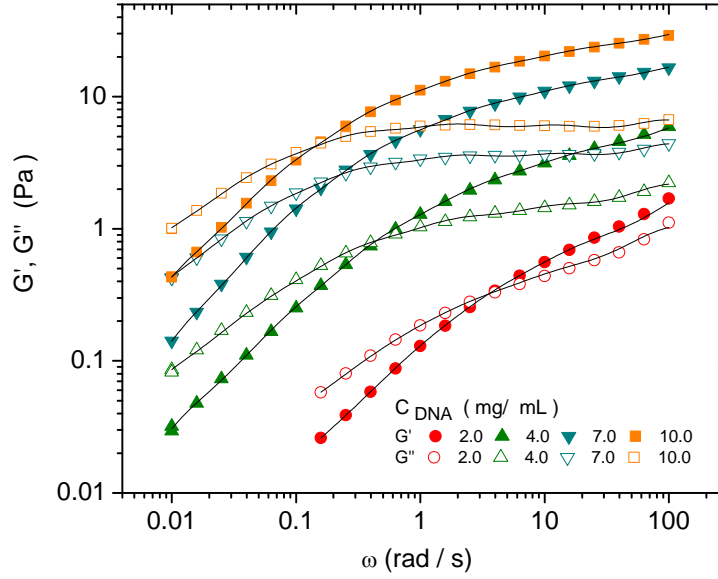
Figure 2.37. *Frequency dependence of the storage modulus, G', and the loss modulus, G'' for DNA concentrations of 2.0, 4.0, 7.0 and 10.0 mg/mL at the temperature of 20 °C. The solid lines represent the fit resulting from Maxwell model (Equations 2.42 and 2.43).*

2.4.7.2. Giesekus model

The flow measurements response in dependence of $\dot{g}$ was reproduced using the Giesekus model, based on the concept of deformation-dependent tensorial mobility [69]. DNA flow response is considered as a natural consequence of the molecules orientation effects, which has been simulated with the Giesekus model in order to obtain the rheological parameters of the solutions of entangled DNA chains, i.e.: two relaxation times (λ_{G1} and λ_{G2}) and the plateau modulus (G_{p1} and G_{p2}). *Figure 2.38* presents a set of plots of shear stress as a function of shear rate for DNA concentrations of 3.0, 4.0, 7.0 and 10.0 mg/mL at the temperature of 20 °C. The solid lines represent the fit of the experimental data by using Giesekus model given by *Equation 2.53* [70,71].

$$S = \left[\frac{G_{p1}}{2\dot{g}\lambda_{G1}}\right](a-1) + \left[\frac{G_{p2}}{2\dot{g}\lambda_{G2}}\right](b-1) + h_0\dot{g} \qquad (2.53)$$

$$a = \left[1 + 4\left(\dot{g}\div\emptyset\right)^2(\lambda_{G1}^2)\right]^{1/2} \qquad (2.54)$$

$$b = \left[1 + 4\left(\dot{\gamma}\right)^2 \left(\lambda_{Gl}^2\right) \right]^{1/2} \qquad (2.55)$$
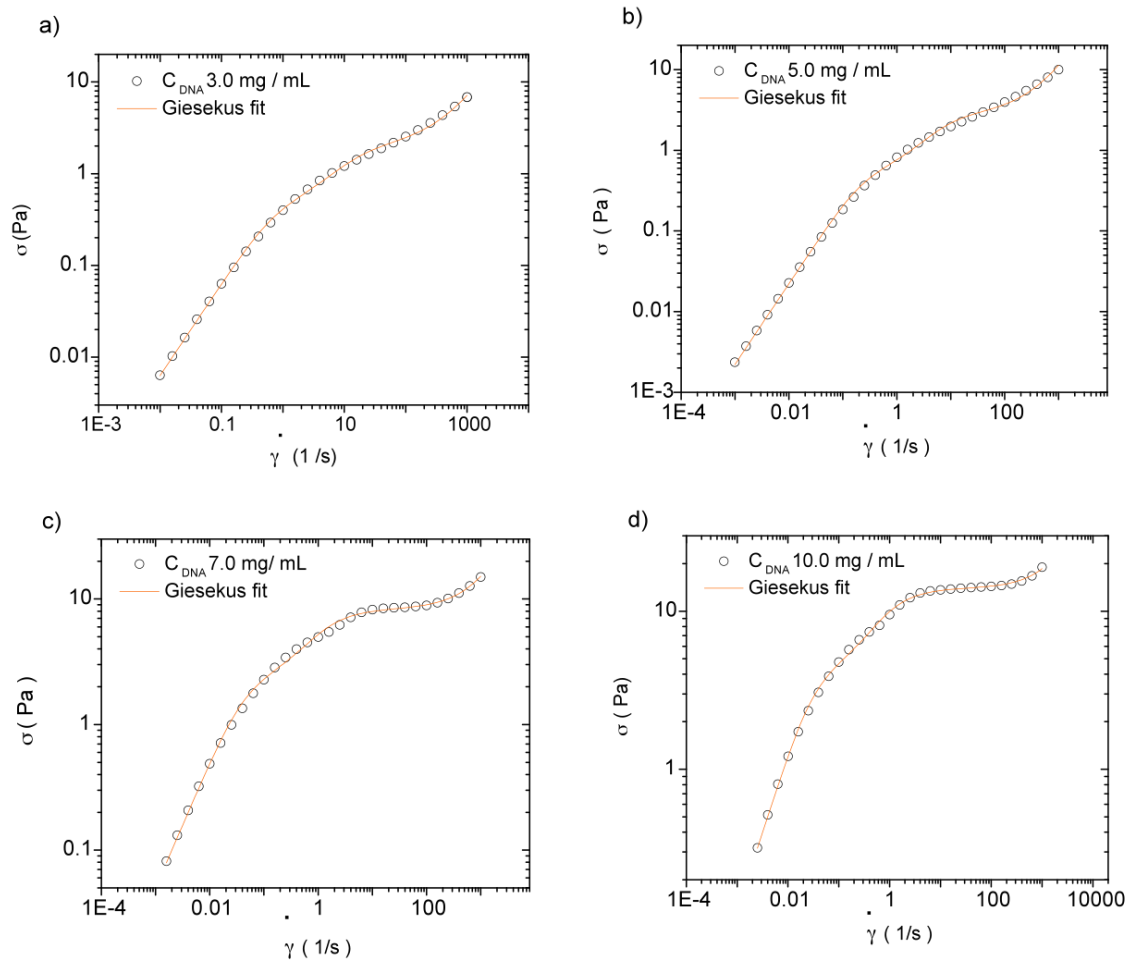
Figure 2.38. *Shear stress as a function of shear rate for DNA concentrations of a) 3.0, b) 5.0, c) 7.0 and d) 10.0 mg/mL at the temperature of 20 °C. The solid lines represent the fit resulting from Giesekus model.*

Table 2.4.- *Resulting values for G_P and λ_G from the fit of the Giesekus model to the experimental data of DNA concentrations of 2.0, 4.0, 7.0 and 10.0 mg/mL at 20 °C.*

DNA concentration (mg/mL) Time constant	3.0		5.0		7.0		10.0	
	G_P	$\lambda_{\Gamma G}$	G_P	$\lambda_{\Gamma G}$	G_P	$\lambda_{\Gamma G}$	G_P	$\lambda_{\Gamma G}$
1	0.278	0.653	0.786	4.074	2.556	18.25	4.715	25.23
2	1.061	0.033	2.447	0.160	5.807	0.598	9.30	0.848

The first relaxation time (λ_1) obtained through the Giesekus model for flow measurements is compared to the Maxwell main relaxation time from dynamic measurements in all the DNA concentration range, showing the same behavior and similar obtained values.

The obtained response for flow measurements was then formulated in terms of the normalized quantities, $\sigma^* = \sigma / G_c$ and $\dot{g}^* = \dot{g}\, t_c$, proposed by *Berret et al.* [72] for the non-linear mechanical response of surfactant wormlike micelles carried under a steady shear flow. A master dynamic phase diagram was obtained at different concentrations for each temperature with the superimposition procedure between flow curves. *Figure 2.39* shows the master curve for σ^* as a function of $\dot{g}^*$ for DNA concentrations between 2.0 and 10 mg/mL at a temperature of 20 °C.
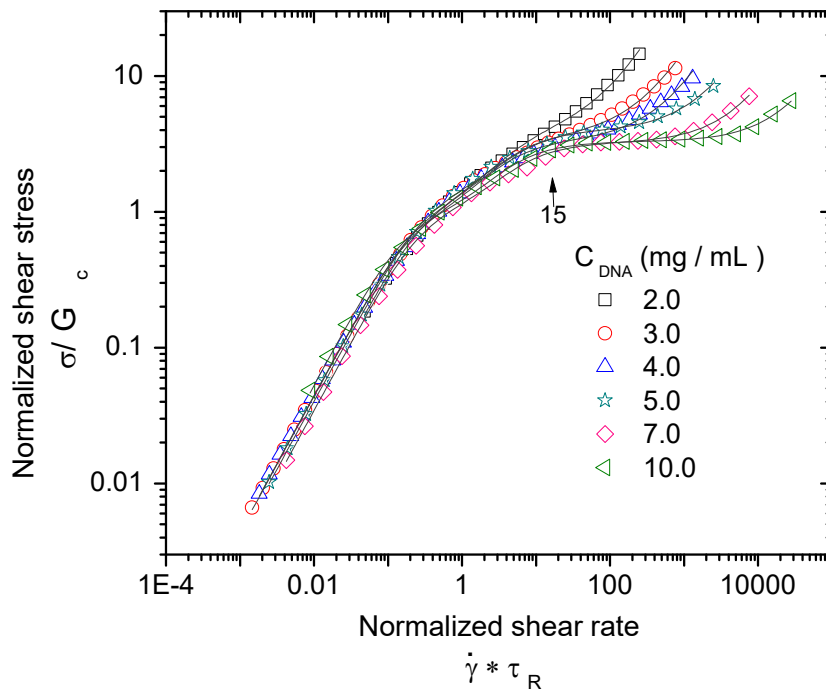
Figure 2.39. *Master dynamic phase diagram of DNA solutions. The normalized shear stress versus the normalized shear rate was obtained for DNA concentrations from 2.0 to 10.0 mg/mL at the temperature of 20 °C. The solid lines represent the fit results obtained with the Giesekus model.*

Below $\dot{g}^* = 0.20$, all data points are superimposed, this is, they are invariant with respect to the relative changes of DNA concentration, as expected for the linear Newtonian regime ($\sigma^* = \dot{g}^*$). At DNA concentrations between 2.0 and 6.0 mg/mL and higher values of $\dot{g}^*$, i.e. $\dot{g}^* \geq 0.20$, the shear stress curve slope decreases, showing the presence of the shear-thinning phenomenon. The onset of a

stress plateau is observed around $\dot{g}^* = 15.0$ at DNA concentrations higher than 6.0 mg/mL, which is related to the appearance of the shear banding flow phenomenon.

2.4.8. Visualizations

In order to explore with more detail the appearance of flow instabilities, a visualization device [42,43] was set up and the deformation of a fine filament of white colored DNA solution injected in the sample, was monitored during the rotation of the plate. It is worth to mention that the injected solution has the same concentration that the one tested. *Figure 2.40* shows the strain dependence of G'and G'' for a DNA concentration of 7 mg/mL at a temperature of 20 °C. We can observe that the elastic moduli (G') is three times higher than the viscous moduli (G''), which is in good agreement with the statement of a greater elastic behavior of DNA solutions at high concentrations due to entanglements.
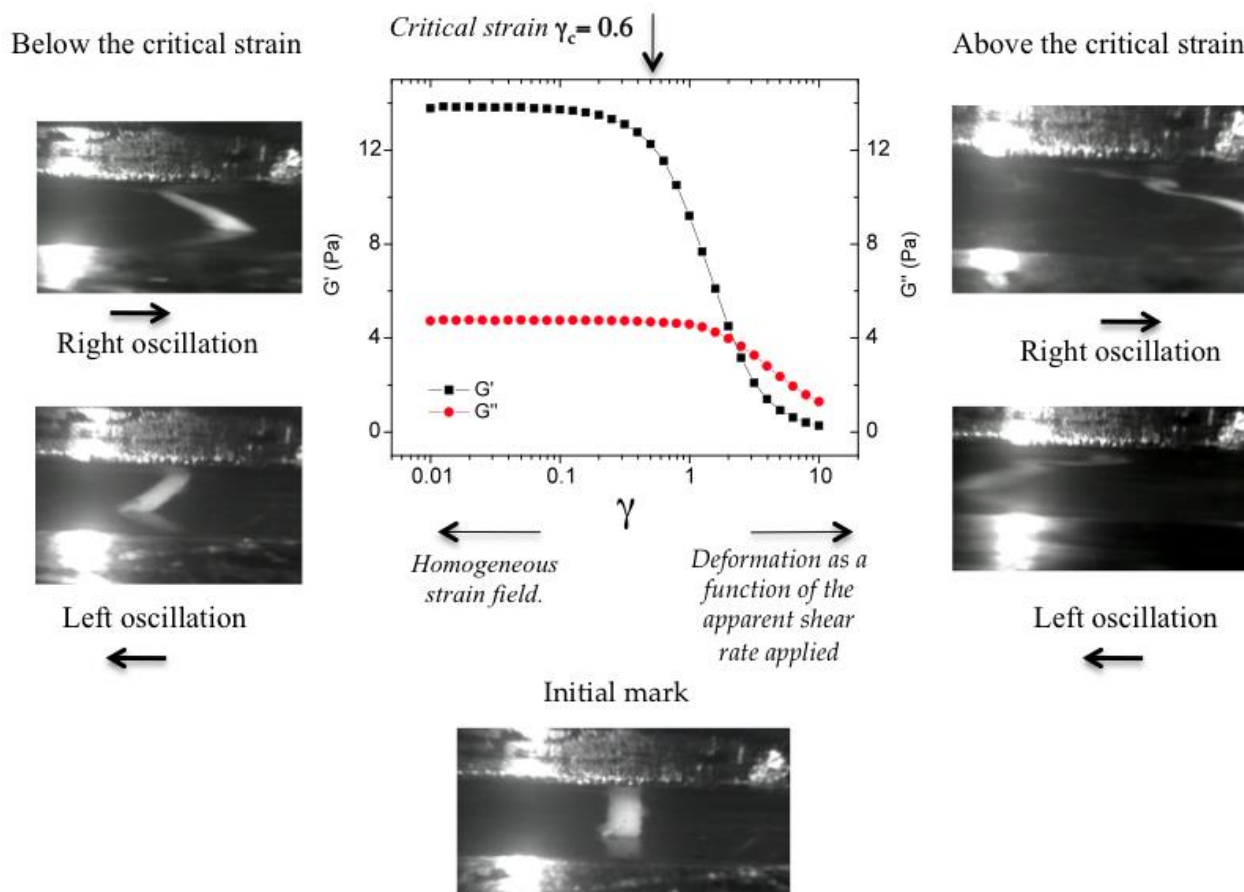
Figure 2.40. *Strain dependence of the storage and the loss modulus, G'and G'', respectively, for a DNA concentration of 7 mg/mL at a temperature of 20 °C. Visualization of the strain field inside the bulk of the solution.*

Here it is possible to identify the critical strain, γ_c, which is around 0.6. Below this critical strain, we have a homogeneous strain field and DNA molecules in solution are deformed in a uniform way, as we can see with left and right oscillations images presented in *Figure 2.38*. Above the critical strain, shear is positioned at half-height of DNA solution, as shown in the same figure. DNA solutions viscoelastic properties change above this strain level, G' breaks down and the deformation becomes a function of the apparent shear rate applied, so the response to stress is not linear anymore.

Figure 2.41 shows the transient response of stress for a DNA concentration of 10 mg/mL at a temperature of 20 ºC to different applied shear rates. As we can see in the three figures, the transient behavior presents the general response to an applied specific level of shear rate: i.e. the stress within DNA solution increases in linear relation with time, then reaches a maximum and finally falls monotonically with time until reaching the steady state.

Three different shear rates were chosen in the range between 1.0 and 30.0 s⁻¹, where DNA instabilities were firstly observed (*Figure 2.39*). *Figure 2.41 a* shows the transient response of stress at a shear rate of 1.0 s⁻¹, from which is possible to observe that the mark representing the strain field is homogeneously deformed. On the contrary, *Figures 2.41 b* and *c* show the brake up of the mark in the middle of the sample after the stress falls, during the steady state, so the strain is no longer homogeneous and is located mostly in a fine layer dividing DNA samples in two. This response was also observed by using this visualization technique in laponite samples [43] and more recently, in NFC suspensions produced from bisulfite pulp [42]. On the other side, shear banding presence during a very long period in steady rheological state was also reported by *Boukany et al.* [69] for a DNA solution of 11 mg/mL with glycerol as solvent, detected by particle-tracking velocimetric (PTV) measurements.

Figure 2.42 shows the shear stress as a function of shear rate for a DNA concentration of 10.0 mg/mL at the temperature of 20 ºC. Visual evidence of the strain field inside the bulk of the solution obtained at the steady state is presented for different shear rates selected in the three different regimes: linear Newtonian regime (0.01 s⁻¹), shear-thinning regime (0.1 and 1.0 s⁻¹) and shear banding flow regime (10.0 and 30.0 s⁻¹). Shear banding in DNA solutions can be probably explained in terms of electrostatic interactions due to ionic contribution of the solvent to the total ionic concentration for a DNA weight at high DNA concentrations, enhancing different chain alignments at high shear rates. The role of electrostatic interactions was also reported by *Hu et al.* for DNA solutions in NaCl 0.01 M as solvent [73]. Other explanations on the occurrence of shear banding is water release in the specific shear band, or local fluctuations in concentrations due to the initial heterogeneous structural organization of the DNA in the volume of the solution [74].
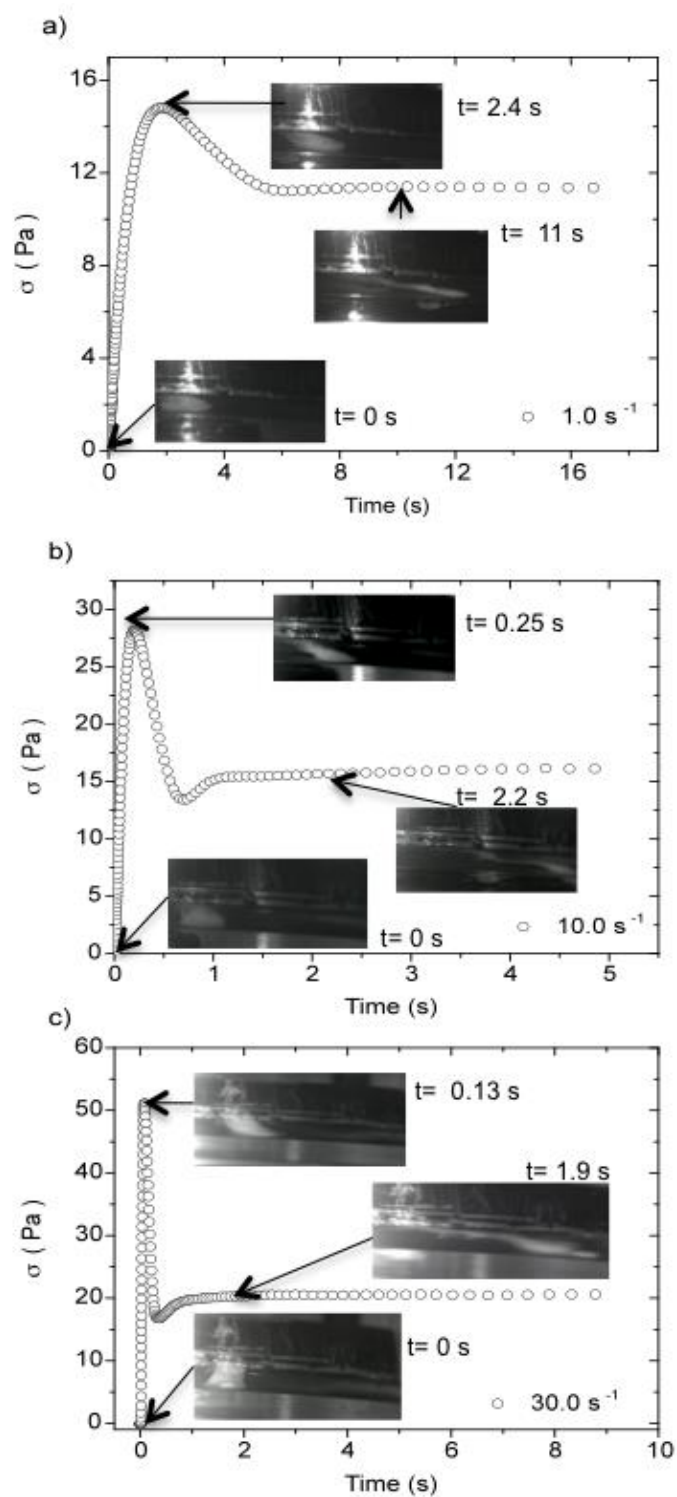
Figure 2.41. *Transient response of stress for a DNA concentration of 10 mg/mL at a temperature of 20 ºC at the following shear rates: a) 1.0 s⁻¹, b) 10.0 s⁻¹ and c) 30.0 s⁻¹. Each image corresponds to a visualization of the strain field inside the bulk of the solution.*
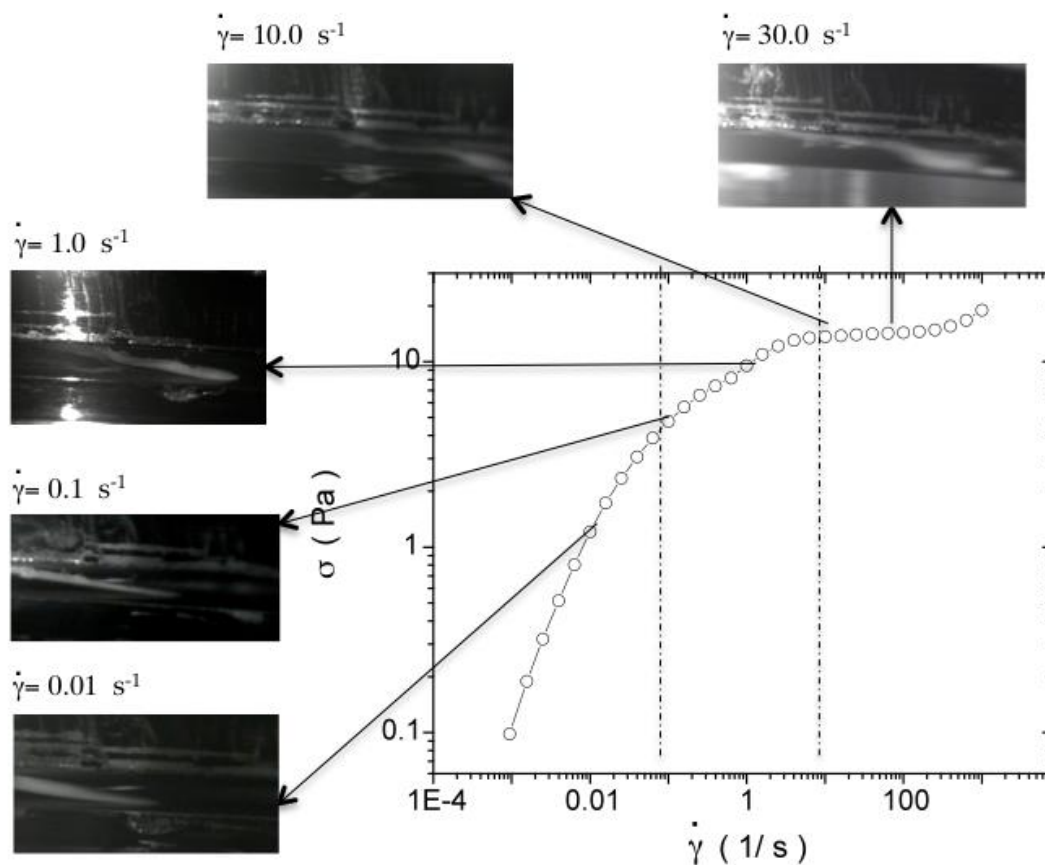
Figure 2.42. *Shear stress as a function of shear rate for a DNA concentration of 10.0 mg/mL at the temperature of 20 ºC. Each image corresponds to a visualization of the strain field inside the bulk of the solution obtained at the steady state.*

In order to identify the appearance of shear banding in terms of DNA concentration, the transient response of stress to an applied shear rate of 10.0 s^{-1} was monitored for several DNA concentrations in the semi-dilute regime with entanglements. *Figure 2.43* shows the transient response of stress for DNA concentrations of 4.0, 5.0, 7.0 and 10.0 mg/mL at a temperature of 20 ºC. We can observe that for DNA concentrations equal and higher than 5.0 mg/mL, the mark representing the strain field is no longer homogeneously deformed, leading to new DNA chain alignments and to the appearance of shear banding at this shear rate.
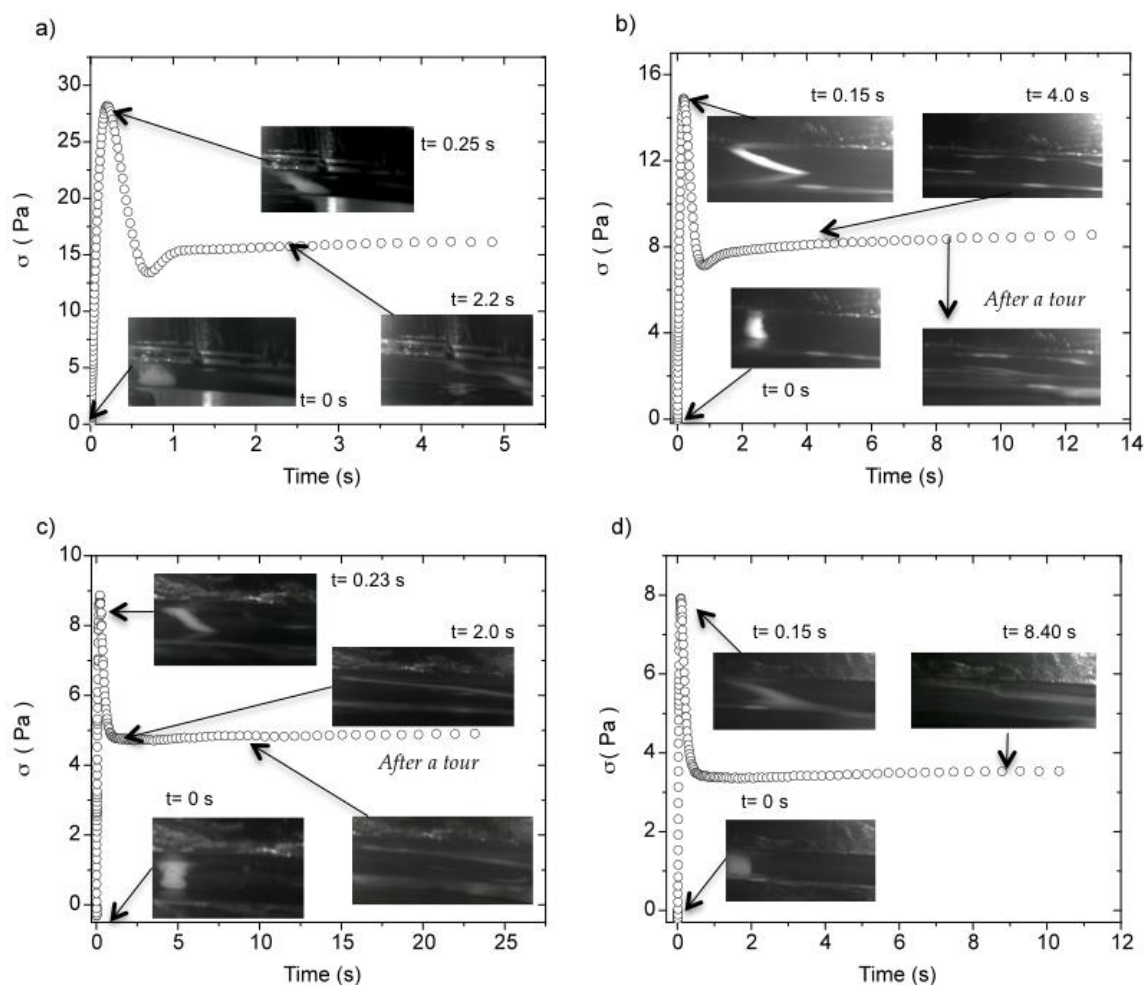
Figure 2.43. *Transient response of stress for DNA concentrations of a) 10.0, b) 7.0, c) 5.0 and d) 4.0 mg/mL at a temperature of 20 °C and at a shear rate of 10.0 s⁻¹. Each image corresponds to a visualization of the strain field inside the bulk of the solution.*

2.5. Particular conclusions on the rheological study of calf-thymus DNA solutions in TE buffer

Calf-thymus DNA solutions in TE buffer were characterized in detail in the dilute and the semi-dilute regimes. The intrinsic viscosity $[\eta]$ was determined from the zero shear-rate viscosity of the Newtonian plateau (η_0), obtained from flow measurements, and is equal to 4 080 mL/g. The molecular weight was then determined, resulting on 8 246 800 g/mol. The first critical concentration (C*) was estimated as a first approach by using the relation $C^{**} \sim [\eta]^{-1}$, obtaining 0.245 mg/mL. The starting point of the semi-diluted entangled domain, C_e, was obtained from the limit of the linear behavior in the higher concentrations domain of η_{sp} as a function of $C_{DNA}[\eta]$ curve, i.e. $C[\eta] \sim 10$, 2.45 mg/mL. The behavior found for calf-thymus DNA/TE buffer solutions corresponds to a semi-rigid polymer behavior.

All experimental data show no considerable temperature dependence between 10 and 40 ºC. All the experimental results are well described in terms of the overlap parameter C[η]. From dynamic and flow measurements, a good superposition of |η*| (ω) and η_0 ($\dot{g}$) as a function of shear rate and radial frequency was obtained in the DNA concentration range between 2.0 and 10.0 mg/mL. A master curve with dynamic measurements data was obtained through a horizontal (ax) and vertical (ay) translation by using a specific DNA concentration as reference, showing that the main relaxation time of the system is only modified by the variation of DNA concentration.

DNA solutions flow response was also formulated in terms of the normalized quantities σ*= σ/G_0 and $\dot{g}$*= $\dot{g}\,t_c$, from which a master dynamic phase diagram was obtained with the superposition between flow curves. Observations of the strain field combined with mechanical measurements were used to demonstrate the appearance of shear banding, i.e. $\dot{g}$=10.0 s^{-1} and C$_{DNA}$≥5.0 mg/mL. In this manner, it is shown by different approaches that for DNA concentrations in the semi-dilute regime with entanglements, DNA chains interactions and entanglements have important effects on linear viscoelasticity and on the different flow regimes.

2.6. References

[1] M. Rinaudo, *Comparison between experimental results obtained with hydroxylated polyacids and some theorical models*, Polyelectrolytes Vol.1, Edited by E. Sélégny, M. Mandel and U.P. Strauss, D. Reidel Publishing Company,157-193 (1974).

[2] S. Forster, M. Schmid, Polyelectrolytes in solution, *Adv Polym Sci* **120**, 51–133 (1995).

[3] A.V. Dobrynin, M. Rubinstein, Theory of polyelectrolytes in solutions and at surfaces, *Prog. Polym. Sci.* 30, 1049–1118, (2005).

[4] M. Doi, S.F. Edwards, *The theory of polymer dynamics*. Oxford: Clarendon Press, (1989).

[5] P.G. de Gennes, *Scaling concepts in polymer physics*. Ithaca, NY: Cornell University Press, (1979).

[6] R.M. Fuoss, Polyelectrolytes, *Discuss. Faraday Soc.* **11**, 125 (1951).

[7] M. Rubinstein, R. H. Colby and A.V. Dobrynin, Dynamics of semidilute polyelectrolyte solutions, *Physical Reviwe Letters* **73**, 2776 (1994).

[8] S. Lifson and A. Katchalsky, The electrostatic free energy of polyelectrolyte solutions. II. Fully stretched macromolecules, *J. Polym. Sci.* **13**, 43 (1954).

[9] I. Roure, *PhD thesis: Rhéologie et Dimensions des chaînes du hyaluronane en solution*, Grenoble, France (1997).

[10] E. Fouissac, *PhD thesis: Contribution à l'obtention d'acide hyaluronique par voie fermentaire et étude de ses propriétés physicochimiques*, Grenoble, France (1992).

[11] F. Oosawa, Polyelectrolytes, M. Dekker, New-York, (1970).

[12] M. Rinaudo, B. Loiseleur, Application du traitement d'Oosawa à l'étude des propriétés thermodynamiques des polyéléctrolytes rigides, *J. Chim. Phys.* **69**, 1606 (1972).

[13] M. Fixman, The Poisson-Boltzmann equation and its application to polyelectrolytes, *J. Chem. Phys.* **70**, 4995-5005 (1979).

[14] C.F. Anderson and M.T. Record, Polyelectrolyte Theories and their Applications to DNA, *Annual Review of Physical Chemistry* **33**,191-222 (1982).

[15] V.V. Anshelevich, A.V. Vologodskii, A.V. Lukashin, M.D. Frank-Kamenetskii, Slow relaxionational processes in the melting of linear biopolymers. A theory of its application to nucleic acids. *Biopolymers* **23**, 39-58 (1984).

[16] M.D. Frank-Kamenetskii, DNA chemistry. How the double helix breathes, *Nature* **328**, 17-18 (1987).

[17] R.M. Fuoss, A.Katchalsky, S.Lifson, The potential of an infinite rod-like molecule and the distribution of the counter ions, *Proceeding of the National Academy of Sciences U.S.* **37** (9), 579-589 (1951).

[18] G.S. Manning, Limiting laws and counterion condensation in polyelectrolyte solutions I. Colligative properties, *J. Chem. Phys.* **51**, 924 (1969).

[19] G.S. Manning, The persistence length of DNA is reached from the persistence length of its null isomer through an internal electrostatic stretching force, *Biophysical Journal* **91**, 3607–3616 (2006).

[20] T. Odijk, Possible scaling relations for semidilute polyelectrolyte Solutions, *Macromolecules* **12**, 688-693 (1979).

[21] J. Skolnick and M. Fixman, Electrostatic persistence length of a wormlike polyelectrolyte, *Macromolecules* **10**, 944 (1977).

[22] T. Odijk, On the ionic- strength dependence of the intrinsic viscosity of DNA, *Biopolymers* **18**, 3111-3113 (1979).

[23] T. Odijk and A.C. Houwaart, On the theory of the excluded-volume effect of a polyelectrolyte in a 1-1 electrolyte solution, *J. Polym. Sci., Polym. Phys.* **16**, 627-639 (1978).

[24] R. E. Harrington, Opticohydrodynamic properties of high-molecular-weight DNA. III. The effects of NaCl concentration, *Biopolymers* **17**, 919-936 (1978).

[25] W.F. Reed, Light-Scattering Results on Polyelectrolyte Conformations, Diffusion, and Interparticle and Correlations, *Macro-ion characterization, From dilute solutions to complex fluids*, Chapter 23, Ed. Kenneth S. Schmitz, ACS Symposium Series 548, American Chemical Society, Washington D.C. (1994).

[26] H. Chen, S. P. Meisburger, S. A. Pabit, J. L. Sutton, W. W. Webb and Lois Pollack, Ionic strength-dependent persistence lengths of single-stranded RNA and DNA, *PNAS* **109**, 799–804 (2012).

[27] G. Maret and G. Weill, Magnetic birefringence study of the electrostatic and intrinsic persistence length of DNA, *Biopolymers* **22**,2727-2744 (1983).

[28] H. Benoit and P. Doty, Light scattering from non-Gaussian chains, *J. Phys. Chem.* **57**(9), 958-963 (1953).

[29] A. Tsortos, G. Papadakis and E. Gizeli, The intrinsic viscosity of linear DNA, *Biopolymers* **95**, 824-832 (2011).

[30] R. Pamies, G.H.J. Cifre, C.L.M. Martínez and García de la Torre, Determination of intrinsic viscosities of macromolecules and nanoparticles. Comparison of single-point and dilution procedures, *J. Colloid Polym Sci* **286**, 1223-1231 (2008).

[31] M.T. Record Jr., Effects of Na+ and Mg++ Ions on the Helix-Coil Transition of DNA, *Biopolymers* **14**, 2137-2158 (1975).

[32] G.C. Berry, The hydrodynamic and conformational properties of denatured proteins in dilute Solutions, *Protein Sci* **19**, 94-98 (2010).

[33] A. Dondos, Denaturated proteins: draining effect and molecular dimensions, *Physica. B.* **405**, 3572-3575 (2010).

[34] J. Eigner and P. Doty, The native, denatured and renatured states of deoxyribonucleic acid, *J. Mol. Biol.* **12**, 549-580 (1965).

[35] D.M. Crothers, B.H. Zimm, Viscosity and sedimentation of the DNA from bacteriophages T2 and T7 and the relation to molecular weight, *J. Mol. Biol.* **12**, 525-536 (1965).

[36] H. Yamakawa, *Modern Theory of Polymer Solutions*, Harper and Row, New York (1971).

[37] W.M. Graessley, Polymer chain dimensions and the dependence of viscoelastic properties on concentration, molecular weight and solvent power, *Polymer* **21**, 258-262 (1980).

[38] P. M. Tuchinsky, *Poiseuille's law* 68, Cornell University (1976).

[39] ASTM Ubbelohde Viscometer, Rheotek USA.

[40] H.A. Barnes, J.F. Hutton and K.Walters, *An Introduction to Rheology*, Amsterdam - London - New York-Tokyo (1993).

[41] C.W. Macosko, *Rheology principles, measurements, and applications*, Wiley-VCH Inc., 111, (1994).

[42] O. Nechyporchuk, M. N. Belgacem and F. Pignon, Rheological properties of micro-/nanofibrillated cellulosesuspensions: Wall-slip and shear banding phenomena, *Carbohydrate Polymers* **112**, 432-439 (2014).

[43] F. Pignon, A. Magnin and J.-M. Piau, Thixotropic colloidal suspensions and flow curves with minimum: Identification of flow regimes and rheometric consequences, *J. Rheol.* **40**(4), 576 (1996).

[44] G.S. Manning, On the application of polyelectrolyte "limiting laws" to the helix-coil transition of DNA. I. Excess univalent cations, *Biopolymers* **11**, 937-949 (1972).

[45] M. Alatorre-Meda, P. Taboada, F. Hartl, T. Wagner, Michael Freis and J. R. Rodríguez, The influence of chitosan valence on the complexation and transfection of DNA: The weaker the DNA–chitosan binding the higher the transfection efficiency, *Colloids and Surfaces B: Biointerfaces* **82**, 54–62 (2011).

[46] P. Sauer, M. Müller, and J. Kang, *QIAGEN GmbH*, 2, 23-26 (1998).

[47] W.W. Wilfinger, K. Mackey and P. Chomczynski, Effect of pH and ionic strength on the spectrophotometric assessment of nucleic acid purity, *Biotechniques* 22(3), 474-6, 478-81, (1997).

[48] C. Schildkraut and S. Lifson, Dependence of the melting temperature of DNA on salt concentration, *Biopolymers* 3, 195-208 (1965).

[49] R.J. Owen, L.R. Hill and S.P. Lapage, Determination of DNA base compositions from melting profiles in dilute buffers, *Biopolymers* **7**, 503 (1969).

[50] M. Gawrońska, I. Kulamowicz, R. Oliński, M. Żbikowska, and Z. Walter, Physico Chemicals characteristics of DNA chromatin fractions from calf thymus, *Z. Naturforsch.* **36c**, 361-365 (1981).

[51] B. Porsch, R. Laga, J. Horský, Č. Koňák, K. Ulbrich, Molecular weight and polydispersity of calf-thymus DNA: static light-scattering and size-exclusion chromatography with dual detection, *Biomacromolecules* **10**, 3148–3150 (2009).

[52] M. Milas, M. Rinaudo and B. Tiniand, The viscosity dependence on concentration, molecular weight and shear rate of xanthan solutions, *Polymer Bulletin* **14**, 157-164 (1985).

[53] H.A. Barnes, J.F. Hutton and K. Walters, *An Introduction to Rheology*, Elsevier Science, Amsterdam, (1989).

[54] J.D. Ferry, *Viscoelastic Properties of Polymers*, 3rd Edition, John Wiley & Sons, New York, (1980).

[55] T.G. Mason, A. Dhople and D. Wirtz, Linear viscoelastic moduli of concentrated DNA Solutions, *Macromolecules* **31**, 3600 (1998).

[56] E. Raspaud, D. Lairez, M. Adam, On the number of blobs per entanglement in semidilute and good solvent solution: melt influence, *Macromolecules* **28**, 927-933 (1995).

[57] Y. Heo, R.G. Larson, The scaling of zero-shear viscosities of semi-dilute polymer solutions with concentration, *J. Rheol.* **49**, 1117 (2005).

[58] N. Berriaud, M. Milas and M. Rinaudo, Rheological study on mixtures of different molecular weight hyaluronates, *Int. J. Biol. Macromol.* **16**, 137-142 (1994).

[59] M. Milas, M. Rinaudo, I. Roure, S. Al-Assaf, G. O. Phillips and P. A. Williams, Comparative rheological behavior of hyaluronan from bacterial and animal sources with cross-linked hyaluronan (hylan) in aqueous solution, *Biopolymers* **59**, 191-204 (2001).

[60] E. Fouissac, M. Milas and M. Rinaudo, Shear-rate, concentration, molecular weight, and temperature viscosity dependences of hyaluronate, a wormlike polyelectrolyte, *Macromolecules* **26**, 6945-6951 (1993).

[61] M. Milas, M. Rinaudo and B. Tinland, The viscosity dependence on concentration, molecular weight and shear rate of xanthan solutions, *Polymer Bulletin* **14**, 157-164 (1985).

[62] M. K. Cowman and S. Matsuoka, Viscosity of Polymer Solutions Revisited in *Hyaluronan, Vol. 1, Chemical, Biochemical and Biological Aspects* Viscosity of polymer solutions revisited, 79-88, Editors J.F. Kennedy, G.O. Phillips, P.A. Williams and V.C. Hascall, Woodhead Publishing Ltd., England (2002).

[63] M. Rinaudo, Relation between the Molecular Structure of Some Polysaccharides and Original Properties in Sol and Gel States, *Food Hydrocoll* **15**, 433 (2001).

[64] M. Milas, M. Rinaudo, M. Knipper and J.L. Schuppiser, Flow and viscoelastic properties of xantan gum solutions, *Macromolecules* **23**, 2506-2511 (1990).

[65] R.H. Colby, M. Rubinstein, M. Daoud , Hydrodynamics of polymer solutions via two-parameter scaling, *J. Phys. II France*, **4**, 1299-1310 (1994).

[66] W. W. Graessley, The entanglement concept in polymer rheology, *Adv. Polym. Sci.* **16**, 1-179 (1974).

[67] P.G. de Gennes, Dynamics of entangled polymer solutions II. Inclusion of hydrodynamic interactions, *Macromolecules* **9**, 587-594 (1976).

[68] N. Berriaud, M. Milas and M. Rinaudo, Characterization and properties of hyaluronic acid (Hyaluronan) in *Polysaccharides: structural diversity and functional versatility*, S. Dumitriu Ed., Marcel Dekker, New-York (USA), 313-334 (1998).

[69] P. E. Boukany and S-Q. Wang, Shear banding or not in entangled DNA solutions, *Macromolecules* **43**, 6950-6952 (2010).

[70] S.-H. Tung, Y.-E. Huang, S.R. Raghavan, Contrasting effects of temperature on the rheology of normal and reverse wormlike micelles, *Langmuir* **23**, 372-376 (2007).

[71] P. Fischer and H. Rehage, Non-linear flow properties of viscoelastic surfactant solutions, *Rheologica Acta* **36**, 13-27 (1997).

[72] J.-F. Berret, G. Porte and J.-P. Decruppe, Inhomogeneous shear flows of wormlike micelles: A master dynamic phase diagram, *Physical Review E*, **55**, 1668-1676 (1997).

[73] Y.T. Hu, C. Palla and A. Lips, Role of Electrostatic Interactions in Shear Banding of Entangled DNA Solutions, *Macromolecules* **41**, 6618-6620 (2008).

[74] F. Martoïa, C. Perge, P.J.J. Dumont, L. Orgéans, M.A. Fardin, S. Manneville and M.N. Belgacem, Heterogeneous flow kinematics of cellulose nanofibril suspensions under shear, *Soft Matter* **11**(24), 4742-4755 (2015).

CHAPTER 3

Experimental study of the adsorption of DNA molecules in solution at different metal surfaces using Electrochemical Impedance Spectroscopy (EIS).

3. Experimental study of the adsorption of DNA molecules in solution at different metal surfaces using Electrochemical Impedance Spectroscopy (EIS).

The results of this chapter are the object of the following publication:

DNA Conformational Transitions at Different Concentrations and Temperatures Monitored by EIS.

L. M. Bravo-Anaya, E. R. Macías, F. Carvajal Ramos, V. V. A. Fernández, N. Casillas, J. F. A. Soltero and E. R. Larios-Durán .

ECS Electrochem. Lett. 2012, Volume 1, Issue 2, Pages G1-G3. doi: 10.1149/2.014202eel.

One integral part of this chapter was published in the following paper:

DNA Transitions by an Adsorption Impedance Study.

L. M. Bravo-Anaya, E. R. Macías, F. Carvajal Ramos, J.G. Álvarez-Ramírez, N. Casillas, J. F. A. Soltero and E. R. Larios-Durán.

J. Electrochem. Soc. 2013, Volume 160, Issue 4, Pages G69-G74, doi: 10.1149/2.029306jes.

3.1. Introduction

Electrochemical Impedance Spectroscopy (EIS) is a novel and non-destructive technique suitable for studying electrically charged surfaces that interact with molecules such as DNA. The response of DNA to an applied electric field has been studied for many years using several electrochemical techniques such as amperometry, potentiometry and voltammetry, among others [1-4]. However, the EIS technique is more sensitive and favorable than the above-mentioned techniques when current and electrical potential differences are negligible at low concentrations [5]. This technique is a useful tool for the study of DNA adsorption process onto metal surfaces without disturbing them by a chemical reaction [6]. Recent reports in the literature show the advantages for studying DNA hybridization processes, enabling the development of DNA biosensing platforms, immunosensors and gene therapy protocols [7,8]. The process of gene transfection achieves the success of gene therapy, as metioned on *Chapter 1*, which corresponds to its principal step and includes the introduction of DNA into cells by a specific agent known as vector [9-11]. The efficiency of gene therapy is determined by this process, and requires an extensive knowledge of DNA conformational changes before performing the transfection process [12, 13]. Since DNA molecule is a polyelectrolyte, then the conformational changes of DNA in

solution and DNA at an interface while interacting with charged surfaces will depend on several parameters such as DNA concentration, salt concentration, pH, temperature and polarization potential [6].

In this chapter, a study of calf thymus DNA molecules adsorption onto platinum and gold electrodes by Electrochemical Impedance Spectroscopy is presented. Impedance measurements were performed at open circuit potential (OCP), therefore, the response leads to a non-faradaic process with DNA adsorption onto the metal surface. The obtained response is interpreted in terms of the impedance adsorption theory [14-18], transforming the impedance results into complex capacitance data by using an equivalent circuit similar to the one proposed by Frumkin-Melik-Gaikazyan-Randles (FMGR) [19]. For Pt-DNA/TE buffer interface, the results cover the temperature range from 20 to 40 °C, while for the Au-DNA/TE buffer interface they cover from 25 to 35 ºC, in order to be used on the whole with the obtained results with the Surface Plasmon Resonance (SPR) technique and discussed in *Chapter 5* of this work. An analysis of each electric element of the equivalent circuit, i.e. double layer capacitance (C_{dl}), adsorption capacitance (C_{ad}), adsorption resistance (R_{ad}) and the time-constant average of the process, was carried out as a function of DNA concentration and temperature, making possible to study the electrochemical double layer structure and the transitions at the interface caused by DNA molecules entanglements and interactions between DNA chains and with the metal surface.

3.1.1. Electrochemical double-layer and overview of the adsorption process

The formation of a specific interfacial region is obtained when a surface is immersed in an aqueous solution. There, the electrochemical properties such as the electrical potential and the electrolyte concentration vary along the metal-solution interface [20]. A charge separation generally takes place at the interface region because of the difference between chemical potentials of the two phases. This interfacial region, along with the charged surface, is known as the electrochemical double layer, EDL. It can range from a few angstroms in highly concentrated solutions to 100 nm in a very diluted solution [21]. The study of the double layer is of great importance in electrochemistry, colloid science and surface chemistry [22]. Some their applications are: metals electrosorption, energy storage devices production, water purification, nanomaterials processing and development of sensors, among others [23].

A large number of studies have been carried on because of the importance of the electrochemical double layer. Several models for the double layer have also been proposed, however, there is no general model that can be used in all the experimental cases. This is due since the structure of the double layer and its capacity depend on various parameters such as the material of the electrode (i.e. metal, carbon, semiconductors, the electrode porosity, the presence of other films on the surface), the type of solvent, the type of supporting electrolyte, the temperature and the specific adsorption degree of ions and

molecules [24]. In the Gouy-Chapman model, ions are considered as punctual charges, water as a continuous medium and the electric potential distribution can be described and predicted using the Poisson-Boltzmann equation [20]. This model has been used in various processes such as heavy metal adsorption and ion transport through membrane channels [25,26]. For higher ions concentrations and higher superficial charge density, it is possible to obtain a better description of the electrochemical double layer using the Monte Carlo method [27]. *Torrie et al.* used this method to generate more accurately numerical results for the original model of electrolytes 2:1 and 2:2, near to a flat wall uniformly charged within the concentration range from 0.005 to 0.50 M and for positive and negative charged surfaces up to 25 $\mu C/cm^2$ [28].

3.1.1.1. The adsorption process

The adsorption corresponds to the accumulation process of particles on a surface. Molecules of a solute get concentrated on a surface by the action of intermolecular forces between them during the adsorption process. The adsorbed species is known as the adsorbate and the surface on which takes place the adsorption process is called substrate or adsorbent [29]. The adsorption processes are used in the production of several biotechnological materials, such as amino acids, proteins and antibiotics, among others [30,31] materials. In order to obtain a greater efficiency in each one of them, different factors have to be studied and considered in detail: the adsorption type according to the interaction type that occurs between the solute and the adsorbent, the type of adsorbent, the relations at the equilibrium and the adsorption kinetics.

We can distinguish two general types of adsorption, although there is also the possibility of having an intermediate behavior. First type corresponds to the physical adsorption, also known as physisorption. This process is similar to a condensation process and is not a specific adsorption. Molecules are generally kept together through weak interactions, i.e. Van der Waals interactions type, like bipolar, dispersion and/or induction interactions. Thus, the physisorption is an exothermic process in which the released heat, ΔH_{ads}, whose value varies between 20 and 40 kJ/mol, is similar to condensation enthalpies of adsorbed species [32]. Physical adsorption cannot explain the catalytic activity of the solids in the case of interactions between stable molecules, since it is not possible to obtain a significant decrease in the activation energy. In the cases when superficial reactions of atoms and free radicals sometimes involve small changes in the activation energies, the physical adsorption is considered as an important process. As the temperature increases, the physical adsorption degree decreases rapidly [33]. This process does not depend on the heterogeneity or the irregularities in the nature of the surface; however, it is directly proportional to the extent of the surface. Physisorption studies are useful to determine properties of solid catalysts [34].

The second type of adsorption corresponds to a non-specific adsorption [35], which involves stronger forces than the physical adsorption forces and is known as chemisorption. *Langmuir* [36] proposed that the adsorbed molecules are retained on the metal surface through valence forces of the same type as the forces occurring between atoms. The values for the chemisorption heats are higher than those of the physisorption processes and support the theory that this type of adsorption is based on valence bonds. Due to the high adsorption heat, the energy of molecules that have been adsorbed through a chemisorption process may be different from the energy of the molecule [37]. Thus, the activation energy for such reactions can be smaller than that of a homogeneous process. There are two types of chemisorption: the activated and the non-activated. In first type, the chemisorption rate varies with temperature, following the finite activation energy of Arrhenius equation. The non-activated chemisorption occurs very quickly, suggesting an activation energy close to zero [38]. *Figure 3.1* shows the effect of temperature on physisorption and chemisorption and *Table 3.1* summarizes the differences between both processes.
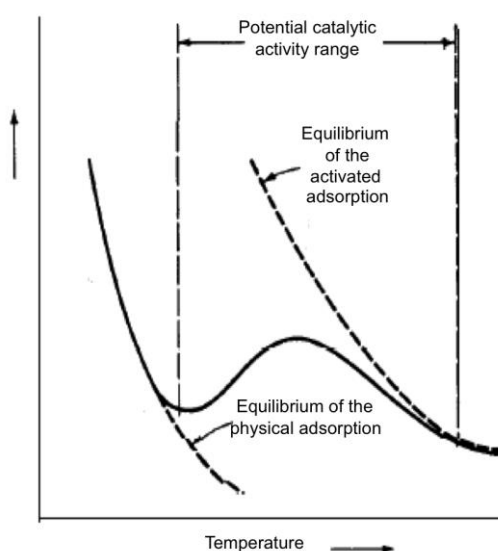
Figure 3.1. *Schematic representation of the temperature effect on the physical and chemical adsorption processes* [39].

Table 3.1.– *Differences between physisorption and chemisorption.*

Parameter	Physical adsorption	Chemical adsorption
Temperature range	Low temperatures	Generally high temperatures.
Adsorption heat	Low (ΔH_{cond})	High, as heat reaction.
Activation energy rate	Very fast, low E_a.	Un-activated: low E_a. Activated: high E_a.
Action rate	It is possible with multiple layers.	Monolayer
Reversibility	Highly reversible.	Generally irreversible.
Importance	Important for determining the surface area and pore size.	Important for determining the active centers are and for the evaluation of surface reactions kinetics.

3.1.1.1.1. Adsorption isotherms

The relation between adsorption and the adsorbate concentration in the bulk solution is known as an adsorption isotherm. The adsorption of the component *i* depends on the temperature and concentration of the components within the phase, C_{vi} (*Equation 3.1*).

$$A_i = f(T, C_{vi}) \tag{3.1}$$

Generally, for one monolayer adsorption, the adsorption isotherm is described by the following expression [40]:

$$q_i = f(C_{vi}) \tag{3.2}$$

where θ represents the fraction covered.

Henry's isotherm [41] describes the simplest case of adsorption, in which the surface coating is proportional to the adsorbate concentration in the bulk of the solution (*Equation 3.3*).

$$q = BC_v \tag{3.3}$$

where C_v is the concentration in the bulk of the solution and B is the adsorption coefficient on m³/mol and depends on the adsorption heat as follows:

$$B = B^0 \exp\left(q_{ad} / RT\right) \tag{3.4}$$

In 1961, Irving Langmuir determined the equation that relates molecules adsorption on a solid surface with concentration or gas pressure of the medium that is located on the solid surface at a constant temperature. For the Langmuir isotherm, the following assumptions are considered for the development [42]:

1. The surface is homogeneous.

2. There is no lateral interactions, this is, desorption energy is constant.

3. The maximum adsorption corresponds to a monolayer.

4. The number of available sites in the adsorbate for the adsorption is limited.

The expression that describes the values for the coated fraction and the number of available sites for the adsorbate to adhere on the surface is the following:

$$q = \frac{BC_v}{(1 + BC_v)} \tag{3.5}$$

However, the Langmuir isotherm has some limitations because it assumes that the heat of adsorption is independent of the surface coating. It is noteworthy that, in many cases, the adsorption positions are not fully equivalent and the firsts positions that will be occupied will be those in which a more satble bond is present. Furthermore, interactions between adsorbed molecules can be significant. Thus, the adsorption enthalpy will not be constant, allowing the mobility of adsorbed molecules and the formation of other layers by physisorption onto the adsorbed monolayer by chemisorption. The consideration of the exponential variation of the heat magnitude with the surface coating is part of Freundlich's proposal (1909). In this isotherm there is no limit coating and a multimolecular adsorption is proposed, not only monomolecular. The Freundlich adsorption isotherm is expressed as follows:

$$\frac{m_a}{m} = KC^{1/n} \tag{3.6}$$

where m_a is the adsorbate mass, m is the adsorbent mass, K_F and $1/n$ are constants for a given adsorbent and adsorbate at a constant temperature.

Because of the limitations of Langmuir's model, other adsorption isotherms have been proposed in order to reproduce more adequately the observed adsorption behavior. One of these empirical isotherms is Temkin's isotherm [43], which assumes that adsorption is characterized by an uniform distribution of binding energies and that the adsorption heat decreases linearly with increasing the coated fraction due to adsorbent-adsorbate interactions. Langmuir's isotherm was then modified by Frumkin [44] to take account of both attractive and repulsive lateral interactions between the adsorbates. Frumkin proposed an expression for these interactions considering that repulsions or attractions between them decrease or increase the heat of adsorption [44].

3.1.2. Electrochemical double layer

3.1.2.1. Surface properties

The electrochemical double layer characteristics vary and depend on the properties of each interface and can be separated in two types: polarizable or non polarizable, depending on the interfacial resistance [20]. The concept of equivalent circuits can easily explain the separation. An equivalent circuit composed of a capacitor, representing the double layer capacitance, a faradaic resistance and the solution resistance, C_{dl}, R_f and R_s, respectively, can represent the interfacial region. If the value of the faradaic resistance is very large, as for the case of ideally polarizable interfaces, the equivalent circuit can be simplified to the series coupling of a double layer capacitor with the solution resistance. In an ideally polarizable surface, any electrochemical reaction takes place, only non-faradaic processes such as adsorption.

Increasing the electrical potential at the metal surface will cause the accumulation of charge in one of the plates of the double layer capacitor, preventing electric current to pass through the interface. On the other hand, if the faradaic resistance is very small, such as for the Ag/AgCl surface in contact with a NaCl solution, the equivalent circuit can be represented by the series coupling of the solution resistance, the faradaic resistance and a capacitor in parallel. Any change in the electric potential at the surface causes the flow of an electrical current through the interface, which is known as ideally non-polarizable.

3.1.3. Electrochemical double layer structure

3.1.3.1. Helmholtz–Perrin model

The Helmholtz model was introduced in 1879 and is considered as the simplest model that explains interface metal/solution structure. This model proposes that all the charge excess on the side of the solution is located at a fixed distance from the electrode, X_{HP}, and is on the same plane [45]. Helmholtz also considered the arrangement of positive and negative charges rigidly on each side of the interface, i.e. the metal surface and the solution, respectively (*Figure 3.2*). In this model the charge in the solution borders the electrode surface and the presence of two charge planes with different polarity located at a distance X are considered.
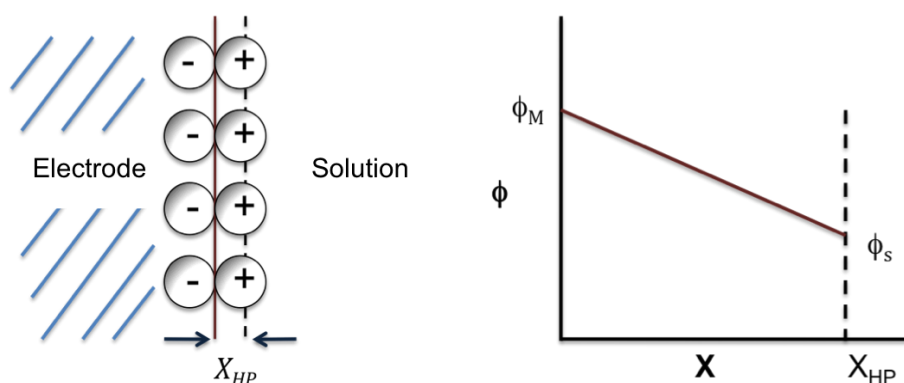
Figure 3.2 *Schematic representation of Helmholtz model.*

According to the Helmholtz-Perrin model, the interface can be compared to a parallel plate capacitor, in which a plate would consist of the metal/solution surface and the other would contain oppositely charged ions in solution [22]. The separation between the two plates corresponds to the distance X_{HP}. For this model, the potential variation in the double layer with respect to the distance from the surface is linear and is given by the following equation:

$$C_{dl} = \frac{e_r e_o}{X_{HP}} \tag{3.6}$$

where C_{dl} corresponds to the double layer capacitance, ε_r to the dielectric constant of the medium, ε_o to the vaccum permittivity, X_{HP} the thickness of the electrical double layer and $\varepsilon_r\varepsilon_o$ is equivalent to the dielectric constant of the medium (ε_r).

However, it is observed experimentally that the capacitance of the double layer varies with the electrode potential and the ion concentration in the solution, which cannot be predicted by the theoretical model of Helmholtz. In this way, the obtained results by using this model are not totally satisfactory.

3.1.3.2. Gouy-Chapman model

Gouy and Chapman proposed a model considering both the potential and the electrolyte concentration contribution on the structure of the electrical double layer. Their proposal was developed between 1910 and 1913. Both of them contributed with several amendments to the Helmholtz model to take into account that the arrangement of the ions takes place along a finite solution thickness, called diffuse layer, which is related to the thermal agitation and to the balance of the metal surface charges [28]. The presence of the ions diffuse layer represents a great difference with Helmholtz model, where the compact layer is the only one considered. The structure of the diffuse double layer proposed by Gouy-Chapman is illustrated in *Figure 3.3 a* and *Figure 3.3 b* shows the potential decay as a function of the distance X.
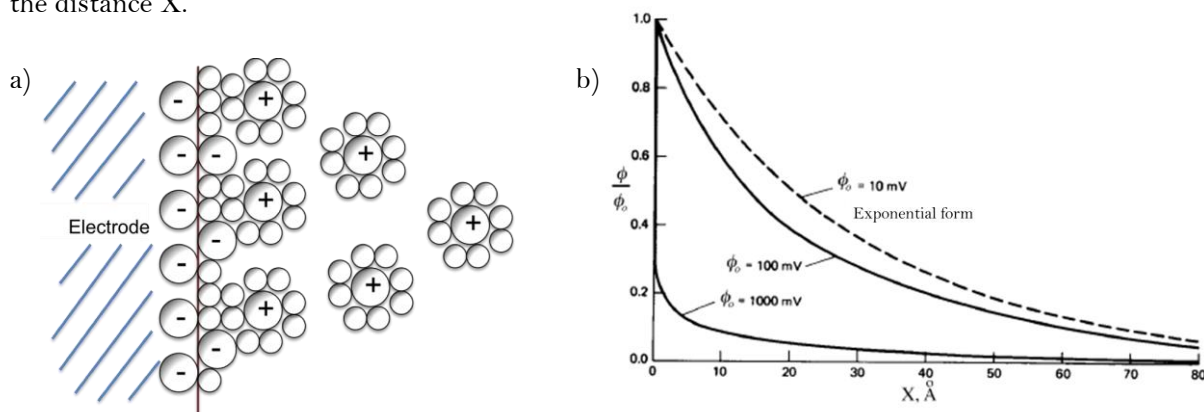
Figure 3.3 *a) Schematic representation of Gouy-Chapman model and b) Potential profiles through the diffuse layer for a solution 10⁻² M in a 1:1 electrolyte at 25 ºC [22].*

In order to maintain the overall electroneutrality of the system, it is necessary that charge excess on the side of the surface attract an equivalent amount of oppositely charged ions in the diffuse layer, wherein the electric potential distribution follows Poisson's equation:

$$\nabla^2 \psi = -\frac{\rho}{\varepsilon} \tag{3.7}$$

where ∇^2 is the Laplacian operator, ψ is the relative electrical potential between the diffused layer and the bulk of the solution, ε_r is the dielectric constant of the medium and ρ is the charge density volume given by:

$$\rho = \sum_i N_i z_i e \tag{3.8}$$

In this equation, z_i is the valence of ion i, e is the electron charge and N_i is the number of ion of the species i. According to the Boltzmann distribution it is possible to express N_i as follows:

$$N_i = N_{io} \exp\left[-\frac{z_i e(\phi - \phi_b)}{kT}\right] \tag{3.9}$$

where k is the Boltzmann constant, T is the absolute temperature, N_{io} is the ions concentration in the bulk of the solution and ϕ and ϕ_b are the absolute electrical potentials in the double layer region and in the bulk of the solution, respectively. It is noteworthy that the electrical potential of reference is located in the bulk of the solution, therefore, $\phi_b =0$ and can be represented by Ψ. By combining *Equations 3.7, 3.8* and *3.9*, the Poisson-Boltzmann equation is obtained:

$$\nabla^2 \psi = -\frac{e}{\varepsilon}\sum_i N_{io} z_i e \exp\left(\frac{-z_i e \psi}{kT}\right) \tag{3.10}$$

If the solution contains only electrolyte type z:z, then *Equation 3.10* can be simplified for a one-dimensional system as follows:

$$\frac{d^2\psi}{dx^2} = \frac{2 N_o z e}{\varepsilon}\sinh\left(\frac{ze\psi}{kT}\right) \tag{3.11}$$

This equation corresponds to a second-order differential equation that can be integrated multiplying both sides by 2 ($d\psi/dx$):

$$\int \frac{d}{dx}\left(\frac{d\psi}{dx}\right)^2 dx = \int \frac{4 N_o z e}{\varepsilon}\sinh\left(\frac{ze\psi}{kT}\right) d\psi \tag{3.12}$$

By integrating *Equation 3.7* from $\psi=0$ and $d\psi/dx=0$, corresponding to the bulk of the solution to any point of the double layer, the following first-order differential equation for ψ is obtained:

$$\frac{dy}{dx} = \frac{-2\kappa kT}{ze}\sinh\left(\frac{ze\psi}{2kT}\right) \qquad (3.13)$$

where κ is the Debye-Huckel parameter for an electrolyte of type 1:1 and N_A is Avogadro's number.

The charge density in the diffuse layer, σ_d, is related to the charge density volume, ρ, as follows:

$$\sigma_d = \int_d^\infty \rho\, dx \qquad (3.14)$$

From *Equation 3.2*, ρ can be also expressed as the second order derivative of the electric potential for a dimensional system, therefore:

$$\sigma_d = \int_\infty^d \varepsilon \frac{d^2 y}{dx^2}\, dx = \varepsilon\left[\frac{dy}{dx}\right]_\infty^d \qquad (3.15)$$

Since ψ=0 when x→∞, then the derivative $(d\psi/dx)_{x\to\infty}=0$ and $\sigma_d=\varepsilon(d\psi/dx)_{x=d}$. From *Equation 3.8* it is possible to obtain a very useful expression between ψ_d and σ_d:

$$\sigma_d = \frac{-2\varepsilon\kappa kT}{ze}\sinh\left(\frac{ze\psi_d}{2kT}\right) \qquad (3.16)$$

It is worth mentioning that, by definition, the differential capacitance of the diffuse double layer, C_{dl}, can be expressed as follows:

$$C_{dl} = -\frac{d\sigma_d}{d\psi_d} \qquad (3.17)$$

Taking the derivative of *Equation 3.16* with respect to ψ_d, then the expression for C_{dl} can be described as:

$$C_{dl} = \varepsilon\kappa\cosh\left(\frac{ze\psi_d}{2kT}\right) \qquad (3.18)$$

Based on the *Equation 3.18*, *Figure 3.4* shows the dependence of C_{dl} with ψ_d. It can be observed that C_{dl} values are very small at low electrolyte concentrations and very high at greater electrolyte concentrations.
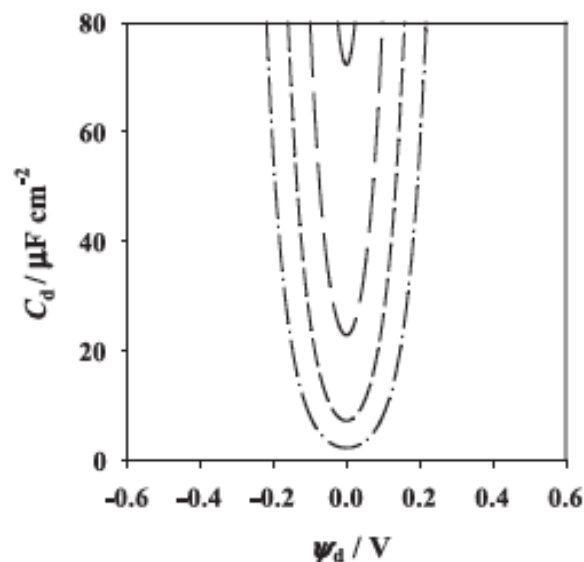
Figure 3.4. *Capacitance of the diffuse layer as a function of potential at various concentrations according to Equation 3.13. Solid line: 0.1 M, long broken line: 0.01 M, short dashed line: 0.001 M, dotted line: 0.0001 M [23].*

The importance of this model is due because it considers the dependence of the capacitance with potential. The experimental behavior of dilute solutions at potentials near to the minimum (zero charge potential where the capacitance has a minimum value) has been well described by this model. However, to apply this model it is required to assume that the dielectric constant does not depend on the distance of the electrode surface, which is not theoretically correct [45]. The electrostatic energy is regarded as the only energy making ions to come to a definite distance, X, from the electrode, ignoring other type of ion-ion interactions, which are considerable at higher adsorbate concentrations.

3.1.3.3. Stern model

Stern's model was proposed in 1924 and features a combination of the two models described above, i.e. the Helmholtz and the Gouy-Chapman models. *Figure 3.5 a* shows the schematic representation of an ideally polarizable interface divided by the inner Helmholtz plane (IHP) and the outer Helmholtz plane (OHP). The IHP corresponds to the geometric place of the adsorbed and dehydrated ions, while the OHP corresponds to the plane of closest rapprochement of the hydrated counterions [21]. Ions found in the outside layer of the OHP are mobile and their distribution depends on the equilibrium between electrostatic interactions and thermal diffusion, therefore, this layer corresponds to the diffuse layer or Gouy Chapman's layer (*Figure 3.5 b*). Moreover, the ions located outside the OHP are immobilized as they are strongly bound to the charged surface (specific adsorption). The immobile ions constitute the Stern layer.

111
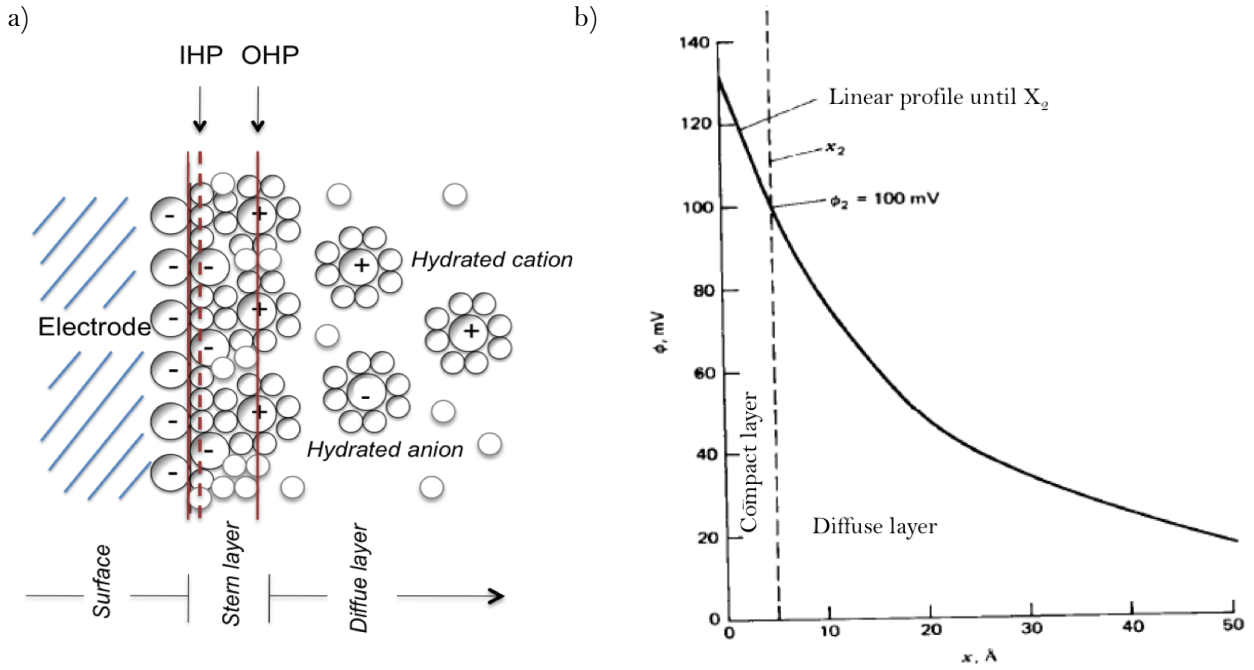
Figure 3.5. *a) Schematic model of the electrochemical double layer showing the specifically adsorbed cations, the highly hydrated anions and the cations in the negatively charged surface and b) potential profiles [23].*

Stern considered that Helmholtz and Gouy-Chapman's models are valid and exist simultaneously, so that some of the charged ions are fixed and form a plane in the proximity of the metal surface (Helmholtz excess charge) (q_H) and the other part of the ions are randomly distributed in the solution, forming the diffuse layer with some charge excess of Gouy Chapman (q_{GC}). In this way, the charge on the surface (q_{SA}) is given by the addition of both charges:

$$q_{SA} = q_H + q_{CG} \tag{3.19}$$

Whereas the electrochemical double layer behaves as an electrical capacitor, then, when the superficial potential increases, the superficial charge density increases too. The separation of the interface in two regions is equivalent to the separation of the double layer total capacitance by the contribution of two capacitances, the Helmholtz capacitance (C_H) and the Gouy-Chapman capacitance (C_{GC}). Therefore, the ratio between the double layer capacitors (C_{dl}) can be represented as follows:

$$\frac{1}{C_{dl}} = \frac{1}{C_H} + \frac{1}{C_{GC}} \tag{3.20}$$

3.1.4. Generalities of polymers and polyelectrolytes adsorption onto a surface

Interactions between polymers and surfaces are controlled by different parameters such as the surface properties (chemical nature and roughness, among others), the nature of the solvent, the polymer properties (molecular weight, concentration, chemical structure) and external factors as temperature and ionic concentration [46, 47]. In the case of polyelectrolytes, electrostatic interactions also contribute during the adsorption process onto the surface. These interactions are related to charge densities of both the polyelectrolyte and the surface, pH and salt concentration of the solution [48].

Polyelectrolytes adsorption has been studied in the last four decades and several theoretical models have been developed in order to understand the adsorption mechanism of theses molecules [49-53]. *Wiegel et al.* [54] proposed one of the first analytical calculations of the polyelectrolyte adsorption at a charged surface by calculating the adsorption threshold and the thickness of the adsorbed chain as a function of salt concentration, supposing the Gaussian statistics of a polyelectrolyte chain. *Borisov et al.* [55] proposed a scaling theory of the conformations of a weakly charged polyelectrolyte near a charged surface, which were confirmed by computer simulations [56]. *Schee* and *Lyklema* [57] showed that very thin adsorbed layers result from strong repulsions between charged monomers and that if the repulsion is screened by adding salt, the adsorbed amount of polyelectrolyte increases and the adsorbed layer gets thicker. Recently, the theoretical interest in the polyelectrolyte adsorption process is due to the importance of understanding the formation of multilayer's resulting from the successive addition of positively and negatively charged polyelectrolytes on charged surfaces from aqueous solutions [58].

A traditional characterization of the adsorption process of a polymer includes the determination of the nature of the interactions, the association constant, the coverage degree, the conformation of the polymer adsorbed at the surface and the structure of the polymer layer. The origin of the interactions between the polymers and the surface depend on the chemical structure of interacting species at local scale range, as hydrogen bounds and hydrophobicity, and at a long-range scale. Usually, adsorption isotherms are made-up in order to determine the association constants and the maximum amounts of adsorbed polymers onto the surface [59].

During the adsorption process of the polymer or polyelectrolyte onto the selected surface, the conformation may vary leading to the formation of segments with polymer in contact with the surface (trains) and segments of polymer that are not in contact with the surface (loops). *Figure 3.6* presents a schematic representation of the equilibrium conformation of a polymer adsorbed onto a surface.
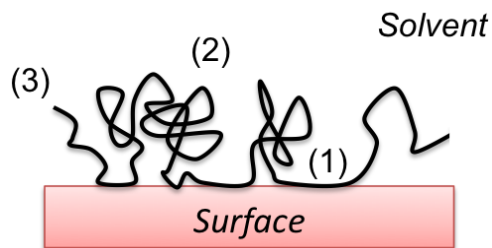
Figure 3.6. *Schematic representation of the equilibrium conformation of a polymer adsorbed onto a surface. 1) trains, 2) loops and 3) the end of the chain free in solution.*

Perkel and Ullman [60] proposed a dependence of the adsorbed amount of polymer (Γ) with the molecular weight, from which it is possible to know about the polymer structure at the surface. In this manner, if Γ is independent on the molecular weight, then the polymer is assumed to adsorb flat on the surface, however, if Γ presents a variation with the molecular weight, then the presence of trains and loops is indicated.

Polyelectrolyte charge density gives information on the conformation of the adsorbed molecule onto the surface. If polymer charge density is low, then the polyelectrolyte chains will only be attached at surfaces sites leading to the formation of extended loops. On the contrary, if polymer charge density is high, then intrachain electrostatic repulsions will make the chains segments to become stiffer, leading to the formation of trains at the surface. *Figure 3.7 a* and *b* show a schematic representation of the conformation models of the adsorption of polyelectrolytes on a charged surface [46, 53].
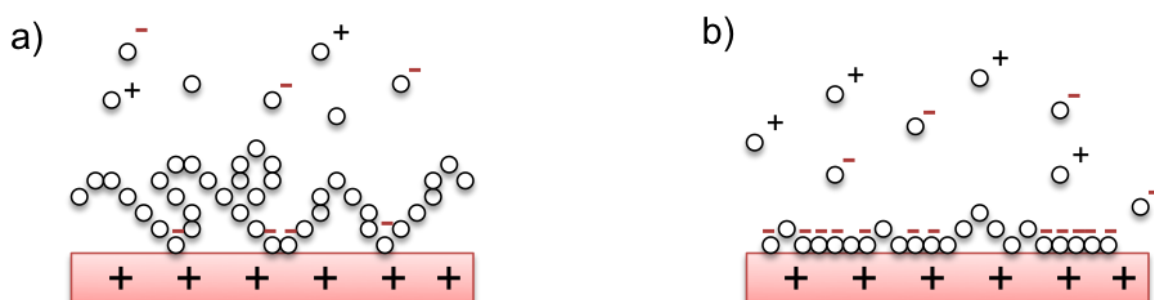
Figure 3.7. *a) Formation of a 3D-layer due to polyelectolyte loops creation (low charge density) and b) flat adsorption on the oppositely charged surface (high charge density)* [53].

3.2. Overview of the Electrochemical Impedance Spectroscopy (EIS) technique

Electrochemical Impedance Spectroscopy (EIS) is considered as a relatively modern technique, sensitive to small changes in the system, allowing the study of the properties of different materials and electrochemical systems even in less conductive medium. This technique is based on applying a sinusoidal potential perturbation to the studied system and recording the current response within the electrochemical cell, at a given frequency range. The relation between the applied potential and the current intensity monitored as a response is known as the impedance of the system and corresponds to a transfer function in the Laplace domain (*Figure 3.8*).

$$\Delta E(\omega) \longrightarrow \boxed{System} \longrightarrow \Delta I(\omega)$$

$$Z(\omega)=\Delta E(\omega)/\Delta I(\omega)$$
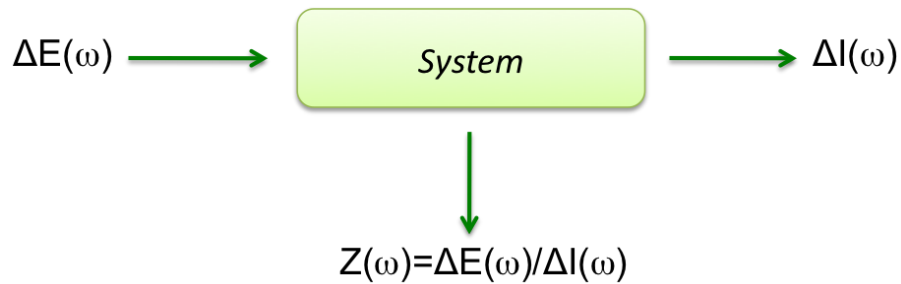
Figure 3.8. *Impedance response of a system.*

3.2.1. Interpretation of the impedance spectra by equivalent circuits

The combination of different passive electrical parameters represents a descriptive method for the impedance response of a system over a wide range of frequencies [61]. The components are usually: resistances (R), associated with the conductivity of the medium, i.e. the solution resistance or the electrode reactions resistance, also known as the charge transfer resistance; capacitors (C), corresponding to the charging of the electrochemical double layer; and inductors (L), related to relaxations taking place at the interface and adsorption processes relaxations. Different combinations of these electrical parameters are known circuits as "equivalent electric circuits".

The representation of the impedance data of a system can be performed by using different types of graphics. One of them corresponds to the complex plane graph or Nyquist plot, in which the response of the imaginary part (-Z") as a function of the real part (Z') of the impedance is shown. The impedance response generated by several well known processes and the equivalent circuits that simulate the obtained behavior are presented in the next figures. The simplest case corresponds to a series combination of a resistance and a capacitor (*Figure 3.9*), where the impedance response is reflected in a number of points at different frequency values, wherein the value -Z" tends to zero with the increase of the frequency. The system behavior reflects the arrangement of charges in the electrochemical double layer. The constant value of the real part of the impedance corresponds to the solution resistance.
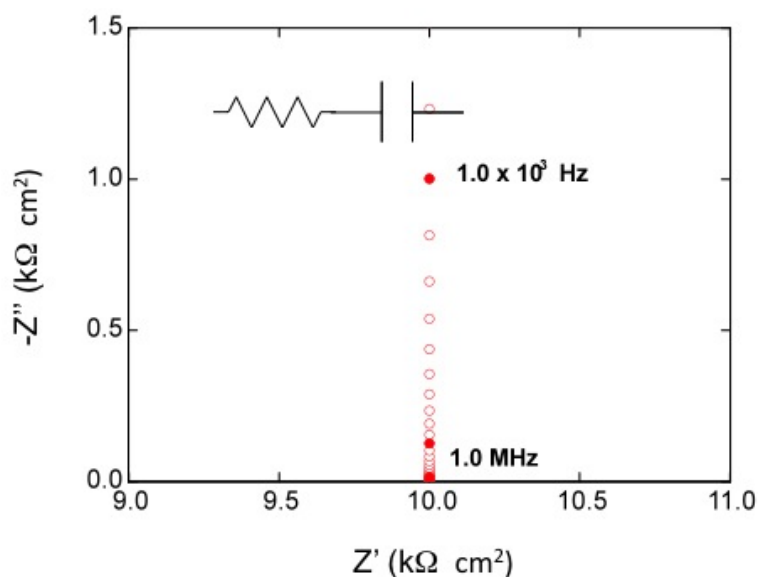
Figure 3.9. *Nyquist diagram for a circuit resistance (R)- capacitor (C) coupled in series. Frequency in Hz. Insert: equivalent circuit representing the impedance response.*

The second case represents the parallel coupling of a resistor and a capacitor. *Figure 3.10* shows the impedance response in a Nyquist plot, where it is possible to observe the presence of a semi-circle in the complex plane that corresponds to the simple analogy of a Faradaic reaction on an electrode, which takes place independently, with an interfacial capacitance C_{dl}, related to the structure of the electrochemical double layer. The time constant of the process can be calculated with the reciprocal of the frequency at the maximum point of the semicircle and corresponds to the coupling of the resistance with the interfacial capacitance.
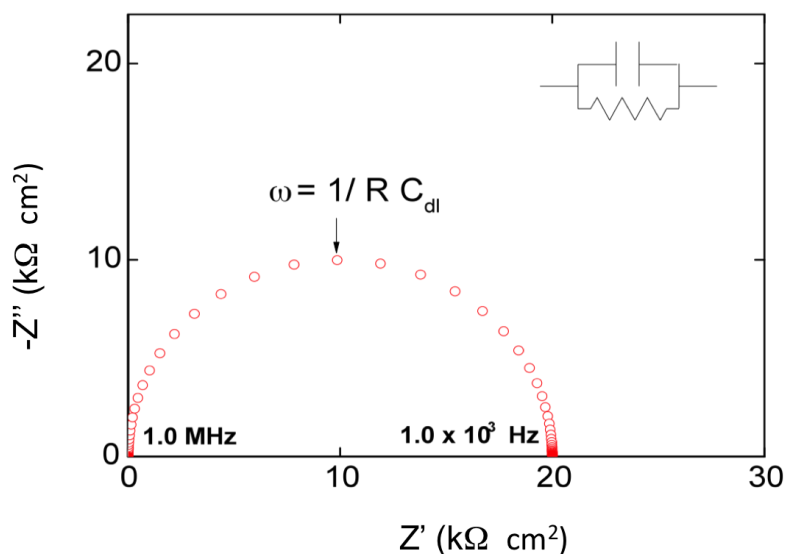
Figure 3.10. *Nyquist diagram for a circuit resistance (R)- capacitor (C) coupled in parallel. Frequency in Hz. Insert: equivalent circuit representing the impedance response.*

Figure 3.11 shows the graphical representation of an electrochemical reaction, in which the presence of a resistance coupled in series with the parallel R–C circuit is depicted by a shift of the semi-circle to higher values of the axis corresponding to the real part of the impedance. This resistance represents the solution resistance, R_s.
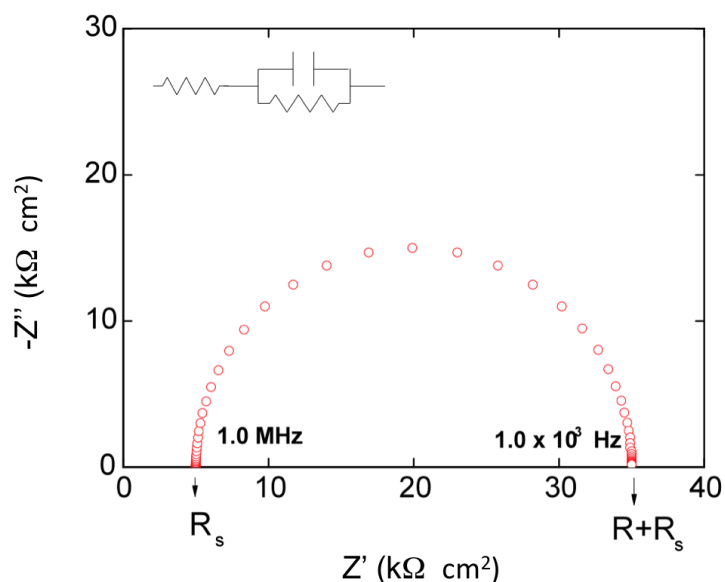
Figure 3.10. *Nyquist diagram for a series coupling of the solution resistance, R_s, with the circuit in parallel: resistance (R)- capacitor (C). Frequency in Hz. Insert: equivalent circuit representing the impedance response.*

Finally, another fundamental equivalent circuit is Randles circuit, in which the charge transfer resistance, R_{ct}, is coupled in series with a Warburg impedance, which depends on frequency and corresponds to a diffusive process.
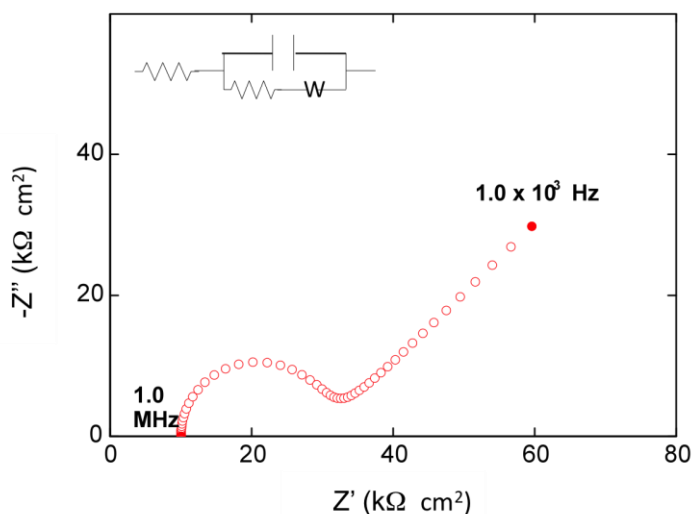
Figure 3.11. *Nyquist diagram of Randles circuit. Frequency in Hz. Insert: equivalent circuit representing the impedance response.*

The analysis of a Randles circuit has two limiting cases: first one is identified at low frequencies, when ω approaches 0, here, the behavior is dominated by the species diffusion and the response corresponds to a straight line and a slope of 0.5. The second is identified at high frequencies, at which the Warburg impedance is a very small value compared to the R_{ct} value, in this case, the answer is a semicircle. *Figure 3.11* shows the impedance response of a charge transfer process controlled by diffusion in semi-infinite layer.

On the other hand, there are also mathematical models that allow obtaining a detailed description of the process under study and to get a greater insight on its kinetics [62]. Such models are known as reaction mechanisms in Electrochemical Impedance Spectroscopy. This approach requires the development of mathematical models that take into account both the experimental factors and the physicochemical properties of the system. The physicochemical properties distribution, such as charge distribution and species concentration is determined by the charge and mass balance subject to the boundary conditions of the system.

In this thesis, the analysis of the experimental data will be performed by using equivalent circuits, with the prospective of taking into account the obtained results and parameters to propose, in a future, a reaction mechanism for the adsorption process of DNA onto metal surfaces.

3.2.2. Adsorption impedance theory

Specific adsorption of ions on metal surfaces has been investigated for several years and by different research groups [14-18,63,64]. Most studies focus on thermodynamic and structural aspects of the adsorption process, which goal was to determine the coated surfaces of a specific surface area by a specific ion to characterize the structure of the adsorbed layer [65,66]. The adsorption impedance theory was initiated by the works of *Ershler* [22], *Frumkin* and *Melik-Gaykazyan* [19] in the 80's. One of the simplest cases that explains the adsorption impedance theory is the adsorption process of a species, which can be simulated by an equivalent circuit including a resistance solution (R_s), a double layer capacitance (C_{dl}) and three electrical parameters coupled in series that describe the adsorption process, i.e. an adsorption resistance (R_{ad}), a Warburg impedance (W_{ad}) and an adsorption capacitance (C_{ad}). The specific meaning of each electrical parameter will be presented in the following section.

3.2.2.1. Adsorption impedance expression and its equivalent circuit

All electrodes show a capacitance called the double layer capacitance (C_{dl}), independently of the Faradaic reactions. While working at open circuit potential, the reflected response in the measurements is due to a non-faradaic process. Therefore, the impedance response observed is the arrangement of

charges at the interface due to the transport of species from the bulk of the solution to the vicinity of the electrode. The response is mostly capacitive. According to the adsorption impedance theory [68], impedance data can be transformed into complex capacitance with the following equation:

$$C(\omega) = \frac{1}{[Z(\omega) - R_s] \times A \times j\omega}$$

(3.21)

where $C(\omega)$ is the complex interfacial capacitance, $Z(\omega)$ is the complex impedance, R_s is the solution resistance, A_e is the area of the electrode and j is the imaginary number. The equivalent circuit that allows simulating this response is represented in *Figure 3.12*.
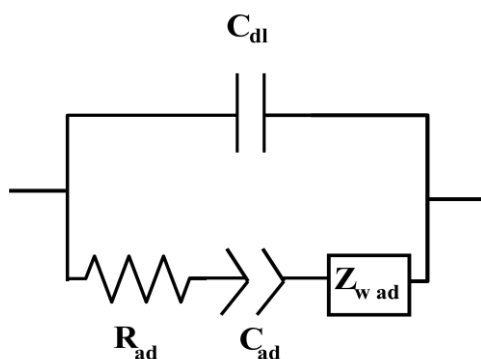
Figure 3.12. *Equivalent circuit representing the complex interfacial capacitance.*

The physical meaning of each of the electrical parameters are described as follows: the double layer capacitance (C_{dl}) is located in the limit when the frequency tends to infinite, $\omega \to \infty$, and is also known as C_{HF}, i.e. capacitance at high frequencies. The adsorption capacitance C_{ad} is located in the limit when the frequency tends to zero, $\omega \to 0$, and is also known as C_{LF}, i.e. capacitance at low frequencies. C_{ad} value can be evaluated as follows: $C_{ad} = C_{LF} - C_{HF}$, and is usually modeled by a constant phase element (CPE) for a non-ideal capacitor. The adsorption resistance, R_{ad}, indicates the ease of the adsorbate to move from adsorbed to the pre-adsorbed state. This value decreases as the concentration increases and tends to zero. The diffusion Warburg impedance, $Z_{w,ad}$ is related to the mass transfer of the adsorbate, including the adsorbate diffusion from the bulk of the solution to the Helmholtz plane.

3.2.2.2. Graphic representation of complex impedance data transformed into complex capacitance data

Due to its physical meaning, $C(\omega)$ is called interfacial capacitance and can be represented through complex diagrams or Bode-type graphics. *Figure 3.13* shows the changes of the capacitance spectra shape with the adsorption rate, i.e. the spectra are arcs, semicircles and "depressed arcs" for the extremes

of slow and fast adsorption, respectively. The capacitance spectra with a skewed-arc shape represents the intermediate cases of the adsorption rate [68].
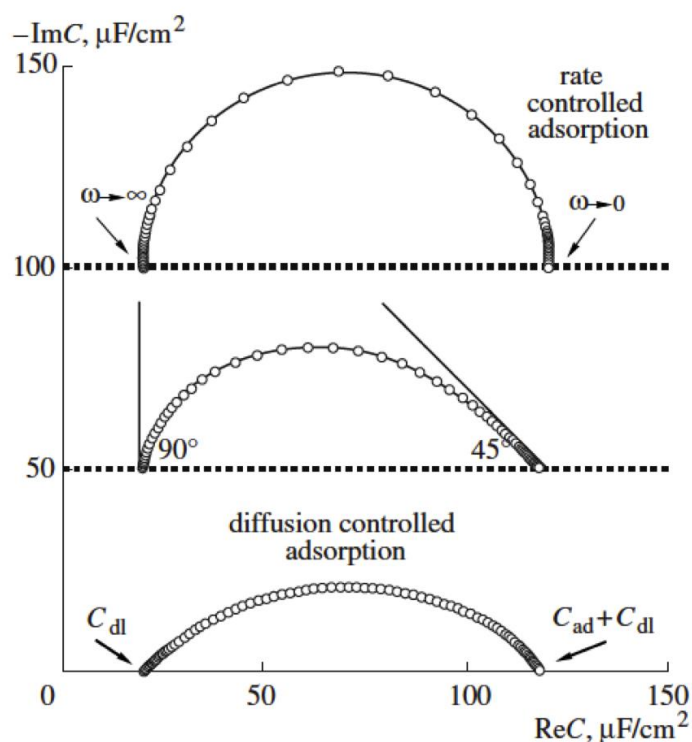
Figure 3.13. *Illustration of the changes on the capacitance spectra shape with the adsorption rate [68].*

3.3. Experimental study of the adsorption of DNA molecules onto platinum electrodes

3.3.1. Experimental conditions for the Pt-DNA/TE buffer interface

The description of the reagents, buffer Tris-HCl/EDTA preparation and DNA/Buffer solutions are presented in *Sections 2.3.1., 2.3.2.* and *2.3.3.* of this work.

3.3.1.1. Double-layer capacitance measurements

DNA adsorption at the electrode was monitored in terms of double-layer capacitance response in a wide range of potentials. Capacitance measurements were carried out in a 1260 FRA instrument coupled to a 1287 potentiostat both from Solartron, Inc. A two identical platinum electrode cell with a surface of 0.25 cm² each was selected for the counter and work electrodes and a satured calomel electrode (SCE) was used as the reference The following parameters were chosen: potential perturbation amplitude 10mV, frequency 1 kHz and a polarization range from -1.1 to 1.3V vs. SCE. All measurements were

carried out at three different temperatures (i.e., 20, 30 and 40 ºC), controlled by the recirculation bath. *Figure 3.14* shows the experimental setup for double-layer capacitance measurements.

3.3.1.2. Impedance measurements

EIS measurements were carried out in a 1260 FRA instrument coupled to a 1287 potentiostat both from Solartron, Inc. Potentiostatic mode at open circuit potential was used for each measurement, applying potential perturbation amplitude of 10 mV in a frequency range of 1 kHz-1 mHz. A two identical platinum electrode cell with a surface of 0.25 cm² each one was used to obtain impedance spectra. Before each EIS experiment routinely a cyclic voltammetry in 0.5 M H_2SO_4 at 50 mV/s was applied to guaranty the cleanliness of the electrodes. Commercial software Zplot® was used to collect impedance data, and commercial software Zview® allowed calculating theoretical parameters from an equivalent circuit able to fit the experimental results. All measurements were also carried out at the temperatures of 20, 30 and 40 ºC, controlled by the recirculation bath and allowing a rest period for each sample to ensure a steady-state measurement. *Figure 3.14* shows the experimental setup for EIS measurements.
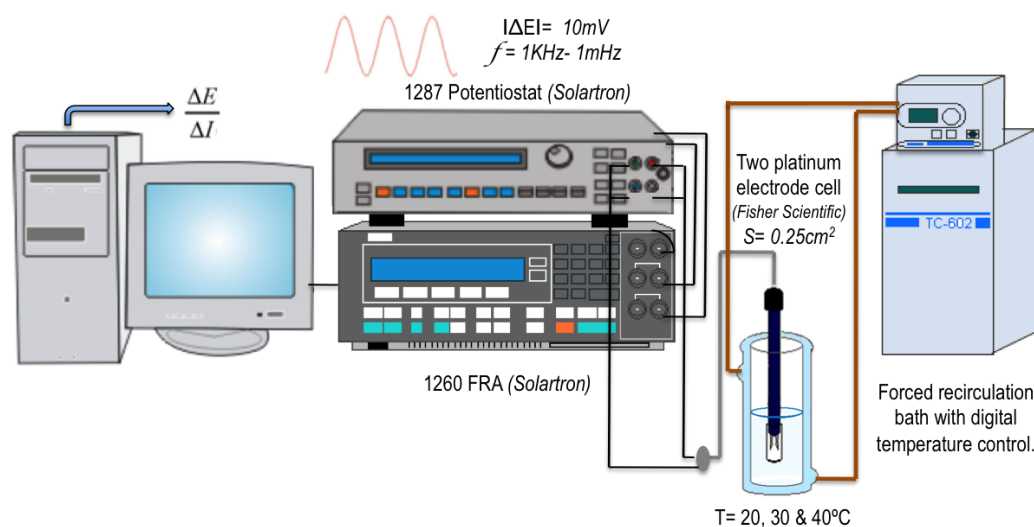
Figure 3.14. *Experimental setup used for double-layer capacitance and EIS measurements.*

3.3.2. Experimental results and discussion for the Pt-DNA/TE buffer interface

3.3.2.1. Differential capacitance curves of the double layer as a function of potential

Figure 3.15 shows the typical double-layer capacitance curves obtained for the TE buffer in absence and presence of DNA concentrations of 0.1, 0.4 and 0.6 mg/mL at 30 °C. In all the cases, when DNA is present, the capacitance-potential dependence shows a decrement of double-layer capacitance values

observed in the TE buffer solutions at more positive polarization potentials than -0.485 V vs. SCE, suggesting that adsorption starts at this polarization. Since the polarization potential is an important parameter in any adsorption-desorption process, it could influence the structure and orientation of any charged adsorbate and consequently, the impedance response will depend on it [15-16]. Since our study is focus on the Pt-DNA/TE buffer interface and taking into account that DNA is negatively charged polyelectrolyte, then the polarization corresponding to the open circuit potential, at which the impedance measurements are carried out needs to be in the polarization range at which DNA is being adsorbed onto the electrode. In this figure it is also possible to observe that double-layer capacitance values increase when DNA concentration increments. On the other hand, at low DNA concentrations, the double-layer capacitance values reach a minimum at 15 mV vs. SCE, which is not visible at higher DNA concentrations. Based on these observations and according to the classical double-layer theory [69-70], we have related the minimum observed in the double-layer curves with the potential of zero charge (PZC), so at more positive potentials than the PZC, DNA adsorption will be highly favorable. In general, the behavior observed at the double-layer capacitance curves shown in *Figure 3.15* is consistent with the double-layer capacitance dependence on the adsorbate concentration as was early demonstrated by Grahame and Devanathan [16,63]. Furthermore, the dependence of PZC with the adsorbate concentration is not described by the Esin-Markov effect [64], this fact strongly suggests that a non-specific adsorption of DNA molecules is taking place at the electrode surface. Thus, all the adsorption process cited in this manuscript is related to the adsorption of the negatively charged DNA molecules. Similar behavior has been observed at the other studied temperatures.
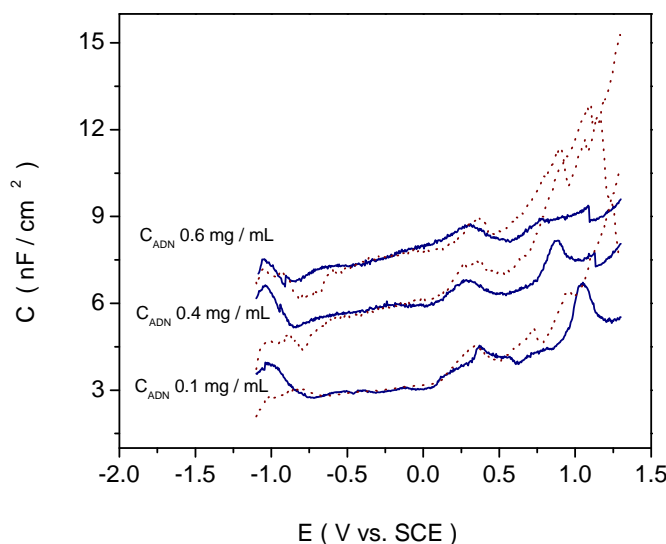
Figure 3.15. *Double-layer capacitance curves as a function of polarization potential obtained for the TE buffer in absence (dotted line) and presence (continuous line) of DNA concentrations of at 30 °C.*

3.3.2.2. Complex impedance and capacitance spectra monitored at OCP

Impedance measurements were carried out at open circuit potential which was around of 300 mV vs. SCE, this potential assures both, adsorption and preservation of DNA molecules (i.e. chemically unmodified). *Figure 3.15* shows some raw impedance data presented as complex plane diagrams for the adsorption of DNA on the platinum electrode with the temperature and concentration of DNA as parameter.
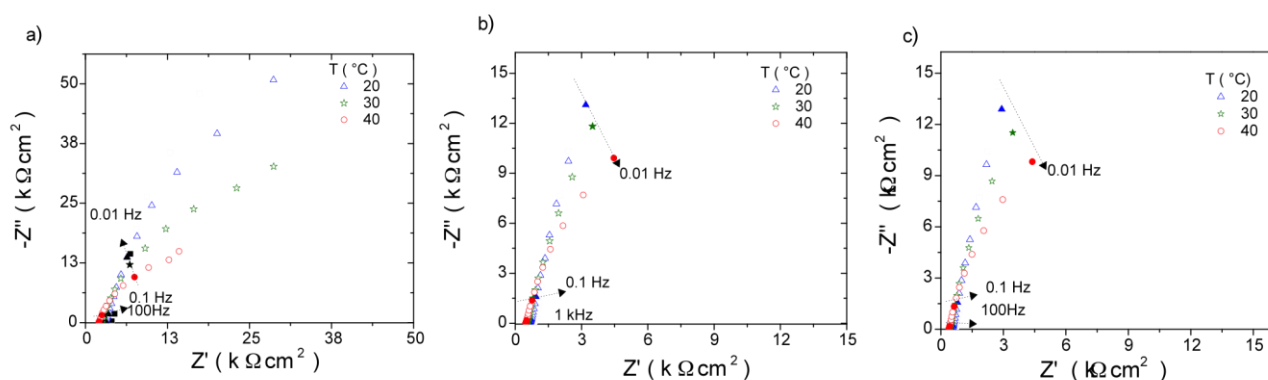
Figure 3.15. *Raw impedance data for DNA concentrations of 0.3, 0.8 and 2.5 mg/mL at the temperatures of 20, 30 and 40 ºC. Frequency in Hz.*

Impedance was then transformed into complex capacitance C(ω) according to *Equation 3.21. Figure 3.16* shows a set of plots that reveal the results obtained from the adsorption study of DNA molecules onto the platinum electrode at different concentrations and temperatures by using impedance measurements. Similar behavior is observed for the other concentrations and temperatures studied in this work. In all cases, the obtained results are presented and interpreted by using the adsorption impedance theory, as has been exhaustively proposed by *Pajkossy et al.,* [71-75] among others authors [63-64].

The trend in all spectra shown in *Figure 3.16* is consistent with the trend of capacitance spectra observed in an adsorption process, as was expected [14-18]. At the three temperatures, the complex capacitance presents a similar typical frequency (f_ω) dispersion depicted as a part of a well-defined depressed arc-shaped (1kHz<f_ω<0.1) and an ascending curve at low frequencies (f_ω< 0.1 Hz). At high frequencies, our spectra can be adequately modeled by a similar equivalent circuit proposed by FMGR [19], thus the complex capacitance dispersion is described by the serial arrangement of three electrical elements: an adsorption resistance (R_{ad}) related to a slow electrosorption process, a constant phase element (CPE), associated to either the surface heterogeneity or to the distributed time constant [71,72], which represents in this case the non-ideal adsorption capacitance (C_{ad}) and a Warburg-like diffusion impedance ($Z_{W,ad}$) associated to the diffusion of the adsorbing DNA molecules at the interface.

In order to completely describe the interface, the double-layer capacitance (C_{dl}) is considered by adding a capacitor in a parallel arrangement. C_{dl} can be associated to the real complex capacitance value obtained at high frequencies limit, while C_{ad} is related to the difference of the real part of the capacitance obtained at low and high frequencies limits. According to the impedance adsorption theory [14-19], the complex capacitance spectra at high frequencies may present two limiting cases either as a perfect loop or a depressed one [15,64]: if the spectra are perfect loops, then the adsorption process is slow and controlled by the electrosorption phenomena. On the other hand, if the spectra depict depressed loop, the adsorption is fast and controlled by the adsorbate diffusion. The ascending curve observed at lower frequencies than 0.1 Hz is associated to an incipient charge transfer process, which was taken into account by adding an additional resistor (R_d) in parallel in one of the branches of the equivalent circuit [73]. R_d is associated to a possible and incipient faradaic process from reaction of impurities or oxygen traces presents at the working solution.
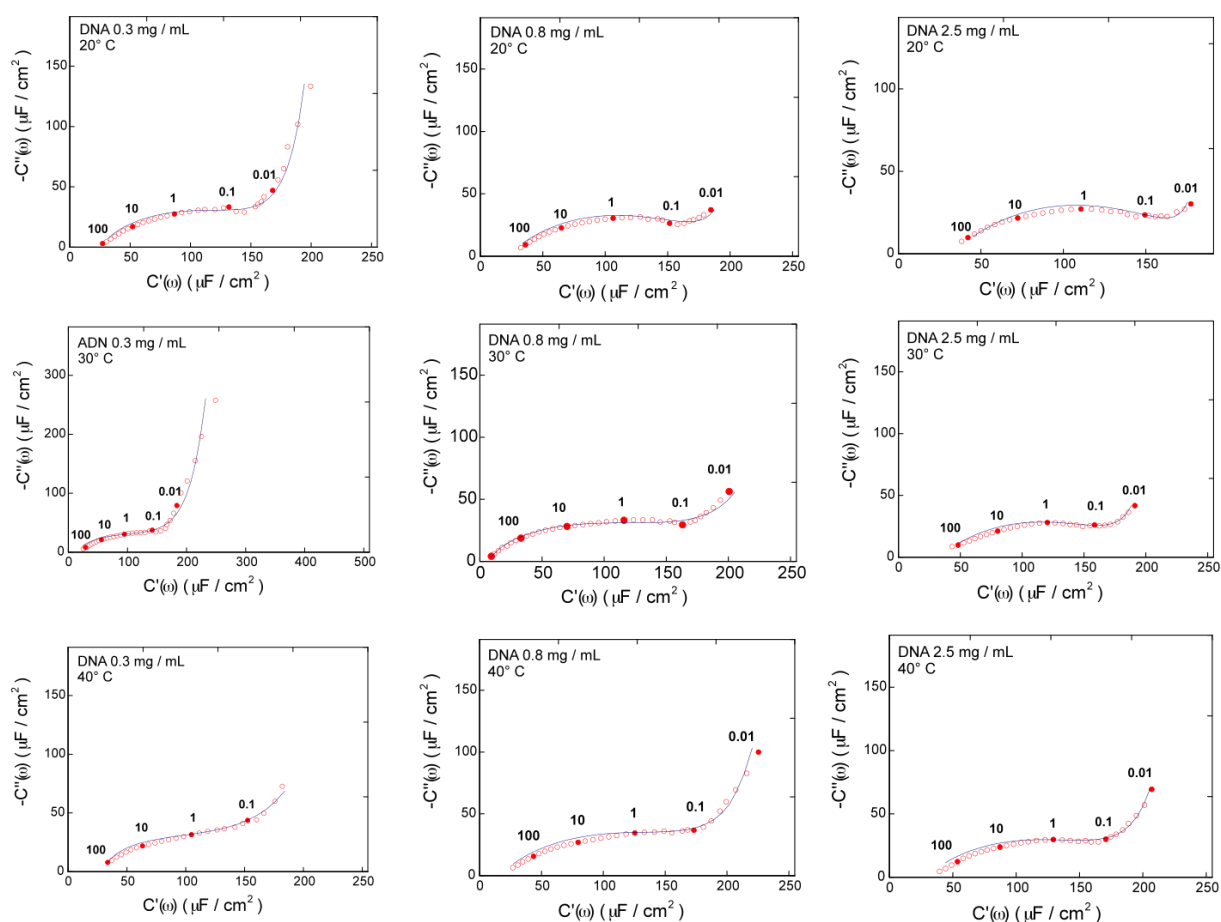
Figure 3.16. *Complex capacitance data for DNA concentrations of 0.3, 0.8 amd 2.5 mg/mL at the temperatures of 20, 30 and 40 ºC. Frequency in Hz.*

A schematic representation of the equivalent circuit is presented in *Figure 3.17* and its corresponding complex capacitance transfer function is given by the following expression:

$$C(W) = C_{dl} + \cfrac{1}{R_{ad}jW + S_{ad}\sqrt{jW} + \cfrac{(jW)^{1-n}}{C_{ad}}} + \cfrac{1}{R_{ct}jW} \tag{3.22}$$

where $\sigma_{ad}(j\omega)^{-1/2}$ corresponds to the diffusional impedance with its coefficient $\sigma_{ad.}$ On the other hand, n is the inherent parameter of the CPE [71,72] according to:

$$CPE = \cfrac{1}{(jW)^n C_{ad}} \tag{3.23}$$
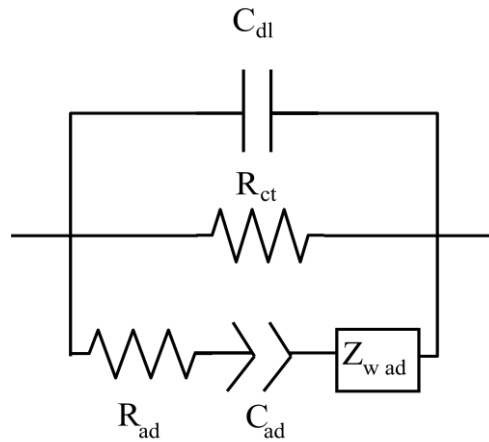
Figure 3.17. *Equivalent circuit representing the complex capacitance for the Pt-DNA/ TE buffer interface.*

The equivalent circuit shown in *Figure 3.17* and *Equation 3.22* were employed to interpret the experimental complex capacitance data obtained at each one of the experimental conditions presented in this work. In *Figure 3.16* it is possible to observe a good correlation between the experimental data and the theoretical spectrum for the equivalent circuit described previously. The resulting fittings are depicted as continuous lines in *Figure 3.16* and the obtained electrical parameters are summarized in *Table 3.2*.

Table 3.2.- *Electrical parameters obtained by fitting the equivalent circuit in Figure 3.17. to the experimental complex data for 0.3, 0.8 and 2.5 mg/ml at 20, 30 and 40 ºC.*

C_{DNA} mg/mL	T ºC	C_{dl} µF/cm^2	C_{ad} µF/cm^2	n	R_{ct} Ω cm^2	R_{ad} Ω cm^2	σ_{ad} Ω cm^{-1} s$^{1/2}$	χ^2
0.3	20	27.3	133.2	0.936	4.7×10^5	13.1	1909.7	0.006
	30	15.6	141.4	0.892	2.4×10^5	4.3	911.3	0.008
	40	30.25	135	0.870	1.3×10^5	13.38	879.7	0.004
0.8	20	22.4	158.9	0.961	5.54×10^5	0.6	1213.5	0.004
	30	9.3	170.5	0.94	2.77×10^5	0.5	666.3	0.004
	40	17.9	175.03	0.927	1.4×10^5	0.5	674.3	0.012
2.5	20	33.4	144.6	0.954	5.9×10^5	0.37	1244.4	0.009
	30	37	132.7	0.96	4.3×10^5	0.06	1191.1	0.003
	40	30.6	152.6	0.932	2.3×10^4	0.25	715.2	0.003

From this table we can observe that the temperature does not have a noticeable effect on C_{dl}, R_{ad}, C_{ad} and R_{ct} parameters, which are at the same order of magnitude in the whole range of temperatures studied. However, the temperature effect becomes evident in the diffusional parameter σ_{ad} which has one order of magnitude difference between the temperature limits, resulting in the largest σ_{ad} value at 20°C. This fact suggests that the diffusional process of DNA molecule inside the interface is slower at this temperature and increases at higher temperatures. It should be point out that at the whole temperature range; DNA adsorption takes place under a diffusional control. This conclusion is derived noticing that R_{ad} is always three orders of magnitude smaller than σ_{ad}. Then, the main contribution to the complex capacitance is rather due to DNA diffusion inside the diffuse layer and not to the electrosorption process, thus the electrosorption phenomenon is not the limiting step [15]. This statement is also in good agreement with the complex capacitance spectra arc-shape shown in *Figure 3.17*, where it becomes evident a depressed loop obtained at high frequencies and it also supports a control by spatially dependent concentration fields. Finally, it is noted from *Table 3.2.* that R_{ct} falls in the range of 10^5 Ω/cm^2, being a high value that limits the charge transfer and confirming that at OCP the interface possess a capacitive behavior and only an incipient and negligible charge transfer is present.

3.3.2.3. Evaluation of the adsorption parameters as a function of temperature and concentration of DNA

Figures 3.18 and *3.19* show the behavior of the electrical parameters C_{dl} and C_{ad}, respectively, included in the equivalent circuit shown in *Figure 3.17*, as a function of the DNA concentration at each one of the temperatures studied. As we can observe, the concentration-dependence in all the electrical parameters is almost the same no matter the temperature studied.
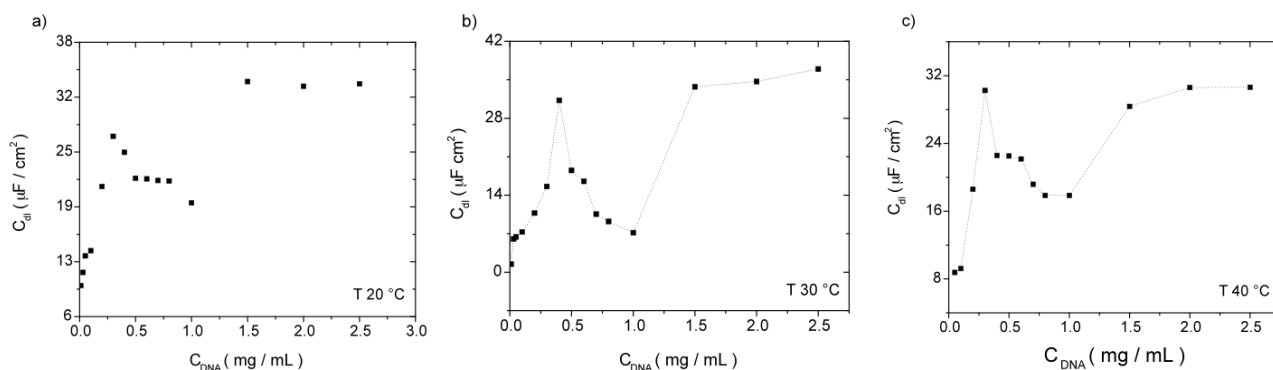
Figure 3.18. *Double-layer capacitance, C_{dl}, as a function of DNA concentration at the temperatures of a) 20, b) 30 and c) 40 °C.*
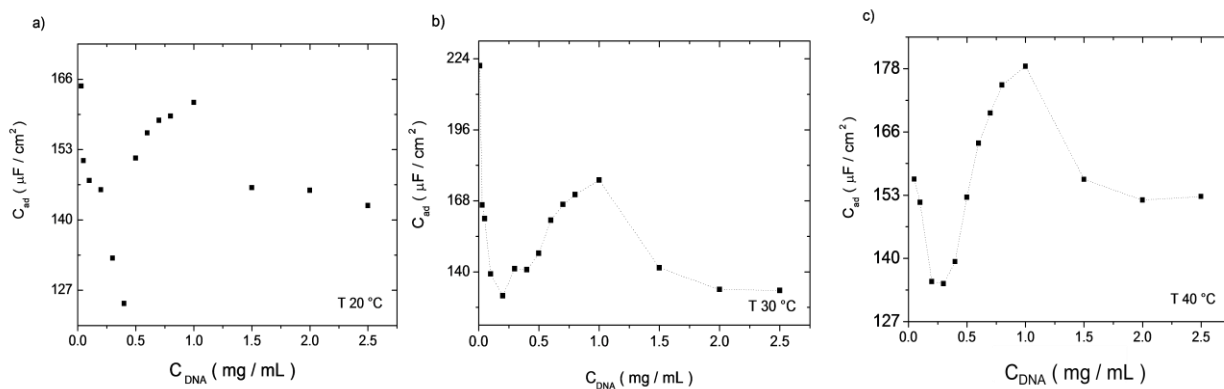
Figure 3.19. *Adsorption capacitance, C_{ad}, as a function of DNA concentration at the temperatures of a) 20, b) 30 and c) 40 °C.*

This feature in these curves strongly suggests that the interfacial double-layer structure is amenably altered when DNA concentration is modified. According to the most simple double-layer model [70,74], the changes on C_{dl} could reflect the changes of the interface thickness d as well as changes on dielectric constant ε. Consequently, if ε is considered as a constant value, changes in C_{dl} and C_{ad} as a function of DNA concentration will be related to the interface thickness [74]. In this way, we

are relating the two noticeable changes on C_{dl} and C_{ad}, observed at 0.36 and 1.5 mg/mL to two possible structural transitions in the adsorbed DNA. These values are close to the ones found for C* and C_e determined though a rheological study carried out at the same experimental conditions to those applied in our work and described in *Chapter 2*. A very good agreement is also found between the values determined in the present work and those reported by *Mason et al.* [77]. This fact allows proposing that the changes on C_{dl} and C_{ad} are related to the double-layer thickness, which is presumably associated to the conformational structure of DNA, and chains interactions such as overlapping and entanglements.

Figure 3.20 shows the R_{ad} concentration-dependence at the three studied temperatures. R_{ad} curves show an adsorption resistance decrement while increasing DNA concentration suggesting that the electrosorption process is less predominant when DNA solution is more concentrated.
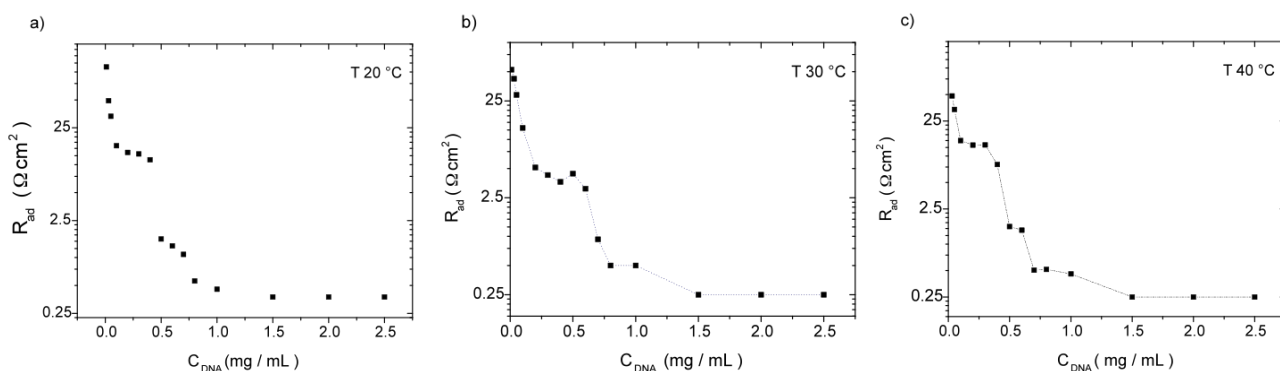
Figure 3.20. *Adsorption resistance, R_{ad}, as a function of DNA concentration at the temperatures of a) 20, b) 30 and c) 40 °C.*

3.3.2.4. Analysis of average time constant of DNA molecules adsorption process onto the platinum surface

An additional analysis can be done if the mean characteristic time constant (τ_c) is evaluated from the high frequency loop observed at the complex capacitance spectra for each one of DNA concentrations studied. An inspection of τ_c at different temperatures, taking the DNA concentration as parameter is shown in *Figure 3.21*, from which is evident that τ_c reaches its higher values at the lowest DNA concentrations and slowly decreases in the millisecond range until suddenly increases at 0.4 mg/mL to start decreasing and remains constant at higher concentration than 1.5 mg/mL. As it can be observed, the evaluation of the mean τ_c is also an useful method to determinate DNA transitions and their correspondence with C* and C_e. Moreover, the τ_c range of values is in adequately agreement with those calculated to the reorganization time of the diffuse double-layer [16, 75, 79]. Furthermore, it

should be notice that at constant temperature and at the semi-diluted regime ($C_{DNA} \leq 0.36$ mg/mL), τ_c decreases while DNA concentration increases.
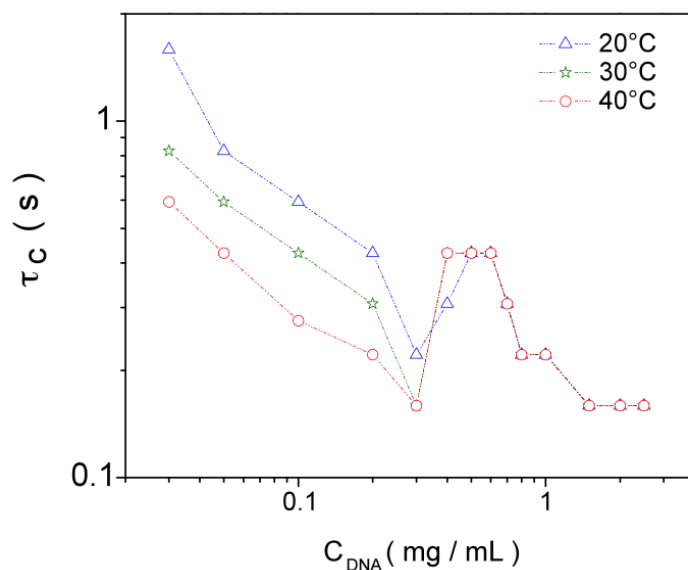
Figure 3.21. *Characteristic time constant of the process, τ_c, as a function of DNA concentration at the temperatures of 20, 30 and 40 °C.*

3.3.3. Particular conclusions for the adsorption of DNA molecules in solution on platinum

A detailed adsorption study of calf thymus DNA onto platinum electrodes was evaluated in a wide concentration and temperature range and was presented by using electrochemical impedance spectroscopy. All the impedance data were transformed into complex capacitance values and were interpreted on the basis of the impedance adsorption theory using a similar FMGR equivalent circuit. We can conclude that at Open Circuit Potential (OCP), a diffusion controlled non-specific adsorption of DNA molecules is taking place at the interface. Moreover, through a detailed analysis of each one of the electrical parameters obtained at each studied temperature it was possible to identify two well-defined interfacial transitions around two DNA concentrations, i.e. 0.36 and 1.5 mg/mL, which were related to the overlap and the entanglement concentrations early determined by rheological methods. Thus, the changes in the interfacial structure, reflected as C_{dl}, C_{ad} and R_{ad} parameters, strongly depend on the DNA nature present inside the solution. All the results allow proposing that impedance measurements interpretation by the impedance adsorption theory is a well suitable method to characterize DNA adsorption and to identify the structural transitions on the metal-DNA/TE buffer interface.

3.4. Experimental study of the adsorption of DNA molecules onto gold electrodes

3.4.1. Experimental conditions for the Au-DNA/TE buffer interface

The description of the reagents, buffer Tris-HCl/EDTA preparation and DNA/Buffer solutions are presented in *Sections 2.3.1., 2.3.2.* and *2.3.3.* of this work.

3.4.1.1. Impedance measurements

EIS measurements were carried out in a 1260 FRA instrument coupled to a 1287 potentiostat both from Solartron, Inc. A convetional three-electrode cell was used for these measurements. A gold cylinder and gold disk were used as the counter and work electrode, respectively, and a satured calomel electrode (SCE) was used as the reference. Potentiostatic mode at open circuit potential was used for each measurement, applying potential perturbation amplitude of 10 mV in a frequency range of 1 kHz-1 mHz. Before each EIS experiment routinely a cyclic voltammetry in 0.1 M $HClO_4$ at 50 mV/s was applied to guaranty the cleanliness of the electrodes. Commercial software Zplot® was used to collect impedance data, and commercial software Zview® allowed calculating theoretical parameters from an equivalent circuit able to fit the experimental results. *Figure 3.14* shows the experimental setup for EIS measurements. All measurements were also carried out at the temperatures of 25, 30 and 25 °C, controlled by the recirculation bath and allowing a rest period for each sample to ensure a steady-state measurement.

3.4.2. Experimental results and discussion for the Au-DNA/TE buffer interface

3.4.2.1. Complex impedance and capacitance spectra monitored at OCP

In order to study the adsorption process of DNA molecules onto gold electrodes by coupling Electrochemical Impedance Spectroscopy technique with Surface Plasmon Resonance technique (SPR), the chosen temperatures for the experimental study were selected in a lower temperature range that the range used for the impedance study of Pt-DNA/TE buffer interface. Therefore, the temperature range for the Au-DNA/TE buffer interface study will be limited to values 5 °C greater and lower than the average room temperature, i.e. 20, 25 and 30 °C. In this chapter, impedance results will be presented and discuss, whereas SPR results will be discuss in detail in *Chapter 5* of this thesis.

Figures 3.22 a, b and *c* show Nyquist plots for several DNA concentrations of 0.05, 0.4 and 2.5 mg/mL at the temperatures of 20, 25 and 30 °C. The results mainly reveal the typical behavior of an unideal double-layer capacitance, which is consistent with the experimental conditions of the study and with the results obtained for the Pt-DNA/TE buffer study. In this way, the experimental results show

that the DNA adsorption process onto gold electrodes is mainly capacitive [80]. This response represents the structural arrangement of DNA molecules on the electrochemical double-layer formed at the gold surface and is in good agreement with the study of the adsorption or calf-thymus DNA molecules onto platinum surfaces previously discussed [80,81]. It is possible to observe a displacement of each spectra towards lower values of the real part of the impedance (Z') at each regime while increasing DNA concentration. A greater amount of negatively charged DNA molecules at higher DNA concentrations causes an increment in the solution's conductivity [82].
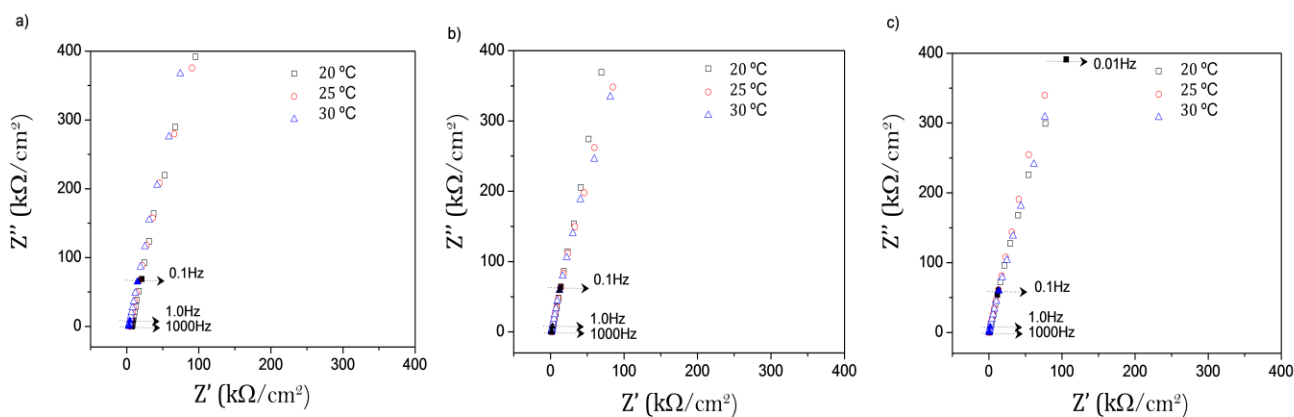
Figure 3.22. *Nyquist plots for Au-DNA/TE buffer interface at DNA concentrations a) 0.05, b) 0.4 and c) 2.5 mg/mL and at the temperatures of 20, 25 and 30 ºC.*

Impedance data was transformed into complex capacitance according to the adsorption impedance theory used by *Pajkossy* and *Kolb* and recently applied to DNA molecules adsorption onto platinum surfaces [14-19, 80, 81], using *Equation 3.21*. The equivalent circuit presented in *Figure 3.17* and its complex capacitance transfer function given by *Equation 3.22* were used to interpret the experimental complex capacitance obtained in this study.

The arrangement of three electrical parameters in series represents the complex capacitance dispersion observed at high frequencies (1 kHz $< f_\omega <$ 1.0 Hz) and describes DNA molecules adsorption process taking place at the electrode surface. An adsorption resistance (R_{ad}), a constant phase element (CPE) representing a non-ideal adsorption capacitance (C_{ad}) and a Warburg-like diffusion impedance ($Z_{W,ad}$) make up this arrangement. A double-layer capacitance (C_{dl}) was added in order to explain Au/Calf-thymus DNA interface. An ascending curve was observed at low frequencies ($f_\omega <$ 1.0 Hz) and is related to an incipient charge transfer resistance (R_{ct}). Since the adsorption process is carried out at open circuit potential, this parameter is associated to a possible reaction of impurities or oxygen traces in the working solution [73]. The physical meaning of each electrical parameter is explained in detail in *Section 3.3.2.2.* of this thesis.

Figures 3.23 a, b and c show the complex capacitance data obtained for DNA concentrations of 0.05, 1.0 and 3.0 mg/mL, representing the typical behavior of the complex capacitance response in each characteristic regime of DNA solutions, i.e. dilute, semi-dilute without entanglements and semi-dilute regime with entanglements, respectively. At high frequencies a depressed loop can be observed, showing that the adsorption carried out on the electrode surface is rapid and is controlled by adsorbate diffusion [64].
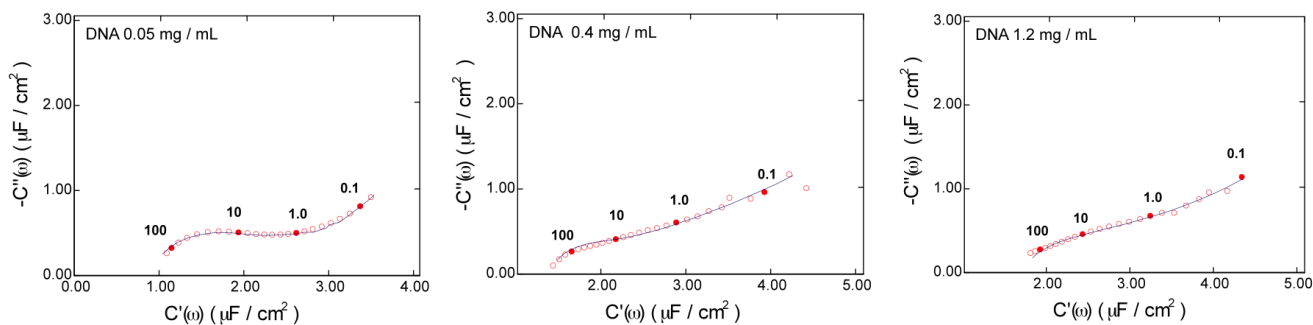
Figure 3.23. *Complex capacitance data for DNA concentrations 0.05, 0.4 and 2.5 mg/mL and at the temperatures of 20, 25 and 30 ºC. Frequency in Hz.*

The equivalent circuit presented in *Figure 3.17* and the *Equation 3.22* were used to fit the experimental data to obtain the value for each electrical parameter involved in the adsorption process at the gold electrode surface. The continuous lines observed in the set of plots of *Figure 3.23* depict the resulting fittings.

Table 3.3 summarizes the estimated parameters for DNA concentrations shown in *Figure 3.23*. In this table we can observe that R_{ad} and σ_{ad} have the same order of magnitude at lower DNA concentrations, suggesting a mixed process, controlled by DNA diffusion and an electrosorption process. However, the diffusional parameter σ_{ad} increases with increasing DNA concentration, showing that the main contribution to the complex capacitance is due to diffusional control [15]. It is evident that R_{ct} values are larger than 10^5 Ω/cm^2, representing the presence of the incipient charge transfer at the interface and confirming the experimental conditions of this study (OCP).

Table 3.3.- *Electrical parameters obtained by fitting the equivalent circuit in Figure 3.17. to the experimental complex data for 0.05, 0.4 and 2.5 mg/ml at a temperature of 25 ºC.*

C_{DNA} mg /mL	C_{dl} μF/cm²	C_{ad} μF/cm²	n	R_{ct} Ω cm²	R_{ad} Ω cm²	σ_{ad} Ω cm⁻¹ s¹ᐟ²	χ^2
0.05	0.985	2.328	0.850	7.653×10^6	3 289.06	3.942×10^4	0.0005
0.4	1.420	2.360	0.774	3.269×10^7	2 621.82	4.174×10^3	0.0013
2.5	1.583	2.559	0.739	8.484×10^8	1 958.00	4.193×10^5	0.0004

3.4.2.2. Evaluation of the adsorption parameters as a function of temperature and concentration of DNA

Double-layer capacitance (C_{dl}) behavior was firstly analyzed as a function of DNA concentration and temperature and is presented in *Figure 3.24*. C_{dl} values were obtained by the fitting the equivalent circuit to the experimental data. It can be observed that C_{dl} values increase as the concentration increases, until C_{DNA} reaches 0.4 mg/mL, where a noticeable change in the trend is depicted, representing a structural rearrangement of DNA molecules on the gold surface. Then a new behavior is then observed between C_{DNA} of 0.4 and 1.5 mg/mL, where DNA concentration starts increasing again. However, C_{dl} values decrease around 1.5 mg/mL and remain constant at higher concentrations, DNA chains get entangled and there is a third behavior of DNA molecules adsorbed in the interface.
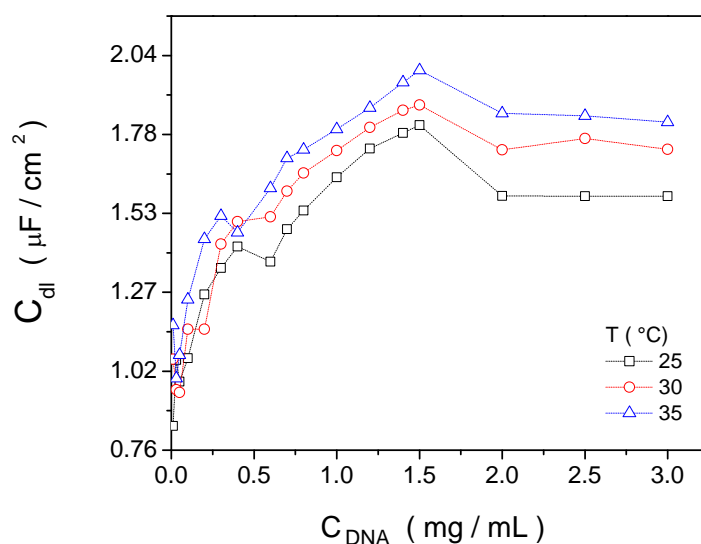
Figure 3.24. *Double-layer capacitance (C_{dl}) behavior as a function of DNA concentration for the temperatures of 25, 30 and 35 ºC.*

Two noticeable transitions are located at DNA concentrations around 0.4 and 1.5 mg/mL. This behavior is in good agreement with C_{dl} behavior for DNA adsorption onto platinum electrodes (previously discussed). The changes observed at C_{dl} are associated to the reorganization of DNA molecules at the double-layer, closely related to the overlapping and entanglement of DNA chains.

Figure 3.25. presents the adsorption capacitance, C_{ad}, as a function of DNA concentration and temperature. As for C_{dl} behavior, two transitions are also identified, related to the structural rearrangement of the electrochemical double layer at each characteristic regime.
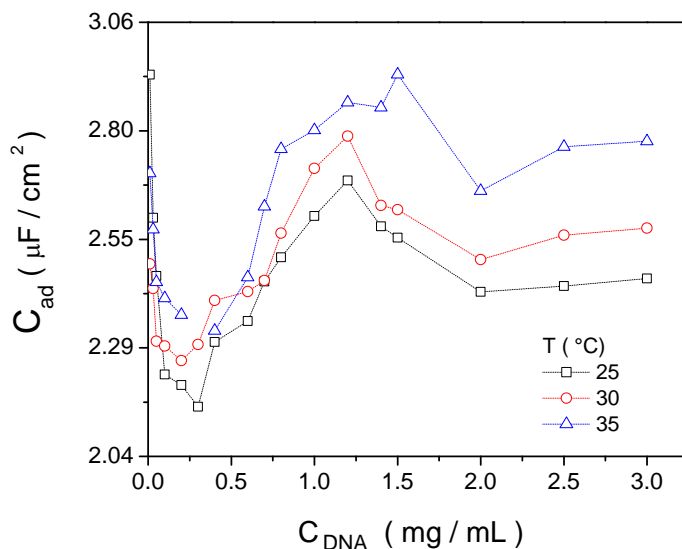
Figure 3.25. *Adsorption capacitance (C_{ad}) behavior as a function of DNA concentration for the temperatures of 25, 30 and 35 °C.*

3.4.3. Particular conclusions for the adsorption of DNA molecules in solution on gold

Electrochemical Impedance Spectroscopy was used to perform a detailed adsorption study of calf-thymus DNA molecules adsorption onto a gold surface. The impedance data was transformed into complex capacitance data using the impedance adsorption theory. C_{dl} and C_{ad} values were obtained through an equivalent circuit similar to the one proposed by Frumkin-Melik-Gaikazyan-Randles (FMGR) and were analyzed as a function of DNA concentration to determine the interfacial structure changes in the electrochemical double-layer. It is possible to conclude that impedance technique is able and sensitive enough to detect the structural changes of DNA molecules in different metal surfaces. In this manner, we can propose EIS as an adequate technique for characterizing the structural nature of the adsorbate based on the changes and the rearrangement of the electrochemical double-layer. On the other side, C_{dl} values were successfully obtained and will be used in *Chapter 5* with SPR measurements, from which DNA molecules adsorption onto a gold surface will be followed by means of an optical

technique. Finally, we can also conclude that the nature of the metal surface at which the adsorption process takes place influences both the double-layer capacitance response and the nature of the adsorption process, i.e. diffusion-controlled or electrosorption-controlled.

3.5. References

[1] J. Flemmig, The adsorption of DNA in the mercury-electrolyte interface, *Biopolymers*, **6**, 1697 (1968).

[2] E. Paleček, Polarographic behaviour of native and denatured deoxyribonucleic acids *J. Mol. Biol.*, **20**, 431, (1966).

[3] W. Yang, J. E. Butler, J. N. Russell Jr. and R. J. Hamers, Interfacial electrical properties of DNA-modified diamond thin films: intrinsic response and hybridization-induced field effects, *Langmuir*, **20**, 6778, (2004).

[4] W. Sun, M. Yang, and K. Jiao, Electrochemical Behaviors of Neutral Red on Single and Double Stranded DNA Modified Electrode, *Int. J. Electrochem. Sci.*, **2**, 93, (2007).

[5] J.-Y. Park and S.-M. Park, DNA hybridization sensors based on electrochemical impedance spectroscopy as a detection tool, *Sensors*, **9**, 9513 (2009).

[6] M. Fojta, R. P. Bowater, V. Stankova, L. Havran, D. M. J. Lilley, and E. Paleček, Two superhelix density-dependent DNA transitions detected by changes in DNA adsorption/desorption behavior, *Biochemistry*, 37, 4853 (1998).

[7] C. Li, X. Li, X. Liu and H.-B. Kraatz, Exploiting the interaction of metal ions and peptide nucleic acids-DNA duplexes for the detection of a single nucleotide mismatch by electrochemical impedance spectroscopy, *Anal. Chem.*, **82**, 1166-1169, (2010).

[8] M. Yi, K.-H. Jeong and L. P. Lee, Theoretical and experimental study towards a nanogap dielectric biosensor, *Biosensors and Bioelectronics*, **20**, 1320-1326, (2005).

[9] A. González-Pérez, R. S. Días, T. Nylander, and B. Lindman, Cyclodextrin-surfactant complex: a new route in DNA decompaction, *Biomacromolecules*, **9**, 772, (2008).

[10] V. A. Bloomfield, DNA condensation, *Curr. Opin. Struct. Biol.*, **6**, 334, (1996).

[11] E. Serres, P. Vicendo, E. Pérez, T. Noel, I. Rico-Lattes, DNA Condensation and transfection of cells in culture by a new polynorbornane polycationic polymer, *Langmuir* **15**, 6956 (1999).

[12] A. Dugaiczyk, S.L.C. Woo, B.W. O'Malley, *Genes in pieces.* In: *Ontogeny of Receptors and Mode of Action of Reproductive Hormones* (Hamilton, Clark, and Sadler, eds) Raven Press, p. 1 (1979).

[13] V. Vijayanathan, T. Thomas and T. J. Thomas, DNA condensation by polyamines: a laser light scattering study of structural effects, *Biochemistry,* **41**, 14086 (2002).

[14] T. Pajkossy, *J. Electroanal. Chem.,* **364**, 111 (1994).

[15] Z. Kerner and T. Pajkossy, Impedance of rough capacitive electrodes – the role of surface disorder, *J. Electroanal. Chem.,* **448**, 139 (1998).

[16] T. Pajkossy, T. Wandlowski, and D. Kolb, Impedance Aspects of the Anion Adsorption on Gold Single Crystal Electrodes, *J. Electroanal Chem.,* **414**, 209 (1996).

[17] T. Pajkossy, and D.M Kolb, An impedance study of Ir (210) in HCl Solutions, *Russ. J. Electrochem.,* **45**, 29 (2009).

[18] T. Pajkossy, and D. M. Kolb, Double layer capacitance of Pt(111) single cristal electrodes, *Electrochim. Acta* **46** 3063 (2001).

[19] A. N. Frumkin, and V. O. Melik-Gaykazyan, Determination of the kinetics of adsorption of organic substances by a.-c. measurements of the capacity and the conductivity at the boundary: electrode-solution, 5, 855 (1951). *Dokl. Akad. Nauk,,* **5**, 855 (1951).

[20] E. Gileadi, *Electrode Kinetics for Chemists Chemical Engineers, and Materials Scientists*; VCH: New York, (1993).

[21] R.J. Hunter, *Foundations of Colloid Science;* Oxford University: New York, Vol. I, (1985).

[22] K.-L Yang, T.-Y. Ying, S. Yiacoumi, C. Tsouris, E.S. Vittoratos, Electrosorption of ions from aqueous solutions by carbon aerogel: an electrical double-layer model, *Langmuir,* **17**, 1961–1969, (2001).

[23] K.-L. Yang, S. Yiacoumi and C. Tsouris, Electrical Double Layer Formation, *Dekker Encyclopedia of Nanoscience and Nanotechnology,* 1001-1014, (2004).

[24] Z. Stojek, *Electroanalytical Methods Guide to Experiments and Applications*, Scholz, Fritz (Ed.), 2nd ed. (2010).

[25] S. Yiacoumi, C. Tien, *Kinetics of Metal Ion Adsorption from Aqueous Solutions: Models, Algorithms, and Applications; Kluwer: Norwell,* MA, (1995).

[26] P. Weetman, S. Goldman and C.G. Gray, Use of the Poisson-Boltzmann equation to estimate the electrostática free energy barrier for dielectric models of biological ion channels, *J. Phys. Chem. B,* **101**, 6073–6078, (1997).

[27] V. Vlachy and A.D.J. Haymet, Salt exclusion from charged and uncharged micropores, *J. Electroanal. Chem.*, **283**, 77–85, (1990).

[28] G.M. Torrie and J.P. Valleau, Electrical double layers. 4. Limitations of the Gouy-Chapman theory, *J. Phys. Chem.*, **86**, 3251-3257 (1982).

[29] K.Y. Foo, B.H. Hameed, Insights into the modeling of adsorption isotherm systems, *Chemical Engineering Journal*, **156**, 2-10, (2010).

[30] G. Narsimhan and F. Uraizee, Kinetics of adsorption of globular proteins at an air-water interface, *Biotechnol. Prog.*, **8**(3), 187-196, (1992).

[31] J. Mcguire and O. Joshi, Adsorption, Proteins with Synthetic Materials. Encyclopedia of Industrial Biotechnology, 1-10, (2009).

[32] D. J. Lavrich, S. M. Wetterer, S. L. Bernasek and G. Scoles, Physisorption and chemisorption of alkanethiols and alkyl sulfides on Au(111), *J. Phys. Chem. B*, **102**(18), 3456-3465, (1998).

[33] A. S. Özcan, B. Erdem and A. Özcan, Adsorption of Acid Blue 193 from aqueous solutions onto Na-bentonite and DTMA-bentonite, *Journal of Colloid and Interface Science*, **280**, 44–54, (2004).

[34] D. M. Young and A.D. Crowell, "*Physical Adsorption of Gases*". Butterworths & Co., London, (1962).

[35] D.O. Hayward and B.M.W. Trapnell, "*Chemisorption*", 2ª Ed., Butterworth & Co., London, (1964).

[36] I. Langmuir,The constitution and fundamental properties of solids and liquids, *J. Am. Chem. Soc.* **38** (11), 2221–2295 (1916).

[37] D.C. Grahame, *Annual Review of Physical Chemistry*, **6**, 337-358, (1955).

[38] O. Levenspiel, *Chemical Reaction Engineering, 3d Edition*, John Wiley & Sons, New York Chichester Weinheim Brisbane Singapore Toronto, 473, (1999).

[39] J.M. Smith, "*Ingeniería de la cinética química*", McGraw-Hill, México, (1991).

[40] V. S. Bagotzky. "*Fundamentals of Electrochemestry*", Capítulo 12. Plenum Press., New York and London, (1993).

[41] E. Laviron, L. Roullier, Electrochemical reactions with adsorption of the reactants and electrosorption- simple analytical Solutions for a Henry isotherm, *Journal of Electroanalytical Chemistry*, **443**, 195-207, (1998).

[42] R.J Hunter, *Foundations of Colloid Science, Oxford University: New York*, **Vol. I**, (1985).

[43] K.Y. Foo and B.H. Hameed, Insights into the modeling of adsorption isotherm systems, *Chemical Engineering Journal*, **156**, 2–10, (2010).

[44] A.N. Frumkin, *Adsorption of organic compounds at electrodes. In Modern Aspects of Electrochemistry.* Butterworths, London. 149-223, (1964).

[45] J. Koryta, J. Dvorák and L. Kavan, *Principles of Electrochemistry, 2d Edition*, John Wiley & Sons, Chichester, New York, Brisbane, Toronto, Singapore, 199-222 (1993).

[46] F. Quemeneur, *Relationship between mechanical parameters and behaviour under external stresses in lipid vesicles with modified membranes. Data Analysis, Statistics and Probability.* Université de Grenoble (2010).

[47] G. Partt and C. Rochester, A*dsorption from solution at the solid/liquid interface,* Academic Press, New York, (1983).

[48] R. Netz and D. Andelman, Neutral and charged polymers at interfaces, *Physics Reports* **95**, 380-381 (2003).

[49] A.V. Dobrynin, M. Rubinstein, Theory of polyelectrolytes in solutions and at surfaces, *Prog. Polym. Sci.* **30**, 1049–1118 (2005).

[50] M. Kawaguchi and A. Takahashi, Polymer adsorption at solid liquid interfaces. *Adv. Colloid Interface Sci.* **37**, 219–317 (1992).

[51] A.K. Bajpai, Interface behaviour of ionic polymers, *Prog Polym Sci.* **22**, 523–564 (1997).

[52] V. Anand, P. Gurumoorthy and K.H. Khan, Polymers at interfaces: biological and non-biological applications, *Recent Research in Science and Technology* **3**(2), 80-86 (2011).

[53] G.J. Fleer, M.A. Cohen Stuart, J.M.H.M. Scheutjens, T. Gasgove and B. Vincent, *Polymer at interfaces.* London: Chapman and Hall (1993).

[54] F.W. Wiegel. *Phase transition and critical phenomena VII.* New York: Academic (1983).

[55] O.V. Borisov, E.B. Zhulina, T.M. Birshtein. Polyelectrolyte molecule conformation near charged surface, *J Phys II* **4**, 913–929 (1994).

[56] V. Yamakov, A. Milchev, O. Borisov and B. Dunweg, Adsorption of a polyelectrolyte chain on a charged surface: a Monte Carlo simulation of sealing behavior. *J Phys Condens. Matter* **11**, 9907–9923 (1999).

[57] H.A. van der Schee and J. Lyklema, Lattice theory of polyelectrolyte adsorption. *J Phys Chem* 88, 6661–6672 (1984).

[58] A.V. Dobrynin, A. Deshkovski and M. Rubinstein, Adsorption of polyelectrolytes at oppositely charged surfaces, *Macromolecules* 34, 3421–3436 (2001).

[59] M.A. Cohen Stuart, *Polymers at Interfaces: Statics, Dynamics and Effects on Colloidal Stability, The Structure, Dynamics and Equilibrium Properties of Colloidal Systems,* **324**, NATO ASI Series, 613-617 (1990).

[60] R. Perkel and R. Ullman, The adsorption of polydimethylsiloxanes from solution, J. Polymer Sci., **54**(159), 127-148 (1961).

[61] E. Barsoukov and J. R. Macdonald, *Impedance Spectroscopy Theory, Experiment, and Applications,* Second Edition, John Wiley & Sons, Inc., Publication, New Jersey (2005).

[62] D. A. Harrington, P. van den Driessche, Mechanism and equivalent circuits in electrochemical impedance spectroscopy, Electrochimica Acta **56**, 8005– 8013 (2011).

[63] A. Jänes, G. Nurk, K. Lust, J. Ehrlich and E. Lust, Adsorption kinetics of normal-heptanol on the bismuth single crystal planes, *Russ. J. Electrochem.,* **38** (2002).

[64] M. Sluyters-Rehbach, and J. H. Sluyters, in *Electroanalytical Chemistry* A. J. Bard Editor, p. 1, Marcel Dekker, Inc, New York (1970).

[65] J. Mostany, E. Herrero, J. M. Feliu and Jacek Lipkowski, Determination of the Gibbs excess of H and OH adsorbed at a Pt(111) electrode surface using a thermodynamic method, *Journal of Electroanalytical Chemistry* **558**, 19-24 (2003).

[66] E. Herrero, J. Mostany, J. M. Feliu and J. Lipkowski, Thermodynamic studies of anion adsorption at the Pt(111) electrode surface in sulfuric acid Solutions, *Journal of Electroanalytical Chemistry* **534**, 79-89 (2002).

[67] B. Ershler, Investigation of electrode reactions by the method of charging-curves and with the aid of alternating currents, *Disc. Farad. Soc.,* **1**, 269, (1947).

[68] T. Pajkossy and D.M. Kolb, An Impedance Study of Ir(210) in HCl Solutions, *Russian Journal of Electrochemistry* **45**, 29–37 (2009).

[69] D. C. Grahame, The electrical double layer and the theory of electrocapillarity, *Chem. Rev.,* **41**, 441 (1947).

[70] J. O'M. Bockris, A. K. N. Reddy and M. Gambioa-Aldeco *Modern Electrochemistry 2A. Fundamentals of Electrodics.,* Kluwer Academic Publisher, New York, Boston, Dordrecht, London, Moscow (2002).

[71] J. Ross Macdonald and Robert L. Hurt, Some simple equivalent circuits for ionic conductors, *J. Electroanal Chem.,* **200**, 69, (1986).

[72] B. Hirschorn, M. E. Orazem, B. Tribollet, V. Vivier, I. Frateur and Marco Musiani, Determination of effective capacitance and film thickness from constant-phase-element parameters, *Electrochim. Acta*, **55**, 6218, (2010).

[73] E. R. Larios-Durán and R. Antaño-López, Kinetic study of bromide adsorption on Hg by a combined equivalent-circuit reaction-mechanism modeling of EIS data, *J. Electroanal Chem.*, **658** 10, (2011).

[74] P. N. Bartlett, *Bioelectrochemistry: Fundamentals, Experimental and Application.*, John Wiley & Sons (2008).

[75] F.C. Anson, R.F. Martin and Ch. Yarnitzky, Creation of nonequilibrium diffuse double layers and studies of their relaxation, *J. Phys. Chem.*, **73**, 1835, (1969).

[76] A. J. Bard, and L. R. Faulkner, *Electrochemical Methods Fundamentals and applications*, John Wiley & Sons, Inc (2001).

[77] T.G. Mason, A. Dhople and D. Wirtz, Linear Viscoelastic Moduli of Concentrated DNA Solutions, *Macromolecules*, **31**, 3600 (1998).

[78] N. Nandi, K. Bhattacharyya and B. Baghi, Dielectric relaxation and solvation dynamics of water in complex chemical and biological Systems, *Chem. Rev.*, **100**, 2013 (2000).

[79] S. W. Feldberg, *J. Phys. Chem.*, **74**, 87 (1970).

[80] L.M. Bravo-Anaya, E.R. Macías, F. Carvajal Ramos, J.G. Álvarez-Ramírez, N.Casillas, J.F.A. Soltero and E.R. Larios-Durán, DNA Transitions by an Adsorption Impedance Study, *J. Electrochem. Soc.* **160**, G69–G74 (2013).

[81] L. M. Bravo-Anaya, E. R. Macías, F. Carvajal Ramos, V. V. A. Fernández, N. Casillas, J.F.A., Soltero and E. R. Larios-Durán, DNA Conformational Transitions at Different Concentrations and Temperatures Monitored by EIS, *ECS Electrochem. Lett.* **1**, G1 (2012).

[82] J. Newman, Resistance for Flow of Current to a Disk, J. *Electrochem. Soc.* **113**, 501–502 (1966).

CHAPTER 4

The scaling of electrochemical parameters of DNA molecules through EIS

Chapter 4. The scaling of electrochemical parameters of DNA molecules through EIS

The results of this chapter are the object of the following publications:

1) *Characterization of DNA/Buffer/H₂O System Through Electrochemical Impedance Spectroscopy.*

L. M. Bravo-Anaya, E.R. Larios-Durán, N. Casillas, V.V. Fernández-Escamilla, E.R. Macías Balleza and J. F. A. Soltero

2) *The Scaling of Electrochemical Parameters of DNA Aqueous Solutions with Concentration and Temperature Through an Electrochemical Impedance Spectroscopy Study.*

L. M. Bravo-Anaya, E.R. Macías Balleza, N. Casillas, F. Carvajal Ramos, V.V. Fernández-Escamilla, J. F. A. Soltero and E.R. Larios-Durán.

4.1. Introduction

In the field of polymer studies, molecular dynamics of bio-macromolecules cover a wide range of characteristic length and time scales [1]. In this manner, scaling laws are helpful for both understanding of the origin of the characteristic differences in a system and for generalizing results observed at various scales. The scaling effects usually depend on two quantities proportional at certain orders of magnitude and have been used to predict the behavior and characteristics of many systems with few experiments on a small-sized scale model. Commonly, scaling laws express one variable as a nonlinear function of another variable raised to a power, i.e. $f(x) \langle x^{\alpha}$, with $\alpha \neq 0$. In the polymers field, they provide basis for estimating important parameters of polymer solutions at their different regimes from the knowledge of several properties of the system [2].

Critical concentrations such as C* and C_e and temperatures in viscoelastic aqueous solutions formed by ionic surfactants [3], triblock copolymers [4, 5] and polyelectrolytes such as DNA [6] have been evaluated using rheological measurements of frequency sweeps experiments performed in the linear viscoelastic region (LVR). With this experiments, some parameters can be obtained, i.e. the crossover frequency (ω_c), the principal characteristic time (τ_c), the Newtonian viscosity (η_0) and the plateau modulus (G_0). Through ω_c, which is obtained with the crossover of the elastic (G') and the loss

(G") moduli, it is possible to calculate the principal characteristic time τ_c ($1/\omega_c$). Since rheological methods have been suitable to determine macroscopic properties of DNA chains in solution at semi-diluted and concentrated regimes [7-9], Electrochemical Impedance Spectroscopy (EIS) is proposed as a suitable electrochemical technique to characterize and analyze DNA molecules behavior at a lower concentration range. DNA molecule response to an applied electrical field has been a subject of during several years using different electrochemical techniques such as amperometry, potentiometry and voltammetry [10-12]. However, EIS constitutes an appropriate method for studying DNA molecules response without being perturbed by chemical reactions, due to its sensitiveness at a low concentration range [13].

In this chapter, a detailed investigation of calf thymus DNA solutions in the platinum and gold interfaces through EIS measurements is presented. Aqueous solutions of calf thymus DNA are adjusted to a pH of 7.3 and studied as a function of DNA concentration and temperature (10, 20, 30 and 40 °C for platinum and 25, 30 and 35 °C for gold). EIS measurements are carried out at open circuit potential, leading to an adsorption response of DNA molecules on platinum electrodes. Two methods are used to analyze EIS measurements, first one is based on the classical theory of electrochemical impedance [14-16] and the second one is presented using a methodology similar to the one used in linear rheology, i.e. through log-log Bode plots (Z 'and -Z" *vs.* ω) from which is possible to determine an impedance characteristic cross-over frequency (ω_c), and Z_o, related to the solution resistance (R_s). A characteristic time-constant of the process (τ_c) was determined by means of the reciprocal of ω_c. The analysis of Z_o and τ_c as a function of DNA concentration allows identifying the two critical concentrations of DNA molecules in solution, C* and C_e, respectively. The relation between Z_o and τ_c as a function of DNA concentration exhibit a linear behavior and follows the power law at every studied temperature for each characteristic regime. Through the scaling of the electrochemical parameters of the system, it is proposed a general impedance transfer funtion able to predict the impedance behavior of a chosen DNA concentration within a specific regime at OCP. By using this function it is possible to study and to analyze theoretically the double-layer charging as a function of concentration with only one impedance experiment and makes possible obtaining electrical parameters concerning the interface DNA-TE buffer at each characteristic regime.

4.2. Experimental conditions

The description of the reagents, buffer Tris-HCl/EDTA preparation and DNA/Buffer solutions are presented in *Sections 2.3.1., 2.3.2.* and *2.3.3.* of this work. The experimental conditions and the setup for EIS measurements are described in *Section 3.3.1.2.*

4.3. Experimental results

4.3.1. Classical EIS analysis

A classical approach based on the electrochemical impedance theory using Nyquist diagrams was performed at first instance to describe DNA molecules impedance response. *Figure 4.1 a* shows, a Nyquist plot for DNA concentrations of 0.4, 0.5, 0.6, 0.7 and 0.8 mg/mL at a constant temperature of 30 ºC using a platinum electrode. It is possible to identify that the process, taking place at the interface DNA-Buffer/platinum, is predominantly capacitive and represents the structural arrangement of DNA molecules adsorbed onto the platinum surface. This response is in good agreement with studies reported through DNA adsorption impedance by complex capacitance studies [6, 17] and it is consistent with the experimental conditions of this study, i.e. open circuit potential.
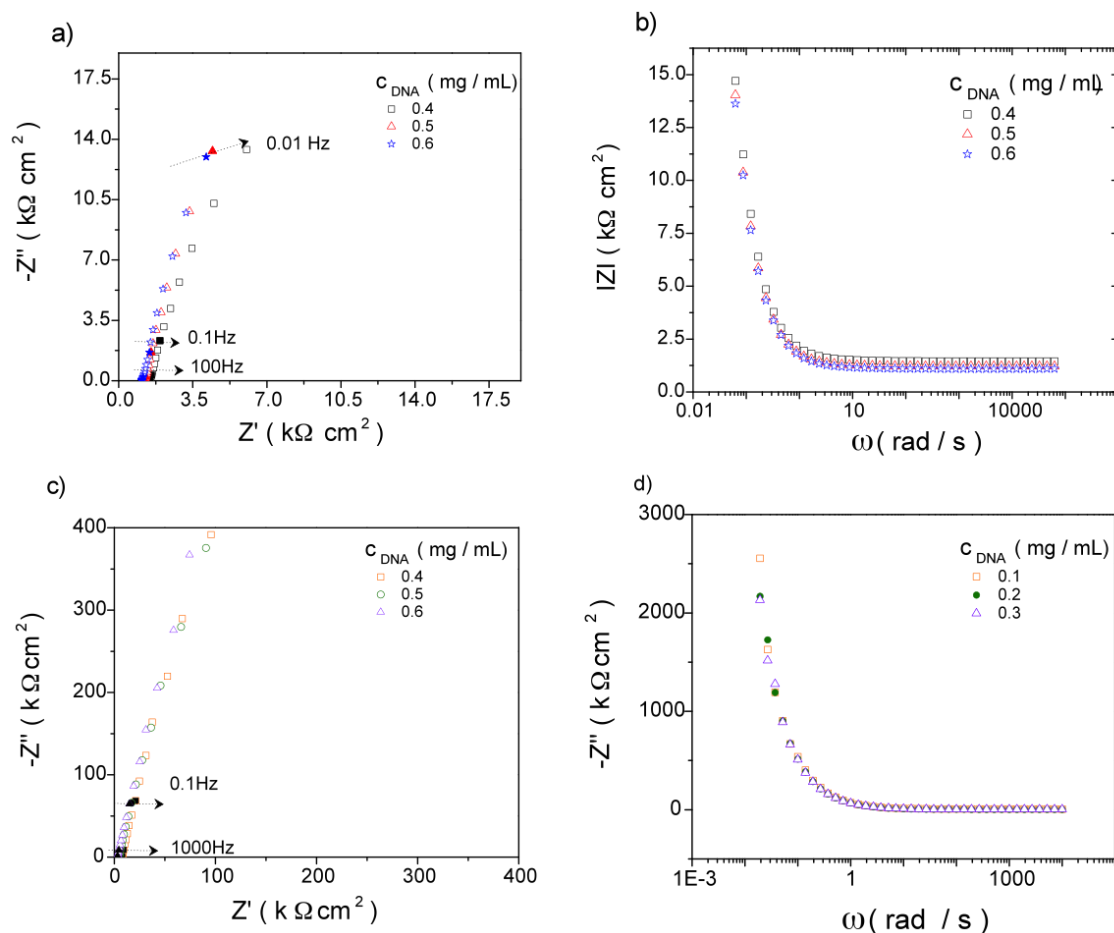
Figure 4.1. *a) Nyquist and b) Bode-module plots for DNA concentrations of 0.4, 0.5 and 0.6 mg/mL at a temperature of 30 ºC using a platinum electrode, respectively c) Nyquist and d) Bode-module plots for DNA concentrations of 0.4, 0.5 and 0.6 mg/mL at a temperature of 30 ºC using a gold electrode, respectively. Frequency in Hz.*

The increment of DNA concentration causes a shift of each spectra towards lower values of Z' at higher frequencies, this means that the solution resistance decreases as expected due to the conductivity raise, caused by the presence of a larger amount of charged DNA molecules [18]. *Figure 4.1 b* shows the complex impedance modulus ($|Z|$) in a Bode diagram where it can be observed that the solution resistance (R_s) diminishes as C_{DNA} increases. *Figure 4.1 c* and *d* show the Nyquist and the Bode diagrams, respectively, for DNA concentrations of 0.4, 0.5 and 0.6 mg/mL at a constant temperature of 30 °C using a gold electrode. The obtained response is consistent with the one previously described for the platinum surface.

Figure 4.2 a shows a Nyquist diagram for a DNA concentration of 0.4 mg/mL as a function of temperature. In this figure it is possible to observe that curves shift to lower Z' values while increasing temperature, indicating a decrement in the solution resistance as a consequence of molecular diffusion increment [19]. This effect is similar to the one observed with augments of DNA concentration (cf. *Figures 1a* and *b*) and is explained as follows: since the viscosity of the medium decreases with a temperature increment [20], the movement of DNA molecules is greater at higher temperatures.
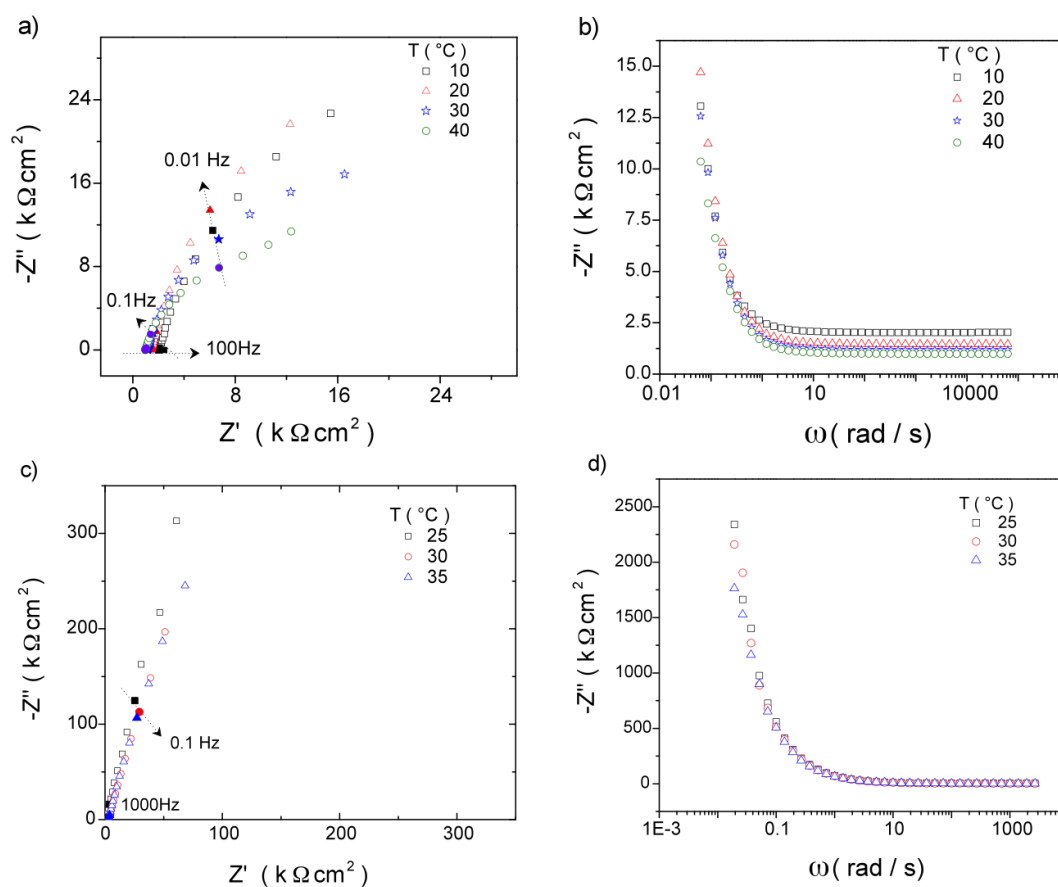
Figure 4.2. *a) Nyquist and b) Bode-module plots for a DNA concentration of 0.4 mg/mL at the temperatures of 10, 20, 30 and 40 °C using a platinum electrode, respectively c) Nyquist and d) Bode-module plots for DNA*

concentrations of 0.4 mg/mL at a temperatures of 25, 30 and 35 ºC using a gold electrode, respectively. Frequency in Hz.

Stokes-Einstein relation sets up that the diffusion coefficient also increases with temperature, producing an augmentation in the molecular diffusion of the species [21, 22]. Therefore, since the conductivity is highly related to mobility and to the diffusion coefficient [23], while increasing temperature, conductivity reaches higher values and is reflected in the decrease of resistivity as it is seen at the decrement on Z'. *Figure 4.2 b* shows the complex impedance modulus (|Z|) in a Bode diagram where it can be observed that the solution resistance (R_s) decreases as temperature increases. *Figure 4.2 c* and *d* show the Nyquist and the Bode diagrams, respectively, for a DNA concentration of 0.4 mg/mL at the temperatures of 25, 30 and 35 ºC using a gold electrode. As well as for the response obtained for the platinum electrode, curves shift to lower Z' values while increasing temperature, as expected. Since the temperatures used for the study of Au/DNA-TE buffer interface are closer from each other, this shift is not as evident as the one obtained for Pt/DNA-TE buffer interface.

According to the Nyquist diagrams, DNA-Buffer/ platinum interface behavior is adequately simulated by an equivalent circuit as the one representing the impedance associated to a faradaic reaction and expressed in terms of a constant phase element (CPE) [24, 25].
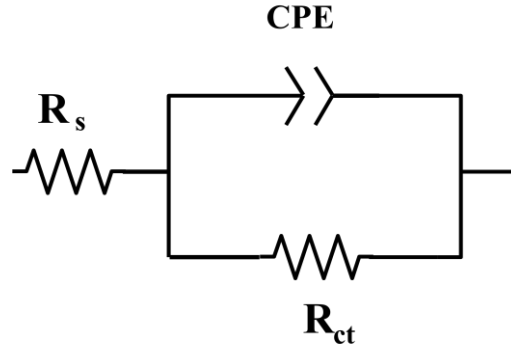
Figure 4.3. *Equivalent circuit representing the complex impedance for Pt-DNA/TE buffer system.*

This equivalent circuit includes an arrangement of the following three electrical parameters: a solution resistance (R_s), a resistance related to an incipient charge transfer (R_{ct}) due to the possible reaction of impurities or oxygen traces present at the working solution [26] and a non-ideal capacitance (CPE). A schematic of the equivalent circuit is presented in *Figure 4.3* and its corresponding complex impedance transfer function is expressed as follows:

$$Z(W) = R_s + \frac{R_{ct}}{1 + (jW)^a Q R_{ct}} \qquad (4.1)$$

where ω and j represent the frequency in rad/s and the imaginary number, respectively. The CPE parameters are Q and α which are independent of the frequency. Furthermore, α can take values between 0 and 1. If $\alpha = 1$, Q represents an ideal interface differential capacitance and has capacitance units, i.e. $\mu F/cm$, but if $\alpha < 1$, the system is affected by several parameters such as superficial heterogeneity or surface roughness and displays a non-ideal behavior [27]. The effective capacitance C_{eff} associated with the CPE is expressed as:

$$C_{eff} = Q^{1/a} R_s^{(1-a)/a} \tag{4.2}$$

Figure 4.4 and *4.5* show the Nyquist diagrams for the impedance results of three DNA concentrations at the four studied temperatures for Pt-DNA/TE buffer interface and at the three studied temperatures for Au-DNA/TE buffer interface, respectively. Continuous lines represent the fittings of the experimental data obtained using *Equation 4.1*. The estimated values for each electrical parameter are summarized in *Table 4.1* for Pt-DNA/TE buffer interface and in *Table 4.2* for Au-DNA/TE buffer interface.
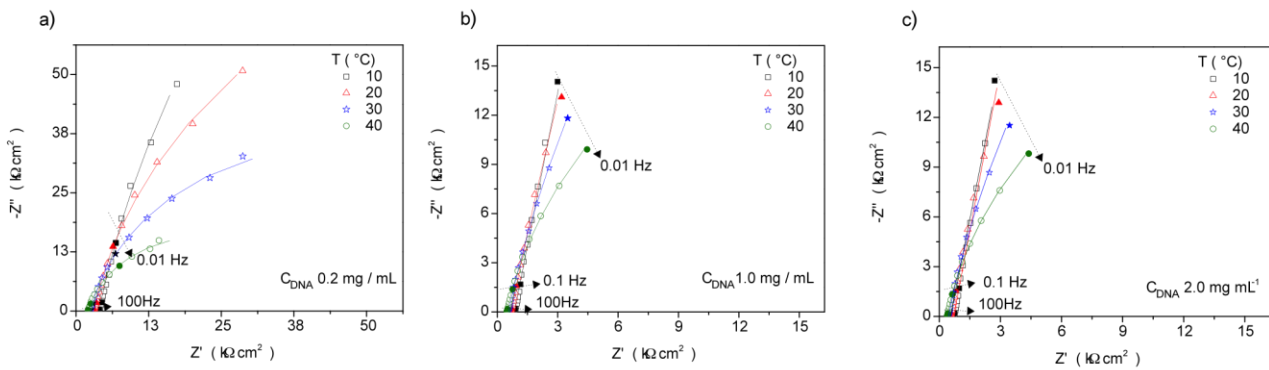
Figure 4.4. *Nyquist plots for Pt-DNA/TE buffer interface: DNA concentrations of a) 0.2, b) 1.0 and c) 2.0 mg/mL at the temperatures of 10, 20, 30 and 40 ºC. Frequency in Hz.*
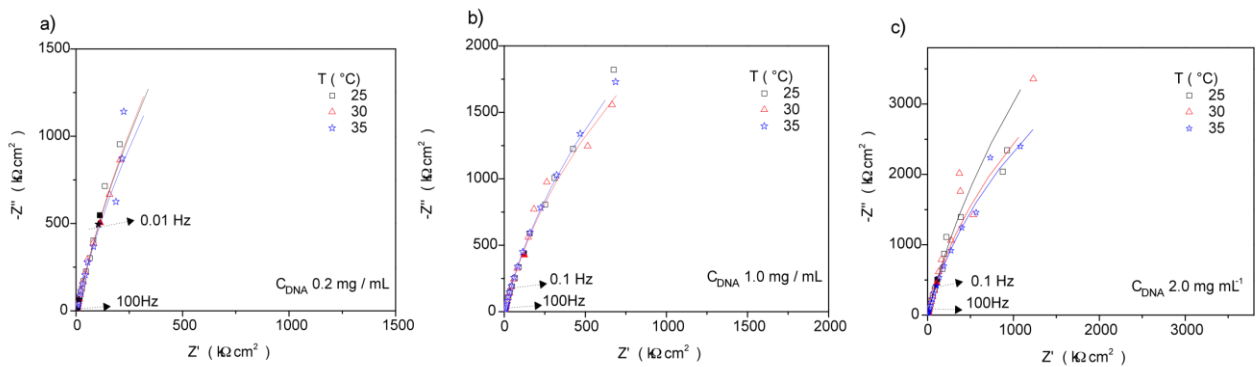
Figure 4.5. *Nyquist plots for Au-DNA/TE buffer interface: DNA concentrations of a) 0.2, b) 1.0 and c) 2.0 mg/mL at the temperatures of 25, 30 and 35 ºC. Frequency in Hz.*

In both interfaces, it is possible to observe that the magnitude order of R_{ct} is higher than 1×10^4 Ω/cm^2, confirming that only an almost negligible charge transfer is present in the process. However, for Au-DNA/Te buffer interface, the R_{ct} obtained values are higher than for Pt-DNA/TE buffer interface, suggesting that in gold electrodes, impurities or oxygen traces present at the working solution are less reactive.

Table 4.1.- *Electrical parameters obtained by fitting the equivalent circuit in Figure 4.3 to the experimental data of Pt-DNA/TE buffer interface for DNA concentrations of 0.2, 1.0 and 2.0 mg/mL at the temperatures of 10, 20, 30 and 40 ºC.*

C_{DNA} mg/mL	T ºC	R_s Ω cm^2	Q $1/\Omega$ cm^2 s$^\alpha$	α	C_{eff} μF /cm^2	R_{ct} Ω cm^2	X^2
0.2	10	3949.75	200.79	0.87	236.69	4.86×10^5	0.006
	20	3061.50	209.82	0.89	234.99	1.92×10^5	0.004
	30	2471.75	214.83	0.86	239.27	8.44×10^4	0.002
	40	2027.75	224.79	0.85	249.07	3.95×10^4	0.003
1.0	10	853.75	218.26	0.89	211.14	2.32×10^6	0.003
	20	682.75	231.27	0.89	219.35	7.95×10^5	0.002
	30	560.25	245.62	0.89	228.71	1.63×10^5	0.002
	40	473.75	262.88	0.89	241.12	5.38×10^4	0.001
2.0	10	706.25	218.25	0.90	207.18	2.11×10^6	0.002
	20	554.25	234.70	0.90	217.99	1.01×10^6	0.002
	30	452.75	253.25	0.90	232.19	1.37×10^5	0.002
	40	383.75	271.96	0.90	246.68	4.77×10^4	0.001

Tables 4.2 and *4.3* show also the dependence with temperature and concentration previously described for the solution resistance, this is: while increasing temperature and concentration, R_s decreases for all DNA concentrations. The obtained values for the effective capacitance show, as expected, an increase with temperature for both interfaces, however a two-order magnitude difference is detected in the C_{eff} values comparing platinum and gold interface, showing that the chosen electrode has an important contribution to the measured capacitance of the metal-DNA/TE buffer interface.

Table 4.2.- *Electrical parameters obtained by fitting the equivalent circuit in Figure 4.3 to the experimental data of Au-DNA/TE buffer interface for DNA concentrations of 0.2, 1.0 and 2.0 mg/mL at the temperatures of 25, 30 and 35 ℃.*

C_{DNA} mg/mL	T ℃	R_s Ω cm^2	Q $1/\Omega$ cm^2 s$^\alpha$	α	C_{eff} μF /cm^2	R_{ct} Ω cm^2	X^2
0.2	25	4455.99	0.662	0.89	0.382	1.24×10^7	0.001
	30	4089.69	0.699	0.88	0.402	7.46×10^6	0.001
	35	3793.78	0.749	0.88	0.421	6.92×10^6	0.0008
1.0	25	1012.34	0.802	0.87	0.346	9.61×10^7	0.001
	30	917.12	0.836	0.87	0.363	7.92×10^6	0.0008
	35	856.30	0.876	0.87	0.380	8.91×10^6	0.001
2.0	25	522.57	0.735	0.88	0.311	1.18×10^8	0.001
	30	476.56	0.801	0.87	0.371	1.05×10^8	0.005
	35	431.68	0.881	0.87	0.390	5.02×10^7	0.002

4.3.2. Impedance spectra analysis through graphs log-log Bode (Z', -Z" vs. ω)

The impedance data obtained for this system are also analyzed by means of an analogous methodology to the one used in studies of oscillatory rheology measurements in the linear viscoelastic regime (LVR) [17-20], so impedance results were plotted by using graphs type log-log Bode.

Figures 4.5 a and *b* show log-log Bode plots (Z' and -Z" vs. ω) for Pt-DNA/TE buffer and Au-DNA/TE buffer interface, respectly, for a variation of DNA concentrations at a constant temperature, from which is possible to determine a characteristic crossover frequency (ω_c) and the Z_o modulus related to the solution resistance (R_s). For both cases, the characteristic time-constant of the process (τ_c) is obtained by calculating the reciprocal of ω_c and is directly related to the metal-DNA solution interface relaxation due to the electrochemical double-layer formation. We can observe that ω_c shifts to higher frequencies when DNA concentration increases. In contrast, the characteristic time-constant and the Z_0 module decrease. This phenomenon may be associated with the diffuse layer thickness decrease caused by DNA concentration increase.
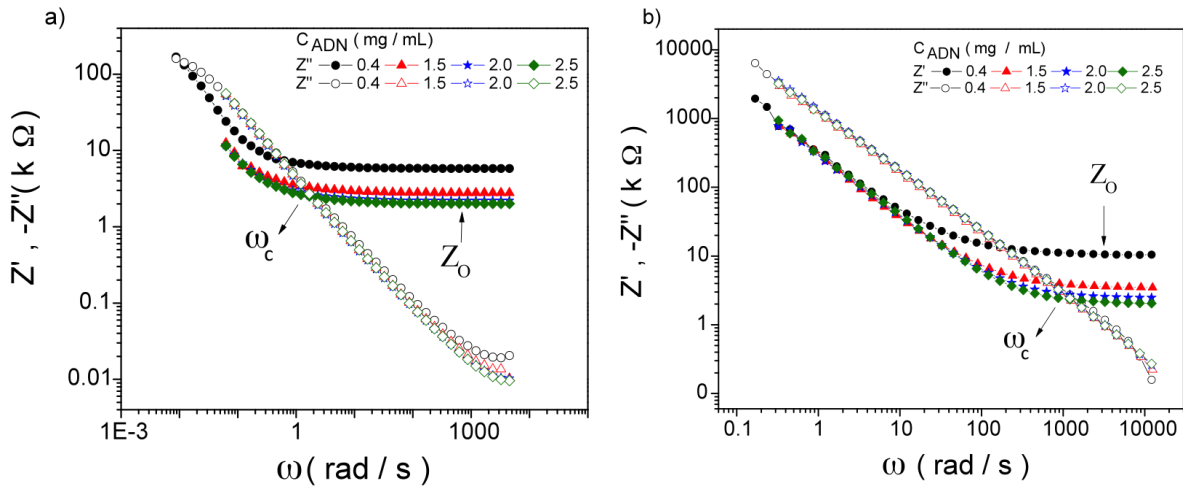
Figure 4.5. *Real (Z') and imaginary (Z'') parts of the impedance as a function of frequency (ω) for a) Pt-DNA/TE buffer interface and b) Au-DNA/TE buffer interface for DNA concentrations of 0.4, 1.5, 2.0 and 2.5 mg/mL at the temperature of 30 °C.*

The results for ω_c, τ_c and Z_0 evaluated for such DNA concentrations at each interface are quantified in *Tables 4.3* and *4.4* for *Pt-DNA/TE buffer* and *Au-DNA/TE buffer*, respectively. It is possible to observe that the time-constant is at least three magnitude orders higher for platinum than for gold, so the nature of the electrode affects the process dynamics, described by τ_c (which will be explained in detail in the following section) taking place at the interface. This could be related with electrostatic interactions of DNA chains with each metal surface.

Table 4.3.- *Cross-over frequency (ω_c), characteristic time-constant (τ_c) and Z_0 module for DNA concentrations of 0.4, 1.5, 2.0 and 2.5 mg/mL in the Pt-DNA/TE buffer at the temperature of 30 °C.*

C_{DNA} mg/mL	ω_c rad/ s	Z_0 Ω	τ_c s
0.4	0.641	4 708.74	1.559
1.5	1.473	2 786.87	0.679
2.0	1.769	2 223.52	0.565
2.5	2.109	2 046.58	0.474

Table 4.4.- *Cross-over frequency (ω$_c$), characteristic time-constant (τ$_c$) and Z$_o$ module for DNA concentrations of 0.4, 1.5, 2.0 and 2.5 mg/mL in the Au-DNA/TE buffer at the temperature of 30 °C.*

C$_{DNA}$ mg/mL	ω$_c$ rad/ s	Z$_O$ Ω	τ$_c$ s
0.4	168.559	4 521.929	5.93 x 10^{-3}
1.5	648.520	3 488.600	1.54 x 10^{-3}
2.0	1 098.678	2 349.203	9.10 x 10^{-4}
2.5	1 413.601	2 049.200	7.07 x 10^{-4}

The physical and quantitative interpretation of τ$_c$ is determined from the analysis of the transfer function shown in *Equation 4.1*, from which is possible to obtain the real and imaginary parts of the impedance, as are given by *Equation 4.3* and *4.4*.

$$Z'(w) = R_s \tag{4.3}$$

$$Z''(w) = \frac{R_{ct}[1 - R_{ct}Q(jw)^a]}{1 - R_{ct}^2(jw)^{2a}} \tag{4.4}$$

Since the time constant is obtained when the real and the imaginary parts of impedance reach the same value, as observed in *Figures 4.5 a* and *b*, we can establish the following relationship:

$$Z'(w) = Z''(w) \tag{4.5}$$

and evaluating the function in the limit when R$_{ct}$ tends to the infinite, i.e. when charge transfer resistance is very large, as in our case where the system is predominantly capacitive, we obtain that the reciprocal of the cross-over frequency corresponds to a time constant related to the coupling in series of the solution resistance and the effective capacitance (*Equation 4.6*).

$$t_c = w_c^{-1} = R_s C_{eff} \tag{4.6}$$

The same expression can be obtained by evaluating *Equation 4.6* in the limit when R$_{ct}$ tends to the infinite.

4.3.3. Temperature dependence in the impedance response

The temperature effect observed in the impedance results is illustrated in *Figures 4.6 a* and *b* for Pt-DNA/TE buffer and Au-DNA/TE buffer interface, respectly, showing Z' and -Z" as a function of frequency for a DNA concentration of 2.0 mg mL^{-1} at the temperatures of 10, 20, 30 and 40 °C for platinum and at 25, 30 and 35 °C for gold. It is possible to observe that ω_c shifts at higher frequencies as temperature increases. On the contrary, the characteristic time-constant (τ_c) and the Z_o module decrease indicating the diminution of the solution resistivity.
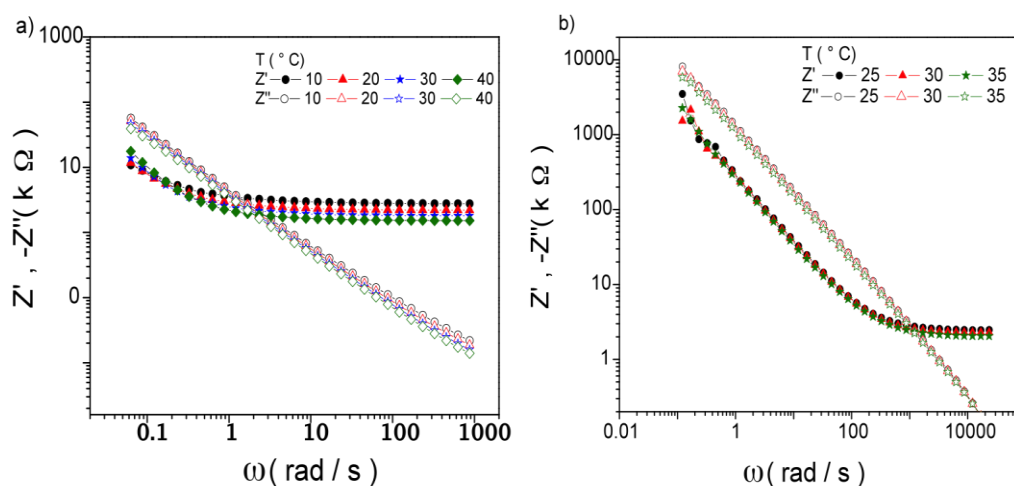
Figure 4.6. *Real (Z') and imaginary (Z'') parts of the impedance as a function of frequency (ω) for a) Pt-DNA/TE buffer interface and b) Au-DNA/TE buffer interface for a DNA concentrations of 2.0 mg/mL at the temperatures of 10, 20, 30 and 40 °C for platinum and 25, 30 and 35 °C for gold.*

Similarly to the effect suggested by DNA concentration, this phenomenon may be associated to the diffuse layer thickness increment with temperature. A diminution in the distance traveled by DNA molecules from the bulk of the solution towards the electrode surface is then produced [28]. In this manner, the characteristic time constant that leads to the arrangement of DNA molecules on the electrochemical double-layer diminishes as temperature increases. The results for ω_c, τ_c and Z_o evaluated for such DNA concentrations at each interface are quantified in *Tables 4.5* and *4.6* for *Pt-DNA/TE buffer* and *Au-DNA/TE buffer*, respectively.

Table 4.5.- *Cross-over frequency (ω_c), characteristic time-constant (τ_c) and Z_o module for a DNA concentrations of 2.0 mg/mL in the Pt-DNA/TE buffer at the temperatures of 10, 20, 30 and 40 °C.*

C_{DNA} Mg/mL	ω_c rad/ s	Z_O Ω	τ_c s
10	1.302	2 769.79	0.768
20	1.597	2 534.43	0.626
30	1.769	2 223.52	0.565
40	2.020	1 500.50	0.495

Table 4.6.- *Cross-over frequency (ω_c), characteristic time-constant (τ_c) and Z_o module for a DNA concentrations of 2.0 mg/mL in the Au-DNA/TE buffer at the temperatures of 25, 30 and 35 °C.*

C_{DNA} mg /mL	ω_c rad/ s	Z_O Ω	τ_c s
25	1 083.056	2 487.907	9.23 x 10^{-4}
30	1 098.678	2 349.203	9.10 x 10^{-4}
35	1 155.151	2 124.819	8.66 x 10^{-4}

On the other hand, in order to evaluate the temperature effect on the interface, *Figures 4.7a* and *b* present the plots of $\ln(\tau_c)$ versus the reciprocal of the absolute temperature for several DNA concentrations on platinum and gold, respectively. A linear behavior of $\ln(\tau_c)$ is observed at each DNA concentration in both figures, which demonstrates that the characteristic time constant of the process follows an Arrhenius-type behavior given by the following expression [29, 30]:

$$t_c = Ae^{-E_a/RT} \tag{4.7}$$

where A_f is the frequency factor, R is the universal gas constant, T is the temperature and E_a corresponds to the minimum amount of energy required for the coupling of the solution resistance and the capacitance in terms of the equivalent circuit representing DNA-platinum interface.
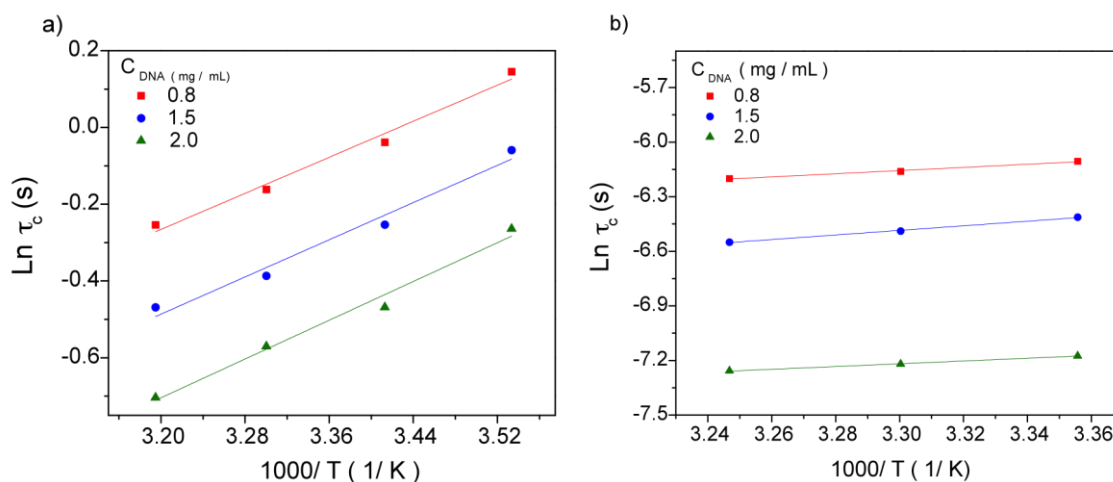
Figure 4.7. *Arrhenius dependence of the characteristic time-constant ($\tau_c = 1/\omega_c$) with the reciprocal of the absolute temperature for DNA concentrations of 0.8, 1.5 and 2.0 mg/mL at the a) Pt-DNA/TE buffer interface and b) Au-DNA/TE buffer interface.*

This Arrhenius-type temperature dependence has been also obtained for the dynamics of DNA solutions studied by dielectric relaxation spectroscopy and dynamic mechanical spectroscopy [1]. As for the temperature dependence of the average relaxation obtained at the higher frequency process (HFP) and at the lower frequency process (LFP) with dielectric measurements, the characteristic time constant obtained through EIS measurements increases while decreasing temperature, as described before. The calculated apparent energy, E_a, for the adsorption process for DNA concentrations presented in *Figure 4.7a*, i.e. 0.8, 1.5 and 2.0 mg/mL at the Pt-DNA/TE buffer interface, are 10.68, 9.94 and 10.55 kJ/mol, respectively, in the temperature range from 10 to 40 ºC, where DNA remains in its native state and the evaporation of water is negligible. The obtained values for E_a increase while augmenting DNA concentration until reaching the first transition of the system, related to C*, i.e. around 0.3 mg/mL, where it is possible to observe an important change on E_a behavior (*Figures 4.8a*). In this manner, is it possible to see that the minimum amount of energy required for the process is dependent on the DNA concentration, on the interactions between DNA chains present in the bulk of the solution and with the metal surface. Using the resulting parameters, it is also possible to estimate τ_c at each temperature between the studied ranges. The calculated apparent energy, E_a, for the adsorption process for DNA concentrations at the Au-DNA/TE buffer interface (*Figure 4.8b*) is slightly lower than the calculated E_a values for the Pt-DNA/TE buffer interface and depict also the change on E_a behavior as a function of concentration. The calculated values for 0.8, 1.5 and 2.0 mg/mL are 7.19, 6.25 and 7.58 kJ/mol, respectively, in the temperature range from 25 to 35 ºC. These results could be related to the energetic nature of the electrodes, however, it will not be discussed in this work.
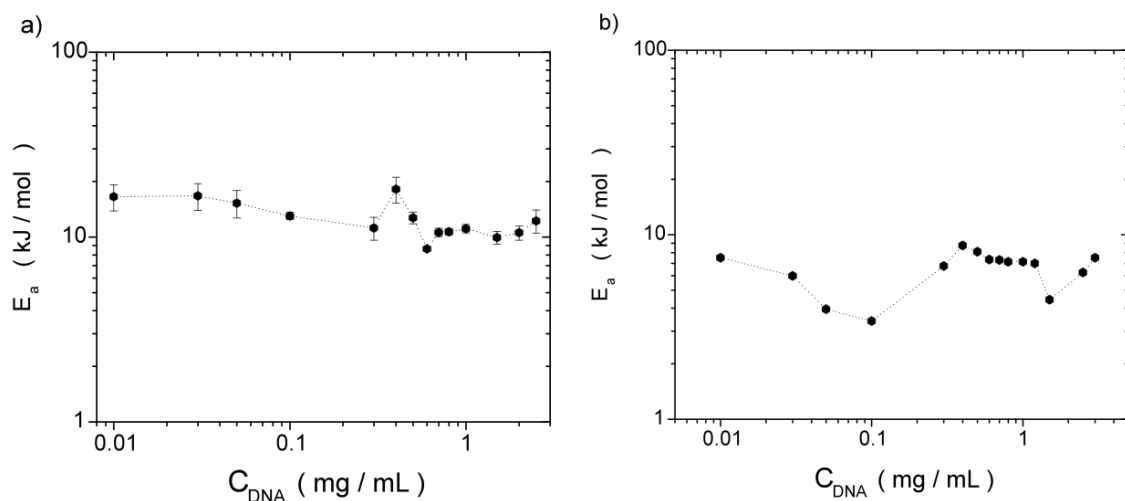
Figure 4.8. *E_a as a function of DNA concentration for a) Pt-DNA/TE buffer interface and b) Au-DNA/TE buffer interface.*

4.3.4. Concentration dependence of DNA in the impedance response

The parameters ω_c, τ_c and Z_o were evaluated from each spectrum obtained for every DNA concentration at each studied temperatures. *Figures 4.9 a* and *b* illustrate the results of τ_c and Z_o as function of C_{DNA} at the temperatures 10, 20, 30 and 40 ºC for Pt-DNA/TE buffer interface and *Figures 4.10 a* and *b* present the results of the same parameters as a function of C_{DNA} at the temperatures 25, 30 and 35 ºC for Au-DNA/TE buffer interface.
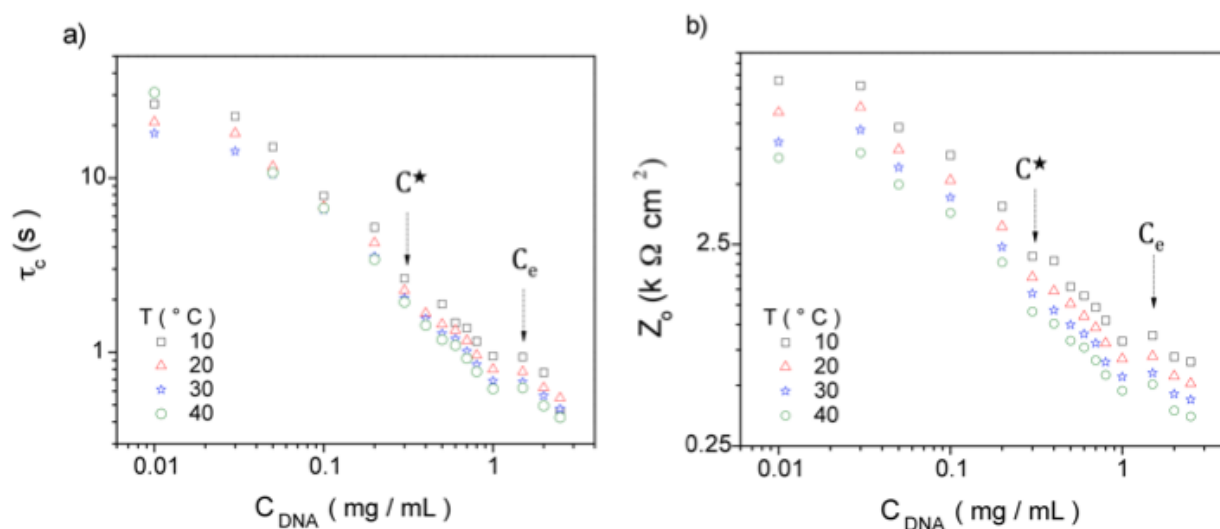
Figure 4.9. *a) Characteristic time-constant (τ_c) and Z_o module for Pt-DNA/TE buffer interface as a function of DNA concentration at the temperatures of 10, 20, 30 and 40 ºC.*
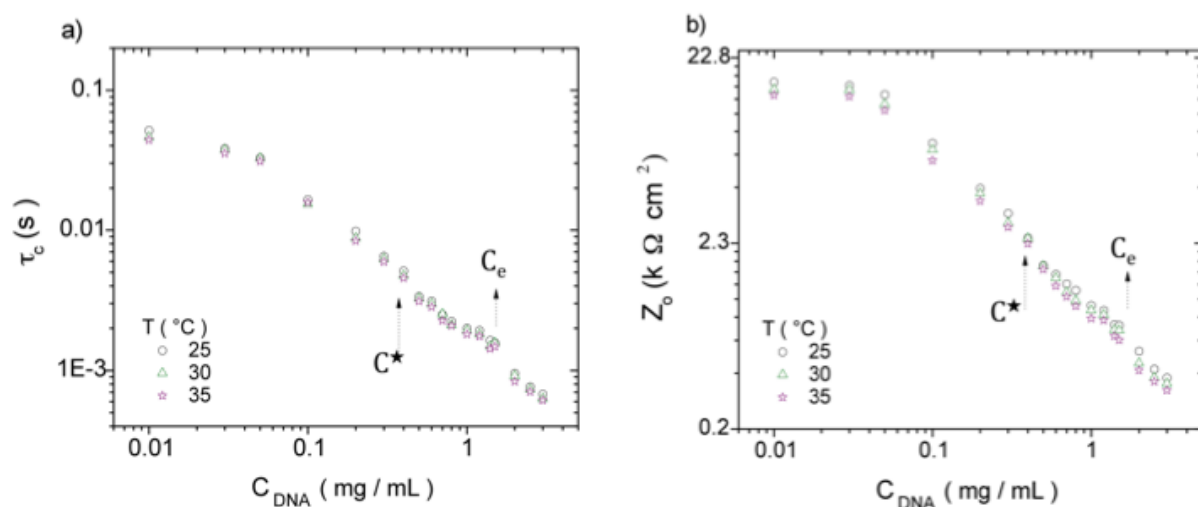
Figure 4.10. *a) Characteristic time-constant (ω_c) and Z_o module for Au-DNA/TE buffer interface as a function of DNA concentration at the temperatures of 25, 30 and 35 °C.*

In all figures, it is possible to identify two transitions located in the slope changes of each isotherm, in a more clearly way for Pt-DNA/TE buffer interface. First transition is located at a DNA concentration around 0.30 mg/mL and is presumably associated with the starting of the interactions between DNA strands. This concentration could be related to the overlap concentration (C*), which represents the transition from the dilute regime to the semi-dilute regime without entanglements (as mentioned in previous chapters of this thesis, i.e. *Chapter 2* and *3*). Second transition is located at a DNA concentration of 1.5 mg/mL, which could be associated to the entanglement concentration (C_e). These results are in fairly agreement with the results previously described in terms of the adsorption study of the Pt-DNA/TE buffer interface [10] (*Chapter 3*) and with the results obtained through rheological measurements described in *Chapter 2*. The characteristic time constant reflects clearly the structural arrangement transitions of the electrochemical double-layer. EIS has been proved to be a suitable technique to characterize microscopically and macroscopically the structural behavior of DNA molecules during the charge arrangement at the electrode surface.

4.3.5. Superposition Z', -Z"/DNA concentration-temperature

Figures 4.11a and *b* shows the results of the impedance response for a) Pt-DNA/TE buffer interface and b) Au-DNA/TE buffer interface, as a function of frequency for several DNA concentrations at the temperatures of 10, 20, 30 and 40 °C for platinum and 25, 30 and 35 for gold. The real and the

imaginary parts of the impedance were divided by Z_o and plotted against the reduced frequency $\omega\tau_c$. It was then possible to obtain a master curve with a Z' and Z"- concentration- temperature superposition. We observe that all the data at frequencies between 2.0 Hz and 10 kHz collapse in a single line for all DNA concentrations, however, at frequencies lower than 2.0 Hz and DNA concentrations higher than 1.0 mg/mL, the results collapse in two lines, showing the transition between the semi-dilute regime without entanglements and the semi-dilute regime with entanglements. This kind of master curves are typically used in rheology studies, here we use the same approach to depict that from a simple visual inspection, normalized impedance curves could give us a qualitative information about the DNA concentration effect.
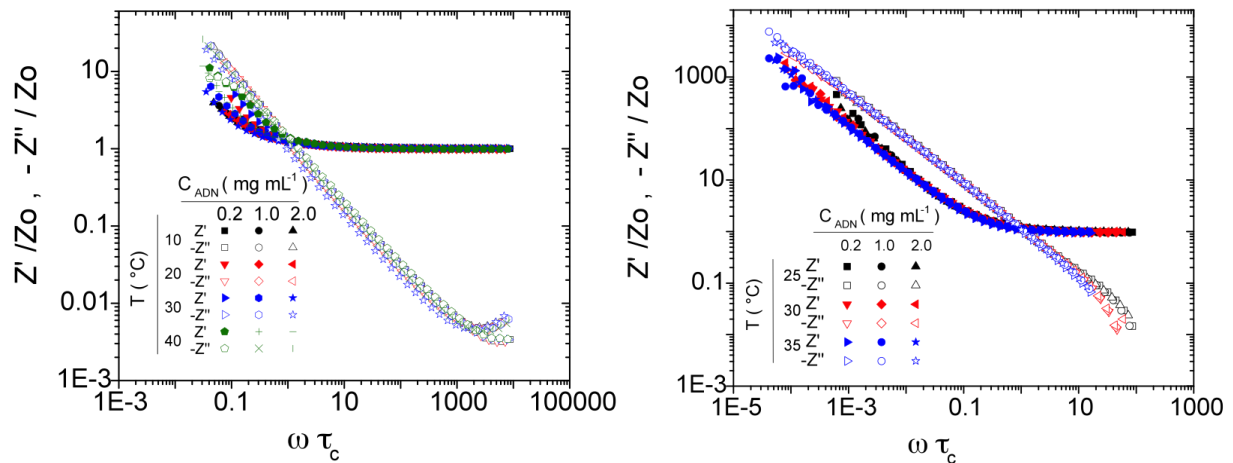
Figure 4.11. *Real and imaginary parts of the impedance in units of Z_o as functions of the rescaled angular frequency $\omega\tau_c$ for a) Pt-DNA/TE buffer interface and b) Au-DNA/TE buffer interface.*

4.3.6. The scaling of electrochemical parameters as a function of DNA concentration and temperature

For impedance studies, the obtained values for the parameters Z_o (*Figure 4.12*) and τ_c (*Figure 4.13*) obtained for the interface Pt-DNA/TE buffer follow a power law behavior as a function of DNA concentration according to: dilute regime ($C_{DNA} < C^*$): $Z_o \sim C_{DNA}^{-0.692 \pm 0.047}$ and $\tau_c \sim C_{DNA}^{-0.793 \pm 0.059}$, semi-dilute regime without entanglements ($C^* < C_{DNA} < C_e$): $Z_o \sim C_{DNA}^{-0.741 \pm 0.023}$ and $\tau_c \sim C_{DNA}^{-0.822 \pm 0.05}$ and semi-dilute regime with entanglements ($C_e < C_{DNA}$): $Z_o \sim C_{DNA}^{-0.668 \pm 0.073}$ and $\tau_c \sim C_{DNA}^{-0.745 \pm 0.046}$. This power law dependence was observed in the whole temperature range studied. The exponent values of the fitting, corresponding to the relation between the solution resistance (Z_o) and DNA concentration are lower in the semi-dilute regime without entanglements. The results for the evaluated parameters (Z_o and τ_c) according to the power law are quantified in *Table 4.7* for each characteristic regime at the four studied temperatures.

Table 4.7.- *Parameters obtained for Pt-DNA/TE buffer by fitting Z_o and τ_c results as a function of DNA concentration according to the law power at the temperatures of 10, 20, 30 and 40 ºC.*

Regime	DNA Concentration mg/mL	T º C	τ_c s		Z_O Ω cm²	
			a	*b*	*c*	*d*
Dilute	$C_{DNA}<C^*$	10	1.284	−0.818	4 846.684	−0.719
		20	0.967	−0.834	3 607.698	−0.732
		30	0.948	−0.815	3 244.702	−0.691
		40	1.227	−0.704	3 155.506	−0.627
Semi-dilute without entanglements	$C^*<C_{DNA}<C_e$	10	0.819	−1.339	3 673.842	−0.768
		20	0.851	−0.763	2 916.883	−0.737
		30	0.661	−0.857	2 353.754	−0.747
		40	0.726	−0.846	2 023.210	−0.713
Semi-dilute with entanglements	$C_e>C_{DNA}$	10	1.580	−1.208	4 490.697	−0.627
		20	1.023	−0.692	3 566.001	−0.633
		30	0.853	−0.772	2 937.819	−0.635
		40	0.902	−0.690	2 729.245	−0.777
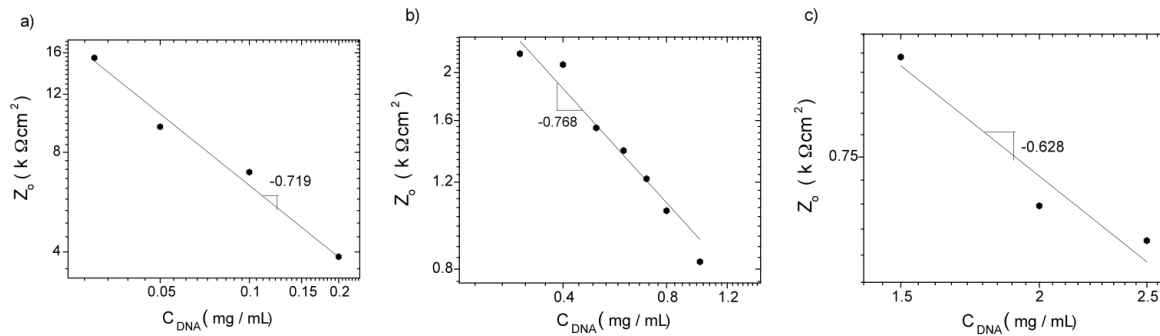
Figure 4.12. *Z_o as a function of DNA concentration at a temperature of 10 ºC evaluated at a) dilute regime, b) semi-dilute regime without entanglements and c) semi-dilute regime with entanglements for Pt-DNA/TE buffer interface.*
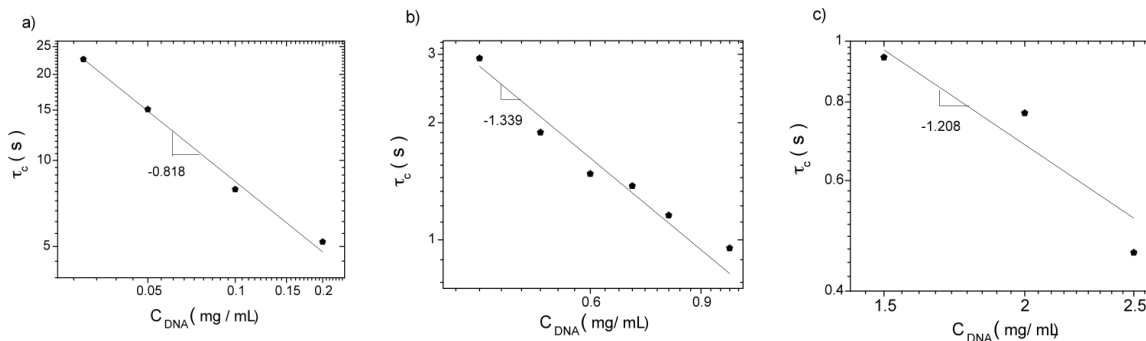
Figure 4.13. *τ_c as a function of DNA concentration at a temperature of 10 ºC evaluated at a) dilute regime, b) semi-dilute regime without entanglements and c) semi-dilute regime with entanglements for Pt-DNA/TE buffer interface.*

The obtained values for the parameters Z_o (*Figure 4.14*) and τ_c (*Figure 4.15*) from Au-DNA/TE buffer interface were also evaluated in terms of a power law behavior as a function of DNA concentration. The following relations were found: dilute regime ($C_{DNA}<C^*$): $Z_o \sim C_{DNA}^{-0.826\pm0.014}$ and $\tau_c \sim C_{DNA}^{-0.939\pm0.027}$, semi-dilute regime without entanglements ($C^*<C_{DNA}<C_e$): $Z_o \sim C_{DNA}^{-0.782\pm0.046}$ and $\tau_c \sim C_{DNA}^{-0.785\pm0.113}$ and semi-dilute regime with entanglements ($C_e<C_{DNA}$): $Z_o \sim C_{DNA}^{-0.634\pm0.021}$ and $\tau_c \sim C_{DNA}^{-0.853\pm0.265}$. This power law dependence was observed in the whole temperature range studied. The results for the evaluated parameters (Z_o and τ_c) according to the power law are quantified in *Table 4.8* for each characteristic regime at the four studied temperatures.

Table 4.8.- *Parameters obtained for Au-DNA/TE buffer by fitting Z_o and τ_c results as a function of DNA concentration according to the law power at the temperatures of 25, 30 and 35 ºC.*

Regime	DNA Concentration mg/mL	T ºC	τ_c s		Z_O Ω cm²	
			a	*b*	*c*	*d*
Dilute	$C_{DNA}<C^*$	25	0.0021	-0.909	5 061.60	-0.842
		30	0.0018	-0.964	4 912.08	-0.812
		35	0.0018	-0.946	4 400.81	-0.825
Semi-dilute without entanglements	$C^*<C_{DNA}<C_e$	25	0.0020	-0.710	4 657.69	-0.763
		30	0.0020	-0.729	4 404.42	-0.736
		35	0.0019	-0.816	4 047.33	-0.779
Semi-dilute with entanglements	$C_e>C_{DNA}$	25	0.0019	-1.010	4 707.82	-0.651
		30	0.0018	-1.000	3 495.28	-0.641
		35	0.0018	-0.547	3 158.09	-0.611
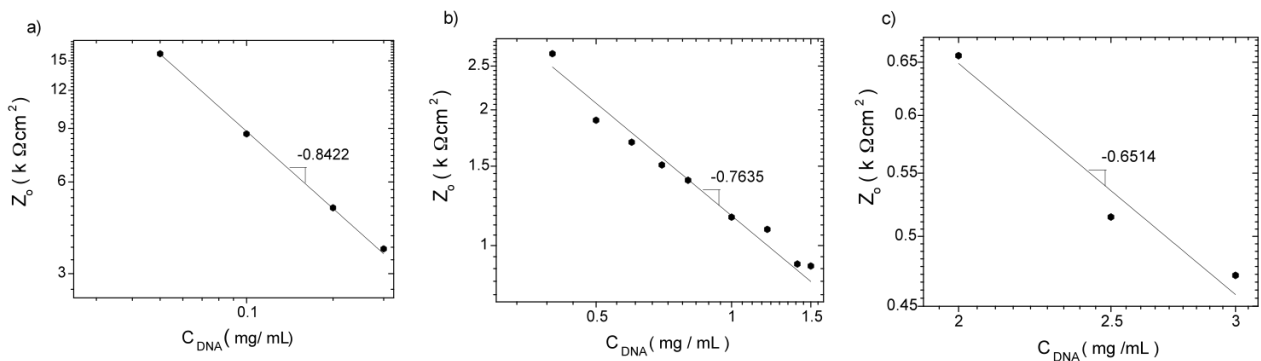
Figure 4.14. *Z_o as a funtion of DNA concentration at a temperature of 25 ºC evaluated at a) dilute regime, b) semi-dilute regime without entanglements and c) semi-dilute regime with entanglements for Au-DNA/TE buffer interface.*
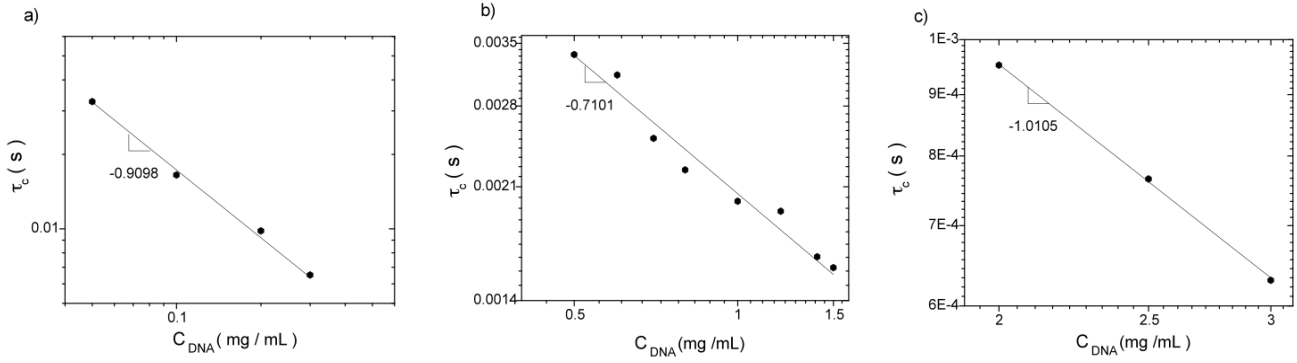
Figure 4.15. *τ_c as a funtion of DNA concentration at a temperature of 25 ºC evaluated at a) dilute regime, b) semi-dilute regime without entanglements and c) semi-dilute regime with entanglements for Au-DNA/TE buffer interface.*

4.3.7. Transfer function designed to simulate the capacitive behavior as a function of the DNA concentration

A transfer function was proposed in order to predict the impedance response generated by the adsorption process of DNA molecules onto the platinum surface for any DNA concentration within the characteristic regimes of the system studied in this work. Simulations were carried out with this transfer function, which was developed as a function of DNA concentration and the electrochemical parameters related to the characteristic time-constant of the process and the solution resistance.

According to *Equation 4.1*, for an ideally polarizable electrode, this expression can be evaluated when R_{ct} boundary tends to infinite. This way, since the values of the charge transfer resistance are very large, the contribution of a resistance due to an oxidation-reduction reaction may be discarded in the final transfer function. Therefore, the expression taking into account this condition is derived as follows:

$$Z(w) = R_s + \frac{1}{(jw)^a Q} \tag{4.8}$$

Since the characteristic time-constant of the process (τ_c) shown in *Equation 4.6* is given in terms of the solution resistance and the effective capacitance, it is possible to replace *Equation 4.2* in *Equation 4.6*, obtaining the following expression:

$$t_c = [R_s Q]^{1/a} \tag{4.9}$$

Solving for Q, we obtain *Equation 4.10* as a function of τ_c, R_s and α:

$$Q = \frac{t_c^a}{R_s} \quad (4.10)$$

By using the mathematic formulation for the general power law, the characteristic time-constant (τ_c) and the Z_o module, related to the solution resistance (R_s), follow the relations given by *Equations 4.11* and *4.12*, respectively.

$$t_c = aC_{DNA}^b \quad (4.11)$$

$$R_s = cC_{DNA}^c \quad (4.12)$$

where *a*, *b*, *c* and *d* are the defined constants for each characteristic regime at each temperature. This way, *Equation 4.10* can be evaluated as a function of DNA concentration according to *Equation 4.11* and *4.12*:

$$Q = \frac{\left[aC_{DNA}^b \right]^a}{cC_{DNA}^b} \quad (4.13)$$

Replacing *Equations 4.12* and *4.13* in the transfer function given by *Equation 4.8*, it is possible to obtain a transfer function able to simulate the impedance response as a function of DNA concentration (*Equation 4.14*).

$$Z(W) = cC_{DNA}^b + \left[1 + \frac{1}{\left(jwaC_{DNA}^d \right)^a} \right] \quad (4.14)$$

To obtain any desired spectra, it is only necessary to model the impedance response at one concentration in a selected characteristic regime by using the Levenberg-Marquardt curve-fitting method. The results will give the information about the alpha coefficient of the constant phase element (CPE), and the power law constants (a, b, c and d), so it will be possible to predict the impedance behavior as a function of concentration and to obtain information about the characteristic time constant of the process and the solution resistance.

Figures 4.16 a, *b*, *c* and *d* show the Nyquist plots for a DNA concentration of 0.4 mg/mL in platinum at the temperatures of 10, 20, 30 and 40 ºC and their respective simulations obtained by using the proposed transfer function given by *Equation 4.14.*
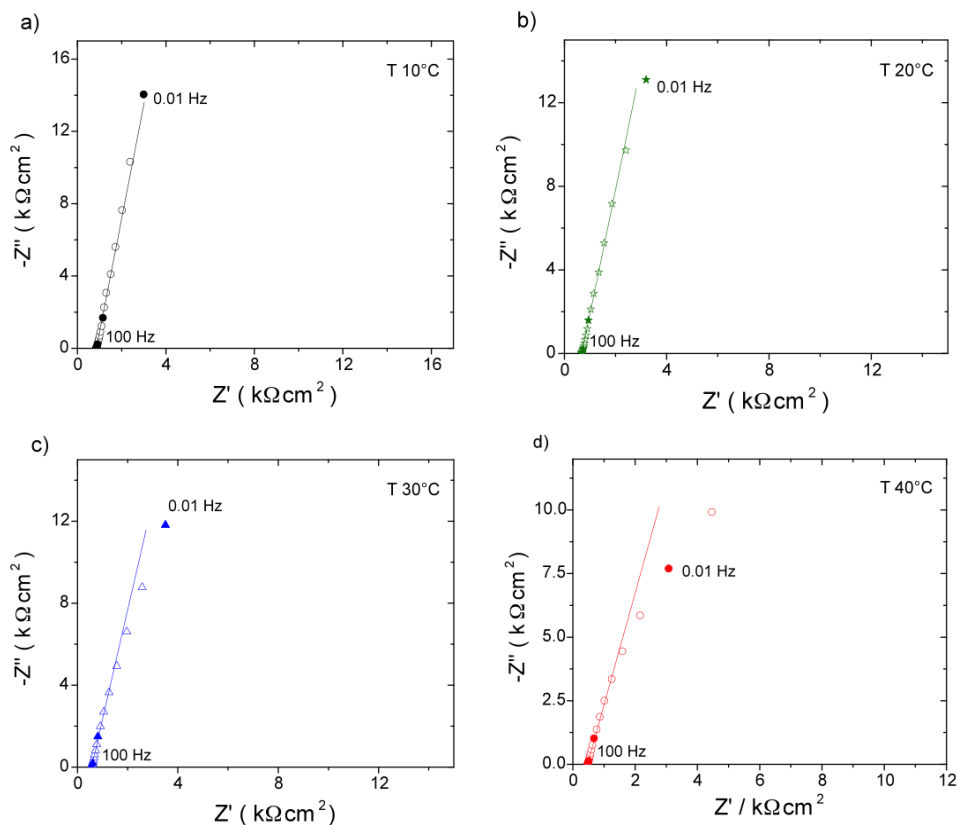
Figure 4.16. *Nyquist plots for Pt-DNA/TE buffer interface at a concentration of 0.4 mg/mL and the temperatures of a) 10, b) 20, c) 30 and d) 40 °C. Frequency in Hz.*

The transfer function was also tested for Au-DNA/TE buffer interface, as we can see in *Figures 4.17a, b* and *c* that show the Nyquist plots for a DNA concentration of 0.4 mg/mL at the temperatures of 25, 30 and 35 °C and their respective simulations obtained by using the proposed transfer function given by *Equation 4.14.* An average of α values obtained through the experimental data of this work and *a, b, c* and *d* values, presented on *Tables 4.7* and *4.8* for platinum and gold, respectively, are considered in these simulations.
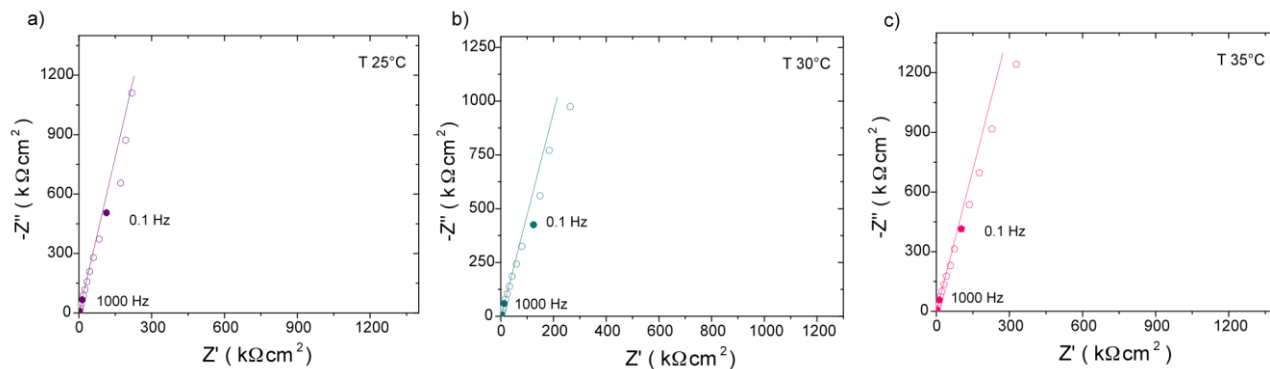
Figure 4.17. *Nyquist plots for Au-DNA/TE buffer interface at a concentration of 0.4 mg/mL and the temperatures of a) 25, b) 30 and c) 35 °C. Frequency in Hz.*

Several advantages have been found by using this transfer function in the study of biopolymeric solutions such as DNA. Through one impedance measurement it is possible to obtain R_s and τ_c profiles as a function of concentration for each characteristic regime of the system. The impedance behavior for every concentration within a specific regime studied at OCP can be predicted, therefore, a double-layer charging analyze as a function of concentration can also be proposed. Since polymeric solutions and several soft material solutions are known by presenting characteristic behaviors within determined concentration and temperature ranges, the electrochemical impedance spectroscopy technique will be able to easily determine the parameters of interest and their profiles by using the transfer function and the power law relations.

4.4. Particular conclusions for scaling of electrochemical parameters of DNA molecules by EIS

Transitional behavior of calf thymus DNA molecules, using platinum and gold electrodes, was investigated through a detailed study performed by electrochemical impedance spectroscopy using the classical impedance analysis by means of equivalent circuits and an analogous methodology to the one used in linear rheology studies. From the analysis of Z_o and τ_c as a function of DNA concentration it was possible to indentify two transitions located around 0.30 and 1.50 mg/mL, related to the overlap (C*) and the entanglement (C_e) concentrations, respectively. A linear behavior of Z_o and τ_c was observed in each characteristic regime of the system, in which the relation between them and C_{DNA} follows the power law at every studied temperature. Arrhenius-type temperature dependence was obtained for the characteristic time constant of DNA molecules arrangement on the electrochemical double-layer. A general impedance transfer function was proposed as a function of DNA concentration through the scaling of the electrochemical parameters, i.e. the Z_o related to the solution resistance and the characteristic time constant of the process, τ_c. Such transfer function allows analyzing theoretically the double-layer charging behavior at OCP as a function of concentration with only one impedance experiment and makes possible obtaining the electrochemical parameters of the interface at a chosen concentration and at a specific regime of the system. In our study, this function was developed through the analysis of the Pt-DNA/TE buffer and the Au-DNA/TE buffer interfaces, but is proposed to be useful in studies of polymeric and surfactant systems, characterized by having different regimes due to their interactions or different kind of structures formed at a wide range of temperature or concentration conditions.

4.5. References

[1] M. Sun, S. Pejanovic, J. Mijovic, Dynamics of deoxyribonucleic acid solutions as studied by

dielectric relaxation spectroscopy and dynamic mechanical spectroscopy, *Macromolecules* **38** (2005) 9854.

[2] Y. Heo, R.G. Larson, The scaling of zero-shear viscosities of semidilute polymer solutions with concentration, *J. Rheol.* **49** (2005) 1117.

[3] F. Carvajal-Ramos, A. González-Álvarez, J. Roger Vega-Acosta, D. Váldez-Pérez, V.V.A. Fernández- Escamilla, E.R. Balleza Escamilla, J.F.A. Soltero, Phase and rheological behavior of cetyldimethylbenzylammonium salicylate (CDBAS) and water, *J. Surfact. Deterg.* **14** (2011) 269-279.

[4] J.G. Álvarez-Ramírez, V.V.A. Fernández, E.R. Macías, Y. Rharbi, P. Taboada, R. Gámez-Corrales, J.E. Puig and J.F.A. Soltero, Phase behavior of the Pluronic P103/water system in the dilute and semi-dilute regimes, *J. Colloid Interface Sci.* **333** (2009) 655-662.

[5] V.V. A Fernandez, N. Tepale, J.G. Álvarez, J.H. Pérez-López, E.R. Macías, F. Bautista, F. Pignon, Y. Rharbi, R. Gámez-Corrales, O. Manero, J.E. Puig and J.F.A. Soltero, Rheology of the Pluronic P103/water system in a semidilute regime: Evidence of nonequilibrium critical behavior, *J. Colloid Interface Sci.* **336** (2009) 842-849.

[6] D.C. Boris and R. H. Colby, Rheology of sulfonated polystyrene solutions, *Macromolecules* **31** (1998) 5746-5755.

[7] T.G. Mason, A. Dhople and D. Wirtz, Linear viscoelastic moduli of concentrated DNA solutions, *Macromolecules* **31** (1998) 3600.

[8] R. Bandyopadhyay and A. K. Sood, Dynamical behavior in the nonlinear rheology of surfactant solutions, *J. Stat. Phys.* (2000) 40-51.

[9] D. Jary, J.- L. Sikorav and D. Lairez, Nonlinear viscoelasticity of entangled DNA molecules, *Europhys. Lett.* **46** (1999) 251-255.

[10] L. M. Bravo-Anaya, E. R. Macías, F. Carvajal Ramos, J. G. Álvarez-Ramírez, N. Casillas, J. F. A. Soltero and E. R. Larios-Durán, DNA Transitions by an Adsorption Impedance Study, *J. Electrochem. Soc.* **160** (2013) G69-G74.

[11] E. Paleček, Polarographic behavior of native and denatured deoxyribonucleic acids, *J. Mol. Biol.*, **20** (1966) 431.

[12] P. Santos-Alvarez, M. J. Lobos-Castanon, A. J. Miranda-Ordieres and P. Tunon-Blanco, Current strategies for electrochemical detection of DNA with solid electrodes, *Anal. Bioanal. Chem.* **378(1)** (2004) 104-118.

[13] J.-Y. Park and S.-M. Park, DNA Hybridization Sensors Based on Electrochemical Impedance Spectroscopy as a Detection Tool, *Sensors* **9** (2009) 9513-9532.

[14] A. Rodríguez-López, D. Torres-Torres, J. Mojica-Gómez, C. Estrada-Arteaga, R. Antaño- López, Characterization by electrochemical impedance spectroscopy of magnetite nanoparticles supported on carbon paste electrode, *Electrochemi. Acta* **56** (2011) 8079-8084.

[15] A. Jänes, G. Nurk, K. Lust, J. Ehrlich, and E. Lust, Adsorption kinetics of normal-heptanol on the bismuth single crystal Planes, *Russ. J. of Electrochem.* **38** (2002) 11-24.

[16] M.E. Orazem, B. Tribollet, *Electrochemical Impedance Spectroscopy*, John Wiley and Sons, Hoboken, New Jersey (2008).

[17] L. M. Bravo-Anaya, E. R. Macías, F. Carvajal Ramos, V. V. A. Fernández, N. Casillas, J. F. A. Soltero and E. R. Larios-Durán, DNA conformational transitions at different concentrations and temperatures monitored by EIS, *ECS Electrochem. Lett.* **1** (2012) G1-G3.

[18] J. Newman, Resistance for Flow of Current to a Disk, *J. Electrochem. Soc.* **113** (1966) 501-502.

[19] M. J. Moorcroft, N. S. Lawrence, B. A. Coles, R. G. Compton, L. N. Trevani, High temperature electrochemical studies using a channel flow cell heated by radio frequency radiation, *J. Electroanal. Chem.* **506** (2001) 28-33.

[20] J. Jacquemin, P. Husson, A. A. H. Padua and V. Majer, Density and viscosity of several pure and water-saturated ionic liquids, *Green Chem.* **8** (2006) 177.

[21] L. Xu, F. Mallamace, Z. Yan, F. W. Starr, S. V. Buldyrev and H. E. Stanley, Appearance of a fractional Stokes-Einstein relation in water and a structural interpretation of its onset, *Nature Physics* **5** (2009) 565.

[22] A. J. Banchio, G. Nägele, and J. Bergenholtz, Viscoelasticity and generalized Stokes-Einstein relations of colloidal dispersions, *J. Chem. Phys.* **111** (1999) 8721.

[23] J. O'M. Bockris, A. K. N. Reddy, and M. Gambioa-Aldeco, *Modern Electrochemistry 2A. Fundamentals of Electrodics., Kluwer Academic Publisher*, New York, Boston, Dordrecht, London, Moscow (2002).

[24] J. R. Macdonald, Impedance spectroscopy and its use in analyzing the steady-state AC response of solid and liquid electrolytes, *J. Electroanal. Chem.* **223** (1987) 25-50.

[25] B. Hirschorn, M. E. Orazem, B. Tribollet, V. Vivier, I. Frateur, M. Musiani, Determination of effective capacitance and film thickness from constant-phase-element parameters, *Electrochim. Acta* **55** (2010) 6218-6227.

[26] E.R. Larios-Durán and R. Antaño-López, Kinetic study of bromide adsorption on Hg by a combined equivalent-circuit reaction-mechanism modeling of EIS data, *J. Electroanal. Chem.* **658** (2011) 10.

[27] Z. Lukacs, The numerical evaluation of the distortion of EIS data due to the distribution of parameters, *J. Electroanal. Chem.* **432** (1997) 79.

[28] A.J. Bard, L Faulkner, *Electrochemical Methods, Fundamentals and Applications*, p.548, 2nd Ed., John Wiley and Sons, Singapore (1980).

[29] S. R. Raghavan and E. W. Kaler, Viscoelastic wormlike micellar solutions formed by cationic surfactants with long unsaturated tails, *Langmuir* **17** (2001) 300-306.

[30] S.-H. Tung, Y.-E. Huang and S. R. Raghavan, Contrasting effects of temperature on the rheology of normal and reverse wormlike micelles, *Langmuir* **23** (2007) 372-376.

CHAPTER 5

Study of the structural rearrangement of the interface DNA-gold by Surface Plasmon Resonance (SPR).

Chapter 5. Study of the structural rearrangement of the interface DNA-gold by Surface Plasmon Resonance (SPR)

The results of this chapter are the object of the following publication:

L. M. Bravo-Anaya, E.R. Macías Balleza, J.L. Hernández-López, V.V. Fernández-Escamilla, A. Carreón-Álvarez, J.R. Rodríguez, J. F. A. Soltero and E.R. Larios-Durán.

5.1. Introduction

The control of surface interactions in the biomaterials field has been widely study for its importance in determining critical parameters such as biocompatibility [1]. Using the Surface Plasmon Resonance (SPR) technique for analyzing such interactions is advantageous due to the possibility of monitoring any dynamic process in real time, such as adsorption or degradation in a wide variety of biomedically relevant interfaces [2]. It is also possible to obtain information on the rate and the degree of adsorption, allowing the determination of dielectric properties, association and dissociation kinetic constants and affinity constants of specific interactions between the analyte-ligand [3]. Currently, the study of ultrathin organic films has gained interest in different fields (i.e. integrated optics, sensors, surface orientation layers, among others [4]), being the deposition of macromolecules such as proteins and DNA particularly analyzed because of its broad application field in the biosensor development [5].

In this chapter we study the adsorption process of calf thymus DNA molecules in TE buffer solution as a function of DNA concentration and at a constant temperature ($25 \pm 1°C$) by Surface Plasmon Resonance (SPR). We report values for the average optical film thickness (d_{opt}) of adsorbed DNA molecules on the surface of the sensor chip for each DNA concentrations studied. The variations of this parameter as a function of DNA concentration are related to transitions in the structural arrangement of the electrochemical double-layer, presumably caused by DNA interactions observed at the concentrations C^* and C_e, previously defined as the overlap and the entanglement concentration, and are in good agreement with the obtained values by EIS and physicochemical techniques (*Chapter 2* and *3* and the C_e value reported by *Mason et al.* [6]). Complementarily, the behavior of the dielectric constant of the system (ε) as a function of DNA concentration was evaluated as a first approximation by using the simplest model of the double layer [7-9] from d_{opt} values and the double layer capacitance values reported in *Chapter 3* for the adsorption of DNA molecules in Au electrodes.

5.2. Overview of the SPR technique

5.2.1. Surface plasmons

The Surface Plasmon Resonance spectroscopy (SPR) is an optical technique that was introduced in the 90's as an underlying technology in affinity biosensors for the analysis of biomolecular interactions (BIA), representing a new concept for the analysis of functional properties of biomolecules [10]. The SPR phenomenon occurs when an incident beam of p-polarized light with a given wavelength gets into the surface at a certain angle through a prism. In such conditions, surface plasmon electromagnetic waves (surface plasmon polaritons) are created in the metal/dielectric interface. Therefore, plasmons are collective charge oscillations of free electrons of a metal in a gaseous medium. A surface plasmon corresponds to a longitudinal charge wave, which propagates in parallel way along the interface of two media, where one is the metal, and the other is the dielectric [10, 11] (*Figure 5.1*). As light, surface plasmons are a form of electromagnetic energy that can only be described by quantum physics.
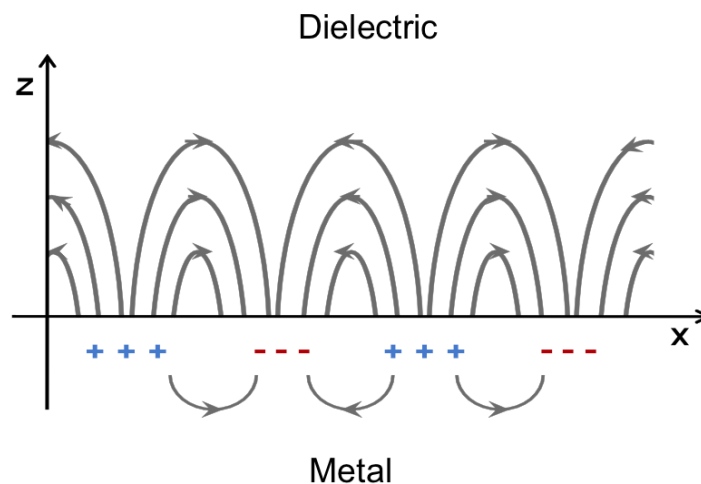
Figure 5.1. *Surface plasmons in the metal-dielectric interface.*

5.2.2. Phenomenon of total internal reflection

The phenomenon of total internal reflection (TIR) is very important in the SPR technique. The propagation of a light beam through a surface from a medium having a high refractive index to a medium having a low refractive index causes the light to be refracted towards the interface. In this way, the incidence angle (θ) increases and a point where the refracted light beam is parallel to the interface is reached, obtaining the critical incidence angle (θ_c) (*Figure 5.2*).

At higher angles of incidence, all the light is reflected within the medium with high refractive index, this phenomena is called total internal reflection. If the medium with lower refractive index

absorbs light at a suitable wavelength, the evanescent field wave can transfer the photon energy corresponding to the medium [12]. This field comes in all circumstances where total internal reflection occurs.
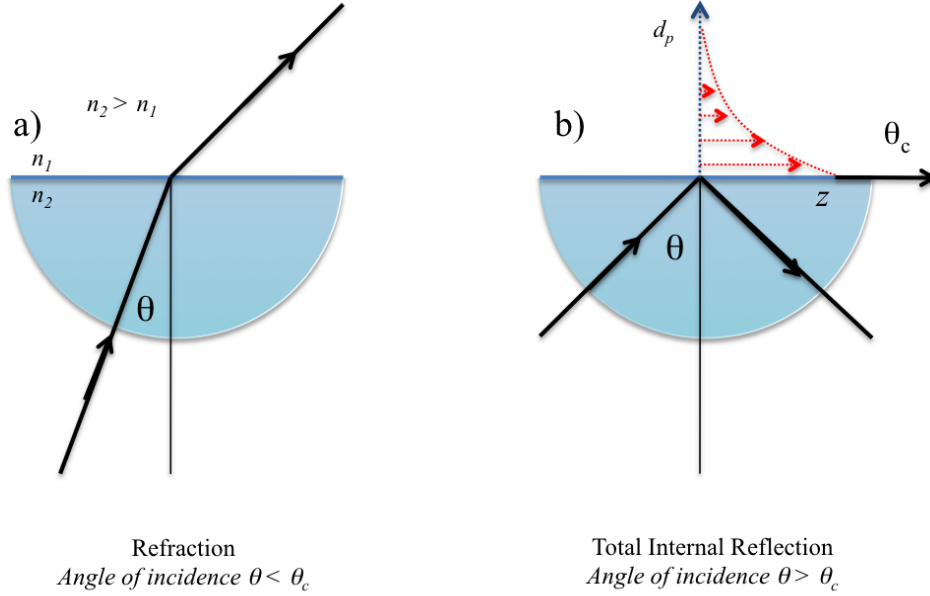
Figure 5.2. *a) The light is directed from the denser medium (n_2) to the lower density medium (n_1) and is refracted to the interface. b) Above the critical incidence angle (θ_c), the total internal reflection (TIR) takes and the light don't pass through the less dense medium.*

Otto [13] and *Kretchmann* [14] developed two different experimental systems for the excitation of surface plasmons. With the Otto configuration it is possible to have a separation of the TIR interface by a thin film of the medium with lower refractive index and is useful in studies of SPR in solid phase media, however, is less suitable for biosensors applications because the liquid film must be controlled carefully. Furthermore, the Kretchmann configuration places directly the metal film in the TIR interface, allowing a greater efficiency in the plasmons generation (*Figure 5.3*).

A source of *p*-polarized monochromatic light is used in SPR and the interface between two dense optical media is coated with a thin metal film. The wave vector of the evanescent field (K_{ev}) is given by:

$$K_{ev} = \left(\frac{w_0}{c}\right)\eta_g \sin\theta \tag{5.1}$$

where ω_0 is the frequency of the incident light, η_g the refractive index of the dense medium (glass), θ the incidence angle of light and c is the speed of light in vacuum. The wave vector of the surface plasmon can be approximated with the following expression:

$$K_{sp} = \left(\frac{w_0}{c} \right) \sqrt{\frac{\varepsilon_m \eta_d^2}{\varepsilon_m + \eta_d^2}} \qquad (5.2)$$

where ε_m is the dielectric constant of the metal film and η_d is the refractive index of the dielectric medium [15].
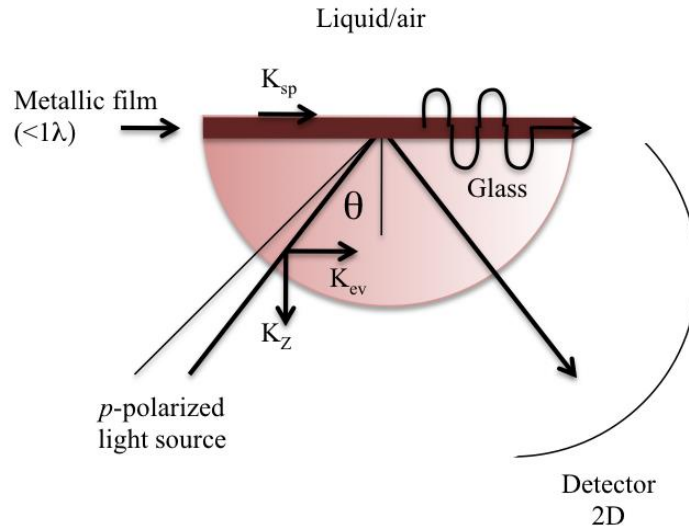
Figure 5.3. *Kretchmann configuration for SPR. The resonance of a surface plasmon is excited in the interface metal/air when the incidence angle of the light beam is such that the evanescent component of the wave vector (K_{ev}) is equal to the wave vector of the surface plasmon that is been propagated (K_{sp}).*

5.2.3. Selection of the metal support

The selection of the metal is very important since it must exhibit a behavior as described in the free electron model [16]. The most suitable metals are silver, gold, copper and aluminum, from which silver and gold are used more frequently. In some cases it has been observed that silver tends to undergo undesirable interactions with the environment (air or water), making it a less attractive metal, however, gold is a stable material and has become the standard metal for SPR studies [17].

5.2.4. SPR phenomenon

When the evanescent wave of the incoming light is capable of being linked with the free oscillating electrons (plasmons) in the metal film and at a specific incidence angle (when $k_{sp} = k_{ev}$), then the response of an excited plasmon is obtained. A decrease in the intensity of the reflected light at a specific incidence angle is obtained as a result of the energy transfer (*Figure 5.4*).

Through the graphical representation of the variation of the laser beam incidence angle we can obtain the minimum corresponding to the light intensity reflected at the metal/dielectric interface, defined by the conditions in which the energy and the momentum of light photons (k_x) and surface plasmon (k_{sp}) are equal.
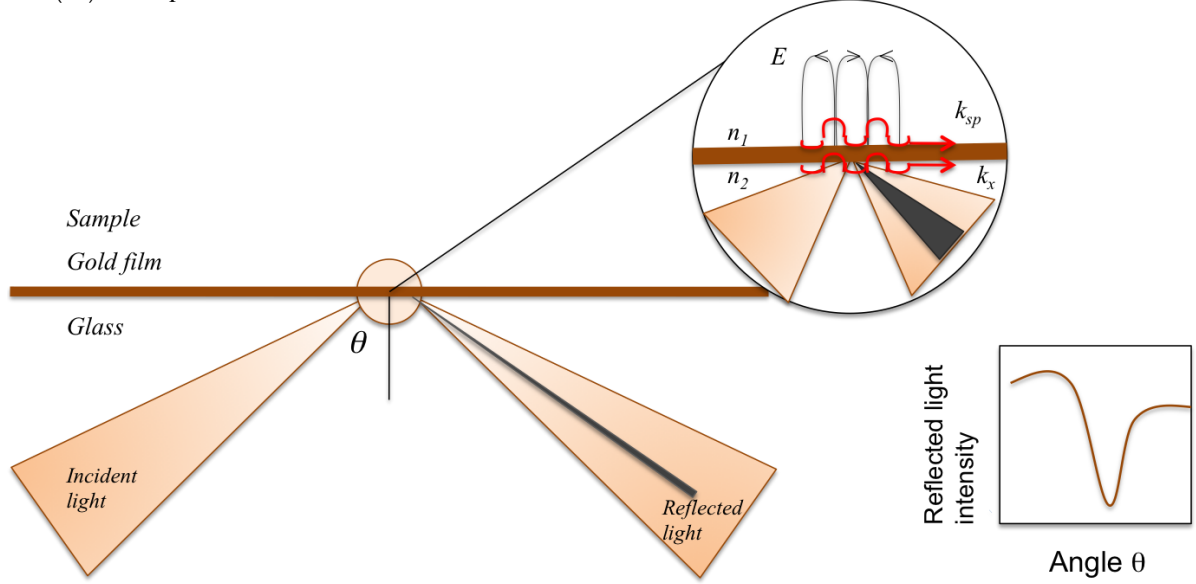
Figure 5.4. *Schematic representation of SPR phenomenon.*

The reflectance of the incident light at a given angle (θ) can be calculated by a three layers Fresnel equation in relation to the *p*-polarization [10]. The detection system consists of three medium *j*, denoted by γ, μ and ρ, corresponding to the prism, the metal film and the sensor film. The reflectance of the incident light (R) is calculated as follows:

$$R = \left| \frac{r_{gm} + r_{mr}e^{2ik_m d_{opt}}}{1 + r_{gm}r_{mr}e^{2ik_m d_{opt}}} \right| \tag{5.3}$$

where $j = \gamma, \mu$ and ρ

$$k_j = \sqrt{e_j \frac{w^2}{c^2} - k_z^2} \tag{5.4}$$

where $k_z = (\varepsilon_\gamma)^{1/2} (\omega/c)\sin\theta$

The amplitude of the reflectance for the interfaces prism-metal and metal-sensor film are given by the following *Equations 5.5* and *5.6.*

$$r_{gm} = \frac{k_g e_m - k_m e_g}{k_g e_m + k_m e_g} \tag{5.5}$$

$$r_{gm} = \frac{k_g e_r - k_r e_g}{k_g e_r + k_r e_g} \tag{5.6}$$

where ε_j is the dielectric constant, k_j is the component of the wave vector perpendicular to the respective media interface j (prism, metal or sensor film), k_z is the component of the wave vector parallel to the interface, ω is the angular frequency of incident light ($\omega(\lambda) = 2\pi c/\lambda$), d_{opt} is the average optical film thickness c is the speed of light.

The application of this mathematical model allows simulating the obtained spectra by SPR and obtaining parameters as the dielectric constants and optical film thickness of the medium studied. The obtained changes in the SPR angle from the reflected light at a particular wavelength are directly related to the constants c_1 and c_2 for the refractive index change at the surface (Δn) and the optical film thickness change (Δd_{opt}) according to the following expression:

$$DQ(/) = c_1 Dn + c_2 Dd_{opt} \tag{5.7}$$

That in the case of proteins, the variations in the optical film thickness (d_{opt}) caused by a conformational change in the molecule can predict a change in the refractive index (Δn) according to the Lorentz-Lorenz relationship [18]:

$$Dn = -\frac{1}{6n}(n^2 + 2)^2 \left(\frac{n^2 - 1}{n^2 - 2} - \frac{n_w^2 - 1}{n_w^2 - 2} \frac{V_p}{V} \right) \frac{Dd_{opt}}{d_{opt}} \tag{5.8}$$

where n is the refractive index of the molecule, n_w is the refractive index of water, V_p is the volume of the molecule and V is the volume of the film formed by the molecule ($V = V_p + V_m$).

5.2.5. Adsorption kinetics

The adsorption processes that are performed on the gold surface can be monitored in real time by selecting a suitable incidence angle and monitoring the reflected light intensity as a function of time. The functionalization of the gold surface with biomolecular receptors can lead to consider the SPR technique as a very effective tool for measuring the kinetics and the equilibrium constants of bioaffinity interactions of the system [19]. Three main stages are considered in the adsorption process monitored through SPR, i.e. association, dissociation and regeneration. Initially, the surface is calibrated with the buffer solution that will create the baseline in the SPR curve. Once the molecule comes in contact with

the surface, a rapid adsorption is produced and can be visualized as an increase in the SPR angle. This process is followed by the formation of a plateau in the adsorption profile, caused by the saturation of the surface with the molecule. Finally, the solution with the molecule is then replaced by the buffer solution in order to remove the material weakly bounded on the surface. The difference between the initial and the final SPR angle provides information about the degree of adsorption and the positive slope of the SPR adsorption curve determines the rate of adsorption [20].

5.3. Experimental conditions

The description of the reagents, buffer Tris-HCl/EDTA preparation and DNA/Buffer solutions are presented in *Sections 2.3.1., 2.3.2.* and *2.3.3.* of this work.

5.3.1. Design of the instrument Nano-SPR 6/321

Measurements of Surface Plasmon Resonance (SPR) were performed on a Nano-SPR 6/321 (USA) instrument that operates according to Kretschmann geometry [21]. It has a 65° retroflexion trapezoidal prism. The right side of the prism allows the reflection and the upper right corner of the prism is equivalent to 90°. The SPR phenomenon takes place in the sensor chip, which is placed on the upper face of the prism by using an immersion liquid. The incidence angle is calibrated by rotating the table on the axis with the prism, in order to match the surface to the glass substrate. *Figure 5.5* shows a schematic representation of the Nano-SPR 6/321 instrument experimental setup.
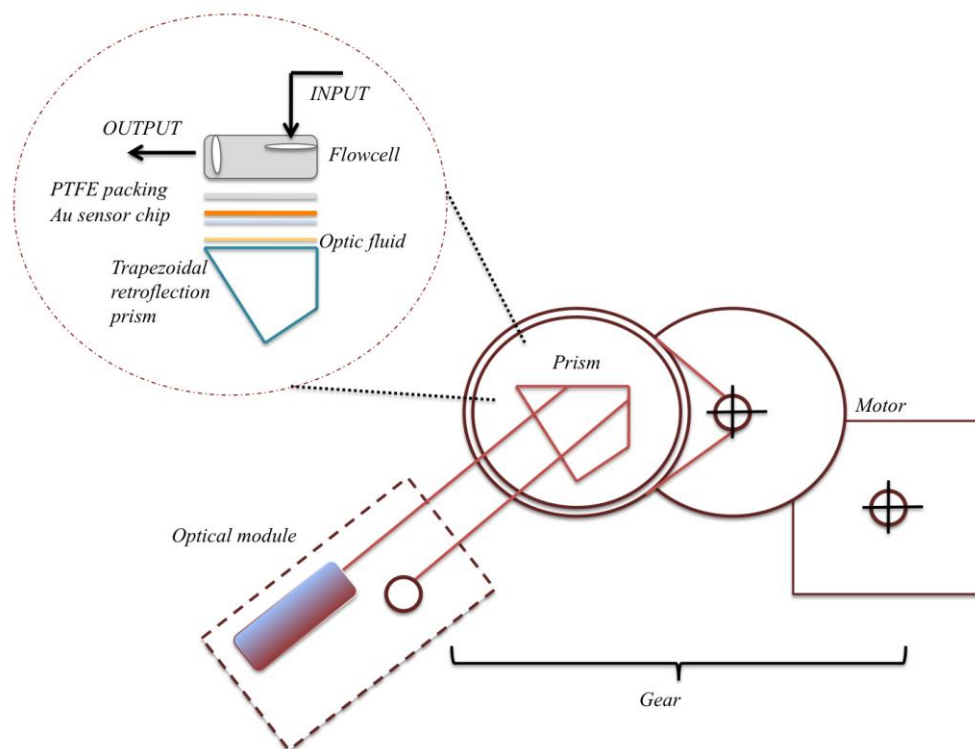
Figure 5.5. *Schematic representation of the experimental setup.*

5.3.2. Preparation of the chip sensor surface

Commercial gold slides used for SPR experiments were supplied by NanoSPR (USA) with the dimensions 20 x 20 x 1 mm. Each slide was coated with a 45 nm gold layer, deposited on a thin 5 nm chromium under layer used to improve the adhesion of the gold layer. Before being modified, the substrates were extensively washed with Milli-Q water, activated with ethanol and finally dried.

5.3.3. SPR measurements

A semiconductor laser beam (Ga-As, λ= 670 nm) was incident on the base of the prism. Due to the Kretschmann configuration of the instrument, the laser was split into two beams. Light reflectivity was monitored as a function of the incidence angle (θ) through a prism (TF1-65). A minimum was observed at the angle where the optimal resonance with the plasmon surface polaritons was reached. The instrument had a flow cell and tubing coupled to a peristaltic pump Masterflex C/L, model 77120-52 from USA. A laminar flow pumped at a speed of 2 rpm was used to carry out the adsorption study of the DNA solutions. For each DNA concentration, the gold slides used as substrate were initially calibrated with buffer EDTA/Tris-HCl for 10 minutes, which provided a baseline. A volume of 1.5 mL of DNA solution was injected into the flow cell and monitored for 90 minutes. After 10 minutes of rinsing with buffer solution, an adsorbed film of DNA molecules was recorded through the minimum angle obtained (θ_{SPR}).

5.3.4. SPR data analysis

Since the minimum angle of reflectivity (θ_{SPR}) is a function of several known parameters, such as refractive indices of glass, gold, chromium and the medium, d_{opt} for the organic layers are calculated using the Fresnel equations [22] through the commercial software Winspall version 3.01. The optical constants of the gold slide film (n_{Au}= 0.15 + 3.6i for gold and n_{Cr} = 2.10 + 3.37i for chromium), the glass substrates (1.616) and the prism were obtained from the supplier's database and were used as the initial parameters in the simulation process. All experiments were performed at room temperature (25 °C).

5.3.5. Transmission Electron Microscopy (TEM) measurements

Transmission Electron Microscopy measurements were carried on with a JEOL JEM-1011 microscope working at an accelerating voltage of 100 kV. One drop of the sample was placed on a carbon-coated copper grid before each examination, then blotted and washed. After this procedure,

phosphotungstic S5 acid 2% (w/v) was used to stain negatively each sample and air to dry them. Samples were incubated during the night prior to the imaging. No dilution was needed prior deposition on the grids. All measurements were performed at a constant temperature of 25 °C.

5.4. Experimental results

5.4.1. SPR angles analysis

The study of the adsorption process of DNA molecules in TE buffer solutions through SPR technique began with the determination of the optimal flow rate to dismiss the mass transport limitations. Such limitations are present when the observed binding between the analyte and the ligand are affected by the diffusion process of the analyte from the bulk of the solution to the surface of the sensor chip. It is known that in the case of biomolecules such as proteins, the binding between analyte and ligand is constant within a range of flow rates of 5 to 75 µL/min and the mass transport limitations are negligible [23]. Therefore, a calibration curve of the peristaltic pump was constructed in order to monitor flow in each one of the channels according to different angular speed (*Figure 5.6*). It was determined that the angular speed range from 0.1 to 2.6 rpm agrees with the criteria mentioned before, so the speed of 2 rpm was selected to perform our measurements.
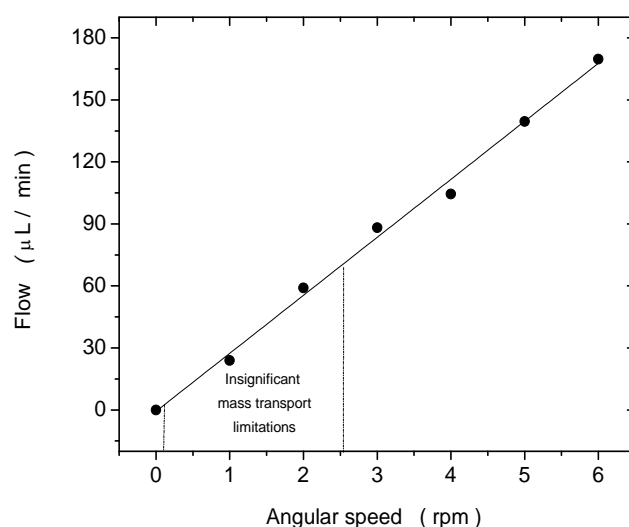
Figure 5.6. *Calibration curve for the peristaltic pump. (r²=0.9945).*

In order to understand the structural arrangement of the electrochemical double-layer formed from the adsorption of DNA molecules onto the Au substrate, several physical parameters obtained through the SPR technique were studied and analyzed.
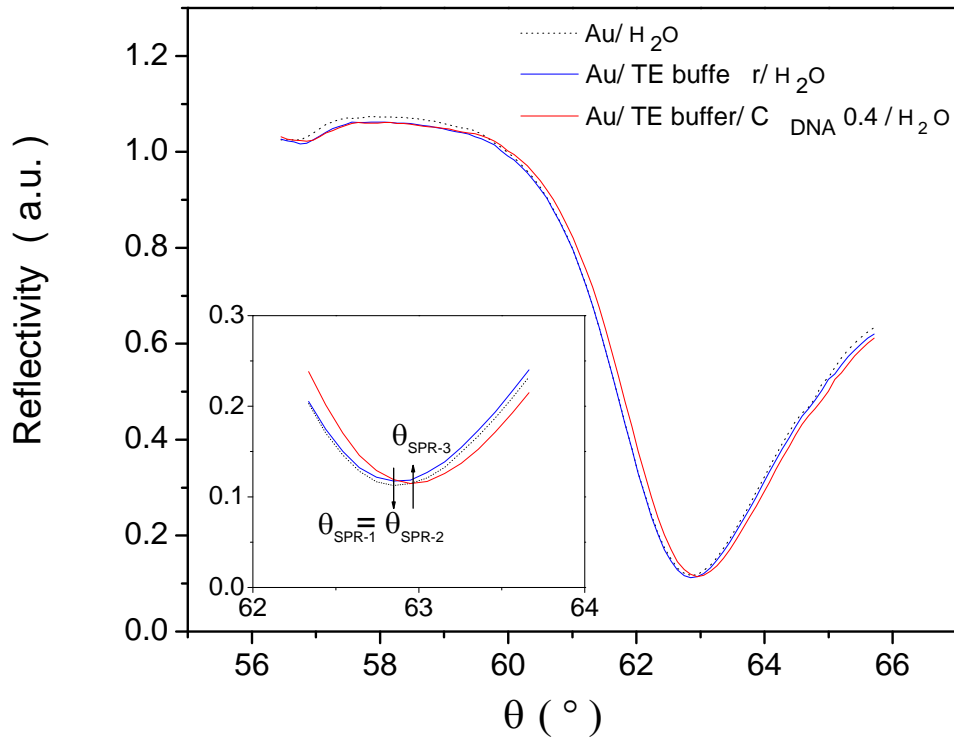
Figure 5.7. *Reflectivity (au) as a function ot the incidence angle (θ in °) for a DNA concentration of 0.4 mg/mL at the temperature of 25 °C. Insert: incidence angles θ_{SPR-1}, θ_{SPR-2} and θ_{SPR-3} for Au/H₂O, Au/TE buffer and Au/TE Buffer/C_{DNA} interfaces, respectively.*

The angle of minimum reflectivity (angle θ_{SPR}) was firstly monitored for each DNA/TE buffer concentrations through the displacement of the calibration angle from the buffer solution towards the largest angle observed after DNA molecules adsorption onto the Au surface. *Figure 5.7* shows, as an example, the normalized reflectivity spectra as a function of the incidence angle for a DNA concentration of 0.4 mg/mL at a constant temperature of 25 ± 1 °C. From these results it is possible to find the positions of the SPR angle for each DNA concentration. In the insert we can be observe the resonance angles θ_{SPR-1} and θ_{SPR-2} for Au/H₂O and Au/TE buffer interfaces, respectively, before the adsorption and θ_{SPR-3} for the Au/TE buffer/C_{DNA} interface after adsorption. It is possible to detect that the SPR angle of the buffer solution does not present significant changes with respect to the angle θ_{SPR-1}. Therefore, any adsorbed film from the buffer solution is neglected. However, after injection of each DNA solution, followed by a 90 minutes adsorption and a 10 minutes rinse with buffer solution, a shift in the minimum incidence angle towards higher values is distinguished. It is then possible to determine the formation of a film with adsorbed DNA molecules onto the metal surface after the set time. The dependence of θ_{SPR-3} with DNA concentration was then analyzed.
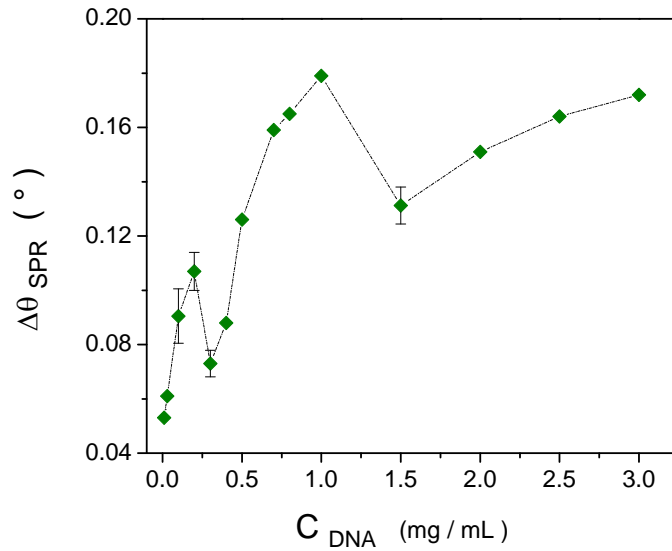
Figure 5.8. *Change of the minimum incidence angle (Δθ_{SPR}) obtained from the difference between θ_{SPR-1} and θ_{SPR-2} as a function of DNA concentration.*

Figure 5.8 shows the change of the incidence angle ($\Delta\theta_{SPR}$) obtained from the difference between the angle θ_{SPR-3} and θ_{SPR-2} as a function of DNA concentration. The resulting curve shows two well-defined minimums located at DNA concentrations of 0.3 and 1.5 mg/mL. These minimums agree acceptably with the values determined by the EIS technique and that were related to C* and C_e (*Chapter 3*), which identify the two transitions of particular interest: the transition between the dilute regime and the semi-dilute regime without entanglements and the transition between the semi-dilute regime without entanglements and the semi-dilute regime with entanglement [5,6]. Both critical concentrations determine changes in the behavior of DNA chains in solution within the three regimes of the system. As in studies of structural conformations of proteins, where $\Delta\theta_{SPR}$ changes as a function of protein concentration allow detection of the conformational changes of the molecules, it is possible to suggest that the transitions represent the variation in the structural arrangement of DNA molecules at the gold slide surface. Furthermore, a more detailed study of the interface was performed simulating the experimental results of the reflectivity as a function of the incidence angle using the Fresnel equations for each DNA concentration. In this way, it was possible to obtain d_{opt} [24, 25] for the Au/ calf thymus DNA interface for every studied C_{DNA}.

5.4.2. Optical film thicknesses determination

Various phenomena such as chemical interactions and dynamic processes of adsorption or degradation can be monitored in real time through the incidence angles, caused by the refractive index variations produced in the metal surface [20]. Such changes may be related to variations in mass and specific interactions between DNA molecules deposited on the surface of Au [26]. The observed shift in the incidence angles can be transformed into increments of the DNA molecules adsorbed films adsorbed on the sensor chip, from which is possible to calculate the average optical film thickness by using *Equation 5.7* through the simulations with the Winspall Software [10, 24, 25]. It is noteworthy to mention that is important to have knowledge of the refractive indices of the films of the interface, since they are parameters that depend on the molecular composition and the packing density of the films, enabling their geometrical thicknesses to be calculated [19]. *Figure 5.9* shows the resulting simulation for the SPR curve obtained for a DNA concentration of 2.0 mg/mL. The simulation allowed obtaining the corresponding values to DNA film optical properties. The obtained values for the optical thicknesses and the refractive indices of each of the films (prism, Cr, Au, DNA and TE buffer solution) are summarized in the insert of *Figure 5.9*. The refractive index for the Tris-HCl buffer solution was taken as 1.334 according to *Diéguez et al.* [27]. The values of the optical properties such as the refractive index and the optical film thickness corresponding to DNA film were evaluated through the simulation. A refractive index of 1.461 was obtained for the DNA film, which is in good agreement with the value reported by *Pei et al.* for the biomolecule [28].

Film	Optical film thickness	n	kappa
Prism	0	1.616	0
Cr	3.89	2.285	1.639
Au	42.77	0.135	3.606
DNA	1.9	1.461	0
Buffer	0	1.334	0
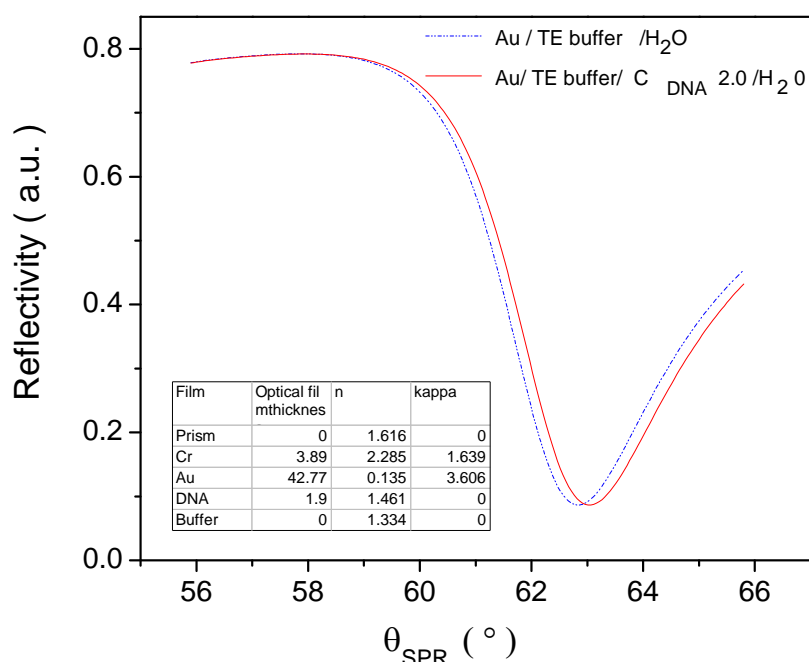
Figure 5.9. *Simulation obtained for the experimental data of the reflectivity versus the incidence angle for the DNA concentration of 2.0 mg/mL at 25 ºC. The optical film thicknesses of each film composing the system are summarized.*

The optical film thickness for a DNA concentration of 2.0 mg mL^{-1} is equal to 1.9 nm, which is close to the thickness reported for the cross section of DNA molecule double helix, 1.8 nm [29]. However, the observed differences could be justified because the values obtained for the optical thicknesses of adsorbed films on metal surfaces by the SPR technique represent the average values monitored during the adsorption process. Simulations were performed for each SPR curve at every DNA concentration and enabled the optical film thickness to be determined for each of them. Several of the calculated values may be validated by some reports, since lower DNA concentrations have been used on the cationic bilayer deposition on self- assembled monolayers [30]. In studies of DNA interactions with cationic lipids, looking for thin DNA film immobilization, the reported values for d_{opt} are in a good agreement with those obtained in this study. In this case, the optical thickness is reported for the adsorbed film of a solution of lambda phage DNA with a concentration of 0.01 mg/mL in a 5 mM Tris buffer and at a pH of 8.5 in three different lipid cationic bilayers each one adsorbed in a MUA monolayer. The thickness of this layer is based on a refractive index of 1.5 and is equal to about 0.8 nm, which is in good agreement with the value obtained for a calf-thymus DNA concentration of 0.01 mg/mL in this analysis (i.e. 0.7 nm) [30].

Figure 5.10 shows a schematic representation of the presumed structural arrangement of the DNA molecules adsorbed onto the gold surface. Previous studies using techniques such as fluorescence measurements show the attraction of the negatively charged strands of DNA due to the positive charges of the metal surface and the efficient energy transfer from the metal [31]. Therefore, DNA strands tend to be attracted to the metal surface in a horizontal manner. In the dilute regime it can be observed that the optical film thickness increases as a function of DNA concentration, being 0.7 nm the lowest value monitored for C_{DNA} of 0.01 mg/mL.
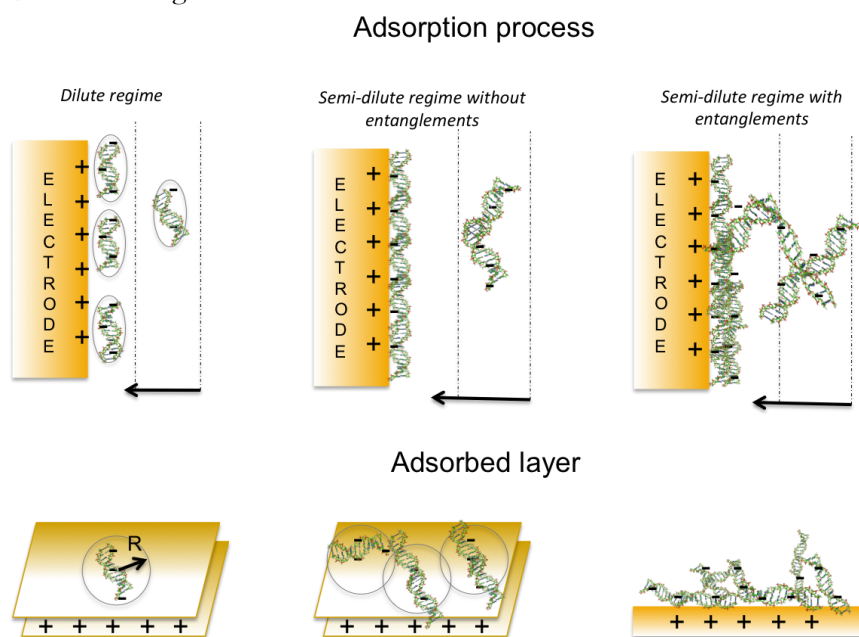
Figure 5.10. *Schematic representation of the presumed structural arrangement of the electrochemical double layer at each characteristic regime.*

Since DNA strands are not immobilize the by any organic compound, the electrochemical double layer formed on the substrate surface is affected only by structural changes at the interface and by the interchains interactions between DNA strands in the different regimes.

An important assumption in dilute solutions is that each unit of the biopolymer has the same possibility to occupy every position adjacent to its neighbor, and that each coil of the molecule is regarded as a hard sphere whose interior is protected from the flow due to hydrodynamic interactions [32]. With increasing DNA concentration and reaching C*, DNA chains begin to overlap and get densely packed, resulting in a change of the optical film thickness behavior and generating a new structural arrangement of DNA molecules on the gold slide surface. A second behavior is then observed from 0.4 to 1.0 mg/mL, in which it is possible to detect a constant augment of d_{opt} while increasing DNA concentration. However, DNA entanglements from C_e show a third behavior for d_{opt} at higher DNA concentrations. The behavior in each regime will be analyzed in the next section.

5.4.3. Evaluation of the optical film thicknesses in each characteristic regime

Figure 5.11 presents the analysis of the optical film thickness as a function of DNA concentration for each characteristic regime in log-log graphics. Linear behavior was observed at each regime and follows the power law [33] according to the following expression:

$$y = ax^b \tag{5.9}$$

where *a* and *b* correspond to the proportionality constant and the power exponent associated with the relation between d_{opt} vs. C_{DNA} ($\Delta d_{opt} / \Delta C_{DNA}$) respectively. This relation follows the *Equation 5.9* according to: dilute regime $C_{DNA} < C^*$): $d_{opt} \sim C_{DNA}^{0.20}$, semi-dilute regime without entanglements ($C^* < C_{DNA} < C_e$): $d_{opt} \sim C_{DNA}^{0.79}$ and semi-dilute regime with entanglements ($C_e < C_{DNA}$): $d_{opt} \sim C_{DNA}^{0.57}$. The obtained values are resumed in *Table 5.1*.

Table 5.1.- *Parameters obtained by fitting d_{opt} as a function of DNA concentration according to the power law at a temperature of 25 ºC.*

DNA concentration range mg/mL	Regime	a	b	r²
$0.01 < C_{DNA} < C^*$	Dilute	1.782	0.201	0.992
$C^* < C_{DNA} < C_e$	Semi-dilute without entanglements	1.898	0.798	0.988
$C_e < C_{DNA} < 3.0$	Semi-dilute with entanglements	1.217	0.567	0.983

We can observe that $\Delta d_{opt}/\Delta C_{DNA}$ increase from dilute regime to semi-dilute regime without entanglements, reaching their maximum value and then decrease when they reach the semi-dilute regime with entanglements. The overlap phenomenon between DNA strands and their dense packing is reflected in the higher value of $\Delta d_{opt}/\Delta C_{DNA}$. However, the strong interaction and entanglement of DNA strands of semi-dilute regime with entanglements exhibited the lowest value of $\Delta d_{opt}/\Delta C_{DNA}$. The values obtained through these fittings by using the power law may predict the d_{opt} for any DNA concentration between each characteristic regime.
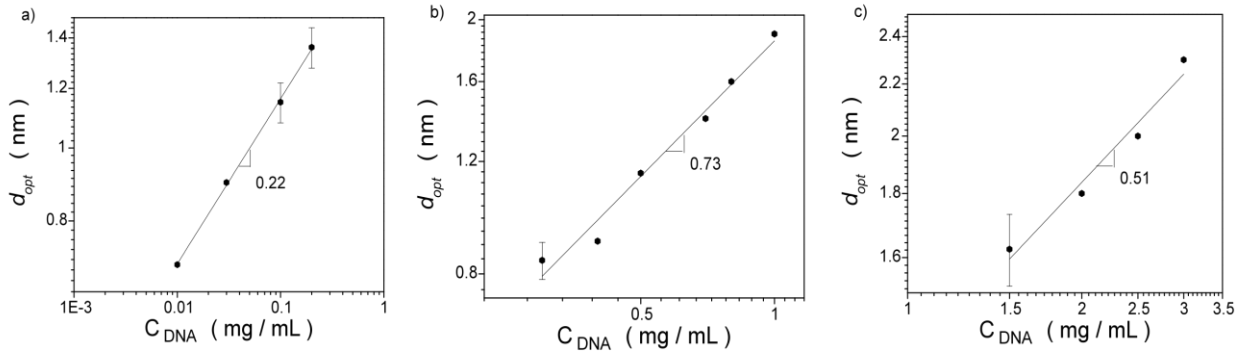
Figure 5.11. *Relation between d_{opt} and DNA concentration fitted according to the power law at each characteristic regime: a) dilute regime, b) semi-dilute regime without entanglements and c) semi-dilute regime with entanglements.*

5.4.4. Surface excess values determination

The results for d_{opt} at each DNA concentration were used to calculate the layer mass per unit area using Feitjer's equation [34,35]:

$$\Gamma = d_{opt}(n_L - n_{buffer}) / \left(\frac{dn}{dc} \right)_{P,T} \tag{5.10}$$

where Γ is the layer mass per unit area (ng/mm²) , d_{opt} is the optical film thickness of the adsorbed layer (nm) and n_L and n_{buffer} are the refractive indices of the layer and the bulk solution, respectively, and $\left(\frac{dn}{dc} \right)_{P,T}$ is the refractive index increment. Feijter's method uses the assumption that the refractive index increment of a protein in solution is a linear function of the protein concentration. The value dn/dc has been reported as 0.175 cm³/gr for DNA [36]. The values obtained for Γ exhibit the same behavior as d_{opt}, showing that variations in the surface excess are also related to structural

rearrangement of the DNA strands adsorbed on the substrate surface. As expected, the obtained values for Γ present the same behavior as d_{opt} at each characteristic regime, showing that the surface coverage variations are also related to the structural arrangement of DNA strands adsorbed onto the substrate. *Table 5.2* summarizes the results for the layer mass coverage obtained using Feitjer's equation, as well as the number of molecules at each DNA concentration. It is noteworthy that the obtained values are in good agreement with those reported for DNA concentrations of the dilute regime through studies of DNA immobilization on preformed alkanethiol SAMs [37]. On the other hand, the number of DNA molecules per square centimeter deduced through quartz crystal microbalance (QCM) experiments for a C_{DNA} of 0.1 mg/mL (4.60×10^{10} molecules/cm²) are the same order of magnitude and we believe this is consistent with the calculated value reported in this work using the SPR technique (4.51×10^{10} molecules/cm²).

Table 5.2.- *DNA dependence for the mass coverage and the amount of DNA molecules present at the interface.*

C_{DNA} mg/mL	Γ ng/mm	Amount of covering DNA molecules molecules/cm²
0.01	60.00	2.87×10^{10}
0.03	77.14	3.69×10^{10}
0.1	94.29	4.51×10^{10}
0.2	111.43	5.33×10^{10}
0.3	68.57	3.28×10^{10}
0.4	77.14	3.69×10^{10}
0.5	98.57	4.71×10^{10}
0,7	120.00	5.74×10^{10}
0.8	137.14	6.56×10^{10}
1.0	162.86	7.78×10^{10}
1.5	132.86	6.35×10^{10}
2.0	154.29	7.38×10^{10}
2.5	171.43	8.19×10^{10}
3.o	197.14	9.42×10^{10}

5.4.5. First approach to the variation of the dielectric constant

In *Chapter 3* we present an adsorption study of DNA molecules onto an Au surface through EIS, in which we show an approach in order to understand the behavior of the differential capacitance C_{dl} as function of DNA concentration and that shows two transitions around 0.36 ± 0.07 and 1.5 mg/mL. Such transitions may be directly related to the film thickness (*d*) by the following equation:

$$C_{dl} = \frac{ee_0}{d} \tag{5.11}$$

where ε_o is the permittivity of the vacuum and ε the dielectric constant [38].

According to the simplest model of the electrochemical double layer [38], changes in differential capacitance can reflect variations in the thickness of the interface as well as in the values of the dielectric constant ε of the system. It is noteworthy that dielectric constants values depend on several parameters such as concentration of the solvent, DNA structure and dielectric field saturation, among others. Furthermore, the interface thickness is directly related to the structure and the rearrangement of DNA molecules at the interface, which is influenced by DNA concentration, causing attractive or repulsive forces and changes in the nature of the DNA molecules [39]. Therefore, changes in the dielectric constant and in the double layer capacitance are also turn related to the average thickness of the interface, evaluated in this study as the average optical film thickness (d_{opt}), resulting in different ways of DNA adsorption such as rolls, slide or twist [39]. *Figure 5.12* shows the results for the dielectric constant as a function of DNA concentration calculated using Equation 5.11 and the C_{dl} values previously obtained by the EIS measurements (*Chapter 3*). The obtained ε values of DNA solutions corresponding to the dilute regime are in good agreement with the values reported for DNA solutions in 1.0 M KH_2PO_4 (1.833) and water (1.945) by *Peterlinz et al.* [40]. Since the electric field intensity of the environment notably influences the dielectric constant [41] and DNA molecules in the surroundings are negatively charged, then the degree of ordering of DNA molecules and dipolar solvent molecules will change with DNA rearrangements, as seen in *Figure 5.12*.
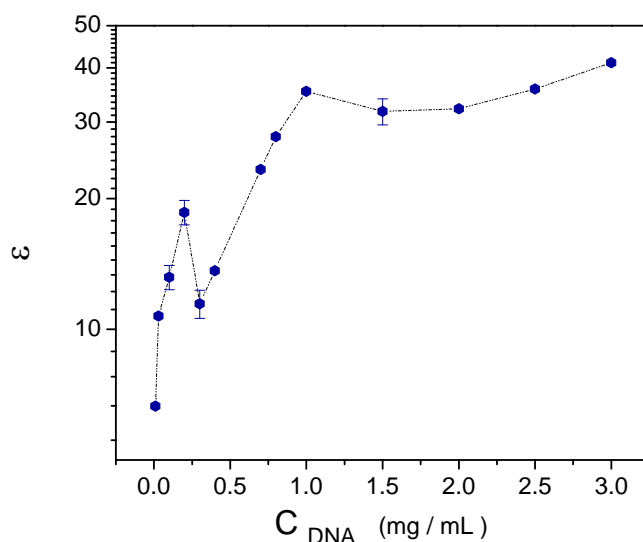
Figure 5.12. *Dielectric constant (ε) as a function of DNA concentration (mg/mL) at a temperature of 25 °C.*

Dielectric constant has a strong influence on the properties of the metal-solution interface, so the double-layer structure should not only depend on the gold electrode but also on the orientation of dipolar solvent molecules near the surface [42]. Hence, catalytic and adsorption properties such as the

metal's adsorptive power, which is low at high interaction energy with solvent, will reflect the interactions between the solvent and the electrode. The displacement of adsorbed solvent molecules and their reorientation will also depend on the structural rearrangement of adsorbed DNA molecules at the metal surface. As seen in *Figure 5.12*, dielectric constant behavior presents two transitions around DNA two concentrations, as observed by several microscopic and macroscopic techniques [6]. As well as small changes in DNA length cause significant changes in the dielectric increment [43], salt concentration is highly related to conformational changes and binding reactions with DNA, which in turn may affect dielectric and ionic strengths. Therefore, the reorientation of DNA molecules permanent dipoles can be associated to the regime transitions, observed at C* and C_e and depicted as a function of DNA concentration.

As well as for d_{opt}, a linear behavior is observed for each regime in log-log graphs, where the relation between ε and C_{DNA} also follows the power law according to: dilute regime (C_{DNA}<C*): $\varepsilon \sim C_{DNA}^{0.31}$, semi-dilute regime without entanglements (C*<C_{DNA}< C_e): $\varepsilon \sim C_{DNA}^{1.02}$ and semi-dilute regime with entanglements (C_e < C_{DNA}): $\varepsilon \sim C_{DNA}^{0.64}$. *Figure 5.13* shows the analysis of the dielectric constant as a function of DNA concentration for each regime in log-log graphics. The values obtained for each fitting are summarized in *Table 5.3*. Just as d_{opt} is a function of C_{DNA}, the values obtained through the power law fittings may predict the ε for any DNA concentration between each characteristic regime.
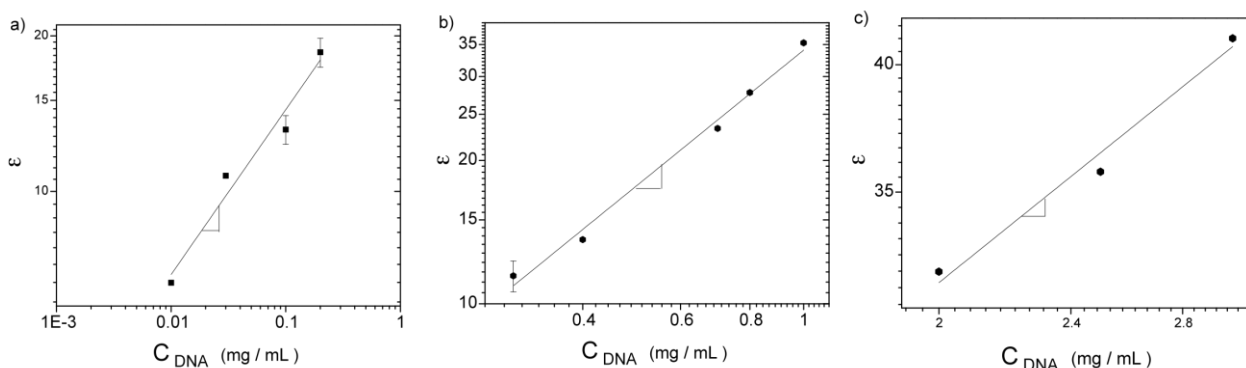
Figure 5.13. *Relation between ε and DNA concentration fitted according to the power law at each characteristic regime: a) dilute regime, b) semi-dilute regime without entanglements and c) semi-dilute regime with entanglements.*

Table 5.3.- *Parameters obtained by fitting ε as a function of DNA concentration according to the power law at a temperature of 25 ºC.*

DNA concentration range *mg/mL*	Regime	a	b	r²
$0.01 < C_{ADN} < C^*$	Dilute	40.772	0.313	0.956
$C^* < C_{ADN} < C_e$	Semi-dilute without entanglements	48.365	1.018	0.990
$C_e < C_{ADN} < 3.0$	Semi-dilute with entanglements	29.517	0.639	0.957

5.4.6. TEM measurements

Figure 5.14 shows three TEM micrographs taken from DNA concentrations of 0.1, 0.5 and 3.0 mg/mL, respectively. *Figure 5.14 a* shows the typical behavior of the dilute regime, where DNA molecules appear like isolated plaits with any interaction between them. Once DNA concentration has reached the C*, DNA molecules start interacting between each other and chains get overlapped, as seen in *Figure 5.14 b*, which represents the semi-dilute regime without entanglements. DNA solutions properties change noticeably at these conditions. *Figure 5.14 c* shows the behavior for a higher DNA concentration. Here it is possible to observe a gellike behavior due to the presence of entanglements between DNA molecules, typical of the semi-dilute regime with entanglements and corresponding to concentrations higher than C_e. These results clearly show the structural nature of DNA molecules when the DNA concentration is taken as a parameter and allows validating transition concentration evaluated by EIS and SPR techniques.
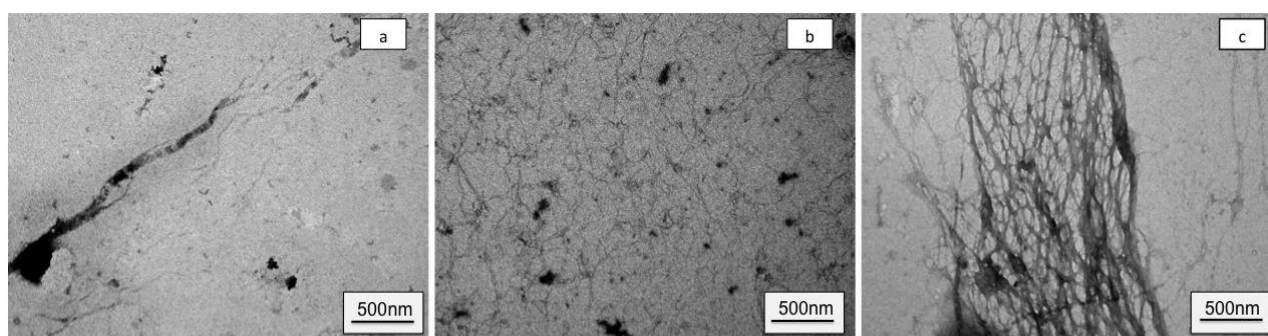
Figure 5.14. *TEM micrographs for DNA concentrations of a) 0.1, b) 0.5 and c) 3.0 mg/mL*

5.5. Particular conclusions for the study of the structural arrangement of the interface DNA-gold by SPR

The optical film thickness (d_{opt}) values observed in the surface of the sensor chip were estimated at each DNA concentrations, whereby two concentrations related to the overlap (C*) and the entanglement (C_e) were identified. The variations of d_{opt} as a function of DNA concentration were related to the transitions in the structural arrangement of the electrochemical double-layer, showing a specific behavior of DNA chains at each characteristic regime. A linear relation between d_{opt} vs. C_{DNA} was observed in each regime, following the power law according to: dilute (C_{DNA} < C*): $d_{opt} \sim C_{DNA}^{0.20}$, semi-dilute regime without entanglements (C*< C_{DNA}< C_e): $d_{opt} \sim C_{DNA}^{0.79}$ and semi-dilute regime with entanglements (C_e < C_{DNA}): $d_{opt} \sim C_{DNA}^{0.57}$. Using the simplest double-layer model, the changes in C_{dl} were related to the changes in d_{opt} as a function of DNA concentration and a dielectric constant behavior was also obtained, showing DNA transitions passing from diluted, semi-diluted unentangled and semidiluted entangled solutions. The power law correlations are proposed as a useful tool to predict interfacial parameters as well as the adsorbate concentration in a wide DNA concentration range. The combination of both EIS and SPR techniques emend an exhaustively characterization of structural behavior of Au-DNA TE buffer interface.

5.6. References

[1] R.J. Green, R.A. Frazier, K. M. Shakesheff, M.C. Davies, C. J. Roberts and S.J.B. Tendler, Surface plasmon resonance analysis of dynamic biological interactions with biomaterials, *Biomaterials*, **21**, 1823-1835 (2000).

[2] R.A. Frazier, G. Matthijs, M.C. Davies, C.J. Roberts, E. Schacht and S.J.B. Tendler, Characterization of protein-resistant dextran monolayers, *Biomaterials*, **21**, 957-977, (2000).

[3] J. Davies, Surface plasmon resonante: The technique and its applications to biomaterial processes, *Nanobiology*, **3**, 5-16, (1994).

[4] Y. Lvov, G. Decher and G. Sukhorukov, Assembly of thin films by means of successive deposition of alternate layers of DNA and Poly(allylamine), *Macromolecules*, **26**, 5396-5399, (1993).

[5] K. Tamada, F. Nakamura, M. Ito, X. Li and A. Baba, SPR-based DNA detection with metal nanoparticles, *Plasmonics*, **2**, 185-191, (2007).

[6] T.G. Mason, A. Dhople and D. Wirtz, Linear Viscoelastic Moduli of Concentrated DNA Solutions, *Macromolecules* **31**, 3600, (1998).

[7] J. O'M. Bockris, A. K. N. Reddy, M. Gambioa-Aldeco, Modern Electrochemistry 2A. Fundamentals

of Electrodics., Kluwer Academic Publisher, New York, Boston, Dordrecht, London, Moscow, (2002).

[8] A. J. Bard, L. R. Faulkner, Electrochemical Methods Fundamentals and applications, John Wiley & Sons, Singapure, (1980).

[9] D. Boda, D. Henderson and K.-Y. Chan, Monte Carlo study of the capacitance of the double layer in a model molten salt, *J. Chem. Phys.* **110**, 5346- 5350, (1999).

[10] P. Englebienne, A. Van Hoonacker and M. Verhas, Surface plasmon resonance: principles, methods and applications in biomedical sciences, *Spectroscopy, IOS Press*, **17**, 255-273, (2003).

[11] M. Yamamoto, *Department of Energy and Hydrocarbon Chemistry*, Kyoto University, 615-8510, (2008).

[12] L.G. Fagerstam, A. Frostell-Karlsson, R. Karlsson, B. Persson and I. Ronnberg, Biospecific interaction analysis using surface plasmon resonance detection applied to kinetic, binding site and concentration analisis, *J. Chromatogr.*, **597**, 397-410, (1992).

[13] A. Otto, Excitation of nonradiative surface plasma waves in silver by the method of frustrated total reflection, *Zeitschrift ffir Physik* **216**, 398-410, (1968).

[14] E. Kretschmann, Die Bestimmung optischer Konstanten von Metallen durch Anregung von Oberflachenplasmaschwingugnen, *Z .Phys.*, **24**, 241-313, (1971).

[15] K. Matsubara, S. Kawata, and S. Minami, A Compact Surface Plasmon Resonance Sensor for Measurement of Water in Process, *Applied Spectroscopy*, **42**, 1375-1379 (1988).

[16] A.D. Boardman, Electromagnetic Surface Modes, John Wiley & Sons, Chichester, *editor. Electromagnetic surface modes, Chichester*, Wiley (1982).

[17] C.E.H. Berger, R.P.H. Kooyman and J. Greve, Surface plasmon propagation near an index step, Optics Communications **167**, 183-189 (1999).

[18] S. Boussaad, J. Pean and N. J. Tao, A High Resolution Multi-wavelength Surface Plasmon Resonance Spectroscopy for Probing Conformational and Electronic Changes in Redox Proteins *Anal. Chem.*, **72**, 222-226, (2000).

[19] C.T. Campbell and G. Kim, SPR microscopy and its applications to high-throughput analyses of biomolecular binding events and their kinetics *Biomaterials*, **28**, 2380-2392, (2007).

[20] M. Mrksich, G.B. Sigal and G.M. Whitesides. Surface plasmon resonante permits in situ measurements of protein adsorption on self-assembled monolayers of alkanethiols on gold, *Langmuir* 11, 4383-4385 (1995).

[21] A. G. Frutos and R. M. Corn, Measurements by surface plasmon resonance monitor changes in thickness or the index of refraction of ultrathin organic films on metal surfaces, *Analytical Chemistry News & Features*, 455 A, (1998).

[22] W. N. Hansen, Electric fields produced by the propagation of plane coherent electromagnetic radiation in a stratified medium, *J. Opt. Soc. Am.*, **58**, 380-390, (1968).

[23] K. Nagata and H. Handa, *Real-Time Analysis of Bomolecular Interactions*, Springer, (2000).

[24] C. E. Jordan and R. M. Corn, Surface plasmon resonance imaging measurements of electrostatic biopolymer adsorption onto chemically modified gold surfaces, *Anal. Chem.*, **69**, 1449-1456, (1997).

[25] R. Georgiadis, K. P. Peterlinz and A. W. Peterson, Quantitative measurements and modeling of kinetics in nucleic acid monolayer films using SPR spectroscopy, *J. Am. Chem. Soc.*, **122**, 3166-3173, (2000).

[26] L. Duque, B. Menges, S. Borros and R. Förch, Immobilization of biomolecules to plasma polymerized pentafluorophenyl methacrylate, *Biomacromolecules*, **11**(10), 2818-2823, (2010).

[27] L. Diéguez, N. Darwish, M. Mir, E. Martínez, M. Moreno and J. Samitier, Effect of the Refractive Index of Buffer Solutions in Evanescent Optical Biosensors, *Sens. Lett.* **7**, 851–855, (2009).

[28] R. Pei, X. Cui, X. Yang and E. Wang, Assembly of Alternating Polycation and DNA Multilayer Films by Electrostatic Layer-by-Layer Adsorption, *Biomacromolecules*, **2**, 463-468, (2001).

[29] Y. Lvov, G. Decher and G. Sukhorukov, Assembly of thin films by means of successive deposition of alternate layers of DNA and Poly(ally1amine), *Macromolecules*, **26**, 5396-5399, (1993).

[30] S. Schouten, P. Stroeve and M. L. Longo, Determination of thickness and dielectric constant of thin transparent dielectric layers using Surface Plasmon Resonance, *Langmuir*, **15**, 8133- 8139, (1999).

[31] U. Rant, K. Arinaga, S. Fujita, N. Yokoyama, G. Abstreiter and M. Tornow, Dynamic Electrical Switching of DNA Layers on a Metal Surface, *Nanoletters*, **4**, 2441- 2445, (2004).

[32] W.W. Graessley, *Polymeric Liquids and Networks: Structure and Properties*, Garland Science, New York, (2004).

[33] J. F. Vega, S. Rastogi, G. W. M. Peters, H. E. H. Meijer, Rheology and reptation of linear polymers. Ultrahigh molecular weight chain dynamics in the melt, *J. Rheol.* **48**, 663-678, (2004).

[34] L. Duque, B. Menges, S. Borros and R. Förch, Immobilization of biomolecules to plasma polymerized pentafluorophenyl methacrylate, *Biomacromolecules*, **11**, 2819 (2010).

[35] L. Lee, A. P. R. Johnston and F. Caruso, Manipulating the salt and thermal stability of DNA

multilayer films via oligonucleotide length, *Biomacromolecules*, **9**, 3072, (2008).

[36] S. M. de Paul, D. Falconnet, S. Pasche, M. Textor, A. P. Abel, E. Kauffmann, R. Liedtke and M. Ehrat, Tuned graft copolymers as controlled coatings for DNA microarrays, *Anal. Chem.* **77**, 5831-5838, (2005).

[37] E. Huang, F. Zhou and L. Deng, Studies of surface coverage and orientation of DNA molecules immobilized onto preformed alkanethiol self-assembled monolayers, *Langmuir*, **16**, 3272-3280, (2000).

[38] A. J. Bard, and L. R. Faulkner, *Electrochemical Methods Fundamentals and applications*, John Wiley & Sons, Inc (2001).

[39] P. N. Bartlett, *Bioelectrochemistry: Fundamentals, Experimental and Application.*, John Wiley & Sons, New York, (2008).

[40] K. A. Peterlinz, R. M. Georgiadis, T. M. Herne and M. J. Tarlov, Observation of hybridization and dehybridization of thiol-tethered DNA using two-color Surface Plasmon Resonance Spectroscopy, *J. Am. Chem. Soc.* 119, 3402, (1997).

[41] J. O'M. Bockris, A. K. N. Reddy, and M. Gambioa-Aldeco, Modern Electrochemistry 2A. *Fundamentals of Electrodics.*, Kluwer Academic Publisher, New York, Boston, Dordrecht, London, Moscow, (2002).

[42] V. S. Bagotsky, *Fundamentals of Electrochemistry*, John Wiley & Sons, Moscow Russia, (2006).

[43] B. Honig, K. Sharp and A.-S. Yang, Macroscopic models of aqueous solutions: biological and chemical applications, *J. Phys. Chem.*, **97**, 1101-1109, (1993).

[44] R.J. Green, J. Davies, M.C. Davies, C.J. Roberts and S.J.B. Tendler, Surface plasmon resonance for real time in situ analysis of protein adsorption to polymer surfaces, *Biomaterials*, **18**, 405-413 (1997).

[45] M. Hnilova, E. E. Oren, U. O. S. Seker, B. R. Wilson, S. Collino, J. S. Evans, C. Tamerler and M. Sarikaya, Effect of molecular conformations on the adsorption behavior of gold-binding peptides, *Langmuir*, **24**, 12440-12445, (2008).

CHAPTER 6

Experimental study of the adsorption of DNA molecules onto metal surfaces by Modulation of the Interfacial Capacitance (MIC)

6. Experimental study of the adsorption of DNA molecules on metal surfaces by Modulation of the Interfacial Capacitance (MIC)

6.1. Introduction

As we have mentioned in previous chapters of this work, DNA adsorption processes onto metal surfaces of different nature have been widely studied for decades. *Miller* [1] was probably the first who studied DNA adsorption, showing that the adsorption of chromosomal DNA was controlled by diffusion for partially covered surfaces and reporting an area per adsorbed nucleotide around 95 Å² for denatured DNA. *Janik and Sommer* [2] followed the adsorption studies, proposing that the chain length of RNA molecules is an important parameter that affects the orientation of these molecules on the electrode. Then, *Brabec and Paleček* [3] showed that all components of DNA nucleotides, this is, the nitrogenous base, the deoxyribose sugar and the phosphate could take part in the adsorption process of DNA onto mercury electrodes.

Usually, the adsorption process depends on temperature, concentration of the adsorbate and the polarization imposed to the electrode, since the species can be adsorbed or desorbed on the electrode in a specific potential region [4]. However, more specifically, DNA adsorption process also depends on the conformation of the molecule, pH and ionic strength of the solvent, solution dielectric constant and on the electric charge of the electrode surface [5]. Many methods have been used and proposed to study adsorption/desorption behavior of nucleic acids at electrodes and are summarized by *Paleček et al.* [5]. Among them, Electrochemical Impedance Spectroscopy (EIS) has been particularly attractive due to the possibility it offers to perform measurements in the frequency domain [6-9]. Previously, we have focused on the study of DNA adsorption onto platinum and gold surfaces by using EIS technique on *Chapters 3* and *4* of this work. Now, we propose a recently developed technique called Modulation of the Interfacial Capacitance (MIC) in order to reach a greater insight on DNA adsorption onto metallic surfaces and to characterize double-layer dynamics during this process.

The Modulation of the Interfacial Capacitance was developed in France in the last decade [10] and is a technique derived of the Electrochemical Impedance Spectroscopy. In this technique, two signals of sinusoidal perturbations are simultaneously applied to the system, i.e. a high and a low frequency signal. In this way, it is possible to measure the modulation of the interfacial capacitance of the electrode, which is determined by the high frequency perturbation that reflects the variations of the capacitance originated by the low frequency perturbation [4]. As reported by *Antaño López* [10], the study of the adsorption processes through this electrochemical technique may give acces to the characteristic frequencies that could be related to adsorption-desorption phenomena of the interface. Then, using an Hg electrode in NaBr and KCl solutions as examples, *Larios-Durán et al.* [11] demonstrated that the MIC was a promising technique for the research and characterization of physicochemical processes that take place inside the diffuse layer. Finally, they reported that the combination of EIS and MIC allowed

improving the understanding of the adsorption processes through the detection of the characteristic frequency of multiple relaxation processes.

In this chapter is presented an adsorption study of calf-thymus DNA molecules in TE buffer (Tris-HCl/EDTA buffer) onto platinum electrodes through Modulation of the Interfacial Capacitance in order to quantify the basic stages of the DNA adsorption-desorption process in each characteristic regime, i.e. dilute, semi-dilute without entanglements and semi-dilute with entanglements. The MIC measurements were performed at open circuit potential in the temperature range between 10 and 40 °C. The experimental response as a function of temperature and DNA concentration gives information of the double-layer relaxation and reorganization dynamics through the time-constants displayed by the loops in the complex plane.

6.2. Overview of the technique

6.2.1. Qualitative description of the MIC

The Modulation of the Interfacial Capacitance is a methodology that is able to measure simultaneously impedance and interfacial capacitance spectra [10]. It was originally developed due to the interest of studying the effect of faradic processes in the differential capacitance of the double layer by a similar method to the impedance; this is, by applying simultaneously two sinusoidal perturbations, one high (f_Ω) and one low (f_ω) frequency, as mentioned in the introduction. In this manner, the idea is to measure the effect of a low frequency perturbation, i.e. less than 100 Hz at which several faradaic processes take place and that can be reached by the impedance technique, in the response of the differential capacitance of the double layer obtained through a second frequency perturbation higher than the first one, i.e. higher than 1 kHz [4]. The results obtained by *Antaño-López et al.* [12,13] using the MIC technique show experimental evidence of the strong relationship between charge transfer and capacitive processes.

The Modulation of the Interfacial Capacitance implies the perturbation with two simultaneous sinusoidal perturbations, unlike impedance technique, which implies a perturbation with one sinusoidal signal. For EIS, the potential or current perturbation as a function frequency, f_ω, allows obtaining the impedance information of the system, that can contain capacitive, charge transfer and/or diffusive transport contributions. However, for the MIC, the high frequency perturbation, f_Ω, allows accessing only to the capacitive response of the interface, that will also show the low frequency perturbation effect. Both techniques, EIS and MIC, measure transfer functions dependent on frequency, where $\Delta E_\omega / \Delta I_\omega$ corresponds to the EIS transfer function and $\Delta C_\Omega / \Delta E_\omega$ to the MIC transfer function. Where

C_Ω represents the differential capacitance of the double layer obtained at the frequency f_Ω and

E_ω represents the potential at the frequency f_ω.

6.2.2. Fundamentals of the MIC

Given the following expression for the current of a system [4,10]:

$$I = \frac{dq}{dt} \tag{6.1}$$

where q represents the charge for a capacitive system and is defined as:

$$q = KE \tag{6.2}$$

In this equation K represents the integral capacitance and E represents the potential.

In this way, the current expression for a capacitive system is the following:

$$I = E\frac{dK}{dt} + K\frac{dE}{dt} \tag{6.3}$$

By applying a sinusoidal perturbation of potential, as an example, the capacitance changes with time, so *Equation 6.3* becomes the following expression:

$$I = E\left(\frac{dK}{dE}\right)\left(\frac{dE}{dt}\right) + K\frac{dE}{dt} \tag{6.4}$$

That can be also written in the subsequent way:

$$I = \left[K + E\left(\frac{dK}{dE}\right)\right]\frac{dE}{dt} \tag{6.5}$$

where the differential capacitance is given by the following term:

$$C_{dl} = \left[K + E\left(\frac{dK}{dE}\right)\right] \tag{6.6}$$

The response in current of a capacitive system can be obtained through the analytic expression of *dE/dt*, which depends on the applied perturbation to the system. The theoretical background for the EIS and the MIC techniques is developed by *Antaño-López* [10] and *Larios-Durán* [4] for the current

expression for a perturbation of the system by a simple signal and for a perturbation of the system by a signal composed of two independent signals.

6.3. Experimental conditions

The description of the reagents, buffer Tris-HCl/EDTA (TE buffer) preparation and DNA/Buffer solutions are presented in *Sections 2.3.1., 2.3.2.* and *2.3.3.* of this work.

6.3.1. MIC measurements on platinum electrodes

MIC measurements were performed using a data acquisition card NI model PC-6251, which makes possible to obtain simultaneously the impedance and the capacitance spectra. A two-platinum electrode cell from Fisher Scientific was used as the working and the counter electrode and a saturated calomel electrode (SCE) was used as the reference. Both platinum electrodes surface is 0.25 cm^2. An electrochemical cleaning of the cell was routinely carried out applying cyclic voltammetry in a potential range between -1.5 and 1.0 V vs. SCE using a 0.5 M H$_2$SO$_4$ solution. The temperature of the samples was monitored using a forced circulation bath with digital temperature control. The measurements were carried out for DNA concentrations from 0.01 to 8.0 mg/mL at the temperatures 10, 20, 30 and 40 ° C. It was allowed a stabilization period of 30 min to each sample at each temperature to ensure a steady-state measurement. Homemade software was used to monitor and calculate the EIS and Modulation of the Interfacial Capacitance Transfer Function (MICTF).

6.3.2. Experimental setup

The experimental setup consists of the interconnection of the data acquisition card (NI model BNC-2110), a lock-in amplifier SR530 from Stanford Research Systems and a Bipotentiostat from Pine Instrument Company. A diagram of this setup is presented in *Figure 6.1*. The lock-in provides a high frequency perturbation ΔE_Ω (where f_Ω=1 kHz and $|\Delta E_\Omega|$= 20 mV rms), which allows obtaining the fluctuations of a low frequency perturbation ΔE_ω (where f_ω is between 100 Hz and 0.01 Hz and $|\Delta E_\omega|$=20 mV rms), generated by the data acquisition card. The electronic addition of both perturbations, ΔE_Ω and ΔE_ω, is carried on in a home made electronic signal adding box. The resulting signal from the addition is then sent to the bipotentiostat and finally imposed to the work electrode. The current and potential responses of the system, ΔI and ΔE, respectively, are obtained from the output

196

channels of the bipotentiostat. ΔI is sent to the input of the lock-in and then the in-phase component $\Delta I_\Omega{}^0$ is sent to the channel AI3 of the card. Subsequently, the output of ΔE from the bipotentiostat is sent directly to channel A1 of the card.
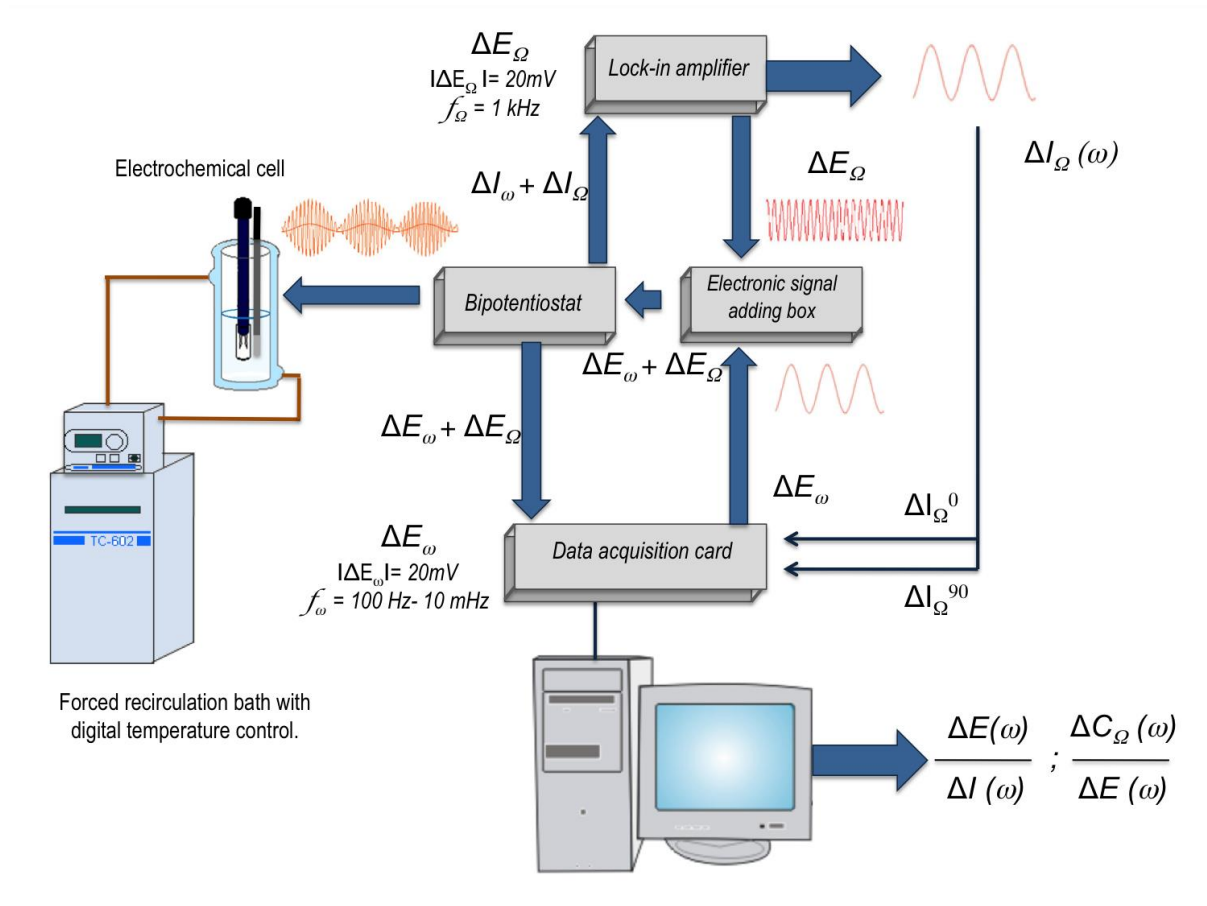
Figure 6.1. *Experimental setup used to measure EIS and MIC simultaneously [11].*

The home made software calculates the EIS as a function of ω following the next expression, as reported by *Larios-Durán et al.* [11]:

$$Z(w) = \frac{\mathrm{D}E(w)}{\mathrm{D}I(w)} = \frac{R_{st} \cdot \mathrm{D}E_w}{\mathrm{D}I_w(w)} \tag{6.7}$$

where R_{st} corresponds to the standard resistance through which the current signal was measured by the potentiostat.

From *Equation 6.7* is possible to calculate the corresponding admittance as the reciprocal of the complex impedance, i.e. $Y(\omega)=1/Z(\omega)$, from which it is possible to access to the capacitance transfer

function. In this way, the intermediate step in the computation of the Modulation of the Interfacial Capacitance and Associated Transfer Functions (MICTF) is determined by the following expression:

$$X_W(w) = \frac{DI_W^{90}}{R_{st} \cdot DE_W}$$

(6.8)

6.3.3. Filters characterization and data processing

6.3.3.1. Filters characterization

Initially, the measured value for the MIC is altered by the experimental setup since the lock-in amplifier also introduces an additional transfer function, F(ω), proper of the internal filters of the instrument (*Equation 6.9*). This transfer function F(ω) has to be characterized in order to remove it's contribution to the experimental measurements of the system. In this thesis, F(ω) is characterized by applying the MIC technique to a semiconductor diode (1N 41 48) under identical conditions to those used in the electrochemical adsorption studies. *Equation 6.9* describes F(ω) transfer function.

$$F(w) = \frac{Y}{(1 + jwt_1)^n (1 + jwt_2)^m}$$

(6.9)

where Y is the gain of the transfer function, τ_1 and τ_2 are the characteristic time constants and ω is the angular frequency ($\omega = 2\pi f_\omega$). F(ω) order is given by the exponents *n* and *m*.

The theoretical development of the current expression to the perturbation composed by a double signal has been previously described by *Larios-Durán et al.* [14] and allows obtaining the filter transfer function and the gain of the measurement chain.

Considering that for a semiconductor diode, the relation current-potential is given by the following expression:

$$I = I_a \exp(b \times E)$$

(6.10)

where I_a and *b* are the characteristic parameters of the diode.

The application of a polarization potential E_0 will produce a current I_0 and the expression will be:

$$I_0 = I_a \exp(b \times E_0)$$

(6.11)

If the system is perturbed by two sinusoidal potentials at the frequencies f_Ω and f_ω, with a polarization potential E_0, then and the response to the current will be:

$$I = I_a \exp[b \cdot (E_0 + DE_W + DE_W)]$$ (6.12)

$$I = I_0 \cdot \exp(bDE_w) \cdot \exp(bDE_W)$$ (6.13)

Using the Taylor series to separate the different contributions and neglecting the higher order terms, it comes that:

$$I = I_a\left[1 + bDE_W + \frac{(bDE_W)^2}{2} + ...\right] \cdot \left[1 + bDE_w + \frac{(bDE_w)^2}{2} + ...\right]$$ (6.14)

$$I = I_0 + I_0 bDE_w + I_0 bDE_W + I_0 b^2 \cdot DE_W DE_w + \frac{I_0 b^2}{2} DE_W^2 + \frac{I_0 b^2}{2} DE_w^2$$ (6.15)

where $DE_W DE_w$ corresponds to the component in phase of the current at the frequency Ω modulated by the signal at frequency ω.

In this way, the response to the perturbation of sinusoidal potential of the semiconductor diode will be a point on the real axis (or a disperion around the same point), in the predicted value equivalent to the constant coefficient of the term $DE_W DE_w$.

Experimentally, the analytical evaluation of the I vs E curve for the semiconductor diode can lead to the characteristic parameters of the diode, i.e. I_a and b. Subsequently, the sustitution of these values on the *Equation 6.11* will leads us to $I_a b^2$. Any response different to this value would be attributed to the internal filters of the synchronous detector.
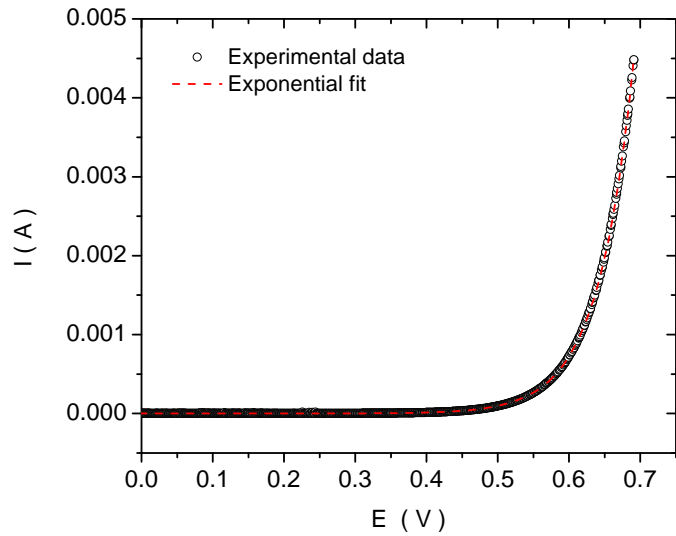
Figure 6.2. *I vs E curve obtained experimentally for the semiconductor diode.*

The polarization curve for the semiconductor diode was fitted through an exponential function using the OriginPro software in order to find I_a and b numerical values and is presented in *Figure 6.2*. The values 4.33 x 10^{-9} and 20.05 were obtained for I_a and b, respectively. Through these parameters, the values for I_0 and I_0b^2 were calculated by using *Equation 6.11* and are equal to 9.77 x 10^{-5} A and 3.93 x 10^{-2} SV^{-1}, respectively. Where the value I_0b^2, corresponding to the coefficient of $\Delta E_\Omega \Delta E_\omega$, as mentioned before, is related to the experimental value obtained through the perturbation of the semiconductor diode to a composed signal.

Figure 6.3 a shows the typical response of the internal filters of the lock-in amplifier measured by a semiconductor diode, analytically described by the *Equation 6.9*. *Figure 6.3 b* corresponds to the normalized spectra which will be used for the arithmetic operations in order to obtain the MICTF values for Pt/DNA-TE buffer interface. The conditions established for the measurement are presented in *Table 6.1* and are identical to the conditions used in the electrochemical experiments. The resistance corresponds to the selected parameter in the biopotentiostat and the sensitivity and time-constant are the selected parameters of the lock-in amplifier.

Table 6.1.- *Standard experimental conditions for the semiconductor diode measurement.*

$f\Omega$	$f\omega$	E_0	$\lvert DE_W \rvert$	$\lvert DE_W \rvert$	Resistance	Sensitivity	Time-constant
1 kHz	100 Hz to 10 mHz	0.5 V	10 mV	10 mV	1 mA	50 mV	30 ms
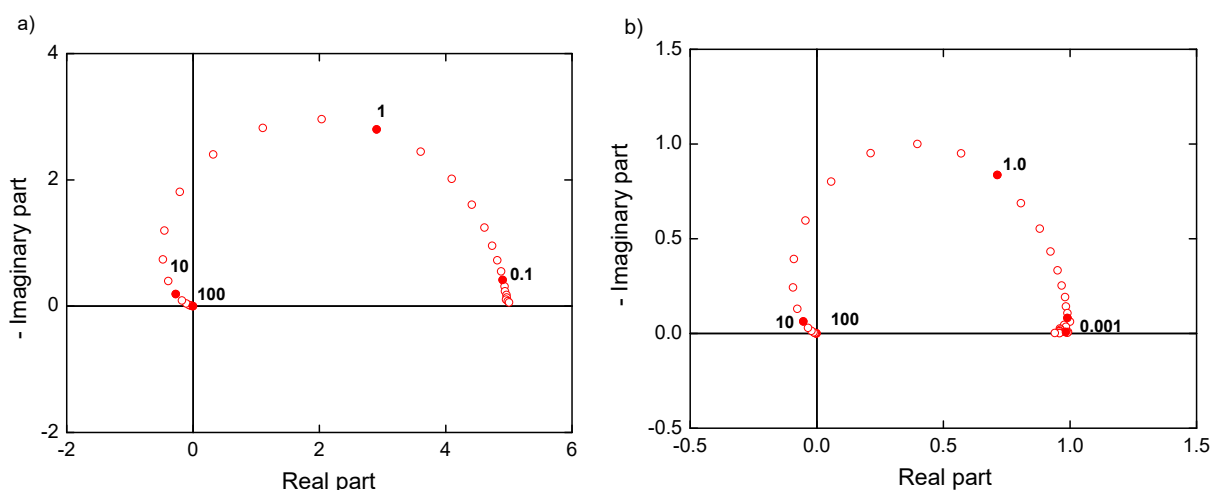
Figure 6.3. *a) Semiconductor diode response to the MIC and b) normalized response of the semiconductor diode.*

The frequency response of this semiconductor diode is fast enough for introducing no distortion at the frequency ω [12]. Theoretically, it would be expected to find a point around the calculated value for I_{ob}^2, however, we obtain a spectra with a semi-circle (*Figure 6.3 a*). This is attributed to the internal filters of the synchronous detector. The original spectra was then fitted in order to know the transfer function for the filter, F(ω), given by *Equation 6.9* and is presented in *Figure 6.4*.
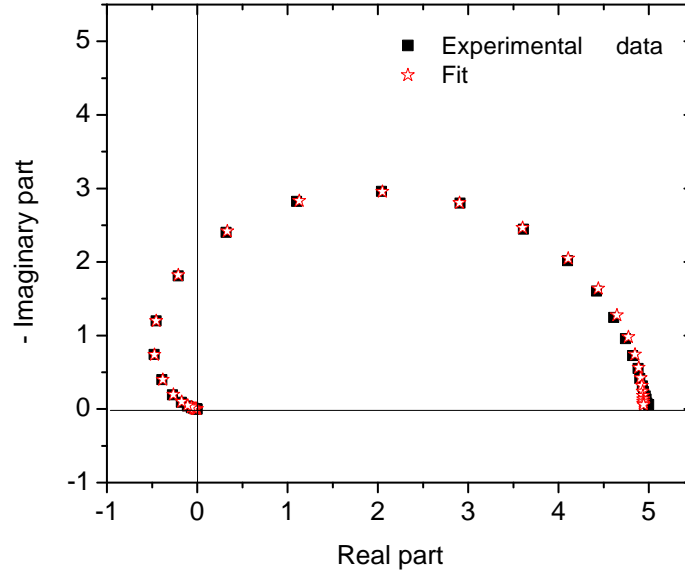
Figure 6.4. *Fitting of the experimental results for the Semiconductor diode response to the MIC.*

Figure 6.4 shows that the loop ends in the second quadrant, so the built-in filter is a second order filter. According to by *Equation 6.9*, the expression can be described by:

$$F(w) = \frac{Y}{(1 + jwt_1) \times (1 + jwt_2)}$$

(6.16)

where the dimensionless coefficient related to the gain equals to 4.80 and the characteristic time constants τ_1 and τ_2 are 0.0142 and 0.1075, respectively.

6.3.3.2. General data processing

Since the experimental values obtained directly through the MIC measurements are not dimensionally capacitance values, the obtained signal, that is properly a potential signal like the input signal that goes to the frequency analyzer, has to be converted into a current signal by applying Ohm's law and using the value of the standard resistance, R_{st}, of the potentiostat. The current value are then converted into capacitance values per area units, A.

Finally, after the determination of the lock-in amplifier response, then the complete correction of $X_\Omega(\omega)$ is given by the following expression:

$$DC_W = \frac{DC_W(w)}{DE(w)} = \frac{1}{F(w)} \cdot X_W(w) \cdot \frac{1}{A \cdot |DE_W| \cdot W} \tag{6.17}$$

where A is the area of the electrode, Ω is the angular frequency of the high frequency potential perturbation ($\Omega = 2\pi f_\Omega$) supplied by the lock-in amplifier and $|\Delta E_\Omega|$ is the amplitude of this perturbation.

The final correction of the experimental data obtained for the semiconductor diode is obtained by dividing them by the transfer function recently obtained (*Equation 6.17*). *Figure 6.5* shows the correction of the semiconductor diode by its transfer function, from which it is possible to obtain a dispersion of points on the real axis around a practically constant value. The discrepancy in the magnitude of the value with the one predicted by *Equation 6.15* is due to the gain of the measuring chain. In this manner, a value of 122 is obtained through a relation between the value obtained through *Equation 6.16* and the value obtained for the transfer function fiven by *Equation 6.15*, and represents the gain of the amplifiers given by the experimental setup.

It is then necessary to divide the response presented in *Figure 6.6* by the value of the gain in order to access to the real response to the double sinusoidal perturbation of potential applied of the semiconductor diode.
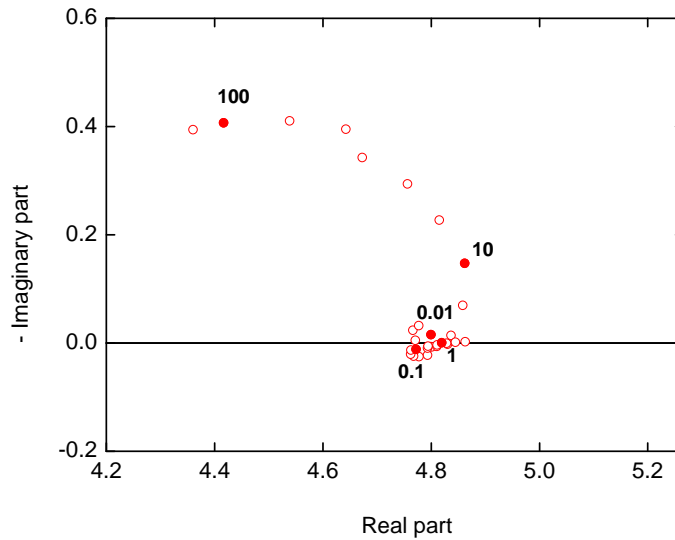
Figure 6.5. *Correction of the experimental values by using the internal filter of the lock-in.*

6.3.3.3. Data processing for Pt-DNA/TE buffer MIC response

In order to obtain the corrected MIC response for Pt-DNA/TE buffer interface, the raw $X_\Omega(\omega)$ data is introduced in *Equation 6.16*. *Figures 6.6 a* to *c* show the MIC data processing diagrams for a DNA concentration of 0.05 mg/mL at the temperature of 20 °C. *Figure 6.6. a* corresponds to the untreated diagram analytically described by the *Equation 6.8*, *Figure 6.6. b* presents the normalized response of the internal filters of the lock-in amplifier measured at the same conditions that Pt-DNA/TE buffer interface measurements *Figure 6.6. c* shows the correction of the experimental values.
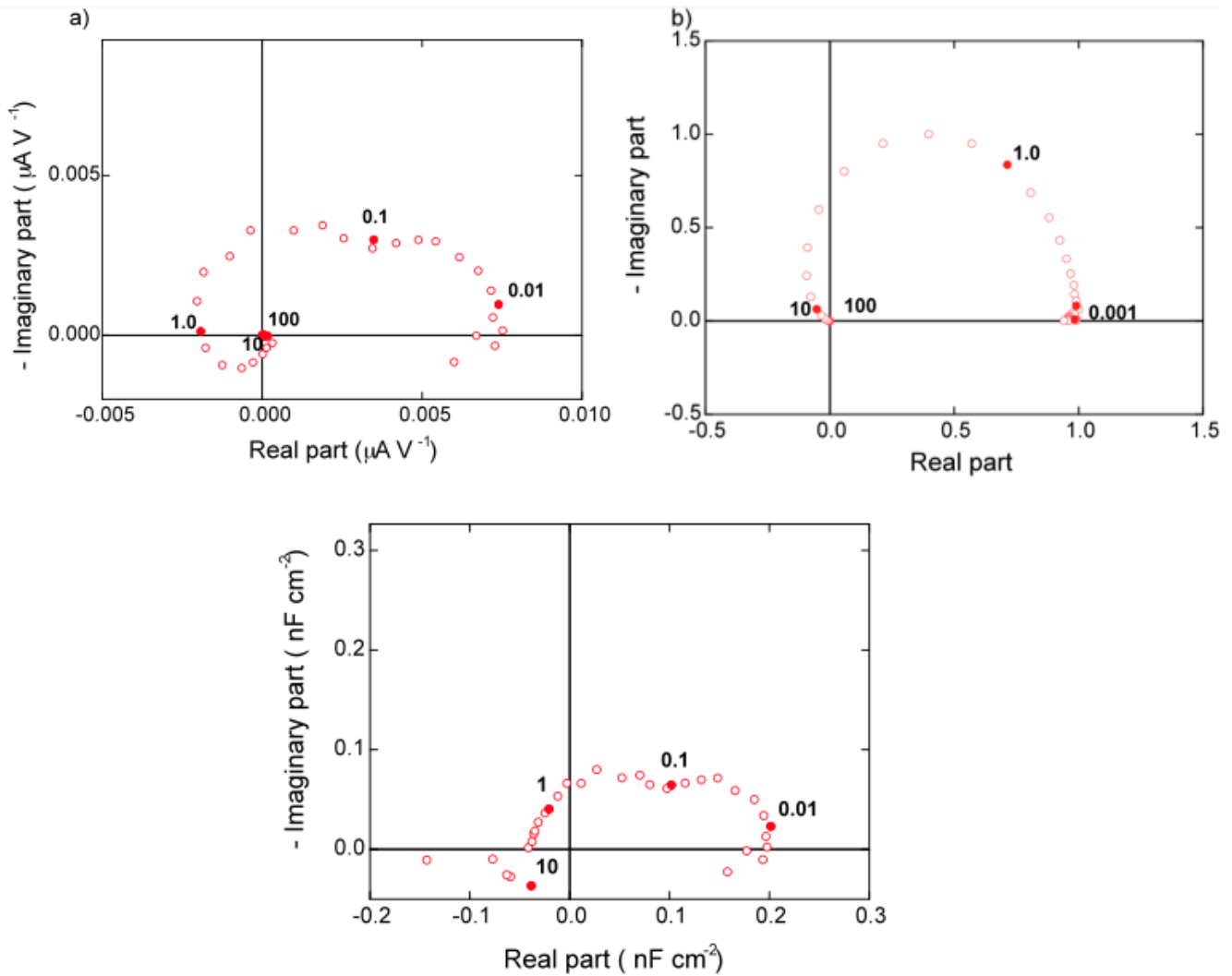
Figure 6.6. *Data processing for obtaining the Pt/DNA-TE buffer MIC spectra.*

a)   Untreated diagram analytically described by the Equation 6.8.
b)   Typical normalized response of the internal filters of the lock-in amplifier measured by a semiconductor diode.
c)   MIC diagram after correction.

6.4. Experimental results and discussion

6.4.1. Response of the Pt/Calf-thymus DNA interface to the MIC

The differential capacitance dependence with potential, evaluated in *Chapter 3* for EIS measurements of Pt/DNA-TE buffer interface, was taken into account in this study in order to attribute the MIC response to the adsorption of DNA molecules onto the platinum surface. In this manner, since MIC measurements were performed at open circuit potential, i.e. around 250 mV vs. SCE, which is a more positive potential than the potential of zero charge (15 mV vs. SCE), the adsorption and preservation of DNA is guaranteed at this potential and this experimental conditions (DNA concentration, ionic strength, pH and temperature) [15]. *Figure 6.7* shows the typical MICTF response for the Pt/DNA-TE buffer interface after the arithmetic treatment for a DNA concentration of 1.0 mg/mL, a temperature of 30 ºC and an ionic strength equivalent to 9.8 mM NaCl, this is, in the semi-dilute regime without entanglements. The electronic conditions stablished for the measurements, selected according to the signal clarity, are presented in *Table 6.2* and correspond to the parameters used for all electrochemical measurements in this work. As mentioned before for the semiconductor diode, the resistance corresponds to the selected parameter in the biopotentiostat and the sensitivity and time-constant are the selected parameters of the lock-in amplifier.

Table 6.2.- *Standard experimental conditions for the MIC measurements of Pt/DNA TE buffer interface.*

f_Ω	F_ω	E_0	$|DE_w|$	$|DE_w|$	Resistance	Sensitivity	Time-constant
1 kHz	100 Hz to 10 mHz	OCP≈0.25 V	10 mV	10 mV	1 mA	50 mV	30 ms
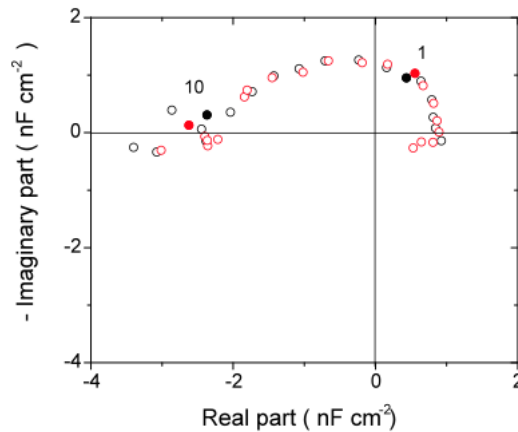
Figure 6.7. *Complex plane diagram and its replica of modulation of interfacial capacitance of the Pt/DNA-TE buffer interface for a DNA concentration of 1.0 mg/mL at a temperature of 30 ºC and an ionic strength equivalent to 9.8 mM NaCl. Parameter f_ω in Hz.*

As observed in *Figure 6.7*, the reproducibility of the measurements is validated with the overlapping of two spectra obtained for the same DNA concentration, i.e. 1.0 mg/ml using the same electronic conditions. For this DNA concentration, temperature and ionic strength, an average single time-constant is observed in the frequency range between 1.0 and 10 Hz, as obtained for the complex capacitance data presented on *Chapter 3* [15,16]. The presence of a depressed loop in this low frequency range shows that DNA adsorption process is a slow process that could be taking place through several steps.

Since DNA MIC spectra present a shift from negative to positive real parts while decreasing the frequency, in order to dismiss or attribute any other contribution to the MIC signal due to the internal filters of the lock-in amplifier or to the experimental setup, firstly, the evaluation of the MICTF response for the Pt/DNA-TE buffer interface was carried out and compared by using different time-constants of the lock-in amplifier (*Figure 6.8*).
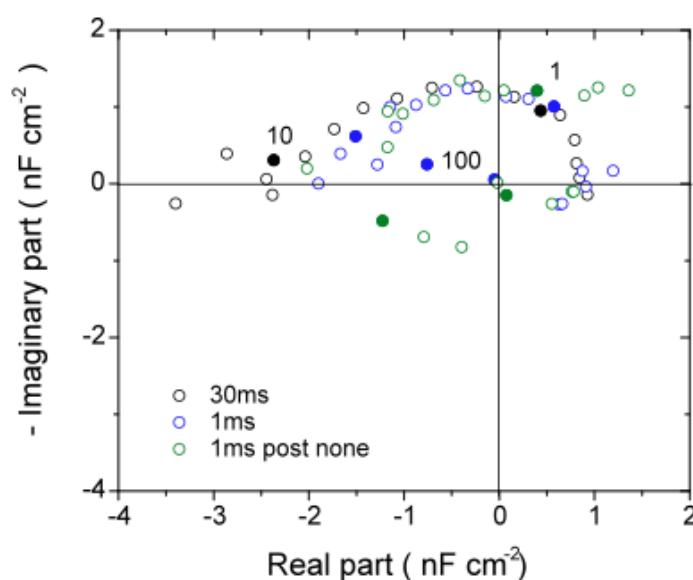
Figure 6.8. *Complex plane diagram of modulation of interfacial capacitance of the Pt/DNA-TE buffer interface for a DNA concentration of 1.0 mg/mL at a temperature of 30 ºC and an ionic strength equivalent to 9.8 mM NaCl with a variation of time-constants of the lock-in amplifier. Parameter f_ω in Hz.*

Figure 6.8 presents the MIC spectra for the Pt/DNA-TE buffer interface obtained after applying a perturbation to the system by a composed signal and using a variation of three different time-constants of the lock-in amplifier for each measurement, i.e. 30 ms, 1 ms and 1 ms post none (which can suppress noise at larger frequencies). A distribution of the capacitance with the frequency is observed at the high frequency range between 100 and 10 Hz, followed by the superposition of the data until arriving to the low frequency range. The single time-constant detected in the frequency range between 1.0 and 10 Hz, and the shift from negative to positive real parts while decreasing the frequency, remain in the obtained

response. In this way, in order to guarantee the validity and reproducibility of the results obtained in this work, one replica of each measurement was carried out at the same the electronic conditions and a second one was also performed with a variation of a time-constant of the lock-in amplifier.

The results allow concluding that the dispersion of the capacitance with frequency indicates a slow adsorption process of DNA molecules onto the platinum surface and does not follow immediately the sinusoidal perturbation.

Since the experimental setup allows obtaining simultaneously the MIC and the EIS response of the interface to the applied sinusoidal potentials, the impedance response for a variation of DNA concentrations was also analyzed in order to confirm the expected capacitive behavior, characteristic of DNA adsorption process onto platinum and gold surfaces, as discussed previously in *Chapters 3* and *4* of this work. *Figure 6.9* presents the impedance spectra for the DNA concentrations of 0.3, 0.5, 0.6 and 1.0 mg/mL at a temperature of 30 ºC.
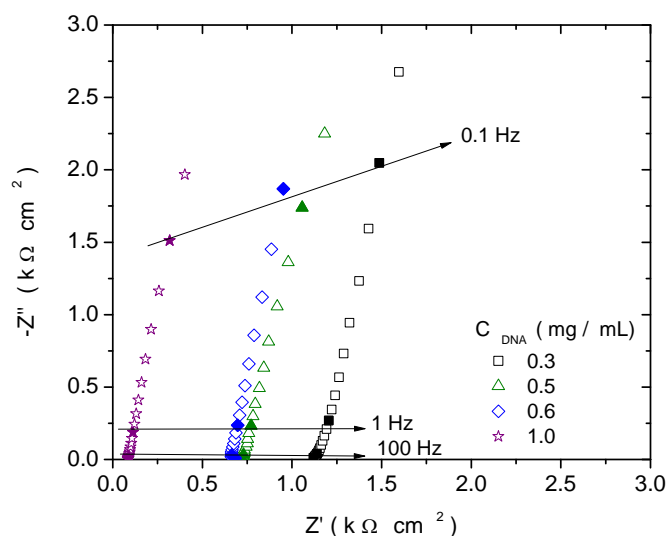
Figure 6.9. *Raw impedance data obtained for a variation of DNA concentrations at the temperature of 30 ºC and an ionic strength equivalent to 9.8 mM NaCl. Parameter f_ω in Hz.*

The obtained spectra correspond, as expected, to a predominantly capacitive process representing the structural arrangement of DNA molecules adsorbed onto the metal surface [17]. The response is in good agreement with the EIS measurements performed with the classical EIS setup and discussed in *Chapter 4* and is also consistent with the experimental conditions of the measurements, i.e. open circuit potential. DNA concentration increment causes a shift of each spectra towards lower values of Z' at higher frequencies, which is related with the decrease of the solution resistance due to the conductivity rise [18], caused by the presence of a large amount of charged DNA molecules.

In this way, the MICTF response for the Pt/DNA-TE buffer interface, obtained with the proposed setup in this work, was validated experimentally through several measurements, taking into account different variations on the electronic conditions selected to perform the measurements. The experimental setup was also validated through the evaluation of the EIS response of the interface, simultaneously collected by our setup, and which is in good agreement with previous EIS measurements for DNA solutions in platinum and gold electrodes [15-17]. Finally, the MIC response at low DNA concentrations is attributed to a slow adsorption process presenting a larger capacitance dispersion with frequency with a depressed loop shape, related to an adsorption process taking place through the superposition of several fundamental steps.

6.4.2. DNA concentration dependence in the response of the MIC

Pt/DNA-TE buffer interface analysis is presented starting from high DNA concentrations, then in the semi-diluted regime with entanglements, i.e. between 2.0 and 10 mg/mL, and finally in the dilute regime. *Figure 6.10* shows the MICTF response for the Pt/DNA-TE buffer interface performed for a DNA concentration of 8.0 mg/mL at a temperature of 30 ºC.
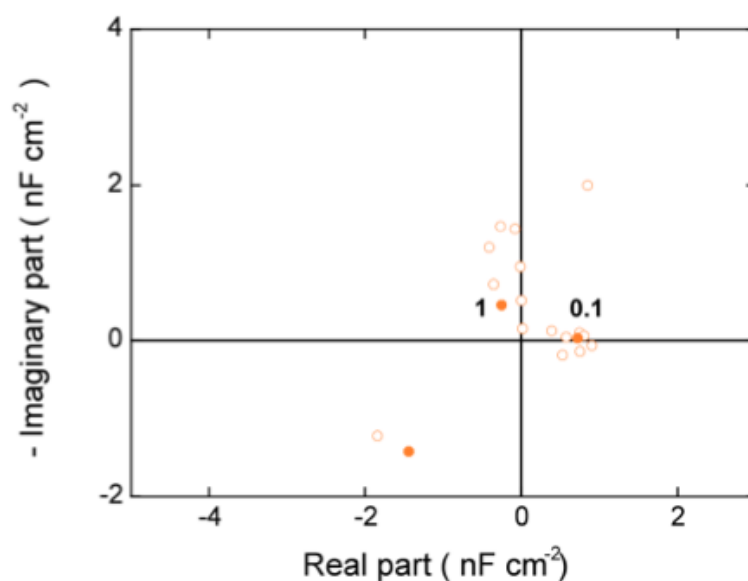
Figure 6.10. *Complex plane diagram of modulation of interfacial capacitance of the Pt/DNA-TE buffer interface for a DNA concentration of 8.0 mg/mL at a temperature of 30 ºC. Parameter f_ω in Hz.*

At high DNA concentrations, the influence of ionic concentration needs to be considered since the increase in DNA concentration leads to an increase of the total ionic concentration, as mentioned in *Chapter 2.* According to the procedure described in *Chapter 2,* for this concentration, the effective ionic

concentration is equal to 2.96 x 10⁻³ equiv/L, from which is possible to calculate the total ionic concentration in the buffer 9:1 and the Debye length, i.e. 12.96 mM and 2.65 nm, respectively. Thus, the ionic concentration influence remains low compared to the ionic contribution of the buffer solution.

As for the reported studies for the adsorption of NaBr and KCl on a mercury electrode, at concentrations higher than 100 mM and at 1M, respectively [11], and for a semiconductor diode, the MICTF diagram for a DNA solution with a $C_T \sim 13$ mM shows a dispersion of points on the real axis around a nearly constant value of around 0.745 nF/cm². A fast adjustment of the electrochemical double-layer takes place under the effect of the potential modulation at the frequency f_ω, so DNA asdorption process follows immediately the applied perturbation. As a first approach, to understand the DNA adsorption process that is taking place in the platinum electrode, it is necessary to take into account the concepts of polyelectrolytes adsorption recently reviewed by *Dobrynin et al.* [19]. In this way, assuming that for this DNA solution, the surface number charge density, σ, related with the thickness of the adsorbed layer, D_{ad}, is higher than the crossover surface charge number density, σ_e, at which the intrachain electrostatic repulsion is on the order of the attraction to the adsorbing surface [19], then DNA chains start getting compressed forming a concentrated polymer solution near the electrode. DNA adsorption is then fast enough (instant adsorption) and is detected by the MIC as a dispersion of points around a constant value. This process could be related to the so-called three-dimensional self-similar adsorbed layer formation for polyelectrolytes, described by *Dobrynin et al.* [20].
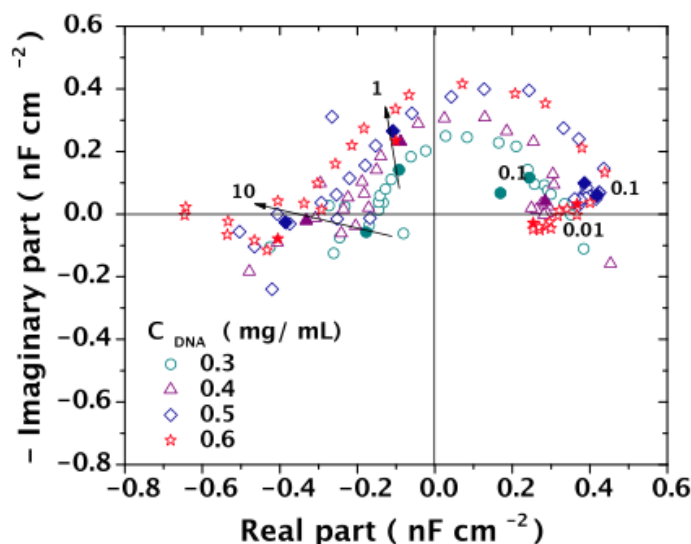

Figure 6.11. *Complex plane diagram of modulation of interfacial capacitance of the Pt/DNA-TE buffer interface for a variation of DNA concentration in the semi-diluted regime without entanglements at a temperature of 20 ºC. Parameter f_ω in Hz.*

At lower DNA concentrations in TE buffer, the influence of ionic concentration is lower and DNA chains in the bulk of the solution are characterized by being in a semi-diluted unentangled regime, as discussed in previous chapters of this work. In this way, the structural arrangement in the electrochemical double-layer will be different and the adsorption process that takes place at the metal surface will be also a different process than the one for the entangled regime. *Figure 6.11* shows the MICTF response for the Pt/DNA-TE buffer interface carried out for DNA concentrations of 0.3, 0.4, 0.5 and 0.6 mg/mL at a temperature of 30 ºC.

Firstly, a depressed loop that may contain the contribution of more than one time constant is observed in the frequency range between 1.0 and 10 Hz, as obtained for the complex capacitance data from EIS measurements through a simple perturbation, and is related to the reorganization time of the diffuse double-layer [21,22]. The results reveal a complex adsorption process including different steps, however, it is possible to quantify the main characteristic time constant of the process. *Figure 6.12* shows the dependence of the characteristic time constant of the process obtained from the high frequency loop of each MIC spectra with DNA concentration, as well as the comparison with the results obtained from EIS measurements at the temperature of 30 ºC (discussed in *Chapter 3*). As we can see, the order of magnitude of the obtained values through MIC measurements is in good agreement with the obtained values from the high frequency loop observed at the complex capacitance spectra from EIS measurements. The diminution of τ_c from MIC measurements as a function of DNA concentration is detected slightly after than the decrease detected by EIS measurements, which starts after 0.6 mg/mL. This could be due to the accuracy of MIC technique to detect the structural rearrangements in the double-layer during the adsorption process.
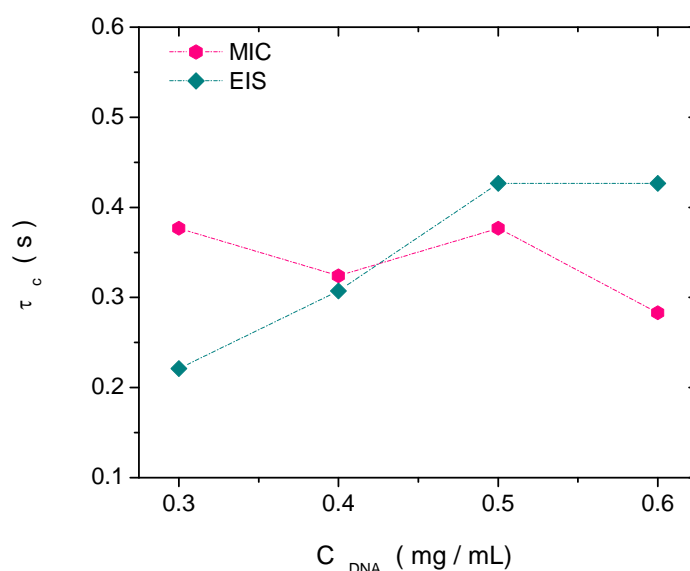
Figure 6.12. *Characteristic time constant of the process, τ_c, obtained from MIC and EIS measurements as a function DNA concentration at the temperature of 30 ºC.*

It is also worth to say that for semi-dilute adsorbed layers, the chain conformation remains the same as in the semi-dilute polyelectrolyte solution [19]. In this manner, the conformation of DNA adsorbed into the metal surface corresponds to the one in the semi-dilute regime in solution (*Chapter 2*). The adsorption process in this regime could be related to a DNA arrangement into a two-dimensional semi-dilute DNA solution with spacing between neighboring chains corresponding to the correlation length of a semi-dilute DNA solution. On the other hand, we can observe the dependence of the MIC response to DNA concentration, from which is possible to conclude that the interfacial double-layer structure is modified with DNA concentration and is sensitive to DNA electrostatic interactions.

Figure 6.13 shows the MICTF response for the Pt/DNA-TE buffer interface carried out for a variation of DNA concentrations in the dilute regime, i.e. 0.01, 0.03, 0.05 and 0.10 mg/mL at a temperature of 30 °C. We can see clearly the dependence of MIC spectra to the frequency when DNA concentration decreases, which is attributed to the charge relaxation of the interface. Two relaxation domains are observed in the MIC response of DNA solutions in the dilute regime. The first loop is in the frequency range between 10 and 0.1 Hz and the second loop below 0.1 Hz. This frequency dependence type with concentration was also found and described by *Larios-Durán et al.* for the adsorption of NaBr and KCl on a mercury electrode by using this technique, showing that at low concentrations (1mM or less) the double-layer capacitance relaxation presents two time-constants: one from a high frequency loop that was attributed to rearrangements inside the diffuse layer, and a second one from the low frequency range, which was attributed to the specific adsorption-desorption processes [11].
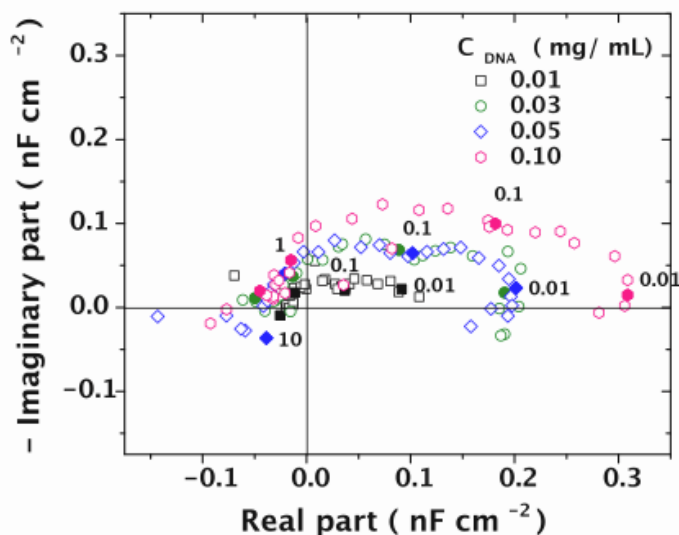
Figure 6.13. *Complex plane diagram of modulation of interfacial capacitance of the Pt/DNA-TE buffer interface for a variation of DNA concentration in the dilute regime at a temperature of 20 °C. Parameter f_ω in Hz.*

In the adsorption process of DNA molecules in a dilute solution with buffer concentration c_s, the electrostatic repulsions between chains is high enough to create a layer with DNA molecules with a distance R between chains in a two-dimensional way that is larger than the end-to-end distance of the chain [19]. In this way, the two relaxations that the dynamics of the electrochemical double-layer present during DNA adsorption process in the dilute regime could be related to the structuration of the double-layer due to the repulsions from other DNA adsorbed chains and the attraction to the oppositely charged metal surface.

Figure 6.14 shows the variation of the characteristic time constant of the process obtained from the first loop (high frequencies) of each MIC spectra with DNA concentration, as well as the comparison with the results obtained from EIS measurements at the temperature of 30 ºC. This curve includes the obtained results at higher DNA concentrations and discussed before in order to observe the all behavior as a function of DNA concentration. The obtained values through MIC measurements are in good agreement with the obtained values from EIS measurements.
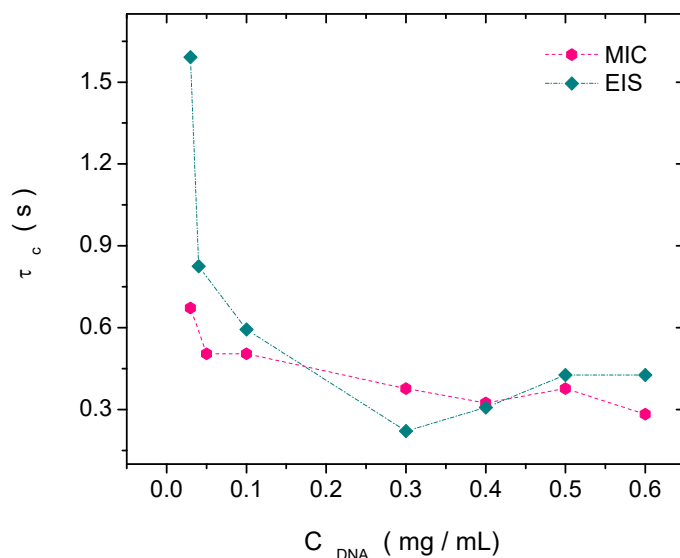
Figure 6.14. *Characteristic time constant of the process, τ_c, obtained from MIC and EIS measurements as a function DNA concentration at the temperature of 30 ºC.*

6.4.3. Temperature dependence in the response of the MIC

The temperature effect on the MICTF response for the Pt/DNA-TE buffer interface is presented in *Figures 6.15* and *6.16* for a DNA concentration in a semi-dilute solution without entanglements and in a dilute solution, respectively. As identified through classical impedance measurements [17], for DNA concentrations in the dilute regime and the semi-dilute regime without entanglements, the relaxation time decreases with temperature. The diffusional process is greater with the increase in temperature, so the adsorption kinetics is also favored. Since a diminution in the traveled distance by DNA molecules

from the bulk of the solution towards the electrode takes place, the relaxation time related to the arrangement of DNA molecules on the double-layer diminishes with the temperature increase. In the dilute regime, even if we observe two loops in the MIC spectra at low temperatures, i.e. 10 and 20 °C, and one depressed loop at higher temperatures, i.e. 30 and 40 °C, the capacitance dispersion with frequency and the shape of the loop continue showing a complex adsorption process that includes more than one superposed adsorption step.
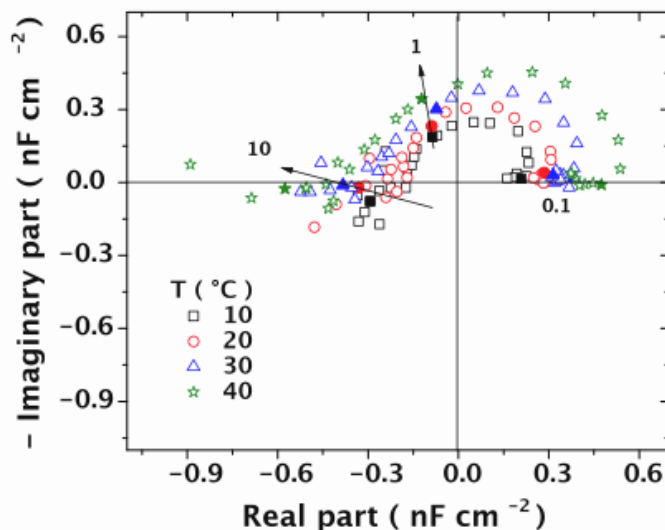
Figure 6.15. *Complex plane diagram of modulation of interfacial capacitance of the Pt/DNA-TE buffer interface for a DNA concentration of 0.4 mg/mL at the temperatures of 10, 20, 30 and 40 °C. Parameter f_ω in Hz.*
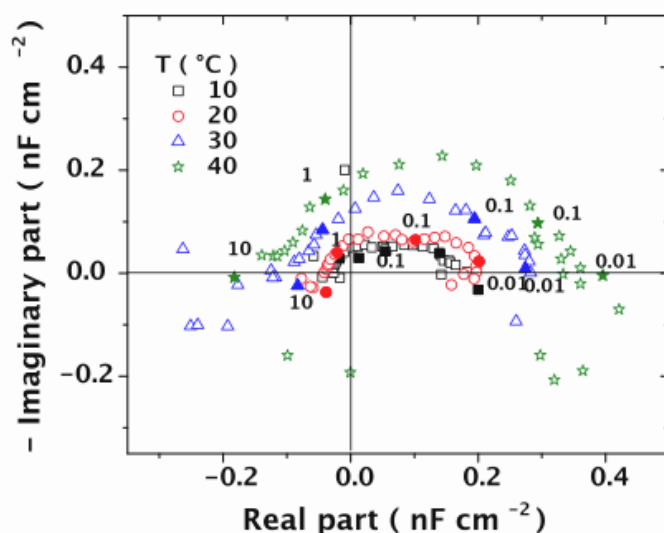
Figure 6.16. *Complex plane diagram of modulation of interfacial capacitance of the Pt/DNA-TE buffer interface for a DNA concentration of 0.05 mg/mL at the temperatures of 10, 20, 30 and 40 °C and an ionic strength equivalent to 9.8 mM NaCl with. Parameter f_ω in Hz.*

Figure 6.17 shows the dependence of the characteristic time constant, τ_c, with temperature for several DNA concentrations in the dilute regime without entanglements, i.e. 0.3, 0.4, 0.5 and 0.6 mg/mL. Here we can clearly observe the decrease of the time-constant with the increase of temperature, showing that the diffusional process is favored and the adsorption process of DNA molecules onto the platinum surface is faster.
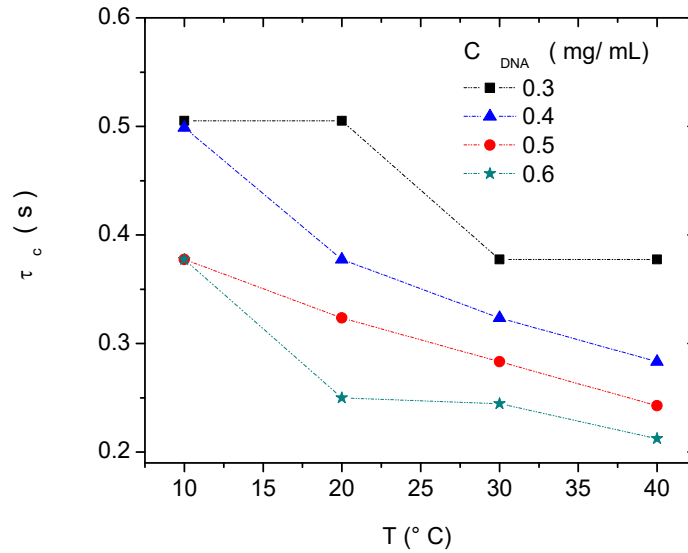
Figure 6.17. *Characteristic time constant (τ_c) dependence with temperature for DNA concentrations of 0.3, 0.4, 0.5 and 0.6 mg/mL.*

Finally, the $\ln(\tau_c)$, obtained from the mean characteristic time constant of the adsorption process, is presented as a function of the reciprocal of the absolute temperature for two DNA concentrations in the semi-dilute regime without entanglements (*Figure 6.18*). A linear behavior is observed and is related to an Arrhenius-type behaviour given by the following equation [17]:

$$\tau_c = Ae^{-Ea/RT} \tag{6.17}$$

where A is the frequency factor, R is the universal gas constant, T is the temperature and E_a is related to the minimum amount of energy required to adsorption process.

This Arrhenius-type temperature dependence is in good agreement with the one obtained for the characteristic time-constant identified through classical EIS measurements [17], as well as the calculated energy E_a, which according to this data is around 13 kJ/mol in the temperature range between 10 and 40 °C.
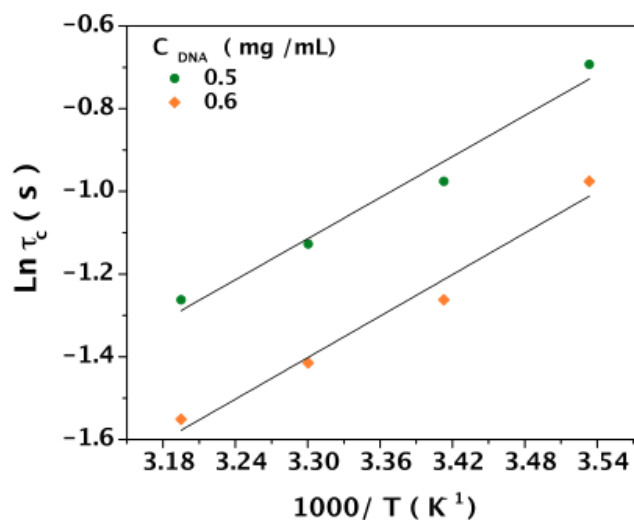
Figure 6.18. *Arrhenius dependence of the relaxation time (τ_c) with the reciprocal of the absolute temperature for DNA concentrations of 0.5 and 0.6 mg/mL.*

6.4.4. Ionic strength dependence in the response of the MIC

In order to put in evidence the electrostatic interchains and intrachains interactions effects in the arrangement of the electrochemical double-layer, the MICTF response for the Pt/DNA-TE buffer interface was also monitored for a constant DNA solution in the dilute regime with a concentration of 0.05 mg/mL at a temperature of 20 °C and a variation of ionic strengths given by the buffer solution (*Figure 6.19*).
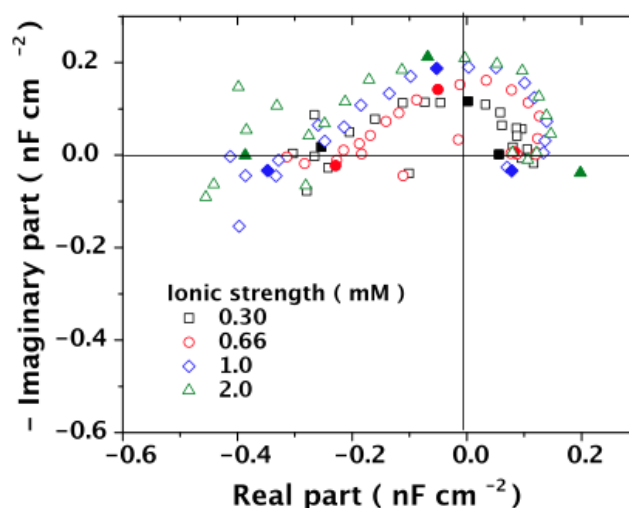

Figure 6.19. *Complex plane diagram of modulation of interfacial capacitance of the Pt/DNA-TE buffer interface for a DNA concentration of 0.05 mg/mL with a variation of ionic strengths. Parameter f_ω in Hz.*

As explained in *Chapter 2*, the ionic strength of TE buffer was determined through conductivity measurements, relating its conductivity to the concentration of a NaCl solution with the same conductivity. For this DNA concentration, the effective ionic concentration is equal to 1.85 x 10^{-5} equiv/L, so the total ionic concentration and the Debye length were calculated for each solution and are resumed in *Table 6.3*.

Table 6.3.- *Total ionic concentration and Debye length for a DNA solution of 0.05 mg/mL with a variation of ionic strength given by the TE buffer solution.*

Ionic strength of TE buffer, C_s (equiv/L)	Total ionic concentration, C_T (equiv/L)	Debye length (nm)
0.30	0.32	16.7
0.66	0.68	11.5
1.0	1.02	9.3
2.0	2.02	6.9

The obtained MIC response shows the presence of a depressed loop including more than one superposed adsorption step. The main characteristic time constant of the process remains constant, i.e. 0.5 s, showing that at this ionic strength range, the adsorption kinetics and the steps of the adsorption process remains the same.

6.4.5. Dependence of the MIC real component at the limit of high frequencies with DNA concentration and temperature.

The MIC real component at the limit of high frequencies was evaluated as a function of temperature and DNA concentration in the three characteristic regimes, i.e. dilute regime, semi-dilute regime without entanglements and semi-dilute regime with entanglements. The results are presented in *Figure 6.20*, which allow observing the increase of the MIC real component with the increase of DNA concentration, so the capacitance dispersion with frequency evolutes until reaching the DNA regime at higher concentrations and at which DNA asdorption process follows immediately the applied perturbation.

A slight increase of the MIC real component with the increase of temperature is also observed and can be explained in terms of the evolution of the MIC spectra due to the facilitation of the diffusion process at higher temperatures.
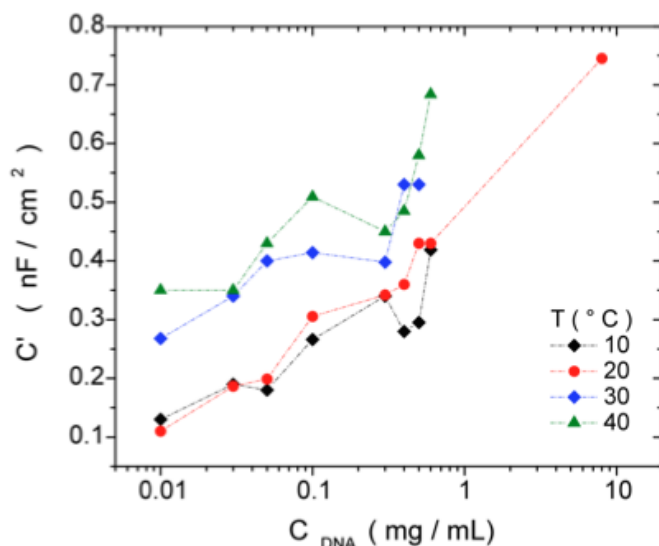
Figure 6.20. *Dependence of the MIC real component at the limit of high frequencies with DNA concentration and temperature.*

6.5. Particular conclusions for the study of DNA molecules adsorption onto metal surfaces by MIC

An adsorption study of calf-thymus DNA in TE buffer in a platinum surface was performed and evaluated through the Modulation of the Interfacial Capacitance technique. As far as we know, this was the first time that this recently developed technique was used to study the double-layer relaxations due to the adsorption process of a polyelectrolyte, i.e. the DNA. The MIC response revealed the double-layer dynamics in the dilute, the semi-dilute regime without entanglements and the semi-dilute regime with entanglements for DNA-TE buffer solutions. At high DNA concentrations, no relaxation process of the double-layer capacitance is observed, however, at low concentrations, more specifically in the semi-dilute regime without entanglements, it is possible to identify more than one superposed time-constant. Finally, for DNA concentrations in the dilute regime, it is shown that the relaxation process clearly exhibits two time constants. The obtained values are in good agreement with the values previously obtained for DNA solutions through classical impedance measurements in the semi-dilute regime without entanglements. The dependence on DNA concentration, temperature and ionic strength for the MIC response was put on evidence and described in this study.

It is demonstrated that MIC technique allows the study of the adsorption kinetics of the simplest species, such as NaBr and KCl, and the most complex species as DNA. It is then possible to identify and explain, semiquantitatively, the fundamental adsorption steps of these species. This technique can become a useful tool in order to reach to a better understanding of the adsorption process of polyelectrolytes such as DNA, maybe more specifically in diluted solutions. In order to get a greater

insight of this process by using different metal surfaces, at each characteristic regime and to analyse the two-dimensional or three-dimensional adsorbed layer formation for DNA solutions, a more detailed analysis including the concepts of the theory of polyelectrolytes in surfaces is needed. Finally, an experimental study with a potential variation with respect to the PZC could give us more information with respect to the negative to positive reals parts of the capacitance response.

6.6. References

[1] I.R. Miller, The structure of DNA and RNA in the water-mercury interface, *J. Mol. Biol.* **3**, 229 (1961).

[2] B. Janik and R.G. Sommer, Polarography of polynucleotides. IV. Effect of the molecular weight of poly(U) On its absorption at a charged surface, *Biopolymers* **12**, 2803 (1973).

[3] V. Brabec and E. Paleček, Adsorption of single-stranded and double-helical polynucleotides on the mercury electrode, *Biopolymers* **11**, 2577 (1972).

[4] E.R. Larios-Durán, Tesis Doctoral "Estudio de procesos de adsorpción sobre electrodos mediante técnicas de modulación", 8 (2011).

[5] E. Paleček, M. Fojta, F. Jelen and V. Vetterl, *Electrochemical analysis of nucleic acids, The Encyclopedia of Electrochemistry*, Bioelectrochemistry, Vol. 9, Eds. A.J. Bard and M. Stratsmann, Wiley-VCH, Weinheim, 365 (2002).

[6] M. Sluyters-Rehbach and J.H. Sluyters, The investigation of the adsorptive behaviour of electroactive species by means of admittance analysis. I. Theory of the case of reversible charge-transfer, *J. Electroanal. Chem.* **136**, 39 (1982).

[7] J.R. MacDonald, *Impedance Spectroscopy*, Wiley, New York, (1987).

[8] S. Hason, J. Dvorak, F. Jelen and V. Vetterl, Interaction of DNA with echinomycin at the mercury electrode surface as detected by impedance and chronopotentiometric measurements, *Talanta* **56**, 905 (2002).

[9] Y.Z. Fu, R. Yuan, L. Xu, Y.Q. Chai, Y. Liu, D.O. Tang and Y. Zhang, Electrochemical impedance behavior of DNA biosensor based on colloidal Ag and bilayer two-dimensional sol-gel as matrices, *J. Biochem. Biophys. Methods* **62**, 163 (2005).

[10] R. Antaño López, These "Sur une nouvelle méthode de caractérisation des processus faradiques a partir de leur couplage avec la capacité de la double couche", Université Paris VI (2001).

[11] E.R. Larios-Durán, R. Antaño-López, M. Keddam, Y. Meas, H. Takenouti and V. Vivier, Dynamics of double-layer by AC Modulation of the Interfacial Capacitance and Associated Transfer Functions, *Electrochimica Acta* **55**, 6292–6298 (2010).

[12] R. Antaño-López, M. Keddam and H. Takenouti, A new experimental approach to the time-constants of electrochemical impedance: frequency response of the double layer capacitance, *Electrochimica Acta* **46**, 3611 (2001).

[13] R. Antaño-López, M. Keddam and H. Takenouti, Interface capacitance at mercury and iron electrodes in the presence of organic compound, *Corr. Engin. Sci. Techn.* **39,** 59, (2004).

[14] E.R. Larios-Durán, Tesis Maestría "Estudio electrocinético de la adsorbión de iones en electrodos líquidos y sólidos mediante técnicas de impedancia y modulación de la capacitancia", (2011).

[15] L.M. Bravo-Anaya, E.R. Macías, F. Carvajal Ramos, J.G. Álvarez-Ramírez, N. Casillas, J.F.A. Soltero and E.R. Larios-Durán, DNA transitions by an adsorption study, *Journal of the Electrochemical Society* **160**, G69-G74 (2013).

[16] L. M. Bravo-Anaya, E.R. Macías, F. Carvajal Ramos, V.V.A. Fernández, N. Casillas, J. F. A. Soltero and E.R. Larios-Durán, DNA conformational transitions at different concentrations and temperatures monitored by EIS, *ECS Electrochemistry Letters* **1 (2),** G1-G3 (2012).

[17] L. M. Bravo-Anaya, E.R. Macías, N. Casillas, F. Carvajal Ramos, V.V.A. Fernández, J.F.A. Soltero and E.R. Larios-Durán, The scaling of electrochemical parameters of DNA aqueous Solutions with concentration and temperature through an Electrochemical Impedance Spectroscopy stuy, *Electrochimica Acta* **167**, 311-320 (2015).

[18] J. Newman, Resistance for flow of current to a disk, *J. Electrochem. Soc.* **113**, 501-501 (1966).

[19] A.V. Dobrynin and M. Rubinstein, Theory of polyelectrolytes in Solutions and at surfaces, *Prog. Polym. Sci* **30**, 1049-1118 (2005).

[20] A.V. Dobrynin, A. Deshkovski and M. Rubinstein, Adsorption of polyelectrolytes at oppositely charged surfaces, *Macromolecules* **34**, 3421-3426 (2001).

[21] T. Pajkossy, T Wandlowski and D. Kolb, *J. Electroanal. Chem.* **414**, 209 (1996).

[22] S.W. Feldberg, *J. Phys. Chem.* **74**, 87 (1970).

[23] S.R. Raghavan, E.W. Kaler, Viscoelastic wormlike micellar solutions formed by cationic surfactants with long unsaturated tails, *Langmuir* **12**, 300-306 (2001).

[24] S.-H. Tung, Y.-E. Huang, S.R. Raghavan, Contrasting effects of temperature on the rheology of normal and reverse wormlike micelles, *Langmuir* **23**, 372-376 (2007).

CHAPTER 7

Chitosan/DNA nanoparticles development for gene therapy

Chapter 7. Chitosan/DNA nanoparticles development for gene therapy

7.1. Introduction

Electrostatic complexes between oppositely charged polyelectrolytes involving natural biopolymers are being developed for biomedical applications [1,2]. More specifically, the attention was focused on cationic polymers due to their potential for DNA complexation and for being used as non-viral vectors for gene delivery [3-5]. Ionic complexes formed between DNA and polycationic liposomes were promising in the 90's [6,7], however, the instability of the complex, the toxicity of the cationic lipids and the short average life of the complexed DNA limit there success. Actually, cationic polymers and phospholipids are the most studied types of non-viral gene delivery vectors [8,9]. Both vectors interact electrostatically with negatively charged DNA forming polyplexes or lipoplexes. Nevertheless, DNA/polymer complexes were found to be more stable than complexes formed with cationic lipids [10]. A great number of characteristics that benefit gene delivery are found in only few natural polycations available, contrary to the abundance of structurally different synthetic non-viral gene delivery vectors. Low immunogenicity, biocompatibility and minimal cytotoxicity are some searched characteristics in polymers in order to develop a better alternative to viral or lipid vectors [11,12]. In this manner, chitosan and its derivatives were identified as safe and efficient cationic carriers with the following characteristics: high biodegradability and biocompatibility, non-toxicity and low cost.

Up to now, chitosan and DNA have been investigated for gene delivery due to the advantages that chitosan provides as a biocompatible non-viral vector which does not produce immunological reactions, contrary to viral vectors [13]. Chitosan has also been used and studied for its ability to protect DNA from nuclease degradation and to transfect DNA into several kinds of cells [14]. Small size complexes ranging from 20 to 500 nm have been previously obtained by using chitosan [15-17], presenting the advantage of entering the cell through endocytosis and/or pinocytosis, which increases the transfection rate. Gene delivery systems based on chitosans offers also to possibility of being modified by adding different kinds of ligands for specific cell interaction, such as transferrin or galatose [8].

In this chapter, DNA-chitosan nanoparticles development for gene transfer is presented. DNA concentration was selected in the dilute regime: 10 times lower than the average value of C*, determined in previous chapters by different techniques. Since DNA chains are separated from each other, a greater stability of the complex formation was expected. Different techniques are used to determine the role of chitosan amount on the formed complex: the obtained data from conductivity, ζ-potential, dynamic light scattering, circular dichroïsm and UV-Vis measurements are combined to determine the complex stoichiometry, the net charge, the dimensions, the conformation and the thermal stability of the complex, respectively. The isoelectric point was found to be related to the protonation degree of chitosan. The influence of chitosan and DNA concentrations on the complex formation is discussed and optimized to get stable nanoparticles.

7.1.1. Chitosan characterization

7.1.1.1. Chitosan structure

Chitosan is the most important derivative of chitin, which is the second most important natural polymer in the world, after cellulose, and is obtained from crustaceans, shrimps and crabs [18]. Chitosan is a linear polysaccharide composed of randomly distributed ®-(1-4)-linked D-glucosamine (deacetylated unit) and N-acetyl-D-glucosamine (acetylated unit) (*Figure 7.1*).
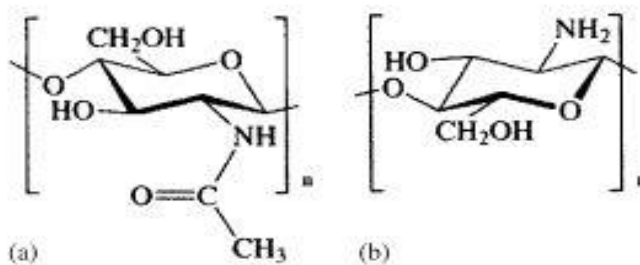
Figure 7.1. *Chemical structure of the repeat unit in a) chitin and in b) chitosan [18].*

In the solid state, chitosan is a semicrystalline polymer, however, it is also possible to obtain sponges, powders and fibers through its regeneration from solutions or its derivatives [18, 19].

7.1.1.2. Solubility

The solution properties of chitosan depend on the following parameters: the average degree of acetylation (DA), the molecular weight and the distribution of the acetyl groups along the chain [20]. *Rinaudo et al.* [21,22] studied chitosan protonation in the presence of acetic acid and the role of HCl on chitosan solubility. Chitosan with a low DA can be solubilized in an average degree of ionization α of chitosan equals to 0.5. This value of α corresponds to a pH between 4.5 and 5.0 in presence of HCl.

Rinaudo et al. [21] proved that the amount of required acid depends on the quantity of chitosan to be dissolved and showed that the solubility is also related to the ionic concentration, the pH, the nature of the acid used for the protonation and the conditions of isolation and drying of the polysaccharide.

7.1.1.3. Degree of acetylation

The degree of deacetylation (DA), determined by the fraction of N-acetylated glucosamine units, is an important property of chitosan that determines the way the polysaccharide can be applied [23]. This

characteristic can be obtained through the following techniques: potentiometric titration, IR, UV, ^{1}H liquid-state NMR and ^{13}C solid-state NMR [19]. DA determination method by ^{1}H NMR spectroscopy was reported to be effective, precise and simple [24]. The fraction of free $-NH_2$ in chitosan can also be obtained by using pH or conductivity measurements dissolving a neutral chitosan with a small excess of HCl on the basis of stoichiometry followed by neutralization of the protonated $-NH_2$ groups by NaOH addition [25].

7.1.1.4. Molecular weight

Chitosan molecular weight can be calculated by means of its intrinsic viscosity using the Mark–Houwink relation (*Equation 2.26*), so solvent needs also to be taken into account. *Rinaudo* [18] summarized several Mark–Houwink parameters for chitosan in various solvents. A set of parameters for the intrinsic viscosity and the molecular radius of gyration $<S^2>^{1/2}$ dependence on molecular weight were previously proposed, stating its validity for all the samples (*Equations 7.1 and 7.2*) [26].

$$[\eta]\ (mL/g) = 0.0843\ M^{0.92} \tag{7.1}$$

$$<S^2>^{1/2}\ (nm) = 0.075\ M^{0.55} \tag{7.2}$$

It is worth to mention that the ionic strength and DA influence also the $[\eta]$, so some parameters K and a for the Mark–Houwink equation were also determined for chitosan with different average DA in 0.3M AcOH/0.2M AcONa as solvent [27].

7.1.2. Chitosan-DNA complex transfection

Transfection of DNA through specific vectors undergoes different challenges before achieving its main goal. *Figure 7.2* presents the necessary steps for DNA complexes in order to transfer DNA into the nucleus of the cell, which are listed as follows [8]:

1) DNA compaction in the presence of chitosan,
2) Interaction of these particles with the anionic proteoglycans at the cell surface,
3) Endocytosis,
4) Accumulation of cationic agents in the acidic vesicles, increase of pH of the endosomes and inhibition of the degradation of DNA by lysosomal enzymes,
5) DNA transport to the nucleus and decomplexation.
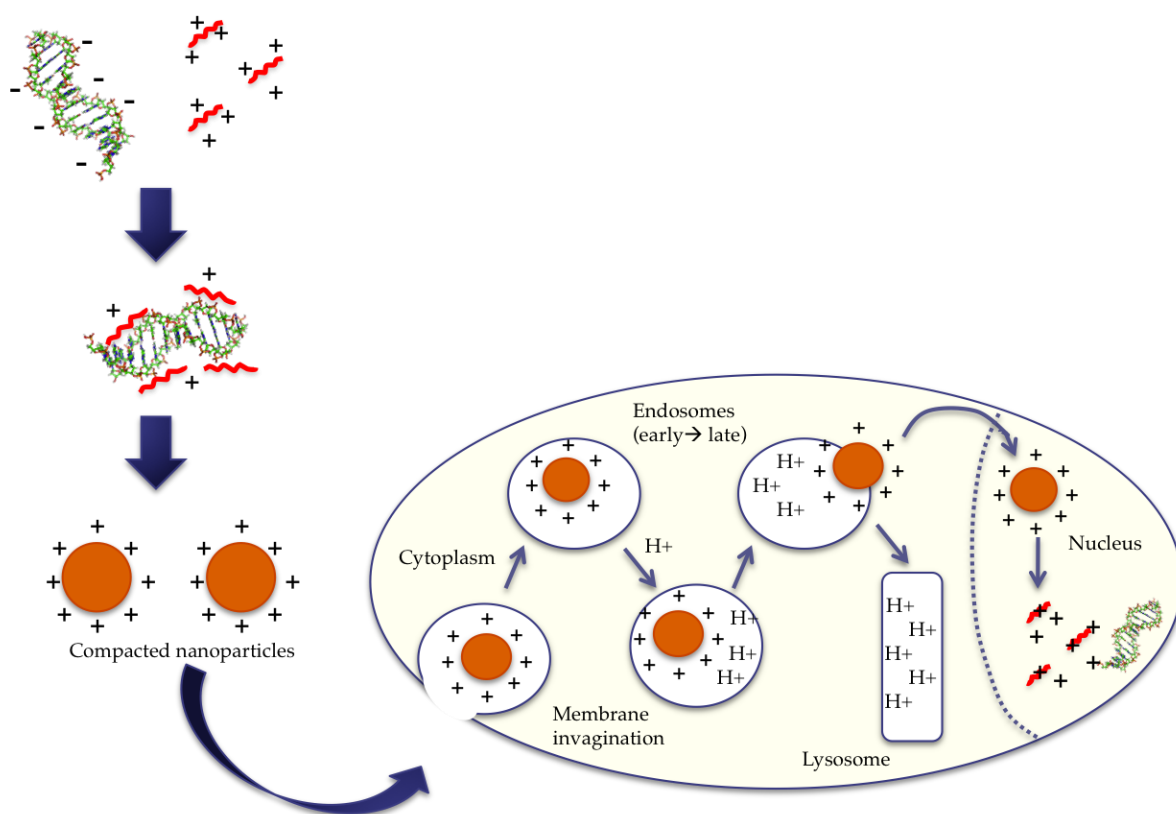
Figure 7.2. *Schematic representation of DNA transfection into a cell.*

7.2. Overview of the techniques

7.2.1. Conductometric measurements

For electrolytic solutions, the current is carried by the ions of the solution, which are in constant random motion in the absence of an electric field due to the action of convection and thermal forces. When ions are subjected to an electric field by applying a potential difference, they present a phenomenon known as ion migration. At these conditions, the solution can be considered as a homogeneous ionic conductor that follows Ohm's Law (*Equation 7.3*):

R= V_E /I   (7.3)

where R is the conductor resistence, V_E is the applied potential difference and I is the intensity of current flowing through the conductor.

The progress of a chemical reaction involving ionic species can be monitored through a measurement of the electrolytic conductivity, i.e. conductometry. In this way, when an ionic reactant is

added to an electrolyte, then the electrolytic conductivity of the mixture is constantly measured. Conductivity measurements can be considered as a tool to locate the end point of the reaction, like in a titration of a HCl solution by the strong base NaOH. In that reaction, highly conducting protons are neutralizad by NaOH addition to form water and conductivity decreases. After reaching the equivalent point, if more NaOH is added, then the conductiviy increases. In this way, the titration of a strong acid with a strong base results in a minimun of the conductivity at the equivalent point.

7.2.2. ζ−potential measurements

Zeta potential (ζ−potential) is a fundamental parameter that affects the stability of particles and corresponds to the magnitude of the electrostatic attraction or repulsion between particles. ζ−potential value is closely related to dispersion, aggregation or flocculation of particles and can be used to improve the formulation of suspensions, dispersions and emulsions.

An electrical double layer is created around a charged colloidal particle in an aqueous solution with properties depending on the characteristics of the solution and the particle. The detection of the particle charge is possible through the imposition of an electric field in the suspension, since the material will migrate towards the electrode of opposite charge. *Figure 7.3* shows a schematic representation of a negatively charged model colloid with its counterions immersed in an aqueous solution and the corresponding potential curve. The applied electric field causes the displacement of the charged colloid with the surface potential Ψ_0 and the counterions retained in the double-layer up to $x = d_{ek}$. The counterions in the low electrostic field domain move in the opposite direction relative to the center particle. These counterions are then sheared off from the electric double layer of the colloid, generating a potential at the plane of shear. The shear plane is located further away but close to the Outer Helmholtz Plane (OHP) at $x = d$, which shows the extend of the Stern layer and the beginning of the diffuse part of the electrical double layer. The ζ-potential is then smaller than the diffuse potential Ψ_d.

The ζ-potential is then defined as the average potential (ψ) in the electrical double layer at the region of shear between the mobile charged particle and the liquid phase. Particle charge is fulfilled by counterions that are attracted by the charged interface between the particle and the solution [27].

Free diffusion of the particles tend to oppose the movement, however, the particle starts moving with a constant velocity when equilibrium has been reached between the two opposing forces. The velocity of a particle in an electric field is known as the electrophoretic mobility of the particle determined by the ζ−potential corresponding to the shear zone, experimentally determined.
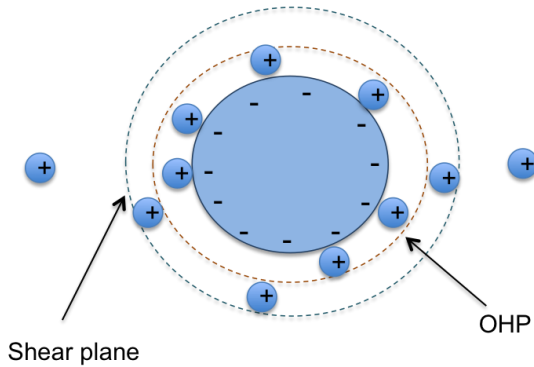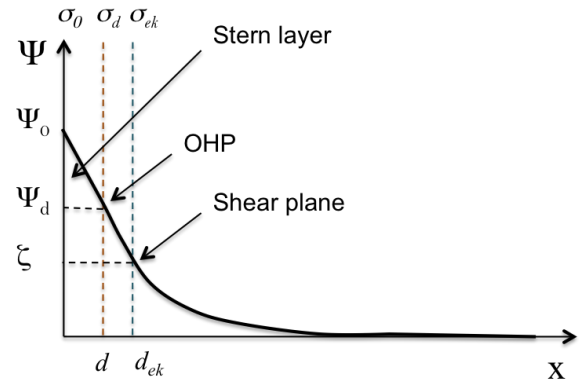
Figure 7.3. *a) Schematic representation of a negatively charged colloid suspended in electrolyte solution and its b) potential curve.*

The electrophoretic mobility increases as the electrical potential of the particle increases in a uniform field. It will depend on the strength of the electric field, the dielectric constant of the liquid the viscosity of the solvent and reflects the surface charge potential, directly conected with the ζ–potential. The ζ–potential can be determined by measuring the electrophoretic mobility of the particle and using the equation of Henry:

$$\mu= 2\varepsilon\varepsilon_0\zeta f(\kappa,a)/3\eta_s \tag{7.4}$$

where ε is the dielectric constant, ε_0 is the permittivity of the vaccum, ζ is the zeta potential, η_s is the solvent viscosity and $f(\kappa,a)$ is Henry's function, which generally has values of 1.0 or 1.5, and μ is the electrophoretic mobility, given by:

$$\mu=\upsilon_e/E \tag{7.5}$$

where υ_e is the measured velocity and E is the applied field.

Henry's function takes into account the Debye-Hückel term, κ, which contains the electrolyte concentration term and leads to the value of the thickness of the double layer surrounding the particle, given by the reciprocal of κ and the particle size, given by the radius a.

If the particle is relatively small compared to the size of the double layer, then $f(\kappa,a)$ =1, so *Equation 7.4* results in:

$$\mu = 2\varepsilon\varepsilon_0\zeta/3\eta_s \qquad (7.6)$$

If the particle is large relative to the double layer distance, $f(\kappa,a) = 1.5$ and *Equation 7.4* results in the Smoluchowski simplified approach given by:

$$\mu = \varepsilon\varepsilon_0\zeta/\eta_s \qquad (7.7)$$

7.2.3. Dynamic Light Scattering measurements

Dynamic light scattering (DLS) is one of the most important techniques of macromolecular characterization [28]. It is usually used to determine the particle size distribution of a specific particle. Scattering phenomena are based in the dependence of the intensity of light scattered by a particle population at a specific angle, to the incident light wavelength, the size, shape and concentration of the scattering particles, the optical properties of the particle and their environment. With this technique it is possible to calculate the shape factor of the particle and to determine its structure. The particles that can be studied by DLS are those whose size is comparable with the wavelength of visible light, so DLS is widely used for the analysis of colloidal dispersions [29]. DLS instruments measuring at a fixed angle can determine the mean particle size in a limited size range and multi-angle instruments can determine the full particle size distribution.

Brownian motion, which is a relevant phenomena in dynamic light scattering measurements, is defined as the arbitrary motion of particles in solution and results from the thermally-driven collisions of the solvent molecules with the studied particles. When a solution of particles diffuses under the Brownian motion phenomena, the light scattered will vary with time. The analysis of the fluctuation of the scattered light leads then to the information of the particles. The characterization of the intensity fluctuations through the intensity correlation function g^2 (q,t), whose analysis provides the diffusion coefficient of the particles.

The standard procedure for obtaining the diffusion coefficient from the correlation function g^2 (q,t) corresponds to the cumulants method , which is given by the following equation [30]:

$$\ln\left|g^2(q,t)\right| = -\Gamma_c t + \frac{1}{2!}m_2 t^2 + \frac{1}{3!}m_2 3t^3 + \dots \qquad (7.8)$$

where Γ_c is the first cumulant, $\langle\Gamma_c\rangle = q_w^2 D$, q_w is the wave vector, and D is the diffusion coefficient.

For spherical particles, the hydrodynamic radius can be calculated through the Stokes-Einstein equation:

$$R_h = \frac{k_B T}{6 \rho h_s D} \tag{7.9}$$

where k_B is the Boltzmann constant, η_s is the viscosity of the solvent and T is the absolute temperature.

7.2.4. Confocal fluorescence microscopy

Confocal microscopes are integrated electronic systems where the optical microscope has a principal role in a configuration that consists of one or more electronic detectors, a computer for image display, processing, output, storage, and several laser systems combined with wavelength selection devices and a beam scanning assembly [31].

The confocal microscope uses an optical imaging technique to increase the contrast and to build three-dimensional images using a spatial pinhole to remove the blurred light in specimens that are thicker than the focal plane. The pinhole is located in front of the photomultiplier and prevents the passage of fluorescence of the sample regions that are not focused. The light from the regions located above or below the focal plane does not converge on the pinhole and is not detected by the photomultiplier.

7.2.5. Circular Dichroïm (CD) measurements

Circular dichroïsm (CD) is a phenomenon originated from interactions of chiral molecules involving asymmetric carbons with circularly polarized electromagnetic rays [32,33]. CD spectroscopy is widely used to study chiral molecules of all types and sizes, but it has its most important applications in the field of large biological molecules, leading to structural, kinetic and thermodynamic information about macromolecules. CD spectroscopy is a technique for electronic absorption, based on the change of electronic molecular configuration from a fundamental state to an excited state due to the absorption of polarized electromagnetic radiation. Circular dichroïm theory was developed by *Biot Neumann* and *Fresnel Snatzke* (1990) [34].

To understand circular dichroïsm, it is necessary to firstly understand the basics of polarization. For linearly polarized light, its oscillations are confined to a single plane [34]. All polarized light states can be described as a sum of two linearly polarized states at right angles to each other. If we take horizontally and vertically polarized light waves with the same amplitude and that are in phase with each other, the resultant light wave is linearly polarized at 45 °. However, if the two polarization states are out of phase, then the resultant wave is not longer linearly polarized. If one of the polarized states is out of phase with the other by a quarter-wave, then the resultant will be a helix known as circularly

polarized light (CPL). The helices can be either right-handed (R-CPL) or left-handed (L-CPL) and are non-superimposable mirror images. In this manner, the optical element that converts between linearly polarized light and circularly polarized light is termed a quarter-wave plate. The basis of CD technique is the difference in absorbance of left-hand and right-hand circularly polarized light and can be applied to molecules that absorb R-CPL and L-CPL differently, i.e that are optically active (chiral) [34-36].

Circular dichroism response is represented in diagrams showing the difference of molar absorption coefficients for R-CPL and L-CPL in front of a given wavelength. CD spectra can be compared with conventional absorption spectra to appreciate other information. With CD spectroscopy it is possible to identify the absolute configurations of chiral compounds with similar electron configurations, as CD spectra will present the same sign. Since the great majority of biological molecules are chiral, they can by studied through CD spectroscopy, i.e. amino acids [37], proteins [38], DNA [39] and RNA [40]. This technique has been extensively used for studying the higher order structures of macromolecules and conformational changes of nucleic acids (DNA) [41-43]. Each structure has a specific circular spectra, which can be used to identify different structural elements and to follow the structural or conformational changes of chiral macromolecules.

The characterization of A and B forms of DNA through CD spectroscopy was firstly reported by *Tunis-Schneider* and *Maestre* [44] and Z conformation of DNA was identified for the first time with this optical technique [45]. The nearest neighbor composition of nucleic acids and their secondary structures highly influence the CD spectrum above 210 nm, so information of both, composition and structure, are available from CD measurements.
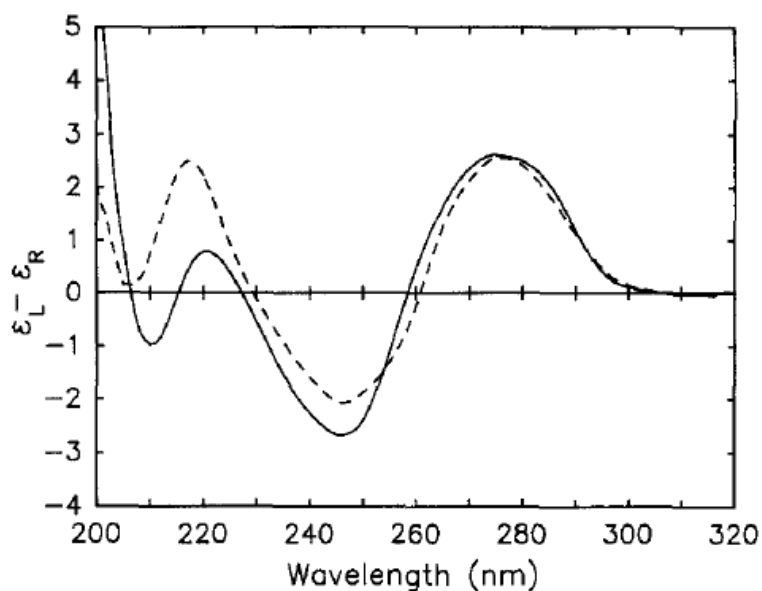
Figure 7.4. *CD spectra of T7 phage DNA before (—) and after (---) heat denaturation. Solvent: 2mM Na^+(phosphate buffer), pH 7. Extinction coefficient at 260nm: 6570 M^{-1} cm^{-1} for the native DNA. ε_L - ε_R is in units of M^{-1} cm^{-1} per molar concentration of nucleotide [46].*

For denaturation of double-stranded B-form DNA, only slight CD changes above 210 nm can be detected. *Figure 7.4* shows the CD spectra of T7 phage DNA before and after thermal denaturation. The denatured DNA was cooled rapidly after being denatured at 80 ºC, so both spectra were obtained at 20 ºC [46]. The values of the major CD bands above 230 nm do not present major variations due to denaturation. Greater CD changes can be detected at wavelengths below 230 nm, which include an increase in the magnitude of the band near 220 nm. A shift of the long-wavelength crossover in the range between 258 and 261 nm usually indicates denaturation.

7.3. Experimental conditions

7.3.1. Reagents

Calf thymus DNA with 13 000 base pairs (bp), NaOH in pellets with impurities $\leq$ 0.001 % and NaCl anhydrous were supplied by Sigma-Aldrich Company. Chitosan sample with a molecular weight (Mw) of 500 000 and a DA of 0.19 was purchased from Kitomer (Marinard, Canada). HCl 0.1 N (Titrisol) was supplied by Merck Millipore.

7.3.2. DNA solutions preparation

DNA solutions were prepared using appropriate amounts of DNA in water and NaCl 1×10^{-2} M, as solvents. The vials were closed and sealed with parafilm to prevent water evaporation and changes in the concentration. DNA concentrations are chosen usually around 0.03 mg/mL in order to avoid experimental difficulties as turbidity during chitosan addition. All solutions were stored in a refrigerator at a temperature of 4 °C in order to prevent degradation.

7.3.3. Chitosan solution preparation

The solutions of chitosan are prepared at 5.3 mg/mL by dissolving a known amount of polysaccharide with the stoechiometric amount of HCl 0.1 N (previously titrated with NaOH 0.1 N) on the basis of NH_2 content (which final pH is around 3.35). The solution was placed under constant stirring for 1 night at room temperature, until complete solubilization, then it was stocked at a temperature of 4 ºC. Chitosan solution was then diluted to 1 mg/mL, then filtered with a 0.2µm membrane and then adjusted to the selected pH with a solution NaOH 0.1 N.

7.3.4. Conductometric measurements

Conductometric measurements were performed in a Crison CM 35 conductivity Instrument at a constant temperature of 25 ±0.01 ºC. Conductimetric titration was firstly performed to determine chitosan DA in presence of HCl by progressive NaOH addition. Then, it was used to follow the chitosan-DNA complex formation by adding progressively a given volume of chitosan 1 mg/mL to a volume of 20 mL DNA solution at a concentration of 0.03 mg/mL under continuous agitation. Each measurement was taken after 5 minutes of stabilization.

7.3.5. ζ–potential measurements

ζ–potential measurements were performed in a Malvern Zetasizer NanoZS at a temperature of 25 ºC. Complex formation was carried on as follows: a given volume of chitosan 1 mg/mL was added to the DNA solution (0.03 mg/ml) at controlled pH, under continuous agitation. After stabilization of the obtained chitosan-DNA complex (i.e. 5 min), 1 mL of the solution was injected to the cell, which was then placed inside the instrument and finally the measurement was taken. After each measurement the whole solution was collected from the Zetasizer Nano cell and reintroduced into the bulk solution (to keep a nearly constant volume of solution) before the addition of the next volume of chitosan solution. The instrument measured the electrophoretic mobility of the particles and converted it to the ζ–potential using the classical Smoluchowski expression.

7.3.6. Dynamic Light Scattering measurements

Dynamic light scattering (DLS) measurements were performed in a Malvern zetasizer 5000 apparatus equipped with a 7132 multibit correlator and multiangles goniometer. The light source was a He-Ne 5mW laser with a wavelength of 632.8 nm. The scattering intensity was measured through a 400 μm pinhole. The correlation functions were averaged over 30 s in equilibrated sample. DLS measurements were carried out at 90 °. The corresponding hydrodynamic radius was calculated using the Stokes−Einstein equation.

7.3.7. Confocal microscopy observations

Optical observations of fluorescein labeled chitosan-DNA complexes were made using a laser fluorescence microscope (TCS SP8) with a 488 nm excitation wavelength. Fluorescence acquisitions at this excitation wavelength are obtained successively. In order to observe the chitosan-DNA complex formation by using fluorescence microscopy, chitosan (1mg/mL) was labeled with fluorescein. The

degree of labeling is determined from the fluorescence intensity of diluted solutions of the free fluorescent probe compared with the fluorescence of a diluted solution of the labeled chitosan (it is found around 2 % of modified sugar unit).

7.3.8. Circular Dichroism (CD) measurements

CD measurements were performed in a Chirascan CD Spectrometer with a 150W air-cooled Xe arc lamp as light source. Spectra were acquired in a 10 mm length quartz cuvette at 25 ° C. Three scans were averaged per spectrum, operating from 200 to 320 nm at a scan speed of 30 nm/min and a bandwidth of 1 nm. Measurements were performed under a constant nitrogen flow, to purge the ozone generated by the light source of the instrument. All results were normalized using the solvent spectra. The protocol for chitosan-DNA complexes preparation explained on *Section 7.3.4.* was performed to obtain each CD measurement.

7.3.9. UV-Vis measurements

DNA melting temperatures (T_m) were measured by recording the absorbance A_{260} as a function of temperature (T) using a Cary 400 Scan UV-Vis Spectrophotometer. Quartz cuvettes were used for all measurements. The solvent cuvettes were filled with water or NaCl 10^{-2} M and were used as the blank. The temperature was raised at a rate of 1 °C/min, from 25 to 90 °C. Then the temperature was decrease from 90 to 25 °C at a rate of 5 °C/min. The protocol for chitosan-DNA complexes preparation explained on *Section 7.3.4.* was performed to obtain each T_m measurement.

7.4. Experimental results and discussion

7.4.1. Chitosan characterization

Chitosan solution was firstly characterized in order to verify the degree of deacetylation (DA) reported by the suppliers and to determine the protonation percentage of a function of pH. A conductometric titration with NaOH 0.1 N was carried out for a chitosan solution of 5.3 mg/mL at a temperature of 25 °C (*Figure 7.5*). The fraction of [NH_3^+] in chitosan was found to be 0.4875, from which was possible to calculate, as a first approach, the DA of our sample, i.e. DA~ 0.22, which is in good agreement with the information provided by the supplier.
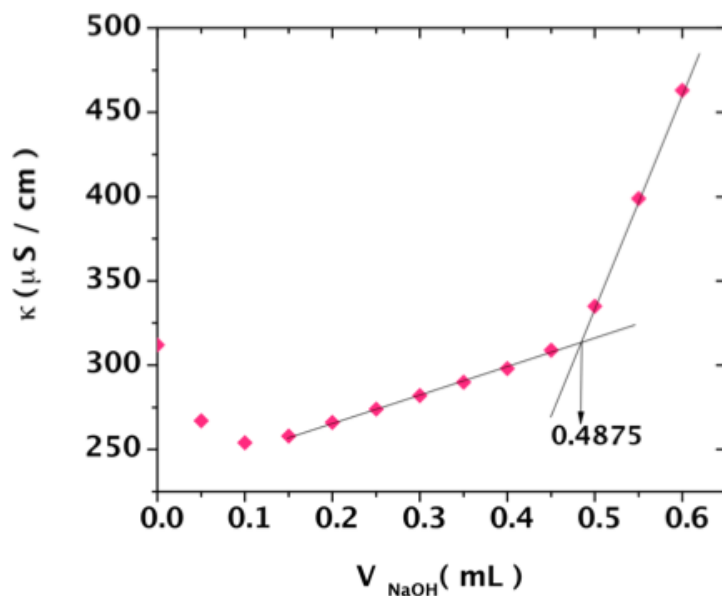
Figure 7.5. *Conductometric titration curve for a chitosan solution 5.3 mg/mL as a function of added volumen of NaOH 0.1 N.*

Figures 7.6 a and *b* present the ζ-potential and the potentiometric titration of chitosan with NaOH 0.1 N, respectively. The fully protonated solution of chitosan (dissolved in stoichiometric amount of HCl) presents a ζ-potential around + 47 mV at a pH of 3.35, showing that under these conditions, chitosan is strongly positively charged since the 100 % of the amino groups are protonated. While the fraction of $[NH_3^+]$ in the solution of chitosan decreases, the ζ-potential decreases and pH increases, so it is possible to calculate the protonation percentage at a given pH.
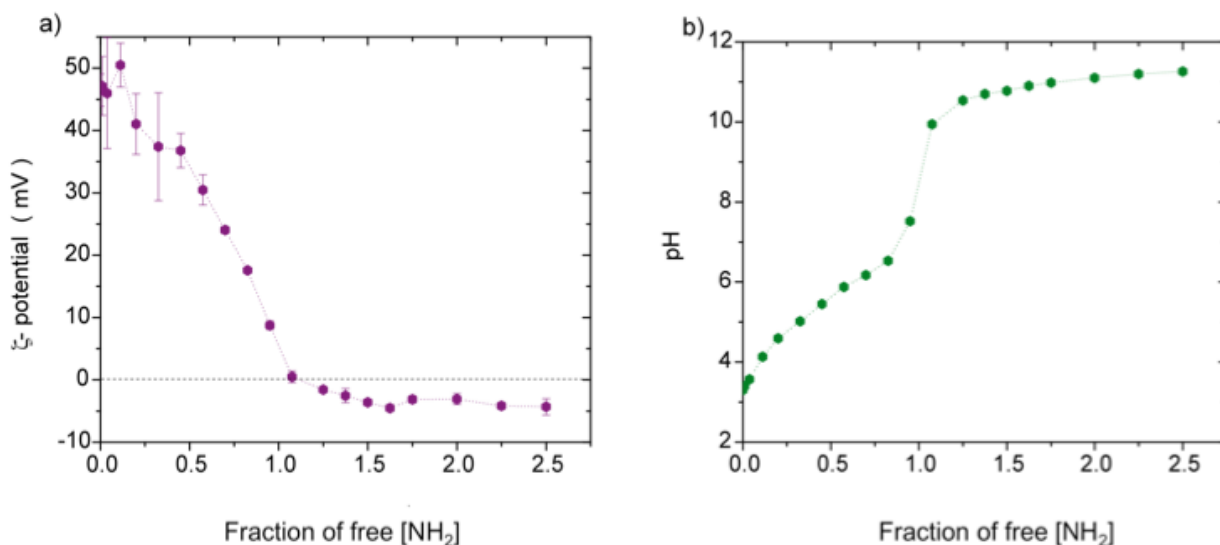
Figure 7.6. *a) ζ-potential and b) potentiometric titration of a chitosan solution 1.0 mg/mL with NaOH 0.1 N.*

Table 7.1 summarizes the charge fraction of chitosan at the different pH's selected for chitosan-DNA complex development in this work. It is shown that at the pH of 6.5, which is a closer value to the average pH at physiological conditions, chitosan is only partially positively charged since 17 % of the amino groups are protonated.

Table 7.1.- *Fractions of [NH$_2$] and [NH$_3^+$] as a function of pH.*

| pH	Fraction of [NH$_2$]	Protonated fration [NH$_3^+$]
4.5	0.20	0.80
4.7	0.23	0.77
5.0	0.33	0.67
6.5	0.83	0.17

7.4.2. Stoichiometry of chitosan-DNA complex

Chitosan-DNA complexes were prepared by using DNA solutions at a concentration of 0.03 mg/mL, which is 10 times lower than the average of C* value determined in previous chapters by different techniques. In order to study the stoichiometry of chitosan-DNA complexes with different ionic forces and conformations, the complexes were prepared with DNA in water and in NaCl 10^{-2} M, as solvents. It is noteworthy that DNA in water is partially denatured at 25 ºC (*Figure 2.12*) and DNA in NaCl 10^{-2} M is in its double-helical conformation, as described previously in *Chapter 2*.

The mixture of oppositely charged compounds leads to electrostatic interactions between both molecules and to the formation of complexes with counterions release [47-49], in this manner, conductometry can be used to evaluate chitosan-DNA interactions and the degree of complexation. The ratio given by the total NH$_2$ concentration (i.e. free [NH$_2$] + protonated [NH$_3^+$]) and the ionic concentration of Phosphates/L (i.e. [P$^-$] supposed to be fully ionized in normal conditions), will lead to the determination of the stoichiometry during the complex formation. For a chitosan concentration of 1 mg/mL, [NH$_2$] equals to 4.7 x 10^{-3}, and considering the average molar mass of a nucleotide as 379 g/mol, for a DNA concentration of 0.03 mg/mL, [P$^-$] equals to 7.9 x 10^{-5} eq/L. The ratio [NH$_2$]/[P$^-$] increases progressively with the addition of small amounts of chitosan until getting to [NH$_3^+$]/[P$^-$]=1, representing full complexation of DNA.

Figure 7.7 shows the electrical conductivity as a function of [NH$_2$]/[P$^-$] during the chitosan-DNA complex formation at a constant temperature of 25 ºC. Small amounts of chitosan 1.0 mg/mL at a pH of 3.35 (with 100 % of the amino groups protonated) were progressively added to a DNA solution with a concentration of 1.0 mg/mL in water, at a pH of 6.5. In this figure we can observe a linear increase of conductivity with the addition of chitosan, however, a clear change in slope is depicted at a [NH$_2$]/[P$^-$]=1, corresponding to the charge stoichiometry between strongly positively charged

chitosan and strongly negatively charged DNA. The increase in conductivity due to the counterion release from the added chitosan is attributed to an increase of the counterions release (Na$^+$ for DNA and Cl$^-$ for chitosane) resulting from the complex formation [49].
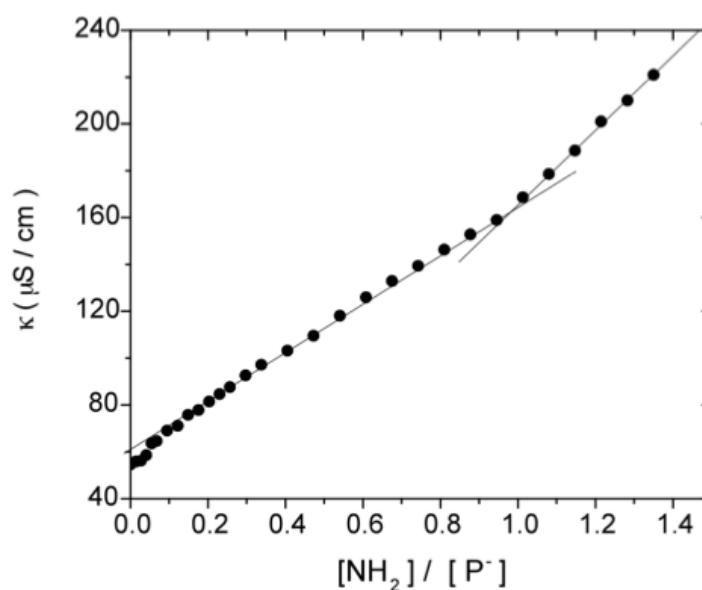
Figure 7.7. *Electrical conductivity (κ) dependence on the ratio [NH$_2$]/[P$^-$] during the formation of the chitosan-DNA complex at a temperature of 25 °C. C$_{DNA}$= 1 mg/mL at a pH of 6.5 and added C$_{Chitosan}$= 1 mg/mL at a pH of 3.35.*
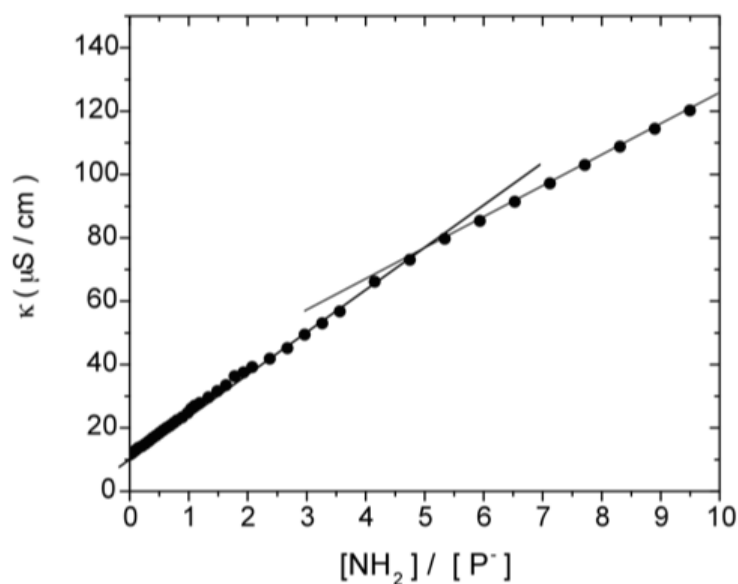
Figure 7.8 shows the electrical conductivity as a function of [NH$_2$]/[P$^-$] during the chitosan-DNA complex formation using a chitosan 1.0 mg/mL at a pH of 6.5 (with 17 % of the amino groups protonated). Since chitosan is weakly protonated, then the amount of chitosan needed to reach the stoichiometry equivalence is greater for a chitosan-DNA complex formed at a constant pH of 6.5 than for a complex formed with chitosan pH 3.35. Here we also observe a linear increase of conductivity with the addition of chitosan and a clear change in slope around [NH$_2$]/[P$^-$]=5.3, corresponding to the charge stoichiometry between weakly positively charged chitosan and strongly negatively charged DNA, taking into account the percentage of protonated amino groups. The lower slope obtained after the equivalent point at [NH$_2$]/[P$^-$]=5.3 could be related to the contribution of the excess of ionized chitosan.

Figure 7.8. *Electrical conductivity (κ) dependence on the ratio $[NH_2]/[P^-]$ during the formation of the chitosan-DNA complex at a temperature of 25 °C. C_{DNA}= 0.03 mg/mL at a pH of 6.5 and added $C_{Chitosan}$= 1 mg/mL at a pH of 6.5.*

In order to study the influence of pH in chitosan-DNA complex formation, we firstly determine the ζ-potential of DNA in the initial aqueous solution as a function of the adopted pH (*Figure 7.9*).
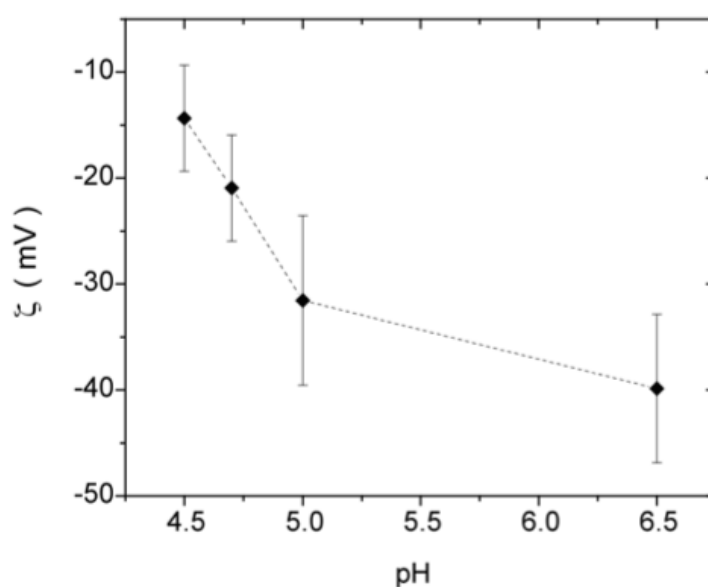
Figure 7.9 *ζ–Potential as a function of pH for a DNA concentration of 0.03 mg/mL in water at 25 °C.*

The stoichiometry during the formation of chitosan-DNA complexes at lowers pH, i.e. 4.5, 4.7 and 5.0 was also studied through conductometric titrations by using DNA solutions adjusted with HCl to the selected pH. An example is given in *Figure 7.10*. It shows the electrical conductivity as a function of $[NH_2]/[P^-]$ obtained from the complex preparation with a DNA solution of 0.03 mg/mL at a pH of 5.0 and a chitosan solution 1.0 mg/mL at a pH of 5.0. The trend of the curve is similar to the one obtained for the complex formation at a constant pH of 6.5, however, the stoichiometry does not correspond to the calculated ratio $[NH_2]/[P^-]$ between partially positively charged chitosan and negatively charged DNA (assuming that the net charge is given by complete dissociation of $[P^-]$), taking into account the percentage of amino groups protonated in chitosan, which experimentally equals to 0.83. This could be related to a slight protonation of DNA bases at lower pH's, i.e. protonation of adenine's N_1 and cytosine's N_3 eliminates these as proton acceptor sites for H-bonding and leads to acquire a relative positive charge decreasing the net charge of DNA as indicated by lower ζ-potential values (*Figure 7.9*) [50]. As for chitosan-DNA complex at a pH of 6.5, the lower slope depicted after the inflection point may be related to the lower protonation of chitosan at pH 5.0 compared to 3.35. From *Figure 7.9*, as a first approximation, the net fraction of charge of DNA is around 0.76 (assuming that ζ-potential is directly proportional to the net charge) when the degree of protonation of chitosan is 0.67 at pH 5.0. Then, the calculated equivalence is 0.88, very near to the experimental value.
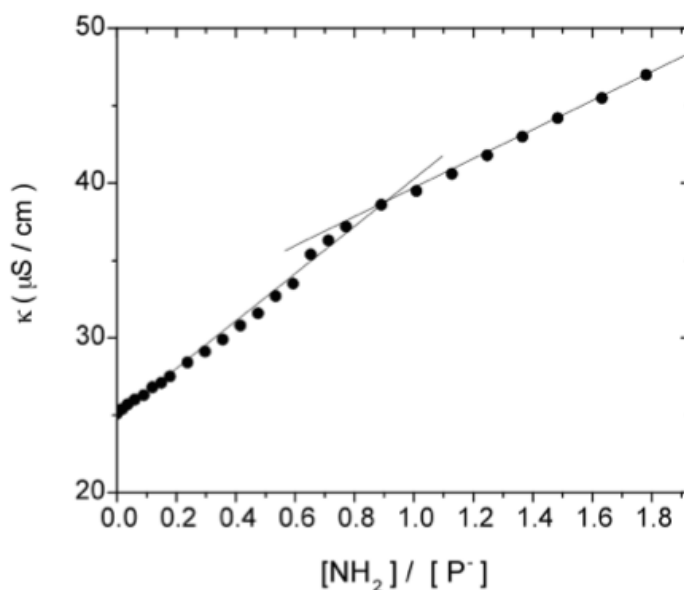

Figure 7.10. *Electrical conductivity (κ) dependence on the ratio $[NH_2]/[P^-]$ during the formation of the chitosan-DNA complex at a temperature of 25 °C. $C_{DNA}= 0.03$ mg/mL at a pH of 5.0 and added $C_{Chitosan}= 1$ mg/mL at a pH of 5.0.*

Until now, our results indicate that chitosan-DNA complex is purely electrostatic and formed between fully ionized phosphates and the fraction of protonated chitosan. Since a slight protonation of

the bases starts in acidic conditions, even above than pH 3.5, then the amount of chitosan needed to reach the stoichiometry of the charges in the complex is less than the calculated one from protonation of chitosan. On the other hand, conductomeric titration was performed for complexes prepared in a solution free of salts, in order to reach a greater insight to the stoichiometry of the reaction without the contribution of any other compound (due to lack of sensitivity in presence of external salt). The complex formation with DNA in NaCl 10^{-2} M as solvent will be then discussed in the following sections and compared to the complex formation with DNA in water.

7.4.3. Net charge of chitosan-DNA complex evaluation

Electrostatic interactions between chitosan and DNA, as a cationic vector and a higly negatively charged molecule, respectively, can be monitored during DNA complexation through electrophoretic mobility measurements by means of the ζ-potential of the resulting particles. The crossover from a negative to a positive ζ-potential is related to the isoelectric point of the particle, at which the ratio between negative charges of DNA and positive charges of the cationic vector corresponds to the stoichiometric neutralization of negative charges [49, 51]. In this manner, ζ-potential is expected to be zero when $[NH_3^+]/[P^-]=[NH_2]/[P^-]=1$, for strongly positively charged chitosan and strongly negatively charged DNA complexes, as presented for a complex obtained from a chitosan solution at its original pH (3.35) and a DNA solution at neutral pH (6.5) (*Figure 7.11*).
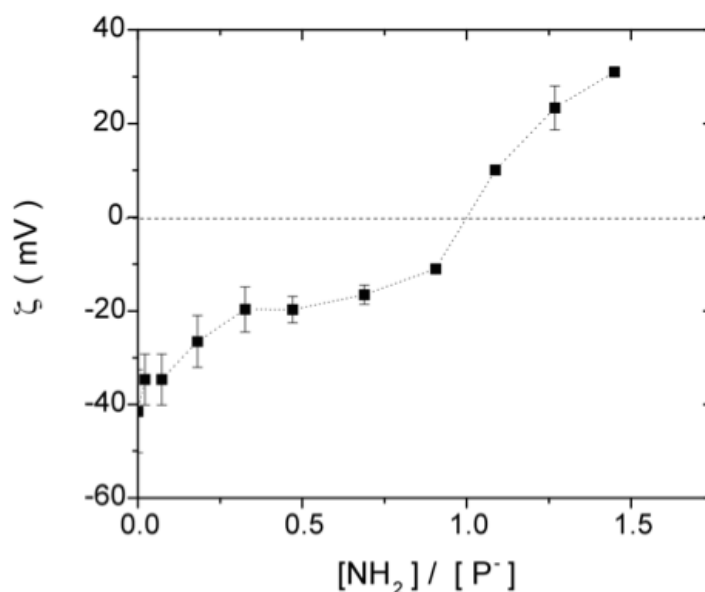
Figure 7.11. *ζ–Potential as a function of [NH₂]/[P⁻] during the formation of the chitosan-DNA complex at a temperature of 25 °C. C_DNA= 0.03 mg/mL at a pH of 6.5 and added C_Chitosan= 1 mg/mL at a pH of 3.35. The results are the average of 5 runs, so uncertainty bars represent the standard deviation.*

For chitosan-DNA complexes obtained from the electrostatic interactions between partially protonated chitosan and DNA at pH 6.5, the isoelectric point is expected to correspond to the calculated equivalence by taking into account the percentage of amino groups protonated. *Figure 7.12* shows the ζ-potential dependence with the $[NH_2]/[P^-]$ ratio during the complexation process using a DNA concentration of 0.03 mg/mL at a pH of 6.5 with the addition of small chitosan amounts at a pH of 6.5. We can observe that the initial highly negative ζ-potential (around -40 mV, corresponding to DNA molecules) decreases with the addition of the cationic vector to DNA solution, showing that electrostatic interactions between chitosan and DNA take place in the solution and represent the starting of the complexation process of DNA, as presented by number (1) in the figure. A plateau is then observed around a ζ-potential of -20 mV, showing that electrostatic interactions are stronger between positively charged chitosan and negatively charged DNA (number (2) in the figure), obtaining a stable complexed nanoparticles dispersion that will be discussed later. A third section (number (3) in the figure) is then observed when the ratio $[NH_2]/[P^-]=5.3$ is reached and ζ-potential= 0 mV, which corresponds to the stoichiometric equivalence charge value determined through conductometric measurements and the theoretical calculations for a chitosan-DNA complex at a pH of 6.5. Finally, a fourth section section is observed when $[NH_2]/[P^-]>5.3$ and ζ-potential> 0 mV (number (4) in the figure), corresponding to overcharging of DNA. A second plateau is then observed around a ζ-potential of +15 mV, which is in good agreement with the reported final ζ-potential value for chitosan-DNA complexes by *Pouton et al.* [52] and *Alatorre-Meda et al.* [49].
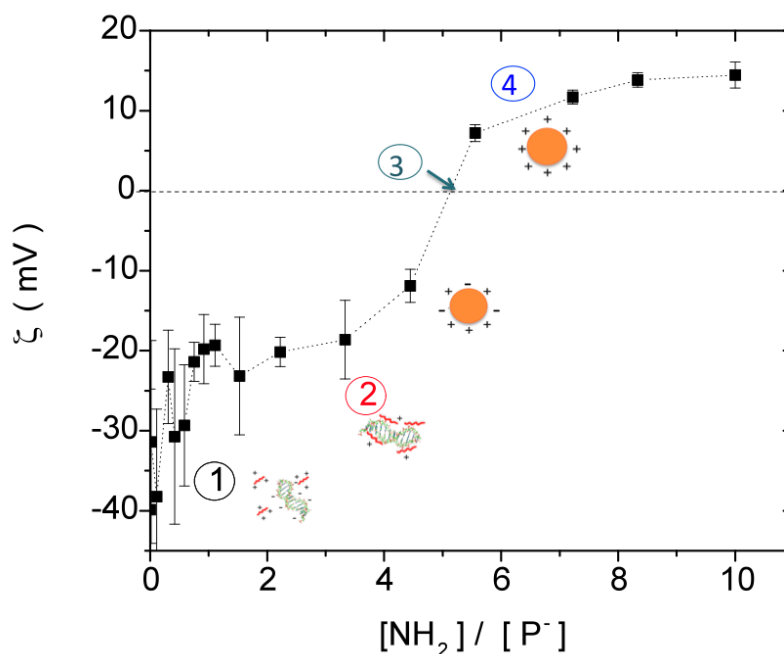
Figure 7.12. *ζ−Potential as a function of $[NH_2]/[P^-]$ during the formation of the chitosan-DNA complex at a temperature of 25 °C. $C_{DNA}= 0.03$ mg/mL at a pH of 6.5 and added $C_{Chitosan}= 1$ mg/mL at a pH of 6.5. The results are the average of 5 runs, so uncertainty bars represent the standard deviation.*

From these results we can conclude that the chitosan-DNA complex is formed by electrostatic interactions between protonated fraction of [NH$_3^+$] and [P$^-$], nevertheless, the stability of the complex could be modified in dependence of the pH.

Figure 7.13 shows the comparison of ζ-potential dependence with the [NH$_2$]/[P$^-$] ratio for the two chitosan-DNA complexes, first one prepared with a chitosan solution at a pH of 3.35 and second one prepared with a chitosan solution at a pH of 6.5. In a different way that for the complex formed at a constant pH of 6.5, the maximum plateau ζ-potential attained by using the chitosan solution at a pH of 3.35 will be higher than + 30 mV.
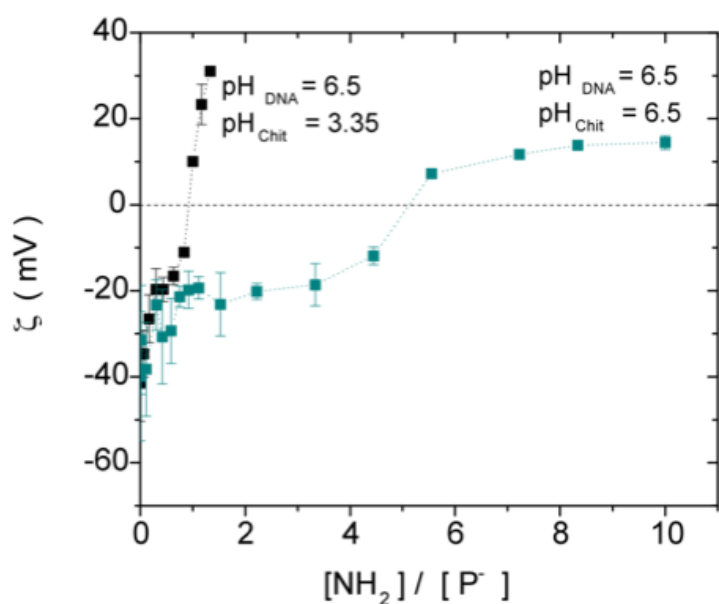
Figure 7.13. *ζ–Potential as a function of [NH$_2$]/[P$^-$] during the formation of chitosan-DNA complexes at a temperature of 25 ºC. C$_{DNA}$= 0.03 mg/mL at a pH of 6.5 and added C$_{Chitosan}$= 1 mg/mL at a pH of 6.5 and at a pH of 3.35.*

Figure 7.14 shows the ζ-potential dependence with the [NH$_2$]/[P$^-$] ratio during the complexation process of DNA in water with chitosan, the two solutions being adjusted to different pH's before complex formation, i.e. 4.5, 4.7, 5.0 and 6.5. It is possible to observe a shift to lower [NH$_2$]/[P$^-$] ratios with the decrease of the pH (5.0> 4.7> 4.6), which values are slightly lower than the calculated stoichiometry of charges, as discussed previously in *Section 7.4.2.* This could be explained in terms of DNA bases protonation (*Figure 7.9*). As discussed before for pH 5.0, the ζ–potential= 0 mV occurs at ratio [NH$_2$]/[P$^-$] lower than 1, as predicted from the net charge of DNA and the degree of protonation of chitosan.
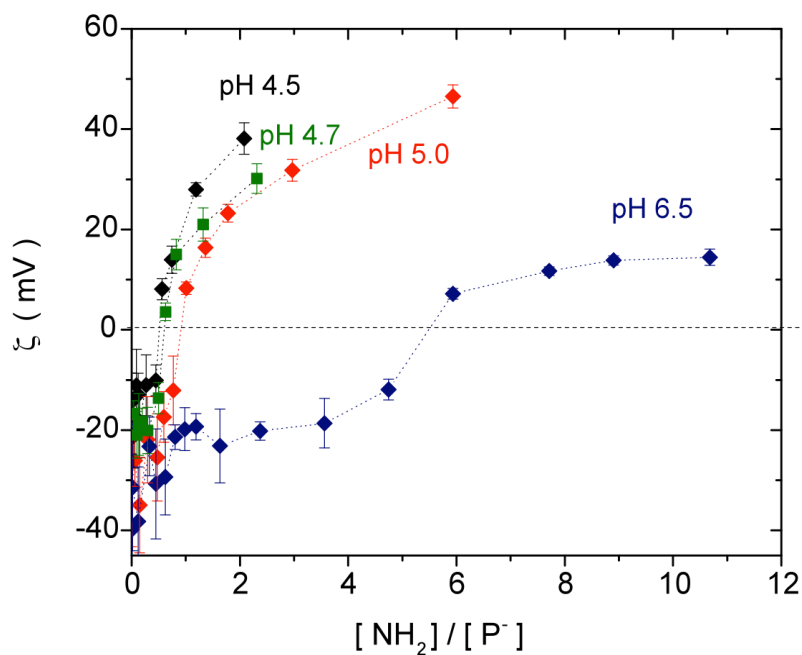
Figure 7.14. *ζ–Potential as a function of [NH₂]/[P⁻] during the formation of chitosan-DNA complexes at a temperature of 25 °C. C_DNA= 0.03 mg/mL and added C_Chitosan= 1 mg/mL at the same pH, i.e.: 4.5, 4.7, 5.0 and 6.5.*

In order to study the ionic strength and DNA conformation influence on chitosan-DNA complex properties, a comparison between the ζ-potential dependence with the [NH₂]/[P⁻] ratio was carried out for two complexes using a DNA concentration of 0.03 mg/mL: first complex was prepared with DNA in water as solvent and second one with DNA in NaCl 10^{-2} M as solvent. The other conditions remain constant, i.e. a chitosan solution with a concentration of 1 mg/mL, a constant pH of 6.5 and a temperature of 25 °C.

Figure 7.15 presents the results of the ζ-potential variation as a function of [NH₂]/[P⁻] for chitosan-DNA complexes in water and in NaCl 10^{-2} M, where we can observe the same behavior for both complexes: a decrease of ζ-potential with the addition of chitosan, a first plateau around -20 mV and a second plateau after the isoelectric point of the complex. However, we also can distinguish a slight shift in [NH₂]/[P⁻] ratio, corresponding to 5.3 for the complex in water and to 5.9 for the complex in NaCl 10^{-2} M. On the other side, the second plateau is located around a ζ-potential of +15 mV for the complex in water and around a ζ-potential of + 5 mV.
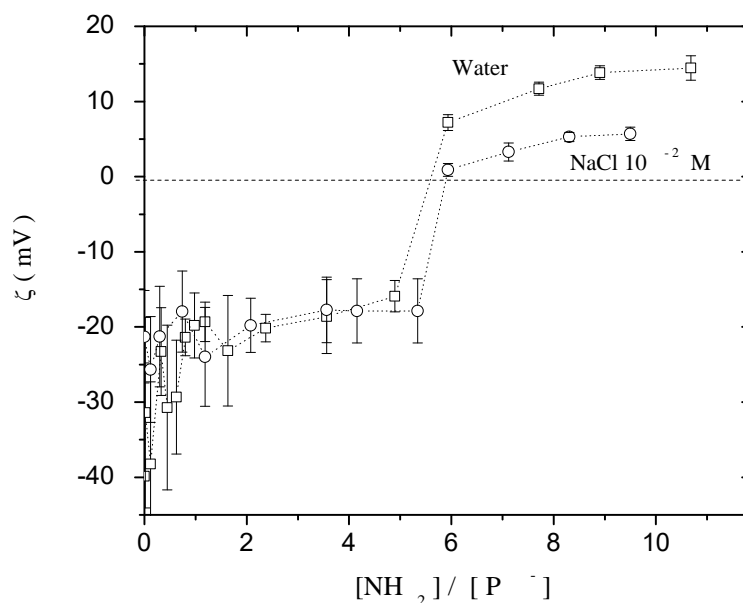
Figure 7.15. *ζ–Potential as a function of [NH₂]/[P⁻] during the formation of chitosan-DNA complexes at a temperature of 25 ºC and a constant pH=6.5. C_DNA= 0.03 mg/mL using water as a solvent (squares) and using NaCl 10⁻² M as a solvent (diamonds) and added C_Chitosan= 1 mg/mL.*

From these last results it is possible to conclude that the complexation of DNA in water, partially denatured as shown by UV-Vis measurements, and double-helical DNA in a solution with an ionic strength of 10^{-2} M NaCl present the same electrostatic behavior and almost the same stoichiometry, given by the ratio between fully ionized phosphates and the fraction of protonated chitosan.

7.4.4. Chitosan-DNA complex dimensions determination

Measurements of dynamic light scattering (DLS) allowed following chitosan-DNA complex formation by measuring the hydrodynamic radius (R_h) and the scattered light intensity (KCps) as a function of $[NH_2]/[P^-]$ ratio. *Figure 7.16* shows a first approximation of R_h values as a function of the $[NH_2]/[P^-]$ ratio during the complexation process of DNA in water and DNA in NaCl 10^{-2} M at a constant pH of 6.5. The average value of R_h decreases upon the addition of chitosan, representing the compaction of the long DNA molecule into a compact nanoparticle by means of the neutralization of the negative charges. *Figure 7.16* presents the first plateau, as the one observed with ζ-potential measurements, obtained before the stoichiometric ratio $[NH_2]/[P^-]$. Here, the dimensions of the nanoparticles have an average radius of 280 nm. In order to study the stability of these nanoparticles with time, they were stocked at a temperature of 3 ºC and their size was monitored each day during at least one week. Finally, it was observed that at $[NH_2]/[P^-]$ >1.0, the size of the particles increases

suddenly and the appearance of a precipitate is evident in the solution, which is expected due to the total neutralization of negative charges and even overcharging with aggregation. DNA precipitation was also observed for the compaction with cationic surfactants [53,54], cationic lipids [55] and different molecular weight chitosans [56].
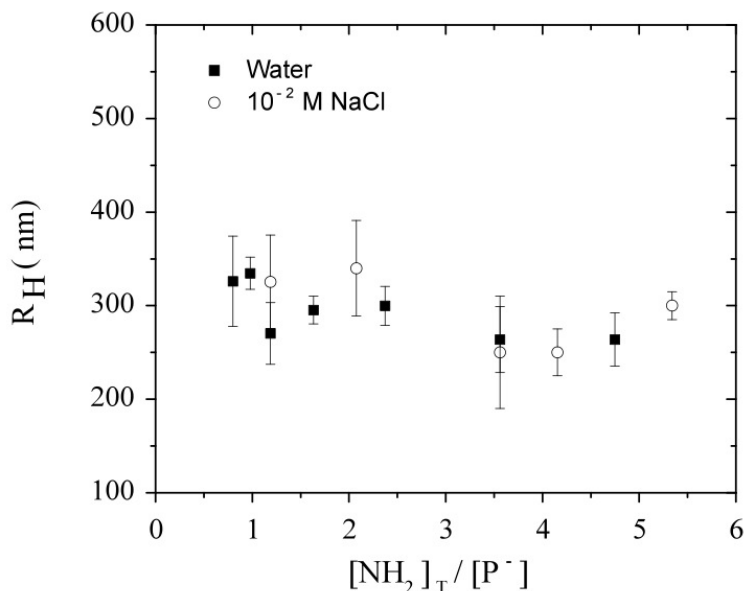
Figure 7.16. *R_h (nm) as a function of [NH_2]/[P^-] during the formation of chitosan-DNA complexes at a temperature of 25 ºC. C_{DNA}= 0.03 mg/mL at a pH= 6.5 using water as a solvent (black squares) and using NaCl 10^2 M as a solvent (circles) and added $C_{Chitosan}$= 1 mg/mL at a pH=6.5.*

Fluorescence confocal observations allowed visualizing chitosan-DNA complexes formed in the first plateau section before reaching the stoichiometry given by [NH_2]/[P^-] and before the ζ-potential = 0 mV. Since labeling the chitosan with a fluorescent dye does not change its ζ-potential or complexes ζ-potential, then chitosan-DNA complexes were prepared by using a chitosan solution labeled with fluorescein. *Figure 7.17* shows fluorescence confocal observations of chitosan-DNA complexes prepared with a DNA solution at a concentration of 0.03 mg/mL, a ratio [NH_2]/[P^-] of 4, a constant pH of 6.5 and a constant temperature of 25 ºC. The spherical red dots in the figure are chitosan-DNA complexes in the solution. An average radius around 200 nm was measured with the analytical software, which is in good agreement with the obtained values through dynamic light scattering in the first plateau region before [NH_2]/[P^-]= 5.3 for a pH of 6.5.
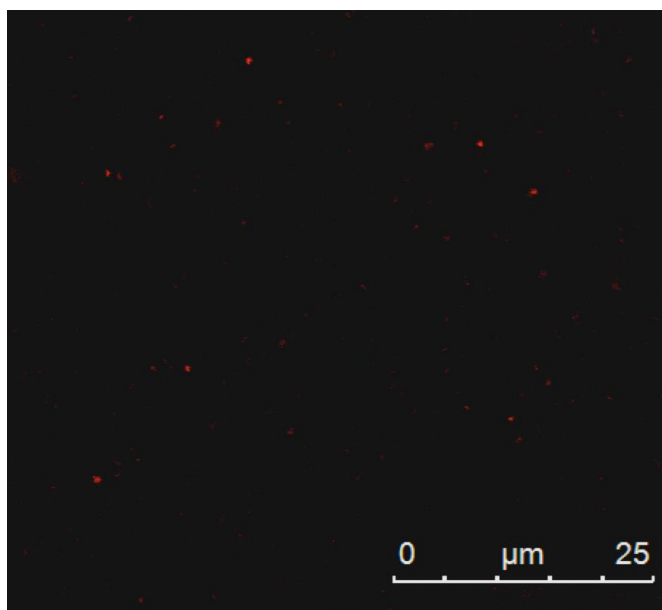
Figure 7.17. *Fluorescence confocal observation of chitosan-DNA complexes at a constant pH of 6.5.*

7.4.5. Chitosan-DNA complex conformation

DNA conformation was firstly evaluated through CD measurements for different DNA concentrations in a solvent with an ionic strength of 10^{-2} M NaCl. *Figure 7.19* shows the CD spectra for three DNA concentrations, i.e. 0.01, 0.03 and 0.05 mg/mL, in a solvent with an ionic strength of 10^{-2} M NaCl and at a temperature of 25 °C. The obtained CD spectra correspond to the characteristic spectra of the double-stranded B-form DNA, with an isodichroic point at the wavelength of 258.5 nm. The dependence with the concentration is well defined with the increase in the magnitude of the band near 280 nm and the decrease in the magnitude of the band near 250 nm.

CD spectra of B-form DNA is presented in *Figure 7.18* for a DNA concentration of 0.03 mg/mL in water, where it is partially denatured, and in 10^{-2} M NaCl where it is in a double-stranded conformation. It is possible to detect a slight shift of the long-wavelength crossover from 258.5 nm to 260.5 nm, which indicates denaturation of DNA strands. We observe also a minor increase in the magnitude of the band near 220 nm, which is also characteristic of denaturation [46], and slight CD changes above 220 nm. These results are in good agreement with the ones obtained through UV-Vis measurements discussed on *Chapter 2*, suggesting that DNA in water as a solvent is partially denatured and that the addition of salt at an ionic concentration of NaCl 10^{-2} M allows maintaining the double-stranded B-form.
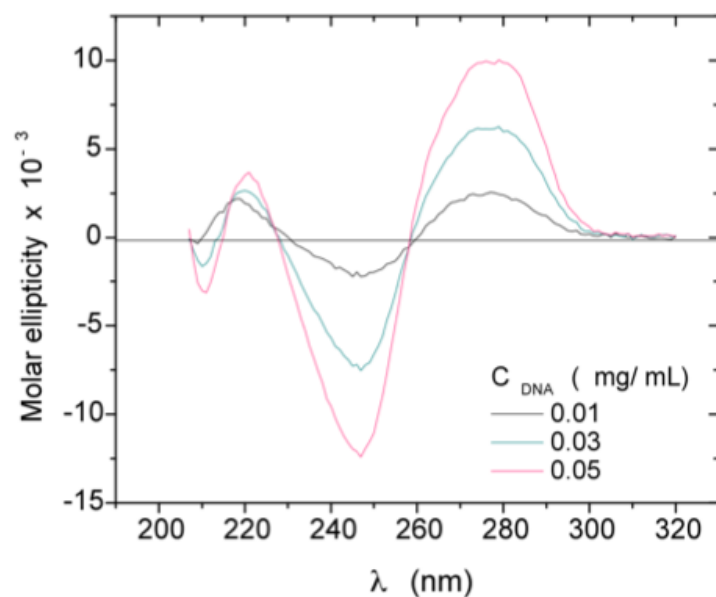
Figure 7.18. *CD spectra of DNA concentrations of 0.01, 0.03 and 0.05 mg/mL at a temperature of 25 °C, a pH of 6.5 and an ionic strength of 10^{-2} M NaCl. The spectra were corrected by subtracting the background of water and three spectra were accumulated and averaged for each sample.*
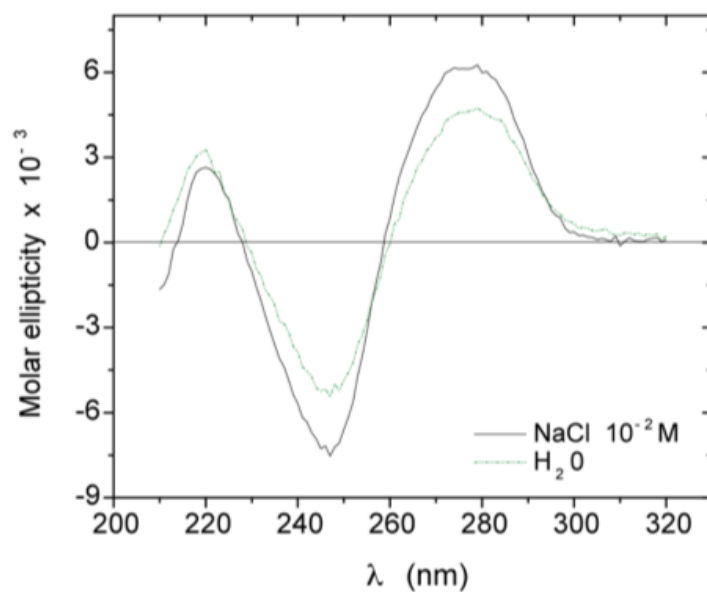
Figure 7.19. *CD spectra of two solutions of DNA at concentration of 0.03 mg/mL in water and in 10^{-2} M NaCl at a temperature of 25 °C and a pH of 6.5. The spectra were corrected by subtracting the background of water and three spectra were accumulated and averaged for each sample.*

DNA conformation in water as a solvent was then evaluated through CD measurements at the different pH's, i.e. 2.0, 4.5, 5.0 and 6.5. *Figure 7.20* shows the CD spectra of DNA solutions in water at a constant concentration of 0.03 mg/mL and at a temperature of 25 ºC.
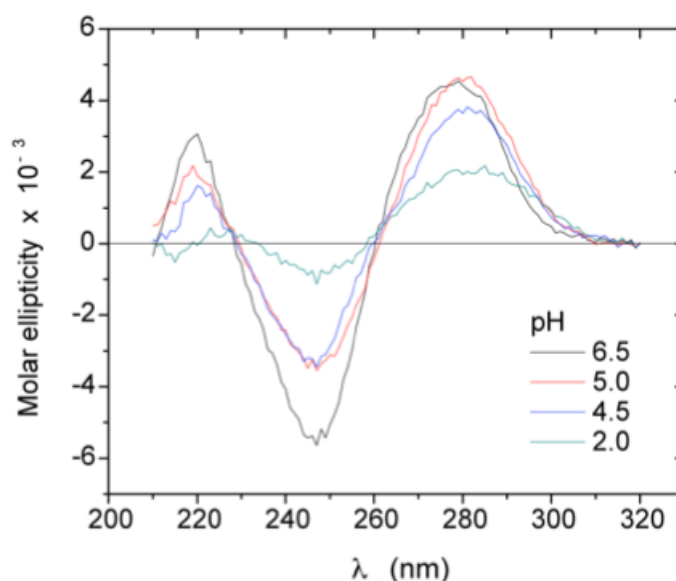
Figure 7.20. *CD spectra of DNA solutions in water at a constant concentration of 0.03 mg/mL, a temperature of 25 ºC and the following pH's: 2.0, 4.5, 5.0 and 6.5. The spectra were corrected by subtracting the background of water and three spectra were accumulated and averaged for each sample.*

Chitosan-DNA complex conformation was then followed by CD measurements using different $[NH_2]/[P^-]$ ratios. *Figure 7.21* shows CD spectra of chitosan-DNA complexes in water at a constant concentration of 0.03 mg/mL and at a temperature of 25 ºC and the following $[NH_2]/[P^-]$:0, 4.0 and 6.4. Firstly, a slight shift in the long-wavelength crossover (260.5 nm) is observed in comparison to the DNA initial conformation and the ratio $[NH_2]/[P^-]$=4.0, corresponding to the stable complex region before the stoichiometry at ζ-potential= 0 mV, suggesting a slight conformational variation as a result of the compaction between chitosan and DNA. Then, a second conformational change is detected at $[NH_2]/[P^-]$=6.4, corresponding to the region after the stoichiometry in chitosan excess with ζ-potential>0 mV. Here, an excess of positive charges leads to a different response in the CD spectra for chitosan-DNA complex. These results differ from those obtained by *Liu et al.* [57], which observed a decrease in the intensity of peaks with the increase in the ratios of chitosan to DNA, but the cotton effect remained constant, showing that DNA remained in its B conformation upon complexing with chitosan.
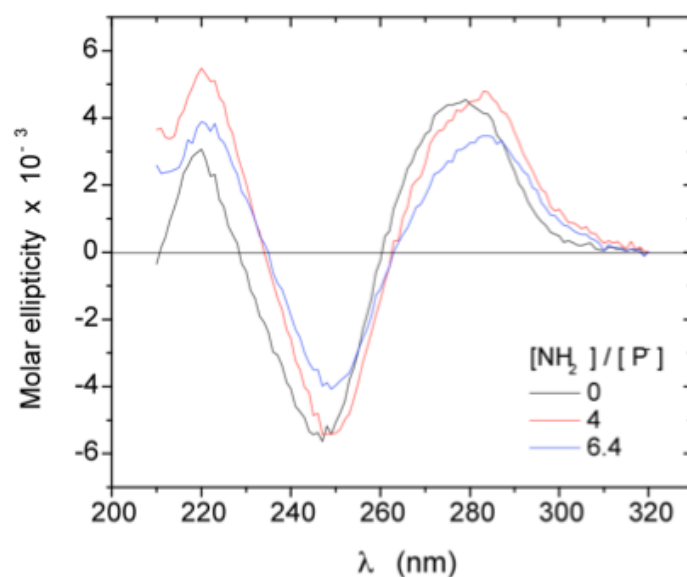
Figure 7.21. *CD spectra of DNA and chitosan-DNA complexes in water at a constant concentration of 0.03 mg/mL, pH=6.5 and at a temperature of 25 °C and the following [NH₂]/[P] ratios: 0, 4.0 and 6.4. The spectra were corrected by subtracting the background of water and three spectra were accumulated and averaged.*

Figure 7.22 a and *b* show the comparison between CD spectra of DNA in water and the spectra of the final chitosan-DNA complex formed in excess of chitosan at the three different pH's: 4.5, 5.0 and 6.0. The influence of pH on the complex formation confirms a slight DNA conformational change at pH 6.5 compared to pH 4.5 and 5.0, which final conformations are very similar between them in the initial DNA conformation and in the complexed DNA nanoparticles.
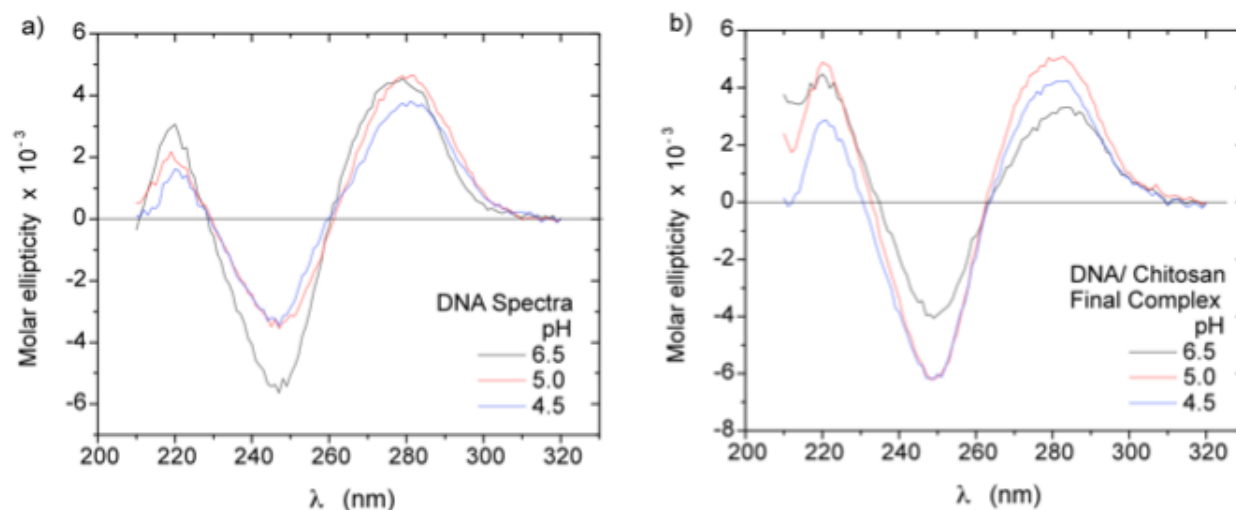
Figure 7.22. *a) CD spectra of DNA in water at the pH 4.5, 5.0 and 6.0. b) CD spectra of the complex chitosan-DNA complex at the pH 4.5, 5.0 and 6.0 in excess of chitosan. DNA concentration: 0.03 mg/mL, added chitosan: 1 mg/mL, temperature: 25 °C. The spectra were corrected by subtracting the background of water and three spectra were accumulated and averaged for each sample.*

7.4.6. Chitosan-DNA complex thermal stability

Thermal stability of chitosan-DNA complexes was studied through UV-Vis measurements by monitoring the melting curves of the formed complexes in NaCl 10^{-2} M with $[NH_2]/[P^-]$ ratios between 0 and 2.7, i.e. ζ-potential < 0 mV.

Figure 7.23 presents the melting curves for chitosan-DNA complexes in NaCl 10^{-2} M with $[NH_2]/[P^-]$ ratios between 0 and 2.7. Here it is possible to observe a shift of the curves to higher temperatures with the increment of $[NH_2]/[P^-]$ ratios of the complexes. The melting temperature is then detected at higher temperatures than the initial T_m of DNA. In this way, it is possible to say that the complex formation between chitosan and DNA leads to a greater thermal stability of DNA in the complex.

The melting temperature dependence of chitosan-DNA complexes in NaCl 10^{-2} M with the ratio $[NH_2]/[P^-]$ is presented in *Figure 7.24*.
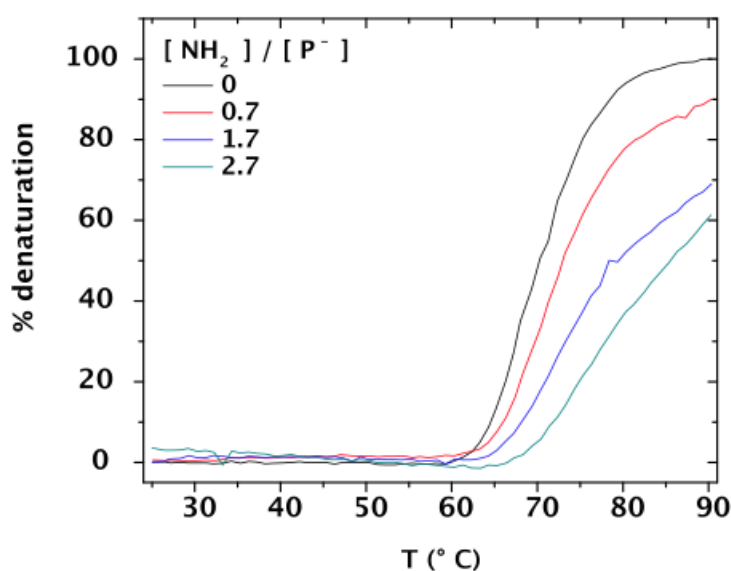
Figure 7.23. *Melting curves of chitosan-DNA complexes in NaCl 10^{-2} M prepared with a DNA concentration of 0.03 mg/mL and a chitosan concentration of 1.0 mg/mL at pH 6.5. Variation of $[NH_2]/[P^-]$ ratios: from 0 to 2.7.*
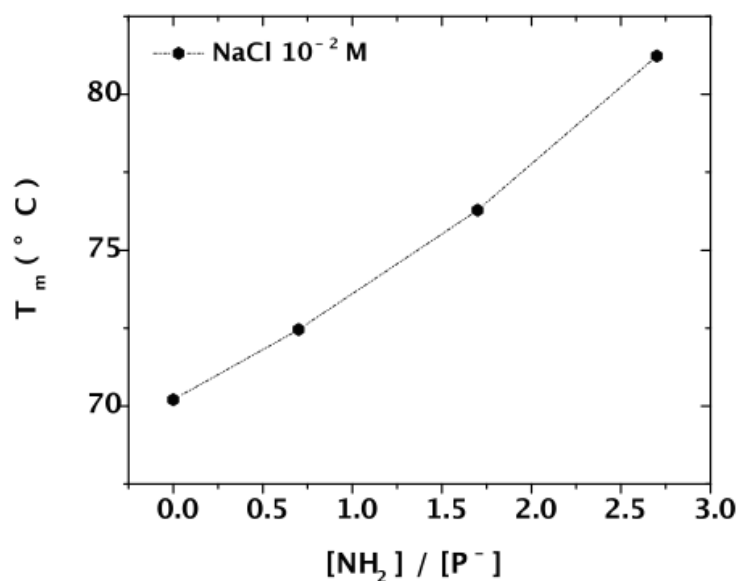
Figure 7.24. *Melting temperature dependence with the ratio [NH₂]/[P⁻] for chitosan-DNA complexes NaCl 10⁻² M.*

We can clearly observe that the T_m increases with the increase of the [NH₂]/[P⁻] ratio. Nevertheless, it is difficult to determine the exact value of the T_m due to experimental conditions, i.e.: it is not possible to perform experiments at temperatures higher than 90 ºC. Tentatively, it was supposed a complete denaturation at higher temperatures and we calculated a possible T_m value for the different complexes studied. The T_m values are obtained for chitosan-DNA complexes in NaCl 10⁻² M in the [NH₂]/[P⁻] range between 0 (DNA solution) and 2.7 (around ζ =-20 mV). These curves indicate a partial denaturation under 90 ºC due to a higher thermal stability of DNA chains in the complex. A second hypothesis may be suggested concerning the partial transition observed, i.e.: a two steps process taking place, in which a fraction of DNA is stabilized in the complex and is not able to be thermally denatured.

7.5. Particular conclusions for Chitosan-DNA complex formation

Here it is demonstrated that chitosan-DNA complex are formed between fully ionized phosphates and the fraction of protonated chitosan. For the first time, it is clearly shown that the net charge of the complex can be expressed in terms of the ratios [NH₂]/[P⁻] and [NH₃⁺]/[P⁻], showing that electrostatic interactions between chitosan and DNA take place in the solution and originate the complexation process of DNA. For progressive additions of chitosan, before reaching the ζ-potential=0mV, a plateau is observed around a ζ-potential of −20 mV, which matches with the obtained chitosan-DNA nanoparticles with stable average hydrodynamic radius around 280 nm. After ζ-

potential=0 mV, all DNA negative charges are neutralized by chitosan positive charges. It is demonstrated that whatever the pH is, chitosan-DNA complex formation can be interpreted on the basis of the electrostatic model, in which the net charge of chitosan as well as that of DNA are taken into account.

The evolution of the hydrodynamic radius and the scattered light intensity was also evaluated in terms of $[NH_2]/[P^-]$. The scattered light increases with the addition of chitosan, corresponding to chitosan association with DNA. The R_h decreases to 280 nm corresponding to the compaction of DNA molecule into compact nanoparticles visualized through fluorescence confocal microscopy. It is worth to mention that these stable nanoparticles are obtained for partial neutralization of phosphate ionic sites ($[NH_3^+]$ fraction between 0.35 and 0.80).

Slight conformational changes of DNA were detected through CD measurements at differents pH and could be related to partial protonation of DNA bases suggested also by ζ-potential measurements. The CD spectra of chitosan-DNA complex was studied for different ratio $[NH_2]/[P^-]$ and pH values, which also indicate small conformational changes of DNA. Finally, the thermal stability of the complexes was studied by UV-Vis absorption measured as a function of temperature. It was observed that the melting temperature of DNA in chitosan-DNA complex increases compared to free DNA in NaCl 10^{-2} M.

7.6. References

[1] V. Vijayanathan, T. Thomas and T. J. Thomas, DNA Nanoparticles and Development of DNA Delivery Vehicles for Gene Therapy, *Biochemistry*, **41**, 14086 (2002).

[2] T. Blessing, J.S. Remy J.P. and Behr, Monomolecular collapse of plasmid DNA into stable virus-like particles, *Proc. Natl. Acad. Sci. U.S.A.* **95**, 1427-1431 (1998).

[3] C.W.S. Richardson, H.V.J. Kolbe and R. Duncan, Potential of low molecular mass chitosan as a DNA delivery system: biocompatibility, body distribution and ability to complex and protect DNA, *International Journal of Pharmaceutics* **178**, 231–243 (1999).

[4] H.-Q. Mao, K. Roy, V.L. Troung-Le, K. A. Janes, K. Y. Lin, Y. Wang, J.T. August and K. W. Leong, Chitosan-DNA nanoparticles as gene carriers: synthesis, characterization and transfection efficiency, *Journal of Controlled Release* **70**, 399–421, (2001).

[5] C.W. Pouton, L.W. Seymour, Key issues in non-viral gene delivery, *Adv. Drug Deliv. Rev.* **34** (1) 3–19, (1998).

[6] M. Cotten and E.Wagner, Non-viral approaches to gene therapy, *Curr. Opin. Biotechnol.* **4**, 705–710 (1993).

[7] J.P. Schonfield and C.T. Caskey, Non-viral approaches to gene therapy, *Br. Med. J.* **51**, 56 (1995).

[8] G. Borchard, Chitosans for gene delivery, *Advanced Drug Delivery Reviews* **52**, 145–150 (2001).

[9] D. Deshpande, P. Blezinger, R. Pillai, J. Duguid, B. Freimark and A. Rolland, Target specific optimization of cat ionic lipid-based systems for pulmonary gene therapy, *Pharm. Res.* **15**, 1340–1347 (1998).

[10] S.C. De Smedt, J. Demeester and W.E. Hennink, Cationic polymer based gene delivery systems, *Pharm. Res.* **17**, 113–126 (2000).

[11] D. Deshpande, P. Blezinger, R. Pillai, J. Duguid, B. Freimark and A. Rolland, Target specific optimization of cationic lipid-based Systems for pulmonary gene therapy, *Pharm. Res.* **15**, 1340–1347 (1998).

[12] S.C. De Smedt, J. Demeester and W.E. Hennink, Cationic polymer based gene delivery systems, *Pharm. Res.* **17**, 113–126 (2000).

[13] M. Lavertu, S. Méthot, N. Tran-Khanh and M. D. Buschmann, High efficiency gene transfer using chitosan/DNA nanoparticles with specific combinations of molecular weight and degree of deacetylation, *Biomaterials* **27**, 4815 - 4824 (2006).

[14] Z.-X. Liao, S.-F. Peng, Y.-C. Ho, F.-L. Mi, B. Maiti and H.-W. Sung, *Biomaterials* **33**, 3306-3315 (2012).

[15] G. Maurstad, Signe Danielsen, and Bjørn T. Stokke, The Influence of Charge Density of Chitosan in the Compaction of the Polyanions DNA and Xanthan, *Biomacromolecules* **8**, 1124-1130 (2007).

[16] F.C. MacLaughlin, R.J. Mumper, J.Wanf, J.M. Tagliaferri, I. Gill, M. Hinchcliffe and A.P. Rolland, Chitosan and depolymer ized chitosan oligomers as condensing carriers for in vivo plasmid delivery, *J. Control. Rel.* **56** , 259–272 (1998).

[17] M. Thanou, B. Florea, M. Geldof, H.E. Junginger, G. Borchard, Quaternized chitosan oligomers as novel gene delivery vectors in epithelial cell lines, *Biomaterials* **23**, 153–159 (2001).

[18] M. Rinaudo, Chitin and chitosan: Properties and applications, *Prog. Polym. Sci.* **31**, 603–632 (2006).

[19] N. Cartier, A. Domard and H. Chanzy, Single crystals of chitosan, *Int J Biol Macromol* **12**, 289–294 (1990).

[20] S. Aiba, Studies on chitosan: 3. Evidence for the presence of random and block copolymer structures in partially N-acetylated chitosans, *Int. J. Biol. Macromol.*13, 40–44 (1991).

[21] Rinaudo M, Pavlov G, Desbrières J. Influence of acetic acid concentration on the solubilization of chitosan, *Polymer* **40**, 7029–7032 (1999).

[22] Rinaudo M, Pavlov G, Desbrières J. Solubilization of chitosan in strong acid medium, *Int. J. Polym. Anal. Charact.* **5**, 267–276 (1999).

[23] S. C. Tan, E. Khor, T. K. Tan and S. M. Wong, The degree of deacetylation of chitosan: advocating the first derivative UV-spectrophotometry method of determination, *Talanta* **45** (4), 713–719 (1998).

[24] A. Hirai, H. Odani and Akio Nakajima, Determination of degree of deacetylation of chitosan by ^{1}H NMR spectroscopy *Polymer bulletin* **26**, 87-94 (1991).

[25] L. Rusu-Balaita, J. Desbrières and M. Rinaudo, Formation of a biocompatible polyelectrolyte complex: chitosan-hyaluronan complex stability. *Polym Bull* **50**, 91–98 (2003).

[26] J. Brugnerotto, J. Desbrières, G. Roberts and M. Rinaudo, Characterization of chitosan by steric exclusion chromatography, *Polymer* **42**, 9921–9927 (2001).

[27] R. J. Zasoski, Zeta potential, *Encyclopedia of Soil Science*, Edited by Ward Chesworth, Springer, The Netherlands, 841-845 (2008).

[28] B.J. Berne and R. Pecora, *Dynamic Light Scattering*, John Wiley and Sons, Inc, New York, (1976).

[29] M.E. Cates and M.R. Evans. *Soft and Fragile Matter. Nonequilibrium Dynamics, Metastability and Flow.* SUSSP, (2000).

[30] G. Landazuri, V. V. A Fernandez, J. F. A. Soltero and Y. Rharbi, Kinetics of the Sphere-to-Rod like Micelle Transition in a Pluronic Triblock Copolymer, *J. Phys. Chem. B*, **116**, 11720−11727, 2012.

[31] J.B. Pawley, *Handbook of Biological Confocal Microscopy*, 3d Edition, Springer, Berlin, (2006).

[32] K. Nakanishi, N. Berova and R.W. Woody, *Circular Dichroism Principles and Applications*, VCH Publishers Inc., New York, (1991).

[33] J. Kypr, I. Kejnovská, D. Renčiuk and M. Vorlíčková, Circular dichroism and conformational polymorphism of DNA, *Nucleic Acids Research* 37(6), 1713–1725 (2009).

[34] N. Berova, K. Nakanishi and R.W. Woody, *Circular Dichroism, Principles and Applications*, Second Edition, Canada, (2000).

[35] T. B. Freedman, X. Cao, R. K. Dukor and L. A. Nafie, Absolute configuration determination of chiral molecules in the solution state using vibrational circular dichroism, *Chirality* **15** (9), 743-758 (2003).

[36] S. M. Kelly, T. J. Jess and N. C. Price, How to study proteins by circular dichroism, Biochimica et Biophysica Acta (BBA) - Proteins and Proteomics 1751 (2), 119–139 (2005).

[37] T. Suzuki, K. Igarashi, K. Hase and K. Tuzimura, Optical Rotatory Dispersion and Circular Dichroism of Amino Acid Hydantoins, *Agricultural and Biological Chemistry* **37**(2), 411-416 (1973).

[38] N. Sreerama, S. Y. Venyaminov and R. W. Woody, Estimation of Protein Secondary Structure from Circular Dichroism Spectra: Inclusion of Denatured Proteins with Native Proteins in the Analysis, *Analytical Biochemistry*, 287(2), 243–251 (2000).

[39] J. Kypr, I. Kejnovská, D. Renčiuk and M. Vorlíčková, Circular dichroism and conformational polymorphism of DNA, *Nucl. Acids Res.* **37** (6), 1713-1725 (2009).

[40] D. S. Moore and T. E. Wagner, Double-helical DNA and RNA circular dichroism. Calculations on base–sugar-phosphate helix interactions, *Biopolymers* **13**(5), 977-986 (1974).

[41] V. I. Ivanov, L. E. Minchenkova, A. K. Schyolkina andA. I. Poletayev, Different conformations of double-stranded nucleic acid in solution as revealed by circular dichroism, *Biopolymers* **12**(1), 89-110 (1973).

[42] C.A. Sprecher, W.A. Baase and W.C. Johnson Jr., Conformation and circular dichroism of DNA, *Biopolymers* 18(4), 1009-1019 (1979).

[43] M.K. Cowman and G.D. Fasman, Circular dichroism analysis of mononucleosome DNA conformation, *Proc. Nati. Acad. Sci. USA* **75**(10), 4759-4763 (1978).

[44] M.J.B. Tunis-Schneider and M.F. Maestre, Circular dichroism spectra of oriented and unoriented deoxyribonucleic acid films--a preliminary study, *J. Mol. Biol.* **52**, 521 (1970).

[45] F.M. Pohl and T.M. Jovin, Salt-induced co-operative conformational change of a synthetic DNA: equilibrium and kinetic studies with poly (dG-dC). *J. Mol. Biol.* **67**, 375 (1972).

[46] D.M. Gray, R.L. Ratliff and M.R. Vaughan, Circular Dichroism Spectroscopy of DNA, *Methods in enzymologhy* **211**, 389-406 (1992).

[47] G.S. Manning, Molecular theory of polyelectrolyte solutions with applications to electrostatic properties of polynucleotides, *Q. Rev. Biophys.* **11**, 179–246 (1978).

[48] D. Matulis, I. Rouzina, V.A. Bloomfield, Thermodynamics of DNA binding and condensation: isothermal titration calorimetry and electrostatic mechanism, *J. Mol. Biol.* **296**, 1053–1063 (2000).

[49] M. Alatorre-Meda, P. Taboada, F. Hartl, T. Wagner, Michael Freis and J. R. Rodríguez, The influence of chitosan valence on the complexation and transfection of DNA: The weaker the DNA–chitosan binding the higher the transfection efficiency, *Colloids and Surfaces B: Biointerfaces* **82**, 54–62 (2011).

[50] J. Stenesh, *Biochemistry*, Vol. *3*, Plenum Press, New York (1998).

[51] M.X. Tang, F.C. Szoka, The influence of polymer structure on the interactions of cationic polymers with DNA and morphology of the resulting complexes, *Gene Ther.* **4**, 823–832 (1997).

[52] C.W. Pouton, P. Lucas, B.J. Thomas, A.N. Uduehi, D.A. Milroy and S.H. Moss, Polycation DNA complexes for gene delivery: a comparison of the biopharmaceutical properties of cationic polypeptides and cationic lipids, *J. Control. Release* **53**, 289–299 (1998).

[53] M. Rosa, R. Dias, M. da G. Miguel and B. Lindman, DNA-Cationic Surfactant Interactions Are Different for Doubleand Single-Stranded DNA, *Biomacromolecules* **6**, 2164-2171 (2005).

[54] R. S. Dias, J. Innerlohinger, O. Glatter, M. G. Miguel and B. Lindman, Coil-Globule Transition of DNA Molecules Induced by Cationic Surfactants: A Dynamic Light Scattering Study, *J. Phys. Chem. B* **109**, 10458-10463 (2005).

[55] J. O. Rädler, I. Koltover, A. Jamieson, T. Salditt and C. R. Safinya, Structure and Interfacial Aspects of Self-Assembled Cationic Lipid-DNA Gene Carrier Complexes, *Langmuir* **14**, 4272-4283 (1998).

[56] P. L. Ma, M. Lavertu, F. M. Winnik and M. D. Buschmann, New Insights into Chitosan-DNA Interactions Using Isothermal Titration Microcalorimetry, *Biomacromolecules* **10**, 1490–1499 (2009).

[57] W. Liu, S. Suna, Z. Cao, X. Zhanga, K. Yao, W. W. Lub and K.D.K. Luk, An investigation on the physicochemical properties of chitosan/DNA polyelectrolyte complexes, *Biomaterials* **26** 2705–2711 (2005).

Conclusions

→ Calf-thymus DNA solutions in TE buffer were firstly characterized in detail in the dilute and the semi-dilute regimes through physicochemical and rheological methods. The intrinsic viscosity $[\eta]$ (4 080 mL/g) was determined from the zero shear-rate viscosity of the Newtonian plateau (η_0) obtained from flow measurements, from which was possible to access to the viscometric-average molecular weight of our samples (6 559 000 g/mol).

→ The overlap concentration (C*) was estimated as a first approach by using the relation $C^* \sim [\eta]^{-1}$, obtaining 0.245 mg/mL. The starting point of the semi-diluted entangled domain, C_e, was then obtained from the limit of the linear behavior in the higher concentrations domain of η_{sp} as a function of $C_{DNA}[\eta]$ curve, i.e. $C[\eta] \sim 10$, equivalent to 2.45 mg/mL.

→ A master curve with dynamic measurements data was obtained through a horizontal (ax) and vertical (ay) translation by using a specific DNA concentration as reference. The imposed shifts were analyzed as a function of DNA concentration, the main parameter controlling the solution behavior at constant molecular weight.

→ A master dynamic phase diagram was obtained with the superimposition procedure between flow curves normalized in terms of $\sigma^* = \sigma/G_0$ and $\dot{g}^* = \dot{g}\, t_c$

→ Observations of the strain field combined with mechanical measurements were used to demonstrate the appearance of shear banding, i.e. $\dot{g} = 10.0$ s^{-1} and $C_{DNA} \geq 5.0$ mg/mL. For high DNA concentrations in the semi-dilute regime with entanglements, DNA chains interactions and entanglements were found to have important effects on linear viscoelasticity and on the different flow regimes.

→ After studying and characterizing DNA behavior in the bulk of the solution, a detailed adsorption study of calf thymus DNA onto platinum and gold electrodes was evaluated in a wide concentration and temperature ranges by using Electrochemical Impedance Spectroscopy (EIS). For both Pt-ADN/TE buffer and Au-ADN/TE buffer interfaces, all the impedance data were transformed into complex capacitance values and were interpreted on the basis of the impedance adsorption theory using a similar FMGR equivalent circuit.

→ It was determined that at Open Circuit Potential (OCP), a diffusion controlled non-specific adsorption of DNA molecules is taking place at the Pt-ADN/TE buffer interface and a mixed process, controlled by DNA diffusion and an electrosorption process is taking place at the Au-ADN/TE buffer interface.

→Through a detailed analysis of each one of the electrical parameters, C_{dl}, C_{ad} and R_{ad}, obtained at each studied temperature it was possible to identify two well-defined interfacial transitions around two DNA concentrations, i.e. 0.36 and 1.5 mg/mL. In this way, the changes in the interfacial structure, reflected in these parameters, strongly depend on the DNA structure solution.

→ It is possible to conclude that the impedance technique is able and sensitive enough to detect the structural changes of DNA molecules in different metal surfaces. In this manner, we can propose EIS as an adequate technique for characterizing the structural nature of the adsorbate based on the changes and the rearrangement of the electrochemical double-layer.

→ The transitional behavior of calf thymus DNA molecules, using platinum and gold electrodes, was aslo investigated through a study performed by EIS using an analogous methodology to the one used in linear rheology studies. A linear behavior of the Z_o modulus, related to the solution resistance, and the characteristic time-constant of the process τ_c was observed in each characteristic regime of the system, in which the relation between them and C_{DNA} follows the power law at every studied temperature. Arrhenius-type temperature dependence was obtained for the characteristic time constant of DNA molecules arrangement on the electrochemical double-layer.

→ A general impedance transfer function, proposed as a function of DNA concentration through the scaling of the electrochemical parameters, Z_o and τ_c, allows analyzing theoretically the double-layer charging behavior at OCP as a function of concentration with only one impedance experiment and makes possible obtaining the electrochemical parameters of the interface at a chosen concentration and at a specific regime of the system. This function is proposed to be useful in studies of polymeric and surfactant systems, characterized by having different regimes due to their interactions or different kind of structures formed at a wide range of temperature or concentration conditions.

→ Through the optical technique Surface Plasmon Resonance (SPR), the adsorption process of DNA onto a gold surface allowed obtaining the optical film thickness (d_{opt}) values observed in the surface of the sensor chip for each DNA concentrations. The variations of d_{opt} as a function of DNA concentration were related to the transitions in the structural arrangement of the electrochemical double-layer, showing a specific behavior of DNA chains at each characteristic regime.

→ Using the simplest double-layer model, the changes in C_{dl} obtained from the Au-DNA/TE buffer interface were related to the changes in d_{opt} as a function of DNA concentration and a dielectric constant behavior was also obtained, showing DNA transitions passing from diluted, semi-diluted unentangled and semidiluted entangled solutions.

→ The combination of both EIS and SPR techniques leads to a complete characterization of the structural behavior of Au-DNA/TE buffer interface.

→ The recently developed technique Modulation of the Interfacial Capacitance (MIC) was used to study the double-layer relaxations due to the adsorption process of a polyelectrolyte: DNA. The MIC response revealed the double-layer dynamics in the dilute, the semi-dilute regime without entanglements and the semi-dilute regime with entanglements for DNA-TE buffer solutions.

→ No relaxation process of the double-layer capacitance was observed at high DNA concentrations, in the semi-dilute regime with entanglements, however, at low concentrations, in the dilute and the semi-dilute regime without entanglements, it was possible to identify more than one superposed time-constant.

→ The obtained values for the main characteristic-time constants of the adsorption process are in good agreement with the values obtained through impedance data transformed into complex capacitance data. The dependence on DNA concentration, temperature and ionic strength for the MIC response was put on evidence and described in terms of the main characteristic time constants of the adsorption process and the shape of the obtained MIC spectra.

→ It is demonstrated that MIC technique allows the study of the adsorption kinetics of the simplest species, such as NaBr and KCl, and the most complex species as DNA. It is then possible to identify and explain, at least qualitatively, the fundamental adsorption steps of these species.

→ Chitosan-DNA nanoparticles were produced by using DNA concentrations in the dilute regime and were studied and characterized by using different methods.

→ The formation of chitosan-DNA complexes was obtained between fully ionized phosphates and the fraction of protonated chitosan. The net charge of the complex was evaluated in terms of the ratio $[NH_2]/[P^-]$, showing that electrostic interactions between chitosan and DNA take place in the solution and originate the complexation process of DNA. Before reaching the ζ-potential=0mV, a plateau is observed around a ζ-potential of -20 mV, which matches with the obtained chitosan-DNA nanoparticles stables on dimension with an average hydrodynamic radius of 220nm.

→ The evolution of the hydrodynamic radius and the scattered light intensity was also evaluated in terms of $[NH_2]/[P^-]$, showing that R_h decreases and the scattered light increases with the addition of chitosan, representing the compaction of the long DNA molecule into a compact nanoparticle by means of the neutralization of the negative charges.

→ Slight conformational changes of DNA were detected through CD measurements and were evaluated for different $[NH_2]/[P^-]$ ratios and different pH.

→ The melting temperature of chitosan-DNA complexes increases with $[NH_2]/[P^-]$ ratio, showing a greater thermal stability than the initial one for DNA in its original conformation and without the addition of any cationic vector.

Perspectives

→ The dynamics of DNA molecules in their different characteristic regimes may represent important keys to the understanding of the functions of this biomacromolecule and its biochemical activiy. A further study taking into account the variation of ionic strength, molecular weight and even the interactions with different cationic molecules may give information about the influence that the variation of these parameters produces in DNA dynamics and in its biological functions.

→ The knowledge of DNA molecules behavior in the dilute regime and their electrostatic interactions with cationic polymers allows an optimal design of non-viral vectors for gene therapy, and may be applied for the study of DNA complexation with different cationic molecules, at different ionic strengths, pH's, concentrations or molecular weights, among other variations.

→ For non-viral vectors applications, the stability of DNA-chitosan complexes must be further studied, specially with chitosan having different degree of acetylation and different molecular weights.

→ The impedance adsorption theory was successfully applied to DNA adsorption process onto metallic surfaces, offering new possibilities and approaches to the study of adsorption processes of polyelectrolytes (and even different biological macromolecules), in order to obtain important information about their structural behavior, the kinetics of the process and their thermodynamics during the adsorption.

→ The combination of both EIS and SPR techniques allows obtaining a detailed characterization of the structural behavior on the metal-DNA/TE buffer interface and can be implemented for the research of the electrochemical double-layer structural variations due to the conformational changes of different biological macromolecules.

→ A development of a reaction mechanism for DNA adsorption process, by taking into account the parameters involved in each step (DNA conformation, persistence length, ionic strength, charge parameter, among others) in each characteristic regime can lead to obtain more information about the kinetics of the adsorption process of DNA onto metallic surfaces.

→ From the obtained results of this thesis it is possible to propose the MIC technique as a useful tool in the research field of the adsorption processes of polyelectrolytes such as DNA and different kind of biological macromolecules. It may be possible to get a greater insight of DNA adsorption process by performing a more detailed analysis including the concepts of the theory of polyelectrolytes on surfaces in each characteristic regime and studying the two-dimensional or three-dimensional adsorbed layer formation for DNA solutions. An experimental study with a potential variation with respect to the PZC may give us more information with respect to the negative to positive real parts of the capacitance response.

A. List of symbols

Nomenclature

a_0	radius of the macromolecular phase in Oosawa's model
A	radius of the cylindrical space in Katchalsky's model
ax	horizontal translation coefficients
ay	vertical translation coefficients
A	Absorbance
A_e	area of the electrode
A_f	frequency factor
A_i	adsorption of the component i
b_i	distance between two ionized sites for a polyelectrolyte
B	adsorption coefficient
c	speed of light in vacuum
C	concentration in Chapter 2
	capacitance in Chapter 3 and 4
$C(\omega)$	complex interfacial capacitance
C'	real part of the capacitance
C''	imaginary part of the capacitance
C_{ad}	adsorption capacitance
C_{DNA}	DNA concentration (in mg/mL)
C_{dl}	double-layer capacitance
C_{eff}	effective capacitance
C_{GC}	Gouy-Chapman capacitance
C_H	Helmholtz capacitance
C_{HF}	capacitance at high frequencies
C_i	concentration of ions (in equi/L)
C_{LF}	capacitance at low frequencies
C_v	concentration in the bulk of the solution
C_{vi}	concentration of the component i
C_m	concentration of ionized groups (counterions)
C**	overlap concentration
C** or C_e	entanglement concentration
CPE	constant phase element
d_{opt}	optical film thickness
D	diffusion coefficient
e	electron charge
E	electric potential
E_a	activation energy
f	transport coefficient in Chapter 2
	frequency range in Chapter 3

$f(\kappa,a)$	Henry's function
f_{Ω}	high frequency
f_{ω}	low frequency
$F(\omega)$	filter transfer function
g	gravity
G	proportionality constant
$G'(\omega)$	shear elastic modulus
$G''(\omega)$	shear viscous modulus
G_p	plateau modulus
$|G^*|$	complex modulus
$k_B T$	Boltzmann term
h	Length
I	current
j	imaginary number
K	Mark-Houwink parameter in Chapter 2
	integral capacitance in Chapter 6
K_F	constants for a given adsorbent and adsorbate at a constant temperature in Freundlich adsorption isotherm
k	vector component
k_x	energy and momentum of light photons
k_{sp}	energy and momentum of surface Plasmon
K_c	Cross model constant
K_{ev}	wave vector of the evanescent field
K_H	Huggins coefficient
K_K	Kraemer coefficient
l_B	Bjerrum length
l_e	electrostatic persistence length
l_o	intrinsic persistence length
l_p	persistence length
L	inductor
m	dimensionless parameter related to the degree of shear thinning in Chapter 2
m_a	adsorbate mass
M	molecular weight
M_c	molecular weight for chain entanglement in undiluted state
n	inherent parameter of the CPE
n	refractive index
n^{-1}	Freundlich adsorption isotherm constant
N_A	Avogadro's number
N_i	number of ion of the species i

N_{io}	ions concentration in the bulk of the solution
q	charge for a capacitive system
q_H	Helmholtz excess charge
q_{GC}	Gouy Chapman excess charge
q_{SA}	charge on the surface
q_w	wave vector
Q	ideal interface differential capacitance
R	Resistance
R_a	Radius
R_{ad}	adsorption resistance
R_{ct}	charge transfer resistance
R_f	faradaic resistance
R_s	solution resistance
R_{st}	standard resistance of the potensiostat
s	slope from flow curves
t	Time
T	temperature
T_m	melting temperature
V	Volume
V_E	potential difference
W_{ad}	Warburg impedance
X_{HP}	thickness of the electrical double layer
Y	admittance
z_i	valence
$Z_{W,ad}$	Warburg-like diffusion impedance
Z_o	impedance plateau module
$Z(\omega)$	complex impedance
Z'	real part of the impedance
Z''	imaginary part of the impedance
$|Z|$	complex impedance modulus
α	Mark-Houwink parameter in Chapter 2
	inherent parameter of superficial heterogeneity or surface roughness in Chapter 4
α_i	ionization degree
Γ	adsorbed amount of polymer
Γ	layer mass per unit area
Γ_c	first cumulant
γ	Strain
γ_a	activity coefficient of the counterions
$\dot{g}$	shear rate
$\dot{g}^*$	normalized shear rate

$\dot{g}_c$	critical shear rate
$\delta\psi$	potential difference
ε	dielectric constant
ε_r	dielectric constant of the medium
ε_o	vaccum permittivity
ε_m	dielectric constant of the metal film
η	Viscosity
η_g	refractive index of a dense medium
η_0	shear viscosity in the Newtonian plateau
η_∞	infinite shear-rate viscosity
η_{rel}	relative viscosity
η_d	refractive index of the dielectric medium
η_{sp}	specific viscosity
η_{red}	reduced viscosity
$[\eta]$	intrinsic viscosity
η_s	solvent viscosity
$|\eta^*|$	complex dynamic viscosity
μ	electrophoretic mobility
θ	covered fraction in Chapter 3
	incidence angle in Chapter 4
θ_c	critical incidence angle
κ	conductivity
κ^{-1}	Debye length
λ	charge parameter chapter 2
	wavelength chapter 5 and 8
λ_G	relaxation time from the Giesekus model
λ_{eff}	critical value of the charge parameter
υ	number of ionic sites on the chain of the polyelectrolyte
υ_e	Velocity
ρ	density in Chapter 2
	charge density volume in Chapter 3
σ	stress in Chapter 2
	charge density in Chapter 3
σ_{ad}	coefficient of the diffusional impedance
σ_d	charge density in the diffuse layer
σ^*	normalized stress
τ_c	characteristic time-constant
τ_R	Maxwell relaxation time-constant
ϕ	osmotic coefficient in Chapter 2

	absolute electrical potentials in the double layer region in Chapter 3
ϕ_b	absolute electrical potentials in the bulk of the solution
φ	volume fraction
ψ	relative electrical potential
ψ_d	relative electrical potential in the diffuse layer
$\Psi_{(a)}$	electrostatic potential at the surface of a polyion
ζ	zeta potential
ω	Frequency
ω_o	frequency of the incident light
ω_C	crossover frequency
$<S^2>$	gyration radius
∇^2	Laplacian operator

B. Abbreviations

CD	Circular Dichroism
CPE	Constant Phase Element
CPL	Circularly polarized light
DA	Degree of deacetylation
DLS	Dynamic light scattering
DNA	Deoxyribonucleic acid
EDL	Electrochemical double layer
EDTA	Ethylenediaminetetraacetic acid
EIS	Electrochemical Impedance Spectroscopy
FMGR	Frumkin-Melik-Gaikazyan-Randles
HFP	Higher frequency process
IHP	Inner Helmholtz plane
IR	Infrared
LFP	Lower frequency process
LVR	Linear viscoelastic region
MIC	Modulation of the Interfacial Capacitance
MICTF	Modulation of the Interfacial Capacitance and Associated Transfer Functions
NMR	Nuclear magnetic resonance
OCP	Open Circuit Potential
OHP	Outer Helmholtz plane
PZC	Potential of Zero Charge
R-CPL	Right-handed Circularly polarized light
L-CPL	Left-handed Circularly polarized light
RNA	Ribonucleic acid
TE	Tris-HCl/EDTA
TEM	Transmission Electron Microscopy
TIR	Total internal reflection
SCE	Saturated Calomel Electrode
SPR	Surface Plasmon Resonance
UV	Ultraviolet
FDA	Food and Drug Administration

The role of micellar dynamics and rheology in drug controlled release

PART II

CONTENT

Introduction

Amphiphilic block copolymers are macromolecules composed of a hydrophobic block and a hydrophilic block. In water, they aggregate into micelles, in which the hydrophobic part forms the heart and the hydrophilic segments form the corona [1,2]. These copolymers are characterized by having a critical micellization concentration (CMC) and a critical micellization temperature (CMT). According to the ratio between the length of the blocks and the quality of the solvent, these copolymers can form spherical micelles, cylindrical or lamellar structures [3-5]. These materials are of great interest because of their applications in drug delivery, cosmetics, synthesis of mesostructured materials and detergency, among many others [6,7]. The kinetics of the transition from one morphology to another is critical to define their spectrum of application. Unlike surfactants, which are dynamically active, the block copolymers have a slower dynamic. In particular, in the case where the surface tension between the blocks is high, they can be trapped in metastable states without reaching thermodynamic equilibrium [8,9]. Thus, understanding the kinetics of these transitions remains a major challenge for the design and control of many aspects of their applications.

The copolymers stimulable by temperature, based on ethylene polyoxide (PEO) and polypropylene polyoxide (PPO) have have been used for basic and applicative research. The commercially available triblock copolymers $(PEO)_x$-$(PPO)_y$-$(PEO)_x$ are among the most studied amphiphilic copolymers [10]. These triblock copolymers are commercially known under the following names: Pluronic ™ and Polaxamers™. Other varieties of Pluronics, in which the PPO was replaced by more hydrophobic blocks such as poly(butylene oxide), poly(styrene oxide) or poly (phenylglycidyl ether) [11] have been also investigated. Unlike other copolymers, Pluronics are dynamically active even at relatively high molecular weight (M_w) [12,13]. Due to their thermo-stimulable properties, triblock copolymers are particularly interesting for several applications such as mesoporous materials development and drug delivery. In this way, drug delivery by PEO-PPO-PEO copolymers uses the structure transition by temperature stimuli. *Barichello et al.* [14] performed studies of insulin release in vivo and in vitro by using gels formed by the F127/water system. This system has been also used for the delivery of ophthalmic [15, 16], parenteral [17] and subcutaneous [18] drugs.

The specific delivery of active ingredients, known as vectorization, has actually become a great challenge in therapeutic research [19,20]. This process has been used to control the distribution of active ingredients such as proteins, genes for gene therapy and drugs, to a target by associating it with a vector. Molecules for chemotherapy are frequently hydrophobic and require vectorization to be transported to the target cell [21,22]. Nevertheless, this controlled drug delivery suffers from a phenomenon called "burst release" as the drugs are released before their target [23]. In this manner main objective is to understand the exchange dynamics between vectors and cells via collective mechanisms. Understanding these dynamics becomes essential for the design and the control of new materials and new processes effective in drug delivery. In this work, our study system is composed by

amphiphilic block copolymer micelles modeling the transporting vehicles, liposomes representing cells and highly hydrophobic alkylated pyrene representing the active ingredient introduced into the micelles. In order to understand, control, and study in detail this system, the characterization of each part of it is also necessary.

The understanding of the dynamics in systems composed by homogeneous micelles is of great importance before complicating the system by adding other type of molecules. In this way, we study the collective dynamics at the equilibrium of triblock copolymer P104/water micelles [24]. The dynamics of these systems were reported to occur via two main mechanisms, the first one is an individual process that involves the expulsion and insertion of chains [25]. The second mechanism is a collective process that occurs through fusion and fission of micelles [26], which are crucial for controlling the behaviour of amphiphilic aggregates particularly in drug delivery and for the synthesis of controlled nano-objects. In this work we show that fusion and fission take place at equilibrium in P104/water micelles. We investigated the role of fusion and fission processes in the sphere to cylindrical micelles transition in P104/water micelles [27]. This transition was followed by a temperature jump from the sphere phase to the rod-like-micelles phase and monitored with dynamic light scattering (DLS). Then, we used a fluorescent technique, which uses the random distribution of hydrophobic pyrene derivative between micelles as a tool to probe the fusion and fission of micelles at equilibrium.

After characterizing amphiphilic block copolymers structure and studying their dynamics in and out of equilibrium, liposomes were prepared and characterized in order to identify their shape, size and their physicochemical properties [28-32]. In order to firstly explore electrostatic interactions between liposomes and P104 micelles, we used different techniques such as Dynamic Light Scattering (DLS) and ζ-potential. Then, the time-scan fluorescence technique, which is used to quantify the kinetics between amphiphilic block copolymer micelles [24], is proposed to quantify the vectorization kinetics between P104 micelles and liposomes. The effect of the variation of several parameters such as liposome concentration, P104 micelles concentration and liposome coating whit chitosan are investigated in order to control the vectorization dynamics between amphiphilic block copolymer micelles and liposomes.

Justification

The structure of amphiphilic block copolymers ensures their ability to interact with the cell membrane and to change its properties. The addition of amphiphiles to cell culture modifies the functional activity of the proteins in the membrane [33] and changes the electrical properties of biological membranes [34]. The high efficiency and relatively low toxicity of amphiphilic block copolymers, as Pluronics, explain their application in various fields of medicine and pharmacology [35, 36].

Very few studies have examined the role of dynamics in amphiphilic block copolymers micelles during the transport and expulsion of drugs. Understanding these dynamics, as well as quantifying and controlling the exchange kinetics become crucial for the design and the control of new materials and new effective vectorization processes in controlled drug release.

Assumptions

Micelles are continuously structured on a microscopic scale: they can be formed and they can dissociate themselves into monomers, they can merge to form larger micelles and they can break up into small micelles. These mechanisms are certainly crucial for the encapsulation and transport of hydrophobic molecules, especially for controlled drug delivery applications. The time characteristics of these dynamics can vary from 10^{-10} s, for conventional surfactants, to years for high molecular weight copolymers [9, 37,38]. These times depend on the hydrophilic corona structure, the length of the chains, the nature of the interaction between micelles (steric/electrostatic), among others parameters.

Recently *Rharbi et al.* [37] developed a technique based on stopped-flow fluorescence to distinguish, analyze and quantify the different dynamics. With this technique it is possible to distinguish fusion mechanisms of micelles from fission and separation of micelles into individual monomers by using hydrophobic fluorescent probes that can be only exchanged via fusion and fission processes. This technique can detect fusion and fission processes that take place in a time range between the ms to a month [37]. This technique will be used to study the exchange dynamics in amphiphilic triblock copolymers and in more complicated systems that include the interactions between macromolecules of different nature, i.e. liposomes and amphiphilic block copolymers.

Objectives

General objective

To study the exchange dynamics between vectors and cell models for the design and the control of new materials and new effective processes in drug delivery. In order to achieve this, we propose a study system composed by amphiphilic block copolymer micelles modeling the vectors to transport the hydrophobic molecules, liposomes as the simplest membrane model and highly hydrophobic alkylated pyrene representing the active ingredient introduced into the micelles.

Specific objectives

- To study the phase behavior and the rheological behavior of amphiphilic block copolymer P104/water.

- To study the mechanisms of fusion and fission of amphiphilic block copolymer P104 micelles in water.

- To investigate the role of fusion and fission processes in the sphere to rod-like micelles transition in P104/water micelles.

- To study the exchange dynamics between amphiphilic block copolymer P104 micelles in water with liposomes based on phospholipids for controlled drug delivery applications.

- To study the influence of chitosan adsorption on amphiphilic block copolymer micelles and liposomes on the exchange dynamics between both particles.

References

[1] J.G. Álvarez-Ramírez, V.V.A. Fernández, E.R. Macías, Y. Rharbi, P. Taboada, R. Gómez-Corrales, J.E. Puig and J.F.A. Soltero, Phase behavior of the Pluronic P103/water system in the dilute and semi-dilute regimes, *Journal of Colloid and Interface Science* **333**, 655–662 (2009).

[2] P. Alexandridis, D. Zhou and A. Khan, Lyotropic Liquid Crystallinity in Amphiphilic Block Copolymers: Temperature Effects on Phase Behavior and Structure for Poly(ethylene oxide)-b-poly(propylene oxide)-b-poly(ethylene oxide) Copolymers of Different Composition, *Langmuir* **12** (11), 2690-2700 (1996).

[3] W. Hamley, Block Copolymers in Solution, ed. I. W. Hamley, John Wiley &Sons, San Francisco, (2005).

[4] P. Alexandridis and B. Lindmann, *Amphiphilic Block Copolymers: Self-Assembly and Applications, ed. P. Alexandridis and B. Lindmann, Elsevier*, Amsterdam, (2000).

[5] E.B. Jørgensen, S. Hvidt, W. Brown and K. Schillén, Effects of Salts on the Micellization and Gelation of a Triblock Copolymer Studied by Rheology and Light Scattering, *Macromolecules* **30**, 2355, (1997).

[6] G. Pembouong, N. Morellet, T. Kral, M. Hof and D. Scherman, M.-F. Bureau and N. Mignet, A comprehensive study in triblock copolymer membrane interaction, *Journal of Controlled Release* **151**, 57–64 (2011).

[7] M. Hamidi, M.-A. Shahbazi and K. Rostamizadeh, Copolymers: Efficient Carriers for Intelligent Nanoparticulate Drug Targeting and Gene Therapy, Macromolecular Bioscience **12**, 144-164 (2012).

[8] A.G. Denkova, E. Mendes and M.O. Coppens, Non-equilibrium dynamics of block copolymer micelles in solution: Recent insights and open questions, *Soft Matter* **6**, 2351 (2010).

[9] T. Nicolai, O. Colombani and C. Chassenieux, Dynamic polymeric micelles versus frozen nanoparticles formed by block copolymers, *Soft Matter* **6**, 3111 (2010).

[10] K. Mortensen and W. Brown, Poly(ethylene oxide)-poly(propylene oxide)-poly(ethylene oxide) triblock copolymers in aqueous solution. The influence of relative block size, *Macromolecules* **26**, 4128 (1993).

[11] A. Cambón, M. Alatorre-Meda, J. Juárez, A. Topete, D. Mistry, D. Attwood, S. Barbosa, P. Taboada and V. Mosquera, Micellisation of triblock copolymers of ethylene oxide and 1,2-butylene oxide: Effect of B-block length, *Journal of Colloid and Interface Science* **361**,154–158 (2011).

[12] G. Waton, B. Michels and R. Zana, Dynamics of block copolymer micelles in aqueous solutions,

Macromolecules **34**, 907 (2001).

[13] V.V.A. Fernández, J.F.A. Soltero, J.E. Puig and Y. Rharbi, Temporal Evolution of the Size Distribution during Exchange Kinetics of Pluronic P103 at Low Temperatures, *The Journal of Physical Chemistry B*, **10**, 1520-6106 (2009).

[14] J.M. Barichello, M. Morishita, K. Takayama and T. Nagai, Absorption of insulin from Pluronic F-127 gels following subcutaneous administration in rats, *Int. Journal of Pharm.* **184** 189-198 (1999).

[15] S.D. Desai, J. Blanchard, In vitro evaluation of pluronic F127 based controlled release ocular delivery systems for pilocarpine, *J. Pharm. Sci.* **87**, 226-230 (1998).

[16] K. Edsman, J. Carlfors and R. Petersson, Rheological evaluation of poloxamer as an in situ gel for ophthalmic use, *Eur. J. Pharm. Sci.*, **6**, 105-112 (1998).

[17] A. Paavola, J. Yliruusi and P.J. Rosenberg, Controlled release and dura mater permeability of lidocaine and ibuprofen from injectable poloxamer-based gels, *Control. Release.* **52**, 169-178 (1998).

[18] B.J. Lee, T.S. Lee, B.J. Cha, S.H. Kim and W.B. Kim, Percutaneous absorption and histopathology of a poloxamer-based formulation of capsaicin analog, *Int. J. Pharm.*, 159, 105-114, (1997).

[19] Y. Liu, T.-S. Niu, L. Zhang and J.-S. Yang, Review on nano-drugs, *Natural Science*, **2**, 41-48, 2010.

[20] P. Soni, S. K. Sar and R. Patel, New Approach for the Determination of Tricyclic Antidepressant Amitriptyline Using *β*-Cyclodextrin-PEG System via Spectrophotomerty, *Journal of Analytical Sciences, Methods and Instrumentation* **2**, 103-107 (2012).

[21] C. Peetla, A. Stine and V. Labhasetwar, Biophysical interactions with model lipid membranes: applications in drug discovery and drug delivery, *Mol Pharm.* **6**(5), 1264–1276 (2009).

[22] R. Duncan, Drug–polymer conjugates: potential for improved chemotherapy, *Anti-cancer Drugs* **3** 175–210 (1992).

[23] X. Huang and C. S. Brazel, On the importance and mechanisms of burst release in matrix-controlled drug delivery Systems, *Journal of Controlled Release* **73**, 121–136 (2001).

[24] Y. Rharbi, Fusion and Fragmentation Dynamics at Equilibrium in Triblock Copolymer Micelles, *Macromolecules* **45**, 9823−9826 (2012).

[25] A. Halperin and S. Alexander, Polymeric micelles: their relaxation kinetics, *Macromolecules* **22**, 2403, (1989).

[26] E.E. Dormidontova, Micellization kinetics in block copolymer solutions: Scaling model, *Macromolecules* **32**, 7630, 1999.

[27] G. Landazuri, V. V. A Fernández, J. F. A. Soltero and Y. Rharbi, Kinetics of the Sphere-to-Rod like Micelle Transition in a Pluronic Triblock Copolymer, *J. Phys. Chem. B* **116**, 11720−11727 (2012).

[28] R. Koynova and M. Caffrey, Phases and phase transitions of the phosphatidylcholines, *Biochimica et Biophysica Acta* **1376** , 91−145 (1998).

[29] A. Moscho, O. Orwar, D. T. Chiu, B. P. Modi and R. N. Zare, Rapid preparation of giant unilamellar vesicles, *Proc. Natl. Acad. Sci. USA* **93**, 11443-11447 (1996).

[30] S. Šegota and D. Težak, Spontaneous formation of vesicles, *Advances in Colloid and Interface Science* **121**, 51−75 (2006).

[31] P. Walde, S. Ichikawa, Enzymes inside lipid vesicles: preparation, reactivity and applications, *Biomolecular Engineering* **18**, 143−177 (2001).

[32] D. A. Bricarello, M. J. Prada and N. Nitin, Physical and Chemicals modifications of lipid structures to inhibit permeation of free radicals in a supported lipid membrane model, *Soft Matter* **8**, 11144 (2012).

[33] G.J. Strugala, B. Elsenhans and W. Forth, Active transport inhibition in rat small intestine by amphiphilic amines: an In Vitro study with various local anaesthetics, *Biochem Pharmacol.* **59**, 907-913, (2000).

[34] J. Meszaros, Effect of palmitoylcarnitine on the passive electrical properties of isolated guinea pig ventricular myocytes, *Eur. J. Pharmacol.* **194**, 107-110 (1991).

[35] A.V. Kabanov, E.V. Batrakova, V.Y. Alakhov, Pluronic block copolymers for overcoming drug resistance in cancer, *Adv. Drug Delivery Rev.* **54**, 759 (2002).

[36] A.V. Kabanova, P. Lemieux, S. Vinogradov, V. Alakhov, Pluronic® block copolymers: novel functional molecules for gene therapy, *Advanced Drug Delivery Reviews* **54**, 223−233 (2002).

[37] Y. Rharbi, L.S. Chen L.S. and M.A. Winnik, Exchange Mechanisms for Sodium Dodecyl Sulfate Micelles: High Salt Concentration, *J. Am. Chem. Soc.*, **126** (19), 6025-6034 (2004).

[38] A.G. Denkova, E. Mendes and M.O. Coppens, Rheology of worm-like micelles composed of tri-block copolymer in the limit of slow dynamics, *J. of Rheology* **53**, 5, 1087 (2009).

CHAPTER 1

Self-assembling systems: amphiphilic block copolymers and liposomes

1. Self-assembling systems: amphiphilic block copolymers and liposomes

1.1. Introduction

The self-assembly of surfactants and amphiphilic polymers in solution has been extensively studied due to the great number of applications that take into account the resulting multimolecular aggregates of these materials. The structure of these aggregates has different effects on the properties of surfactant or amphiphilic polymer solutions, as their solubilization capacity for hydrophobic substances, their viscoelastic properties, among many others [1].

It is important to know how the molecular structure of the surfactant, the amphiphilic polymer or the liposome controls the shape and size of the aggregates in order to chose the molecules that produce a specific structure such as spherical micelles, globular micelles, rod-like micelles or spherical bilayer vesicles, as well as to design novel amphiphilic molecules that generate any aggregate morphology.

1.2. Surfactants

Surface-active agents, also known as surfactants, are amphiphilic substances that lower the surface tension of the medium in which they are dissolved, or lower the interfacial tension between two liquid phases immiscible with each other [2,3]. These substances can associate in polar and non-polar solvents to form a variety of structures depending on the concentration or the temperature [4-6]. A surfactant is also characterized by its affinity to be adsorbed on the air-water interface or the water-oil interface. They are widely used in food and pharmaceutical industry, in cosmetics, plastics production, in enhanced oil recovery, agriculture and in many other fields [7-10]. In the field of pharmaceutical sciences, the surfactants are used as emulsifiers, wetting agents solubilizers, among others applications [11]. Actually, they are considered important molecules as therapeutic agents for combating several diseases due to their antibacterial and antiviral functions [12]. They are also suitable anti-adhesive coating agents for medical insertional materials, which lead to a decrease in a great number of hospital infections without using chemicals or synthetic drugs.

Surfactants are composed by two parts with different affinities for solvents. One of them has affinity for water (polar solvents) and the other one for oil (non-polar solvents). If the solvent is water, each part is called hydrophilic and hydrophobic [13]. In this way, they are soluble in both organic solvents and water. Surfactants are indicated by the presence of a polar head and a tail as the non-polar region (*Figure 1.1*). The hydrophobic part of the molecule can have different unsaturated portions or aromatic entities and it may also be partially or fully halogenated, like in fluorocarbon compounds. The hydrophilic part of the molecule can contain functional groups such as -COOH, -OH, -NH$_2$, among others, which give sufficient affinity for water, allowing the interactions with polar medium and to form aqueous solutions [14].
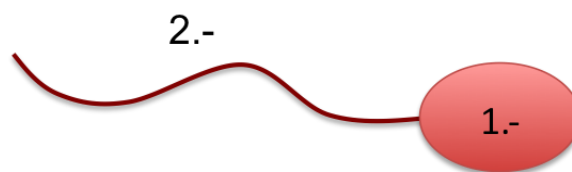
Figure 1.1. *Schematic representation of a surfactant 1.- hydrophilic head and 2.- hydrophobic tail.*

Usually, the hydrophobic group is a long-chain hydrocarbon residue and less frequently a halogenated or oxygenated hydrocarbon or siloxane chain, whereas the hydrophilic group is an ionic or polar group [15]. Surfactants can be classified according to the electric charge of their polar part, so they are divided in ionic and non-ionic surfactants. Ionic surfactants are in turn divided in anionic, cationic, amphoteric and zwitterionic surfactants [16] (*Figure 1.2.*).
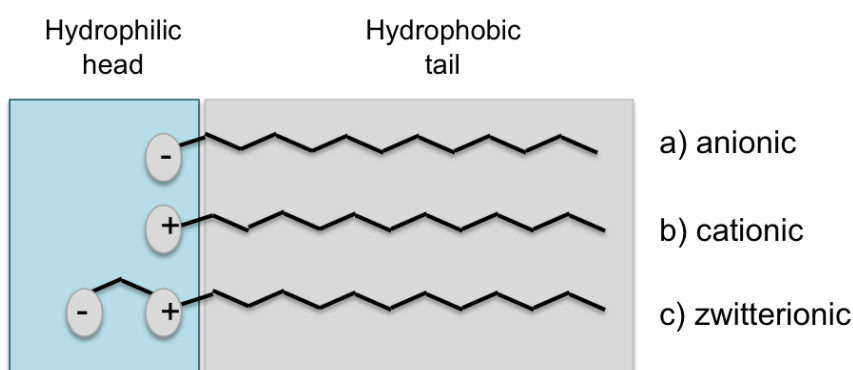
Figure 1.2. *Surfactant classification according to their polar part: a) negatively charged, b) positively charged and c) two oppositely charged groups.*

1.2.1. Ionic surfactants

1.2.1.1. Anionic surfactants

This type of surfactants is largely used due to its low cost of production and its easy way to be applied [17]. They are characterized by having polar groups such as sulfates, sulfonates, carboxylates and phosphates radicals [18]. The counterions mostly used with these surfactants are sodium, potassium, ammonium, calcium and several protonated alkylamines. Sodium and potassium promote water solubility, whereas calcium generates oil solubility. Finally, both oil and water solubility is propitiated in the case of protonated alkylamines.

The most common anionic surfactants are carboxylic acids, phosphoric and polyphosphoric acid esters, sulfonic acids, sulfuric acid esters and perfluorinated anionic surfactants, among others [19]. Anionic surfactants are the most abundant group of surfactants but they are not compatible with cationic surfactants. They are sensitive to hard water, however, this sensitivity decreases in the following order: carboxylates, phosphates, sulfates and sulfonates.

1.2.1.2. Cationic surfactants

Cationic surfactants represent only about 5% of surfactants produced in the world and they are generally more expensive than anionics because of the high-pressure hydrogenation reaction needed during their synthesis. Most of them are usually based on a nitrogen atom with positive charge, since amines can only function as surfactants in their protonated state [20]. Therefore, this type of surfactant cannot be used in solutions with high pH values. Cationic surfactants are compatible with nonionic and zwitterionic surfactants, but usually they are not compatible with anionic surfactants, except the amine oxides. They adsorb easily on many surfaces and they are used to modify them.

1.2.1.3. Amphoteric or zwitterionic surfactants

Amphoteric or zwitterionic surfactants act depending on the medium in which they are, so they can function as anionics and as cationics surfactants depending on the pH of the solution [21]. These surfactants, also known as ampholytes, contain at least one anionic and one cationic group. The isoelectric point is the pH where the net charge is null. Therefore, in basic medium they behave as anionic surfactants and in acidic medium they behave as cationic surfactants. The cationic part is based on primary, secondary or tertiary amines, or quaternary ammonium cations. The anionic part may vary and can include sulfonates. The most common biological zwitterionic surfactants have a phosphate anion with an amine or ammonium, such as the phospholipids phosphatidylserine, phosphatidylethanolamine and phosphatidylcholine, among others [22].

Several methods are used to produce these surfactants, which mostly contain a quaternary ammonium ion (a cation) and a negatively charged group that can be a carboxylate ($-CO_2^-$), a sulfate ($-OSO_3^-$) or a sulfonate ($-SO_3^-$). They are compatible with all other types of surfactants, they are not sensitive to hard water and they are generally stable in acidic and basic media. Zwitterionic surfactants generally maintain their properties in high alkaline medium.

1.2.2. Nonionic surfactants

Nonionic surfactants are surfactants that can be solubilized by the combined effect of a number of weak solubilizing groups (hydrophilic), such as ether or hydroxyls groups in the molecule. Most of the nonionic surfactants contain a polyether group, composed by oxyethylene obtained by the polymerization of ethylene oxide [23]. These surfactants form the second wider group of surfactants. They are usually compatible with other types of surfactants but they are not sensitive to hard water. Contrary to nonionic surfactants, their physicochemical properties are not affected by electrolytes. Finally, their physicochemical properties depend mainly on the temperature since they are less soluble in water at high temperatures.

Table 1.1 summarizes some examples of each type of surfactant.

Table 1.1.- *Classification of surfactants and some examples [15].*

Surfactant type		Nature of the hydrophilic group	Example
Ionic	Anionic	Negative charge	$RCOO^-Na^+$ (soap) $RC_6H_4SO_3^-Na^+$ (alkylbenzene sulfonate)
	Cationic	Positive charge	$RNH_3^+Cl^-$ (salt of a long-chain amine) $RN(CH_3)_3^+Cl^-$ (quaternary ammonium chloride)
	Amphoteric or Zwitterionic	Positive and negative charges	$RN^+H_2CH_2COO^-$ (long-chain amino acid) $RN^+(CH_3)_2CH_2CH_2SO_3^-$ (sulfobetaine)
Nonionic		No apparent ionic charge	$RCOOCH_2CHOHCH_2OH$ (monoglyceride long-chain fatty acid) $RC_6H_4(OC_2H_4)_xOH$ (polyoxyethylenated alkylphenol) $R(OC_2H_4)_xOH$ (polyoxyethylenated alcohol)

1.2.3. Surfactant structures

The great variety of structures formed by surfactants is studied and determined through different techniques such as Nuclear Magnetic Resonance (NMR), neutron scattering, Small Angles X-ray Scattering (SAXS), Dynamic Light Scattering (DLS) and Quasielastic Light Scattering (QLS), among others. Some of the identified structures are spherical micelles, cylindrical micelles, mesophases and liquid crystals as cubic phases.

In aqueous solution, a surfactant micelle is formed with its lipophilic tails oriented towards the interior, presenting in this way its hydrophilic surface to the polar ambient. The simplest micelles are spheres but as surfactant concentration increases the micelles grow and form rods. At high surfactant

concentrations the rods form larger structures tan can be hexagonally packed rods or palisade arrangements (*Figure 1.3*). As these structures increase in size, they take on a greater degree of order until they become liquid crystals (for the biggest structures).
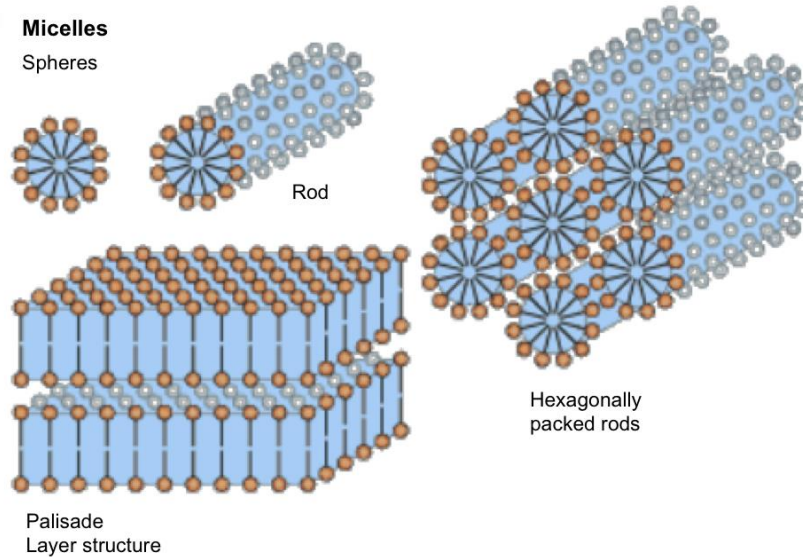
Figure 1.3. *Some structures formed by surfactants [24].*

1.3. Critical Micellar Concentration (CMC)

Micelles are small colloidal particles, relative to the wavelength of light. When micelles form, the behavior of the aqueous surfactant solution is such as a microheterogeneous medium. The value of the CMC can be determined by the change in the physicochemical properties of the surfactant solution as the surfactant concentration increases [25-28].

The CMC depends on several parameters, such as temperature, pressure, the nature of the amphiphile, the solvent composition and the presence of solubilized substance. It decreases with increasing hydrocarbon chain-length of the apolar groups, and for ionic surfactants it also depends on the nature and concentration of counterions in solution. CMC also decreases with the addition of electrolytes.

Most of the physical properties of amphiphilic solutions change drastically in the CMC. In this manner, the CMC was defined as the concentration at which takes place the maximum change in the slope of the curve presenting an ideal colligative property ϕ as a function of the total concentration of amphiphile, C_T (*Equation 1.1*).

$$\left[\frac{d^3 f}{dC_T^3} \right]_{C_r = CMC} = 0 \tag{1.1}$$

Generally, the CMC is located at the intersection of two extrapolated curves of a determined physical property as a function of concentration (*Figure 1.4.*). The calculated CMC values using different properties can be slightly different since the CMC is not a defined concentration, but a small interval of concentrations.
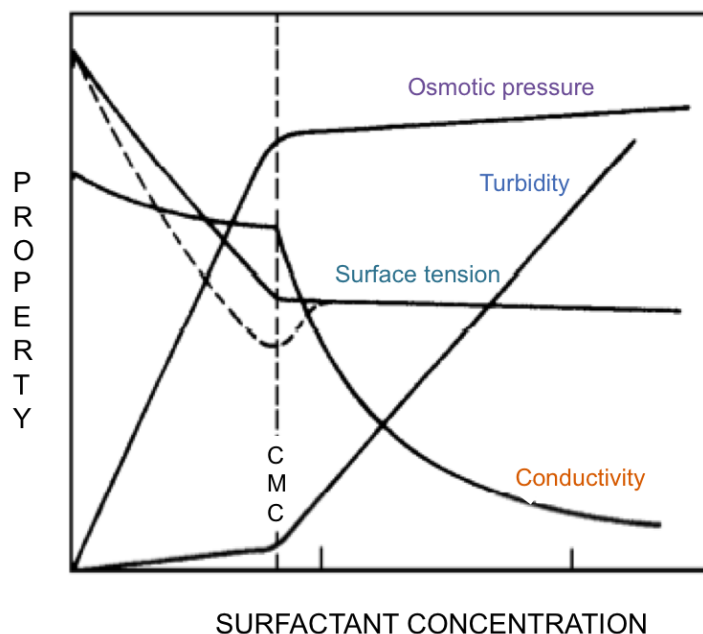
Figure 1.4. *Variation of each physicochemical property as a function of surfactant concentration.*

1.4. Critical Micellar Temperature (CMT)

The critical micelle temperature, also known as the Krafft temperature, is the minimum temperature at which surfactants form micelles. Micelle formation is a process greatly dependent on temperature and is also known as an entropy-driven process, which results in a important decrease in the CMC with the increase of temperature [29]. This behavior allows the extensive applicability of the critical micellar temperature CMT as a suitable micellar parameter. Above the CMT, unimers and micelles exist in the state of equilibrium with most of the surfactant molecules in the micellar form. The effects of temperature on the properties and structures of surfactants solutions have been extensively studied and represent an important key of their applications [30-32].

1.5. Cloud Point Temperature (CPT)

The cloud point corresponds to the temperature above which an aqueous solution of a water-soluble surfactant becomes turbid [33]. The determination of the cloud point temperature is of great importance for the storage stability of the solutions. Storing formulations at temperatures significantly

higher than the cloud point may result in phase separation and instability. Several processes such as wetting, cleaning and foaming can be different above and below the cloud point. Nonionic surfactants usually show optimal effectiveness when they are used near or below their cloud point and low-foam surfactants may be used at temperatures slightly above their cloud point.

CPT is classically measured using 1% aqueous surfactant solutions. Cloud points temperature are usually found between 0 and 100 °C, limited by the freezing and boiling points of water. Cloud points are characteristic of nonionic surfactants [34]. Anionic surfactants are more water-soluble than nonionic surfactants and have much higher cloud points (above 100°C). The presence of other components in a surfactant solution may decrease or increase the cloud point of the solution.

1.6. Surfactants solubility

Micellar solutions can solubilize nonpolar substances (such as oils) in important amounts within or on the surface of the micelles. These high solubilization systems can be microemulsions or liquid crystals due to the structures adopted in the surfactant system oil-water. By increasing temperature, the solubility of nonionic surfactants also increases. The increase of solubility becomes a relatively slow process from the Kraft temperature, since in this point the solubility increases rapidly and can reach miscibility in the whole range of concentration after a few degrees. Below the Kraft temperature, the surfactant is reasonably soluble and the concentration is not sufficient to form micelles, so that the balance is made between a monomolecular surfactant solution and the solid precipitate [35].

1.7. Amphiphilic block copolymers

Amphiphilic block copolymers are functional polymers that may be used in a great number of applications mostly related to the energetic and structural control of materials interfaces [36]. The interest in the synthesis and characterization of amphiphilic block has increased extremely in the last years. This is due to their molecular structure, which consists of at least two parts with different chemical natures. Amphiphilic copolymers are used as emulsifiers, foamers, thickeners, dispersants and vectors for drug deliver, among others applications [36,37].

Block copolymers are substances formed by macromolecules consisting of blocks arranged in a linear sequence. A block is a portion of a macromolecule that is composed by several units with at least one characteristic that is not present in the neighboring portion [38]. Copolymers may contain two or three blocks which are usually represented as AB, ABA and BAB, where A and B are the polymer blocks (*Figure 1.4*). Other block copolymers containing repeated units formed by two blocks $(AB)_n$ have also been synthesized.
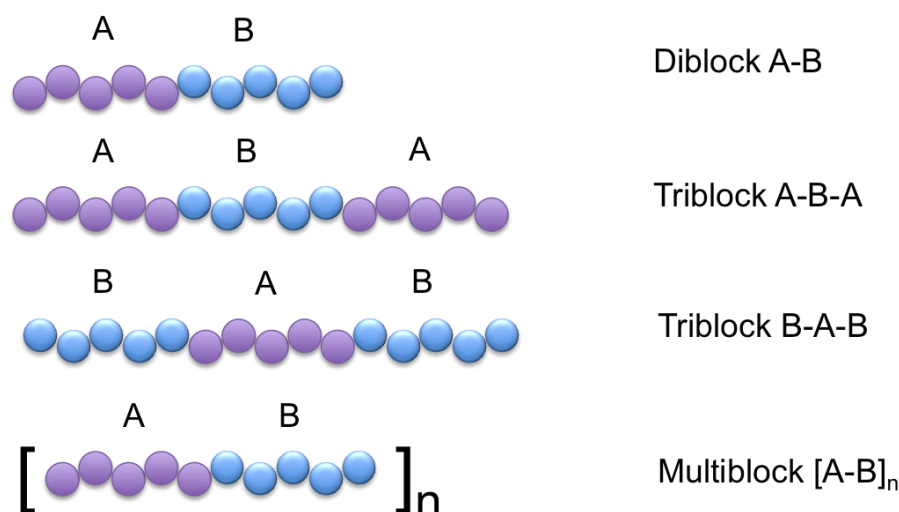
Figure 1.5. *Schematic representation of block copolymers.*

1.8. Triblock copolymers

Amphiphilic triblock copolymers are synthesized through a simultaneous polymerization of more than one type of monomer at which the individual monomers come as blocks of a variety of lengths in the copolymer molecule. As the two blocks within the copolymer are not compatible between each other, amphiphilic block copolymers assemble in melts and solutions [39]. Copolymers can assemble in aqueous solutions as microstructures similar to micelles formed by low-molecular-weight surfactants.

Some commercially available copolymers are the water-soluble triblock copolymers of poly(ethylene oxide) (PEO) and poly(propylene oxide) (PPO), also represented as PEO-PPO-PEO, and are considered as nonionic macromolecular surfactants. The production of many molecules with different properties that meet with specific requirements in different areas can be obtained from the synthesis of a variety of block copolymers with different compositions in their PPO/PEO ratio and/or a diverse molecular weight, given by the PEO and PPO block length.

1.8.1. Synthesis and nomenclature

The synthesis of PEO-PPO-PEO triblock copolymers is carried on by the sequential addition of first propylene oxide (PO) and then ethylene oxide (EO) to a low molecular weight water-soluble propylene glycol, a poly(propylene oxide) oligomer. An alkaline catalyst, usually NaOH or KOH, is used during the oxyalkylation and is then neutralized and removed from the final product [39,40].

The Pluronic PEO-PPO-PEO block copolymers can be obtained in a great range of molecular weights and PPO/PEO composition ratios [41]. The following notation is used for these materials: L for liquids, P for paste and F for flakes. Then the first or two numbers denote the molecular weight of the PPO block and the last number represent the molecular weight of the PEO block.

Figure 1.6 shows the Pluronic grid that present the arrangement of Pluronic PEO-PPO-PEO block copolymers depending on their composition (PPO and PEO block groups).
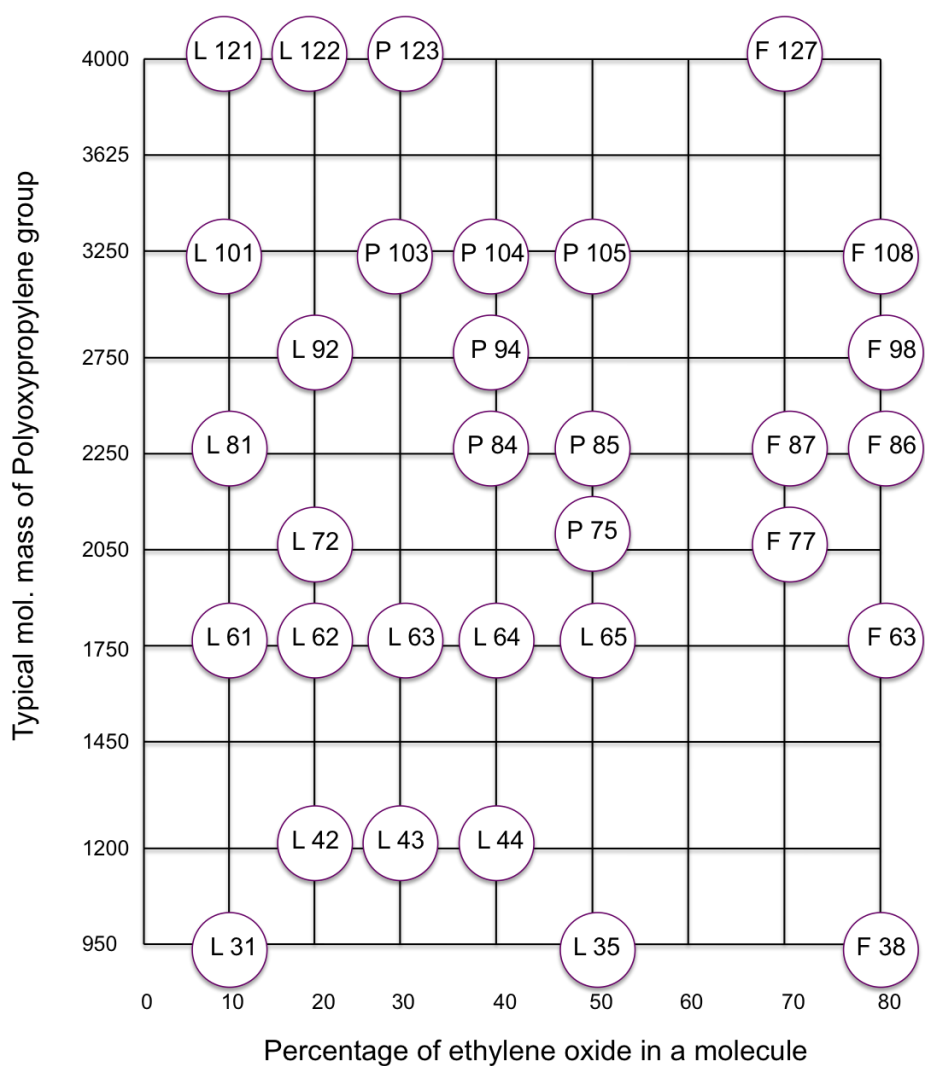
Figure 1.6. *Pluronic grid [39].*

1.8.2. Physical properties

Block copolymers present a reversible solubility with temperature, they are more soluble in cold water than in warm water and exhibit a clouding point temperature. Copolymers with low EO content

have low properties for foaming, so the best antifoam is obtained with the ratio of EO/PO from 1:4 to 1:9. The inverted materials PO/EO/PO produce less foam.

Copolymers with high molecular weight and high content in PO groups possess good wetting properties. The biodegradability is low, particularly for products with high PO content groups.

1.8.3. Micelle formation in PEO-PPO-PEO triblock copolymers

The micellization of amphiphilic block copolymers is a more complex process than micellization of standard low-molecular weight surfactants. In fact, a certain CMC range has been usually observed with some ambiguity. The CMC values determined by different methods and different techniques may vary depending on the sensitivity of the technique to the amount of molecularly dispersed copolymers (unimers) present in the solution [42]. In this manner, the values reported in the literature differ considerably due the several reasons such as the lack of sufficient temperature control and batch-to-batch variations [39,43].

The sensitive nature of triblock copolymers micellization leads to the possible alteration of the aggregation characteristics due to the addition of different compounds. In fact, it has been found that the addition of co-solvents or solutes to aqueous triblock copolymer solutions can influence the CMT and the CMC [44]. Experimentally, Small-Angle Neutron Scattering (SANS) scattering curves can be fitted by using the model of Pedersen, which gives information about the core size, the corona thickness, and the aggregation number of micelles. *Figure 1.7* shows a schematic of the Pedersen model for block copolymer micelles, where R_c is the core radius, R_{int} is the interaction radius, and $R_{g(PEO)}$ is the radius of gyration of the PEO segment.
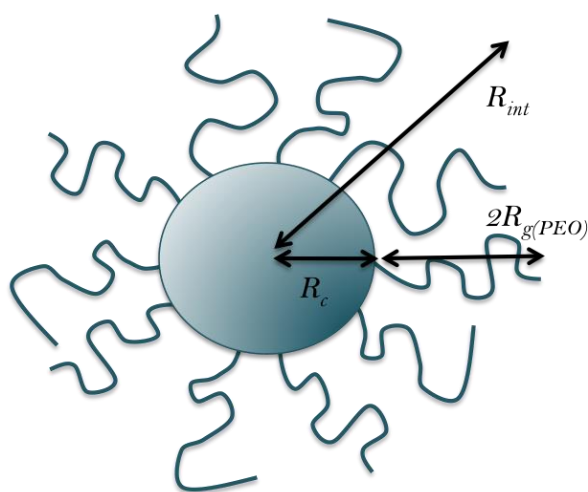
Figure 1.7. *Schematic representation of the Pederson model for block copolymer micelles [44].*

1.8.4. Micellization thermodynamics

Diblock and triblock copolymers form micelles in selective solvents that can be thermodynamically good solvents for one of the blocks and precipitants for the other block [39]. Micellization of block copolymers follows the closed association model, which assumes equilibrium between molecularly dispersed copolymer (unimer) and multimolecular aggregates (micelles). Two main approaches have been previously discussed to the thermodynamic analysis of the micellization process [39]. First one is the phase separation model, here the micelles are supposed to form a separate phase at the CMC. Second one is known as the mass-action model, which considers micelles and unassociated unimers to be in an association-dissociation equilibrium. The standard free energy change for the transfer of 1 mol of amphiphile from solution to the micellar phase is given by *Equation 1.2* for both cases.

$$\Delta G = RT\ln(X_{CMC}) \tag{1.2}$$

where ΔG is the free energy of micellization in the absence of electrostatic interactions, R is the gas law constant, T is the absolute temperature and X_{CMC} is the critical micellization concentration in mole fraction units.

Here, the concentration of free surfactant (unimers) in the presence of micelles is considered to be constant and equal to the CMC value. The standard enthalpy of micellization can be expressed by applying the Gibbs Helmholtz equation (*Equation 1.3*).

$$\Delta H = -RT^2[\partial\ln(X_{CMC})/\partial T]_P \tag{1.3}$$

The standard entropy of micellization per mole of surfactant, ΔS can be also determined by using *Equation 1.4*.

$$\Delta S = (\Delta H - \Delta G)/T \tag{1.4}$$

It comes that for block copolymer micellization:

$$\partial\ln(X_{CMC})/\partial(1/T) = \partial\ln(X)\partial(1/T_{CMT}) \tag{1.5}$$

where X is the concentration (in mole fraction) and T_{CMT} is the critical micellization temperature.

In this way, *Equation 1.3* can be written as follows:

$$\Delta H = R[\partial(X)/\partial(1/T_{CMT})]_P \tag{1.6}$$

The standard enthalpy of micellization, ΔH^o, can be then calculated from the inverse slope of the linear fit to the $1/T_{CMT}$ vs. ln(mole fraction) data.

The standard enthalpy of micellization, ΔH°, is positive [39], showing that the transfer of unimers from solution to the micelle is an enthalpically unfavorable endothermic process. The free energy, ΔG°, is negative due to the spontaneous formation of thermodynamically stable micelles. Therefore, a negative entropy contribution has to be the driving force for block copolymers micellization. However, it worth's mentioning that contrary to the entropy-driven micellization in water, the micellization of copolymers in non-polar solvents is due to enthalpy interactions between the copolymer segments and the solvent.

1.8.5. Gels formed by PEO-PPO-PEO triblock copolymers

The Pluronic PEO-PPO-PEO block copolymers solutions of high copolymer concentration present a remarkable change in the viscosity at temperatures near to ambient temperature, showing a phenomena known as thermoreversible gelation [39]. Some authors related the gel transition to intrinsic changes in the micellar properties [45] or to the possibility of the development of an ordered three-dimensional structured state [46]. However, recently neutron scattering studies showed that the observed change in viscosity is due to a hard-sphere crystallization, since the micelle concentration gets close to the critical volume fraction of 0.53 (micelles close-packed) [39]. It is possible to dissolve again the gel at higher temperatures. The gelation temperature and the thermal stability range of the gel increase with the increase of the PEO block length.

1.9. Applications of amphiphilic block copolymers

Amphiphilic block copolymers can be used in many applications due to their self-assembling properties. They can be applied either in the solid state or in a specific solvent, which gives a great variety of morphologies. They are useful as compatibilizers, viscosity modifiers, dispersants to stabilize colloidal suspensions, nanocarriers for the encapsulation and controlled release of drugs, templates for mineralization or, more generally, in nanoscience and nanotechnologies [47].

Since amphiphilic block copolymers containing hydrophilic and hydrophobic blocks can form different nanostructures in aqueous solution, such a micelles with an average size between 20 and 100 nm, which is a similar size to the one of a virus or a lipoprotein, they can be used as nanocarriers for small compounds and for drug delivery processes. One of the advantages of these micelles is that they can be used as nanocarriers for small compounds [48]. Nowadays, Pluronic block copolymers have been studied as drug delivery vehicles to treat different multidrug resistant cancers and for cancer chemotherapy [49]. Recent studies showed that the interaction between Pluronic block copolymers and cancer cells result in a chemo-sensitization of the cancer cells [50].

1.9.1. Controlled release and drug delivery

Nowadays, targeting specific cells or specific membrane proteins is being widely studied in order to improve diagnosis and treatments in the field of medicine [51]. Many efforts are currently focused in the development of nanoscale vehicles able to carry complex functionality to cell or membrane targets within the body and that can remain intact and can escape from the defense system. This kind of specific targeting is attractive since several side effects of actual drugs may appear from the undesired impact of a drug molecule on physiological pathways in a cell and that are not involved in the disease process.

Polymer-based nanotechnology is actually one of the most attractive areas of pharmaceutical research and is growing fast since the last decade [52]. The materials more often studied include polymer micelles, polymer-DNA complexes, nanogels, liposomes, and other different nanoscale sized materials for medical applications. Many different preparations of polymeric molecules at the nanoscale represent promising opportunities for the safe and efficient delivery of drugs and genes [53].

Triblock copolymers have been studied and proposed as efficient drug delivery systems that can provide different useful effects [53]. In this manner, the incorporation of drugs into the core of the micelles formed by Pluronic® triblock copolymers produces an increase of solubility, of the metabolic stability and a greater circulation time for the drug [54]. *Figure 1.8* shows a schematic representation of an amphiphilic block copolymer micelle anti-cancer drug. It has also been reported and proved that the interactions of these copolymers with multidrug-resistant cancer cells result in the sensitization of the cells compared to other anticancer agents. Additionally, the single molecular chains of copolymers, i.e. the unimers, inhibit drug efflux transporters in the blood–brain barrier and in the small intestine, which contributes to an improved transport of select drugs to the brain and increases oral bioavailability [53].
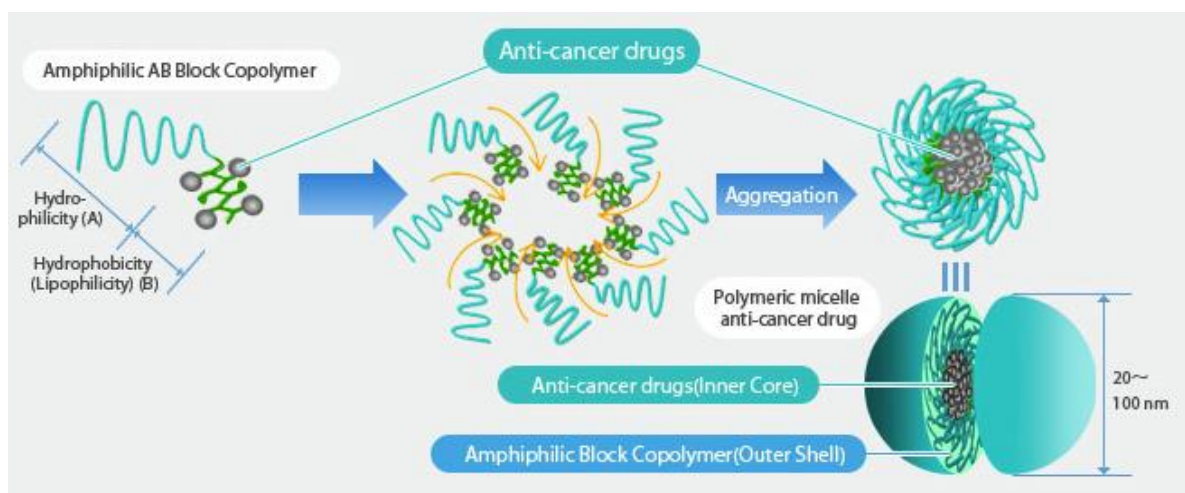
Figure 1.8. *Amphiphilic block copolymer micelle anti–cancer drug [55].*

1.9.1.1. Micellar drug carriers

Amphiphilic block copolymers micelles have been considered as a group of drug delivery complexes with a nanoscale size between 5 and 100 nm characterized by a core/shell structure [56]. The inner core, constituted by the hydrophobic blocks, is able to create a cargo space for the solubilization, storage, controlled release and protection of unstable lipophilic drugs from chemical degradation of the metabolism through biological agents. Additionally, the outer shell or corona is composed of the hydrophilic blocks, which supply a protective interface between the core and the external environment through steric stabilization effects [57]. The solubilization of lipophilic drugs by amphiphilic block copolymers can be obtained by hydrophobic and/or covalent interactions between the polymer structure and the drug molecule. Block copolymer micelles can directly target their encapsulant to specific tissues. In micelles, the miscibility, compatibility and degree of interaction between the drug and the block that form the core are important factors for an efficient drug loading, stability and drug release. Also, several factors as the carrier size, polymer composition and surface characteristics are important factors that influence the long circulation properties [58].

1.9.2. Burst release

Premature release, also known as burst release is one of the recent challenges that limit clinical successes of block copolymer micelles for targeted anticancer drug delivery [59]. Burst release is also considered as a foremost persistent problem in the development of injectable polymeric delivery systems, which occurs during the first minutes of contact with the external medium [60]. Burst release also limits the development of controlled release formulations including drug-loaded micro and nanoparticles, especially with low molecular weight drugs. It's generally assumed that burst drug release in blood circulation is mainly due to blood dilution and subsequent micelle disassembly after i.v. administration. A better prediction of burst release and its reduction can be reached with greater investigations on micelle disassemblies [59].

Several strategies have been employed to reduce burst release by preventing micelle disintegration, such as varying the lengths of hydrophilic and hydrophobic blocks of the block copolymers, crosslinking of the core, and/or crosslinking the shell. These approaches decrease CMC of micelles and prevent micelle disintegration in the bloodstream but might not necessarily eliminate burst release. This finding was useful for developing polymeric micelles with controlled release of lipophilic drugs [59].

Hasan et al. [60] studied the encapsulation, by a double-emulsion method, of polymeric nanoparticles within polymeric microparticles using non-water soluble polymers and an appropriate organic solvent for the preparation of composite microparticles, preventing the dissolution of the nanoparticle suspension as internal phase. They found that burst was significantly lower with the composite microparticles and that could be explained by the slower diffusion of the drugs through the

double polymeric wall formed by the nanoparticle matrix followed by second diffusion step through the microparticle polymeric wall.

Because burst release happens in a very short time compared to the entire release process, it has not been specifically investigated in most published results, and it has been ignored in most mathematical models. *Huange et al.* [61] presented experimental observations of burst release in monolithic polymer controlled drug delivery systems and some of the ideas used to prevent burst and the treatment of burst release in controlled release models. For a prevention of burst release, some advanced technologies are being developed by using surface extraction of the active agent prior to in vivo usage, using double-walled microspheres with layers made of different inert polymers, and modifying the surfaces of the drug-loaded matrix with an outer layer polymer coating. The complete elimination of the burst release effect is complicated, but a better understanding of the phenomena occurring at the early stages of release may help researchers quantifiably predict burst release.

1.10. Lipid vesicles

Membranes play an important role in the internal and external processes of the cell [62,63]. The nuclear membrane protects the DNA inside the cell and examines the molecules that try to enter or leave. The cell has a broad diversity of other internal membranes that are involved in several processes and have different characteristics [62,64]. Proteins, cholesterol and lipids, which are amphiphilic molecules containing hydrophilic and hydrophobic parts that tend to form bi-layered structures, are the most important components of the double-layered membranes that surround the cell and the nucleus [65].

Actually, the development of cell-sized giant unilamellar vesicles, which are referred as a particular type of compartment formed in vitro in an aqueous medium, from natural or non-natural amphiphiles, are of great interest since a giant vesicle membrane can model the self-closed lipid matrix of the plasma membrane of biological cells [66]. Nowadays, giant vesicles are used in the investigation of biomembranes properties, such as lateral lipid heterogeneities, membrane growing and fission, membrane permeabilization caused by the addition chemical compounds, among others [67].

1.10.1. Lipids

Lipids are mostly known as amphiphilic molecules that allow them forming structures such as vesicles, unilamellar or multilamellar liposomes or membranes in aqueous solutions [68]. They are divided in five main categories: glycerophospholipids, sphingomyelins, glycolipids, steroids and eicosanoids [69,70]. The selected lipids for this study are the glycerophospholipids, which are

amphiphilic molecules containing an hydrophilic head, composed of a phosphate group and a polar group, which are connected to two hydrophobic tails by a glycerol group.
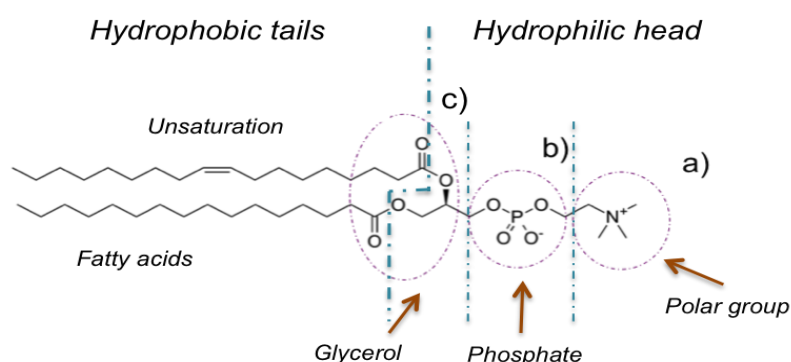
Figure 1.9. *Chemical structure of a phospholipid containing a hydrophilic head formed by the following active sites: 1) a polar group, 2) a negative phosphate group and 3) and two carbonyl oxygen groups that connect the hydrophilic head group with the two hydrophobic tails.*
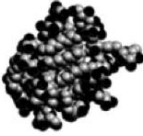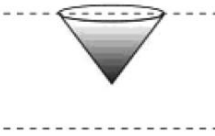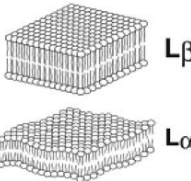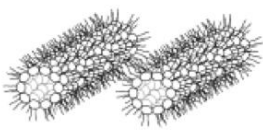
Figure 1.9. shows the chemical structure of a lipid composed by a hydrophilic head formed by three active sites. The net charge of the phospolipid can change depending on the chemical structure of the polar group. Some zwitterionic lipids are the phosphatidylcholine (PC), phosphatidylethanolamine (PE) and phosphatidylserine (PS) and some negatively charged lipids are the phosphatidic acid (PA), phosphatidylglycerol (PG) and phosphatidylinositol (PI) [70,71].

In the conventional nomenclature of phospholipids, the notation Cn:m X is used to refeer to the carbon number on the chain (n), the number of unsaturations (m) and the polar head group (X). As an example, the notation diC18:1 PC corresponds to 1,2-dioleoyl-sn-glycero-3-phosphocholine (DOPC), which has two oleoyl chains, with 18 carbons and one double bond, and a phosphatidylcholine (PC) polar head [70,72].

1.10.2. Self-association of lipids in aqueous solution

Polar lipids are amphipatic and contain hydrophobic and hydrophilic domains, as mentioned before. Due to the hydrophobic effect, the hydrocarbon domains of polar lipids changes the stable hydrogen bonded structure of water causing caje-like structures around the non-polar domain [73]. The structural organization of a polar lipid in aqueous solutions is determined by its concentration and by the law of opposing forces. The lipids are not soluble anymore in water and tend to self-assemble to limit the contact between hydrophobic tails and water at concentrations greater that the CMC (10^{-10} M

for phospoholipids with chain lengths of 16) [73,74]. They can form different structures that depend on the geometrical parameters of the global shape of the lipid [75] (*Figure 1.10*).

LIPIDS	PHASE	MOLECULAR SHAPE
Lysophospholipids Detergents	Micellar	Inverted cone
Phosphatidylcholine Sphingomyelin Phosphatidylserine Phosphatidylinositol Phosphatidic Acid Cardiolipin Digalactosyl diacylglycerol Diglucosyl diacylglycerol	Lβ Lα Bilayer	Cylindrical
Phosphatidylethanolamine Cardiolipin Ca^{2+} Phosphatidic Acid Ca^{2+} Phosphatidic Acid (pH<3.0) Phosphatidylserine (pH<4.0) Monogalactosyl diacylglycerol Monoglucosyl diacylglycerol	Hexagonal (H$_{II}$)	Cone

Figure 1.10. *Polymorphic phases and molecular shapes exhibited by lipids.*

Phospholipid with long alkyl chains do not form micelles, however, they organize into bilayer structures that allow tight packing of adjacent side chains with the greater exclusion of water from the hydrophobic domain. In living cells, phospholipids are not found free as monomers in aqueous solutions, though, they are organized in membrane bilayers or protein complexes [76].

1.10.3. Phases and phase transitions of lipids

The phase behavior of lipids in aqueous solutions is of interest in different disciplines due to the possible biological importance of the different phases they form and the transitions they undergo [76,77]. Until now, all the collected information on lipid mesomorphic and polymorphic transitions and miscibility can be found in the Lipid Thermodynamic Database (LIPIDAT) [78]. This database is considered comprehensive for glycerophospholipids, sphingolipids, glycoglycerolipids and biological membrane lipid extracts.

Lipids self-assemble into different kind of phases depending on their chemical structure and on external variables such as water content, temperature, pressure and aqueous phase composition [79]. These phases are made of aggregates resulting of the hydrophobic effect and have diverse structures that are mutually related (*Figure 1.11*).

The following expression presents a generalized phase sequence of thermotropic phase transitions in membrane lipids (phospholipids and glycolipids) [79,80]:

$$L_c \leftrightarrow L_\beta \leftrightarrow L_\alpha \leftrightarrow Q^{[B]}_{II} \leftrightarrow H_{II} \leftrightarrow Q^{[M]}_{II} \leftrightarrow M_{II}$$

A temperature increase on a lamellar crystalline (subgel) L_c phase results in the formation of a lamellar gel L_β phase, which undergoes a melting transition into the lamellar liquid-crystalline L_α phase. With a greater increase in temperature, several mesomorphic phase transitions follow the sequence L_α, bilayer cubic ($Q^{[B]}_{II}$), inverted hexagonal (H_{II}), inverted micellar cubic ($Q^{[M]}_{II}$) and micellar M_{II}.
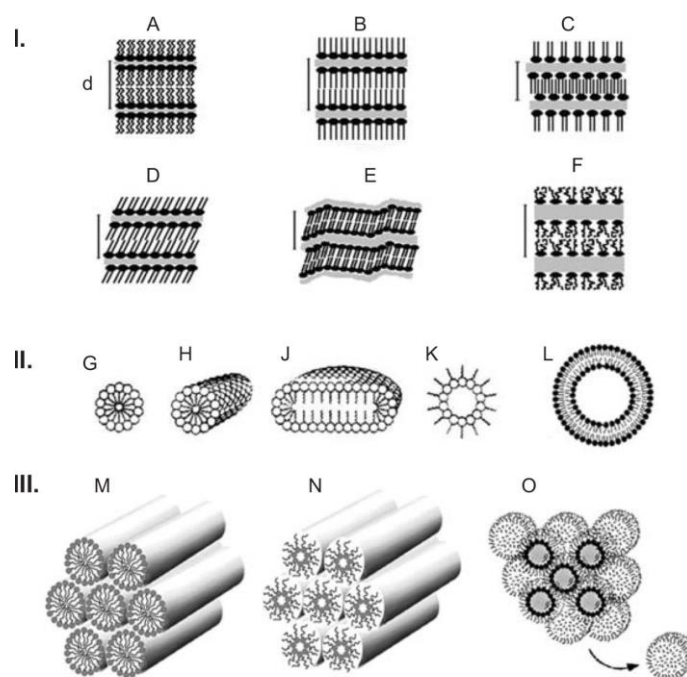
Figure 1.11. *Structures of lipid phases. I) Lamellar phases: A) subgel, L_c; B) gel, L_β, C) interdigitated gel, $L_\beta^{[int]}$, D) gel, tilted chains, $L_{\beta'}$, E) rippled gel, $P_{\beta'}$ and F) liquid crystalline, L_α. II) Micellar aggregates: G) spherical micelles, M_I, H) cylindrical micelles, tubules, J) disks, K) inverted micelles, M_{II} and L) liposomes. III) Non-lamellar liquid-crystalline phases with different topology: M) hexagonal phase H_I, N) inverted hexagonal phase H_{II} and O) inverted micellar cubic phase $Q_{II}^{[M]}$ [79].*

The phase transition from lamellar/gel–lamellar to liquid-crystalline phase (L_β–L_α), also called melting transition, solid-fluid or main transition, is the greatest energetic transition in lipid bilayers, presenting a high enthalpy change. It takes into account rotameric disordering of hydrocarbon chains and the increasing on head-group hydration and intermolecular entropy [77,81]. The gel–liquid-crystalline transitions in fully hydrated lipids involve large increases in lipid surface area (~25%) and specific volume (~4%). This can be evidenced in calorimetric measurements with narrow heat-capacity peaks with enthalpy of approximately 20 to 40 kJ/mol [81].

The hydrocarbon chains mainly influence the melting transition temperature, i.e. it increases if the chains are longer and more saturated. For lipids with unsaturated chains, the position and type of the double bond modifies significantly the melting temperature. Also, the melting temperature is affected by chain branching and by the chemical linkage between the chains and the polar head group. Anhydrous lipids with identical hydrocarbon chains present melting-phase transitions at almost identical temperatures. However, in aqueous dispersions the head-group and lipid–water interactions modify the lipid phase behavior.

1.10.4. Vesicles

For phosphatidylcholines, since the sections of the polar head and the two hydrophobic tails are approximately the same (0.6 nm²), a three dimensionnal self-closed bilayer structure is formed in presence of water. This structure is characterized by an assembly of two separate lipid leaflets with a thickness between 3 to 6 nm, depending of the hydrocarbon chain length, called vesicles (*Figure 1.12*) [69].
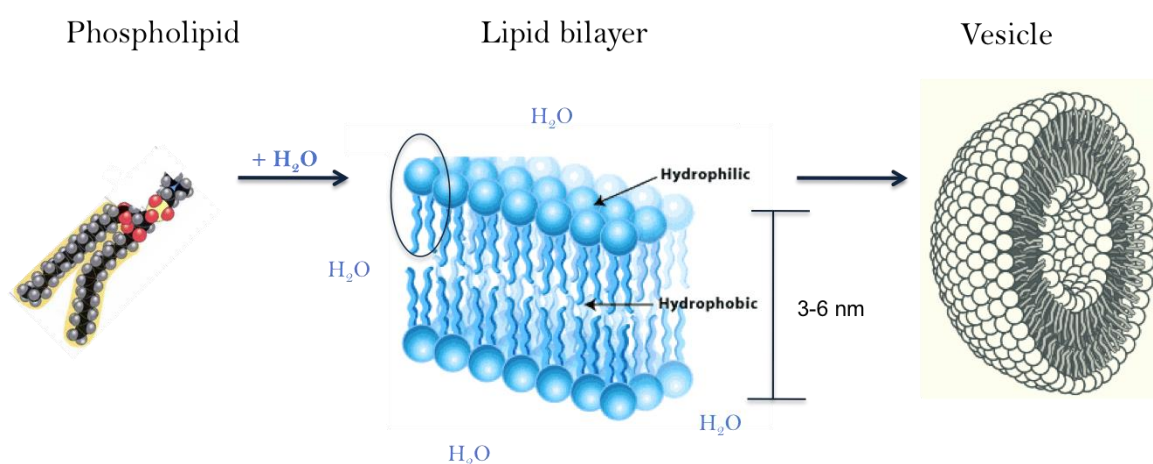
Figure 1.12. *Lipids self-associate in presence of water into bilayer structures that tend to close in order to form lipid vesicles.*

Vesicles can have different sizes depending on the preparation technique used [82], resulting in sizes ranging from nanometers to micrometers in diameter. The three principal kinds of liposomes are the following: Small Unilamellar Vesicles (SUVs) with sizes from 20 to 100 nm, Large Unilamellar Vesicles (LUVs) with sizes from 100 to 500 nm and Giant Unilamellar Vesicles (GUVs) with sizes from 0.5 to 100 μm, which are generally studied as over-simple models of biological cells [83] and can be directly observed by optical microscopy. A giant unilamellar vesicle (GUV) has a similar basic structure of all biological cells, since a vesicle membrane imitates the self-closed lipid matrix of the plasma membrane.

1.10.5. Transport across the bilayer

1.10.5.1. Passive diffusion

Molecules and ions dissolved in water are in constant motion, resulting in movements from regions where their concentration is high to regions where their concentration is lower. This process is called diffusion [84]. When a cell or vesicle with a high interior salt concentration is located in a solution with a low salt concentration it will swell and then burst. Small-uncharged non-polar molecules can diffuse through lipid bilayers many orders of magnitude faster than ions or water. This is valid in fats and in organic solvents like chloroform and ether. In spite of of their polar character larger molecules diffuse more slowly across lipid bilayers than small molecules.

1.10.5.2. Endocytosis and exocytosis

Some molecules or particles are too large or too hydrophilic to pass through a lipid bilayer, however, they can be transported across the cell membrane through fusion or budding of vesicles. Endocytosis is the process in which large particles are wrapped with plasma membrane and moved into the cell in the form of vesicles or vacuoles [85]. Exocytosis is the reverse of endocytosis, here the material is expelled from the cell without ever passing through the membrane as individual molecules [86]. Some particular types of cells move great amounts of bulk material into and out of themselves through endocytosis and exocytosis.
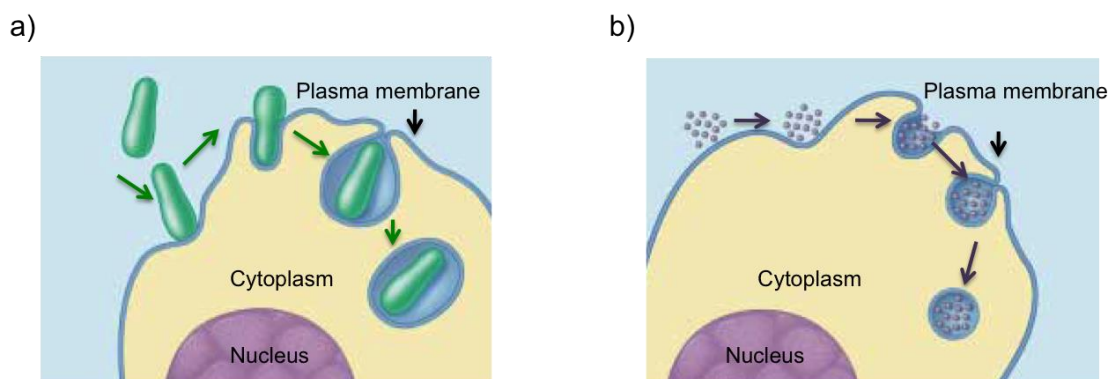
Figure 1.13. *Two forms of endocytosis: a) phagocytosis and a) and pinocytosis [87].*

Phagocytosis is the process where a living cell ingests other cells or particles [88] (*Figure 1.13 a*). Phagocytes may be free-living one-celled organisms, such as amoebas, or a body cell, such as white blood cells. Through pinocytosis, a cell will take in everything that is in the extra-cellular fluid outside of the cell, including solutes (*Figure 1.13 b*) [89]. In this process, only small amounts of material will enter the cell, and a minimal amount of adenosine triphosphate (ATP) is necessary.

1.10.5.3. Electroporation

The application of a large artificial electric field across the membrane results in a rapid increase in the bilayer permeability, known as electroporation [90]. This technique is used to introduce hydrophilic molecules into cells and is very useful for large highly charged molecules such as DNA, that would never diffuse passively across the hydrophobic bilayer core [91]. This way, electroporation is an important methods of transfection [92]. During electroporation, the increase in permeability affects the transport of ions and other hydrated species and the lipid molecules are not chemically modified but only shift the position, opening up a pore that behaves as the conductive pathway through the bilayer as it is filled with water.

1.11. References

[1] R. Nagarajan, Amphiphilic Surfactants and Amphiphilic Polymers: Principles of Molecular Assembly, Molecular Sciences and Engineering Team, Natick Soldier Research, Development & Engineering Center, American Chemical Society: Washington DC. (2011).

[2] D.F. Evans, D.J. Michell and B.W. Ninhan, Oil, water, and surfactant: properties and conjectured structure of simple microemulsions, *J. Phys. Chem.* **90** (13) 2817–2825 (1986).

[3] M. J. Rosen, The relationship of structure to properties in surfactants. IV. Effectiveness in surface or interfacial tension reduction, *Journal of Colloid and Interface Science* **56** (2) 320–327 (1976).

[4] J.F.A. Soltero, J.E. Puig, O. Manero and P.C. Schulz, Rheology of Cetyltrimethylammonium Tosilate-Water System. 1. Relation to Phase Behavior, *Langmuir* **11**, 3337-3346 (1995).

[5] S. Hawgood and K. Shiffer, Structures and Properties of the Surfactant-Associated Proteins, *Annual Review of Physiology* **53**, 375-394 (1991).

[6] J. Hao and H. Hoffmann, Self-assembled structures in excess and salt-free catanionic surfactant solutions, *Current Opinion in Colloid & Interface Science*, 9(3), 279–293 (2004).

[7] M.M. Rieger and L.D. Rhein, *Surfactants in Cosmetics*, Marcel Dekker Inc. New York, Basel, (1997).

[8] M. Nedjhioui, N. Moulai-Mostefa, A. Morsli and A. Bensmaili, Combined effects of polymer/surfactant/oil/alkali on physical chemical properties, *Desalination* **185**, 543–550 (2005).

[9] T. T. Nguyen and D. A. Sabatini, Characterization and Emulsification Properties of Rhamnolipid and Sophorolipid Biosurfactants and Their Applications, *Int. J. Mol. Sci. 12*(2), 1232-1244 (2011).

[10] I. M. Banat, R. S. Makkar and S. S. Cameotra, Potential commercial applications of microbial surfactants, *Applied Microbiology and Biotechnology* **53**, 495-508 (2000).

[11] A. Singh, J. D. Van Hamme, O. P. Ward, Surfactants in microbiology and biotechnology: Part 2. Application aspects, Surfactants in microbiology and biotechnology: Part 2. Application aspects, *Biotechnology Advances* **25**, 99-121 (2007).

[12] L. Rodrigues, I. M. Banat, J. Teixeira and R. Oliveira, Biosurfactants: potential applications in medicine, *Journal of Antimicrobial Chemotherapy* **57**, 609–618 (2006).

[13] C. Taupin, *Chapter: The Physicochemistry of Surfactants in Soft Matter Physics*, Editors M. Daoud, C. E. Williams, Springer Verlag Berlin, 133-154 (1999).

[14] V.B. Fainerman, D. Möbius and R. Miller, S*urfactants: Chemistry, Interfacial Properties, Applications*, Elsevier Science, Amsterdam, The Netherlands (2001).

[15] M.J. Rosen and J.T. Kunjappu, *Surfactants and Interfacial Phenomena*, 4th Edition, John Wiley & Sons, Inc. (2012).

[16] E. W. Kaler, K. L. Herrington, A. K. Murthy, J. A. N. Zasadzinski, Phase behavior and structures of mixtures of anionic and cationic surfactants, *J. Phys. Chem.* **96** (16), 6698–6707 (1992).

[17] S. Che, Alfonso E. Garcia-Bennett, T. Yokoi, K. Sakamoto, H. Kunieda, O. Terasaki and T. Tatsumi, A novel anionic surfactant templating route for synthesizing mesoporous silica with unique structure, *Nature Materials* **2**, 801 - 805 (2003).

[18] K. Tsujii, N. Saito and T. Takeuchi, Krafft points of anionic surfactants and their mixtures with special attention to their applicability in hard water, *J. Phys. Chem.* **84** (18), 2287–2291 (1980).

[19] T. Cserháti, E. Forgács and G. Oros, Biological activity and environmental impact of anionic surfactants, *Environment International* **28**, 337-348 (2002).

[20] S.P. Moulik, M.E. Haque, P.K. Jana and A.R. Das, Micellar Properties of Cationic Surfactants in Pure and Mixed States, *J. Phys. Chem.* **100** (2), 701–708 (1996).

[21] E.G. Lomax, *Amphoteric Surfactants*, Second Edition, Volume 59, Marcel Dekker, Inc., New York (1996).

[22] J. Eastoe, J. S. Dalton and R. K. Heenan, Dynamic Surface Tensions and Micelle Structures of Dichained Phosphatidylcholine Surfactant Solutions, *Langmuir* **14** (20), 5719–5724 (1998).

[23] H. Matsuura and K. Fukuhara, Conformational analysis of poly(oxyethylene) chain in aqueous solution as a hydrophilic moiety of nonionic surfactants, *Journal of Molecular Structure* **126**, 251–260 (1985).

[24] *Surfactants: the ubiquitous amphiphiles*, Royal Society of Chemistry (2015).

[25] M.S. Bakshi, P. Sharma, G. Kaur, S. Sachar and T.S. Banipal, Synergisitc mixing of L64 with various surfactants of identical hydrophobicity under the effect of temperature, *Colloids Surf* A **278**, 218 (2006).

[26] R.J. Hunter, *Foundations of colloid science*, Oxford University Press, New York, 1–565 (1987).

[27] M.S. Bakshi and S. Sachar, Influence of hydrophobicity on the mixed micelles of Pluronic F127 and P103 plus cationic surfactant mixtures, *Colloids Surf A* **276**, 146 (2006).

[28] M.S. Bakshi, J. Singh and G. Kaur, Antagonistic mixing behavior of catonic Gemini surfactant and triblock polymers in mixed micelle, *J Colloid Interface Sci* **285**, 403 (2005).

[29] V. Singh, P. Khullar, P. N Dave and N. Kaur, Micelles, mixed micelles, and applications of polyoxypropylene (PPO)-polyoxyethylene (PEO)-polyoxypropylene (PPO) triblock polymers, *International Journal of Industrial Chemistry* **4**, 12 (2013).

[30] M. A. Ward and T. K. Georgiou, Thermoresponsive Polymers for Biomedical Applications, *Polymers* **3**, 1215-1242 (2011).

[31] B.R. Twaites, C.D.H. Alarcon, M. Lavigne, A. Saulnier, S.S. Pennadam, D. Cunliffe, D.C. Gorecki and C. Alexander, Thermoresponsive polymers as gene delivery vectors: Cell viability, DNA transport and transfection Studies, *J. Control. Releas* **108**, 472-483 (2005).

[32] M.C. Hacker, L. Klouda, B.B. Ma, J.D. Kretlow and A.G. Mikos, Synthesis and characterization of injectable, thermally and chemically gelable, amphiphilic poly(N-isopropylacrylamide)-based macromers. *Biomacromolecules* 9, 1558-1570 (2008).

[33] J.R. Trindade, Z.R. Visak, I.M. Marrucho, J.A.P. Coutinho, J.N. Canongia Lopes and L.P.N. Rebelo, Salting-Out Effects in Aqueous Ionic Liquid Solutions: Cloud-Point Temperature Shifts, *J. Phys. Chem. B* **111** (18), 4737–4741 (2007).

[34] K. Shinoda and H. Arai, The Correlation between Phase Inversion Temperature In Emulsion and Cloud Point in Solution of Nonionic Emulsifier, *J. Phys. Chem.* **68** (12), 3485–3490 (1964).

[35] P. M. Holland and D. N. Rubingh, Mixed Surfactant Systems, *American Chemical Society*, 17-30 (1992).

[36] S. Förster and M. Antonietti/Amphiphilic Block Copolymers, *Adv. Mater.* **10**, 200 (1998).

[37] M. Balcı, A. Allı, B. Hazer, O. Güven, K. Cavicchi and M. Cakmak, Synthesis and characterization of novel comb-type amphiphilic graft copolymers containing polypropylene and polyethylene glycol, *Polym. Bull.*, Springer, (2009).

[38] G. Riess, Micellization of block copolymers, *Prog. Polym. Sci.* **28**, 1107 (2003).

[39] P. Alexandridis, T. Alan Hatton, Poly(ethylene oxide)-poly(propylene oxide)-poly (ethylene oxide) block copolymer surfactants in aqueous solutions and at interfaces: thermodynamics, structure, dynamics, and modeling, *Colloids and Surfaces, A: Physicochemical and Engineering Aspects* **96**, 1-46 (1995).

[40] I.R. Schmolka, A review of block polymer surfactants, *J. Am. Oil Chem. Soc.* **54**, 110 (1977).

[41] P. Bahadur and G. Riess, Block Copolymers: A Special Class of. Surfactants, *Tenside Surf. Det.* **28**, 173 (1991).

[42] E.D. Goddard, C.A.J. Hoeve and G.C. Benson, Heats of Micelle Formation of Paraffin Chain Salts in Water, *J. Phys. Chem.* **61**, 593 (1957).

[43] A. Ben-Naim, *Hydrophobic Interactions*, Plenum, New York (1980).

[44] B. Foster, T. Cosgrove and B. Hammouda, Pluronic Triblock Copolymer Systems and Their Interactions with Ibuprofen, *Langmuir* **25**(12), 6760–6766 (2009).

[45] J. Rassing and D. Attwood, Ultrasonic velocity and light scattering studies on polyoxyethylene-polyoxypropylene copolymer pluronic F-127 in aqueous solution, *Int. J. Phann.* **13**, 47-55 (1983).

[46] P. Wang and T.P. Johnson, *J. Appl. Polym. Sci.* 43 (1991).

[47] M. Lazzari, G. Liu and S. Lecommandoux, *Block Copolymers in Nanoscience*, WIiley-VCH Verlag GmbH&Co. KGaA, Weinheim (2006).

[48] G. A. Husseini and W. G. Pitt, Micelles and Nanoparticles for Ultrasonic Drug and Gene Delivery, *Adv Drug Deliv Rev.* **60**(10), 1137–1152 (2008).

[49] D. Y. Alakhova and A. V. Kabanov, Pluronics and MDR Reversal: An Update, *Mol Pharm.* **11**(8), 2566–2578, (2014).

[50] A. V. Kabanov, E. V. Batrakova and V. Y. Alakhov, An essential relationship between ATP depletion and chemosensitizing activity of Pluronic® block copolymers, *J Control Release* **91**(0), 75–83 (2003).

[51] P. Broz, S. M. Benito, C.L. Saw, P. Burger, H. Heider, M. Pfisterer, S. Marsch, W. Meier and P. Hunziker, Cell targeting by a generic receptor-targeted polymer nanocontainer platform, *Journal of Controlled Release* **102**, 475–488 (2005).

[52] J. Safari, Z. Zarnegar, Advanced drug delivery systems: Nanotechnology of health design A review, *Journal of Saudi Chemical Society* **18**(2), 85–99 (2014).

[53] E. V. Batrakova and A. V. Kabanov, Evolution of Drug Delivery Concept from Inert Nanocarriers to Biological Response Modifiers, *J Control Release* **130**(2), 98–106 (2008).

[54] A.V. Kabanov, E.V. Batrakova and V.Y. Alakhov, Pluronic block copolymers as novel polymer therapeutics for drug and gene delivery, *J Control Release* **82**(2-3), 189-212 (2002).

[55] Nippon Kayaku, Development of "dye-sensitized solar cells" - Development of high-efficiency solar cells using organic dyes -, http://www.nipponkayaku.co.jp/english/company/rd/topics.html.

[56] M. Hamidi, M.-A. Shahbazi and K. Rostamizadeh, Copolymers: Efficient Carriers for Intelligent Nanoparticulate Drug Targeting and Gene Therapy, Macromolecular Bioscience **12**, 144-164 (2012).

[57] S. R. Croy and G. S. Kwon, Polymeric micelles for drug delivery. *Curr. Pharm. Des.* 12, 4669-4684 (2006).

[58] A. V. Kabanov and V. Y. Alakhov, Pluronic block copolymers in drug delivery: from micellar nanocontainers to biological response modifiers, *Crit. Rev. Ther. Drug Carrier Syst.* 19, 1-72 (2002).

[59] P. Zou, H.-W. Chen, H. J. Paholak and D.-X. Sun, Burst Release of Lipophilic Drugs from Poly (Ethylene Oxide)- B- Polystyrene Micelles is not Caused by Micelle Disassembly, *Journal of Tumor* 1(2), 7-15 (2013).

[60] A. Sheikh Hasan, M. Socha, A. Lamprecht, F. El Ghazouani, A. Sapin, M. Hoffman, P. Maincent and N. Ubrich, Effect of the Microencapsulation of Nanoparticles on the Reduction of Burst Release, *International Journal of Pharmaceutics* **344**, 53-61 (2007).

[61] X. Huang and C. S. Brazel, On the Importance and Mechanisms of burst Release in Matrix-Controlled Drug Delivery Systems, *Journal of Controlled Release* **73**, 121-136 (2001).

[62] R. Hodge, *The molecules of life, DNA, RNA and proteins, Genetics & Evolution*, New York, (2009).

[63] B. Alberts, A. Johnson, J. Lewis, M. Raff, K. Roberts and Peter Walter, *Molecular Biology of the Cell*, 4th Edition, New York: Garland Science (2002).

[64] M. Bloom, E. Evans and O. G. Mouritsen, Physical properties of the fluid lipid-bilayer component of cell membranes: a perspective, *Quarterly Reviews of Biophysics* **24**, 293-397 (1991).

[65] H. Lodish, A. Berk, S. L. Zipursky, P. Matsudaira, D. Baltimore and J. Darnell, *Molecular Cell Biology*, 4th Edition, New York: W. H. Freeman (2000).

[66] P.L. Luisi and P. Walde, *Giant Vesicles, Perspectives in Supramolecular* Chemistry,Volume 6, *Ziirich,* Switzerland, John Wiley & Sons, LTD Chichester, New York, Weinheim, Brisbane, Singapore, Toronto (2000).

[67] G. van Meer, D. R. Voelker, and G. W. Feigenson, Membrane lipids: where they are and how they behave, *Nat Rev Mol Cell Biol* **9**(2), 112-124 (2008).

[68] W. Hoppe, W. Lohmann, H. Markl and H. Ziegler, Biophysics, Springer-Verlag, Berlin, Heidelberg, New York, Tokyo, 2nd Edition, (1982).

[69] B. Alberts, A. Johnson, J. Lewis, M. Ra, K. Roberts and P. Walter, *Molecular Biology of the Cell*, 4th revised edition. Garland Science, New York (2002).

[70] F. Quemeneur. Relationship between mechanical parameters and behaviour under external stresses in lipid vesicles with modfied membranes. Data Analysis, Statistics and Probability. Université de Grenoble (2010).

[71] C.A. Valcarcel, M. Dalla Serra, C. Potrich, I. Bernhart, M. Tejuca, D. Martinez, F. Pazos, M.E. Lanio and G. Menestrina, Effects of lipid composition on membrane permeabilization by sticholysin I and II, two cytolysins of the sea anemone Stichodactyla helianthus, *Biophys J.* **80**(6), 2761-2774 (2001).

[72] The Nomenclature of Lipids, IUPAC-IUB Commission on Biochemical Nomenclature (CBN), *Eur. J. Biochem.* **79**, 11-21 (1977).

[73] D.E. Vance and J.E. Vance, *Biochemistry of Lipids, Lipoproteins and Membranes*, 1st Edition, The Netherlands (2008).

[74] J. Israelachvili, *Intermolecular and surface forces*, Academic Press, London (1992).

[75] V. A. Frolov, A. V. Shnyrova and Joshua Zimmerberg, Lipid Polymorphisms and Membrane Shape, *Cold Spring Harbor Laboratory Press* **3**, 1-15 (2011).

[76] N. Ridgway and R. Mcleod, *Biochemistry of Lipids, Lipoproteins and Membranes*, 6th Edition, United States of America (2016).

[77] R. Koynova and M. Caffrey, Phases and phase transitions of the phosphatidylcholines, *Biochimica et Biophysica Acta* **1376**, 91–145 (1998).

[78] M. Caffrey, NIST Standard Reference Database 34, Lipid Thermotropic Phase Transition Database (LIPIDAT), Version 1.0. National Institute of Standards and Technology, Gaithersburg, MD 20899, (1993).

[79] R. Koynova and B. Tenchov, Transitions between lamellar and non-lamellar phases in membrane lipids and their physiological roles. *OA Biochemistry* **1**(1), 9 (2013).

[80] B. Tenchov, On the reversibility of the phase-transitions in lipid-water systems, *Chem Phys Lipids* **57**(2–3), 165-77 (1991).

[81] D. Marsh, *Handbook of lipid bilayers*, Second Edition, CRC Press, (1990).

[82] R. Lipowsky and E. Sackmann, *Structure and Dynamics of Membranes, Handbook of Biological Physics*, Elsevier Science, Amsterdam (1995).

[83] P. Walde, K. Cosentino, H. Engel and P. Stanod, Giant vesicles: Preparations and applications, *ChemBioChem*, **11**(7) 848-865, (2010).

[84] G. Camenisch, J. Alsenz, H. van de Waterbeemd and G. Folkers, Estimation of permeability by passive diffusion through Caco-2 cell monolayers using the drugs' lipophilicity and molecular weight, *European Journal of Pharmaceutical Sciences* **6** (4), 313–319 (1998).

[85] F. Zhao, Y. Zhao, Y. Liu, X. Chang, C. Chen and Y. Zhao, Cellular Uptake, Intracellular Trafficking, and Cytotoxicity of Nanomaterials, *Nanotechnology with Soft Matter* **7**(10), 1322–1337 (2011).

[86] J. L. Goldstein, R.G.W. Anderson and M.S. Brown, Coated pits, coated vesicles, and receptor-mediated endocytosis, *Nature* **279**, 679-685 (1979).

[87] B. Alberts, A. Johnson, J. Lewis, M. Raff, K. Roberts and P. Walter, Molecular Biology of the Cell, 4th Edition, New York: Garland Science (2002).

[88] A. Aderem and D. M. Underhil, Mechanisms of phagocytosis in macrophages, *Annual Review of Immunology* **17**, 593-623 (1999).

[89] J.T. Penniston and D.E. Green, The conformational basis of energy transformations in membrane systems: IV. Energized states and pinocytosis in erythrocyte ghosts, *Archives of Biochemistry and Biophysics* **128**(2), 339–350 (1968).

[90] C. Chen, S.W. Smye , M.P. Robinson and J.A. Evans, Membrane electroporation theories: a review, *Medical and Biological Engineering and Computing* **44**(1), 5-14 (2006).

[91] G.L. Andreason and G.A. Evans, Introduction and expression of DNA molecules in eukaryotic cells by electroporation, *BioTechniques* **6**(7), 650-660 (1998).

[92] B. Peng, Y. Zhao, H. Lu, W. Pang and Y. Xu, In vivo plasmid DNA electroporation resulted in transfection of satellite cells and lasting transgene expression in regenerated muscle fibers, *Biochemical and Biophysical Research Communications* **338**, 1490–1498 (2005).

CHAPTER 2

Experimental techniques

2. Experimental techniques

The following experimental techniques: Rheology, Dynamic Light Scattering, ζ-potential and Confocal Microscopy are presented and described in *Sections 2.2* and *7.2*, respectively, of Part I of this thesis.

2.1. Density and sound velocity

The density (ρ) is an intensive property of the matter defined as the ratio between the mass of an object (M) divided by its volume (V) (*Equation 2.1*).

$$\rho = M/V \tag{2.1}$$

The sound speed is the propagation dynamics of sound waves. It depends on the characteristics of the medium and not in the characteristics of the wave or the generating force. For liquids, the sound velocity (υ) is given by the following expression:

$$\upsilon = (K/\rho)^{1/2} \tag{2.2}$$

where K is the compressibility modulus.

The density is one of the mostly used properties of a solution and is needed for the design of many chemical processes. The experimental measurements of density and sound velocity are used to calculate the apparent molar volume (V_ϕ) and the apparent molar adiabatic compression (K_ϕ), which are expressed with the *Equations 2.3* and *2.4.* [1]. Apparent (molar) properties are not constants, even at a given temperature, but are functions of the composition.

$$V_f = \left[\left(\frac{M_w}{\rho} \right) - \left(\frac{(\rho - \rho_0) \times 10^3}{m \times \rho \times \rho_0} \right) \right] \tag{2.3}$$

$$K_f = \left[\frac{(\beta_s - \beta_{s0}) \times 10^3}{m \times \rho_0} + \left(\beta_s \times V_j \right) \right] \tag{2.4}$$

where ρ is the solution density (g/cm³) at the corresponding molality m, ρ_0 is the solvent density and M_w is the molecular weight of the solute (g/mol). β_s and $\beta_{s,0}$ are the adiabatic compressibilities of the solution and the solvent, respectively, and are given by *Equations 2.5* and *2.6*.

$$b_s = \left(\frac{10^{-3}}{u_s^2 \times r}\right)$$ (2.5)

$$b_{s,0} = \left(\frac{10^{-3}}{u_{s,0}^2 \times r}\right)$$ (2.6)

where υ is sound velocity (m/s).

In previous reports in the literature [2], V_ϕ and K_ϕ data obtained from aqueous solutions of some drug compounds have been qualitatively interpreted in terms of solute–solvent and solute–solute interactions. The adiabatic compressibility was correlated with the hydrational behavior of the solute molecule and was found to be sensitive to the structural features of the solute, such as shape, size, branching, and presence of aromatic rings.

2.2. Viscosity

Viscosity is a measure of its resistance to gradual deformation by shear stress or tensile stress. In this chapter, viscosity measurements are performed in a falling ball viscometer that measures the displacement time of a ball through transparent and opaque liquids according to Höppler's falling ball principle.

The falling ball viscometer measures the viscosity of Newtonian liquids and gases. The method applies Newton's law on a falling sphere ball when it reaches a terminal velocity. The rolling and sliding movement of the ball through the liquid sample are studied in an inclined cylindrical measuring tube. The dynamic viscosity of the sample is obtained through the correlation with the time required by the ball to travel a specific distance [3].

2.3. Fluorescence spectrophotometry

2.3.1. Absorption and emission of light

Fluorophores, also known as chromophores, are substances that produce a molecule to absorb energy of a specific wavelength and then to remit energy at a different wavelength, which will depend on the fluorophore and the chemical environment [4].

To account sufficiently for the processes of absorption and emission of light, we need to assume that radiant energy can only be absorbed in definite units, or *quanta*. The energy, E, carried by any

quanta is proportional to its frequency of oscillation as follows:

$$E = h\upsilon_f = hc/\lambda \qquad\qquad (2.7)$$

where υ_f is the frequency, λ the wavelength and h is Planck's constant (6.624 x 10^{-27} ergs/second).

Since the energy of a single quantum is too small, then it is usual to refer to the energy associated with N_A quanta (where N_A is Avogadro's number 6.023 x 10^{23}), which is called an Einstein. In fluorimetry, the ultraviolet and visible regions of the spectrum are the most interesting regions since absorption causes the excitation of the most electrons of the molecule.

Excitation leads a molecule to reach any of the vibrational sub-levels associated with each electronic state. Since the energy is absorbed as discrete quanta, this should result in a series of distinct absorption bands [5].

A plot of emission against wavelength for any given excitation wavelength is known as the emission spectrum. An excitation spectrum corresponds to the plot of the emission from the sample against the wavelength of exciting light when the wavelength of the exciting light is changed. Additionally, if the intensity of exciting light is constant as its wavelength is changed, the plot of emission against exciting wavelength is known as the corrected excitation spectrum [5].

2.3.2. The fluorescence process

Fluorescence is the result of a three-stage process that takes place in fluorophores (generally polyaromatic hydrocarbons or heterocycles). A fluorescent probe is a fluorophore developed to localize within a specific region of a biological species or to respond to a particular stimulus.
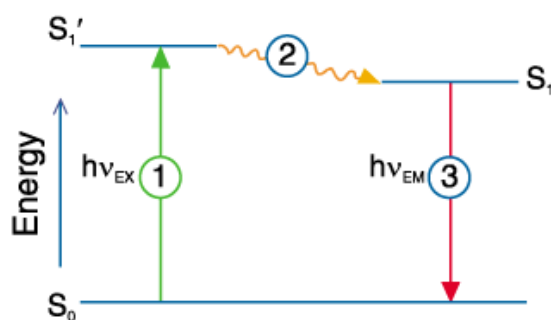
Figure 2.1. *Schematic representation of fluorescence three-stage process* [6].

Jablonski diagram, presented in *Figure 2.1*, illustrates the process involved in the production of an

excited electronic singlet state by absorption and then the emission of fluorescence [6]. First stage (1) corresponds to the excitation stage. Here, a photon of energy $h\upsilon_{ex}$ is supplied by an external source such as a laser and is then absorbed by the fluorophore, creating an excited electronic singlet state (S_1'). This process makes the distinction between fluorescence and chemiluminescence, in which the excited state is occupied by a chemical reaction.

Stage (2) corresponds to the excited-state lifetime. The excited state stays for a finite time (usually from 1 to 10 ns). During this time, the fluorophore undergoes conformational changes and is undergoes several interactions with its molecular environment. These processes have two important consequences: the energy of S_1' is moderately dissipated, yielding a relaxed singlet excited state (S_1) from which fluorescence emission is originated. Then, not all the molecules initially excited by absorption, during stage 1, return to the ground state (S_0) by fluorescence emission.

Finally, stage (3) is the fluorescence emission. A photon of energy $h\upsilon_{em}$ is emitted, returning the fluorophore to its ground state S_0. Here, the energy of the photon is lower, due to energy dissipation during excited-state lifetime, consequently of longer wavelength, than the excitation photon $h\upsilon_{ex}$. *Figure 2.2* shows a schematic representation of the excitation of a fluorophore at three different wavelengths.

All the fluorescence process is a cyclic process. Except if the fluorophore is irreversibly destroyed in the excited state, which is an important phenomenon known as photobleaching, the same fluorophore can be repeatedly excited and detected. The high sensitivity of fluorescence detection techniques is due the fact that a single fluorophore can generate a great amount of detectable photons.
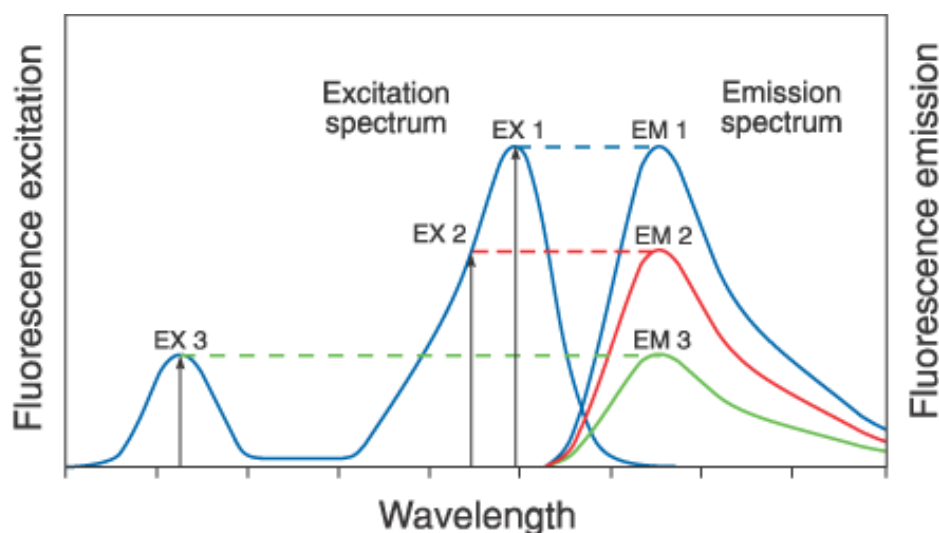
Figure 2.2. *Excitation of a fluorophore at three different wavelengths [6].*

2.4. References

[1] J.G. Álvarez-Ramírez, V.V.A. Fernández, E.R. Macías, Y. Rharbi, P. Taboada, R. Gámez-Corrales, J.E. Puig and J.F.A. Soltero, Phase behavior of the Pluronic P103/water system in the dilute and semi-dilute regimes, *Journal of Colloid and Interface Science* **333**, 655-662 (2009).

[2] M. Iqbal and R. E. Verrall, Apparent molar volume and adiabatic compressibility studies of aqueous solutions of some drug compounds at 25 °C, *Canadian Journal of Chemistry* **67**(4), 727-735 (1989).

[3] P. Yuan and B.-Y. Lin, Measurement of Viscosity in a Vertical Falling Ball Viscometer, technical article EMD Millipore, Germany (2008).

[4] M. Sauer, J. Hofkens, and J. Enderlein Handbook of Fluorescence Spectroscopy and Imaging. WILEY-VCH Verlag GmbH & Co. KGaA, Weinheim (2011).

[5] D.M. Hercules, *Fluorescence and phosphorescence analysts*, Editor Wiley-Interscience Publishers, New York, London, Sydney (1965).

[6] B. Valeur and J.C. Brochon, New trends in Fluorescence Spectroscopy, Applications to Chemical and Life Sciences, Springer Series on Fluorescence, Methos and Applications, Springer, Berlin (2001).

CHAPTER 3

Structural and rheological behavior of P104 triblock copolymer

3. Structural and rheological behavior of P104 triblock copolymer

The results of this chapter are the object of the following proceeding:

Triblock copolymer P104 detailed behavior through a density, sound velocity and DLS study

L. M. Bravo-Anaya, C. Fierro-Castro, Y. Rharbi and J. F. A. Soltero Martínez.

AIP Conference Proceedings **1599**, 481 (2014); doi: 10.1063/1.4876883

3.1. Introduction

Amphiphilic block copolymers are known by their efficiency during drug delivery processes with multiple effects [1,2]. The incorporation of drugs into the micelles core formed by these copolymers may lead to an increment of solubility, metabolic stability and circulation time for the drug [3]. In this manner, the core-shell design of the micelles is crucial for their effectiveness in drug delivery [4]. It is worth to mention that the core is a water-incompatible compartment that is segregated from the aqueous exterior by the hydrophilic chains of the shell, able to receive the incorporation of several therapeutic reagents [5]. It is also possible to select several block copolymers with different properties for specific pharmaceutical applications such as gene delivery [6-8]. Recently, the interactions of the triblock copolymer unimers with multidrug-resistant cancer cells have been studied, resulting in the sensitization of these cells with respect to various anticancer agents [7,9].

All these applications highly depend on the triblock copolymer structure. In this manner, in water, they can form micelles above the critical micellar temperature (CMT) and the critical micellar concentration (CMC). In these amphiphilic triblock copolymers, it has been reported that the CMC decreases rapidly as temperature increases and that the CMT decreases as copolymer concentration increases [10-12]. Furthermore, the spherical micelles grow to form worm-like micelles as the temperature or the amphiphilic triblock copolymer concentration is increased. This growth process is characterized by a drastic viscosity increase of several orders of magnitude [13,14]. The phase behavior of theses copolymers in water is extremely dependent on temperature and the relative block sizes [15]. Moreover, at higher concentrations and temperatures they tend to form a great diversity of lyotropic liquid crystals [16,17].

In order to determine the formation and morphology of P104 structures in aqueous solution, a detailed P104/water phase diagram in the dilute and semi-dilute regions was elaborated using rheology, dynamic light scattering (DLS), viscosity (η), density (ρ) and sound velocity (υ) measurements. With the obtained information we observed the transition zone between monomers and micelles, i.e. where P104 monomers are in thermodynamic equilibrium with micelles, then the formation of spherical micelles, the

sphere to rod-like micelles transition, and finally, the cloud point temperature. It is worth to mention that in the literature there are several reports of different studies on these copolymers, however, their results differ from each other since they were done with different batchs. Here we are relating the results of different techniques on the same batch of P104 triblock copolymer. Also, all the studies that are presented in the following chapters of this thesis were carried out with this P104 block copolymer, so it's characterization is of great interest.

3.2. Experimental conditions

3.2.1. Materials and solutions preparation

Triblock copolymer Pluronic® P104, $[(PEO)_{27}–(PPO)_{61}–(PEO)_{27}]$, has a molecular weight of 5900 g/mol. This material was provided by the BASF Company. $P104/H_2O$ and P104/NaCl solutions were prepared with water obtained through a Millipore Milli-Q purification system and with sodium chloride (NaCl) in powder supplied by Sigma-Aldrich and dissolved in purified water, respectively.

P104 solutions were prepared with adequate amounts of P104 triblock copolymer, respectively, and with distilled, deionized water. They were stored in 20 mL glass vials, which were placed on a mechanical shaker for 12 hours to homogenize the solution. Then, each solution was covered with aluminum foil to avoid contact with light and therefore the degradation of the sample. Each solution reached the equilibrium temperature in 24 hours. The solutions were prepared within the concentration range from $1x10^{-3}$ to 500 mg/mL.

3.2.2. Density and sound velocity measurements

Density and ultrasound velocity were continuously and automatically measured using an Anton Paar DSA 5000 densimeter and a sound velocity analyzer. Since density and ultrasound velocity speed are strongly sensitive to temperature, the Peltier method was used to keep the temperature constant to within $\pm 1x10^{-3}$ K. Density and ultrasound measurements reproducibility are $\pm 1x10^{-6}$ g cm^{-3} and $\pm 1x10^{-2}$ m/s, respectively. The measurements were performed at a P104 concentration range from $1x10^{-3}$ to 150 mg/mL in the temperature range from 5 to 60 °C.

3.2.3. Viscosity measurements

Viscosity measurements were performed in an automatic viscometer AMVn from Anton Paar Company for P104 concentrations from $1x10^{-3}$ to 100 mg/mL at the temperatures of 10, 20, 30, 40 and 50 °C, starting from the highest temperature and including 5 replicates for each measurement. A

temperature sweep was carried out for P104 concentrations of 10, 20 and 30 mg/mL by taking viscosity values every two degrees in the temperature range from 6 to 80 °C. All samples were analyzed at different inclination angles, i.e. 30 °, 50 ° and 70 °.

3.2.4. Dynamic Light Scattering measurements

Dynamic light scattering (DLS) measurements were performed in a Malvern Zetasizer 5000 instrument equipped with a 7132 multibit correlator and multiangles goniometer. The light source was a laser of He-Ne (5 mW) with a wavelength of 632.8 nm. The scattering intensity was measured through a 400 μm pinhole. DLS measurements for P104 were carried out at 45, 90 and 135 ° for a temperature range between 10 and 64 ºC.

3.2.5. Rheological measurements in the linear domain

The rheological behavior of P104/water system was studied in the rheometer AR-G2 from the TA Instruments Company.

Two different geometries were used depending on P104 concentration:

1.- Steel cone with a 60 mm diameter and an angle of 1º was used for P104 solutions with concentrations between 10 and 250 mg/mL.

2.- Steel cone with a 40 mm diameter and an angle of 2º was used for P104 solutions with concentrations between 250 and 600 mg/mL.

3.2.5.1. Strain sweeps

In order to define the linear viscoelastic regimes, the oscillation strain sweeps were carried out at an angular frequency of 10 rad/s in a strain range between 0.1% and 100% and using 10 points per decade. For each P104 sample, each sweep was performed at different temperatures depending on the chosen concentration.

3.2.5.2. Temperature sweeps

These sweeps were performed using a selected strain in the linear viscoelastic region, applying an angular frequency of 10 rad/s in a temperature range from 1 to 90 °C with a heating rate of 1 °C/min.

3.3. Experimental results

3.3.1. P104 micellization in water evaluated through density and sound velocity

The study of the dependence of density and sound velocity with concentration and temperature give information in order to determine the regions where only unimers of amphiphilic block copolymers exist, the formation of spherical micelles as well as their maximum formation rate and the sphere-to-rod like micelles transition [18].

Figure 3.1 shows the behavior of P104 density as a function of temperature for several P104 concentrations. Here we can observe the increase of density with P104 concentration, as expected, and the decrease of density with temperature up to a critical temperature T_i, where a more pronounced decrease is identified. T_i shifts to lower temperature while increasing P104 concentration. A second critical temperature is identified as T_f and is the onset at which density starts decreasing monotonically with temperature. As for P103 [18] and P94 [19] triblock copolymers, this transition is related to micelle formation due to dehydration around the hydrophobic PPO segments, which form the core, and more hydrophilic hydrated PEO segments that for the corona. This transition is then attributed to the critical micellar temperature (CMT) and decreases as P104 concentration increase.
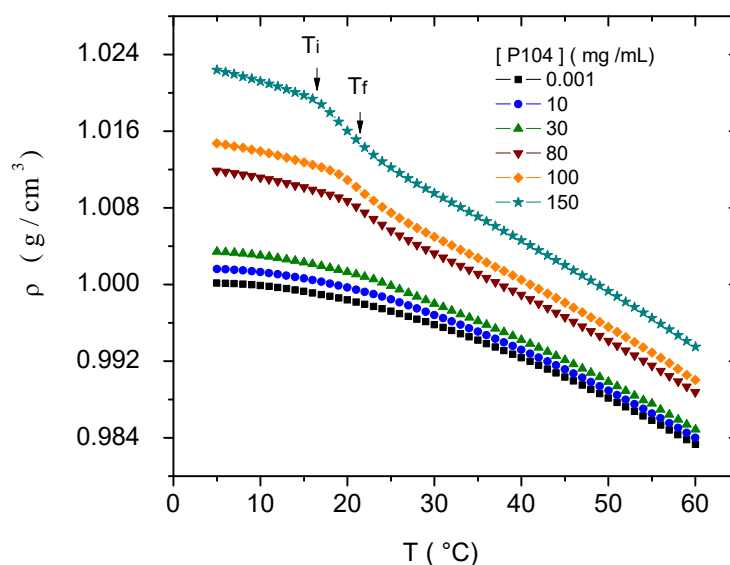
Figure 3.1. *Density (ρ) as a function of temperatures for different P104 concentrations: 0.001, 10, 30, 80, 100 and 150 mg/mL.*

Figure 3.2 shows the dependence of P104 sound velocity as a function of temperature for several P104 concentrations. We can observe that the transition temperature T_i shifts to lower values when P104 concentration increases and is nearly the same than the value determined through density measurements. At lower temperatures than T_i, the P104 unimers increase with concentration, so sound

velocity increases with P104 concentration increment. Nevertheless, at the onset of micellization, the unimers start to aggregate due the increase of temperature and the dehydration of PPO segments, resulting in a drop of sound velocity caused by the decrease on the number of effective particles in the solution [18]. This transition is then related to the critical micellar transition (CMT). The obtained values are consistent with literature reports [10]. After the transition temperature, since P104 concentration and temperature increase, the size of micellar aggregates also increases, leading to stronger interactions among them and to a decrease in their number density, which results in the decrease of sound velocity values.
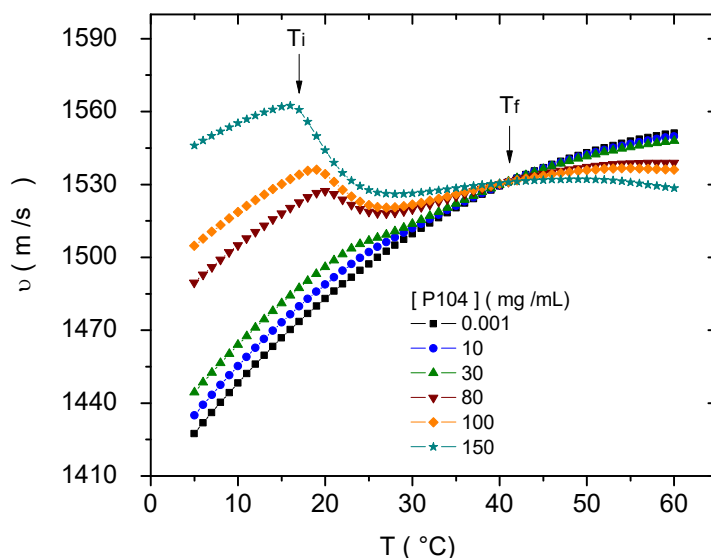
Figure 3.2. *Sound velocity (υ) as a function of temperatures for different P104 concentrations: 0.001, 10, 30, 80, 100 and 150 mg/mL.*

3.3.2. Evaluation of the apparent molar adiabatic compressibility

The apparent molar adiabatic compression (K_ϕ) was calculated by using *Equation 2.4*, which is directly related with the apparent molar volume (V_ϕ). *Figure 3.3* shows the apparent molar adiabatic compressibility (K_ϕ) as a function of temperature for several P104 concentrations. Two linear regions with a sharp increase with temperature are depicted in all the curves. First onset is directly with the CMT, as previously described.

Figure 3.4 shows the temperature dependence of the first derivative of K_ϕ as a function of temperature. A sharp peak is detected for each P104 concentration and is directly related with the onset of micellization, i.e. the CMT. As expected, a shift of the position of the peaks to lower values of

317

temperature is observed with the increase on temperature. At higher temperatures, a slight shoulder is detected around 55 °C, which could be related to a transition from micelles to rod-like micelles. However, since micellization of P104 block copolymer takes place at higher temperatures than other triblock copolymers [10-12,18], the use of techniques such as density measurements is limited.
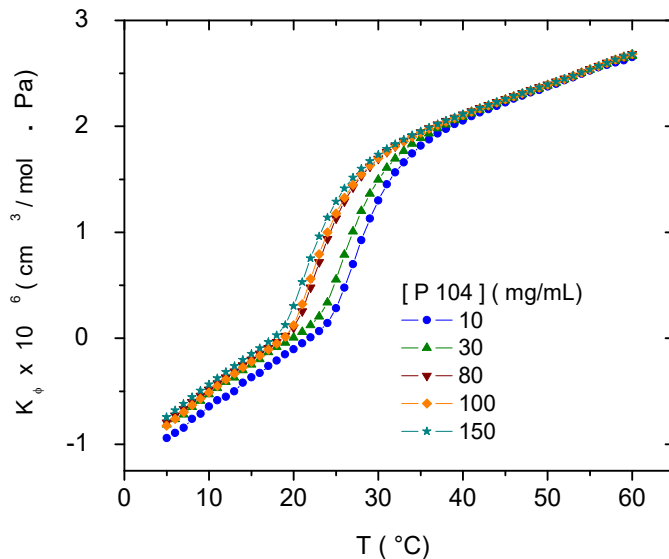
Figure 3.3. *Apparent molar adiabatic compressibility (K_ϕ) as a function of temperature for several P104 concentrations: 10, 30, 80, 100 and 150 mg/mL.*
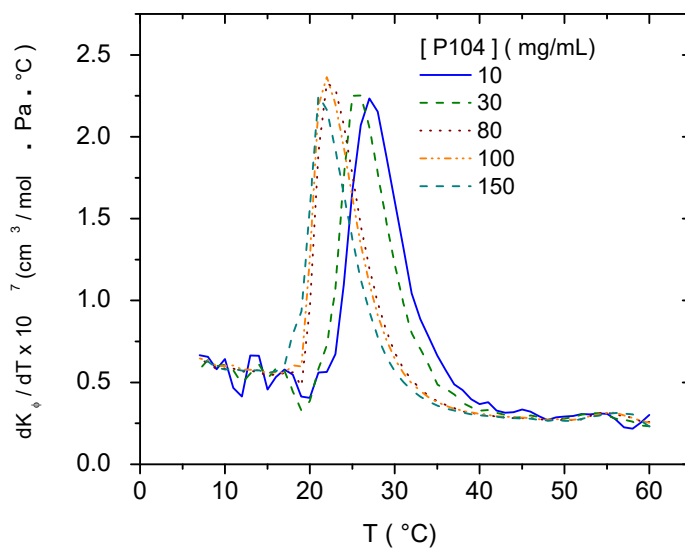
Figure 3.4. *Temperature dependence of apparent molar adiabatic compressibility derivative (dK_ϕ/dT) for different P104 concentrations: 10, 30, 80, 100 and 150 mg/mL.*

3.3.3. P104 micellization in water evaluated through viscosity measurements

The effect of temperature on the viscosity of P104 samples was analyzed to corroborate the phase transitions previously observed and the structural changes determined by ultrasound and density measurements and DLS. *Figure 3.5* shows the obtained profiles for the viscosity as a function of temperature for P104 solutions at the flowing concentrations: 10, 20 and 30 mg/mL. As expected, an increase on viscosity is observed with the increase on P104 concentration, as well as the decrease of viscosity with the increase on temperature.
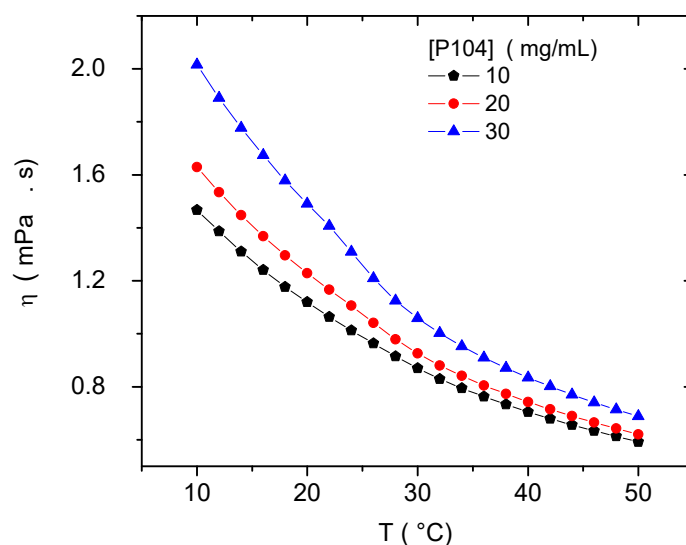
Figure 3.5. *Dynamic viscosity as a function of temperature for P104 concentrations of 10, 20 and 30 mg/mL. The measurements were carried out at 30º, 50º and 70º.*
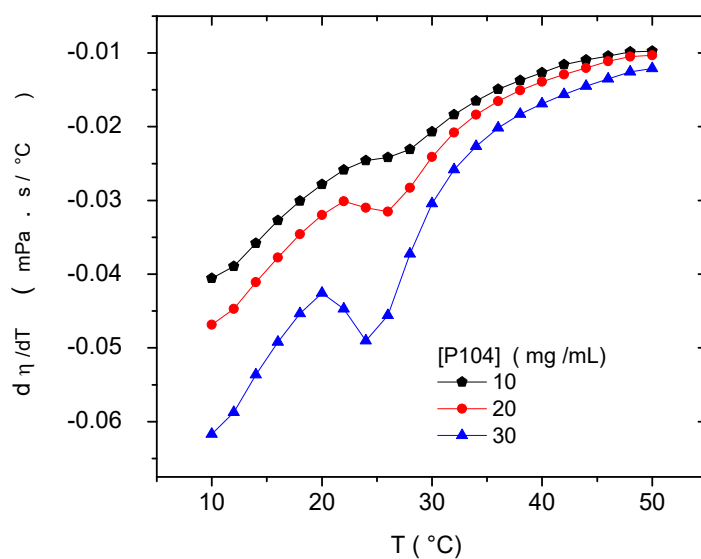
Figure 3.6. *Dependence of dη/dT with temperature for P104 concentrations of of 10, 20 and 30 mg/mL. The measurements were carried out at 30º, 50º and 70º.*

The first derivative of the viscosity with temperature allows detecting the transitions of P104 in water as a function of temperature. *Figure 3.6* shows the variation of $d\eta/dT$ with temperature for P104 concentrations of of 10, 20 and 30 mg/mL. A noticeable change is observed between 24 and 27 °C, depending on P104 concentration, and is related to the critical micellar transition (CMT), representing the onset of micellization when unimers start to aggregate due the increase of temperature and the dehydration of PPO segments. These results are in good agreement with the obtained values through density and sound velocity measurements, previously presented and discussed.

3.3.4. Morphology of P104 micelles in water by Dynamic Light Scattering (DLS)

Dynamic Light Scattering (DLS) measurements were performed in a temperature range from 10 to 64 °C to obtain, as first approximation, information about the shape of the micelles from the combination of the scattering intensity and the hydrodynamic radius [21,22]. DLS measurements normally use the Stokes-Einstein equation (*Equation 3.1*) in order to obtain the information about the hydrodynamic radius through the measured diffusion coefficient (D). The experiments are usually carried out at low concentrations since they are affected by this parameter. However, we noticed that between 10 and 20 mg/mL, we still have reliable data. Above these concentrations, we measure an apparent diffusion coefficient and a smaller apparent hydrodynamic radius is obtained.

$$R_h = \frac{k_B T}{6 \rho h_s D} \tag{3.1}$$

Here, k is the Boltzmann constant, η_s is the viscosity of the solvent and T is the absolute temperature.

Figure 3.7 shows the temperature dependence of the hydrodynamic radius, R_h, and the scattered light intensity for a P104 solution at a concentration of 10 mg/mL in water, from which it is possible to determinate that micelles form in a temperature range between 26 and 54 °C with an average size of 11.4 ± 1 nm. An increment in both the R_h and the scattered light intensity is observed after the temperature of 55 °C. The scattered light intensity is low at the temperatures below 26 °C, which is related with the presence of unimers in the solution [23]. In this manner, the temperature of 26 °C corresponds to the CMT of P104 triblock copolymer at this concentration, which is in good agreement with the CMT temperature reported by *Alexandridis et al.* [24] for a P104 concentration of 10 mg/mL in water. After the CMT, the scattered light intensity starts to increase with temperature and remains almost constant between the temperature range of 26 and 54 °C. However, after 55 °C, it increases progressively until reaching a two-magnitude order difference from the initial value, suggesting the appearance of a new P104 structure. This transition in good agreement with the one obtained through the evaluation of dK_ϕ/dT as a function of temperature. This phenomenum has been presented in terms

of the enhanced dehydration of the micelle corona, consisting essentially of PEO, with temperature increase [24,25].
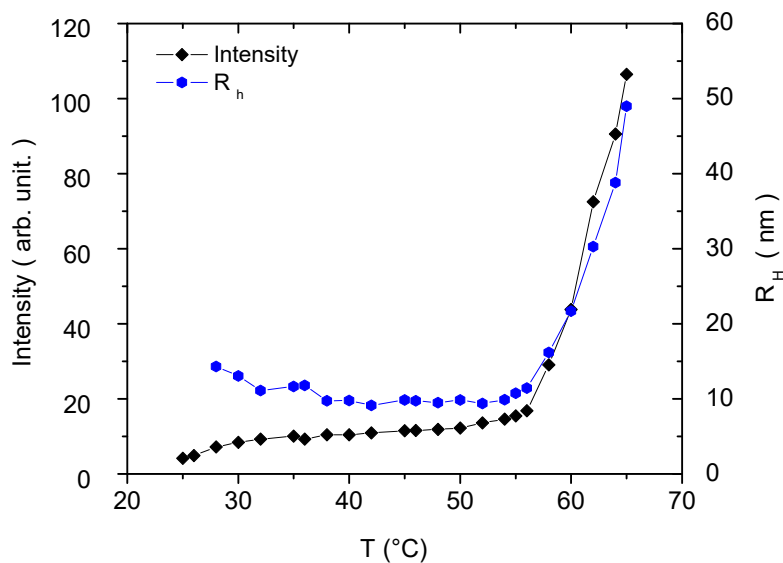
Figure 3.7. *Temperature dependence of the hydrodynamic radius and the scattered light intensity for 10 mg/mL P104 solution in water measured at 90 °. The sample was equilibrated during 24h before each measurement.*

The formation of new structures is determined with the variations of the intrinsic asymmetry [Z], obtained through the relation of the scattering intensity values measured at 45° and the scattering intensity values measured at 135° ($I_{45°}$ /$I_{135°}$).
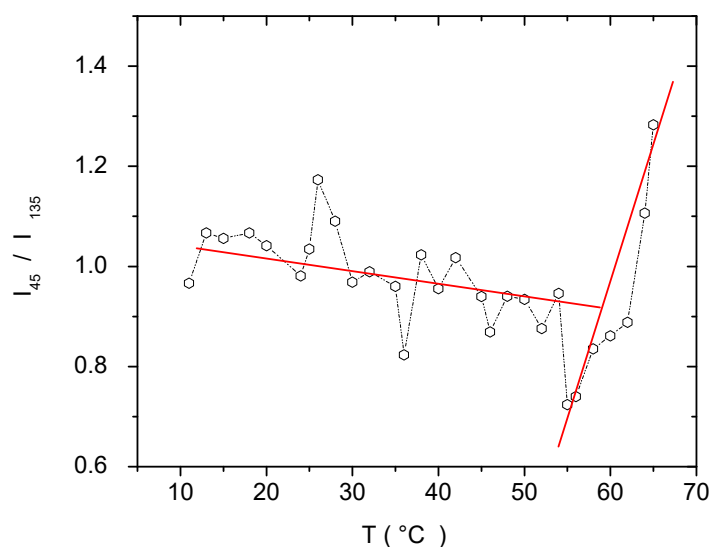
Figure 3.8. *Intrinsic asymmetry [Z]=$I_{45°}$ /$I_{135°}$ as a function of temperature P104 concentration of 10 mg/mL. $I_{45°}$ and $I_{135°}$ are the scattering intensity measured at 45 ° and 135 ° respectively.*

Figure 3.8 presents the aspect factor $I_{45°}/I_{135°}$ as a function of temperature for a P104 solution at a concentration of 10 mg/mL in water, where it is possible to observe the onset of an $I_{45°}/I_{135°}$ ratio different than 1.0 at the temperature of 54 ºC. The ratio between the characteristic dimension of the structure and the wavelength (D/λ) is found to be around 0.04 when $[Z]\approx1$, i.e. between 10 and 54 ºC, suggesting spherical micelle morphology. Then, the growth of micelles is detected at higher temperatures.
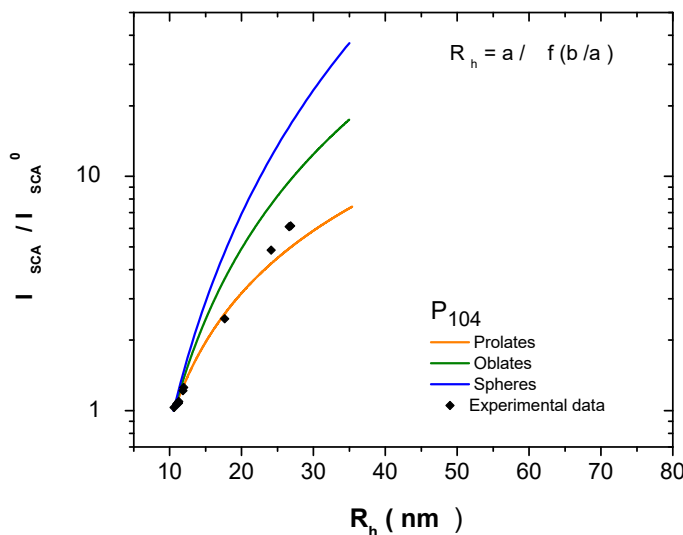
Figure 3.9. *Scattered intensity I_{SCA}/I_{SCA}^0 plotted as a function of the hydrodynamic radius R_h for a 10 mg/mL P104 solution in water. I_{SCA} and R_h are measured at various temperatures and I_{SCA}^0 is the scattering intensity at 38ºC. The plot I_{SCA}/I_{SCA}^0 is compared to the Perrin model of prolate ellipsoids, oblate ellipsoids and spheres.*

On the other side, the combination of the hydrodynamic radius and the scattered light intensity allow obtaining another approximation about the shape of micelles [26]. The Perrin model is used to estimate the dimensions of micelles for prolate and oblate ellipsoids [27-29]. The expression for the prolate case is given by the following equation:

$$R_h = (b/2) \times \frac{\sqrt{p^2-1}}{\ln(P+\sqrt{p^2-1})} \tag{3.1}$$

where $p=a/b$, b corresponds to the semiminor axis and a corresponds to the semimajor axis. For prolate, a is the micelle length L and b corresponds to the diameter of the spherical micelle $b=2R_h^0$. R_h^0 being the hydrodynamic radius at 38 ºC.

On the other side, the expression for the oblate ellipsoid is given by the following equation:

$$R_h = (a/2) \times \frac{\sqrt{(1/p)^2 - 1}}{\arctan(\sqrt{(1/p)^2 - 1})} \qquad (3.2)$$

where $a = 2R_h^0$.

The volume of the micelle (V_{mic}) is given by the following expression:

$$I_{SCA} a V_{mic} P(q) \qquad (3.3)$$

where I_{SCA} is the total scattering intensity and $P(q)$ is the micelle form factor. $P(q)$ for sphere, prolate and oblate ellipsoids can be calculated using the Debye and Anacker equation [29].

Figure 3.9 shows the scattered intensity I_{SCA}/I_{SCA}^0 as a function of the hydrodynamic radius R_h for a 10 mg/mL P104 solution in water. The plot I_{SCA}/I_{SCA}^0 is compared to the Perrin model of prolate ellipsoids, oblate ellipsoids and spheres. I_{SCA} and R_h were measured at six different temperatures from the spherical micelles domain to the elongated micelles domain. I_{SCA}^0 is the scattering intensity taken at 38 ºC, which corresponds to the temperature chosen as the initial one, in the spherical micelles domain. The dependence of I_{SCA}/I_{SCA}^0 with R_h is close to the predicted behavior for prolate ellipsoids, which suggest that P104 micelles grow as prolate rods. This behavior was previously obtained for P103 micelles [23].

From this study, a spherical micelle morphology of P104 triblock copolymer was firstly proposed since the scattering intensity did not show any dependence on the scattering angle. Above 54 °C, both the scattering intensity (I_{SCA}) and R_h increase steadily with increasing temperature, suggesting a structural transition from spheres to elongated micelles. This conclusion was supported by the variation of the aspect factor ($I_{45°}/I_{135}$) from ~1 between 25 and 54 °C to above 1.5 for T > 54 °C. The dependence of I_{SCA} on R_h was also compared with the Perrin model, taking $b = 2R_h^0$ and $a = 2R_h^0$ for prolate ellipsoid and oblate ellipsoid respectively, from which a small problate rod growth was determined.

In terms of the applications, the obtained micellar structure for P104 amphiphilic copolymer in the temperature range between 25 and 55 ºC (spherical micelles domain) can be used as micellar nanocarriers for drug controlled release. Firstly, their nanoscale size makes them a suitable option for targeted drug delivery applications, including storage, controlled release and protection of the hydrophobic drugs. Contrary to P103 triblock copolymer, which starts to aggregate at 37 ºC, the spherical micellar stability of P104 at the temperature of 37 ºC becomes a good selection in order to maintain a determined shape at the average body temperature, which could be then degraded through a determined stimulation (temperature, pH or ionic strength variations) in order to release the hydrophobic drug. It becomes evident that the shape of micelles is affected by temperature, which can be

exploited for the design of new formulations. These stimuli-responsive materials present a great advantage for drug targeting strategies, allowing the drug delivery system to respond in a specific way.

3.3.5. Morphology of P104 micelles in NaCl

It is well known that the self-assembly behaviors of amphiphilic block copolymers in aqueous solutions can be affected by varying temperature [31], water-soluble electrolytes [32] and solvent [33]. For vectorization applications, the effects of salts on triblock copolymers morphology needs to be studied in order to understand the variations caused due to different ionic strength environments.
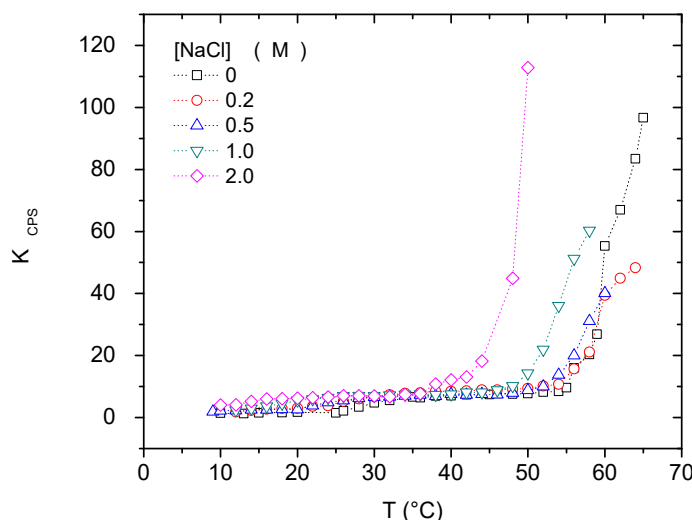
Figure 3.10. *Scattered light intensity measured at an angle of 90º for a P104 solution with a concentration of 10 mg/mL in presence water and in 0.2, 0.5, 1.0 and 2.0 M NaCl.*

Firstly, the scattered light intensity was then monitored as a function of temperature for P104 solutions at a constant concentration of 10 mg/mL P104 but in presence of different concentrations of NaCl, measured at a constant angle of 90 º (*Figure 3.10*). The observed trend is the same for all curves, detecting the presence of a regime with spherical micelles and another one with rod-like micelles [22-25]. However, we can observe a shift of the spherical micelles region to lower temperatures with the increment of salt concentration, so the addition of NaCl facilitates the process of sphere to rod-like micelles transition at lower temperatures [34,35]. In this manner, and according to several reports on the literature, the greater propensity of sphere-to rodlike transition is related to an increase of micelle dehydration (decrease in solubility) [31-35]. As it is possible to observe in our results, it would be possible to work with NaCl concentrations up to 1.0 M at 37 ºC, since at higher NaCl concentrations, the CMT decreases considerably.

The influence of the addition of the inorganic salt NaCl to P104 triblock copolymer solutions was then studied through the determination of the variation of the CMT (critical micellar temperature), the MGT (micellar growth temperature) and the CPT (cloud point temperature) of P104 solutions with different NaCl amounts. *Figure 3.10* shows the dependence of the CMT, MGT and CPT with NaCl concentration for a 10 mg/mL P104 solution. We can observe that the temperature range for solubility of the triblock copolymer or CPT, the CMT and the MGT decrease with the increase on NaCl concentration. The addition of inorganic salts dehydrates the ethylene oxide chains and reduces the critical temperatures of the solutions [32]. The addition of NaCl to amphiphilic block copolymer P104 induces micellization in a similar way that temperature does, this way, the temperatures of the micellar sphere to rod-like micelles transition and cloud points are shifted to lower values [36]. In this manner, the addition of a simple salt is a simple way to modify the properties of an amphiphilic triblock copolymer solution in order to have a specific behavior in a desired temperature range, which can be exploited in the development of drug nanocarriers for the specific drug delivery. In the same way, the increase on the ionic strength is another stimulus that will allow a specific realese of a hydrophobic drug.
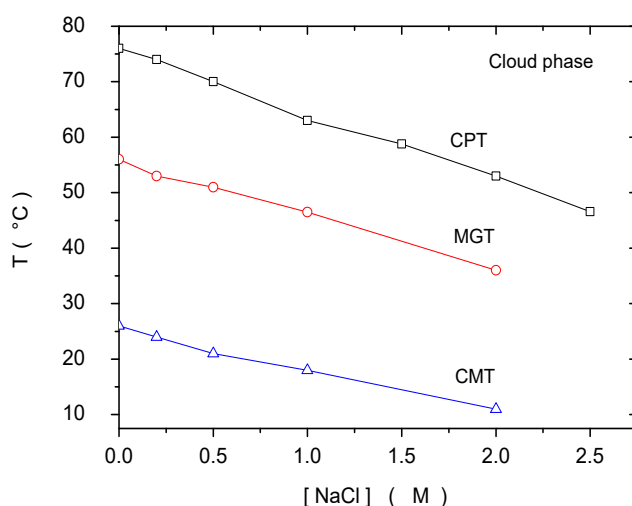
Figure 3.10. *Dependence of the CMT, MGT and CPT of a P104 solution with a concentration of 10 mg/mL with NaCl concentration.*

3.3.6. Rheological measurements

The hydrophobic core of PPO in amphiphilic triblock copolymers is used to give the delayed release of hydrophobic drugs. At higher concentrations and temperatures, some of these copolymers solutions form thermo-reversible and physical gels [37,38]. These gels consist of liquid crystals of packed spherical or rod-like micelles. Rheological measurements allow studying different properties of the materials useful in many biomedical applications [39,40].

3.3.6.1. Linear Viscoelastic Region

Strain sweeps for a P104 concentration range between 50 and 600 mg/mL were performed in order to identify the linear viscoelastic region (LVR) as a function of temperature. *Figure 3.11 a* and *b* show the strain dependence of G' and G'' for P104 concentration of 50 mg/mL at the temperature of 75 ºC and for a P104 concentration of 350 mg/mL at the temperature of 65 ºC, respectively. We can observe that for a P104 concentration of 50 mg/mL, at strains less than the 20%, G' and G'' are independent of γ, however, for a P104 concentration of 350 mg/mL G' and G'' are independent of γ at strains less than the 1.0%. In this manner, it was found that the LVR is highly dependent in both P104 concentration and temperature. *Table 3.1* summarizes the %γ where G' and G'' are independent of γ for several P104 concentrations at different temperatures.
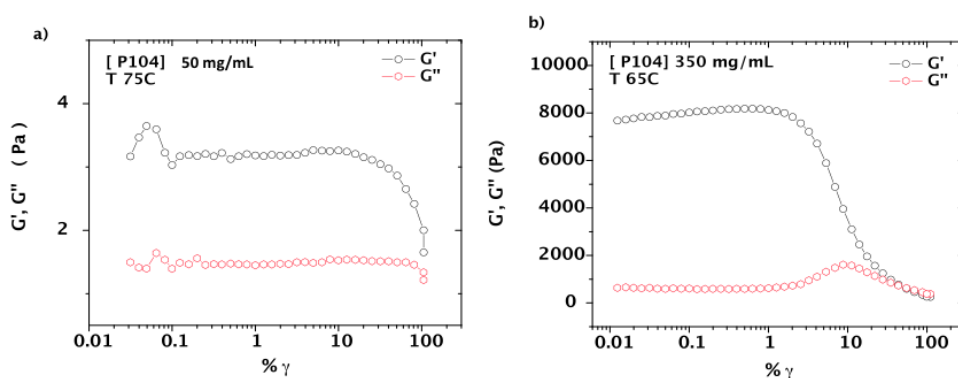
Figure 3.11. *Strain dependence of G' and G'' for a) P104 concentration of 50 mg/mL at the temperature of 75 ºC and for b) P104 concentration of 350 mg/mL at the temperature of 65 ºC.*

Table 3.1.- *Linear viscoelastic region (LVR) for several P104 concentrations at different temperatures.*

[P104] (mg/mL)	T (ºC)	%γ
50	40	40
	75	12
100	20	80
	30	80
	70	2.0
150	40	90
	70	1.0
200	50	90
	70	0.1
250	20	100
	30	0.1
	70	0.5
350	30	0.2
	65	0.7
400	20	0.1
	60	1.0
600	20	0.4
	45	0.4

3.3.6.2. Temperature sweeps

Figure 3.12 presents a set of plots showing the temperature dependence on the storage and loss modulus for different P104 concentrations, i.e. 100, 150, 200 and 225 mg/mL. For P104 concentration of 100 mg/mL (*Figure 3.12 a*), a viscous behavior (G''>G') is firstly observed within the temperature range from 3 to 20 °C. A first crossover of G' and G'' is then observed around the temperature 20 °C. The loss modulus is then independent of the temperature until reaching the temperature of 58 °C, at which a large increase of two orders of magnitude is observed, changing from the dilute to the soft gel domain. A drop of both G' and G'' values is then observed at the temperature of 81 °C, at which the soft gel condition returns to a liquid condition. *Figure 3.12 b* shows the temperature dependence of G' and G'' for the P104 concentration of 150 mg/mL. A similar behavior to the one obtained for P104 concentration of 100 mg/mL is observed. Here, the loss and the storage modulus are independent of the temperature until reaching the temperature of 60 °C, at which a large increase of also two orders of magnitude is observed, changing from the dilute to the soft gel domain. The drop of both G' and G'' values is slightly shifted to higher values of temperature, i.e. 85 °C.
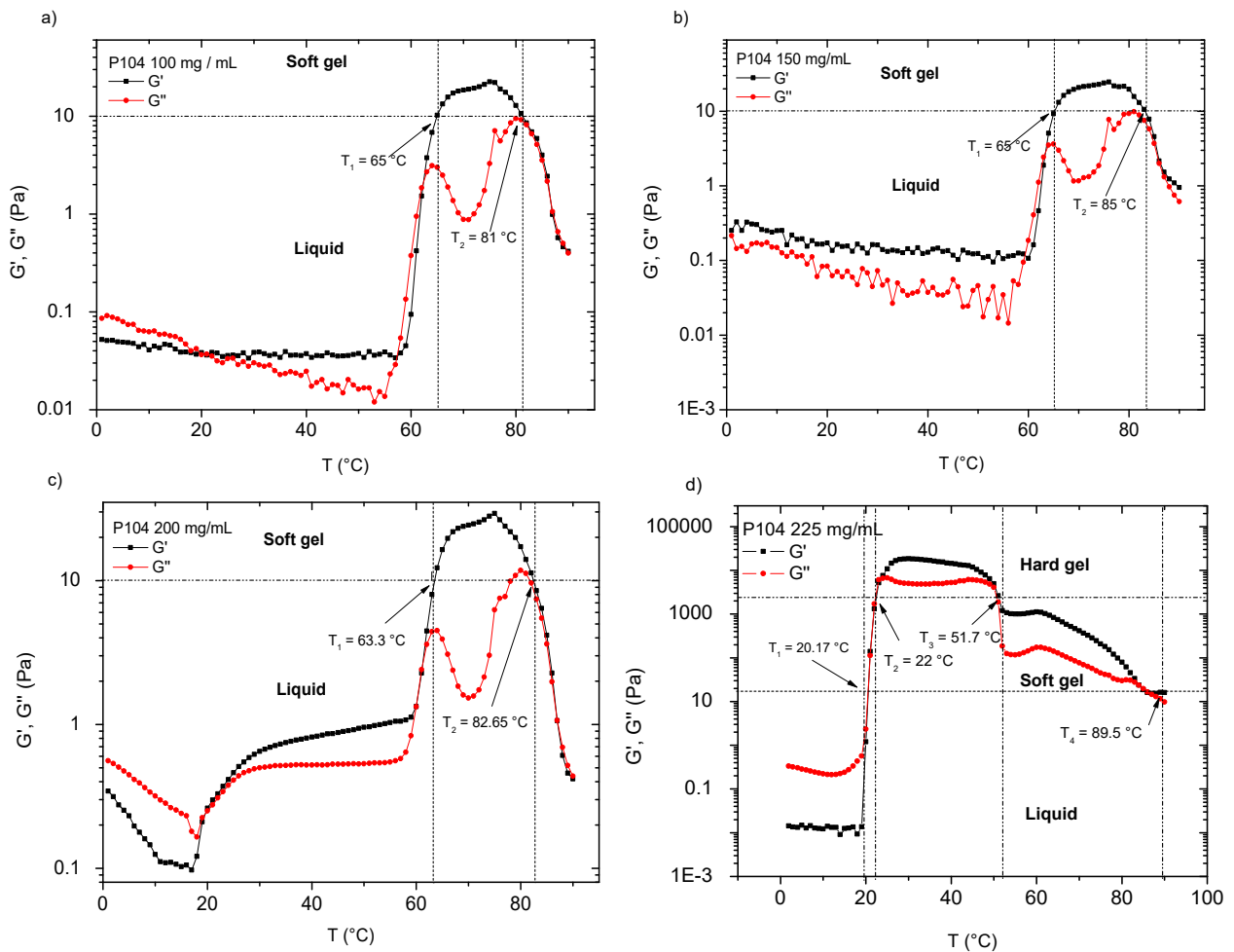
Figure 3.12. *Temperature sweeps of P104 concentrations: a) 100, b) 150, c) 200 and d) 225 mg/mL.*

Figure 3.12 c shows the temperature dependence of G' and G" for the P104 concentration of 200 mg/mL. As for P104 concentration of 100 mg/mL, a viscous behavior (G">G') is firstly observed within the temperature range from 3 to 18 ℃. A first crossover of G' and G" is also observed around the temperature 20 ℃. A slight increase in both modulus is then observed from around 20 to 58 ℃. Then, an increment on G' of one order of magnitude is detected, changing from the dilute to the soft gel domain in a temperature range between around 63 and 83 ℃. A pronounced drop of G' and G" is detected around 83 ℃. Finally, a new behavior of P104 solutions is presented in *Figure 3.12 d*, in which the material reaches the hard gel domain between a temperature range of around 22 and 52 ℃. In this manner, an increase of around three orders of magnitude is reached from this P104 concentration in a ΔT of around 30 ℃. In this manner, P104 solutions form thermo-reversible gels that depend on P104 concentrations and on temperature, which could be used for different applications at physiological temperatures [37,41,42].

3.3.7. Temperature-composition phase diagram of P104/water

Figure 3.13 shows the phase diagram for P104/water system in the concentration range from 0 to 150 mg/mL. Here we can observe that the CMT slightly decreases with the increase of P104 concentration, as previously reported for several P104 concentrations [10].
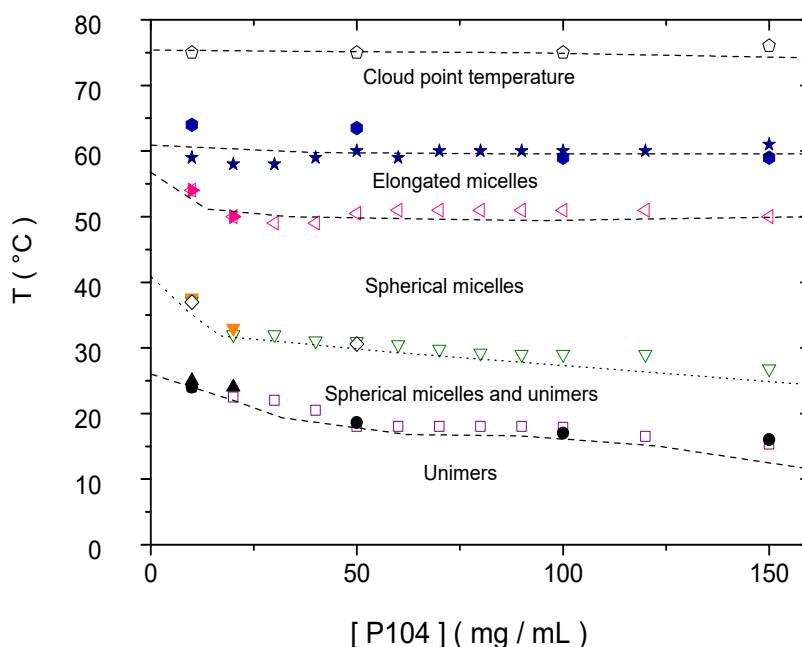
Figure 3.13. *Temperature-composition phase diagram of P104/water binary composition.*

The existence of micelles and unimers in a wide range of temperatures was detected through density and sound velocity measurements, dynamic light scattering and viscosity. The CMT and the temperature at which the micellization is finished were determined from the start and the end of the peak of the derivative of the apparent molar adiabatic compressibility (represented by the dashed line). After the MGT (micellar growth temperature), spherical micelles grow into rod-like micelles (prolates, according to the first approximation by using Perrin´s model). At higher temperatures, a reversible phase separation takes place and the clouding point is reached, at which a great storage modulus (G') is detected.

3.4. Particular conclusions for the structural behavior of P104 triblock copolymer

A study of amphiphilic block copolymer P104 was performed through density, sound velocity, viscosity and dynamic slight scattering (DLS) measurements in the dilute and semi-dilute regimes between 10 and 65ºC. The results made possible to analyze the structural behavior of the system, to determine the critical micellar temperature (CMT) and the micellar growth temperature (MGT) as a function of P104 concentration. The temperature domains at which P104 spherical micelles and P104 elongated micelles exist are greater than for other triblock copolymers, allowing their applications in a wider field. I_{SCA} and R_h were obtained through DLS measurements at six different temperatures from the spherical micelles domain to the elongated micelles domain. As first approximation for a morphology study, the dependence of I_{SCA}/I_{SCA}^0 with R_h was compared to the Perrin model of prolate ellipsoids, oblate ellipsoids and spheres, which was found to be close to the predicted behavior for prolate ellipsoids, which suggest that P104 micelles grow as prolate rods. The effect of NaCl addition on CMT, MGT and CPT was described. Rheological properties were studied in a P104 concentration range from 50 to 600 mg/mL and were found to be greatly dependent on temperature and concentration, since the storage modulus increase between two and three orders of magnitude.

3.5. References

[1] M.L. Adams, A. Lavasanifar and G.S. Kwo, Amphiphilic Block Copolymers for Drug Delivery, *Journal of Pharmaceutical Sciences* **92**, 1343–1355 (2003).

[2] S. Zamani and S. Khoee, Preparation of coreeshell chitosan/PCL-PEG triblock copolymer nanoparticles with ABA and BAB morphologies: Effect of intraparticle interactions on physicochemical properties, *Polymer* **53**, 5723-5736 (2012).

[3] K.T. Oh, T.K. Bronich and A.V. Kabanov, Micellar formulations for drug delivery based on mixtures of hydrophobic and hydrophilic Pluronic block copolymers. Journal of controlled release, *J*

Control Release. **94**(2-3), 411-22 (2004).

[4] X. Zhao and P. Liu, Reduction-Responsive Core–Shell–Corona Micelles Based on Triblock Copolymers: Novel Synthetic Strategy, Characterization, and Application As a Tumor Microenvironment-Responsive Drug Delivery System, *ACS Appl. Mater. Interfaces* **7** (1), 166–174 (2015).

[5] M. Morell and J. Puiggalí, Hybrid Block Copolymers Constituted by Peptides and Synthetic Polymers: An Overview of Synthetic Approaches, Supramolecular Behavior and Potential Applications, *Polymers* **5**(1), 188-224 (2013).

[6] X.-B. Xiong and A. Lavasanifar Amphiphilic Block Copolymer Based Nanocarriers for Drug and Gene Delivery in *Intracellular Delivery*, Editors: Aleš Prokop, Vol. 5 of the series Fundamental Biomedical Technologies, Springer, 251-289 (2011).

[7] A. V. Kabanov, E. V. Batrakova and V. Y. Alakhov, Pluronic® block copolymers as novel polymer therapeutics for drug and gene delivery, *Journal of Controlled Release* **82** (2–3), 189–212 (2002).

[8] T.-il Kim, H. J. Seo, J. S. Choi, H.-S. Jang, J.-un Baed, K. Kim and J.-S. Park, PAMAM-PEG-PAMAM: Novel Triblock Copolymer as a Biocompatible and Efficient Gene Delivery Carrier, *Biomacromolecules* **5** (6), 2487–2492 (2004).

[9] A. V. Kabanov, E. V. Batrakova and V. Y. Alakhov, Pluronic® block copolymers for overcoming drug resistance in cancer, *Advanced Drug Delivery Reviews* **54** (5), 759-779 (2002).

[10] P. Alexandridis, T. Alan Hatton, Poly(ethylene oxide)-poly(propylene oxide)-poly (ethylene oxide) block copolymer surfactants in aqueous solutions and at interfaces: thermodynamics, structure, dynamics, and modeling, *Colloids and Surfaces, A: Physicochemical and Engineering Aspects* **96**, 1-46 (1995).

[11] P. Alexandridis and B. Lindmann, *Amphiphilic Block Copolymers: Self-Assembly and Applications, ed. P. Alexandridis and B. Lindmann, Elsevier*, Amsterdam, (2000).

[12] P. Alexandridis, Thermodynamics and Dynamics of Micellization and Micelle Solute Interactions in Block- Copolymer and Reverse Micellar Systems, Ph.D. Thesis, Massachusetts Institute of Technology, Cambridge MA, (1994).

[13] G. Waton, B. Michels and R. Zana, Dynamics of block copolymer micelles in aqueous solutions, *Macromolecules* **34**, 907 (2001).

[14] M. Duval, G. Waton, R. Zana, Evidence of micelle growth in aqueous solutions of the amphiphilic poly(ethylene oxide)-poly(propylene oxide)-poly(ethylene oxide) triblock copolymers from differential scanning microcalorimetry, *Colloids Surf. A* **183**, 55 (2001).

[15] G. Wanka, H. Hoffmann and W. Ulbricht, The aggregation behavior of poly-(oxyethylene)-poly-

(oxypropylene)-poly-(oxyethylene)-block-copolymers in aqueous solution, *Colloid and Polymer Science* **268**, 101 (1990).

[16] K. Mortensen and W. Brown, Poly(ethylene oxide)-poly(propylene oxide)-poly(ethylene oxide) triblock copolymers in aqueous solution. The influence of relative block size, *Macromolecules* **26**, 4128 (1993).

[17] J.K. Pedersen and C. Svaneborg, Scattering from block copolymer micelles, *Curr. Opinion in Colloid and Interface science* **7**, 158 (2002).

[18] J.G. Álvarez-Ramírez, V.V.A. Fernández, E.R. Macías, Y. Rharbi, P. Taboada, R. Gámez-Corrales, J.E. Puig and J.F.A. Soltero, Phase behavior of the Pluronic P103/water system in the dilute and semi-dilute regimes, *Journal of Colloid and Interface Science* **333**, 655-662 (2009).

[19] M. Iqbal and R. E. Verrall, Apparent molar volume and adiabatic compressibility studies of aqueous solutions of some drug compounds at 25 °C, *Canadian Journal of Chemistry* **67**(4), 727-735 (1989).

[20] G. Landazuri, V. V A Fernandez, J. F. A. Soltero and Y. Rharbi, Kinetics of the Sphere-to-Rod like Micelle Transition in a Pluronic Triblock Copolymer, *J. Phys. Chem. B* **116**, 11720−11727 (2012).

[21] G. Fritz, G. Scherf and O. Glatter, Applications of densiometry, ultrasonic speed measurements, and ultralow shear viscosimetry to aqueous fluids, *J. Phys. Chem.* **104**, 3463 (2000).

[22] G. G. Warr and F. Grieser , Determination of micelle size and polydispersity by fluorescence quenching. Theory and numerical results, *J. Chem. Soc., Faraday Trans.* **1**, 1986,82, 1813-(1828).

[23] Y. Liu, S.-H. Chen and J. S. Huang, Light-Scattering Studies of Concentrated Copolymer Micellar Solutions, *Macromolecules* **31**, 6226-6233 (1998).

[24] T. Sakai and P. Alexandridis, Size- and shape-controlled synthesis of colloidal gold through autoreduction of the auric cation by poly(ethylene oxide)-poly(propylene oxide) block copolymers in aqueous solutions at ambient conditions, *Nanotechnology* **16**, S344–S353 (2005).

[25] P. Alexandridis, T. Nivaggioli and T. A. Hatton, Temperature Effects on Structural Properties of Pluronic P104 and F108 PEO-PPO-PEO Block Copolymer Solutions, *Langmuir* **11** (5), 1468−1476 (1995).

[26] N.A. Mazer, G.B. Benedek and M.C. Carey, An Investigation of the Micellar Phase of Sodium Dodecyl Sulfate in Aqueous Sodium Chloride Using Quasielastic Light Scattering Spectroscopy, *J. Phys. Chem.* **80**, 1075-1085 (1976).

[27] F. Perrin, Mouvement Brownien d'un ellipsoïde. II: Rotation libre et dépolarisation des fluorescences. Translation et diffusion de molécules ellipsoïdales. *J. Phys. Radium* **7**, 1-11 (1936).

[28] S. A. Willis, G. R. Dennis, G. Zheng, W. S. Price, Hydrodynamic size and scaling relations for linear and 4 arm star PVAc studied using PGSE NMR, *Journal of Molecular Liquids* **156**, 45–51 (2010).

[29] H. G. Thomas, A. Lomakin, D. Blankschtein and G. B. Benedek, Growth of Mixed Nonionic Micelles, *Langmuir* **13**, 209-218 (1997).

[30] P. Debye and E.W. Anacker, Micelle shape from dissymmetry measurements, *J. Phys. Colloid Chem* **55**, 644-655 (1951).

[31] S. Hvidt, E. B. Joergensen, W. Brown, K. Schillen, Micellization and Gelation of Aqueous Solutions of a Triblock Copolymer Studied by Rheological Techniques and Scanning Calorimetry *J. Phys. Chem* **98**, 12320 (1994).

[32] P. Bahadur, P. Li, M. Almgren and W. Brown, Effect of potassium fluoride on the micellar behavior of Pluronic F-68 in aqueous solution, *Langmuir* **8**, 1903 (1992).

[33] R. Ivanova, B. Lindman and P. Alexandridis, Effect of glycols on the self-assembly of amphiphilic block copolymers in water. 1. Phase diagrams and structure identification, *Langmuir* **16**, 3660 (2000).

[34] R. Ganguly, V.K. Aswal, P.A. Hassan, I.K. Gopalakrishnan and J.V. Yakhmi, Sphere-to-rod transition of triblock copolímero micelles at room temperature, *Indian Academy of Sciences* **63**, 277-283 (2004).

[35] M.K. Sharma, V.K. Aswal and P.A. Hassan, Self-Assembly of PEO-PPO-PEO triblock copolymers in aqueous electrolyte solution, *Founder's Day Special Issue* **285**, 84-87 (2007).

[36] N.J. Jain a, V.K. Aswal b, P.S. Goyal b, P. Bahadur, Salt induced micellization and micelle structures of' PEO/PPO/PEO block copolymers in aqueous solution, *Colloids and Surfaces A: Physicochemical and Engineering Aspects* **173**, 85–94 (2000).

[37] S. Hvidt and K. Keiding, Rheology and Structures of EO-PO-EO Block Copolymers in Aqueous Solutions, *Annual Transactions of the Nordic Rheology Society* **17** (2009).

[38] L. Guo and E. Luijten, Reversible Gel Formation of Triblock Copolymers Studied by Molecular Dynamics Simulation, *Journal of Polymer Science: Part B: Polymer Physics* **43**, 959–969 (2005).

[39] I. Chamradová, L. Vojtová, L. Michlovská, P. Poláček and J. Jančář, Rheological properties of functionalised thermosensitive copolymers for injectable applications in medicine, *Chemical Papers* **66**, 977-980 (2012).

[40] T. Vermonden, M. Na, M.J. Van and W.E. Hennink, Rheological studies of thermosensitive triblock copolymer hydrogels, *Langmuir* **22**(24),10180 (2006).

[41] V. K. Garripelli, J.-K. Kim, R. Namgung, W.J. Kim, M.A. Repka and S. Jo, A novel thermosensitive polymer with pH-dependent degradation for drug delivery, *Acta Biomater* **6**(2), 477 (2010).

[42] L. Klouda and A. G. Mikos, Thermoresponsive hydrogels in biomedical applications - a review, *Eur J Pharm Biopharm* **68**(1), 34–45 (2008).

CHAPTER 4

Collective dynamics of P104 amphiphilic block copolymer in and out of equilibrium

4. Collective dynamics of P104 amphiphilic block copolymer in and out of equilibrium

4.1. Introduction

Amphiphilic block copolymers can self-assemble in water forming micelles, spheres, cylinders, vesicles and other types of structures [1,2]. Because of their high molecular weights, they present slow dynamics to frozen, which can catch those structures in metastable states without reaching the equilibrium [1-3]. Amphiphilic block copolymer dynamics can be studied at the equilibrium or out of the equilibrium [4], as in the sphere-to rod like micelles transition.

Surfactant micelles kinetics at equilibrium are dominated by two mechanisms [5-10]. First mechanism has been described by Anniasson and Wall (A−W) and involves unimer/micelle interactions via insertion−expulsion of unimers [11-13]. The second mechanism involves micelle−micelle interactions via fusion and fragmentation [14-16]. However, the dynamics in block copolymer micelles differs from the surfactant kinetics due to the chain correlation in the core and the strong steric repulsion of the corona. *Halperin et al.* proposed insertion−expulsion as the main dynamic process in diblock copolymers [2], nevertheless, *Dormidontova* reported that fusion and fragmentation were favorable in the early stage of micellization while unimer insertion−expulsion is the main process at equilibrium [17]. Recently, the detection of fusion-fission mechanisms at equilibrium was reported in P103 triblock copolymer micelles (pluronics) by *Rharbi* [5].

On the other side, for the study of the dynamics out of equilibrium, structural transitions such as the sphere to cylinder transition have been caused by a jump of co-solvent, which consist in the addition of a second solvent in small quantities to modify the solvent influence of the medium. Usually, experiments known as jumps represent the abrupt change of a selected variable for the study of the system response to the perturbation [19,20]. In two recent studies, the slow dynamics of the transition from sphere to cylinder of the triblock copolymer Pluronic P123 were investigated in a mixture of water, salt, and ethanol [20,21]. One of these studies reported that the transition could exist through the mechanisms of fusion and fragmentation-exchange of unimers [20]. Recently, *Landazuri et al.* [22] presented a kinetics study of the sphere-to-rod transition in aqueous micelle solutions of triblock copolymer P103. This transition was followed by a temperature jump from the sphere phase to the rod phase and monitored with dynamic light scattering.

In the field of controlled drug release, molecules for chemotherapy are usually hydrophobic and require vectorization to be transported to the target cell [23,24]. Micelles made of amphiphilic block copolymers with a nanoscale size between 5 and 100nm, have an inner core that is comprised of the hydrophobic blocks and creates a space for the solubilization, storage, controlled delivery and protection of hydrophobic drugs [25]. Many studies have been performed in order to develop a variety of

nanostructures, including micelles, polymersomes and hydrogels for an efficient drug delivery [25-28]. However, very few studies have examined the collective mechanisms as fission-fusion on micelles in the transport and expulsion of active ingredients. Understanding these dynamics at the equilibrium state and during specific stimuli for the release of the active ingredient becomes crucial for the design and the control of new materials and new processes effectives in controlled drug delivery.

In this chapter, a study of the dynamics of the sphere to rod–like micelle transition of the triblock copolymer P104 in water is presented in first place. This transition was obtained by increasing the temperature of the micellar spherical domain to the cylindrical domain. The scattering intensity and the hydrodynamic radius of the micelles were monitored throughout the experiment using Dynamic Light Scattering. The influence of salt addition in the sphere to ro–like micelle transition was also studied. Then, the micellar dynamics at equilibrium of the triblock copolymer P104 in aqueous solution were studied by fluorescence spectroscopy. A fluorescent technique proposed several years ago by *Rharbi et al.* [18,29-31], which uses the random distribution of hydrophobic pyrene derivatives (PyC$_{18}$) between micelles is selected as a tool to investigate the fusion and fission dynamics between P104 micelles.

4.1.1. Surfactant micelles dynamics

Two main principal mechanisms have been proposed in order to explain the surfactant micelles dynamics [5-10]. First one consists in the gradual expulsion and insertion of surfactants unimers (*Figure 4.1*) and second one consists in the fusion and fission of complete micelles (*Figure 4.2*).
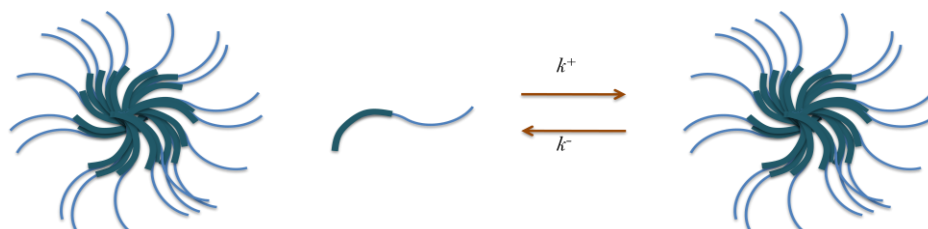
Figure 4.1. *Schematic representation of expulsion and insertion of surfactants unimers where k $^+$ corresponds to the kinetic constant of the insertion process and k $^-$ corresponds to the kinetic constant of the expulsion process [22].*

Figure 4.2. *Schematic representation of fussion and fission of complete micelles, where k$_{fus}$ corresponds to the kinetic constant of the fusion process and k$_{fra}$ corresponds to the kinetic constant of the fission process [22].*

Most experiments in surfactants kinetics that study the return to equilibrium after a small perturbation has reported two relaxations with two different time scales. The fast kinetics have been attributed by *Aniansson et. al.* [11,12] to the insertion of existing free surfactant in micelles. This process changes micelle size without affecting its number. Moreover, the slow kinetics was related to the slow dissociation-growth of micelles through the insertion and subsequent expulsion of unimers [11-13] or the fusion and fission of micelles [14-16]. The equilibrium dynamics in surfactant micelles was performed through time sweeps experiments using fluorescence hydrophobic probes of pyrene [29-31]. In these studies it was concluded that the fusion and fission occurs at the equilibrium in non-ionic surfactant. Finally, wormlike micelles dynamics was studied by *Turner et. al* [32] and discussed in terms of fusion and fission mechanisms. Their model proposes an exponential distribution of the average length, L, of micelles, with respect to the surfactant concentration surfactant as follows: $L \approx [\text{surfactant}]^{0.5}$.

4.1.2. Amphiphilic block copolymer micelles dynamics

Amphiphilic block copolymer micelles dynamics are very sensitive to the type of solvent, unlike surfactants dynamics, so it may be affected and may vary from slow to frozen dynamics [22, 33-35]. The unimer insertion-expulsion mechanisms were proposed by *Haperin et al.* [2] to be the dominant processes for block copolymer micelles dynamics. However, *Dormidontova* [17] proposed that fusion-fission mechanisms were favorable in the early stage of micellization. Two different kind of kinetics experiments in amphiphilic block copolymers allow studying the dynamics at equilibrium and the transition dynamics from one morphology to another.

4.1.2.1. Dynamics at equilibrium in amphiphilic block copolymers

The dynamics at equilibrium of amphiphilic block copolymers can be studied and discussed in terms of the randomization kinetics of block copolymer micelles [33,34,36]. Experimentally, these dynamics can be detected and quantified by using time-resolved neutron scattering on mixtures of deuterated and hydrogenated copolymers, or by copolymers labeled with fluorescent probes.

The dynamics at equilibrium in amphiphilic block copolymers have recently been proved to be collective mechanisms that can be monitored through the exchange of fluorescent probes hydrophobic between micelles [29-31]. The exchange of solutes between micelles takes place in the same way that the exchange of copolymer chains (*Figure 4.3*). The transfer of a hydrophobic probe molecule (P) from a filled micelle to an empty micelle takes place through three major routes, as it is possible to observe in *Figure 4.3*. In the first mechanism (a), the probe leaves the filled micelle to go to the aqueous phase and then enters into the empty micelles. In the second mechanism (b), the filled micelle is broken into two

micelles, each one of them retaining one probe molecule, followed by the growth of the fragments through the insertion of copolymer chains or the fusion with an empty micelle. In the third mechanism (c), complete micelles can fuse with empty micelles to form large micelles that break giving rise to two normal size micelles containing one probe molecule each one. The exit-entry and fission-growth processes are first order process, which can lead to the rate constants k_{exit} and k_{fiss}, respectively. The fusion-fission a second order kinetics process. When the concentration of empty micelles is much larger than the filled micelles concentration, the fusion-fission process leads to a first order kinetics with a rate k_{fus} x[micelles]. The exchange rate is then given by the following expression:

$$k_{decay} = k_{fis} + k_{fus} \text{ x[micelles]} \tag{4.1}$$
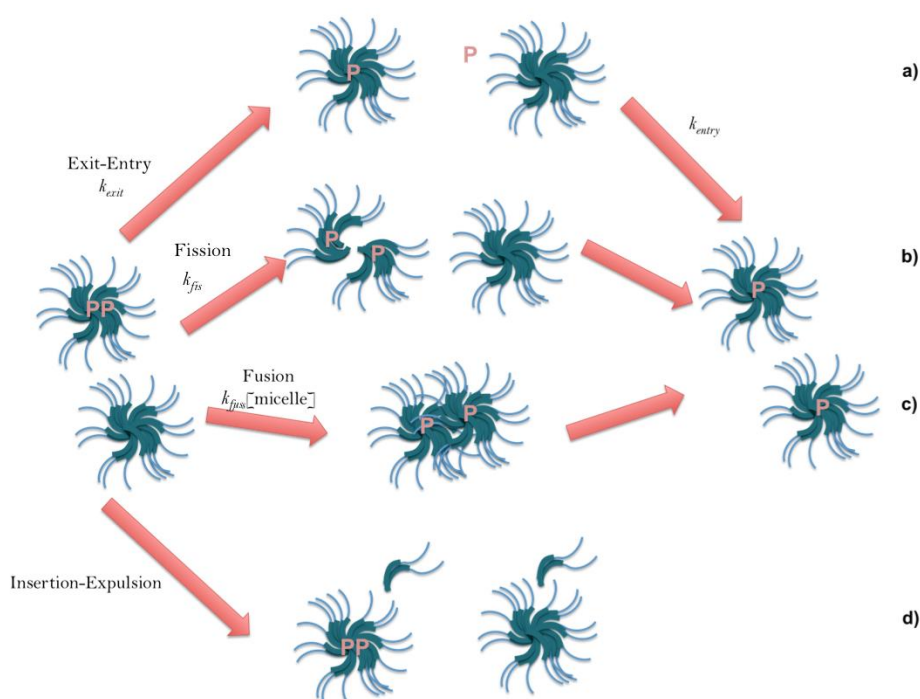
Figure 4.3. *Different processes for exchanging copolymer chains and probes (P) between micelles: a) Exit–entry of the probe, b) fission-growth, c) fusion-fission and d) insertion-expulsion of single chains [18].*

4.1.2.2. Dynamics of micellization in amphiphilic block copolymers

In this case, as well as for surfactant micelles kinetics, the transition from monomer to micelle presents two processes [29-31]. First one corresponds to a fast process associated with the formation of metastable micelles through the insertion of free copolymers in the existing micelles [35] Second one is a slow process that is related to either fusion-fission or to insertion-expulsion mechanisms.

4.1.2.3. Sphere-to-rod like micelles transitions in amphiphilic block copolymers

The transition from sphere-to-rod like micelles has been studied through experiments called "jumps", which could be cosolvent jumps [19], salt jumps [20] or temperature jumps [37]. The dynamics of the sphere-to-rod-like transition in polystyrene-poly(acrylic acid) (PS-PAA) copolymers were reported by *Burke et al.* [3], attributing this transition to a three-steps mechanism, i.e. the adhesion of spherical micelles, the formation of a pearl necklace shaped rods and the smoothing of the rods. The sphere-to-rod dynamics in the pluronic triblock copolymer P123 in a mixture of water, salt and ethanol were also studied [20]. The obtained results allowed proposing that the transition could take place through both fusion-fission and unimer exchange. Recently, *Landazuri et al.* [22] studied the sphere-to-rod transitions in aqueous solutions of P103 triblock copolymer, showing that the transition was dominated by a mechanism involving fusion and fission of micelles.

4.2. Experimental conditions

Materials and solutions preparation are described in *Chapter 3* of this part of the thesis.

4.2.1. Solutions preparation for fluorescent measurements

For fluorescent measurements, the fluorescent probe 1-pyrenyloctadecanone, $C_{34}H_{44}O$ (PyC$_{18}$), was prepared using a Friedel-Crafts acylation of pyrene with stearoyl chloride in dichloroethane in the presence of aluminum chloride (AlCl$_3$) [15]. The PyC18 was solubilized into the P104 micelles by mixing triblock copolymer P104 (20 mg/ mL) with PyC18 at a temperature greater than 75 ° C. The solution was strongly stirred for 10 min with a Vortex genie 2 model G 650 mechanical shaker at its maximum frequency (>10 Hz).

4.2.2. Dynamic Light Scattering measurements

Dynamic Light Scattering (DLS) measurements were performed on a Malvern Zetasizer 5000 instrument equipped with a particle analyzer with variable angle, between 45° and 135°, and a multi-bit correlator 7132. A He-Ne laser (5 mW) with a wavelength of 632.8 nm was used as a light source. The scattered light intensity was measured through a pinhole of 400 μm. The correlation functions were averaged from 5 measurements of 60 s each one. The temperature was controlled with an internal Peltier in the instrument. The intensity correlation function is analyzed by the *Cumulants* method, from which is possible to calculate the apparent hydrodynamic radius and the total intensity of the scattered light [328,39]. The size distribution of micelles is obtained using the application of the Laplace

transform to the autocorrelation function of the measured scattering intensity data with the *Contin* program [22]. DLS measurements for P104 were carried out at the angles 45 º, 90 º and 135 º at the equilibrium for a temperature range between 10 and 64 ºC.

4.2.3. Kinetics experiments through DLS

Studies of micellar dynamics out of the equilibrium were carried out by experiments called "temperature jumps", which consist in monitoring the evolution of the hydrodynamic radius and the scattering intensity versus time during a sudden change of temperature for a micellar solution at the equilibrium from a temperature T1 to a temperature T2. To perform these experiments, the sample was stabilized at a temperature T1 during 24 hours; in this way, it was possible to ensure the micellar equilibrium. Then, the sample was introduced to the instrument previously calibrated at the temperature T2 and the measurements were initiated immediately.

The autocorrelation decays were measured each 5s and averaged over the same time. The kinetics measurements were carried out at 45º, 90º and 135º. The measurements were performed carrying out a temperature jump from T1= 38ºC at which spherical micelles are stable to a temperature T2 which yields rod-like micelles (T2= 42, 50 55, 58 and 64 ºC). Cell 1 cm. We investigated the required time to reach the desired temperature and we found that this temperature can be reached in 2 min., which means that the kinetics below 2 min. should not be taken into account. In this Chapter we are forced to work at higher P104 concentrations since fusion and fission cannot be identified at lower triblock copolymer concentrations.

4.2.4. Fluorescence measurements

Fluorescence measurements were performed with a Jobin Yvon spectrometer Fluorolog III (2-2) in the S/R mode. Kinetic experiments were carried out mixing a solution with micelles of P104 containing PyC$_{18}$ (B) with probe-free P104 micelles (A) in a 2 mm thick cell (*Figure 4.4*). A ratio of 1:20 (P104 solution with PyC$_{18}$: Probe free P104 solution) was used to study the dynamics. All the measurements were carried in a temperature range between 30 and 62 °C. An excitation wavelength of 344 nm was used for each measurement, monitoring the emission every 30 s at λ_{ex}= 480 nm for the excimer and λ_{mon} = 376 nm for the monomer. Measurements were performed in the concentration range between 10 and 100 mg/mL. *Figure 4.4* presents a schematic representation of the mechanism used to perform these kinetic experiments.
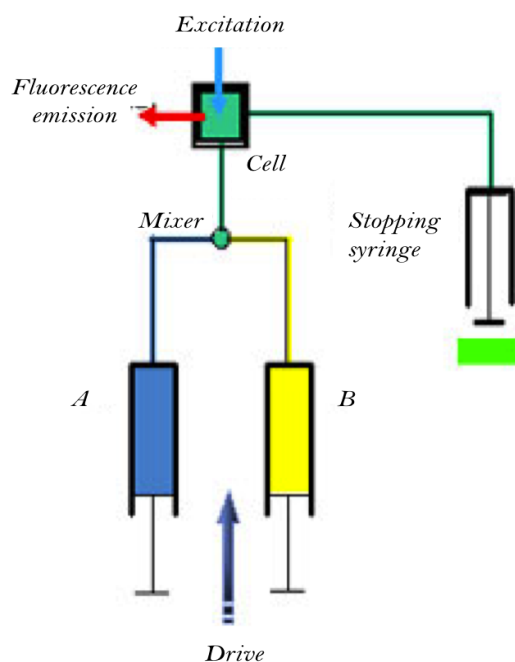
Figure 4.4. *Schematic representation of the kinetic experiments performed with a stopped flow mechanism.*

4.3. Experimental results

4.3.1. Collective dynamics of P104 triblock copolymer out of equilibrium

4.3.1.1. Growth kinetic observed on the evolution of the hydrodynamic radius and the scattering intensity

The total scattering intensity contains information of the average size of micelles, the polydispersity of the solution, the size distribution and the water content in the micelles. In the case of monodisperse micelles, scattering intensity can be described by the following expression:

$$I_{disp} \; \alpha \; (n_{mic} - n_w)^2 \; \varphi_{mic} \; \alpha \; V_{mic} \tag{4.2}$$

where I_{disp} the total intensity scattered, V_{mic} corresponds to the volume fraction of micelles, φ_{mic} is the volume fraction of surfactant, n_{mic} and n_w are the refraction indices of the micelles and water, respectively.

During kinetics of the structure transition, all these parameters can vary simultaneously and may complicate the description of the dynamic process. The more accelerated process, identified during the rapid increase of the scattering intensity can be attributed to the increase on the micellar size or the dehydration of the micelles. Thus, the change of each of the micellar parameters must be monitored individually.

While increasing the temperature of the spherical micelles domain T1 (which have an average hydrodynamic radius of 11 nm) to the temperature of the rod-like micelles domain T2, both the hydrodynamic radius and the total scattering intensity increase as a function of time (*Figures 4.5 a and b*). The sphere to rod-like micelle transition in P104 amphiphilic block copolymer is then slow enough to be monitored by Dynamic Light Scattering measurements, as P103 amphiphilic block copolymer transition. *Figure 4.5 a* shows the dependence of the hydrodynamic radius as a function of time for a P104 solution in water with a concentration of 20 mg/mL by changing the temperature from 38 to 64 ºC. We observe that a single process (*Equation 4.3*) describes the increase of the hydrodynamic radius (R_h) as a function of time, showing that the process involving monomer-micelle interactions is negligible in this temperature range. The increasing decay of R_h can be adequately simulated by using an mono-exponential expression with a rate $k_{growth}^{Rh} = 1/\tau$

$$R_h(t) = [R_h(\infty) - R_h(0)]*\exp(-t/\tau) + R_h(\infty) \tag{4.3}$$
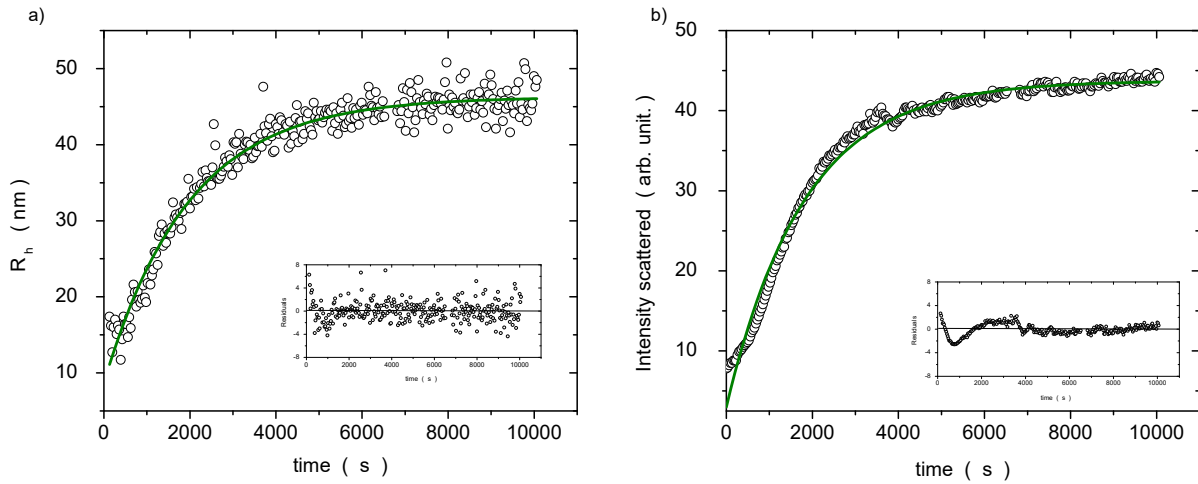
Figure 4.5. a) *Hydrodynamic radius, R_h, and b) scattered intensity versus time for a P104 solution with a concentration of 20 mg/mL obtained after a temperature jump from a T1=38 °C to T2 = 64 °C. The solid line represents the obtained fitting using a mono-exponential expression that simulates the intensity decay. Inset: residual of the fit to the single exponential function.*

Figure 4.5 b shows the response of the total scattering intensity as a function of time for the P104 solution with a concentration of 20 mg/mL by changing the temperature from 38 ºC to 64 ºC. The kinetic decay can be also adequately simulated using a mono-exponential function with an apparent relaxation time according to the next expression:

$$I_{SCAT}(t) = [I_{SCAT}(\infty) - I_{SCAT}(0)]*\exp(-t/\tau + I_{SCAT}(\infty) \tag{4.4}$$

where I_{SCAT} is the dispersed intensity and τ represents the apparent relaxation time.

The fits of the experimental data were obtained beyond 2 min. since the desired temperature can be reached in 2 min. after the sample is placed in the measuring cell.

The results allow proposing that the increasing decay consists on a single process. However, in some literature reports, the temperature jumps experiments of triblock copolymers as L64 [29,40,41] and F85 [42] show two processes, one fast and one slow. They mention that the scattering intensity is increased in the rapid process and then decreases during the second process, which means that the slow process is obtained at slightly higher temperatures than the CMT. The first process is related to the incorporation of free copolymer to the micelles, generating metastable micellar structures. Furthermore, for P104 triblock copolymer, the critical micellar concentration was detected around 0.07 mg/mL at the temperature of 38 °C and decreases with increasing temperature, therefore, it is consider as a negligible parameter (cmc <0.1 mg/mL) [29]. Since the concentration of free copolymer is negligible compared to the concentration of micellization, the increase on the temperature does not cause the growth of the micelles by incorporating free monomer on them. The slow kinetics may include the following mechanisms: dehydration of the micelles, cooperative condensation and monomer dissolution, a fusion process or a fission-growth process.

4.3.1.2. Growth kinetic observed on the intrinsic asymmetry [Z]

The intrinsic asymmetry, given by the ratio between the intensity observed at an angle of 135° and an angle of 45°, allows identifying the longitudinal growing process of the micelles.
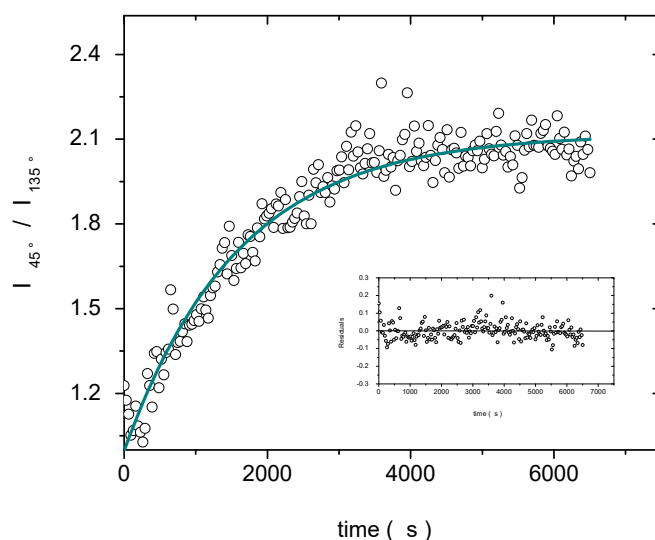
Figure 4.6. *Intrinsic asymmetry, $I_{45°}/I_{135°}$, as a function of time for a solution of P104 at a concentration of 25 mg/mL after carrying the solution from a temperature T1 = 38 °C to a temperature T2 =64 °C. The solid line represents the fitting using a mono-exponential expression that simulates the decay of the intensity. $I_{45°}$ and $I_{135°}$ are the intensities of scattering measured at 45° and 135°, respectively.*

Figure 4.6 shows the intrinsic asymmetry, $I_{45°}/I_{135°}$, versus time, of a solution of P104 with a concentration of 20 mg/mL after carrying the solution from a temperature $T1 = 38$ °C to a temperature $T2 = 64$ °C. After this temperature jump from 38 to 64 ° C, $I_{45°}/I_{135°}$ increases progressively with time and reaches a maximum value at 1.4, indicating the presence of elongated micelles. This curve can also be simulated with a mono-exponential function having one characteristic time constant, similar to the one used for evaluating the behavior of R_h. This way, it can be inferred that micelles grow longitudinally during the relaxation process and their length increases with time.

4.3.1.3. Exchange rate

The structural transition rate from spherical micelles to elongated micelles depends directly on the relation between the blocks PPO/PEO and from PPO block length. P103 triblock copolymer $[(PEO)_{17}–(PPO)_{60}–(PEO)_{17}]$, with a ratio PPO/PEO=1.76 has relaxation times between the range of 100s to 6000s, depending on the concentration. A more hydrophobic system, Pluronic P123 $[(PEO)_{20}–(PPO)_{70}–(PEO)_{20}]$, with a ratio PPO/PEO=1.75 and a longer PPO block, exhibits relaxation times that can last days in the absence additives. In our case, the relaxation times of P104 $[(PEO)_{27}–(PPO)_{61}–(PEO)_{27}]$, with a ratio PPO/PEO=1.13, are in the range from 800s to 4000s.

Figure 4.7 a and *b* show the hydrodynamic radius and the scattering light, respectively, as a function of time for several concentrations of P104 solutions. For the evolution of the hydrodynamic radius, the maximum values reached by the kinetics decrease while increasing P104 concentration at the studied concentration range. The growth rate calculated through the scattering intensity and the hydrodynamic diameter, $k_{growth} = 1/\tau$ is between 0.00031 s^{-1} and 0.00125 s^{-1} for the concentration range of P104 between 10 mg/mL and 100 mg/mL.
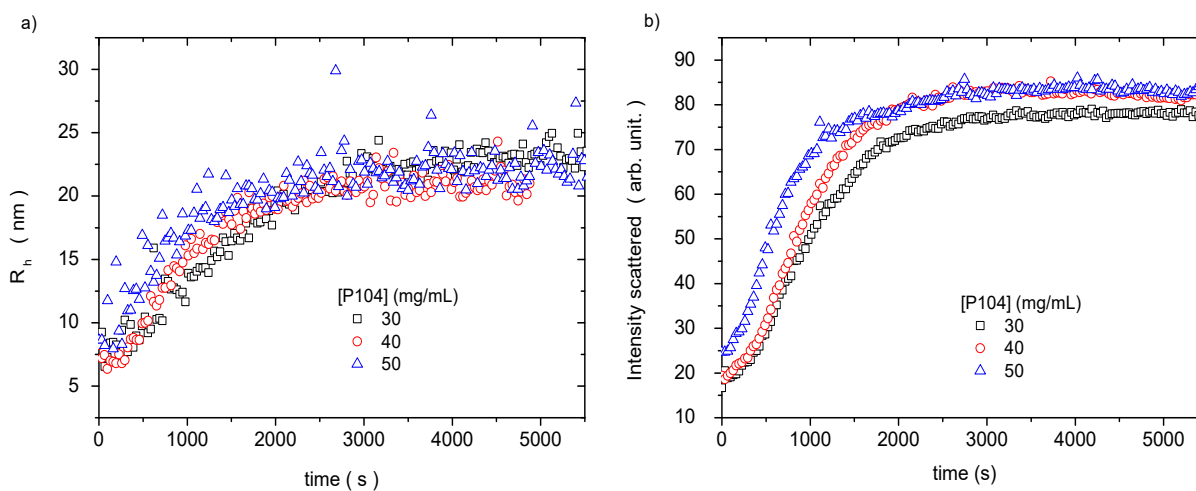
Figure 4.7. *a) Hydrodynamic radius and b) intensity scattered as a function of time for P104 solutions with concentrations of 30 , 40 and 50 mg/mL after the temperature jump from T1 = 38 °C to T2 = 64 °C.*

The exchange kinetics in triblock copolymers involve changing various parameters such as the number of copolymers per micelle or the aggregation number (N_{agg}), the size distribution and the content of water [29]. If the growth is sphere to sphere, the relation between the growth rate calculated from the scattering intensity (k_{growth}^{I}) and the growth rate calculated from the hydrodynamic diameter (k_{growth}^{Dh}) should be the following: $k_{growth}^{I} = 3\ k_{growth}^{D_h}$.

Figure 4.8 shows the dependence of growth rate with the triblock copolymer concentration obtained from the mono-exponential fits of the hydrodynamic radius, the scattering light intensity and the aspect factor in the concentration range of P104 triblock copolymer in water between 10 and 60 mg/mL. In all cases, we observe a linear increase with the concentration that corresponds to a second-order process including fusion of micelles into a long micelle. Through these results, it is found that the growth process of P104 triblock copolymer micelles in water follows two mechanisms. The first mechanism involves the integration of copolymer chains and micelles to form thermodynamically stable micelles. The second mechanism involves fusion-fission processes of aggregates/chains of triblock copolymer into micelles to produce micelle with any size until reaching a thermodynamically stable micellar size. The growth dynamics exhibit a relatively slow process with a characteristic time with values from 800s to 4000s. A simulation of this process is possible in order to take into account the reduction of micelles and an exponential behavior, however it will be done in order to analyse the process in a more detailed way in a future.
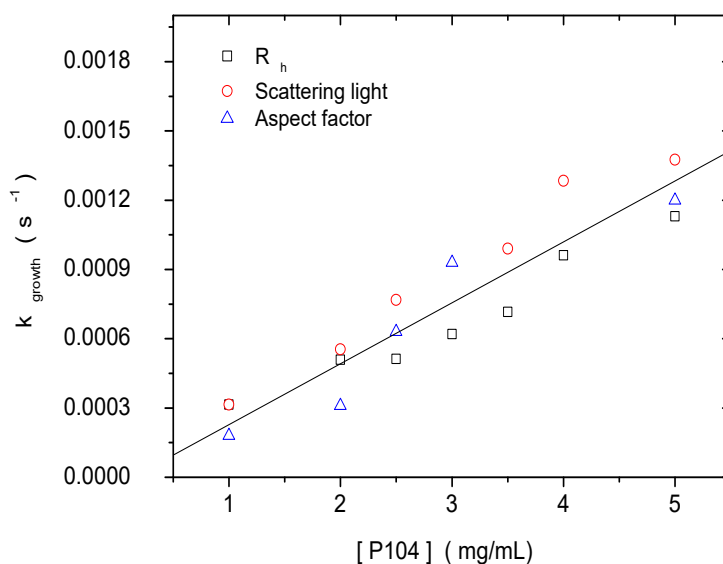
Figure 4.8. *Growth rate (k_{growth}) calculated from the evaluation of the hydrodynamic radius, R_h, the scattering light and the aspect factor decays by using the mono-exponential expression as a function of P104 concentration.*

4.3.1.4. Temperature effect on the growth process

*Figure 4.9 a* and *b* show the growth kinetics through the response of the hydrodynamic radius and the light scattering intensity, respectively, as a function of time for a P104 solution with a concentration of 20 mg/mL, after the temperature jump from the temperature T1= 38 °C to the temperatures of 42, 50, 55 and 58 °C. We can observe that the final values for R_h increase with the temperature increase, i.e. 22 nm at 42 °C, 24 nm at 50 °C, 38 nm at 55 °C and 54 nm at 58 °C. With light scattering intensity measurements, it is possible to observe that he growth process becomes evident after a temperature of 50 °C.
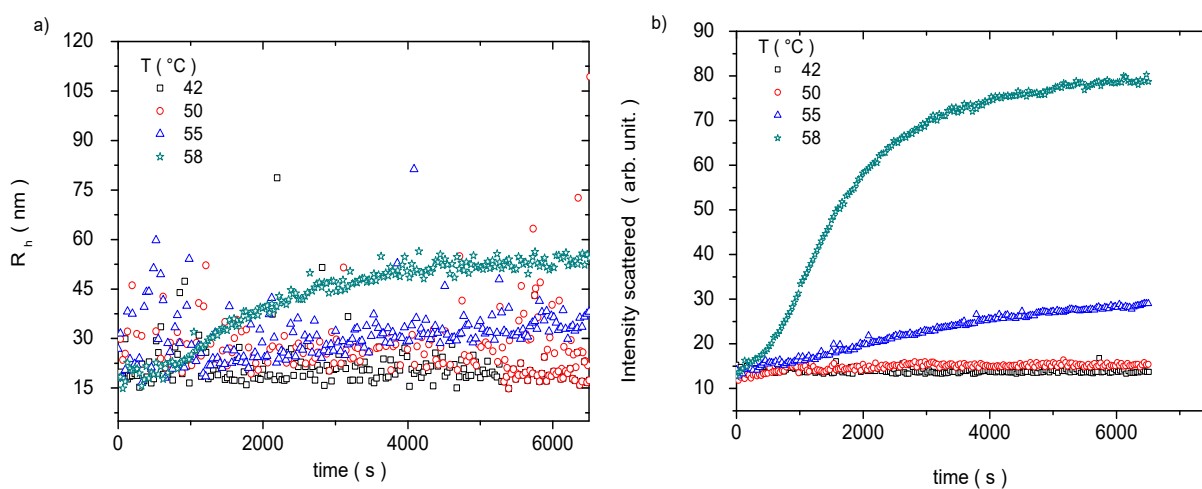
Figure 4.9. *a) Hydrodynamic radius and b) scattering light intensity as a function of time for a P104 solution with a concentration of 20 mg/mL after the temperature jump from T1 = 38 °C to the temperatures of 42, 50, 55 and 58 °C.*

4.3.1.5. NaCl effect on the growth process

Figure 4.10 a shows the dependence of the hydrodynamic radius as a function of time for a P104 solution with a concentration of 20 mg/mL in 0.5 M NaCl by changing the temperature from 38 °C to 64 °C. We can observe that a single process describes also the increase of the hydrodynamic radius (R_h) as a function of time, in the same way that for a P104 solution in water. In this manner, at this NaCl concentration, the increasing decay of R_h can be also be simulated by using an mono-exponential expression with a rate k_{growth} ^{Rh} = $1/\tau \square \square$ However, here the k_{growth} obtained from the R_h decay differs to the one obtained from the Scattering Light Intensity, suggesting the formation of a different structure during the growth process. This effect will be further studied. *Figure 4.10 b* shows the influence of NaCl concentration on the growth rate for a P104 solution with a concentration of 20 mg/mL. We can observe that k_{growth} increases with the increase of NaCl concentration, suggesting a slower transition from spherical micelles to rod-like micelles compared to P104 micelles in water as a solvent.
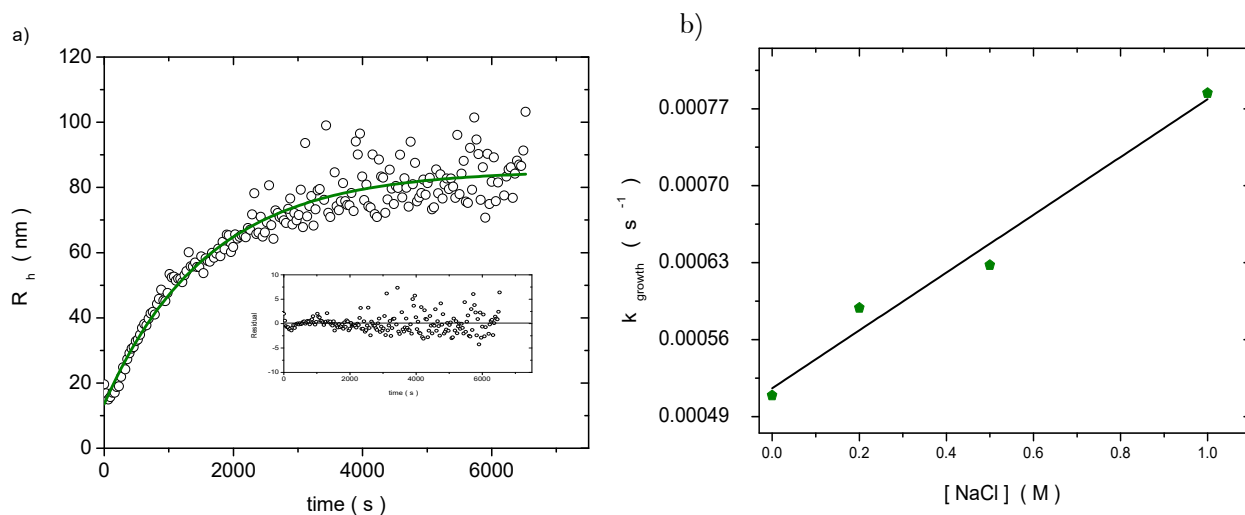
Figure 4.10. *a) Hydrodynamic radius, R_h, versus time for a P104 solution with a concentration of 20 mg/mL in 0.5 M NaCl obtained after a "temperature jump" from a $T_1 = 38$ °C to $T_2 = 64$ °C. The solid line represents the obtained fitting using a mono-exponential expression that simulates the intensity decay. b) Growth rate (k_{growth}) calculated from the evaluation of the scattered intensity by using the mono-exponential expression as a function of P104 concentration.*

## 4.3.2. Collective dynamics of P104 triblock copolymer in water at the equilibrium

The availability of a hydrophobic core region within triblock copolymer micelles (Pluronics) allows for stable loading of poorly soluble hydrophobic drugs during micellization. The encapsulation of hydrophobic drugs in nanoparticles can increase the accumulation of drugs in tumors, reduce toxicity for healthy tissue and improve pharmacokinetics in comparison to administration processes of free drug [43]. However, when developing nanoparticles for drug delivery, it is important to understand the interaction mechanisms between the nanoparticles and the delivery mechanisms of the encapsulated drug to achieve efficient delivery and release of drugs to the target [44].

4.3.2.1. Micellar dynamics

The micellar dynamics at equilibrium of aqueous solutions of P104 triblock copolymer were studied by using a fluorescent hydrophobic substance (PyC_{18}) in order to follow the exchange between micelles at equilibrium. Fluorescence measurements were performed by mixing P104 micelles containing PyC_{18} with micelles probe-free at the same temperature and with the same P104 concentration. Through these measurements it is possible to analyze different exchange mechanisms between micelles in order to determinate the dominant ones.

4.3.2.2. Solubilization and fluorescence of PyC_{18} in P104 triblock copolymer micelles

As previously determined from DLS measurements, P104 aqueous solutions form spherical micelles between the temperatures of 26 °C and 55 °C with a hydrodynamic radius of 11.85 ± 1 nm (for a P104 concentration of 10 mg/mL). Therefore, P104 amphiphilic copolymer presents a range of temperatures where it is possible to obtain spherical micelles at low temperature (25 °C - 54 °C) and rod-like micelles below 54 °C. The dynamics at equilibrium at both domains (spherical micelles and rod-like micelles) were studied using the formation of an excimer of a highly hydrophobic pyrene as a function of time. For the incorporation of the hydrophobic probe (PyC_{18}) (*Figure 4.11*), P104 aqueous solutions were heated above the clouding point and then cooled to a temperature within the range in which spherical micelles are formed. This way, micelles dissolve the modified pyrene PyC_{18} randomly. The fluorescent spectra of the copolymer micelles containing more than one molecule of PyC_{18} depict a wide excimer emission band with a peak at 480 nm and a monomer band between 375.5 and 400 nm.
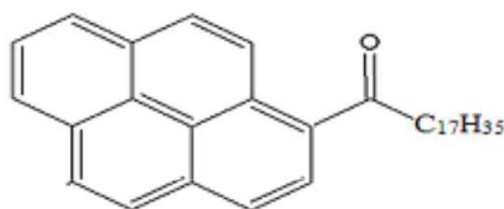
Figure 4.11. *Molecular structure of the hydrophobic fluorescent probe PyC_{18}.*

Figure 4.12 a shows the fluorescence spectra for various concentrations of PyC_{18} in P104 aqueous solutions at a concentration of 50 mg/mL. By diluting the 50 mg/mL P104 solution filled with PyC_{18} with probe-free copolymer, the spectrum evolves and shows a greater monomer emission. At the lowest concentration of PyC_{18}, the excimer emission is barely detectable, however, at higher concentrations it is very important, with a peak at 480 nm. The ratio of the excimer to monomer intensities, I_{ex}/I_{mon}, is very sensitive to the distribution of PyC_{18} in the P104 micelles. When two PyC_{18} molecules are present in the micelles, their signal is emitted in the excimer regime (i.e. between 450 and 550 nm) and when one PyC_{18} molecule is in the micelle, its signal is emitted in the monomer form (376 nm). When the distribution of PyC_{18} in the micelles follows the Poisson distribution, the ratio between I_{ex} and I_{mon} is proportional to *<n>* (i.e. [PyC_{18}]/[Micelles], where [Micelles]=([P104] − CMC)/N_{agg}) [29]. N_{agg} corresponds to the aggregation number, which is a temperature dependent parameter and has been take from the reported values by *Liu et al.* [46]. An UV-Vis analysis allows calculating PyC_{18} concentration present on the initial solution (i.e. 2.9×10^{-4} M).

a)

b)
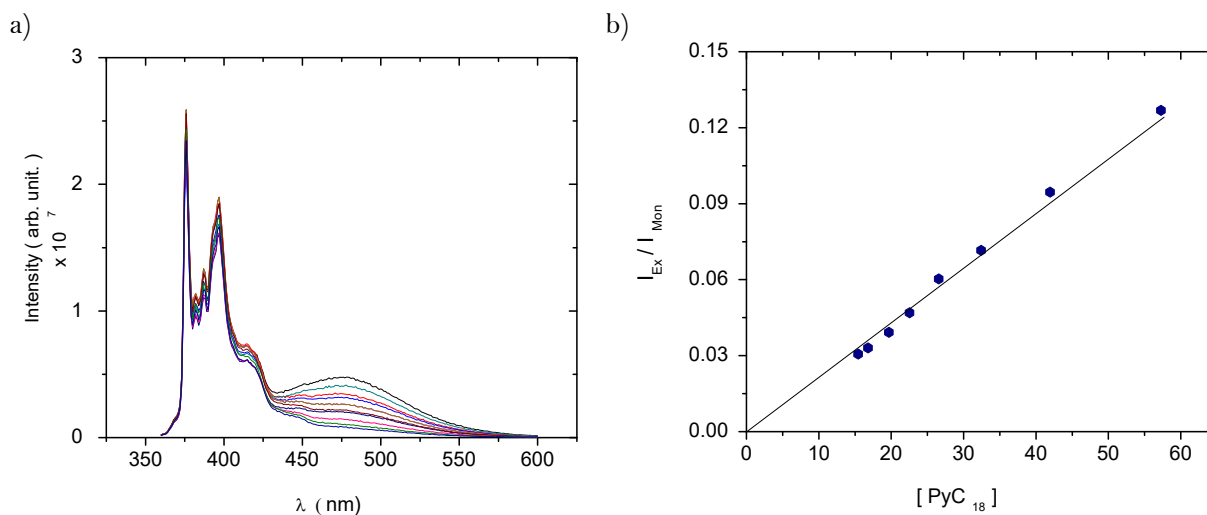
Figure 4.12. *a) Emission spectra (λ_ex=344nm) for various concentrations of PyC₁₈ in P104 aqueous solutions at a concentration of 50 mg/mL monitored at ac onstant temperature: 37 °C. b) Linear dependence between I_ex/I_mon with PyC₁₈ concentration in a 50 mg/mL P104 solution at a temperature of 37 °C (r² = 0.971).*

Figure 4.12 b shows the linear dependence between I_{ex}/I_{mon} and the PyC$_{18}$ concentration in a 50 mg/mL P104 sample. The relation between the excimer intensity (λ_{ex} = 480 nm) and the monomer intensity (λ_{mon} = 375 nm), I_{ex}/I_{mon}, increases linearly with the increase of the average number of hydrophobic probe per micelle <*n*>. This linear dependence suggests that the PyC$_{18}$ follows a random Poisson distribution for all P104 concentrations at all the studied temperatures in this work. The exchange kinetics was then performed taking into account low values of the average number of PyC$_{18}$ per micelle, <*n*>.

4.3.2.3. PyC$_{18}$ exchange kinetics in P104 triblock copolymer micelles

Figure 4.13 shows the fluorescence spectra of PyC$_{18}$ solubilized in a P104 aqueous solution with a concentration of 50 mg/mL before and after the addition of a probe-free P104 aqueous solution with the same concentration at a temperature of 37 °C. In this figure it is possible to observe clearly that the value of the excimer intensity, detected at a wavelength at 480 nm and identified as "before the exchange", is lower than the value of the monomer intensity, located at a wavelength at 376 nm and labeled as "after the exchange." The spectrum has a broad excimer emission with a peak at 480 nm and monomer fluorescence at 376-400 nm. The existence of the excimer emission at 480 nm infers the presence of micelles bearing two or more PyC$_{18}$ molecules [29].
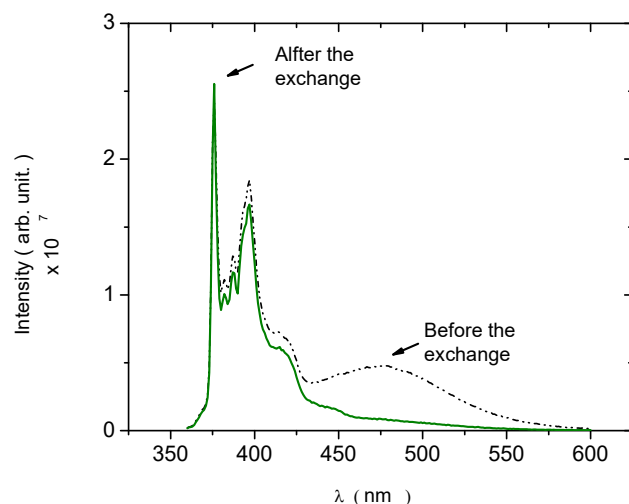
Figure 4.13. *Emission spectra (λ_{ex}= 344 nm) of PyC$_{18}$ in 50 mg/mL P104 solution. The spectrum labeled "before exchange" identifies the P104 solution containing the hydrophobic probe PyC$_{18}$. The spectrum labeled "after exchange" identifies the solution obtained by mixing 0.05 mL of micelles filled with PyC$_{18}$ and 1 mL of empty P104 micelles (50 mg/mL) measured after 2 hours.*

Figure 4.14 shows the excimer and monomer decays obtained after mixing a 40 mg/mL P104 solution filled with PyC$_{18}$ and a 40 mg/mL free-probe P104 solution as a function of time. A volume ratio of 0.05:1 ([PyC$_{18}$ in P104 micelles]:[Probe free P104 micelles]) was used for the mixing process of the P104 solutions filled with hydrophobic probe and the P104 micelles probe-free, respectively. This behavior follows an exponential function.
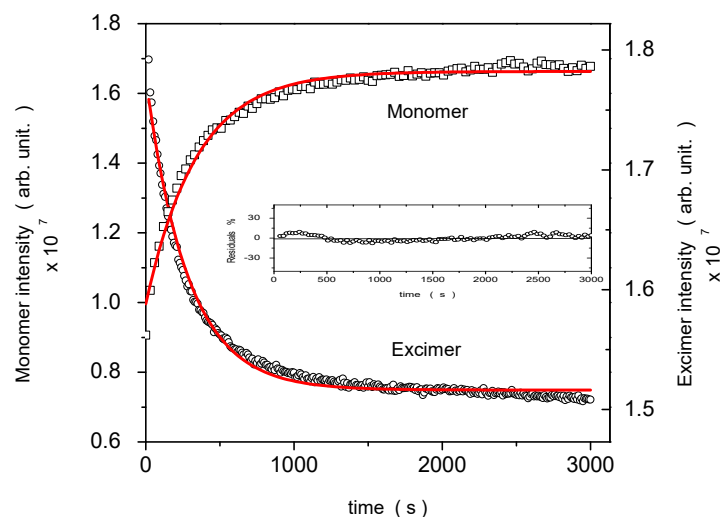
Figure 4.14. *Decay of the excimer band (λ_{em} = 480 nm) and the monomer band (λ_{em} = 376 nm) after mixing 0.05 mL of a 40 mg/mL P104 solution with PyC$_{18}$ and 1mL of a 40 mg/mL P104 probe-free solution at the temperature of 40 °C. The solid line represents the fit to a single exponential expression (r^2 = 0.988).*

The fitting of each of the decays was performed using a mono-exponential function in order to determine the kinetic constants from the inverse of the relaxation times ($k_{decay}=1/\tau$). The relaxation time (τ) from the mono-exponential function is similar to the average value $<\tau>$ calculated from the fit to two exponentials.

4.3.2.4. Concentration dependence on the exchange dynamics

Kinetic experiments were performed in a P104 concentration range between 10 and 100 mg/mL for the temperatures from 30 ºC to 64 °C, this way, the dynamic micellar profiles were obtained within the spherical micelles region and the cylindrical elongated micelles region before the clouding point. *Figure 4.15* shows the excimer decays obtained after mixing a 30, 50, 80 and 100 mg/mL P104 solution filled with PyC$_{18}$ with their respective free-probe P104 solution as a function of time.
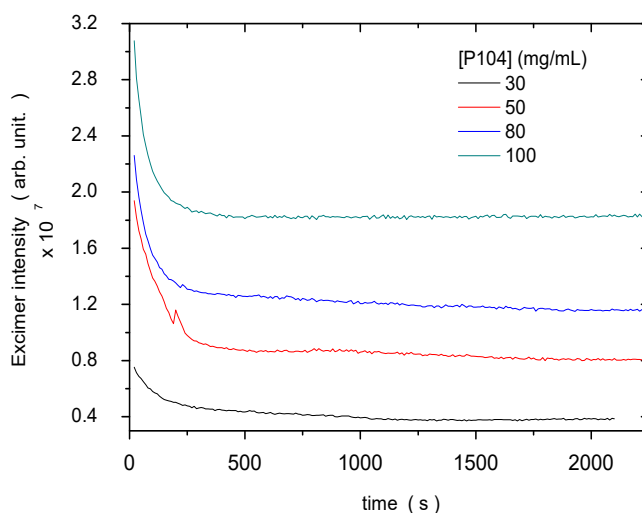

Figure 4.15. *Decay of the excimer band (λ_{em} = 480 nm) and the monomer band (λ_{em} = 480 nm) after mixing 0.05 mL of a 30, 50, 80 and 100 mg/mL P104 solution with PyC$_{18}$ and 1mL of a 30, 50, 80 and 100 mg/mL P104 probe-free solution at the temperature of 30 °C. The solid line represents a fit to a single exponential expression ($r^2 = 0.988$).*

Figure 4.16. shows the linear dependence of the kinetic constant (k_{decay}) with [micelles] at the temperature of 30 ºC, as described by *Equation 4.5*.

$$k_{decay} = k_1 + k_2 \, [micelles] \tag{4.5}$$

This behavior suggests the existance of a first order process with a rate k_1 independent of free-probe micelles and a secong order process with a linear dependence of k_{decay} with [micelles].

As presented in *Figure 4.3*, the exchange of the probe could take place by fission-growth of micelles, exit-entry of the probe and fusion-fission of micelles, which could occur simultaneously. Since the rates of these processes have different sensitivities to copolymer concentration, their individual contribution can be separated. If the exchange is carried out via exit-entry of the probe and via fission-growth of micelles, it is characterized by a first-order kinetics, whereas the collision fusion-fission mechanism exhibits a second-order kinetics with a second-order rate constant. The second-order process k_2 is dominated by fusion−fission, involving several steps: collision of a full and an empty micelle, adhesion of these micelles, fusion of the two micelles to form a large one, exchange of the solute within the large micelle, and fission of the large micelle into two micelles containing one PyC_{18} each one. It was shown that the fusion rate is independent of the polarity of the probe in Triton X-100 and synperonic surfactants, so the second-order fusion rate reflects the rate of fusion [29-31].

When the concentration of empty micelles is larger than the concentration of micelles containing PyC_{18}, we obtain a pseudo-first-order exchange rate constant dependent on the concentration of empty micelles (*Equation 4.6*).

$$k_{decay} = k_{exit} + k_{fiss} + k_{fus} \, [micelles] = k_{exit} + k_{fiss} + k_{fus} \, ([P104] - CMC) / N_{agg} \tag{4.6}$$

where k_{exit} is the exit-entry kinetic constant, k_{fiss} corresponds to the fission micelles kinetic constant and k_{fus} to the fusion kinetic constant between micelles filled with PyC_{18} and probe-free micelles.
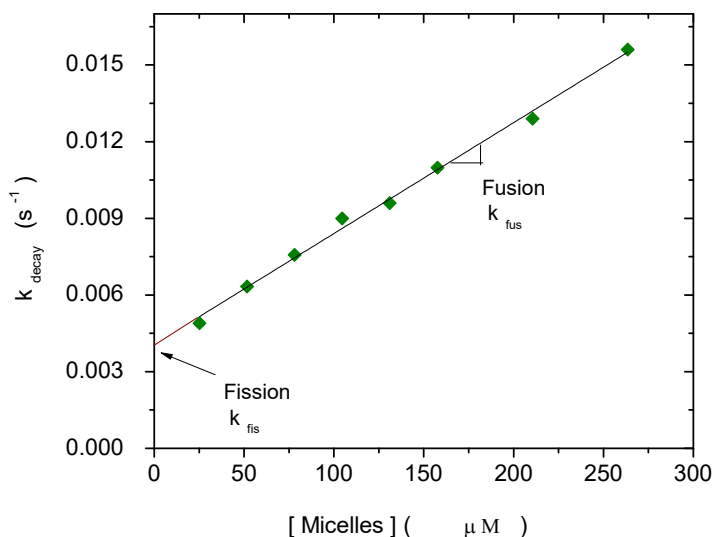
Figure 4.16. *Linear dependence of the kinetic constant (k_{decay}) with micelle concentration for P104 triblock copolymer at the temperature of 30 °C, where $[Micelles]=([P104] - CMC) / N_{agg}$.*

As shown on *Figure 4.3*, the first order mechanism may be due to the exit-entry (k_{exit}) and the fission (k_{fiss}) processes. The limiting rate for the exit-entry mechanism of the probe is water solubility (C_w) and diffusion through the core/corona. If water solubility is the dominant barrier, then the exit rate can be estimated through the following expression:

$$k_{exit} = k_{entry*}c_\omega/n_m \tag{4.7}$$

where n_m is the average number of probe per micelle at the equilibrium.

A water-soluble probe soluble such as pyrene (10^{-7} mol/L) can be exchanged mainly through an exit-entry mechanism. However, the C_{18} chain present on the hydrophobic probe, PyC_{18}, reduces its water solubility and makes insignificant the exit rate. This way, the first order mechanism is related to the fission process.

In *Figure 4.26*, the intercept represents the first order mechanism that describes an exchange due to a fission of a micelle filled with PyC_{18} in two micelles, followed by the growth of this resulting micelle (by association or fusion). The second order mechanism, with linear dependence on k_{decay} on the [micelles] is related to a fusion-fission process, which involves the following steps: collision of a micelle filled with PyC_{18} and an empty micelle, exchange of the solute inside that big micelle and fission of this micelle in two normal size micelles with a fluorescent probe inside each one of them.

Halperin et al. [12] suggested that fission and fusion mechanisms are negligible in comparison to the expulsion-insertion of the copolymer chain. They reported that the coronal energetical barrier (steric barrier) and the interfacial barrier (surface tension) lead to fission-fusion rates extremely small, which are not possible to identify. However, our results show that fission and fussion mechanisms take place at equilibrium in block copolymer micelles. Even if k_{fiss} and k_{fus} *are 10^6* times slower, they are still important and are crucial for controlling the structure of the block copolymer micelles. This has been presented in the sphere to rod-like micelles transition, which is dominated by the fussion and fission rates. Furthermore, we will show in the following chapter that these mechanisms are important in the vectorization process.

4.3.2.5. Temperature dependence on the exchange dynamics

Figure 4.17 a shows the linear dependence of k_{decay} with [micelles] for the temperatures between 30 and 50 °C, where spherical micelles are thermodinamically stable. *Figure 4.17 b* presents the k_{obs} versus [micelles] in the rod-like micelles regime between 50 °C and 57 °C. Here it is possible to identify that k_{decay} values decrease in the spherical regime and increase in the rod-like micelles regime.
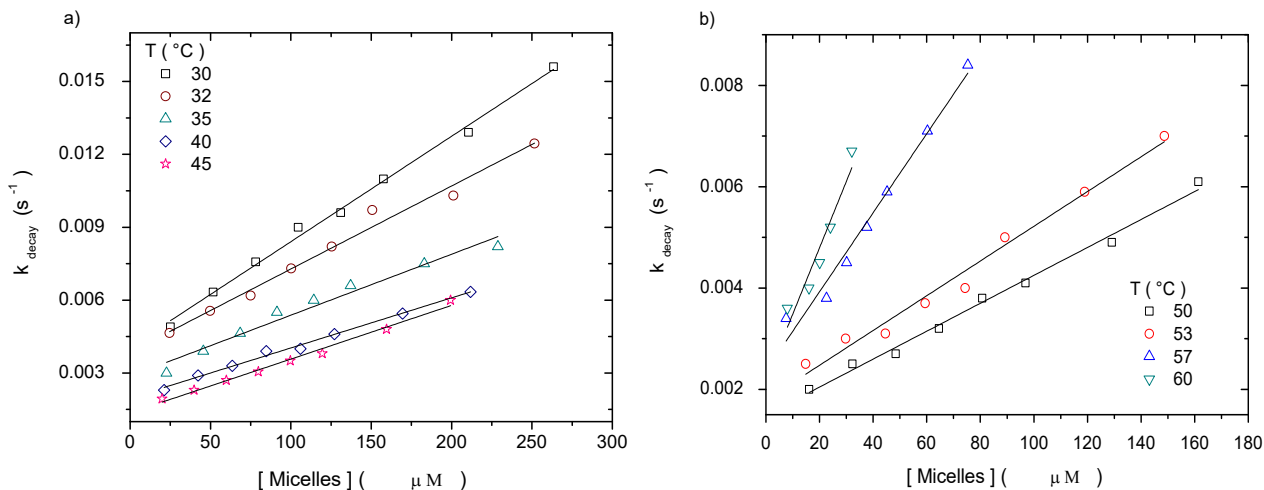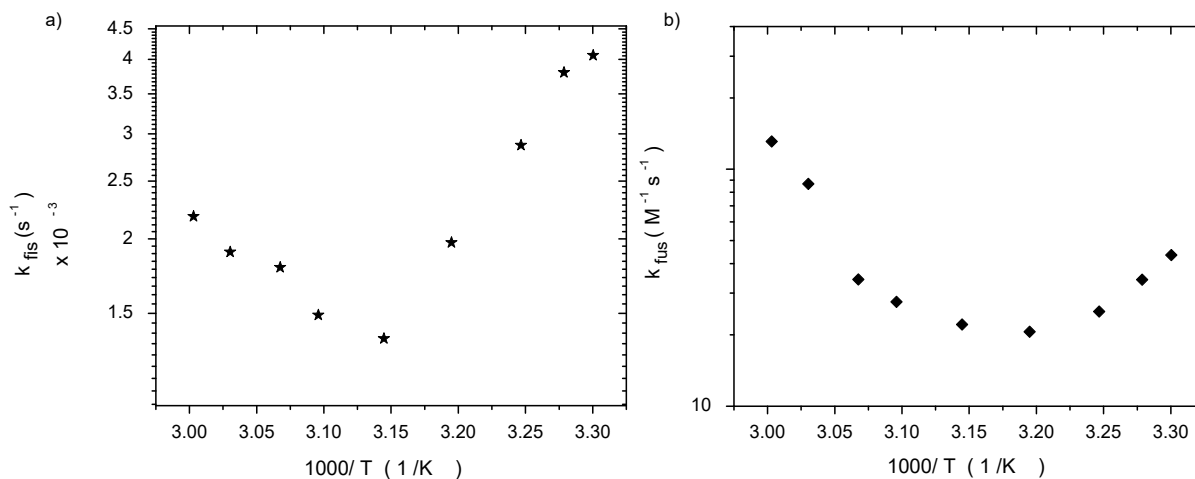
Figure 4.17. *Kinetic constant (k_{decay}) obtained through the fitting of the exchange decays of PyC_{18} in P104 solutions with a mono-exponential function plotted as a function of empty micelles concentration at the temperatures of a) 30, 32, 40, 45 and 50 °C and b) 50, 53, 57 and 60 °C.*

Figures 4.18 a and *b* present k_{fiss} and k_{fus} in Arrhenius plots. In both figures it is possible to observe that the fission and fusion constants present two apparent activation energies with opposite sign, a negative apparent activation energy in the micelles regime and a positive apparent activation energy in the rod-like micelles regime. In the spherical regime, both kinetic constants (k_{fiss} and k_{fus}) decrease with the increase of temperature, with almost similar apparent activation energy, suggesting that they have a similar energy barrier. According to *Halperin et al.* [12], the energy barrier to fission can be estimated from the combination of surface tension energy and core elastic energy ($\gamma_{PPO/water}$). When increasing the temperature in the spherical regime, $\gamma_{PPO/water}$ increases, enhancing the barrier to fussion and leading to the reduction of k_{fiss}. The similarity in the slope of k_{fiss} and k_{fus} versus the inverse of temperature suggests that the barrier to fusion in the spherical regime is also the core surface tension. This is not consistent with Halperin's suggestion, since they proposed that the coronal steric energy is the main contribution to the energy barrier. Here we show that the core surface tension and the coronal energy are important barriers to fusion of micelles.

When the sphere to rod-like micelles transition is approached, k_{fus} shows a plateau and then drastically increases in the rod regime. In this regime, the PEO corona collapses, reducing the steric coronal repulsion and leading to a decrease of the barrier energy to fusion. The fission rate also increases in the rod-like micelles regime, with a lower magnitude than fusion, which suggests that the coronal energy contributes to the fission barrier to some extent. Surface instabilities can appear when the corona collapses, promoting micelles pinching and micelles breaking. This was recently seen in surfactant micelles and reported by *Rharbi et al.* [47].

Our results show that the barrier energy to fission is controlled by the core surface tension in the spherical micelles regime and by a combination of the surface tension and the coronal energy in the rod-like micelles regime. The fusion process is mainly affected by the core surface tension in the spherical regime and the collapse of the corona in the rod-like micelles regime.

Figure 4.18. *Arrhenius plots for the a) fission kinetic constant, and the b) fusion kinetic constant calculated by the linear dependence of the kinetic constant k_{decay} as a function of P104 empty micelles concentration.*

4.4. Particular conclusions for the collective dynamics of P104 amphiphilic block copolymer in and out of equilibrium

In this study we described the transition dynamics of spherical micelles to elongated cylindrical micelles in aqueous solutions of P104 triblock copolymer. Were carried out experiments called "temperature jumps", obtaining the variation of the scattering intensity and the hydrodynamic radius as a function of time with dynamic light scattering (DLS). The growth dynamics present a relatively slow process with characteristic times within the range of 800s to 4000s. The scattering intensity, the hydrodynamic radius and the aspect factor evolution as a function of time were analyzed by using a mono-exponential function with an apparent relaxation time. The linear increase of the growth rate with P104 triblock copolymer concentration shows that the structural transition is dominated by a fusion-fission mechanism with normal size micelles. The growth constant increases with the increase of NaCl concentration, suggesting a slower transition from spherical micelles to rod-like micelles compared to P104 micelles in water as a solvent.

Additionally, we demonstrated that collective dynamics take place between P104 spherical micelles and P104 rod-like micelles at the equilibrium. The exchange mechanism depicted by k_{decay} consists on two processes: a first order mechanism with linear velocity independent of the empty micelles concentration, related to the fission process, and a second order mechanism with linear dependence on

k_{decay} as a function of the empty micelles concentration, related to the fusion process. Fission and fusion constants present two apparent activation energies with opposite sign, a negative apparent activation energy in the micelles regime and a positive apparent activation energy in the rod-like micelles regime. We show that the barrier energy to fission is controlled by the core surface tension in the spherical micelles regime and by a combination of the surface tension and the coronal energy in the rod-like micelles regime.

4.5. References

[1] T. Nicolai, O. Colombani and C. Chassenieux, Dynamic polymeric micelles versus frozen nanoparticles formed by block copolymers, *Soft Matter* **6**, 3111 (2010).

[2] A. Halperin and S. Alexander, Polymeric micelles: their relaxation kinetics, *Macromolecules* **22**, 2403 (1989).

[3] S.E. Burke and A. Eisenberg, Kinetics and mechanisms of the sphere-to-rod and rod-to-sphere transitionsin the ternary system PS310-b-PAA(52)/dioxane/water, *Langmuir* **17**, 6714 (2001).

[4] B. Michels, G. Waton and R. Zana, Dynamics of micelles of poly(ethylene oxide)- poly(propylene oxide)-poly(ethylene oxide) block copolymers in aqueous solution. *Langmuir* **13**, 3111−3118 (1997).

[5] C. K. Kim, P. Ghosh, C. Pagliuca, Z.-J. Zhu, S. Menichetti and V. M. Rotello, Entrapment of Hydrophobic Drugs in Nanoparticle Monolayers with Efficient Release into Cancer Cells, *J. Am. Chem. Soc.* **131** (4) 1360−1361 (2009).

[6] P. Broz, S. M. Benito, C.L. Saw, P. Burger, H. Heider, M. Pfisterer, S. Marsch, W. Meier and P. Hunziker, Cell targeting by a generic receptor-targeted polymer nanocontainer platform, *Journal of Controlled Release* **102**, 475−488 (2005).

[7] M. Hamidi, M.-A. Shahbazi and K. Rostamizadeh, Copolymers: Efficient Carriers for Intelligent Nanoparticulate Drug Targeting and Gene Therapy, *Macromol. Biosci.* **12**, 144-164 (2012).

[8] E.V. Batrakova and A. V. Kabanov, Evolution of Drug Delivery Concept from Inert Nanocarriers to Biological Response Modifiers, *J Control Release* **130**(2), 98−106 (2008).

[9] A.V. Kabanov, E.V. Batrakova and V.Y. Alakhov, Pluronic block copolymers as novel polymer therapeutics for drug and gene delivery, *J Control Release* **82**(2-3), 189-212 (2002).

[10] M. Hamidi, M.-A. Shahbazi and K. Rostamizadeh, Copolymers: Efficient Carriers for Intelligent Nanoparticulate Drug Targeting and Gene Therapy, Macromolecular Bioscience **12**, 144-164 (2012).

[11] E.A.G. Aniansson and S.N. Wall, Kinetics of step-wise micelle association, *J. Phys. Chem.* **78**, 1024-1030 (1974).

[12] E.A.G. Aniansson, S.N. Wall, M. Almgren, H. Hoffmann, H. Kielmann, W. Ulbricht, R. Zana, J. Lang and C. Tondre, *J. Phys. Chem.* **80**, 905−922 (1976).

[13] S.N. Wall and E.A. Aniansson, Numerical calculations on the kinetics of stepqise micelle association, *J. Phys. Chem* **84**, 727-736 (1980).

[14] M. Kahlweit, Kinetics of formation of association colloids**,** *J. Colloid Interface Sci.* **90**, 92−99 (1982).

[15] E. Lessner, M. Teubner, and M. Kahlweit, Relaxation experiments in aqueous solutions of ionic micelles. 2. Experiments on the system water-sodium dodecyl sulfate-sodium perchlorate and their theoretical interpretation *J. Phys. Chem.* **85**, 3167−3175 (1981).

[16] P. Rene and P.G. Bolhuis, Prediction of an Autocatalytic Replication Mechanism for Micelle Formation *Phys. Rev. Lett.* **97** (2006).

[17] E.E. Dormidontova, Micellization kinetics in block copolymer solutions: Scaling model, *Macromolecules* **32**, 7630−7644 (1999).

[18] Y. Rharbi, Fusion and Fragmentation Dynamics at Equilibrium in Triblock Copolymer Micelles, *Macromolecules 45,* 9823-9826 (**2012).**

[19] J. Zhang, J. Xu, S. Liu, Chain-Length Dependence of Diblock Copolymer Micellization Kinetics Studied by Stopped-Flow pH-Jump, *J. Phys. Chem. B* **112**, 11284 (2008).

[20] A.G. Denkova, E. Mendes and M.-O. Coppens, Rheology of worm-like micelles composed of tri-block copolymer in the limit of slow dynamics, *J. Phys. Chem B.* **113**, 989 (2009).

[21] Y. Kadam, R. Ganguly, M. Kumbhakar, V.K. Aswal, P.A. Hassan and P. Bahadur, Time dependent sphere-to-rod growth of the pluronic micelles: investigating the role of core and corona solvation in determining the micellar growth rate, *J. Phys. Chem. B* **113**, 16296 (2009).

[22] G. Landazuri, V. V. A Fernandez, J. F. A. Soltero and Y. Rharbi, Kinetics of the Sphere-to-Rod like Micelle Transition in a Pluronic Triblock Copolymer, *J. Phys. Chem. B* **116**, 11720−11727 (2012).

[23] C. K. Kim, P. Ghosh, C. Pagliuca, Z.-J. Zhu, S. Menichetti and V. M. Rotello, Entrapment of Hydrophobic Drugs in Nanoparticle Monolayers with Efficient Release into Cancer Cells, *J. Am. Chem. Soc.* **131** (4) 1360−1361 (2009).

[24] P. Broz, S. M. Benito, C.L. Saw, P. Burger, H. Heider, M. Pfisterer, S. Marsch, W. Meier and P. Hunziker, Cell targeting by a generic receptor-targeted polymer nanocontainer platform, *Journal of Controlled Release* **102**, 475–488 (2005).

[25] M. Hamidi, M.-A. Shahbazi and K. Rostamizadeh, Copolymers: Efficient Carriers for Intelligent Nanoparticulate Drug Targeting and Gene Therapy, *Macromol. Biosci.* **12**, 144-164 (2012).

[26] E. V. Batrakova and A. V. Kabanov, Evolution of Drug Delivery Concept from Inert Nanocarriers to Biological Response Modifiers, *J Control Release* **130**(2), 98–106 (2008).

[27] A.V. Kabanov, E.V. Batrakova and V.Y. Alakhov, Pluronic block copolymers as novel polymer therapeutics for drug and gene delivery, *J Control Release* **82**(2-3), 189-212 (2002).

[28] M. Hamidi, M.-A. Shahbazi and K. Rostamizadeh, Copolymers: Efficient Carriers for Intelligent Nanoparticulate Drug Targeting and Gene Therapy, Macromolecular Bioscience **12**, 144-164 (2012).

[29] Y. Rharbi, M. Li, M.A. Winnik and K.G. Hahn, Temperature Dependence of Fusion and Fragmentation Kinetics of Triton X-100 Micelles, *J. Am. Chem. Soc.* **122**, 6242–6251 (2000).

[30] Y. Rharbi, N. Bechthold, K. Landfester, A. Salzman and M.A. Winnik, Solute exchange in synperonic surfactant micelles, *Langmuir* **19**, 10-17 (2003).

[31] Y. Rharbi, M.A. Winnik and K.G. Hahn, Kinetics of Fusion and Fragmentation Nonionic Miedles: Triton X-100, *Langmuir* **15**, 4697–4700 (1999).

[32] M.S. Turner and M.E. Cates, Flow-induced gelation of rodlike micelles, *Europhysics Letters* **11**, 681 (1990).

[33] R. Lund, L. Willner, D. Richter and E.E. Dormidontova, Equilibrium chain exchange kinetics of diblock copolymer micelles: Tuning and logarithmic relaxation, *Macromolecules* **39**, 4566–4575 (2006).

[34] Y.Y. Won, H.T. Davis and F.S. Bates, Molecular exchange in PEO-PB micelles in water, *Macromolecules* **36**, 953–955 (2003).

[35] B.K. Johnson and R.K. Prud'homme, Mechanism for Rapid Self-Assembly of Block Copolymer Nanoparticles, *Phys. Rev. Lett.* **91** (2003).

[36] R.S. Underhill, J. Ding, V.I. Birss and G. Liu, Chain Exchange kinetics of polystyrene-block-poly(2-cinnamoylethyl methacrylate) micelles in THF cyclopentane, *Macromolecules* **30**, 8298–8303 (1997).

[37] I. LaRue, M. Adam, M. Pitsikalis, N. Hadjichristidis, M. Rubinstein, S.S. Sheiko, *Macromolecules* **39**, 309–314 (2006).

[38] B.J. Berne and R. Pecora, *Dynamic Light Scattering*, John Wiley and Sons, Inc, New York, (1976).

[39] M.E. Cates and M.R. Evans. *Soft and Fragile Matter. Nonequilibrium Dynamics, Metastability and Flow*. SUSSP, (2000).

[40] N. Muller, *Kinetics of Micellization in Solution Chemistry of Surfactants, Vol. I*, Mittal, K. L., Ed. Plenum, New York, 267 (1979).

[41] J. Gormally, W.J. Gettins, E. Wyn-Jones, K*inetic Studies of Micelle Formation in Surfactant in Molecular 1nteractions*, Vol. 2, H. Ratajczak, W.J. Orville-Thomas, Eds., Wiley, New York, 143 (1980).

[42] I. Goldmints, J.F. Holzwarth, K.A. Smith, T.A. Hatton, Micellar dynamics in aqueous solutions of PEO-PPO-PEO block copolymers. *Langmuir*, **13**, 6130 (1997).

[43] S. Snipstad, S. Westrom, Y. Morch, M. Afadzi, A. K. Aslund and C. De L. Davies, Contact-mediated intracellular delivery of hydrophobic drugs from polymeric nanoparticles, *Cancer Nanotechnology* 5, 8 (2014).

[44] J. Panyam and V. Labhasetwar, Biodegradable nanoparticles for drug and gene delivery to cells and tissue. *Adv Drug Deliv Rev* 55 ,329-347 (2003).

[45] D.M. Hercules, *Fluorescence and phosphorescence analysts*, Editor Wiley-Interscience Publishers, New York, London, Sydney (1965).

[46] Y. Liu, S.-H. Chen and J. S. Huang, Small-Angle Neutron Scattering Analysis of the Structure and Interaction of Triblock Copolymer Micelles in Aqueous Solution, *Macromolecules* **31**, 6226-6233 (1998).

[47] Y. Rharbi, M. Karrouch, and P. Richardson, Fusion and Fission Inhibited by the Same Mechanism in Electrostatically Charged Surfactant Micelles, *Langmuir*, **30** (27), 7947−7952 (2014).

CHAPTER 5

Exchange dynamics between amphiphilic block copolymers and lipidic membranes

5. Exchange dynamics between amphiphilic block copolymers and lipidic membranes

5.1. Introduction

Nowadays, the specific delivery of active ingredients, known as vectorization, represents a great challenge in therapeutic research [1-3]. This process has been used to control the distribution of active ingredients such as proteins, genes for gene therapy and drugs, to a target by associating it with a vector [4,5] and allows maximizing the therapeutic effects of the drug and may minimize the side effects [6]. Vectorization may be achieved by chemical, physical or biological methods, and is considered an important process in cases where the drug is chemically unstable or presents weak characteristics pharmacokinetics [7,8]. Vectorization proposes benefits such as increasing the therapeutic effect, decreasing toxicity causing the active principle, increasing half-life of the active ingredient and releasing the active ingredient release in time among others [9,10].

The three main types of physical vectors are liposomes, microparticles and nanoparticles [11,12]. Liposomes are different from the microparticles and nanoparticles due to their nature and composition. However, the main difference between microparticles and nanoparticles is the size of both structures, i.e., greater or less than 1 μm, respectively [13,14]. More specifically, it is noteworthy that the liposomes are vesicles consisting of concentric membranes with single or multiple phospholipid bilayers [15] that contain an aqueous volume within and are used as the simplest models of cells [16]. They are formed spontaneously as a result of lipid-water interactions. Various techniques exist for preparing liposomes, which can allow obtaining vesicles with different sizes, internal volume and encapsulation capacity [16,17].

Vectorization has undergone significant development in the last few years [18,19]. Currently, molecules used in chemotherapy are generally hydrophobic and require a vectorization process to be transported to the target cell [20,21]. However, this controlled release of drugs suffers from a phenomenon known as "burst release", in which the active ingredient is released before reaching its target [22-24]. The focus of this chapter is related to these dynamics between triblock copolymers and liposomes for the vectorization of hydrophobic molecules, using a fluorescence technique. Very few studies have examined the collective mechanisms of micelles in the transport and removal of the active ingredients. Understanding the exchange dynamics becomes crucial for the design and control of new materials and new effective processes in controlled drug release.

Our study system is composed by liposomes representing cells, amphiphilic block copolymer micelles modeling the transporting vehicles and highly hydrophobic alkylated pyrene representing the active ingredient introduced into the micelles. Time scan fluorescence technique, which has been previously used to quantify the collective dynamics between amphiphilic block copolymer micelles [25],

was used in this work to quantify the vectorization dynamics between micelles and liposomes. We first used different techniques such as dynamic light scattering (DLS) and ζ–potential to characterize liposomes and block copolymer micelles and to explore liposome/micelles interactions. Then, we investigated several parameters that control the collective vectorization dynamics between micelles to liposomes, i.e. liposomes concentration and a chitosan coating on liposomes and micelles.

## 5.2. Experimental conditions

5.2.1. Materials

Triblock copolymer Pluronic® P104, [(PEO)$_{27}$–(PPO)$_{61}$–(PEO)$_{27}$], has a molecular weight of 5900 g/mol. This material was provided by the BASF Company. Solutions P104/H$_2$O were prepared with water obtained through a Millipore Milli-Q purification system. Chitosan sample with a molecular weight (M$_w$) of 500 000 and a DA of 0.19 was purchased from Kitomer (Marinard, Canada). HCl 0.1 N (Titrisol) was supplied by Merck Millipore. L-α-Phosphatidylcholine, also known as 1,2-Diacyl-*sn*-glycero-*3*-phosphocholine (from egg yolk) (*Figure 5.1*), C$_{42}$H$_{82}$NO$_8$P, with a molecular weight of 776 g/mol, was selected to prepare the lipid structures and was supplied by Sigma Aldrich. It is a zwitterionic phospholipid with two chains of 18 carbons having one unsaturation per each carbon chain (*Figure 5.1*). Its main transition temperature, T$_m$, is evaluated to -15 ºC [26]. We used an organic solvent prepared with chloroform and methanol. Both reagents were supplied also by Sigma Aldrich.
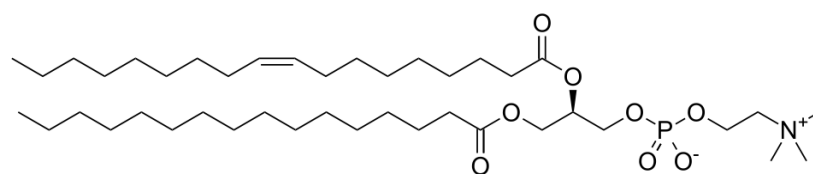
Figure 5.1. *Chemical structure of L-α-Phosphatidylcholine [27].*

5.2.2. Formation of GUVs and LUVs

The phospholipids were dissolved in a solution of chloroform and methanol with a ratio of 2:1 [28]. The aqueous phase (distilled water) was added carefully to the solution. The vesicles were formed in distilled water at a concentration of 25 mg/mL. The organic solvent was removed through a hydration and evaporation process during 72 hours at a temperature of 37 ºC. The obtained solution contains giant unilamellar vesicles, known as GUV's. *Figure 5.2* shows a schematic representation of GUV's formation [28]. The liposomes were stored at 4 ºC.
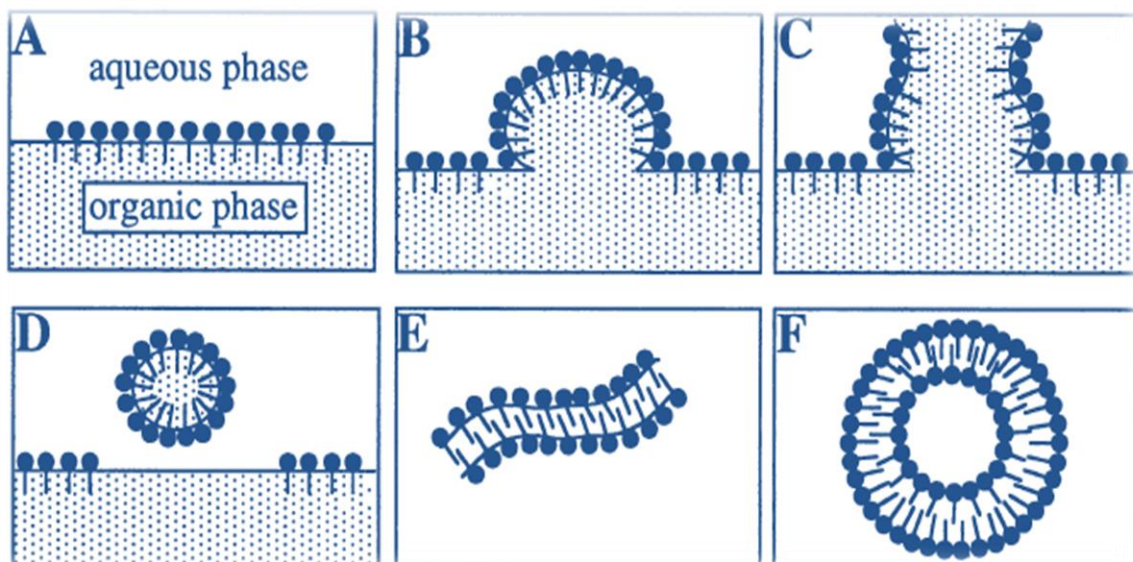
Figure 5.2. *Schematic representation of GUV's formation. a) Formation of an ordered monolayer of phospholipids at the interface between the aqueous phase and the organic phase. b) Formation of bubbles observed during evaporation. c) Rupture of a phospholipid film causing its fragmentation. d) Formation of micellar structures. e) Spontaneous vesiculation. f) Formation of phospholipid fragments with bilayers [28].*

The LUVs were obtained by extrusion of a suspension of GUVs, using a 0.2 μm filter (*Figure 5.3*). At these conditions, LUVs are unilamellar and have diameters of around 200 ± 10 nm [29,30]. LUVs were prepared from the GUVs solution in order to obtain a suspension with the same lipid composition [31] and were used to perform Dynamic Light Scattering (DLS) measurements in convenient conditions.
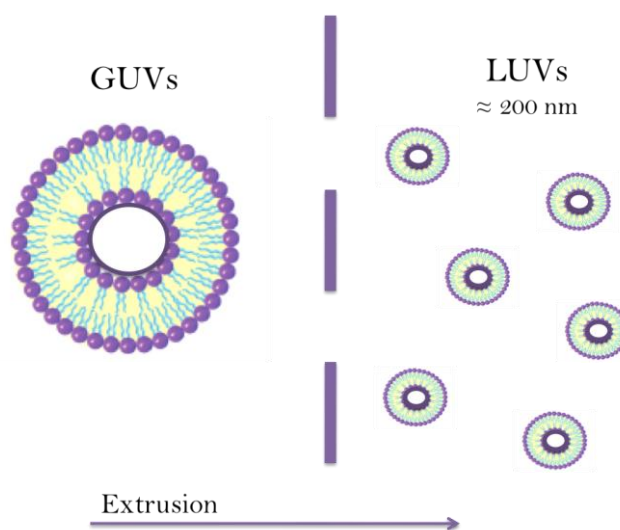
Figure 5.3. *Schematic representation of LUV's formation by extrusion of a GUVs suspension.*

Taking into account the structure of GUVs and LUVs, it is assumed that half of the lipid heads (Lipid out) are outside the vesicle and contribute to the interactions with the external medium.

5.2.3. Preparation of triblock copolymer solutions

A fluorescent solution 1-pyrenyl-octadecanone $C_{34}H_{44}O$ (PyC_{18}) was prepared using a Friedel-Crafts acylation of pyrene with stearoyl chloride in dichloroethane in the presence of aluminum chloride ($AlCl_3$). The PyC_{18} was solubilized in micelles of triblock copolymer P104 mixing an aqueous copolymer solution (10 mg/mL) with PyC_{18} at a temperature of 75 °C or higher, this way the clouding point of the copolymer is exceeded. The solutions were stirred vigorously for 10 min. in a Vortex Genie 2 model G 650 with a mechanical stirrer at its maximum frequency (> 10 Hz). The vials were covered with aluminum foil to prevent samples degradation caused by contact with light. An UV-Vis analysis allowed calculating the PyC_{18} concentration present on the initial solution (i.e. 2.1 x 10^{-4} M).

5.2.4. Chitosan solution preparation

The solutions of chitosan are prepared at 5.3 mg/mL by dissolving a known amount of polysaccharide with the stoechiometric amount of HCl 0.1 N (previously titrated with NaOH 0.1 N) on the basis of NH_2 content (final pH is around 3.35). The solution was placed under constant stirring for 1 night at room temperature, until complete solubilization, then it was stocked at a temperature of 4 ºC. Chitosan solution was then diluted to 1 mg/mL, filtered with a 0.2μm membrane and adjusted to the selected pH with a solution NaOH 0.1 N. (Chitosan properties and characteristics are described in *Chapter 7* of *Part I* of this thesis).

5.2.5. Confocal microscopy measurements

In order to observe the chitosan coating on GUVs by using fluorescence microscopy, chitosan (1mg/mL) was labeled with fluorescein. The degree of labeling is determined from the fluorescence intensity of diluted solutions of the free fluorescent probe compared with the fluorescence of a diluted solution of the labeled chitosan (it is found around 2 % of modified sugar unit). Optical observations of GUVs suspensions and fluorescein labeled chitosan-GUVs suspensions were made using a laser fluorescence microscope (TCS SP8) with a 488 nm excitation wavelenght. Fluorescence acquisitions at this excitation wavelength are obtained successively.

5.2.6. Dynamic Light Scattering measurements

Dynamic light scattering (DLS) measurements of P104 triblock copolymer micelles and LUV's were performed in a Malvern zetasizer 5000 apparatus equipped with a 7132 multibit correlator and multiangles goniometer. The light source was a He-Ne 5mW laser with a wavelength of 632.8 nm. The scattering intensity was measured through a 400 µm pinhole. The correlation functions were averaged over 30 s in equilibrated sample. DLS measurements were carried out at 90°. The corresponding hydrodynamic radius was calculated using the Stokes-Einstein equation.

5.2.7. Fluorescence measurements

Fluorescence measurements were carried out on a Jobin Yvon Spectrometer Fluorolog III (2-2) in the S/R mode. Kinetic experiments were performed mixing a P104 solution containing PyC_{18} with a suspension of L-α-phosphatidylcholine liposomes at a pH of 6.5 without hydrophobic probe. Measurements were performed for different liposome concentrations and a constant P104 micelles concentration (10 mg/mL) with PyC_{18}. Measurements were carried out at a temperature of 37 °C. An excitation wavelength of 344 nm was used, monitoring the emission every 30 s at λ_{em}= 480 nm for the excimer and at λ_{mon}= 376 nm for the monomer. The exchange dynamics between chitosan-coated liposomes and P104 micelles were performed by mixing a GUVs suspension at a pH= 6.5 with a specific coating of chitosan at a pH= 6.5 and with a selected ζ-potential, with P104 triblock copolymer micelles at a concentration of 10 mg/mL.

5.2.8. ζ-potential measurements

ζ–potential measurements were performed in a Malvern Zetasizer NanoZS at a temperature of 37 ºC. The results are the average of 5 runs. The instrument measured the electrophoretic mobility of the particles and converted it to the ζ–potential using the classical Smoluchowski expression. For each ζ–potential during chitosan-coating of liposomes, the following protocol was performed: a given volume of chitosan solution at a constant pH was added to the liposome suspension, after homogenization, 1 mL of the solution was injected to the cell, which was then placed inside the instrument and finally the measurement was taken. After each measurement the whole solution was collected from the Zetasizer Nano cell and reintroduced into the bulk solution (to keep a nearly constant volume of solution) before the addition of the next volume of chitosan solution.

5.3. Experimental results

### 5.3.1. Micellar structure and net charge of P104 amphiphilic triblock copolymer in aqueous solutions

Dynamic light scattering measurements were used to identify conditions at which we can observe the formation of spherical and elongated micelles in P104 triblock copolymer solutions in water. As discussed in *Chapter 3*, the hydrodynamic radius remains constant within the temperature range from 30 to 54 °C, indicating the formation of spherical micelles with an average size of 11.4 ± 1 nm [32].

The net charge of P104 micelles was then evaluated with ζ–potential measurements at a temperature of 37 °C and at a pH of 6.5, obtaining a value of -5.8 ±0.4 mV, which reveals a slight negative charge due mostly to traces of sodium or potassium hydroxide used as catalysts during the oxyalkylation step of P104 triblock copolymer synthesis [32].

5.3.2. L-α–phosphatidylcholine liposomes characterization

5.3.2.1. Confocal microscopy observations of GUVs

Confocal observations allowed visualizing L-α–phosphatidylcholine GUVs suspension in water at a concentration of 2 mg/mL and a pH of 6.5. *Figures 5.4 a, b* and *c* show confocal observations of liposomes in water with a ζ-potential of around -26 mV. The average hydrodynamic radius for the observed GUVs in the images is around 12 μm, however, a polydisperse suspension is obtained for GUVs formation (*Figure 5.4 c*).
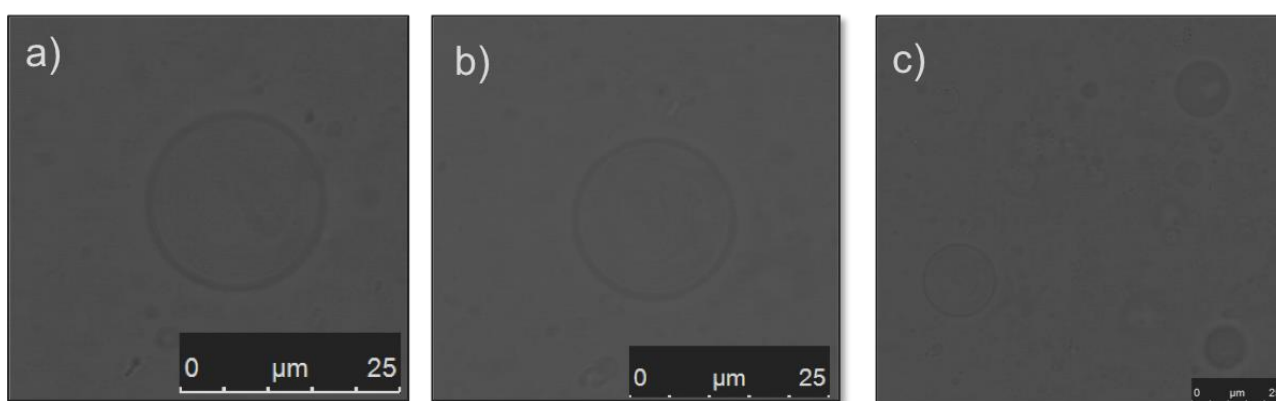

Figure 5.4. *a)-c) Confocal observations of GUVs in water at a concentration of 2 mg/mL and a pH of 6.5.*

5.3.2.2. LUVs size measurements through DLS

The morphology of L-α-phosphatidylcholine large unilamellar vesicles (LUVs) was studied by Dynamic Light Scattering (DLS). The values of the hydrodynamic diameter and the intensity of scattering light were determined using 10 consecutive measurements at a constant temperature of 37 °C and an incident light angle of 90°. We obtained an average value of 160 ± 20 nm for the hydrodynamic diameter. The formation of LUVs is then confirmed with the obtained size [1,33].

5.3.2.3. Net charge of liposomes

ζ-potential is a measure of the electric charge of a liposome, which is an important parameter since charge affects both the particle stability and liposomal pharmacology [34]. At a pH of 6.5, corresponding to the pH of the liposomes preparation (GUVs and LUVs), ζ-potential is negative and has a value around to -22 mV, which is in good agreement with the values previously reported by several authors [34,35]. This negative value is probably due to the presence of carboxylic groups caused by the lipid degradation and to the phosphate and the quaternary amino groups of the phosphatidylcholine polar head, as we can see in *Figure 5.5*.
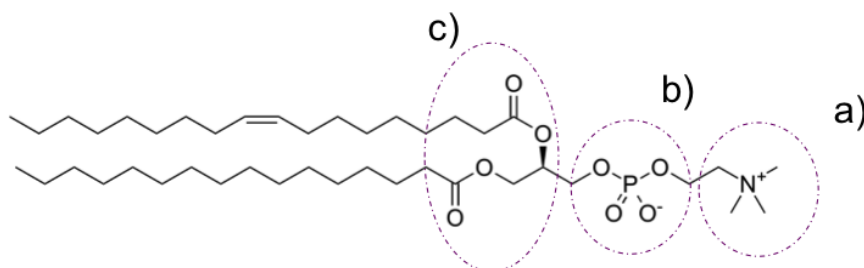

Figure 5.5. *Active sites of L-α-phosphatidylcholine: a) polar head group with a positive quaternary amino group, b) a negative phosphate group and c) two carbonyl oxygen groups, connecting the hydrophilic head group with the two hydrophobic tails.*

Figure 5.6 shows the ζ-potential dependence with pH of L-α-phosphatidylcholine GUVs suspension. We can observe that ζ-potential increases with the addition of HCl, which decreases the pH of the suspension. The isoelectric point (IEP) is found when ζ-potential= 0 mV around a pH of 4.0, in good agreement with the literature [36]. Then, the ζ-potential becomes positive and reaches a constant value of +14 mV at a pH around 2.0. When pH decreases, the dissociation of the phosphate acid and carboxyl groups is reduced, so the relative positive contribution of the quaternary amino group

increases [31]. On the other side, the ζ-potential decreases with the addition of NaOH until reaching a constant value of around -30 mV at a pH of 8. The presence of a plateau, which slightly decreases with the addition of NaOH, was attributed to the complete dissociation of the phosphate and carboxyl groups of the lipids.
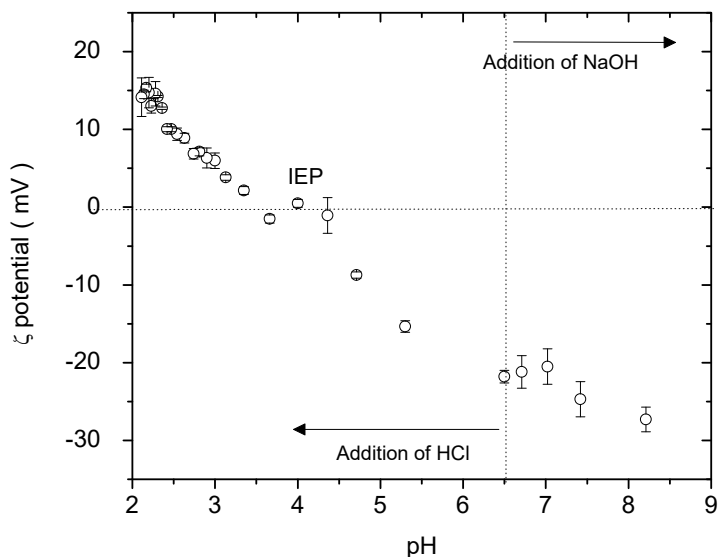

Figure 5.6. *ζ-potential variation of L-α-phosphatidylcholine GUVs as a function of pH. The isoelectric point (IEP) is obtained around a pH=4.0.*

In the following study, the pH value of GUVs and LUVs suspension is maintained at pH=6.5, where the membrane is negatively charged and stable [34].

5.3.3. Interactions between L-α–phosphatidylcholine LUVs and P104 micelles.

5.3.3.1. Electrostatic interactions through ζ-potential measurements

Since liposomes are stable and highly negatively charged, and P104 amphiphilic triblock copolymer micelles are weakly negatively charged probably due to catalysts residues [32], the electrostatic interactions between both particles were studied through ζ-potential measurements. *Figure 5.7* shows the ζ-potential dependence with the ratio given by the P104 micelles concentration and the lipid out concentration, i.e. [P104]/[Lipid out], at a constant pH of 6.5 and a temperature of 37 °C. Different amounts of a P104 micelles solution with a concentration of 10 mg/mL were mixed with a GUVs suspension with an initial concentration of 25 mg/mL, resulting on different [P104]/[Lipid out] ratios. We can observe that the ζ-potential slightly decreases with the increase of the amount of P104 micelles in the mixture, suggesting the presence of weak electrostatic interactions between micelles and the lipidic membrane.
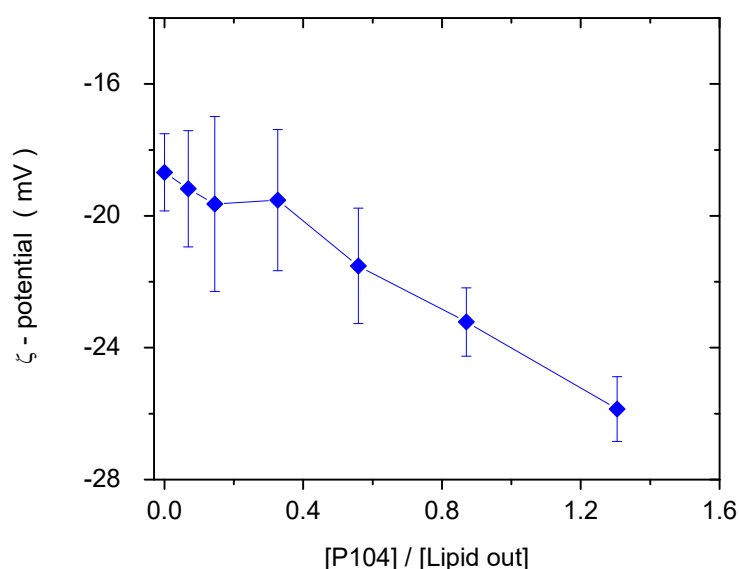
Figure 5.7. *ζ-potential variation with the [P104]/[Lipid out] ratio, measured at a constant temperature of 37 °C and a pH=6.5.*

5.3.3.2. Interactions through DLS measurements

Interactions between P104 micelles and LUVs were also studied through DLS measurements by following the evolution of the hydrodynamic radius of different concentration LUVs suspensions upon the addition of various amounts of P104 micelles solution to the liposomes suspension. *Figure 5.8* shows the variation of the hydrodynamic radius as a function of liposomes concentration for different amounts of P104, measured at a constant temperature of 37 °C and a pH=6.5. We observe that the average hydrodynamic radius presents a constant value of 160 ± 20 nm.

It is then of our interest to analyze the possibility of full coverage of liposomes with P104 micelles, unimers or if micelles can be completely independent. In this manner, as an example, the mixture of P104 micelles at a concentration of 2 mg/mL and liposomes at a concentration of 1.6 mg/mL is studied. Firstly, the number of micelles present in the mixture is calculated using the aggregation number (N_{agg}) of the amphiphilic triblock copolymer. For P104, an average value of $N_{agg} = 74$, reported for a P104 at a temperature of 35 °C was taken from *Liu et al.* reports [37]. In this way, for a P104 concentration of 2 mg/mL, the amount of micelles is 2.8×10^{15} micelles/mL. Then, the number of liposomes is obtained for a concentration of 1.6 mg/mL by calculating the average number of lipids per liposomes (with an average radius of 160 nm) knowing the area per polar head (0.71 nm) [38], this number equals to 2.45×10^{12} liposomes/mL. Then, from these two numbers of particles, micelles are able to cover liposomes, but due their small dimensions, the increase on the hydrodynamic radius (R_h) of eventually covered liposomes by micelles is not detected as shown in *Figure 5.8*, due to lack of precision of this technique. In

addition, due to the large molar mass of liposomes, it is not possible by DLS to identify the presence of a fraction of free micelles.
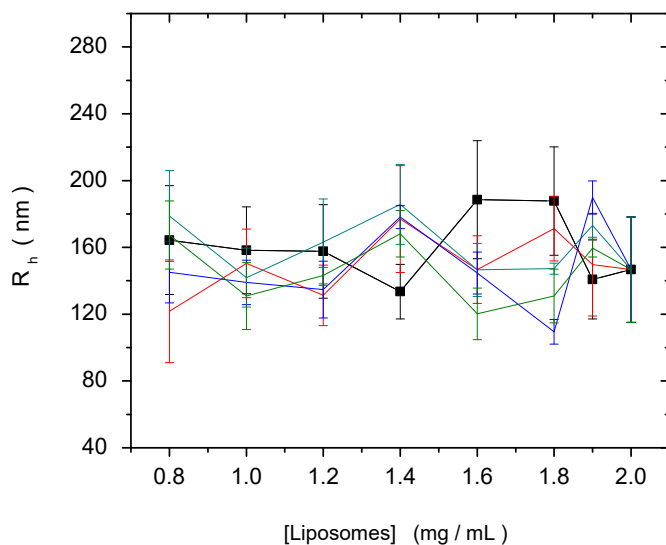
Figure 5.8. *R_h variation with the liposomes concentration, measured at a constant temperature of 37 °C and a pH=6.5. P104 concentrations: 0.5 mg/mL (black line), 1 mg/mL (red line), 2 mg/mL (dark green line), 3 mg/mL (light green line), 4 mg/mL (blue line) and 5 mg/mL (purple line).*

5.3.3.3. Interactions through fluorescence measurements

P104 triblock copolymer forms spherical micelles in water in a temperature range from 30 to 54 °C with an average size of 11.4 ± 1 nm. When a P104 solution containing micelles is mixed with a liposomes suspension, the total concentration of P104 is diluted. Some of the micelles will go to the liposomes and they will fuse together, some micelles will be adsorbed on the liposomes and another part of the copolymer will go into water since the CMC is approached.

The micellar behavior of P104 in water was investigated using the excimer and the monomer formation of PyC_{18}. The evolution of the PyC_{18} emission spectra contained in a P104 solution at different concentrations in a liposome suspension of fixed concentration of 25 mg/mL, was then studied and is illustrated in *Figure 5.9 a*. Here it is possible to observe the increase in the excimer and monomer bands, located at λ_{ex}=480 nm and λ_{mon}=376 nm, respectively, with increasing the micelles concentration in the final solution. *Figure 5.9 b* shows the evolution of the PyC_{18} emission spectra contained in a P104 solution in water at different concentrations. The variation on the excimer and monomer bands was quantified by using the ratio between the monitored intensities, i.e. I_{mon}/I_{ex}, for the P104 micelles and liposomes mixture and for the dilution of P104 micelles in water. *Figure 5.10 a* shows the obtained results in terms of the inverse of P104 triblock copolymer concentration. In both cases it is possible to

identify a change localized around the P104 concentration of 0.67 mg/mL in water and around the P104 concentration of 0.53 mg/mL in liposome suspensions, related to the CMC of the amphiphilic block copolymer at the temperature of 37 °C, in good agreement with previous results. With these results, we can see that the value of P104 CMC at 37 °C remains almost constant in the liposomes environment. *Figure 5.10 b* shows a schematic representation of P104 structural behavior in GUVs suspension.

The control of the stability of the structures of drug delivery vectors to a particular variation in the environment plays an important role in the efficiency of controlled drug release. The low CMC is taken as an indicator that shows that the dilution after administration will not lead to the breakdown of micelles, allowing them to circulate in the environment in which they are released and accumulate in their specific target [43].
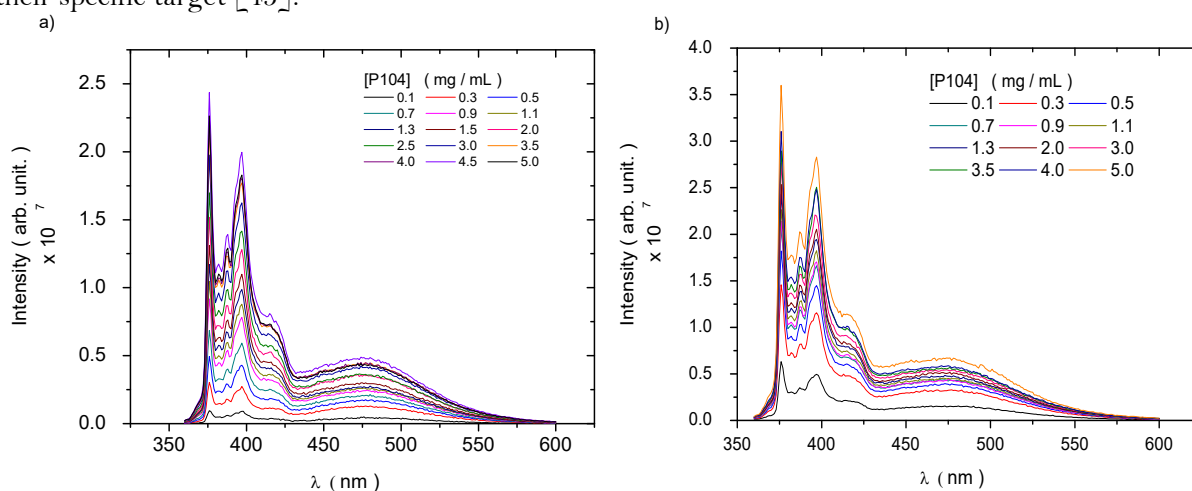
Figure 5.9. *Emission spectra of PyC$_{18}$ in a) P104 aqueous solutions mixed with GUVs suspensions evaluated at different concentrations of P104 and b) different P104 concentrations in water at a temperature of 37 °C.*
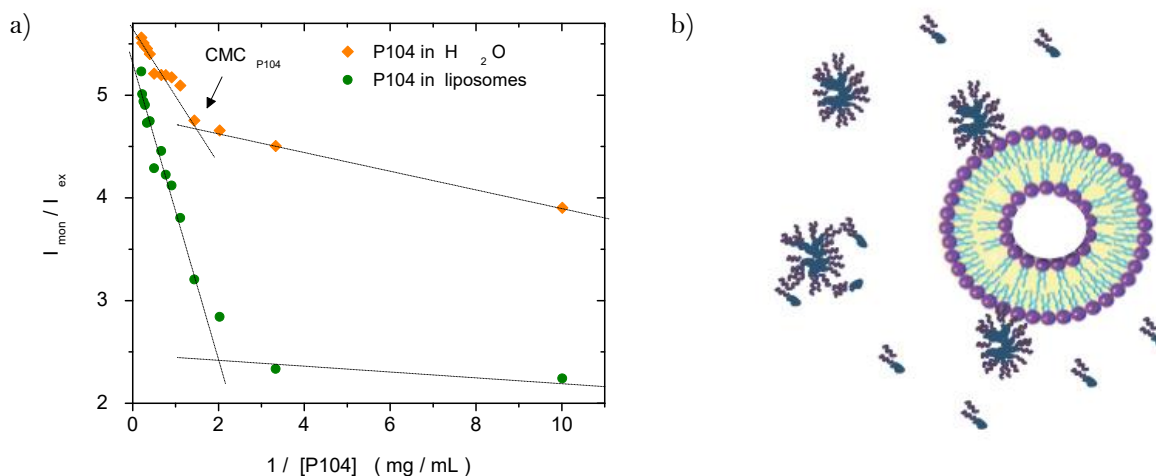

Figure 5.10. *a) CMC evaluation of P104 triblock copolymer in water and in L-α-phosphatidylcholine GUVs suspension at a constant pH=6.5 and a temperature of 37 °C. b) Schematic representation of P104 in GUVs suspension.*

5.3.4. Experimental conditions to monitor the exchange dynamics between amphiphilic block copolymers and L-α-phosphatidylcholine GUVs suspensions through fluorescence measurements

The dynamics between P104 amphiphilic triblock copolymer, selected as vectors, and GUVs prepared with L-α-phosphatidylcholine are studied in this section. PyC_{18} was firstly solubilized in P104 micelles by mixing P104 (10 mg/mL) with PyC_{18} at higher temperatures than 70 ºC. P104/water solutions were used at concentrations and at a temperature above the critical conditions at which spherical micelles are formed. The experimental conditions were selected close to the physiological conditions, i.e. controlled pH of 6.5 and a temperature of 37 ºC, in order to facilitate the understanding of micellar drug delivery vehicles interactions with phospholipid membranes.

Figure 5.11a and *b* show the spectra of a GUVs suspension at a concentration of 25 mg/mL and the emission spectra of PyC_{18} in an aqueous solution of P104 with a concentration of 10 mg/mL mixed with GUVs suspension 17.5 mg/mL and the emission of the liposome, respectively. In our study, we used an excitation wavelength of 344 nm. The fluorescence spectra of copolymer micelles containing more than one molecule of PyC_{18} exhibit an emission excimer band at 480 nm and an emission monomer band at 376 nm. We noticed that L-α-phosphatidylcholine presents a fluorescence spectrum in the wavelength range between 350 and 600 nm with a characteristic peak around 425 nm. This response is related to impurities of liposomes suspensions.

a)

b)
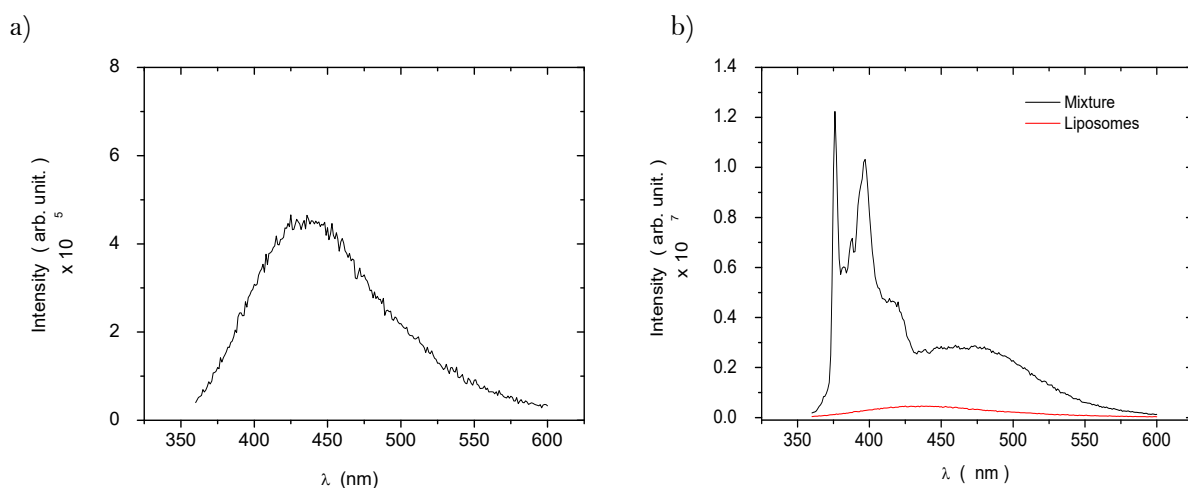
Figure 5.11. *a) Emission spectra of GUVs suspension at a concentration of 25 mg/mL and b) emission spectra of PyC_{18} in an aqueous solution of P104 with a concentration of 10 mg/mL mixed with GUVs at a concentration of 17.5 mg/mL, both measured at a temperature of 37 ºC and at a pH=6.5.*

We can observe that the intensity signal obtained for liposomes suspension is considerably lower than the intensity signal obtained for PyC_{18} in P104 micelles, however, it is important is important to avoid the emission spectra of liposomes. In this way, in further analysis, the emission spectrum of liposomes will be subtracted from PyC_{18} in P104 micelles emission spectra in order to remove any other contribution to the fluorescence intensity that gives us the information about the exchange dynamics by following PyC_{18} bands evolution [25,40-42]. It is worth to mention that the contribution of the liposome intensity signal depends on its concentration, while increasing liposomes suspension concentration the intensity increases, however, at low concentrations, the signal is almost negligible. *Figure 5.12* shows the initial emission spectra of PyC_{18} in P104 micelles mixed with GUVs suspensions and the spectra after after subtraction of the liposomes emission signal. A slight decrease in the excimer band is detected after removing the fluorescence signal of liposomes.
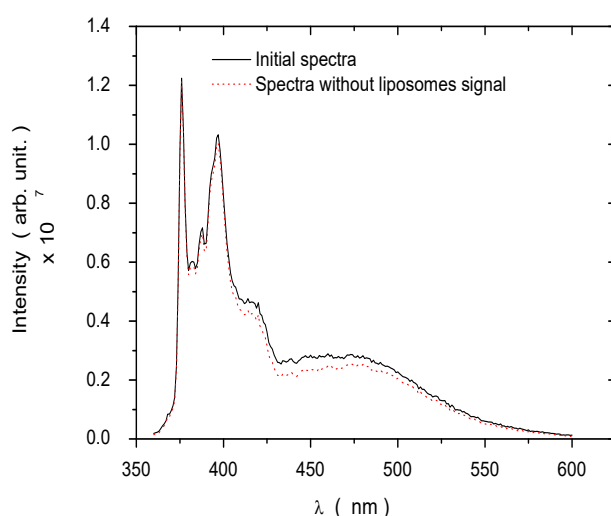
Figure 5.12. *Emission spectra PyC₁₈ in an aqueous solution of P104 with a concentration of 10 mg/mL mixed with GUVs at a concentration of 17.5 mg/mL before and after the subtraction of liposomes fluorescence intensity, both measured at a temperature of 37 ºC and at a pH=6.5.*

Additionally, and contrary to P104 micelles kinetic measurements, in these experiments it was not possible to measure the excimer and monomer decays as a function of time with a simple kinetic measurement. It was then necessary to measure consecutively the emission spectra of the mixture of P104 micelles and GUVs suspensions every 5 minutes. The evolution of the obtained spectra as a function of time was treated in terms of the ratio given by the value obtained from the integration of the excimer intensity peak (440 nm< I_{ex} <550 nm) and the integration of the monomer intensity peak (366 nm< I_{mon}<425 nm). Several wavelength intervals were tested in order to remove any other liposomes signal contribution to the emission spectra, resulting in the same values. A special program using OriginPro software was developed in order to subtract the intensity signal of liposomes from each emission spectra and to integrate the excimer and monomer intensity peaks. Finally, measurements

lasted about a week, so it was necessary to inspect that liposomes remained unaffected during the exchange period. Figure 5.13 shows the evolution with time of the emission spectra of PyC_{18} in an aqueous solution of P104 at a concentration of 10 mg/mL mixed with GUVs.
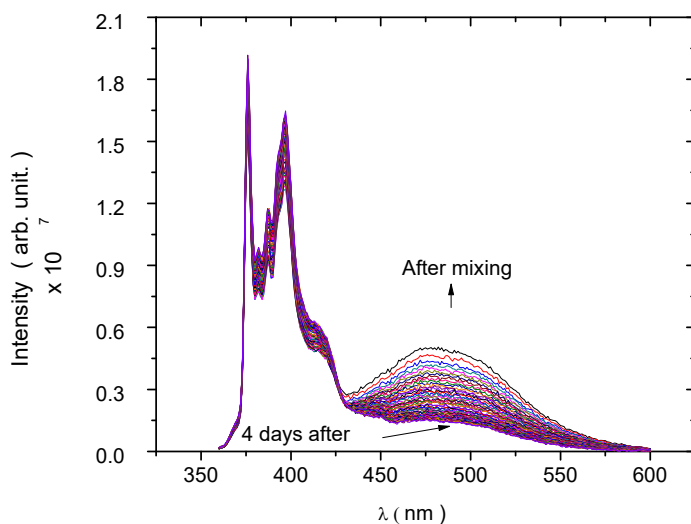
Figure 5.13. *Evolution with time of the emission spectra of PyC_{18} in an aqueous solution of P104 at a concentration of 10 mg/mL mixed with GUVs suspension at a concentration of 17.5 mg/mL. The temperature was maintained at 37 ºC and at the pH=6.5.*

5.3.5. Experimental study of the exchange dynamics between P104 micelles and liposomes.

Firstly, it is worth to mention that the difference in the hydrophobicity of P104 triblock copolymer micelles and L-α-phosphatidylcholine contributes to the exchange of PyC_{18}. *Figure 5.14* shows the emission spectra of PyC_{18} in an aqueous solution of P104 with a concentration of 3 mg/mL before and after the exchange with a GUVs suspension at concentration of 17.5 mg/mL and a constant pH of 6.5. The emission spectrum presents a broad excimer emission with a peak at 480 nm and monomer fluorescence at 376-400 nm, as for the case of PyC_{18} spectrum in amphiphilic block copolymer micelles [25]. The existence of the excimer emission at 480 nm infers the presence of micelles bearing two or more PyC_{18} molecules. The response of the monitored emission 4 days after the mixture of P104 micelles and GUVs shows a decrease in the value of the excimer and an increase of the monomer intensity.
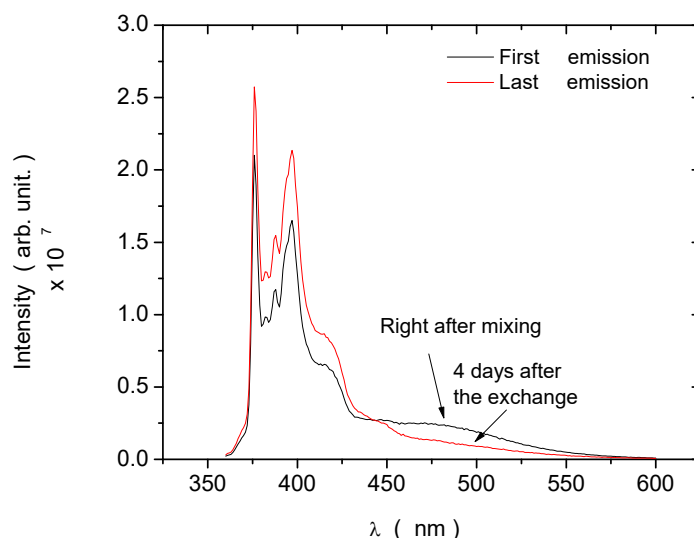
Figure 5.14. *Emission spectra of PyC₁₈ in 3 mg/mL P104 aqueous solution mixed with a 17.5 mg/mL GUVs suspension (right after mixing) before and 4 days after the exchange, both measured at a temperature of 37 °C.*

Figures 5.15 a and *b* show the time-scan analysis for the evolution of the monomer and the excimer intensities, respectively, after mixing a 3 mg/mL P104 solution, containing PyC₁₈, with 6, 8, 10 and 15 mg/mL GUVs suspensions. During the mixing, a change on the environment of P104 micelles with PyC₁₈ is caused, modifying the overall fluorescence intensity, which increases rapidly in the first hour and then decreases progressively. This phenomenon is probably due to some of the additives of the liposomes that could migrate into the micelles and change the fluorescence of the PyC₁₈. The increase is most likely due to oxygen reduction in P104 micelles, leading to an increase of the total fluorescence intensity. We can also observe that the intensity of the peak reached after the increase of the overall fluorescence intensity varies with the concentration of liposomes.
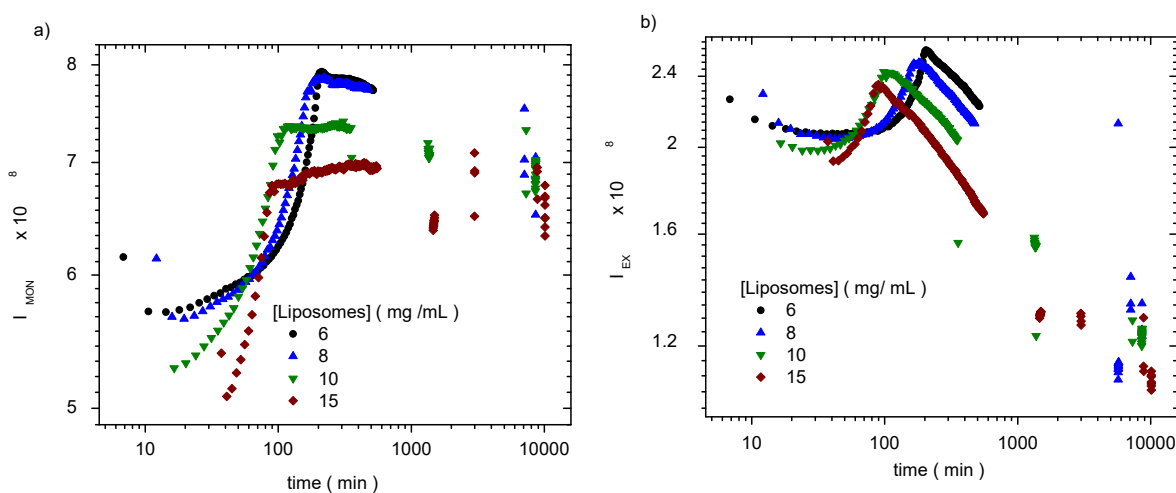
Figure 5.15. *a)* I_{mon} *decay and b)* I_{ex} *decay as a function of time obtained during the exchange of 3 mg/mL P104 micelles containing PyC₁₈ with a 6, 8, 10 and 15 mg/mL GUVs suspension. The measurement temperature is 37 °C.*

Figure 5.16 shows the I_{ex}/I_{mon} decay as a function of time for a mixture of 3 mg/mL P104 micelles containing PyC_{18} with GUVs suspension at a concentration of 17.5 mg/mL. The observed peak from the evolution of the monomer and the excimer intensities disappears here. Since $I_{ex}/I_{mon} \alpha I/I_0$, this ratio will depend mainly on the average number of PyC_{18} per micelles, resulting in the best way to measure the exchange dynamics between P104 micelles containing PyC_{18} and liposomes. From the time-scan analysis of I_{mon}/I_{ex} it is possible to obtain the main relaxation time (τ) of the global exchange dynamics between micelles and liposomes (i.e. 420 min for these specific conditions). The kinetic decay can be simulated by a mono-exponential function with an apparent relaxation time (τ), which equals to 740 min for this case.
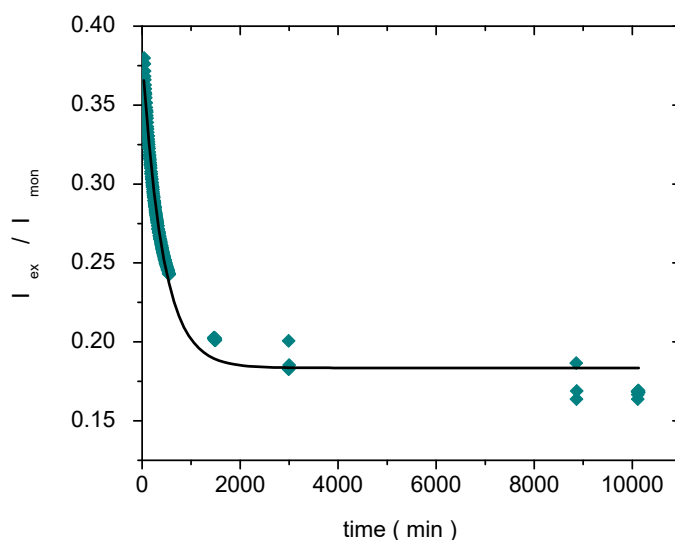
Figure 5.16. *I_{ex}/I_{mon} decay as a function of time obtained during the exchange of 3 mg/mL P104 micelles containing PyC_{18} with a 17.5 mg/mL GUVs suspension. The measurement temperature is 37 °C. The solid line represents the fit with a mono-exponential function that simulates the decay of I_{ex}/I_{mon}.*

A similar behavior to the one obtained for the interactions between amphiphilic triblock copolymers micelles at the equilibrium, in which the response follows a mono-exponential function, is observed. The kinetic decay can be simulated by a mono-exponential function with an apparent relaxation time (τ). The kinetic constant, k_{decay}, of P104 micelles-GUVs exchange can be then quantified from the reciprocal of the apparent relaxation time obtained from the following expression:

$$I_{ex}/I_{mon} = Ae^{-t/\tau} + B \tag{5.1}$$

where A and B are the constants obtained from the fit of the experimental results.

It is worth to mention that the apparent relaxation time (τ) obtained from the mono-exponential function is similar to the average value $<\tau>$ calculated from the fit to two exponentials.

5.3.5.1. Dependence on liposomes concentration

When the kinetics are repeated with different GUVs concentrations and with a P104 solution with a constant concentration, we observe a linear dependence of the exchange rate $k_{decay}=1/\tau$ on the concentration of liposomes (GUVs). *Figure 5.17* shows the kinetic constant (k_{decay}) dependence with the concentration of liposomes in a mixture containing P104 micelles filled with PyC_{18} at a concentration of 3 mg/mL. We can observe an increment on k_{decay} values with the increase of liposomes concentration in the mixture and a linear dependence within the concentration range from 8 to 17.5 mg/mL according to the following equation:

$$k_{decay}= k_1+ k_2 \,[liposomes] \tag{5.2}$$
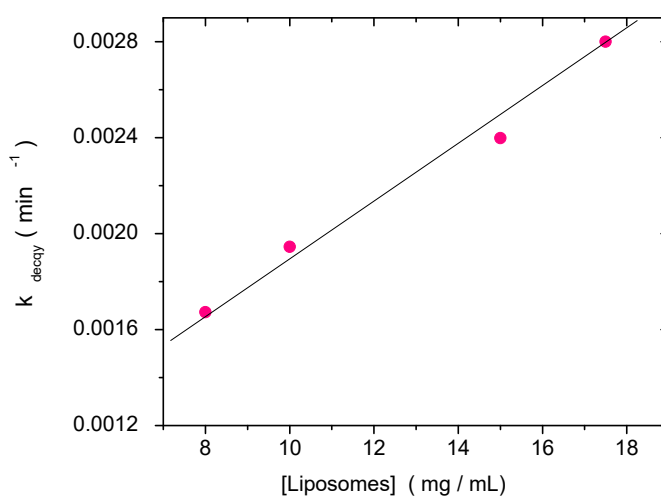
Figure 5.17. *Kinetic constant (k_{decay}) calculated from the fits of the exchange decays obtained for P104 micelles containing PyC_{18} and GUVs suspension as a function of liposomes concentration. The measurement temperature is 37 ºC and the pH= 6.5.*

5.3.5.2. Exchange dynamics between P104 micelles and liposomes

The linear dependence on k_{decay} as a function of the liposomes concentration with a kinetic constant called k_2 or fusion-adherence kinetic constant is considered a second order mechanism. From this we can say that the exchange dynamics between P104 amphiphilic block copolymers and liposomes is a collective mechanism involving adhesion-fusion, exchange and separation. It depends on the variation of the amount of liposomes in the suspension.

Now it is possible to compare the collective dynamics obtained from the exchange between P104 micelles and from the exchange between P104 micelles and liposomes. *Figure 5.18* shows the kinetic

constant (k_{decay}) dependence with [liposomes] in different mixtures containing P104 micelles filled with PyC$_{18}$ at a concentration of 3 mg/mL and the kinetic constant (k_{decay}) dependence with [P104] at a temperature of 37 ºC. A three magnitude-order difference of k_{decay} values calculated for P104 micelles-liposomes exchange is obtained in comparison with k_{decay} values calculated for micelle-micelle exchange.
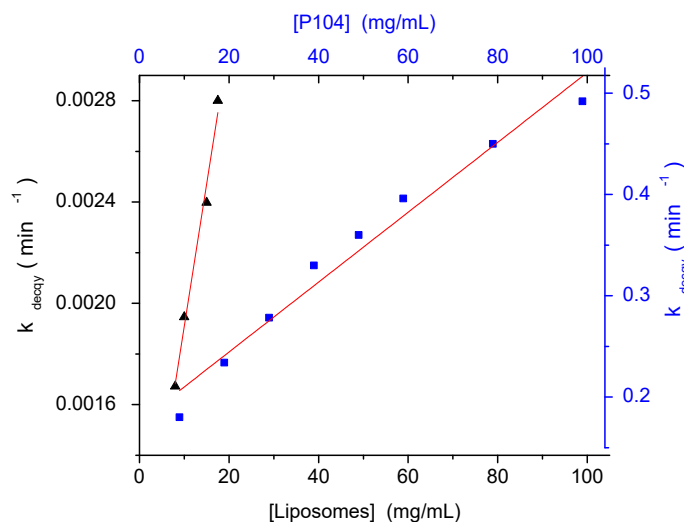
Figure 5.18. *Kinetic constant (k_{decay}) calculated from the fitting of the exchange decays of a sample of PyC$_{18}$ in P104 and L-α-phosphatidylcholine vesicles as a function of P104 triblock copolymer concentration. The measurement temperature is 37 ºC.*

However, a better comparison of these two systems is performed through the analysis of k_{decay} as a function of the number of empty micelles and empty liposomes (*Figure 5.19 a* and *b*). The rate of collision-adhesion exchange, k_2, calculated from the slope of the k_{decay} as a function of the molar concentration of liposomes is $k_2 = 1256$ M^{-1} s^{-1}. This value is 50 times the fusion rate of P104 micelles–micelles, which is equal to 25 M^{-1}s^{-1}.

The exchange rate via collision-adhesion-exchange process is the product of a diffusion controlled rate k_{diff} and the probability of adhesion-exchange (P_{reac}) (*Equation 5.3*).

$$k_2 = k_{fus} = k_{diff} \cdot P_{reac} \tag{5.3}$$

The diffusion controlled rate k_{diff} can be written as:

$$k_{diff} = 4\pi \, N_A \, (R_{h1} + R_{h2})(D_1 + D_2) * 1000 \tag{5.4}$$

where N_A is the Avogadro number, R_{h1} and R_{h2} are the hydrodynamic radius of liposomes and P104 micelles, respectively. D_1 and D_2 are the diffusion coefficients of liposomes and the P104 micelles, respectively. When using Stokes-Einstein equation for the diffusion-controlled coefficient (*Equation 3.1* of this part of the thesis), *Equation 5.4* becomes:

$$k_{diff} = 4\ N_A . k_B T / 3\eta\ (R_{h1}+R_{h2})^2/(R_{h1}\ R_{h2})\ .\ 1000 \tag{5.5}$$

where k_B is the Boltzmann constant, T is the temperature and η is the water viscosity. For the liposome-micelles case, $k_{diff} = 5\text{x}10^{10}\ M^{-1}\ s^{-1}$ while for micelle-micelle case $k_{diff} = 7\text{x}10^9\ M^{-1}\ s^{-1}$. The collision rate of micelle-liposome is higher than that of micelle-micelles due to the liposome size. Therefore, the probability of adhesion-exchange (P_{reac}) is $1.25\text{x}10^{-8}$, which is in the same order of magnitude of P104 micelle-micelle P_{reac} ($2.4\text{x}10^{-8}$). This suggests that P104 micelles control the adhesion-exchange process of P104-liposome system.
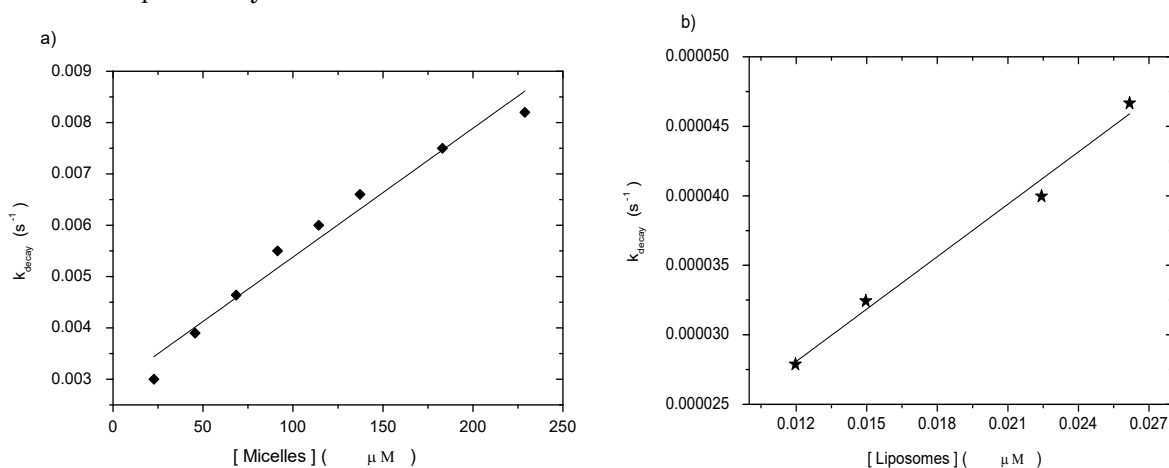
Figure 5.19. *a) Kinetic constant (k_{decay}) vs [Micelles] and b) Kinetic constant (k_{decay}) vs [Liposomes]. The measurement temperature is 37 °C.*

On the other hand, a first order mechanism with a rate independent of the liposomes concentration and with a kinetic constant called k_1 is related to the exit-entry process of the probe (dominated by water solubility and which is very low), to the exchange-assisted by the unimer (almost negligible) of the probe or to fission-fusion exchange.

A moderately water soluble molecule as pyrene (10^{-7} mol/L) can be mainly exchanged through an exit-entry process with a rate of certain orders of magnitude greater than the rate observed in this dynamic. In addition, the C_{18} chain present in the pyrene derivative, PyC_{18}, reduces its solubility in water and causes the exit ratio to be negligible during the experiment. To confirm this statement, complementary experiments were performed, as the limitation for the exit-entry process of the PyC_{18} is the insolubility in water (C_w) or the diffusion through the core/corona of micelles. GUVs suspensions

was left in contact for a week with a dialysis bag dialysis tubing cellulose membrane (which is supposed to be permeable for free pyrene) with P104 micelles containing PyC_{18}. The emission spectra of GUVs suspensions shows a very low signal allowing concluding that exit-entry of PyC_{18i} into GUVs suspension (25 mg/mL) has to be experimentally discarded (*Figure 5.20*). Some results are also obtained for PyC_{18} in water. Then, the emission spectra of the liposome suspensions in contact with the bag containing P104 micelles with PyC_{18} and water with PyC_{18} do not present any appearance of a specific fluorescent peak. These results show that the exchange of the probe by exit-entry of the micelles to the liposomes is most likely not crucial in the mechanism.
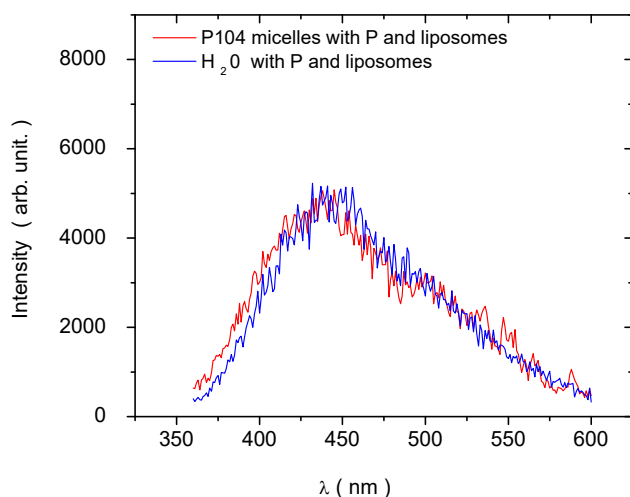
Figure 5.20. *Emission spectra of a GUVs suspension containing PyC_{18} (P) (black line), emission spectra of GUVs suspension left in contact with a membrane filled with P104 micelles containing PyC_{18} (P) (red line), emission spectra of GUVs suspension left in contact with a membrane filled with water containing PyC_{18} (P) (blue line).*

Finally, we propose an interaction mechanism between P104 triblock copolymer micelles and L-α-phosphatidylcholine GUVs suspensions dominated by collective dynamics that could involve the following steps: collision of a micelle and a GUV, adhesion of micelles on the lipidic membrane, transfer of solute inside the lipidic membrane of the GUV and followed by a possible separation (*Figure 5.21*). As conclusion, the vectorisation dynamics of hydrophobic drugs through vectors such as amphiphilic block copolymers can be followed, studied and quantified by using this fluorescence technique.
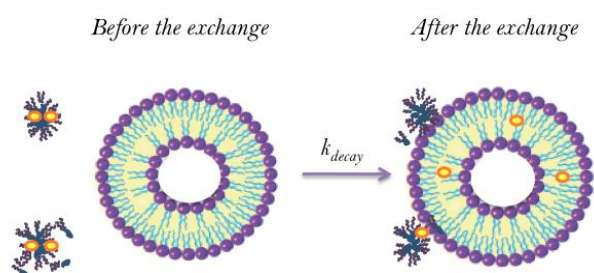

Figure 5.21. *Schematic representation of the exchange mechanism between P104 micelles and liposomes.*

5.3.6. Role of chitosan interactions in the exchange dynamics between amphiphilic block copolymers and L-α-phosphatidylcholine liposomes suspensions

In liposomes applications, polymer coating can improve the structural stability of membranes, the biocompatibility and drug delivery efficiency [44,45]. Chitosan has been recently used to improve liposomes biocompatibility, biodegradability and mucoadhesivity [44,46]. *Quemeneur et al.* [44] previously reported that chitosan adsorbs flat on the surface of a zwitterionic phosphatidylcholine membrane of vesicles and demonstrated that the origin of the interactions is mainly electrostatic. They also reported that the net charges of positively charged chitosan and DOPC phospholipid membranes depend on the pH (passing from positive to negative net charge when pH increases). In our work, the role of the addition of chitosan on liposomes in the interactions between amphiphilic block copolymer micelles and liposomes is firstly studied through DLS and ζ–potential measurements. Then, we investigated the role of chitosan-liposomes coating in the collective exchange mechanisms between micelles and liposomes through fluorescence measurements.

5.3.6.1. Chitosan coating on GUVs observed by fluorescence confocal microscopy

GUVs suspensions were incubated with fluorescein labeled chitosan at a pH of 6.5 and were then observed by confocal imaging. The lipidic membrane can be visualized if an adsorption of the labeled polyelectrolyte is obtained from the electrostatic interactions between negative and positive charges of chitosan and GUVs, respectively. The obtained ζ-potential of labeled chitosan coated GUVs, which represents the net charge of the particle, is not affect by the fluorescein dye, as reported previously by *Quemeneur et al.* [46]. *Figure 5.22* shows the observation of the fluorescent lipid bilayer and polymer decoration of a chitosan coated GUV, in which all the surface of the liposome vesicle looks homogeneously covered by the chitosan without any apparent modification of the vesicle shape.
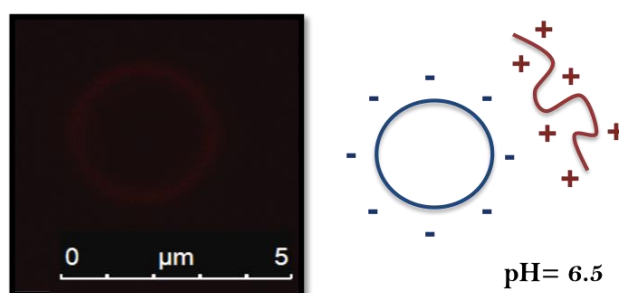
Figure 5.22. *Fluorescence confocal observations of a chitosan (Mw=500 000 and a DA of 0.19) coated GUV incubated at a pH= 6.5. We visualize the lipid membrane with the polyelectrolyte coating.*

5.3.6.2. Chitosan adsorption on L-α-phosphatidylcholine LUVs and GUVs

The role of chitosan adsorption on LUVs was determined through DLS and ζ-potential measurements and observed through fluorescence confocal microscopy on GUVs. The pH of both initial chitosan and LUVs suspension, which is equal to 6.5, was controlled in order to maintain the net charge of each component constant during the adsorption process. As reported before [44], the influence of vesicle size on chitosan adsorption, determined through ζ-potential measurements of LUVs and GUVs as a function of added cationic chitosan is negligible, so both LUVs and GUVs present the same behavior with chitosan coating.

Figure 5.23 a shows the ζ-potential and particle size variation upon the addition of cationic chitosan to a LUVs suspension of 2.0 mg/mL at a temperature of 37 ºC, as a function of the molar ratio $[NH_2]_{added}/[Lipid\ out]$; $[NH_2]$ represents the total concentration of amino groups added whatever is the degree of protonation. It is possible to observe that upon the first additions of the positively charged chitosan, the negative net charge of the GUV decreases until reaching a value of 0 mV, i.e. the isoelectric point (IEP), corresponding to a molar ratio $[NH_2]_{added}/[Lipid\ out]= 3$ at which the neutralization of the global negative charges of the liposomes is reached.

The information obtained through DLS for the hydrodynamic radius of the particles reveals a maximum around the IEP, corresponding to the presence of aggregation of of partially chitosan-coated LUVs with a maximum size of around 1600 nm. Then, upon progressive addition of chitosan, adsorption still takes place on liposomes but aggregates dissociate until resulting in isolated positively charged LUVs with the same average size as LUVs in the bare state. This is due to an overcharging of liposomes upon the addition of chitosan, which originates electrostatic repulsion. Then, the concentration of chitosan in the obtained ζ-potential plateau corresponds to the dissociation of aggregates, from which it is possible to work with isolated chitosan-coated vesicles. *Figure 5.23 b* shows a schematic representation of LUVs suspension structure for the cases previously described: (1) corresponds to isolated bare LUVs without the addition of chitosan, (2) aggregation of LUVs upon the addition of chitosan up to the IEP, ζ-potential= 0 mV, and (3) isolated chitosan-coated LUVs at coating saturation. As proposed by *Quemeneur et. al* [31,44], this mechanism is due to the equilibrium between long range repulsions and short range attractions of electrostatic nature related to a patch-like structure model for membrane coating [47]. *Figure 5.23 c* presents the different states described in *Figure 5.23 b* with confocal fluorescence microscopy by using fluorescein labeled chitosan at a pH of 6.5. Firstly it is presented the visualization of a bare GUV with a ζ-potential=-26 mV, then we observe the aggregation of GUVs at the isoelectric point and finally, the isolated chitosan-coated GUVs with a ζ-potential=20 mV, corresponding to the ζ-potential plateau at overcharging state. In this manner, the coating of GUVs with cationic chitosan at different ζ-potentials, at which liposomes present a different behavior

(isolation or aggregation), will be used to study their effects on the interactions with P104 amphiphilic block copolymer micelles.

a)

b)

c)
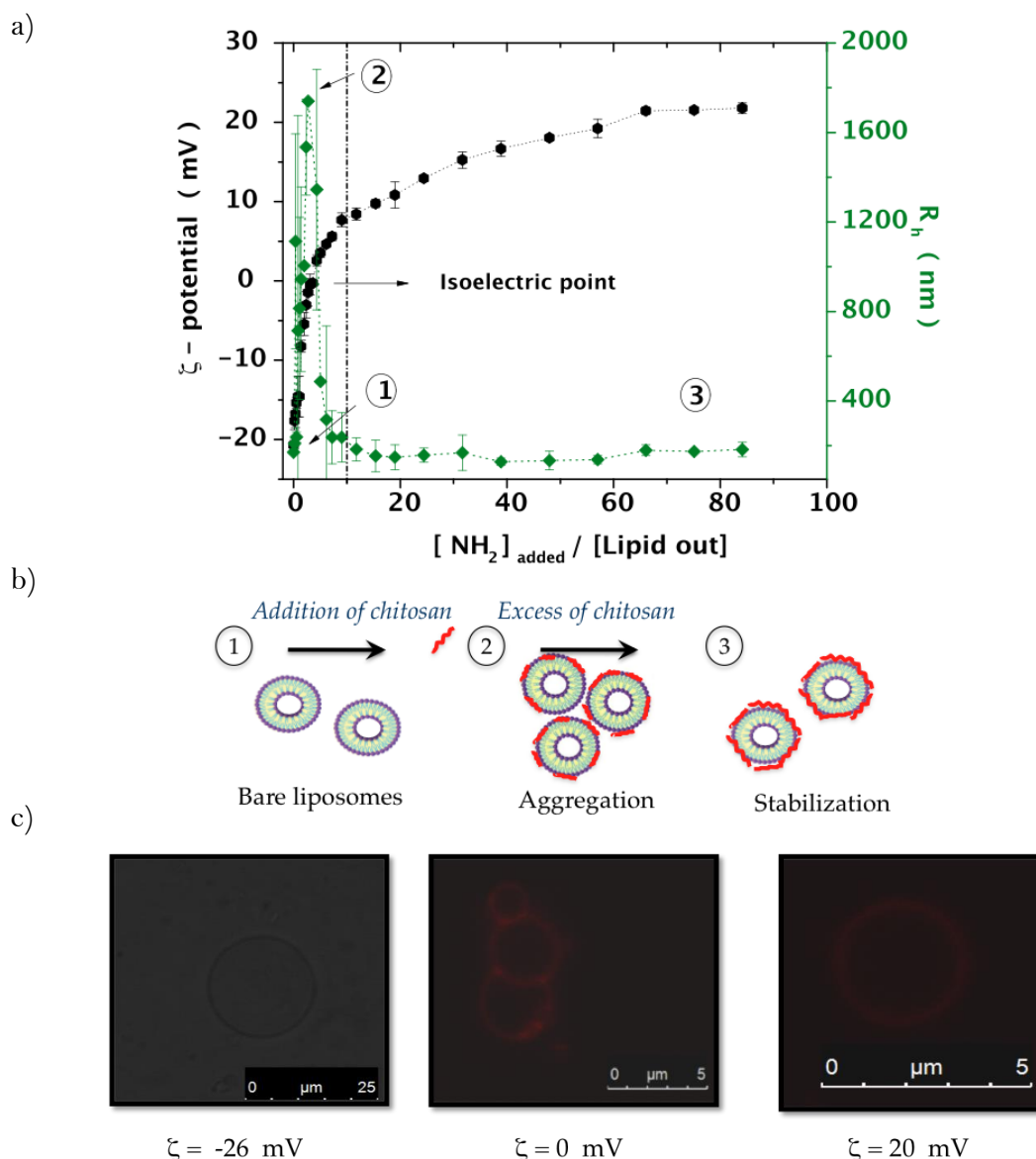
Figure 5.23. *a) ζ-potential and R_h variation upon the addition of cationic chitosan to LUVs, expressed by the molar ratio [NH₂]added/[Lipid out] at a pH=6.5. b) Schematic representation of LUVs suspension structure for the following cases: (1) isolated bare LUVs without the addition of chitosan, (2) aggregation of LUVs upon the addition of chitosan up to the isoelectric point, ζ-potential= 0 mV, and (3) isolated chitosan-coated LUVs at coating saturation. c) Aggregation-separation process observed on GUVs with confocal fluorescence microscopy.*

5.3.6.3. Chitosan adsorption on P104 triblock copolymer micelles

After studying the role of chitosan adsorption on LUVs and GUVs, a chitosan adsorption study on P104 triblock copolymer micelles was also performed through DLS and ζ-potential measurements. The pH of both initial chitosan and P104 micelles solution, which is equal to 6.5, was controlled in order to maintain the net charge of each component constant during the adsorption process. The concentration and temperature of P104 were maintained at the conditions at which stable spherical micelles are preserved, i.e. 10 mg/mL and 37 °C. *Figure 5.24 a* shows the ζ-potential and particle size variation upon the addition of cationic chitosan to P104 micelles as a function of the molar ratio $[NH_2]_{added}/[P104]$. As for the case of LUVs, we can observe that upon the first additions of the positively charged chitosan, the slightly negative net charge of P104 micelles decreases until reaching a value of 0 mV, i.e. the isoelectric point (IEP), corresponding to a molar ratio $[NH_2]_{added}/[P104]= 0.05$, so a very small amount of chitosan is needed in order to neutralize all the negative charges of P104 micelles resulting from the synthesis residues.
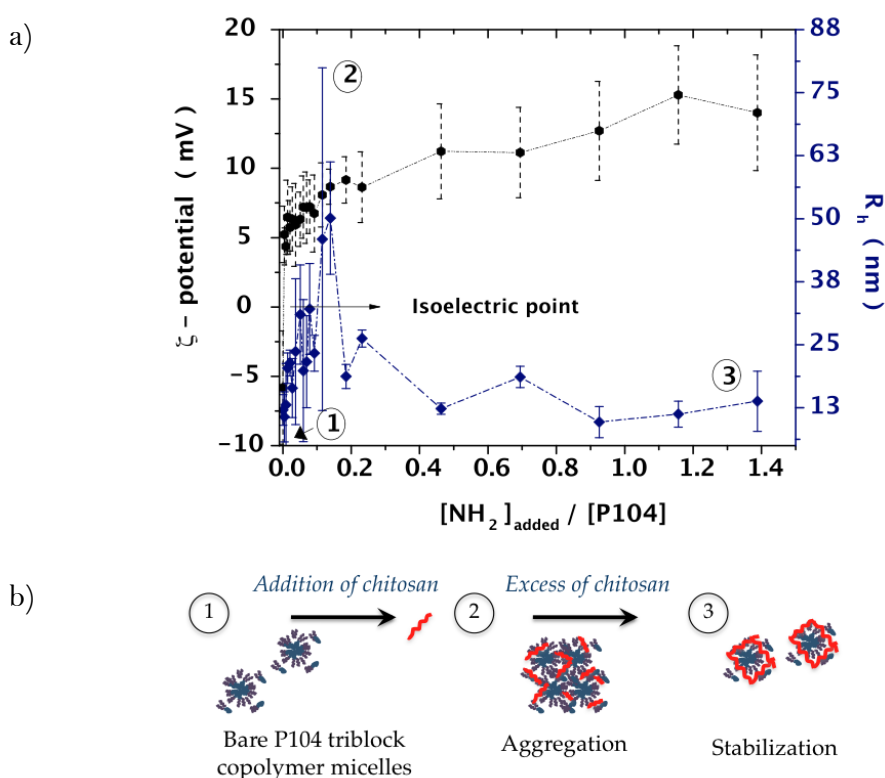
Figure 5.24. *a) ζ-potential and R_h variation upon the addition of cationic chitosan to P104 block copolymer micelles at a concentration of 10 mg/mL, pH=6.5 and a controlled temperature of 37 °C, expressed by the molar ratio $[NH_2]_{added}/[P104]$. b) Representation of micelles structure for the following cases: (1) isolated bare P104 micelles without the addition of chitosan, (2) aggregation of P104 micelles upon the addition of chitosan up to the isoelectric point, ζ-potential= 0 mV, and (3) isolated chitosan-coated P104 micelles at coating saturation.*

From DLS measurements, we can observe that the hydrodynamic radius of P104 micelles, which is initially around 12 nm, shows a maximum around the IEP, corresponding to the presence of aggregates of partially chitosan-coated P104 micelles with a maximum size of around 50 nm. Upon progressive addition of chitosan, the adsorption on P104 micelles continues, but aggregates also dissociate until resulting in isolated positively charged P104 micelles with the same average size as an initial micelle in the bare state. As for the liposomes, this is due to an overcharging of P104 upon the addition of chitosan, which originates electrostatic repulsion. *Figure 5.24 b* shows a schematic representation of P104 micelles structure during the addition of cationic chitosan: (1) corresponds to isolated bare P104 micelles without the addition of chitosan, (2) aggregation of P104 micelles upon the addition of chitosan up to the IEP, ζ-potential= 0 mV, and (3) isolated chitosan-coated P104 micelles at coating saturation.

These modifications on P104 micelles characteristics could improve the storage stability of hydrophilic drugs in micelles core and could prevent their release before reaching the specific target and receiving the adequate stimuli to achieve an efficient and controlled drug delivery. As an example, a drug delivery vector was recently developed with chitosan coated iron oxide nanoparticles, which was capable of being internalized by cells, was able to escape the endosome and inhibited the production of pro-inflammatory cytokines (small proteins important in the immune system) [48].

5.3.6.4. Influence of GUVs suspensions concentration on chitosan adsorption

The influence of liposome concentration in the mechanism of adsorption of chitosan on the lipidic membrane was studied through ζ-potential measurements. *Figure 5.25* shows the dependence of the ζ-potential with the added $[NH_3^+]$ for three different liposome suspensions concentrations: 0.02, 2.0 and 10.0 mg/mL.
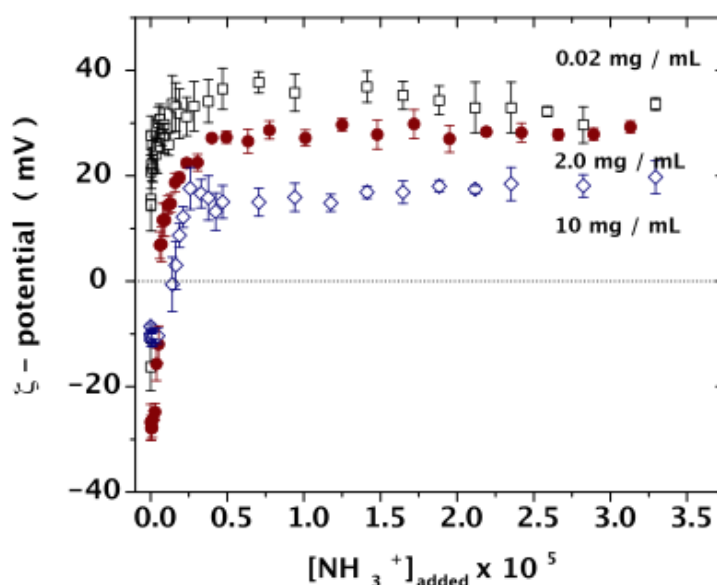
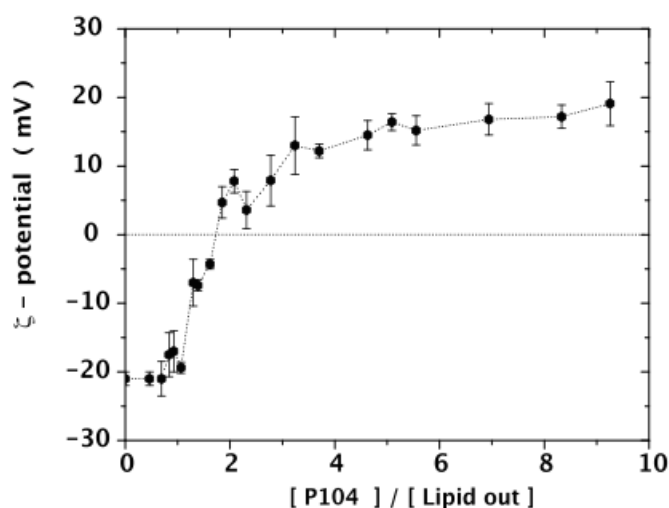**Figure 5.25.** *Variation of the ζ-potential as a function of the added $[NH_3^+]$ for three different liposome suspensions concentrations: 0.02, 2.0 and 10.0 mg/mL at a constant pH of 6.5.*

Both chitosan solution and GUVs suspension were used at a constant pH of 6.5. The initial ζ–potential values for each GUVs suspensions are negative due to the dissociation of phosphates and possibly carboxylates resulting from lipid oxidation. However, with the progressive addition of chitosan, the ζ–potential values become positive reaching a constant value that will dependent in the concentration of liposomes. The amount of chitosan added to get ζ–potential= 0 mV increases with liposome concentration. For a liposome concentration of 0.02 mg/mL, a plateau in ζ–potential values is reached around 35 mV, though, for higher liposome concentrations, the ζ–potential values decrease, reaching constant value around 27 mV and 18 mV, for concentrations of 2.0 and 10 mg/mL, respectively. In this manner, we can observe that the ζ–potential in the plateau presents a dependence on liposome concentration for the adsorption process of chitosan on the lipidic membrane. Some interactions between liposomes coated by excess of chitosan may form supramolecular structures (with some turbidity).

5.3.6.5. Interactions between chitosan coated P104 micelles and chitosan coated GUVs

Figure 5.26 shows the dependence of the ζ-potential with the ratio [P104]/[Lipid out] obtained through the progressive addition of chitosan-coated P104 micelles in excess (ζ-potential average of 22 mV) to a GUVs suspension of 10 mg/mL coated with 30 μL chitosan (ζ-potential average of -20 mV). The obtained results could be interpreted by an adsorption mechanism of positively charged chitosan coated P104 on the lipidic membrane. However, this needs to be more studied in order to determine a detailed mechanism. A plateau is observed around a ζ-potential value of +20 mV, which corresponds to the isolated chitosan-coated P104 micelles adsorbed in the lipidic membranes.

Figure 5.26. *Variation of the ζ-potential as a function of the ratio [P104]/[Lipid out] for the progressive addition of chitosan-coated P104 micelles to chitosan-coated GUVs at a constant pH of 6.5. All measurements were performed at a constant temperature of 37 ℃.*

5.3.6.6. Exchange between P104 triblock copolymer micelles and GUVs with chitosan coatings

P104 triblock copolymer micelles and chitosan-coated GUVs exchange dynamics where studied through ζ-potential and fluorescence measurements, by using the highly hydrophobic PyC_{18} as the simulation of the hydrophobic drug. The fluorescence emission spectra of PyC_{18} (P) in P104 micelles were firstly compared with the fluorescence emission spectra of PyC_{18} (P) in chitosan-coated P104 micelles. These measurements were performed in order to identify any kind of variation due to the addition of the cationic chitosan to the micelles. *Figure 5.27* shows the emission spectra of PyC_{18} (P) in P104 micelles at a concentration of 10 mg/mL, with and without a chitosan-coating. The emission response for both systems can be superposed, so the chitosan adsorption on the lipid membrane does not interfere in the emission spectra of PyC_{18} at the chosen environment.
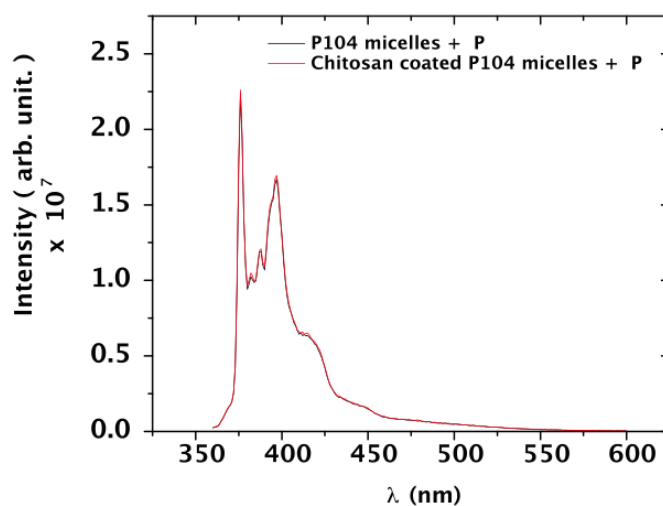
Figure 5.27. *Emission spectra of PyC_{18} (P) in P104 aqueous solutions at a concentration of 10 mg/mL, with and without a chitosan-coating at a temperature of 37 °C.*

In a second step, the influence of chitosan adsorbed on liposomes and/or micelles is examined to evidence its role on PyC_{18} transfer. In *Figure 5.28 a*, negatively charged P104 micelles are added progressively to chitosan-coated liposomes at ζ-potential around zero (form aggregates, see *Figure 5.28 b*). The ζ-potential becomes negative as a proof of P104 micelle interactions. After 9 hours, a small modification of the fluorescence spectrum is observed (*Figure 5.28 c*). When liposomes are highly positively charged, they are stable and isolated, as seen in *Figure 5.28 b*. In this case, the fluorescence spectrum shows only a slight modification. This indicates that the transfer of PyC_{18} into the liposome is even slower. One hypothesis should be that micelles adsorb the excess of chitosan and that these two types of particles repel each other, both being positively charged.

a)

b)

c)
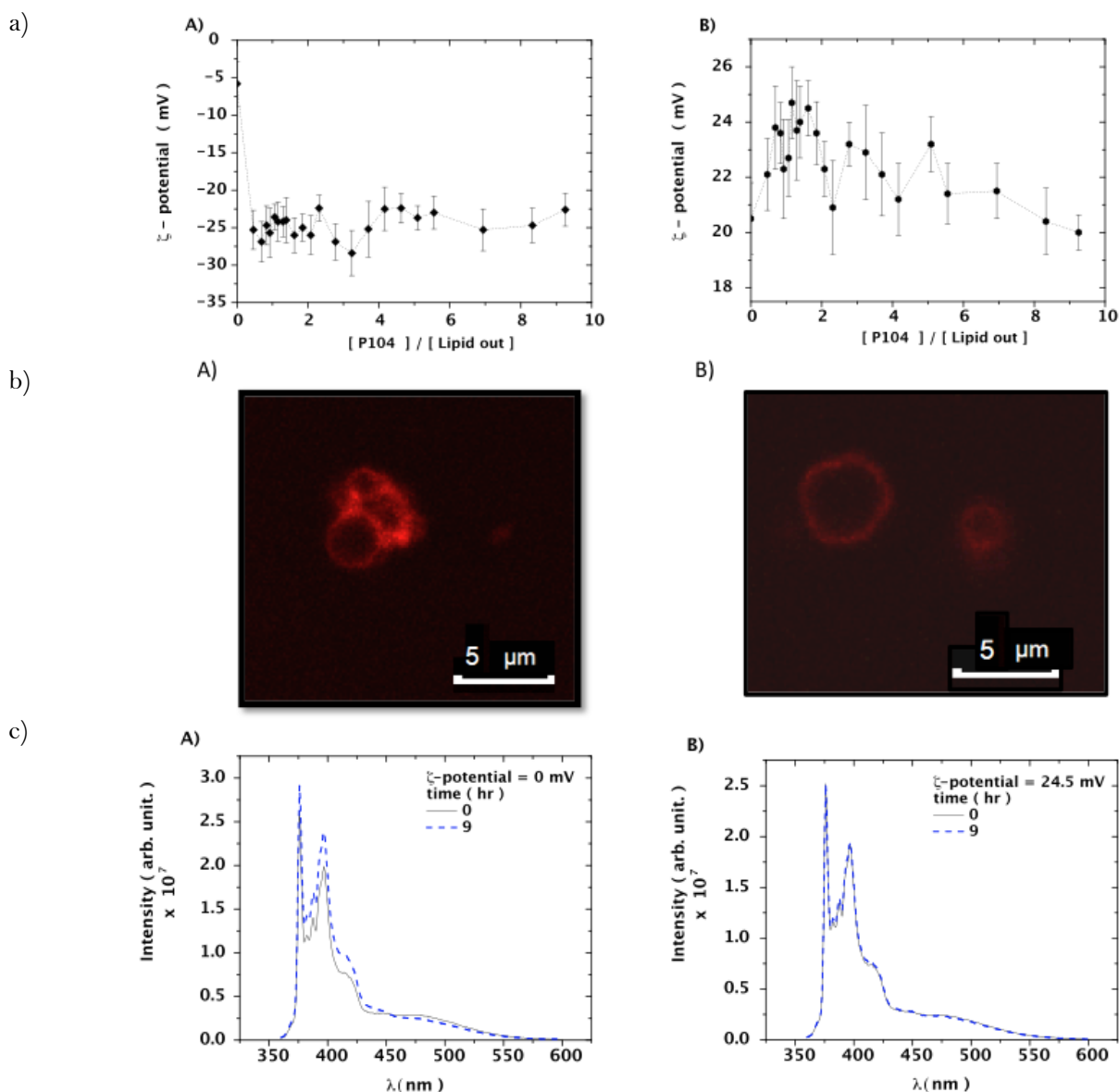
Figure 5.28. *a) ζ-potential variation upon the addition of P104 micelles to chitosan-coated GUVs suspension at a concentration of 10 mg/mL: A) ζ-potential=0 mV and B) ζ-potential= 24.5 mV. b) Visualizations of liposome initial state A) aggregation of chitosan-coated GUVs at the IEP and B) isolated chitosan-coated GUVs observed with confocal fluorescence microscopy. c) First and last emission spectra of PyC₁₈ (P) in P104 aqueous solutions at a concentration of 10 mg/mL mixed with chitosan-coated GUVs: A) ζ-potential=0 mV and B) ζ-potential= 24.5 mV. The temperature was always controlled at 37 °C.*

Finally, the schematic representations of the role of chitosan in the exchange mechanism between P104 micelles and chitosan-coated liposomes with a ζ-potential near to the IEP and with ζ-potential in the adsorption plateau of the ζ-potential curve are presented in *Figures 5.29 a* and *b*, respectively.

388
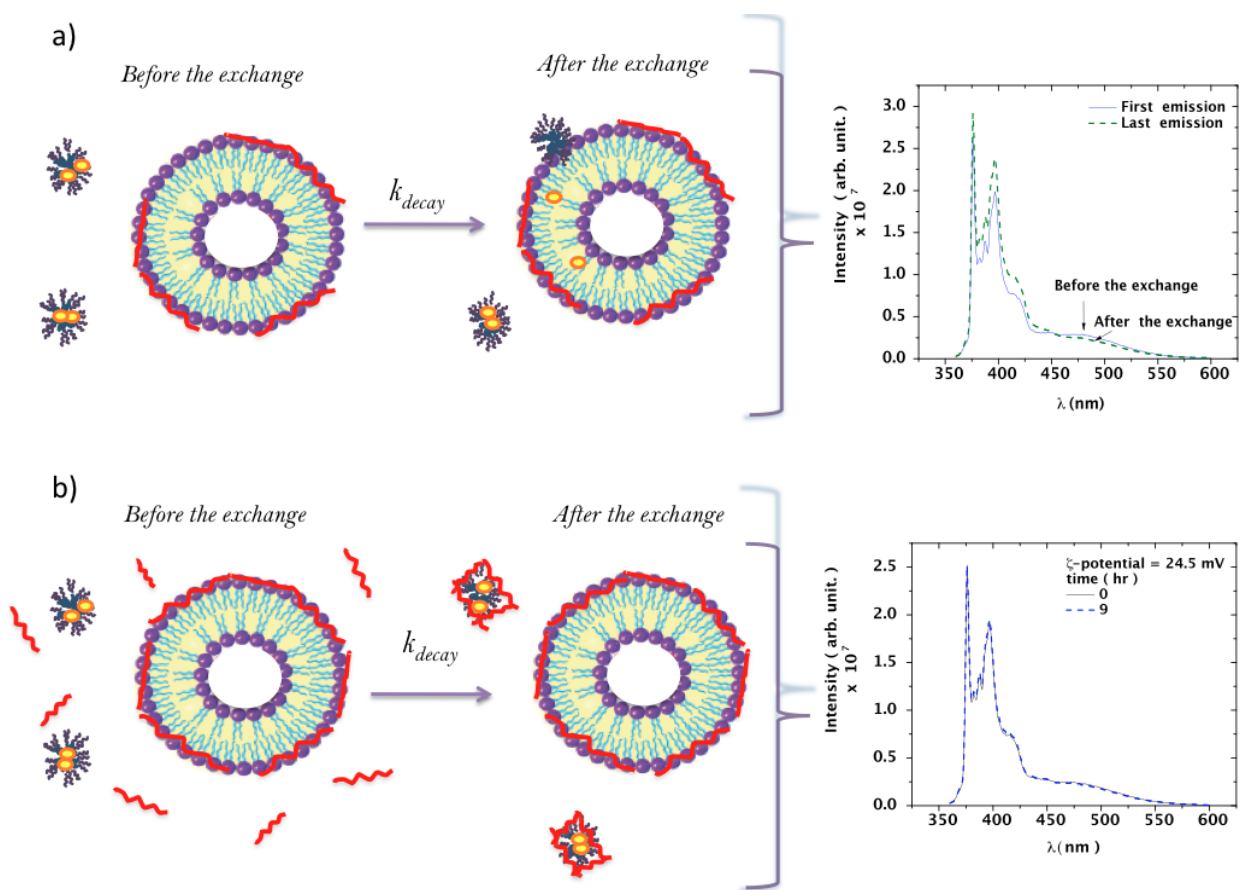
Figure 5.29. *Schematic representations of the role of chitosan in the exchange mechanism between liposomes and P104 micelles for a) ζ-potential near to the IEP and b) ζ-potential in the adsorption plateau of the ζ-potential curve.*

5.4. Particular conclusions for the exchange dynamics between amphiphilic block copolymers and lipidic membranes

P104 triblock copolymer micellization was firstly studied in water and in a GUVs suspension in order to determine P104 CMC at these conditions. A CMC value was found around the P104 concentration of 0.53 mg/mL in the GUVs suspensions. The exchange dynamics between amphiphilic block copolymers and GUVs suspensions were successfully monitored by using a hydrophobic fluorescent probe that can be exchanged via different mechanisms. The evolution of the emission spectra as a function of time was treated in terms of the ratio given by the values obtained from the integration of the excimer intensity peak (440 nm< I_{ex} <550 nm) and the integration of the monomer intensity peak (366 nm< I_{mon} <425 nm). We found that the decrease of the ratio I_{ex}/I_{mon} with time follows a single-exponential decay after mixing GUVs suspension with P104 micelles containing PyC$_{18}$, from which it is possible to quantify the exchange time constant. Finally, we demonstrated that the exchange dynamics between amphiphilic block copolymer micelles and liposomes is a collective mechanism that follows a

389

first order mechanism with linear velocity rate independent of the liposomes concentration and a second order mechanism with linear dependence of k_{decay} as a function of the liposome concentration.

On the other side, we demonstrated that electrostatic interactions play an important role in the adsorption of chitosan on amphiphilic block copolymer micelles and liposomes. The collective exchange mechanisms between chitosan coated liposomes and micelles could be reduced in presence of chitosan (near the isoelectric point) and the chitosan addition slows down the exchange rate of collective mechanisms.

5.5. References

[1] E. Soussan, S. Cassel, M. Blanzat and I. Rico-Lattes, Drug Delivery by Soft Matter: Matrix and Vesicular Carriers, *Angew. Chem. Int. Ed.* **48**, 274 - 288, (2009).

[2] Y. Liu, T.-S. Niu, L. Zhang and J.-S. Yang, Review on nano-drugs, *Natural Science* **2**, 41-48 (2010).

[3] P. Ramos-Cabrer and F. Campos, Liposomes and nanotechnology in drug development: focus on neurological targets, *International Journal of Nanomedicine* **8**, 951–960 (2013).

[4] R. Waehler, S. J. Russell and D. T. Curiel, Engineering targeted viral vectors for gene therapy, *Nature Reviews Genetics* **8**, 573-587 (2007).

[5] M. Morille, C. Passirani, A. Vonarbourg, A. Clavreul and J.-P. Benoit, Progress in developing cationic vectors for non-viral systemic gene therapy against cancer, Biomaterials **29**, 3477-3496 (2008).

[6] Srinivas Ganta, Harikrishna Devalapally, Aliasgar Shahiwala and Mansoor Amiji, A review of stimuli-responsive nanocarriers for drug and gene delivery, *Journal of Controlled Release* **126**, 187-204 (2008).

[7] D.E. Owens and N.A. Peppas, Opsonization, biodistribution, and pharmacokinetics of polymeric nanoparticles, *Int J Pharm* **307**, 93–102 (2006).

[8] H. Laroui, D.S. Wilson, G. Dalmasso, K. Salaita, N. Murthy, S.V. Sitaraman and D. Merlin, Nanomedicine in GI, *Am J Physiol Gastrointest Liver Physiol.* **300**(3), G371–G383 (2011).

[9] M. Murillo, S. Espuelas, S. Prior, A. I. Vitas, M. J. Renedo, M. M. Goñi, J. M. Irache, C. Gamazo, Liberación controlada de principios activos mediante el empleo de formulaciones galénicas *Rev. Med. Univ. Navarra*, **45**, 19-34, 2001.

[10] C. Capasso, M. Hirvinen and V. Cerullo, Beyond Gene Delivery: Strategies to Engineer the Surfaces of Viral Vectors, *Biomedicines* **1**, 3-16 (2013).

[11] M. Malmsten, *Surfactants and Polymers in Drug Delivery*, Marcel Dekker, New York, (2002).

[12] K.K. Jain, *Drug Delivery Systems, Methods in molecular biology*, Humana Press (2008).

[13] C. M. Pitsillides, E. K. Joe, X. Wei, R. R. Anderson, Charles P. Lin, Selective Cell Targeting with Light-Absorbing Microparticles and Nanoparticles, *Biophysical Journal* **84**, 4023–4032 (2003).

[14] D. S. Kohane, Microparticles and nanoparticles for drug delivery, *Biotechnology and Bioengineering* **96**, 203-209 (2007).

[15] A. Akbarzadeh, R. Rezaei-Sadabady, S. Davaran, S. W. Joo, N. Zarghami, Y. Hanifehpour, M. Samiei, M. Kouhi and K. Nejati-Koshki, Liposome: classification, preparation, and applications, *Nanoscale Research Letters* **8**, 102 (2013).

[16] T. P. de Souza, P. Stano Dr. and P. L. Luisi, The Minimal Size of Liposome-Based Model Cells Brings about a Remarkably Enhanced Entrapment and Protein Synthesis, *ChemBioChem* **10**, 1056–1063 (2009).

[17] F. Szoka and D. Papahadjopoulus, Procedure for preparation of liposomes with large internal aqueous space and high capture by reverse-phase evaporation, *Proc. Natl. Acad. Sci. USA* **75**, 4194-4198 (1978).

[18] P. Couvreur, Drug vectorization or how to modulate tissular and cellular distribution of biologically active compounds, *Ann. Pharm. Fr.* **59**(4), 232-238 (2001).

[19] S. Laurent, D. Forge, M. Port, A. Roch, C. Robic, L. V. Elst and R. N. Muller, Magnetic Iron Oxide Nanoparticles: Synthesis, Stabilization, Vectorization, Physicochemical Characterizations, and Biological Applications, *Chem. Rev.* **108**, 2064–2110 (2008).

[20] A. Llevot and D. Astruc, Applications of vectorized gold nanoparticles to the diagnosis and therapy of cancer, *Chem. Soc. Rev.* **41**, 242-257 (2012).

[21] A. M. Mohs, J. M. Provenzale, Applications of Nanotechnology to Imaging and Therapy of Brain Tumors, *Neuroimaging Clinics of North America* **20**, 283-292 (2010).

[22] Xiao Huang, Christopher S. Brazel, On the Importance and Mechanisms of burst Release in Matrix-Controlled Drug Delivery Systems, *Journal of Controlled Release* **73**, 121-136 (2001).

[23] X. Huang and C. S. Brazel, On the importance and mechanisms of burst release in matrix-controlled drug delivery systems. J Control Release, *Journal of Controlled Release* **73**, 121–136 (2001).

[24] Peg Zou, Hong-Wei Chen, Hayley J Paholak, Du-Xin Sun, Burst Release of Lipophilic Drugs from Poly (Ethylene Oxide)- B- Polystyrene Micelles is not Caused by Micelle Disassembly, *Journal of Tumor* 1(2), 7-15 (2013).

[25] Y. Rharbi, Fusion and Fragmentation Dynamics at Equilibrium in Triblock Copolymer Micelles, *Macromolecules* **45**, 9823-9826 (**2012).**

[26] R. Koynova and M. Caffrey, Phases and phase transitions of the phosphatidylcholines, *Biochimica et Biophysica Acta* **1376**. 91–145 (1998).

[27] P3556, L-α-Phosphatidylcholine, Sigma Aldrich Catalog.

[28] P. Walde, K. Cosentino, H. Engel and P. Stano, Giant Vesicles: Preparations and Applications, *ChemBioChem* **11**, 848-865 (2010).

[29] M.J. Hope, M.B. Bally, G. Webb P.R. and Cullis, Production of large unilamellar vesicles by a rapid extrusion procedure. characterization of size distribution, trapped volume and ability to maintain a membrane potential, *Biochim. Biophys. Acta* **812**, 55-65 (1985).

[30] R. Nayar, M.J. Hope and P.R. Cullis, Generation of large unilamellar vesicles from long-chain saturated phosphatidylcholines by extrusion technique, *Biochim. Biophys. Acta* **986**, 200-206 (1989).

[31] F. Quemeneur. Relationship between mechanical parameters and behaviour under external stresses in lipid vesicles with modfied membranes. Data Analysis, Statistics and Probability. Université de Grenoble (2010).

[32] P. Alexandridis, T. Alan Hatton, Poly(ethylene oxide)-poly(propylene oxide)-poly(ethylene oxide) block copolymer surfactants in aqueous solutions and at interfaces: thermodynamics, structure, dynamics, and modeling, *Colloids and Surfaces, A: Physicochemical and Engineering Aspects* **96**, 1-46 (1995).

[33] F. Madani and A. Gräslund, Investigating Membrane Interactions and Structures of CPPs, *Cell-Penetrating Peptides*, Springer Protocols, Second Edition, 73-87 (2015).

[34] S. T. Crooke, *Antisense Drug Technology: Principles, Strategies, and Applications*, Second Edition, CRC Press (2007).

[35] P.L. Luisi and P. Walde, Giant Vesicles in *Perspective in Supramolecular Chemistry*, John Wiley & Sons, Chichester, U.K. (2000).

[36] A. Petelska and Z. Figaszewski, Effect of pH on the interfacial tension of lipid bilayer membrane, *Biophys. J.* **78**, 812-817 (2000).

[37] Y. Liu, S.-H. Chen and J. S. Huang, Light-Scattering Studies of Concentrated Copolymer Micellar Solutions, *Macromolecules* **31**, 6226-6233 (1998).

[38] C. Pidgeon and C. A. Hunt, Calculating Number and Surface Area of Liposomes in Any Suspension, *Journal of Pharmaceutical Sciences* **70**, 173 (1981).

[39] P.P. Infelta and M. Gratzel, Statistics of solubilizate distribution and its application to pyrene fluorescence in micellar systems. A concise model. *J. Chem. Phys.*, 70, 179 (1979).

[40] Y. Rharbi, M. Li, M.A. Winnik and K.G. Hahn, Temperature Dependence of Fusion and Fragmentation Kinetics of Triton X-100 Micelles, *J. Am. Chem. Soc.* **122**, 6242–6251 (2000).

[41] Y. Rharbi, N. Bechthold, K. Landfester, A. Salzman and M.A. Winnik, Solute exchange in synperonic surfactant micelles, *Langmuir* **19**, 10-17 (2003).

[42] Y. Rharbi, M.A. Winnik and K.G. Hahn, Kinetics of Fusion and Fragmentation Nonionic Micelles: Triton X-100, *Langmuir* **15**, 4697–4700 (1999).

[43] R. Savic, A. Eisenberg and D. Maysinger, Block copolymer micelles as delivery vehicles of hydrophobic drugs: Micelle-cell interactions, *Journal of Drug Targeting* **14**(6), 343-355 (2006).

[44] F. Quemeneur, M. Rinaudo, G. Maret and B. Pépin-Donat, Decoration of lipid vesicles by polyelectrolytes: mechanism and structure, *Soft Matter* **6**, 4471-4481 (2010).

[45] T. Xu, N. Zhang, H.L. Nichols, D. Shi and X. Wen, Modification of nanostructured materials for biomedical applications, *Mater. Sci. Eng. C* **27**, 579-594 (2007).

[46] F. Quemeneur, M. Rinaudo and B. Pépin-Donat, Influence of Polyelectrolyte Chemical Structure on their Interaction with Lipid Membrane of Zwitterionic Liposomes, *Biomacromolecules* **9**, 2237-2243 (2008).

[47] C. Cametti, Polyion-induced aggregation of oppositely charged liposomes and charged colloidal particles: the many facets of complex formation in low-density colloidal Systems, *Chem. Phys. Lipids* **155**, 63-73 (2008).

[48] F. Kratz, P. Senter and H. Steinhagen, *Drug Delivery in Oncology: From Basic Research to Cancer Therapy*, Volume 1, page 894, Wiley-VCH Verlag & Co., Germany (2012).

Conclusions

→ A study of amphiphilic block copolymer P104 in water was performed through density, sound velocity, viscosity and dynamic slight scattering (DLS) measurements in the dilute and semi-dilute regimes between 10 and 65 ºC.

→ The structural behavior of the P104/water system was analyzed and allowed determining the critical micellar temperature (CMT), the micellar growth temperature (MGT) and the clouding point temperature (CPT) as a function of P104 concentration.

→ The temperature domains at which P104 spherical micelles and P104 elongated micelles exist are greater than for other triblock copolymers, allowing their applications in a wider field.

→ The dependence of I_{SCA}/I_{SCA}^0 with R_h was compared to the Perrin model of prolate ellipsoids, oblate ellipsoids and spheres, and was found to be close to the predicted behavior for prolate ellipsoids, suggesting that P104 micelles grow as prolate rods.

→ The determined micellar structures for P104 amphiphilic copolymer in the temperature range between 25 and 55 ºC (spherical micelles domain), can be used as micellar nanocarriers for drug controlled release. Their nanoscale size makes them a suitable option for targeted drug delivery applications, including storage, controlled release and protection of the hydrophobic drugs. The shape of micelles is affected by temperature, which can be exploited for the design of new formulations.

→ The effect of NaCl addition on CMT, MGT and CPT was described.

→ Rheological properties were studied in a P104 concentration range from 50 to 600 mg/mL and were found to be greatly dependent on temperature and concentration, since the storage modulus increases between two and three orders of magnitude. At higher concentrations and temperatures, this copolymer solutions form thermo-reversible and physical gels. After the MGT, spherical micelles grow into rod-like micelles (prolates), which increases the viscoelasticity of the solutions.

→ We described the growth dynamics of spherical micelles to elongated micelles in aqueous solutions of P104 triblock copolymer by performing "temperature jumps" experiments, from which it was possible to obtain the variation of the scattering light intensity and the hydrodynamic radius as a function of time.

→ The scattering intensity, the hydrodynamic radius and the aspect factor evolution as a function of time were analyzed by using a mono-exponential function with an apparent relaxation time. The growth dynamics present a relatively slow process with characteristic times within the range of 800s to 4000s.

→ The linear increase of the growing rate with P104 triblock copolymer concentration shows that the structural transition is dominated by a fusion-fission mechanism with normal size micelles.

→ We demonstrated that collective dynamics take place between P104 spherical micelles and P104 rod-like micelles at the equilibrium. The exchange mechanism, depicted by k_{decay}, consists on two processes: a first order mechanism with linear velocity independent of the empty micelles concentration, related to the fission process, and a second order mechanism with linear dependence on k_{decay} as a function of the empty micelles concentration, related to the fusion process.

→ It was found that fission and fusion constants present two apparent activation energies with opposite sign, a negative apparent activation energy in the micelles regime and a positive apparent activation energy in the rod-like micelles regime. We show that the barrier energy to fission is controlled by the core surface tension in the spherical micelles regime and by a combination of the surface tension and the coronal energy in the rod-like micelles regime.

→ P104 triblock copolymer micellization was studied in water and in GUVs suspension, from which was possible to detect a similar CMC of P104 in both environments.

→ The exchange dynamics between amphiphilic block copolymers and GUVs suspensions were successfully monitored by using a hydrophobic fluorescent probe that can be exchanged via different mechanisms.

→ The emission spectra obtained from fluorescence measurements during the interactions between P104 amphiphilic block copolymers filled with PyC_{18} and GUVs suspensions show an increase on the monomer, representing the presence of the PyC_{18} (which simulates the hydrophobic drug) interacting with GUVs lipidic membrane

→ The evolution of the emission spectra as a function of time can be treated in terms of the ratio given by the values obtained from the integration of the excimer intensity peak (440 nm< I_{ex} <550 nm) and the integration of the monomer intensity peak (366 nm< I_{mon} <425 nm).

→ We found that the decrease of the ratio I_{ex}/I_{mon} with time, obtained after mixing GUVs suspension with P104 micelles containing PyC_{18}, follows a single-exponential decay, from which it is possible to quantify the exchange time constant.

→ We demonstrated that the exchange dynamics between amphiphilic block copolymer micelles and liposomes is a collective mechanism that follows a first order mechanism with linear velocity rate independent of the liposomes concentration and a second order mechanism with linear dependence of k_{decay} as a function of the liposome concentration.

→ The collision rate of micelle-liposome was calculated and was found to be higher than that of micelle-micelles due to the liposome size. It is proposed that P104 micelles control the adhesion-exchange process of P104-liposome system.

→ We demonstrated that electrostatic interactions play an important role in the adsorption of chitosan on amphiphilic block copolymer micelles and liposomes.

→ The modifications on P104 micelles characteristics with a chitosan coating could improve the storage stability of hydrophilic drugs in micelles core and could prevent their release before reaching the specific target and receiving the adequate stimuli to achieve an efficient and controlled drug delivery.

→ The collective exchange mechanisms between chitosan coated liposomes and micelles could be reduced in presence of chitosan (near the isoelectric point) and the chitosan addition slows down the exchange rate of collective mechanisms.

Perspectives

→ The experimental results of the growth dynamics of P104 spherical micelles to elongated micelles in water and in NaCl should be simulated in order to analyze the process in a more detailed manner.

→ Now that we successfully monitored the exchange dynamics between P104 triblock copolymer and L-α-phosphatidylcholine GUVs suspensions by using a hydrophobic fluorescent probe, the variation of amphiphilic block coplymers, ionic strength of the GUVs suspension, pH and temperature could be studied in order to control the vectorization rate.

→ A theoretical model should be proposed in order to simulate the experimental results obtained through the kinetics between amphiphilic block copolymers and lipidic membranes and to obtain more information about the mechanism.

→ The interactions between chitosan-coated micelles and chitosan-coated liposomes could be deepened in order to indentify conditions at which the vectorization dynamics are accelerated.

→ Since the vectorization dynamics were studied by using L-α-phosphatidylcholine liposomes as the simplest cell models, it would be of great interest to study the exchange dynamics by using real cells.

A. List of symbols

Nomenclature

a	semimajor axis of a prolate in Perrin model
b	semiminor axis of a prolate in Perrin model
C_T	total concentration of amphiphile
E	Energy
G'	elastic modulus
G''	viscous modulus
H	Planck's constant
I_{ex}	excimer intensity
I_{mon}	monomer intensity
I_{SCA}	total scattering intensity
$I_{SCA}{}^0$	scattering intensity taken at a reference temperature
I_{disp}	total intensity scattered
k^+	kinetic constant of the insertion process
k^-	kinetic constant of the expulsion process
k_B	Boltzmann constant
k_{diff}	diffusion controlled rate
k_{fus}	kinetic constant of the fusion process
k_{fiss}	kinetic constant of the fission process
k_{decay}	general exchange constant
k_{growth}	growth constant
K	compressibility modulus
KCps	scattering light intensity
K_ϕ	apparent molar adiabatic compression
L_α	lamellar liquid-crystalline phase
L_β	lamellar gel phase
L_c	lamellar crystalline phase
L	micelle length
M	molality
M	mass of an object
M_{II}	micellar phase
M_w	molecular weight
n_{mic}	refraction indices of micelles
n_w	refraction indices of water
N_A	Avogadro's number

N_{agg}	aggregation number
H_{II}	inverted micellar cubic phase
$P(q)$	micelle form factor in Perrin's model
P_{reac}	probability of adhesion-exchange
$\underset{\sim}{Q}^{[B]}_{II}$	bilayer cubic phase
$\underset{\sim}{Q}^{[M]}_{II}$	inverted micellar cubic phase
R	gas law constant
R_c	core radius of a block copolymer micelle
$R_{g(PEO)}$	radius of gyration of the PEO segment of a block copolymer micelle
R_h	hydrodynamic radius
T	temperature
X_{CMC}	critical micellization concentration in mole fraction units
V	volume of an object
V_{mic}	volume of a micelle
V_ϕ	apparent molar volume
ΔG	free energy of micellization per mole of surfactant
ΔH	standard enthalpy of micellization per mole of surfactant
ΔS	standard entropy of micellization per mole of surfactant
Φ	ideal colligative property
β_s	adiabatic compressibility of the solution
$\beta_{s,0}$	adiabatic compressibility of the solvent
γ	strain
η	Viscosity
Λ	Wavelength
ρ	density
ρ_0	solvent density
υ	sound velocity
υ_f	frequency
φ_{mic}	volume fraction of surfactant
τ	relaxation time
ζ	zeta potential
$<n>$	average number of hydrophobic fluorescent probe per micelle

B. Abbreviations

ATP	Adenosine Triphosphate
CMC	Critical Micellization Concentration
CMT	Critical Micellization Temperature
CPT	Cloud Point Temperature
DA	Degree of Deacetylation
DNA	Deoxyribonucleic Acid
DLS	Dynamic Light Scattering
DOPC	Lipid 1,2-dioleoyl-sn-glycero-3-phosphocholine
GUVs	Giant Unilamellar Vesicles
IEP	Isoelectric Point
LUVs	Large Unilamellar Vesicles
LIPIDAT	Lipid Thermodynamic Database
LVR	Linear Viscoelastic Region
MGT	Micellar Growth Temperature
NMR	Nuclear Magnetic Resonance
PA	Phosphatidic Acid
PC	Phosphatidylcholine
PE	Phosphatidylethanolamine
PEO	Ethylene Polyoxide
PG	Phosphatidylglycerol
PI	Phosphatidylinositol
PPO	Polypropylene Polyoxide
PS	Phosphatidylserine
PyC_{18}	Fluorescent probe 1-pyrenyloctadecanone, $C_{34}H_{44}O$
SUVs	Small Unilamellar Vesicles
QLS	Quasielastic Light Scattering
SAXS	Small Angles X-ray Scattering

Résumé étendu géneral

1. Étude du comportement d'ADN en solution et aux interfaces

1.1. Introduction

Les études de molécules d'ADN dans des solutions aqueuses effectuées par différentes approches permettent d'évaluer la forte influence de la nature de la molécule et ses propriétés physico-chimiques quand elles interagissent avec d'autres types de molécules en solution ou avec des surfaces métalliques. Les résultats nous permettent d'aspirer à une meilleure compréhension des interactions moléculaires et de chercher une meilleure efficacité de leurs applications. Maintenant, la capacité de détecter l'ADN et de l'ARN en utilisant des capteurs d'hybridation d'ADN est utilisé en génomique et les attentes dans les procédés électrochimiques augmentent chaque jour, ainsi que le développement de biocapteurs d'ADN, l'évaluation des interactions ADN-protéines et des études de thérapie génique. Aujourd'hui, l'objectif de parvenir à une plus grande efficacité dans les processus de compaction de l'ADN, l'innovation du développement des capteurs d'ADN et l'étude des changements de propriétés interfaciales générés entre les surfaces métalliques et les molécules d'ADN sont devenus des sujets de grand intérêt en bioingénierie.

La possibilité de prendre quelques concepts de la théorie des solutions de polymères utilisés dans les études physico-chimiques et rhéologiques peut ouvrir de nouvelles possibilités dans le domaine des systèmes comme l'ADN en solution, en utilisant différentes techniques dont les méthodes électrochimiques et optiques. Des techniques électrochimiques telles que la Spectroscopie d'Impédance Électrochimique (EIS, en anglais) et la Modulation de la Capacité Interfaciale (MIC, en anglais) sont proposées pour déterminer les paramètres caractéristiques qui permettront d'identifier et d'étudier les transitions des interfaces formées par de molécules d'ADN adsorbées sur différentes surfaces métalliques d'une manière détaillée. De cette manière, ce travail propose le couplage des techniques rhéologiques, électrochimiques et optiques pour effectuer une étude détaillée du comportement de molécules d'ADN en solution et aux interfaces (utilisant deux surfaces métalliques différentes), en fonction de paramètres tels que la température, la concentration de l'ADN, la concentration en sel et le potentiel électrique.

1.2. Caractérisation et propriétés rhéologiques de l'ADN en solution

Initialement, le comportement rhéologique des solutions ADN/tampon, ainsi que la détermination des concentrations critiques (C* et C_e), sont présentés et discutés à partir des expériences d'écoulement et des expériences dynamiques. La viscosité intrinsèque $[\eta]$ (4 080 ml/g) a été déterminée à partir de l'extrapolation à concentration d'ADN nulle, de la viscosité de cisaillement (η_0) au plateau Newtonien

obtenue par écoulement. Cette valeur a été utilisée pour accéder à la masse moléculaire de nos échantillons d'ADN (8246 800 g/mol).

L'influence du gradient de cisaillement sur la viscosité des échantillons d'ADN a été étudiée dans une large gamme de concentrations de ADN (0.1 à 10 mg/mL) à des températures de 10, 20, 30 et 40 ° C. Les données obtenues à la température de 20 °C sont présentées dans la *Figure 1*. Les courbes d'écoulement sont caractérisées par trois paramètres importants: la viscosité η_0 du plateau Newtonien, le gradient de cisaillement critique $\dot{g}_c$ et la pente *s*. Le gradient de cisaillement critique est lié au temps caractéristique τ_R de l'ADN en solution. Un gradient de cisaillement plus élevé que le temps de relaxation de la solution d'ADN conduit à la manifestation de changements structurels tels que desenchevêtrements, alignements des molécules dans l'écoulement, entre autres, ou à des modifications conformationnelles de la molécule. La viscosité dans le plateau Newtonien correspond à la viscosité lorsque $\dot{g} < \dot{g}_c$. Aussi, $\dot{g}_c$ diminue avec l'augmentation de la concentration de l'ADN.
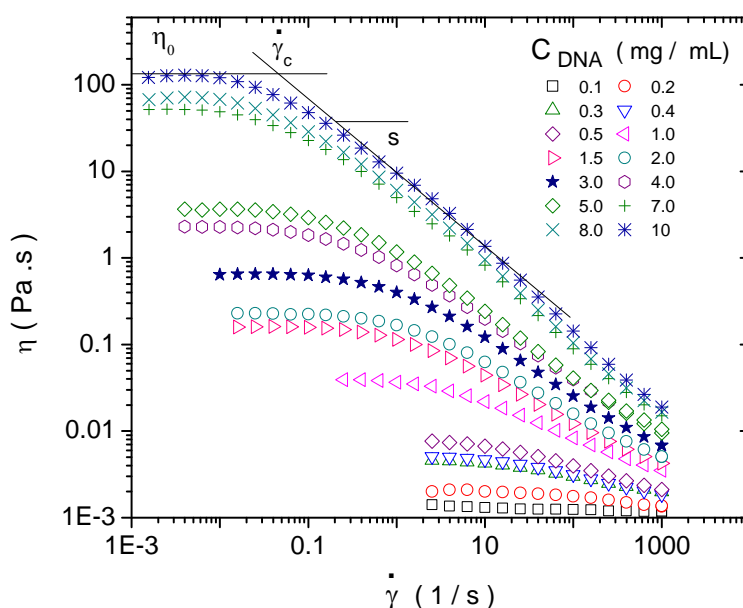
Figure 1. *Influence du gradient de cisaillement sur la viscosité de solutions d'ADN de thymus de veau, pour differentes concentrations d'ADN et à une température de 20 ° C.*

Les courbes d'écoulement $\eta(\dot{g})$ en fonction de $\dot{g}$ et la détermination de la viscosité sur le plateau Newtonien permettent d'estimer les viscosités spécifiques à gradient de cisaillement nulle pour la gamme suivante de valeurs de C[η]: $C_{DNA}[\eta] < 40$. On obtient une courbe maîtresse à partir de la variation de la viscosité spécifique en fonction du paramètre de recouvrement C[η], à partir dequel on peut déterminer les deux concentrations d'ADN critiques (*Figure 2*). La première concentration critique

(C*) a été estimée, comme première approche, en utilisant la relation C*~[η] $^{-1}$, et est égal à 0.245 mg/mL. Le point de départ du domaine semi-dilué enchevêtré, C_e, a été obtenu à partir de la limite du comportement linéaire en representation log-log pour le domaine de concentrations plus élevées dans la courbe η_{sp} en fonction de $C_{DNA}[\eta]$, i.e. $C_{DNA}[\eta] \sim 10$, c'est à dire: 2.45 mg/mL.
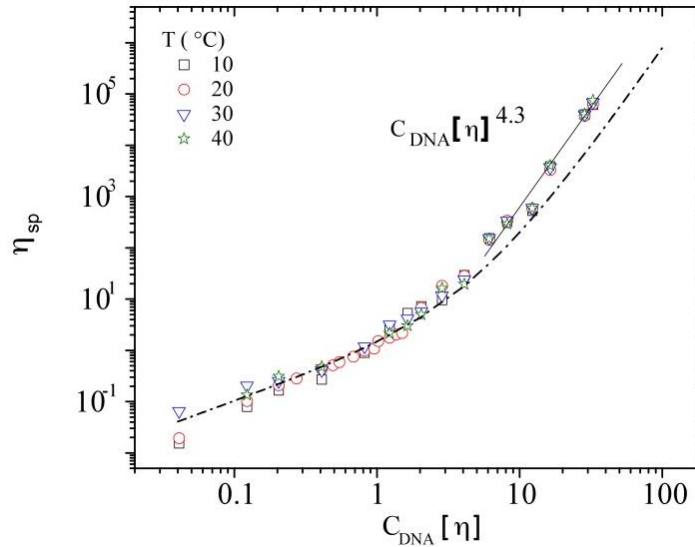
Figure **2.** D*épendance de la viscosité spécifique en fonction du paramètre de chevauchement C[η] pour des solutions d'ADN de thymus de veau dans du tampon TE à un pH de 7.3 et pour les températures de 10, 20, 30 et 40 °C.*

Le deuxième paramètre qui caractérise le comportement de l'ADN est le gradient de cisaillement critique $\dot{g}_c$, obtenu au début de l'écoulement non Newtonien. À partir d'un graphique log-log de $\dot{g}_c$ en fonction de $C_{DNA}[\eta]$ pour des concentrations d'ADN dans le régime semi-dilué il est possible d'obtenir la relation $\dot{g}_c \sim C_{DNA}[\eta]^{-1.9}$, avec une pente moyenne de -2, laquelle a été également constaté pour hyaluronanes de différentes masse moléculaire par *M. Milas et al.*. On peut aussi constater que les résultats à toutes les températures ont un comportement identique et la même pente moyenne.

A partir d'une translation horizontale (ax) et d'une translation verticale (ay), en utilisant une concentration d'ADN comme une référence spécifique, on obtient une courbe maîtresse qui montre que le temps de relaxation principal du système est modifié seulement par la variation de la concentration de l'ADN. Le paramètre de translation horizontale représente le coefficient de translation des fréquences et le deuxième représente le coefficient de translation du module. La *Figure 3* montre la courbe maîtresse de l'ADN obtenu pour une gamme de concentrations entre 1.5 et 10.0 mg/mL à la température de 20 °C, en utilisant comme référence 4 mg/mL. La même procédure a été utilisée pour l'analyse de la température pour chaque concentration d'ADN.
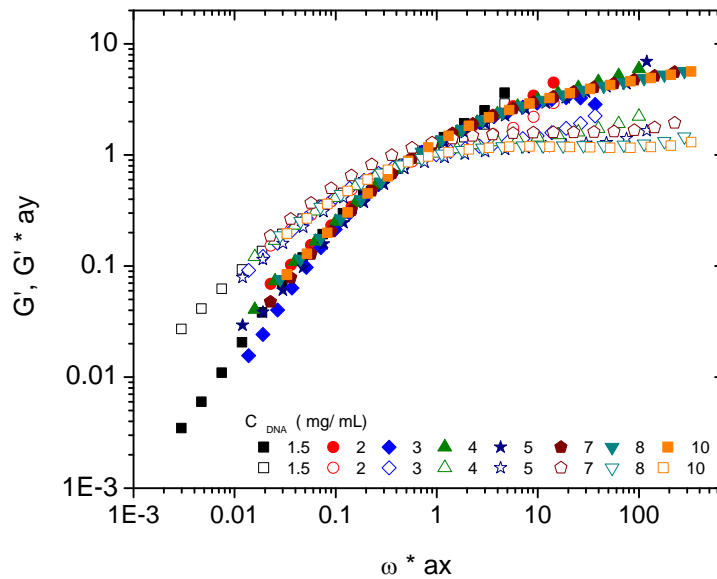
Figure 3. *Courbe maîtresse pour les modules élastique (G ') et visqueux (G'') réduits en fonction de la fréquence réduite pour la variation de concentrations d'ADN entre 1.5 et 10.0 mg/mL à la température de 20 ° C.*

À partir des mesures dynamiques et d'écoulement on obtient une bonne superposition de |η*| (ω) et

η_0 ($\dot{g}$) en fonction du gradient de cisaillement et de la fréquence radiale dans la gamme de concentrations d'ADN comprise entre 2.0 et 10.0 mg/mL, en accord un comportement de polymere en solution. De la meme facon, la pente s obtenue en ecoulement suit le meme comportement que les valeurs obtenues a partir de la dynamique (*Figure 4*).

On détermine aussi la pente de la région de loi de puissance de |η*| (ω) en fonction de la fréquence radiale pour chaque concentration d'ADN et à chaque température. Dans la région de loi de puissance de

η, en fonction de $\dot{g}_c$, la pente *s* dépend du paramètre de chevauchement C[η], tel que décrit par *Graessley et. al.* Pour C_{DNA}[η]>35, la pente tend vers une limite, comme prévu dans la théorie de l'enchevêtrement de Graessley, et est égal à -0.818.

Les résultats sont présentés dans la *Figure 4* et montrent que la valeur limite pour l'ADN thymus de veau dans du tampon TE à un pH de 7.3 présente une pente moyenne de -0.82, ce qui correspond au comportement décrit par Graessley et qui a également été rapporté pour une grande gamme d'échantillons d'acide hyaluronique avec différentes masses moléculaires.
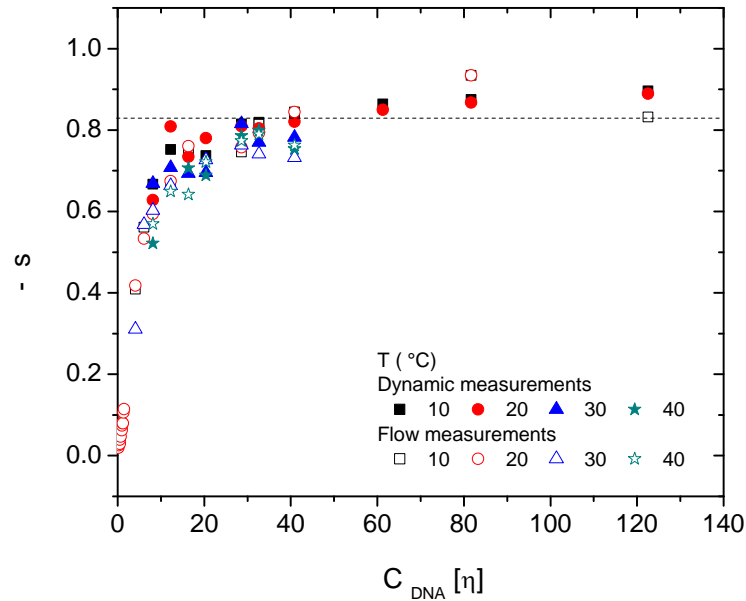
Figure 4. *Pente s dans la région de loi de puissance déterminé à partir des courbes d'écoulement et des courbes dynamiques pour l'ADN de thymus de veau dans du tampon TE à des températures de 10, 20, 30 et 40 °C.*

En utilisant une approche complémentaire pour l'étude des solutions d'ADN enchevêtrées, i.e. concentrations d'ADN supérieures à 2.0 mg/mL, le comportement non-linéaire a été formulée en termes de quantités normalisées $\sigma^* = \sigma/G_0$ et $\dot{g} = \dot{g}^* \tau_c$, à partir desquelles on obtient une courbe maîtresse avec la superposition des courbes d'écoulement et de dynamique. Le comportement non-linéaire de solutions ADN/tampon est reproduit en utilisant le modèle de Giesekus avec deux temps caractéristiques, sur la base du concept de déformation dépendante de la mobilité tenseur.

La *Figure 5* montre la courbe maîtresse de σ^* en fonction de $\dot{g}^*$ pour la gamme de concentrations d'ADN entre 2.0 et 10 mg/mL à une température de 20 °C. En dessous de $\dot{g}^* = 0.20$, tous les données sont superposées, c'est à dire qu'ils sont invariants par rapport aux variations relatifs de la concentration d'ADN, comme prévu pour le régime Newtonien linéaire ($\sigma^* = \dot{g}^*$). À des concentrations d'ADN entre 2.0 et 6.0 mg/mL et à des valeurs plus élevées de $\dot{g}^*$, c'est à dire $\dot{g}^* \geq 0.20$, la pente de la courbe de contrainte diminue, montrant la présence du phénomène de rhéofluidification. L'apparition d'un plateau de contrainte est observée autour de $\dot{g}^* = 15.0$, à des concentrations d'ADN supérieures à 6.0 mg/mL, ce qui est liée à l'apparition du phénomène de bandes de cisaillement.
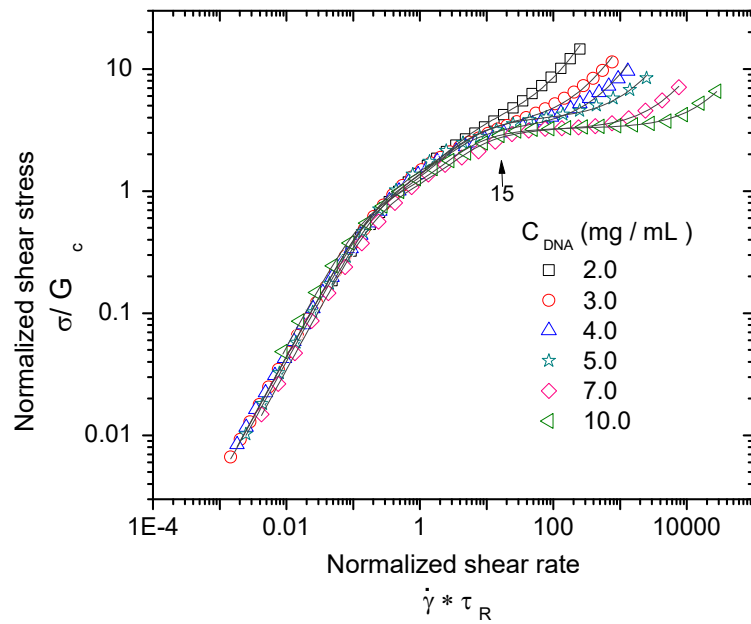
Figure 5. *Courbe maîtresse pour les solutions d'ADN. Contrainte de cisaillement normalisé, en fonction du gradient de cisaillement normalisé, pour des concentrations d'ADN de 2.0 à 10.0 mg/mL à la température de 20 °C. Les lignes en trait plein représentent les simulations obtenus avec le modèle de Giesekus.*
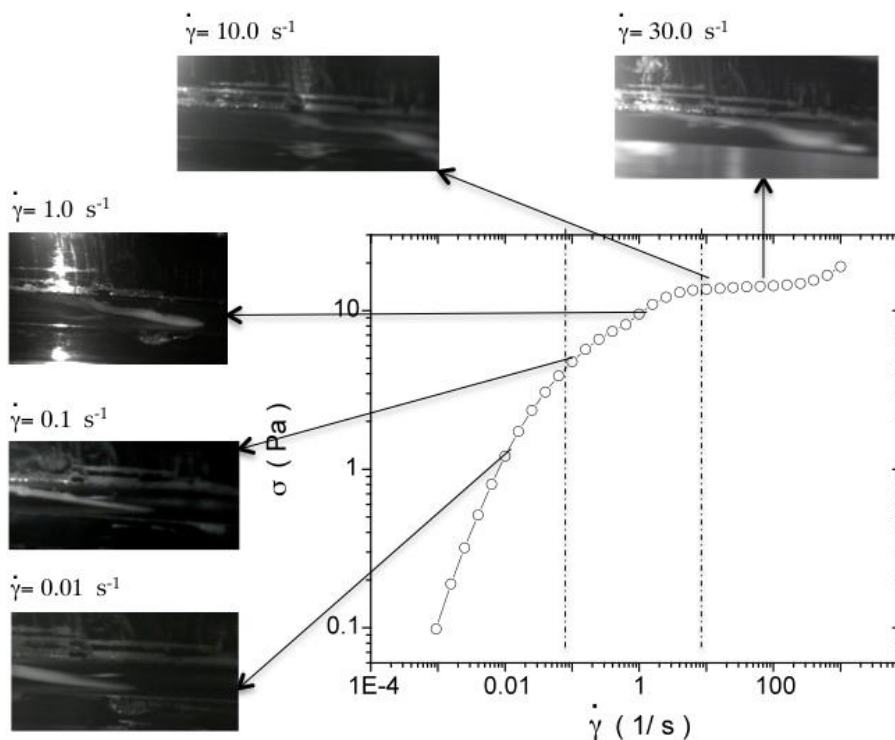
Figure 6. *Contrainte de cisaillement en fonction du gradient de cisaillement pour une concentration d'ADN de 10.0 mg/mL à la température de 20 °C. Chaque image correspond à une visualisation du champ de déformation à l'intérieur de la solution obtenue à l'état d'équilibre.*

L'apparition des bandes de cisaillement est démontré a partir d'observations du champ de déformation combinée avec des mesures mécaniques. Les conditions trouvées sont les suivantes: $\overset{.}{g}$ =10.0 s^{-1} and C$_{DNA}$> 5.0 mg/mL. Des preuves visuelles du champ de déformation à l'intérieur de la solution, obtenues à l'état d'équilibre sont présentées pour différents gradients de cisaillement sélectionnés dans les trois régimes différents: le régime Newtonien (0.01 s^{-1}), le régime de rhéofluidification (0.1 et 1.0 s^{-1}) et le régime d'écoulement avec bandes de cisaillement (10.0 et 30.0 s^{-1}) (*Figure 6*). Pour les concentrations en ADN plus élevées dans le régime semi-dilué avec enchevêtrements, les interactions entre chaînes d'ADN et les enchevêtrements ont des effets importants sur la visco-élasticité linéaire des solutions dans les différents régimes d'écoulement.

1.3. Etude expérimentale de l'adsorption des molécules d'ADN en solution en différentes surfaces métalliques

Après avoir étudié les propriétés des molécules d'ADN en solution, on a utilisé des techniques électrochimiques et optiques pour identifier les changements structurels aux interfaces Au/ADN et Pt/ADN et pour décrire le comportement des chaînes d'ADN dans la double couche électrochimique en fonction de la concentration d'ADN pour chaque régime caractéristique, c'est-à dire, les régimes dilué et semi-dilué. Les résultats d'impédance obtenus par Spectroscopie d'Impédance Électrochimique ont été transformés en valeurs de capacité complexes et interprétés sur la base de la théorie de l'impédance d'adsoption en utilisant l'approche des circuits équivalents proposé par Frumkin-Melik-Gaikazyan-Randles (FMGR). La *Figure 7* montre les spectres de capacité complexe pour des concentrations d'ADN de 0.3, 0.8 and 2.5 mg/mL à des températures de 20, 30 et 40 ºC avec une electrode de platine.

La tendance de tous les spectres montrés dans la *Figure 7* correspond à celle des spectres de capacité observés pour un processus d'adsorption. Pour les trois températures, la capacité complexe présente une dispersion typique en fonction de la fréquence (f_ω), avec une forme d'arc déprimé bien défini (1 kHz <f$_\omega$ <0.1) et une courbe ascendante dans les basses fréquences (f_ω <0.1 Hz).

Aux fréquences élevées, les spectres peuvent être adéquatement modélisée par un circuit équivalent similaire proposé par FMGR, de cette façon, la dispersion de la capacité complexe est décrite par l'arrangement en série de trois éléments électriques: une résistance à l'adsorption (R$_{ad}$), liée avec un processus d'électrosorption lent, un élément de phase constante (CPE), associé avec l'hétérogénéité de surface, qui représente dans ce cas la capacité d'adsorption non idéale (C_{ad}) et une impédance de diffusion de Warburg ($Z_{W,ad}$), associé à la diffusion des molécules d'ADN qui s'adsorbent à l'interface. Pour décrire complètement l'interface, on considère une capacité à double couche (C_{dl}) par l'ajout d'un condensateur en parallèle dans le circuit équivalent.
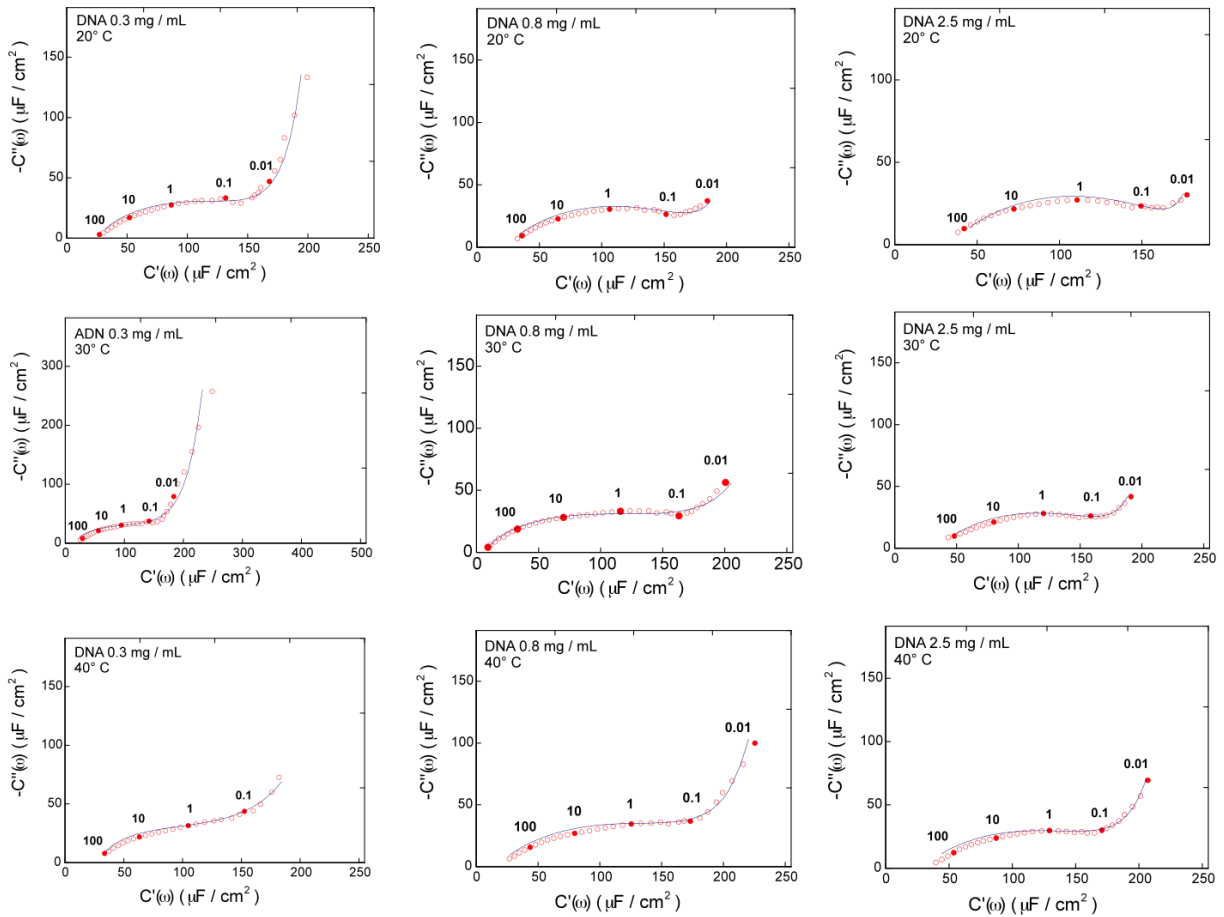
Figure 7. *Spectres de capacité complexes pour les concentrations d'ADN de 0.3, 0.8 et 2.5 mg/mL à des températures de 20, 30 et 40 ºC. Fréquence en Hz.*

Le circuit équivalent représenté dans la *Figure 8* et *l'Équation 1* ont été utilisés pour interpréter les données expérimentaux de capacité complexe obtenus à chacune des conditions expérimentales présentées dans ce travail.
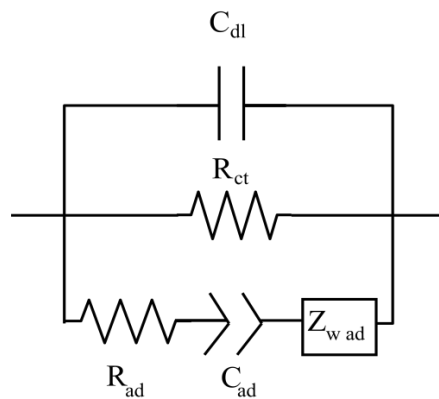
Figure 8. *Circuit équivalent représentant la capacité complexe pour l'interface Pt-ADN/tampon.*

$$C(W) = C_{dl} + \cfrac{1}{R_{ad}jW + S_{ad}\sqrt{jW} + \cfrac{(jW)^{1-n}}{C_{ad}}} + \cfrac{1}{R_{ct}jW} \qquad (1)$$

Où $\sigma_{ad}(j\omega)^{-1/2}$ correspond à l'impédance de diffusion avec son coefficient σ_{ad}. D'autre part, le paramètre n est inhérent au CPE selon:

$$CPE = \frac{1}{(jW)^n C_{ad}} \qquad (2)$$

On établit ensuite les dépendances de chaque paramètre du circuit équivalent, soit la capacité de la double couche (C_{dl}), la capacité d'adsorption (C_{ad}), la résistance d'adsorption (R_{ad}) et la résistance au transfert de charge (R_{ct}) en fonction de la concentration en ADN (*Figure 9 et 10*). L'analyse de ces paramètres, ainsi que la constante de temps caractéristique τ_c, permettent de détecter deux changements remarquables dans la structure de la double couche autour des concentrations d'ADN de 0.30 et 1.50 mg/mL, lesquelles sont reliées avec le recouvrement et l'enchevêtrement des molécules d'ADN, déterminées par des méthodes rhéologiques. Le réarrangement de la structure de la double couche est expliquée selon les interactions des molécules d'ADN à l'interface, résultant du recouvrement et des enchevêtrements des chaînes d'ADN. Ainsi, les changements dans la structure interfaciale, reflétés dans les paramètres C_{dl}, C_{ad} et R_{ad}, dépendent fortement de la nature de l'ADN présent dans la solution.

Les *Figures 9* et *10* montrent la dependence de la capacité de la double couche (C_{dl}) pour les interfaces Pt-ADN et Au/ADN, respectivement, en fonction de la concentration d'ADN à différentes températures. Puisque la nature du processus d'adsorption dépend aussi des électrodes utilisées, l'arrangement des charges dans la double-couche éléctrochimique varie d'une électrode à autre. Néanmoins, les variations de la capacité de la double couche (C_{dl}) en fonction de la concentration d'ADN sont détectées avec les deux electrodes.
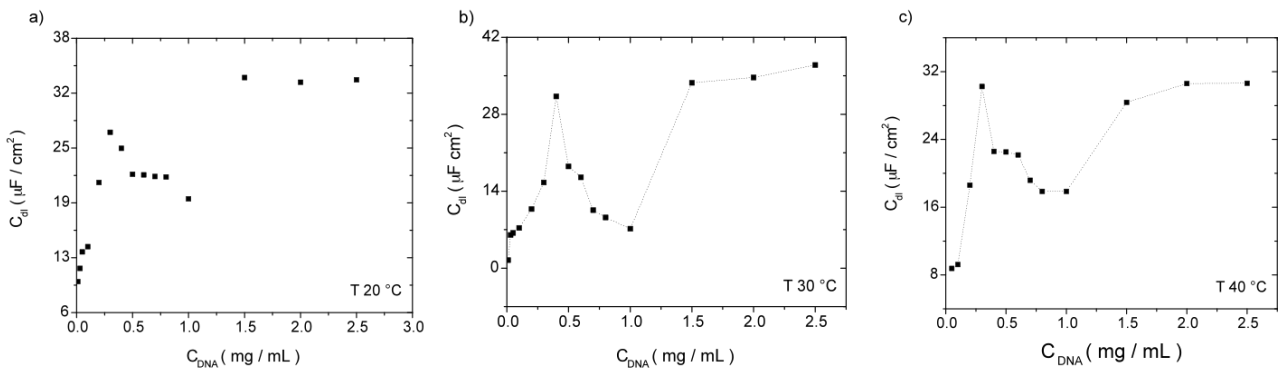

Figure 9. *Capacitance de la double-couche (C_{dl}) en fonction de la concentration d'ADN à des températures de a) 20 b) 30 c) 40 °C.*
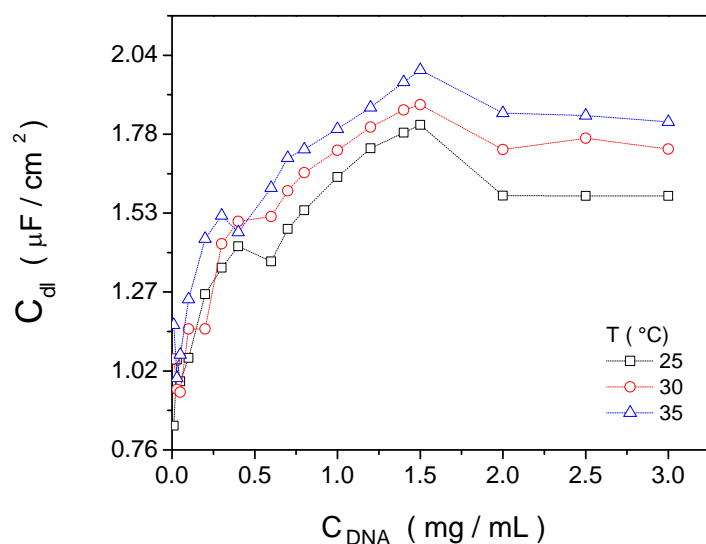
Figure 10. *Capacitance de la double-couche (C_{dl}) en fonction de la concentration d'ADN pour les températures de 25, 30 et 35 °C.*

On a déterminé qu'à potentiel de circuit ouvert (OCP), une adsorption non spécifique contrôlée par la diffusion de molécules d'ADN se déroule à l'interface Pt-ADN/tampon, par contre un processus mixte, contrôlée par la diffusion de l'ADN et par un processus de électrosorption se déroule à l'interface detampon Au-ADN/tampon. Tous les résultats permettent de proposer que l'interprétation des mesures d'impédance par la théorie impédance d'adsorption est un procédé bien adapté pour caractériser les procesus d'adsorption d'ADN et qui permet d'identifier les transitions structurelles sur l'interface metal-ADN/tampon. De cette manière, nous pouvons proposer EIS comme une technique adéquate pour caractériser la nature structurelle des adsorbats sur la base des changements et du réarrangement de la double couche électrochimique.

Ensuite, les effects du comportement structurel des molécules d'ADN de thymus de veau aux interfaces platine et or ont été étudiés par Spectroscopie d'Impédance Électrochimique en utilisant une méthodologie analogue à celle utilisée dans les études de rhéologie linéaires. Les *Figures 11 a* et *b* montrent les graphiques Bode en log-log (Z' et -Z" vs ω) pour les interfaces Pt-ADN/tampon et Au-ADN/tampon, respectivement, pour une variation de concentrations d'ADN à une température constante. À partir de ce type de graphiques il devient possible de déterminer une fréquence caractéristique de coupure (en ω_c) et le module Z_o associé à la résistance à la solution (R_s). Pour les deux interfaces, la constante de temps caractéristique du processus ($\tau_c = 1/\omega_c$) est obtenue en calculant l'inverse de ω_c et peut être directement liée à la relaxation de l'interface métal-ADN adsorbé, en raison de la formation d'une double couche électrochimique.
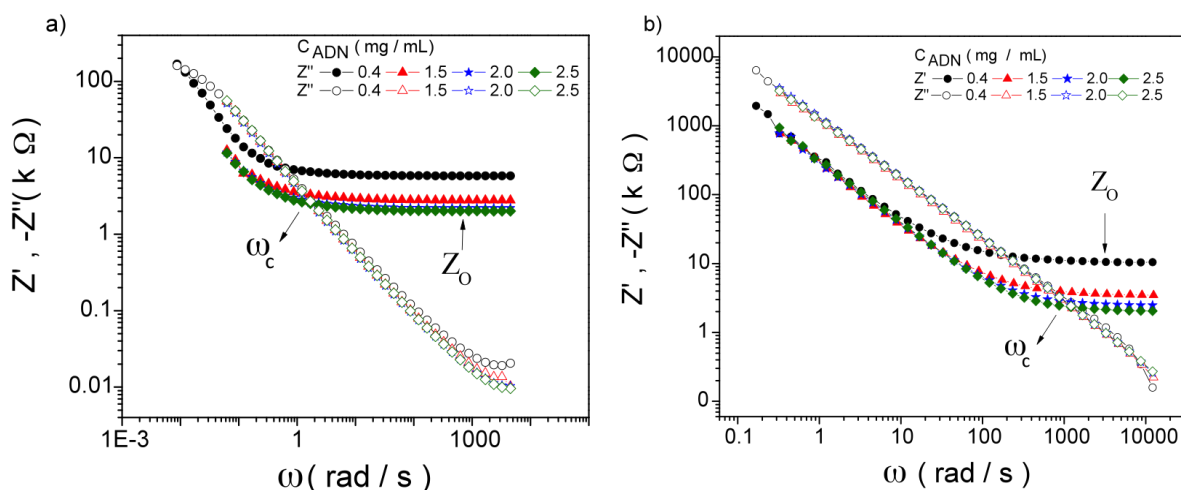
Figure 11. *Parties réel (Z ') et imaginaire (Z' ') de l'impédance en fonction de la fréquence (ω) pour les interfaces a) Pt-ADN/tampon et b) Au-ADN/tampon.*

À partir de l'information obtenue des deux interfaces, on obtient un comportement linéaire du module Z_o et de τ_c dans chaque régime caractéristique du système, dans lequel la relation avec la concentration d'ADN suit une loi de puissance à chaque température étudiée. Une fonction de type Arrhenius pour la température a été obtenue au niveau de la constante de temps caractéristique pour l' l'arrangement des molécules d'ADN dans la double couche électrochimique, à partir de laquelle on peut accéder à l'énergie d'activation (E_a) du processus d'adsorption.
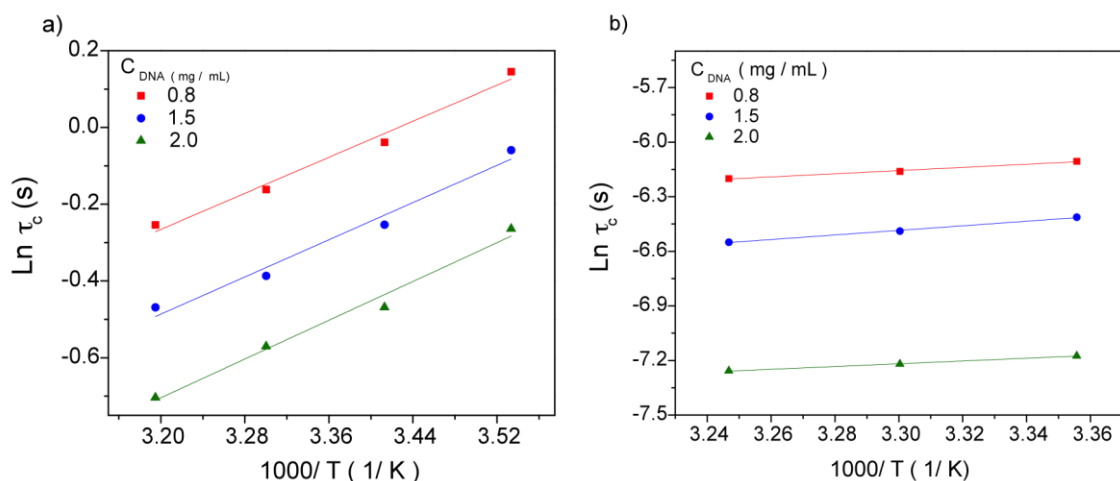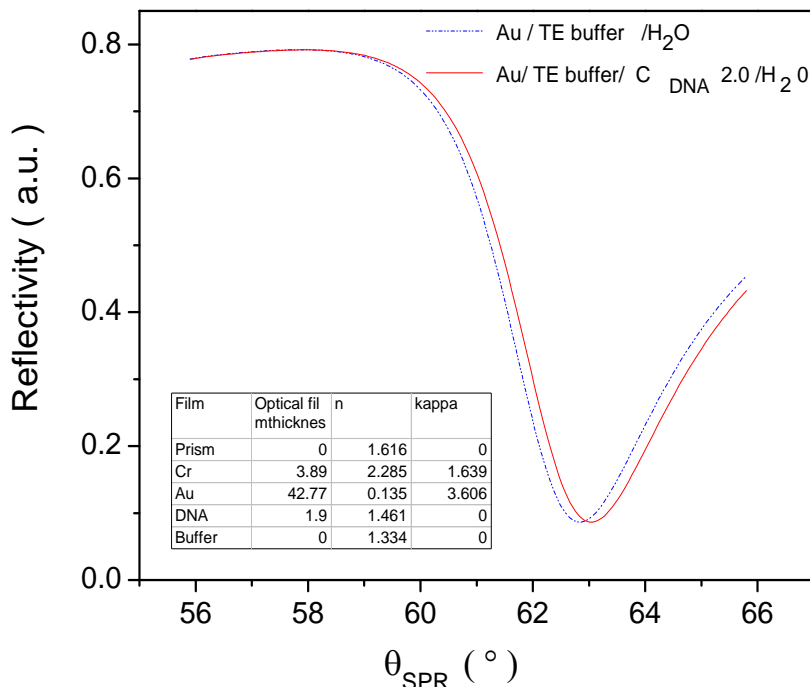

Figure 12. *Dépendance du type Arrhenius pour la constante caractéristique de temps ($\tau_c=1/\omega_c$) avec l'inverse de la temperature absolue pour les concentrations d'ADN de 0.8, 1.5 et 2.0 mg/mL aux interfaces a) Pt-ADN/tampon et b) Au-ADN/ tampon.*

Une fonction de transfert d'impédance générale a été proposée en fonction de la concentration d'ADN à partir des paramètres électrochimiques, Z_o liée à la résistance de la solution et la constante de temps caractéristique du processus, τ_c (*Équation 3*).

$$Z(W) = cC_{DNA}^{b} + \left[1 + \frac{1}{(jWaC_{DNA}^{d})^{a}}\right] \tag{3}$$

Cette fonction de transfert permet l'analyse théorique du comportement de la double couche éléctrochimique à OCP en fonction de la concentration avec seulement une mesure expérimentale d'impédance et rend possible l'obtention des paramètres électrochimiques de l'interface dans un régime particulier du système. Dans notre étude, cette fonction a été développé grâce à l'analyse des interfaces Pt-ADN/tampon et Au-ADN/tampon, mais elle peut être utile dans les études de systèmes polymères et d'agents tensioactifs, caractérisés par des régimes différents en raison de leurs interactions ou des différentes types de structures formées sur une large gamme de conditions de température ou de concentration.

Avec la technique optique Résonance de Plasmons de Surface (SPR, en anglais), on a completé l'étude du processus d'adsorption des molécules d'ADN sur une surface d'or et on a pu a obtenir les valuers moyens des épaisseurs de film optique (d_{opt}) des molécules d'ADN adsorbées (*Figure 13*).

Film	Optical film thicknes	n	kappa
Prism	0	1.616	0
Cr	3.89	2.285	1.639
Au	42.77	0.135	3.606
DNA	1.9	1.461	0
Buffer	0	1.334	0

Figure 13. *Simulation obtenue pour les données expérimentales de la réflectivité par rapport à l'angle d'incidence pour la concentration d'ADN de 2.0 mg/mL à la température de 25 °C. Les épaisseurs de film optiques de chaque film composant le système sont résumées dans le tableau.*

Les variations de d_{opt} en fonction de la concentration de l'ADN sont liés à des transitions dans l'arrangement structurel de la double couche électrochimique, telle que celles détectées avec les techniques électrochimiques. Un comportement linéaire a été observée pour chaque régime et suit la loi de puissance en fonction de la concentration: en régime dilué ($C_{ADN} < C^*$) $d_{opt} \sim C_{ADN}^{0.20}$, en régime semi-dilué sans enchevêtrements ($C^* < C_{ADN} < C_e$) $d_{opt} \sim C_{ADN}^{0.79}$ et en régime semi-dilué avec enchevêtrements ($C_e < C_{ADN}$) $d_{opt} \sim C_{ADN}^{0.57}$ (*Figure 14*).
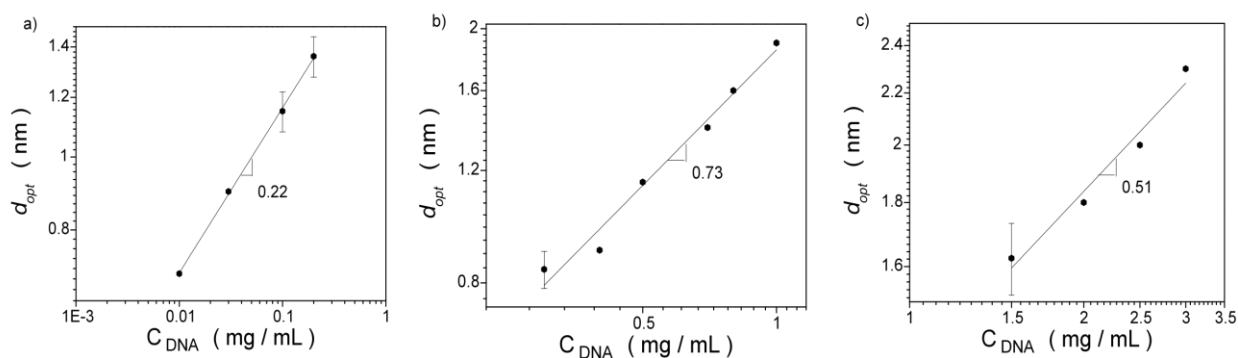

Figure 14. *Relation entre d_{opt} et la concentration de l'ADN en utilisant conformément la loi de puissance pour chaque régime caractéristique: a) régime dilué, b) régime semi-dilué sans enchevêtrements et c) régime semi-dilué avec enchevêtrements.*

En utilisant le modèle de la double couche la plus simple, les changements de C_{dl} obtenus à partir de l'étude de l'interface Au-ADN/tampon par impédance ont été associées aux changements dans les valeurs de d_{opt} en fonction de la concentration de l'ADN. De cette façon, on peut obtenir le comportement de la constante diélectrique, présentant les transitions de l'ADN aux interfaces.

D'autre part, la technique de Modulation de la Capacité Interfaciale (MIC), en combinaison avec des mesures de EIS, a été développé pour étudier les dynamiques de la double couche formée dans l'interface Pt-ADN/buffer dans les régimes dilué et semi-dilué. Cette technique est appliquée pour la première fois dans l'étude de la dynamique de la double couche d'un polyélectrolyte tel que l'ADN dans une large gamme de concentrations d'ADN et à des températures où la double hélice de l'ADN est bien préservée. La réponse MIC a révélé la dynamique de la double couche dans le régime dilué, le régime semi-dilué sans enchevêtrements et le régime semi-dilué avec enchevêtrements. À des concentrations élevées d'ADN, aucun processus de relaxation de la capacité à double couche n'est observée (*Figure 15*), cependant, à de faibles concentrations, et plus spécifiquement dans le régime semi-dilué sans enchevêtrement (*Figure 16*), il est possible d'identifier plusieurs constantes de temps superposées. Pour des concentrations d'ADN dans le régime dilué (*Figure 17*), il est démontré que le processus de détente présente clairement deux constantes de temps.
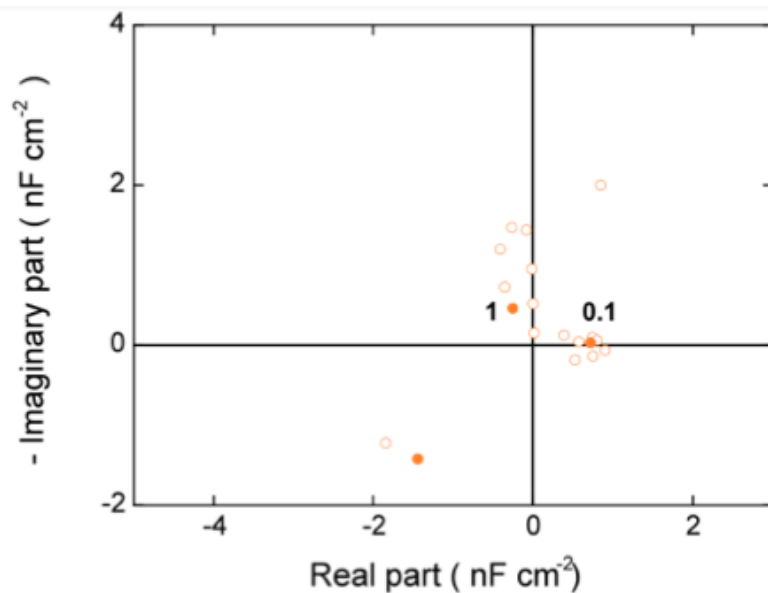
Figure 15. *Diagramme du plan complexe pour la modulation de la capacité interfaciale à l'interface Pt-ADN/tampon à une concentration d'ADN de 8.0 mg/mL et à une température de 30 °C. Paramètre f_ω en Hz.*
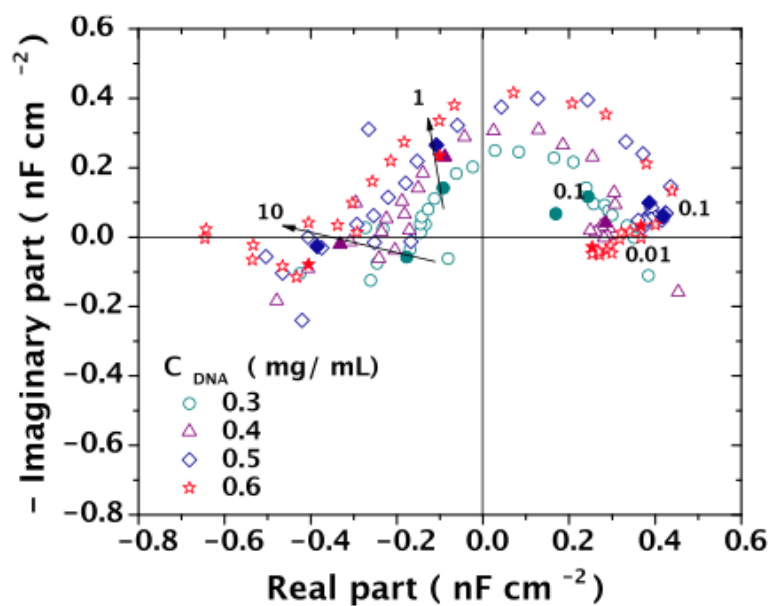
Figure 16. *Diagramme du plan complexe pour la modulation de la capacité interfaciale à l'interface Pt-ADN/tampon pour une variation de concentrations d'ADN dans le régime semi-dilué sans enchevêtrements et à une température de 20 °C. Paramètre f_ω en Hz.*
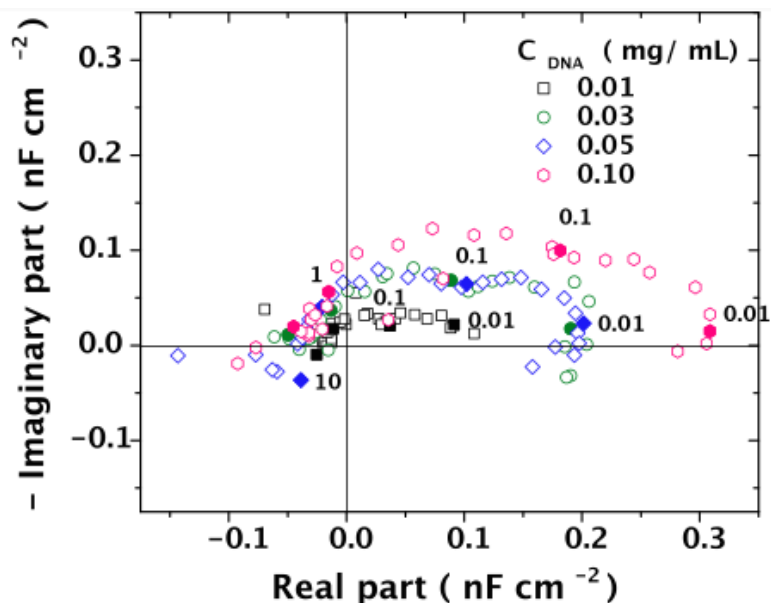
Figure 17. *Diagramme du plan complexe pour la modulation de la capacité interfaciale à l'interface Pt-ADN/tampon pour une variation de concentrations d'ADN dans le régime dilué et à une température de 20 °C. Paramètre f_ω en Hz.*

Les valeurs obtenues pour les constantes de temps characteristiques du processus d'adsorption par MIC sont en bon accord avec les valeurs précédemment obtenues pour des solutions d'ADN par des mesures d'impédance classiques (*Figure 18*).
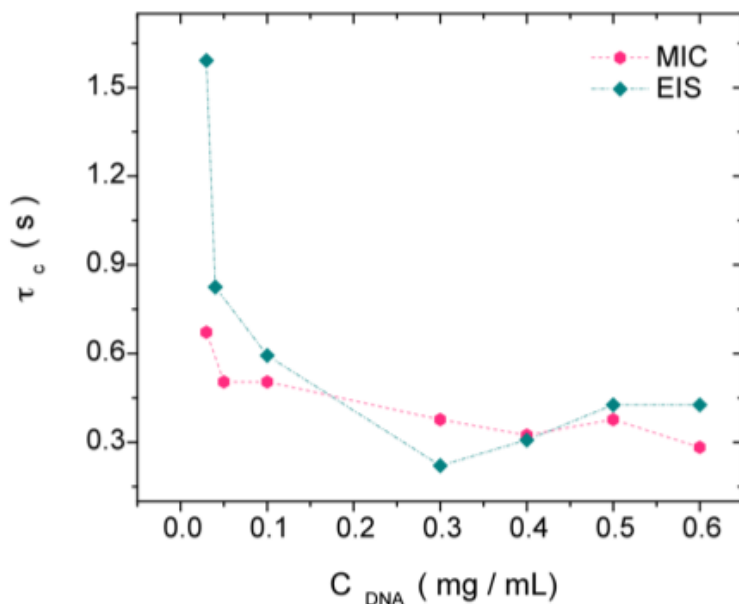

Figure 18. *Constantes de temps caractéristiques du processus d'adsorption, τ_c, obtenues à partir des mesures de MIC et de EIS en fonction de la concentration d'ADN et à la température de 30 °C.*

416

La fonction de la concentration d'ADN, de la température et de la force ionique de la réponse de MIC pour l'interface Pt-ADN/tampon a été mis en évidence et décrite dans cette étude. Il est démontré que la technique MIC permet l'étude de la cinétique d'adsorption des espèces les plus simples, tels que KCl et NaBr, et des espèces les plus complexes, tel que l'ADN. Il est alors possible d'identifier et d'expliquer, au moins qualitativement, les étapes fondamentales d'adsorption de ces espèces.

1.4. Développement de nanoparticules Chitosane/ADN pour la thérapie génique

Nous avons étudié finalement la formation de nanoparticules de chitosane-ADN pour le transfert de gènes comme application. Des concentrations d'ADN ont été choisies dans le régime dilué, 10 fois plus faibles que la valeur trouvée par C*. Le chitosane forme des complexes électrostatiques avec l'ADN avec une stoechiométrie définie entre des phosphates complètement ionisés et la fraction de chitosane protonée. La charge nette du complexe a été évaluée en fonction du rapport $[NH_2]/[P^-]$, montrant que les interactions électrostatiques entre le chitosane et l'ADN ont lieu dans la solution et proviennent du processus de complexation de l'ADN. Avant d'atteindre le potentiel $\zeta=0$ mV, on observe un plateau autour d'un potentiel ζ de -20 mV (*Figure 19*), ce qui correspond avec la formation des nanoparticules stables de chitosane-ADN avec un rayon hydrodynamique moyen de 220 nm. Le point isoélectrique est liée au degré de protonation du chitosane. Après le potentiel $\zeta =0$ mV, toutes les charges négatives de l'ADN sont neutralisées par des charges positives du chitosane. On a également trouvé que la stabilité du complexe peut être modifié avec le pH (*Figure 20*).
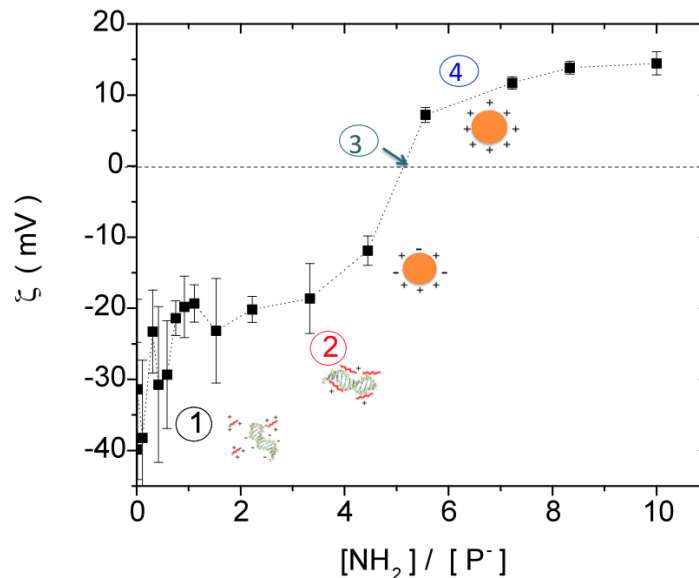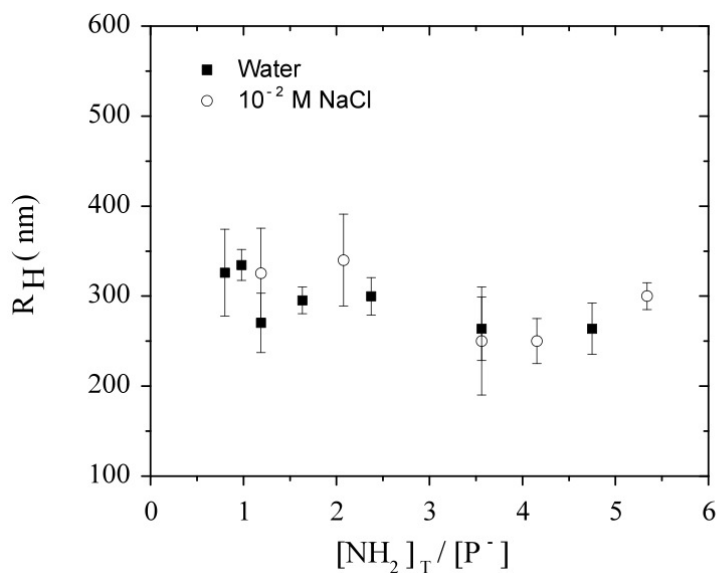

Figure 19. *Potentiel ζ en fonction du ratio $[NH_2]/[P^-]$ au cours de la formation du complexe chitosane-ADN à une température de 25 ° C_{ADN} = 0.03 mg/mL à un pH de 6.5 et $C_{Chitosane}$ = 1 mg/mL à un pH de 6.5. Les résultats sont la moyenne de cinq points, de sorte que les barres d'incertitude représentent la déviation standard.*
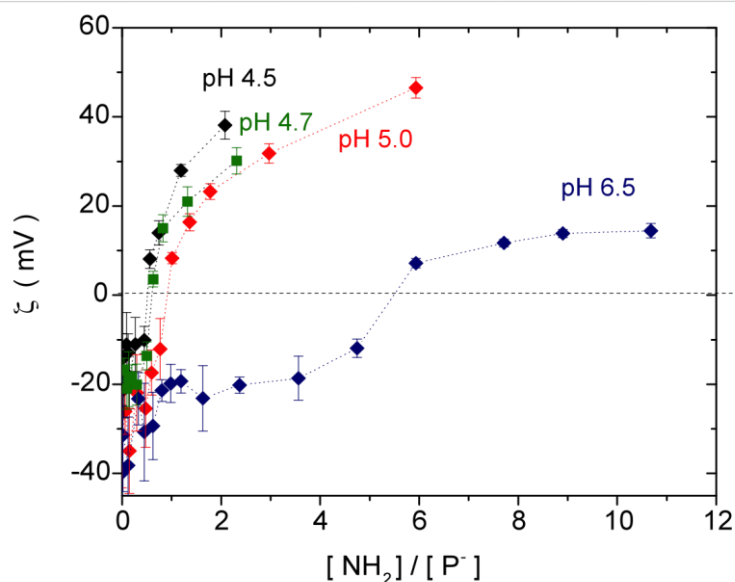
Figure 20. *Potentiel ζ en fonction du ratio [NH₂]/[P -] au cours de la formation du complexe chitosane-ADN à une température de 25 ° C_ADN = 0.03 mg/mL à un pH de 6.5 et C_Chitosane = 1 mg/mL aux pH's de 4.7, 5.0 et 6.0.*

Le processus de compaction de l'ADN dans l'eau, partiellement dénaturé, et l'ADN en double hélice dans une solution ayant une force ionique de 10⁻² M de NaCl, présente le même comportement électrostatique avec la même stoechiométrie, donné par le rapport entre les phosphates complètement ionisés et la fraction de chitosane protoné.

Figure 21. *Rayon hydrodynamique en fonction du ratio [NH₂]/[P ⁻] au cours de la formation du complexe chitosane-ADN à une température de 25 ° C_ADN = 0.03 mg/mL à un pH de 6.5 et C_Chitosane = 1 mg/mL pH de 4.7, 5.0 et 6.0.*

L'évolution du rayon hydrodynamique (R_h) et de l'intensité de la lumière diffusée a été évaluée en

fonction de $[NH_2]/[P^-]$. Le R_h diminue et l'intensité de lumière diffusée augmente avec l'addition de chitosane, représentant la compaction de la longue molécule d'ADN dans une nanoparticule par la neutralisation des charges negatives (*Figure 21*). Les complexes chitosane-ADN formés dans le premier plateau de potentiel ζ, avant d'atteindre la stoechiométrie, ont été visualisés par microscopie confocale de fluorescence, et un rayon moyen a été trouvé autour de 200 nm. De légers changements de conformation de l'ADN ont été détectés mesures CD-travers et ont été évalués pour différents ratios $[NH_2]/[P^-]$ et différents pH.
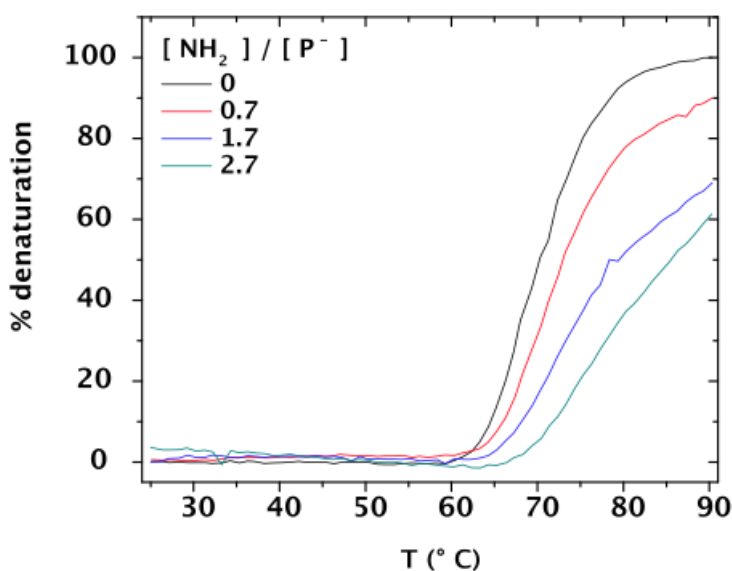
Figure 22. *Dépendance du % de dénaturation avec la température pour des complexes chitosane-ADN dans 10^{-2} M de NaCl à un pH de 6.5. Variation de ratios $[NH_2]/[P^-]$: de 0 à 2.7.*

La stabilité thermique des complexes d'ADN-chitosan a été étudiée par des mesures de UV-Vis en étudiant les courbes de fusion des complexes à différents rapports $[NH_2]/[P^-]$. Ensuite, la température de fusion de l'ADN dans le complexe (T_m) a été détectée à des températures plus élevées que celle de l'ADN en double-hélice en solution. La stabilité thermique est alors supérieure pour les complexes chitosane-ADN formés et dépendant du rapport $[NH_2]/[P^-]$ (*Figure 22*).

1.5. Conclusions

Pour conclure, dans ce travail, nous avons caractérisé un échantillon d'ADN en solution dans un tampon Tris-HCl/EDTA en fonction de la concentration et de la température en utilisant différentes méthodes physico-chimiques (rhéologie, dichroïsme circulaire et spectroscopie UV). La viscosité intrinsèque determinée dans le plateau Newtonian en écoulement a permis d'obtenir la masse molaire (8 246 800 g/mol). Les différents régimes de concentration en polymère C* et C_e ont été caracterisés. Le

comportement rhéologique en écoulement et en dynamique est caractéristique d'un comportement en solution et indépendant de la température entre 10 et 40 ºC, domaine dans lequel l'ADN est en double-hélice.

L'adsorption de l'ADN sur des électrodes de platine et d'or a été déterminée dans une large gamme de concentrations et de températures en utilisant différentes méthodes électrochimiques (Spectroscopie d'Impédance Électrochimique, Modulation de la Capacité Interfaciale et Résonance de Plasmons de Surface). Les résultats d'impédance ont été interprétés en utilisant la théorie d'adsorption d'impédance avec un circuit équivalent similaire a celui de FMGR. Différents régimes de concentrations sont observés et sont en bon accord avec les études de l'ADN en solution par rhéologie.

Enfin, la formation du complexe electrostatique chitosane-ADN a été étudiée et conduit à la formation de nanoparticules stables pour une neutralization partielle de l'ADN. Ces nanoparticules de 200 nm de diamètre correspondent à l'étape de compaction de l'ADN dont la température de fusion augmente par la formation du complexe.

2. Le rôle de la dynamique micellaire et la rhéologie dans la libération contrôlée de médicaments.

2.1. Introduction

Les copolymères amphiphiles à blocs sont des macromolécules constituées d'une partie hydrophobe et d'une partie hydrophile. Dans l'eau, ils s'assemblent en micelles, dans lesquelles la partie hydrophobe forme le coeur et les segments hydrophiles forment la couronne en milieu aqueux. Ces copolymères sont caractérisés par une concentration micellaire critique (CMC) et une température micellaire critique (CMT). Selon le rapport entre la longueur des blocs et de la qualité du solvant, ces copolymères peuvent former des micelles sphériques, cylindriques ou des structures lamellaires. Actuellement, ces matériaux sont d'un grand intérêt en raison de leurs applications dans l'administration contrôlée de médicaments. La cinétique de transition d'une structure à autre est essentielle pour atteindre une meilleure efficacité dans les applications. Contrairement aux agents tensio-actifs, qui sont dynamiquement actifs, les copolymères à blocs ont une dynamique plus lente. En particulier, dans le cas où la tension de surface entre les blocs est élevée, ils peuvent être piégés dans des états métastables sans atteindre l'équilibre thermodynamique. Les copolymères à trois blocs, stimulables par la température, à base de polyoxyde d'éthylène (PEO) et polyoxyde de polypropylène (PPO), sont disponibles dans le commerce et se trouvent parmi les copolymères amphiphiles les plus étudiés.

La libération spécifique d'ingrédients actifs, connue comme vectorisation, est devenue un grand défi pour la recherche thérapeutique. Ce procédé a été utilisé pour contrôler la distribution des ingrédients actifs tels que les protéines, les gènes pour la thérapie génique et les médicaments, à une cellule cible en l'associant à un vecteur. Les molécules de la chimiothérapie sont souvent hydrophobes et ont besoin

d'être vectorisées pour être transportés vers la cellule cible. Néanmoins, cette libération contrôlée de médicaments souffre d'un phénomène appelé «libération en rafale» («burst release»), dans lequel les médicaments sont libérés avant d'arriver vers leur cellule cible. De cette façon, l'objectif principal de cette partie de la thèse est d'étudier la dynamique d'échange entre les vecteurs et les cellules par des mécanismes collectifs. Comprendre cette dynamique devient essentielle pour le développement et le contrôle de nouveaux matériaux et de nouveaux procédés efficaces dans la libération contrôlée de médicaments.

Initialement, nous étudions le rôle des processus de fusion et de fission dans la transition micelles sphériques à micelles allongées de copolymère amphiphile P104 (Pluronic ®) dans l'eau. Cette transition a été induite par un saut de température et a été suivie par diffusion dynamique de lumière (DLS). Après, nous étudions les dynamiques collectives à l'équilibre et hors équilibre des micelles P104 dans l'eau. Les dynamiques de ces systèmes se produisent par l'intermédiaire de deux mécanismes principaux : le premier est un processus individuel qui implique l'expulsion et l'insertion de chaînes et le deuxième est un processus collectif qui se produit à travers le processus de fusion et fission de micelles. Ces mécanismes sont cruciaux pour contrôler le comportement des micelles d'amphiphiles, en particulier dans l'administration de médicaments. Ensuite, nous avons préparé et caractérisé des liposomes, qui seront utilisés comme les modèles les plus simples de cellules, afin d'identifier leur forme, la taille et leurs propriétés physico-chimiques. Tout d'abord, on a exploré les interactions électrostatiques entre les liposomes et les micelles de P104. Ensuite, on a utilisé une technique de fluorescence pour quantifier la cinétique de vectorisation entre les micelles de P104 et les liposomes. L'effet de la variation de plusieurs paramètres tels que la concentration des liposomes et des recouvrements avec un polycation, le chitosane, a été étudiée afin de contrôler la dynamique de vectorisation entre les micelles de copolymères à blocs amphiphiles et les liposomes.

2.2. Comportement structurel et rhéologique du copolymère tribloc P104

Afin de déterminer la formation des structures P104 et leur morphologie en solution aqueuse, on a élaboré un diagramme de phases détaillé du P104 dans l'eau différentes domaines de concentration (régions diluées et semi-diluées) en utilisant des mesures de rhéométrie, de diffusion dynamique de la lumière (DLS), de viscosité (η), densité (ρ) et vitesse du son (υ). On a étudié les transitions de monomère à micelles, c'est à dire, les conditions dans lesquelles les monomères sont en équilibre thermodynamique avec des micelles, puis la formation de micelles sphériques, la transition en micelles allongées et enfin, la température de trouble.

La *Figure 1* montre le comportement de la densité du P104 en fonction de la température pour plusieurs concentrations de P104. Ici, nous pouvons observer l'augmentation de la densité avec la concentration P104, comme prévue, et la diminution de la masse volumique avec la température, jusqu'à

une température critique T_i, où on identifie une diminution plus prononcée. La température T_i diminue quand la concentration de P104 augmente. Une seconde température critique est identifiée comme T_f, le début de la diminution monotone de la masse volumique avec la température. De la même façon que pour les copolymères P103 et P94, cette transition est liée à la formation de micelles due à la déshydratation des segments PPO hydrophobes, qui forment le noyau, et des segments hydrophiles PEO plus hydratée pour la couronne. Cette transition est alors attribuée à la température micellaire critique (CMT) et diminue à mesure que la concentration en P104 augmente.
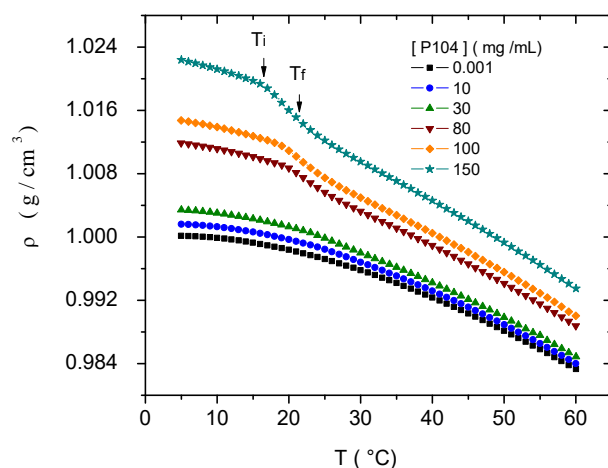
Figure 1. *Masse volumique (ρ) en fonction de la température pour différentes concentrations en P104: 0,001, 10, 30, 80, 100 et 150 mg/mL.*

La *Figure 2* montre la dépendance de la vitesse du son en fonction de la température pour plusieurs concentrations en P104. À des températures inférieures à T_i, la quantité d'unimères de P104 augmente avec la concentration, alors la vitesse du son augmente avec la concentration P104. Pendant l'apparition de micelles, les unimères commencent à s'agréger due à l'augmentation de la température et déshydratation des blocs de PPO, résultant en une baisse de la vitesse du son, causée par la diminution du nombre de particules efficaces dans la solution.
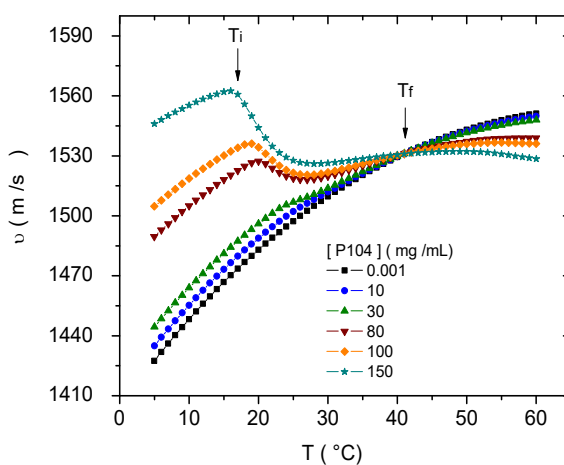

Figure 2. *Vitesse du son (υ) en fonction de la température pour différentes concentrations en P104: 0,001, 10, 30, 80, 100 et 150 mg/mL.*

Des mesures de diffusion dynamique de la lumière (DLS) ont été effectuées dans une gamme de température de 10 à 64 °C afin d'obtenir l'information structurelle des micelles à partir de la combinaison de l'intensité de lumière diffusé et du rayon hydrodynamique. La *Figure 3* montre la dépendance du rayon hydrodynamique, R_h, et de l'intensité de la lumière diffusée avec la température pour une solution de P104 dans l'eau à une concentration de 10 mg/mL, à partir de laquelle il est possible d'identifier la formation des micelles sphériques dans une gamme de température entre 26 et 54 °C, ayant une taille moyenne de 11.4 ± 1 nm.
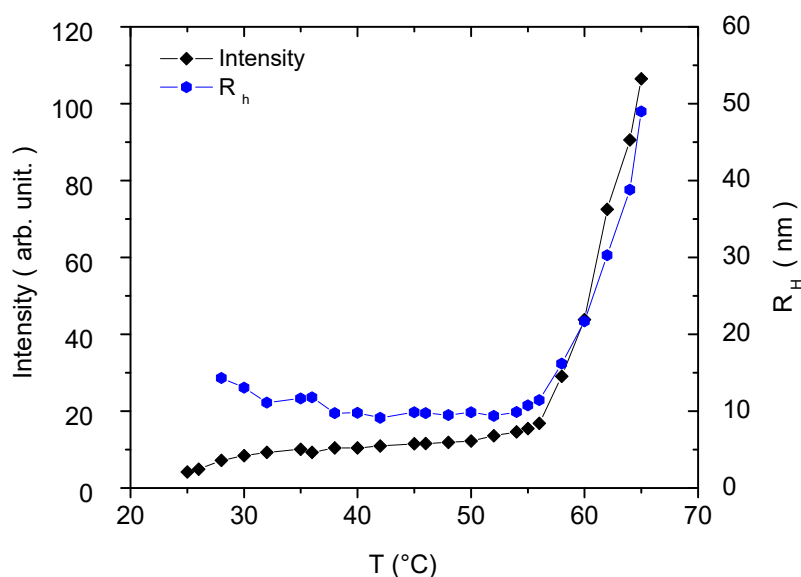

Figure 3. *Dépendance du rayon hydrodynamique et de l'intensité de la lumière diffusée avec la température pour une solution de P104 à une concentration de 10 mg/mL mesurée à 90 °. L'échantillon a été équilibré pendant 24 heures avant chaque mesure.*

L'augmentation du R_h et de l'intensité de lumière diffusée est observée au dessus de la température de 55 °C. Le début de cette transition est directement lié à une transition structurelle du P104 en solution aqueuse. Ce phénomène est expliqué en termes de la déshydratation de la couronne des micelles, constitué essentiellement de PEO, avec l'augmentation de la température.

La combinaison de l'information sur le rayon hydrodynamique et l'intensité de lumière diffusée permettent d'obtenir des informations sur la forme de micelles. Pour cela, on utilise le modèle de Perrin pour estimer les dimensions de micelles pour les ellipsoïdes prolates et oblates. La *Figure 4* montre l'intensité diffusée (Sous la forme du rapport I_{SCA}/I_{SCA}^0 avec I_{SCA}^0 l'intensité initiale de la solution) en fonction du rayon hydrodynamique R_h pour une solution de P104 avec une concentration de 10 mg/mL. La courbe I_{SCA}/I_{SCA}^0 est comparée avec le modèle de Perrin pour les ellipsoïdes prolates, les ellipsoïdes oblates et les sphères. I_{SCA} et R_h ont été mesurées à six températures différentes à partir des températures du domaine de micelles sphériques jusqu'aux températures de micelles allongées.

L'intensité de lumière diffusée I_{SCA}^0 est sélectionnée à 38 °C, ce qui correspond à la l'intensité diffusée à la température initiale dans le domaine des micelles sphériques. La dépendance d'I_{SCA}/I_{SCA}^0 avec R_h est proche du comportement prédit pour ellipsoïdes prolates, ce qui suggère que les micelles P104 poussent comme des tiges applaties. Ce comportement a été précédemment obtenu pour des micelles de copolymère tribloc P103.
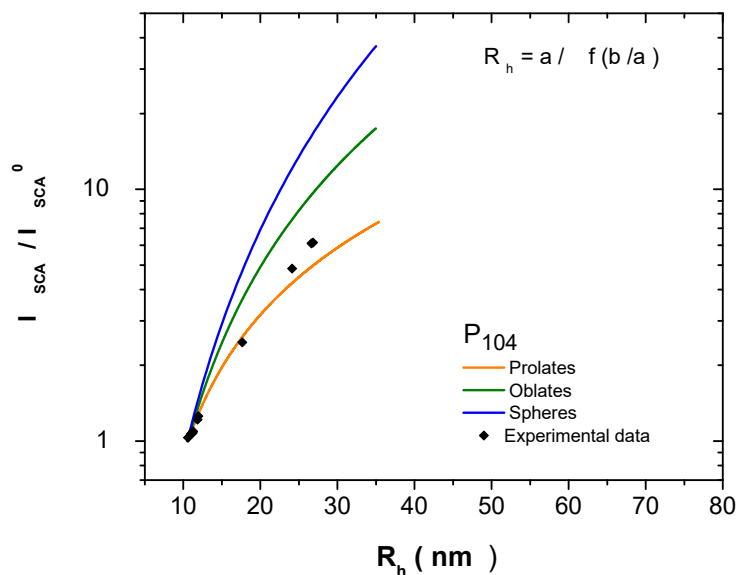
Figure 4. *I_{SCA}/I_{SCA}^0 tracée en fonction du rayon hydrodynamique R_h pour une solution de P104 à 10 mg/mL. I_{SCA} et R_h ont été mesurés à différentes températures et I_{SCA}^0 correspond à l'intensité de lumière diffusée à 38 °C. La courbe I_{SCA}/I_{SCA}^0 est comparée avec le modèle de Perrin pour ellipsoïdes prolates allongé, ellipsoïdes applatis et sphères.*

Les structures micellaires déterminées pour le copolymère amphiphile P104 dans le domaine de température entre 25 et 55 °C, c'est à dire, le domaine de micelles sphériques, peuvent être utilisés comme nanosupports micellaires pour la libération contrôlée de médicaments. Tout d'abord, leur taille nanométrique est une option appropriée pour des applications de vectorisation de médicaments ciblée, y compris le stockage, la libération contrôlée et la protection des médicaments hydrophobes. Ensuite, la stabilité des micelles sphériques à la température de 37 °C devient un bon choix afin de maintenir leur structure déterminée à la température moyenne du corps, laquelle pourrait être ensuite dégradée par une stimulation spécifique (température, pH ou des variations de force ionique) afin de libérer le médicament hydrophobe.

À des concentrations et des températures plus élevées, certaines solutions de copolymères forment des gels physiques thermoréversibles. Ces gels sont constitués de cristaux liquides et de micelles sphériques ou bâtonnets enchevêtrés. Les mesures rhéologiques permettent l'étude des différentes propriétés des matériaux utiles dans de nombreuses applications biomédicales. En rhéologie, des

balayages en contrainte pour des solutions de copolymère P104 dans une gamme de concentration entre 50 et 600 mg/mL ont été effectuées afin d'identifier la région viscoélastique linéaire (LVR) pour différentes températures. Ensuite, des balayages de température ont été effectués pour observer les propriétés viscoélastiques des solutions de P104 dans une grande gamme de température (3-90ºC). La *Figure 5* présente un ensemble de courbes montrant la dépendance de la température sur les modules G' et G'' pour les suivantes concentrations de solutions de P104 : 100, 150, 200 et 225 mg/mL. Pour la solution de P104 à la concentration de 100 mg/mL (*Figure 5 a*), on observe tout d'abord un comportement visqueux (G''>G') dans la gamme de température entre 3 et 20 ° C. Un premier croisement des courbes G' et G'' en fonction de la température ensuite observé à 20 °C. Le module de perte est indépendant de la température jusqu'à la température de 58 °C, à laquelle une forte augmentation de deux ordres de grandeur est observée, passant du domaine dilué au domaine de gel mou (ou faible). On observe ensuite la diminution de G' et G'' à la température de 81 °C, à laquelle le gel revient à un comportement d'état liquide.

La *Figure 5 b* illustre la dépendance de G' et G'' avec la température pour une solution de P104 avec une concentration de 150 mg/mL. On observe un comportement similaire à celui obtenu pour la solution de P104 à la concentration de 100 mg/mL. Ici, les modules G' et G'' sont indépendantes de la température jusqu'à la température de 60 ° C, suivi d'une grande augmentation de deux ordres de grandeur. La *Figure 5 c* montre la dépendance de G' et G'' avec la température pour une solution de P104 à la concentration de 200 mg/mL. On observe un comportement visqueux (G'<G'') dans le domaine de température de 3 à 18 ° C. Un premier croisement entre G' et G'' est observé autour de la température 20 ° C. Ensuite, une légère augmentation des deux modules est identifiée entre 20 à 58 °C. Ensuite, un incrément sur G' d'un ordre de grandeur est détecté, changeant du régime sol au comportement de gel mou dans une gamme de températures entre 63 et 83 °C. Une diminution prononcée de G' et G'' est détectée autour de 83 °C. Enfin, un nouveau comportement des solutions de P104 est présenté dans la *Figure 5 d*, dans lequel le matériel atteint le comportement de gel dur dans la gamme de températures de 22 et 52 °C. De cette façon, une augmentation d'environ trois ordres de grandeur est accessible avec cette solution de P104 à cette concentration. Les solutions de P104 forment donc des gels thermo-réversibles qui dépendent des concentrations des solutions P104 et de la température, ce qui peut être utilisé pour différentes applications thérapeutiques à des températures physiologiques.

La *Figure 6* représente le diagramme de phases pour le système P104/eau dans la gamme de concentration de 0 à 150 mg/mL. L'information obtenue pour le copolymère tribloc P104 dans des solutions aqueuses représente un outil pour les applications de libération de médicaments et de gènes en profitant des structures formées et de leur dépendance avec la température et la concentration.
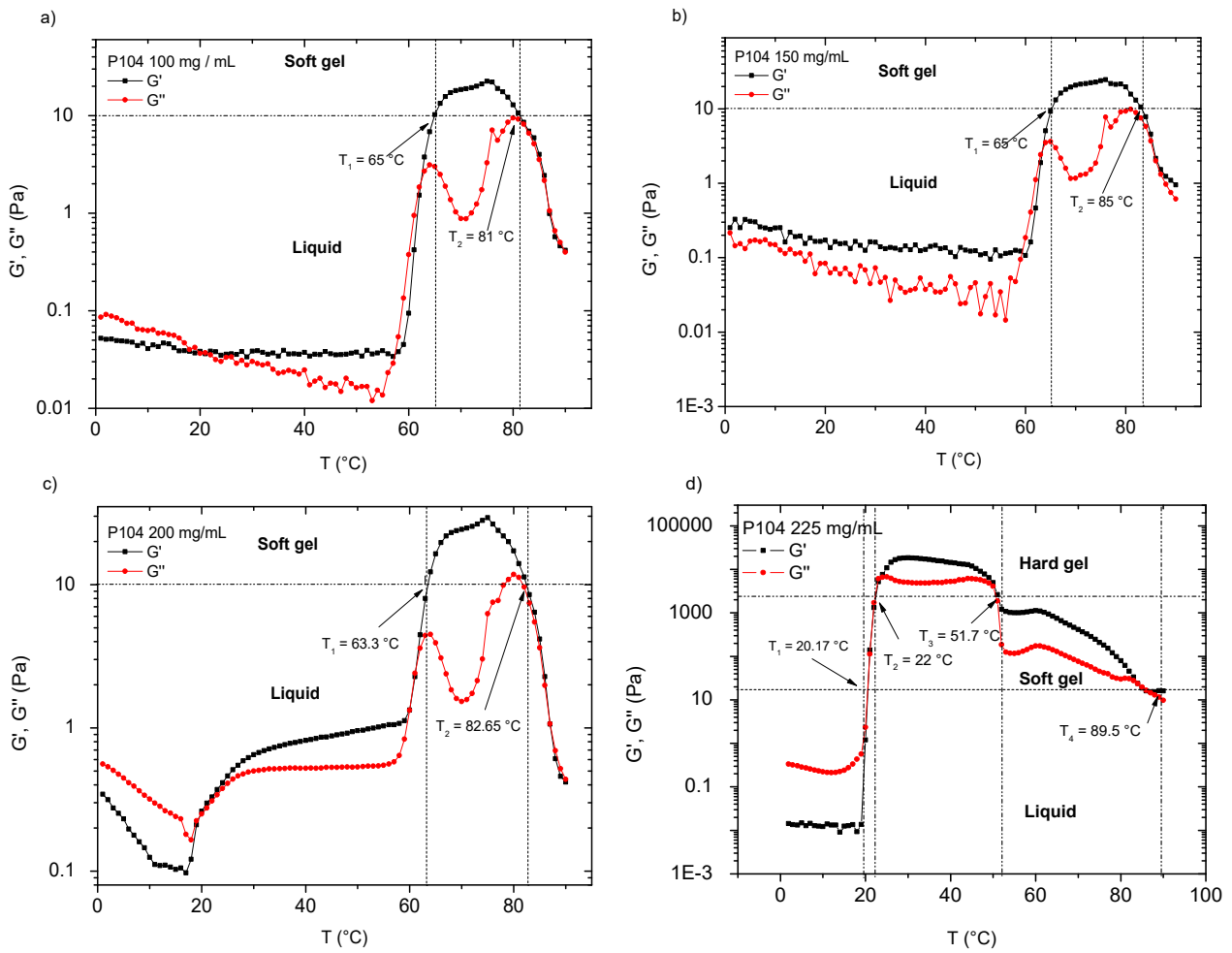
Figure 5. *Balayages en température pour des solutions de P104 à concentration variable: a) 100, b) 150, c) 200 and d) 225 mg/mL.*
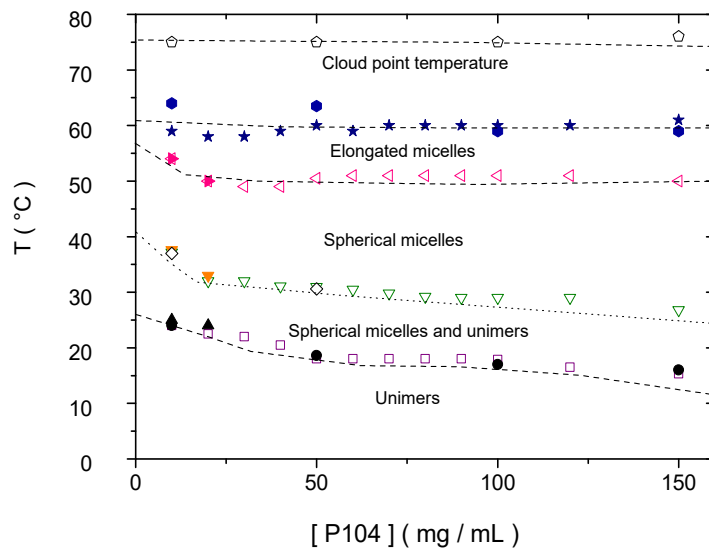

Figure 6. *Diagramme de phase : température-composition du copolymère tribloc P104 dans l'eau.*

2.3. Les dynamiques collectives du copolymère tribloc P104 à l'équilibre et hors équilibre

Après avoir étudié et déterminé les transitions structurelles du P104 en solutions aqueuse, on a étudié le dynamique de croissance et transition de micelles sphériques à micelles allongées. Cette transition a été obtenue en augmentant la température dans le domaine sphérique micellaire (T1) à la température du domaine de micelles allongées (T2). L'intensité de lumière diffusée et le rayon hydrodynamique des micelles ont été contrôlés tout au long de l'expérience en utilisant la technique de diffusion dynamique de la lumière. Pour effectuer ces expériences, l'échantillon a été stabilisé à la température T1 pendant 24 heures, de cette façon, il est possible d'assurer l'équilibre micellaire. Ensuite, l'échantillon a été introduit dans l'appareil déjà stabilisé à la température T2 et les mesures ont été débutées immédiatement.

En augmentant la température du domaine de micelles sphériques T1 (qui ont un rayon hydrodynamique moyen de 11 nm) à la température T2 du domaine de micelles allongées, le rayon hydrodynamique et l'intensité de diffusion augmentent en fonction du temps (*Figures 7 a* et *b*). La transition de micelles sphériques à micelles allongées du copolymère tribloc P104 est   suffisamment lente pour être suivie par des mesures de diffusion dynamique de lumière, comme pour la transition du copolymère amphiphile P103.
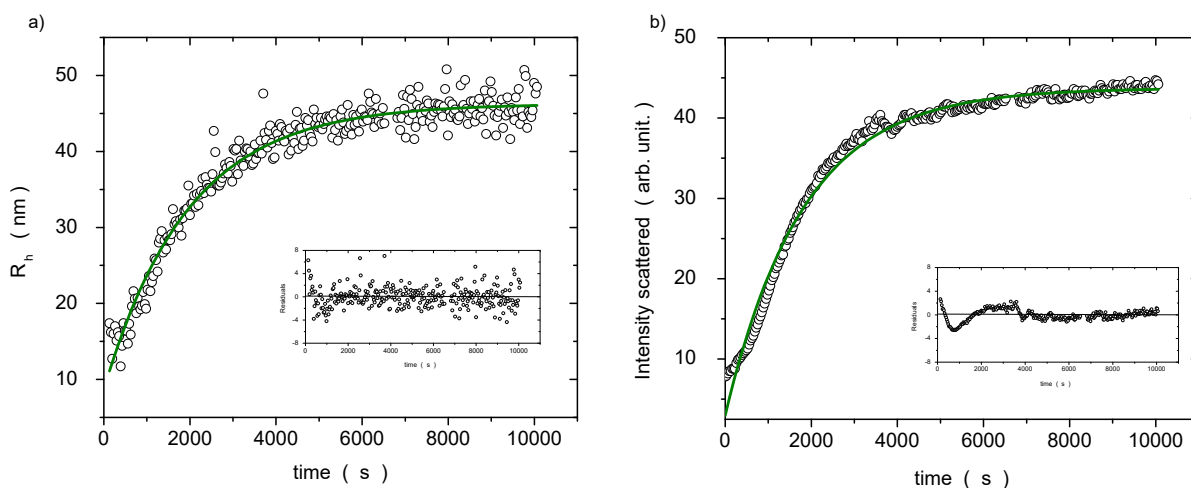
Figure 7. a) *Rayon hydrodynamique, Rₕ, et b) l'intensité diffusée en fonction du temps pour une solution de P104 avec une concentration de 20 mg/mL obtenus après un saut de température à partir d'une temperature T1 = 38 °C à une deuxième température T2 = 64 ° C. La ligne continue représente l'ajustement obtenu en utilisant une expression mono-exponentielle qui simule la croissane de l'intensité. Encart: résiduelle de la forme de la fonction exponentielle unique.*

La *Figure 7 a* montre la dépendance du rayon hydrodynamique avec le temps pour une solution de P104 dans l'eau à une concentration de 20 mg/mL en modifiant la température 38 à 64 ° C. On observe qu'un seul processus (*Équation 1*) décrit l'augmentation du rayon hydrodynamique (R_h) en fonction du temps, montrant que le processus impliquant des interactions monomère-micelles est négligeable dans cette gamme de température.

La croissante du R_h peut être simulé de manière adéquate en utilisant une expression mono-exponentielle avec une vitesse k_{decay} correspondante à k_{obs} $R_h = 1/\tau$

$$R_H(t) = [R_H(\infty) - R_H(0)]*exp(-t/\tau) + R_H(\infty) \tag{1}$$

La *Figure 7 b* représente la variation de l'intensité de diffusion totale en fonction du temps pour la même solution de P104. La cinétique de croissane peut aussi être simulée de manière adéquate en utilisant une fonction mono-exponentielle avec un temps apparent de relaxation selon l'expression suivante:

$$I_{SCAT}(t) = [I_{SCAT}(\infty) - I_{SCAT}(0)]*exp(-t/\tau + I_{SCAT}(\infty) \tag{2}$$

où I_{SCAT} est l'intensité diffusée et τ représente le temps de relaxation apparent.

Le facteur asymétrique, donné par le rapport entre l'intensité observée à un angle de 135 ° et un angle de 45 °, $I_{45°}/I_{135°}$, permet d'identifier le processus de croissance longitudinale des micelles. Les résultats obtenus pour ce rapport en fonction du temps, peuvent également être simulés avec une fonction mono-exponentielle ayant une constante de temps caractéristique, analogue à celle utilisée pour évaluer le comportement de R_h. De cette façon, on peut en déduire que des micelles se développent longitudinalement pendant le processus de relaxation et que leur longueur augmente avec le temps.

Le taux de transition structurelle de micelles sphériques à micelles allongées dépend directement de la relation entre les blocs PPO/PEO et de la longueur du bloc PPO. Le copolymère tribloc P103 $[(PEO)_{17}-(PPO)_{60}-(PEO)_{17}]$ à un ratio PPO/PEO=1.76 et présente des temps de relaxation entre la gamme de 100s à 6000s, en fonction de la concentration. Un système plus hydrophobe, par exemple le Pluronic P123 $[(PEO)_{20}-(PPO)_{70}-(PEO)_{20}]$, avec un ratio PPO/PEO=1.75 et un bloc plus long de PPO, présente des temps de relaxation qui peuvent durer des jours en absence d'additifs. Dans notre cas, les temps de relaxation du P104 $[(PEO)_{27}-(PPO)_{61}-(PEO)_{27}]$, qui a un ratio PPO/PEO = 1.13, se trouvent dans la gamme de 800s à 4000s. La *Figure 8* montre la dépendance des taux de croissance avec la concentration en copolymère tribloc P104 obtenue à partir des fonctions mono-exponentielle du rayon hydrodynamique, de l'intensité de la lumière diffusé et du facteur de forme dans la gamme de concentration de P104 en solution aqueuse entre 10 et 60 mg/mL. Dans tous les cas, on observe une augmentation linéaire avec la concentration qui peut correspondre à un processus de second ordre y compris la fusion des micelles dans une longue micelle.

Grâce à ces résultats, il est alors constaté que le processus de croissance des micelles de copolymère tribloc P104 dans l'eau présente deux mécanismes. Le premier mécanisme possible implique l'intégration de chaînes de copolymère et des micelles pour former des micelles stables thermodynamiquement. Le deuxième mécanisme possible implique des processus de fusion-fission d'agrégats et chaînes de copolymère tribloc dans des micelles pour produire des micelles de différentes tailles jusqu'à atteindre une taille micellaire thermodynamiquement stable. La dynamique de croissance présente un processus relativement lent avec un temps caractéristique variant de 800s à 4000s.
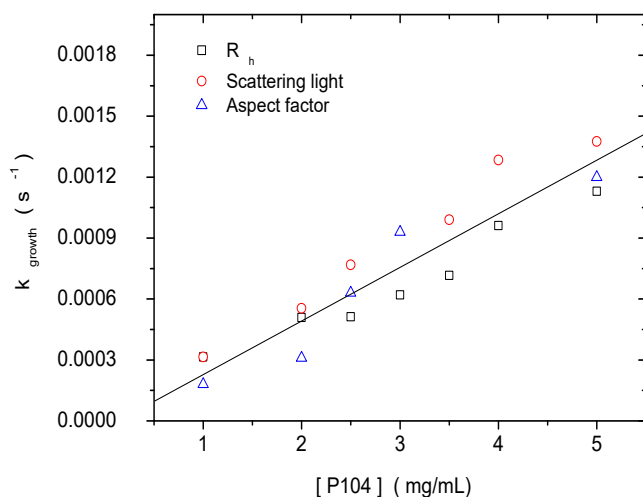

Figure 8. *Taux de croissance (de k_{growth}) calculé à partir de l'évaluation du rayon hydrodynamique, R_h, l'intensité de lumière diffusée et le facteur de forme en utilisant une expression mono-exponentielle, en fonction de la concentration P104.*

D'autre part, on a étudié la dynamique micellaire à l'équilibre du copolymère tribloc P104 en solutions aqueuse par spectroscopie de fluorescence. Une technique de fluorescence avec un dérivé de pyrène hydrophobe (PyC_{18}) est sélectionnée comme un outil pour étudier les mécanismes de fusion et fission entre les micelles de P104. Pour cela, la disponibilité d'une région de coeur hydrophobe à l'intérieur des micelles de copolymère tribloc permet un chargement stable de médicaments hydrophobes peu solubles au cours de micellisation, dont la molécule de PyC_{18} sera utilisée comme modèle. L'encapsulation des médicaments hydrophobes dans des nanoparticules peut augmenter l'accumulation de médicaments dans les tumeurs, réduire la toxicité pour les tissus sains et améliorer la pharmacocinétique par rapport aux processus d'administration de médicament libre. Cependant, lors de l'élaboration des nanoparticules pour l'administration de médicaments, il est important de comprendre les mécanismes d'interaction entre les nanoparticules et les mécanismes de distribution du médicament encapsulée pour obtenir une forme efficace et la libération de médicaments sur la cible.

Les mesures de fluorescence ont été effectuées à partir d'un mélange de micelles de P104 contenant du PyC18 et des micelles de P104 sans marqueur fluorescent en préservant la même température et la

même concentration totale en P104. À partir de ces mesures il est possible d'analyser les différents mécanismes d'échange entre les micelles afin de déterminer les mécanismes dominants. Les dynamiques à l'équilibre dans les deux domaines suivants: domaine de micelles sphériques et domaine de micelles allongées ont été étudiées en utilisant la formation d'un excimère d'un dérivé de pyrène fortement hydrophobe en fonction du temps. Pour l'insertion de lala molécule hydrophobe (PyC$_{18}$) dans le cœur des micelles, des solutions aqueuses P104 ont été chauffés au-dessus du point de trouble et ensuite refroidies à une température située dans la gamme dans laquelle des micelles sphériques sont formées. Ce processus est répété jusqu'à 8 fois. De cette façon, les micelles dissolvent le PyC$_{18}$ de façon aléatoire. Les spectres de fluorescence des micelles de copolymère contenant plus d'une molécule de PyC18 présentent une bande d'émission large correspondant à l'excimère avec un pic à 480 nm et une bande de monomères entre 375,5 et 400 nm.

Les cinétiques d'échange ont été réalisées en tenant compte des valeurs faibles du nombre moyen de molécules hydrophobes par micelles, $<n>$, de sorte qu'il est possible d'obtenir une dépendance linéaire du ratio de l'intensité de l'excimer (I_{ex}) et de l'intensité de monomère (I_{mon}) avec la concentration de micelles de P104. La relation entre l'intensité de excimer ($\lambda_{ex} = 480$ nm) et du monomère ($\lambda_{mon} = 375$ nm), I_{ex}/I_{mon}, augmente linéairement avec l'augmentation du nombre moyen de PyC$_{18}$ par micelles $<n>$. La distribution du PyC18 correspond à une distribution de Poisson aléatoire entre les micelles. La *Figure 9* illustre les spectres de fluorescence du PyC$_{18}$ solubilisé dans une solution aqueuse de micelles de P104 à la concentration de 50 mg/mL avant et après l'addition d'une solution aqueuse de P104 sans molécule fluorescente avec la même concentration (50 mg/mL), à une température de 37 °C. L'existence de l'émission d'un excimère à 480 nm indique la présence de micelles portant deux ou plusieurs molécules de PyC$_{18}$. La diminution de l'excimère représente l'interaction du PyC$_{18}$ avec une autre micelle de la même nature.
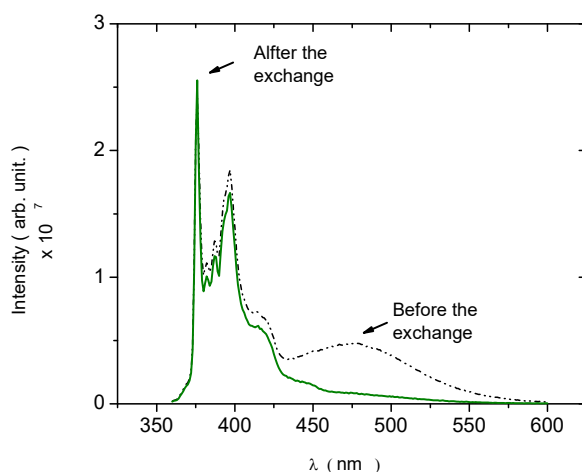
Figure 9. *Spectres d'émission (($\lambda_{ex}= 344$ nm) du PyC$_{18}$ dans une solution de copolymère P104 pa une concentration de 50 mg/mL. Le spectre marqué "before the exchange" identifie la solution initiale de P104 contenant le PyC$_{18}$. Le spectre étiqueté " after the exchange " identifie la solution obtenue en mélangeant 0.05 ml de micelles remplies avec du PyC$_{18}$ et 1 ml de micelles de P104 sans PyC$_{18}$ (50 mg/mL) mesurée après 2 heures.*

La *Figure 10* montre l'excimère et le monomère en fonction du temps obtenue après le mélange d'une solution de P104 40 mg/mL avec du PyC$_{18}$ et d'une solution sans PyC$_{18}$ à la même concentration (40 mg/mL). Ce comportement suit une fonction exponentielle, ce qui représente un échange correspondant à un mécanisme micellaire fusion-fission au premier contact entre deux micelles. L'évaluation de chaque déclin peut être effectuée en utilisant une fonction mono-exponentielle, ce qui permet de déterminer les constantes cinétiques avec l'inverse du temps de relaxation (k$_{decay}$= 1/τ). Le temps de relaxation (τ) obtenu à partir de la fonction mono-exponentielle est similaire à la valeur moyenne <τ> calculé à partir de l'ajustement de deux exponentielles.
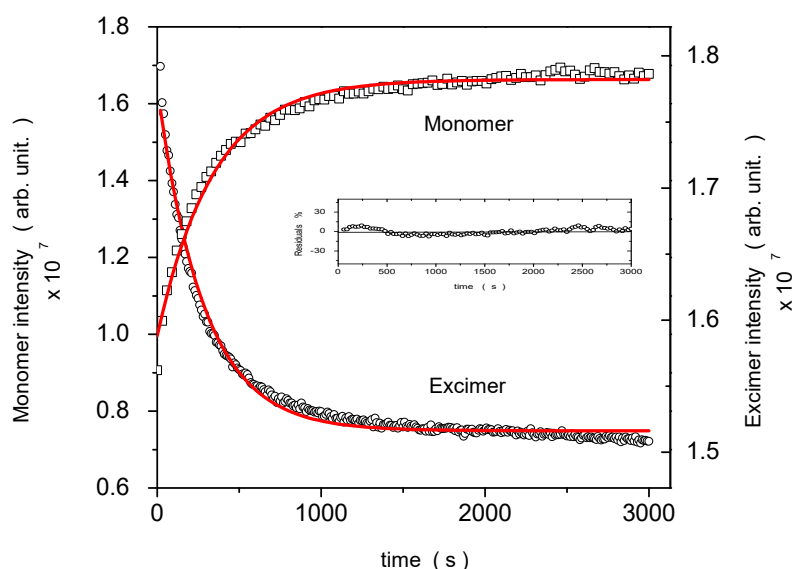
**Figure 10**. *Déclins de la bande de l'excimère (λ_{em} = 480 nm) et de la bande du monomère (λ_{em} = 376 nm) après le mélange de 0.05 mL d'une solution de P104 à 40 mg/mL avec PyC$_{18}$ et 1 ml d'une solution de P104 libre de PyC$_{18}$ à 40 mg/mL à la température de 40 °C. Les lignes solides correspondent aux ajustements utilisant une expression mono-exponentielle (r^2 = 0.988).*

Les expériences cinétique ont été réalisées dans une gamme de concentrations de P104 comprise entre 10 et 100 mg/mL pour les températures de 30 °C à 64 °C, de cette façon, les profils micellaires dynamiques ont été obtenus dans la région des micelles sphériques et la région de micelles allongée avant le point de trouble.

La *Figure 11* montre la dépendance linéaire de la constante cinétique (*k$_{decay}$*) avec la concentration micellaire de copolymère tribloc P104 ([Micelles]=([P104]-CMC)/N$_{agg}$) à la température de 30 °C. Un mécanisme de premier ordre avec une vitesse linéaire indépendante de la concentration en micelles vides avec une constante cinétique *k$_1$* est lié au processus de fission. Un mécanisme de deuxième ordre, avec une dépendance linéaire de *k$_{decay}$* en fonction de la concentration de micelles vides, est liée à un processus de fusion-fission, qui est effectuée par les étapes suivantes: collision d'une micelle remplie avec du PyC$_{18}$

et d'une micelle vide, échange du PyC_{18} à l'intérieur de la grande micelle et fission de cette micelle en deux micelles de taille standard avec du PyC_{18} à l'intérieur de chacune d'elles. L'interception représente le mécanisme de première ordre qui décrit l'échange due à la fission d'une micelle avec du PyC_{18} en deux micelles, suivie par la croissance de la micelle pour entrer dans la micelle vide.
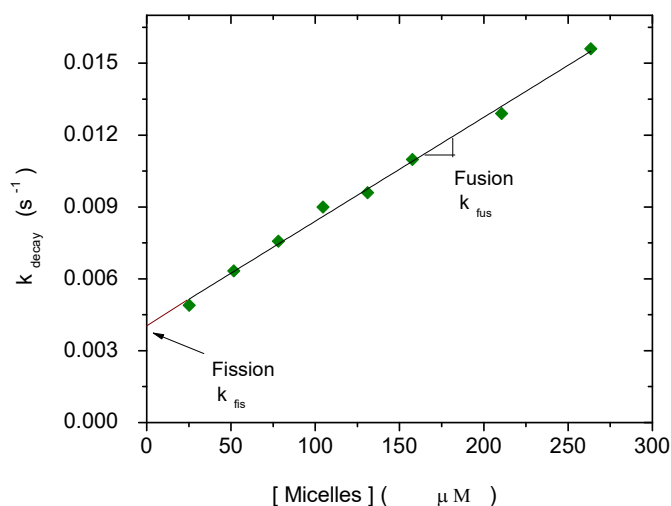
Figure 11. *Dépendance linéaire de la constante cinétique (k_{decay}) avec la concentration micellaire de copolymère tribloc P104 à la température de 30 °C.*

La *Figure 12* illustre la dépendance linéaire entre la constante cinétique k_{obs} et la concentration micellaire ([Micelles]=([P104]-CMC)/N_{agg}) dans la solution de P104 à des températures de 30 à 50 ° C, où des micelles sphériques sont stables micelles thermodynamiquement.
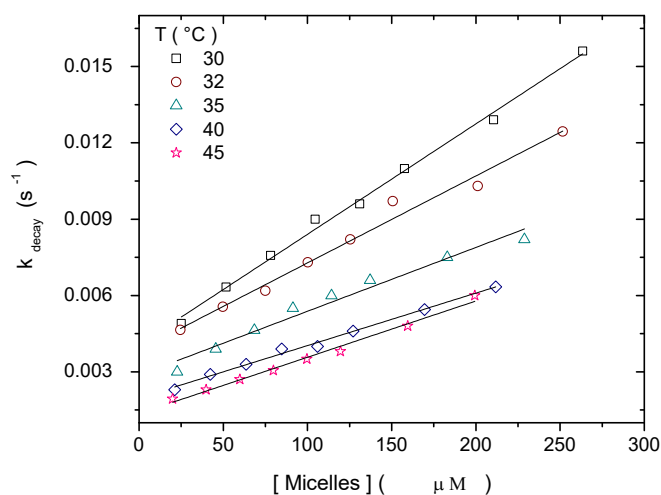
Figure 12. *Constante cinétique (k_{decay}) en fonction avec la concentration micellaire de copolymère tribloc P104 aux températures de 30, 32, 40 et 45 ° C.*

Il est possible d'observer que les valeurs k_{decay} diminuent avec l'augmentation de la température, jusqu'à une température de 45 °C. Ensuite, l'analyse des constantes de fission et de fusion en fonction de la température permet de trouver deux énergies d'activation de signe opposé, l'une à des températures élevées et l'autre à basse température. Quand les températures augmentent, les micelles sphériques sont compactés et les constantes de fission et de fusion, k_1 et k_2, diminuent jusqu'à ce que les micelles commencent à se développer, pour former ensuite des micelles allongées.

2.4. La dynamique d'échange entre copolymères triblocs amphiphiles et membranes lipidiques

Dans cette partie, on a étudié les dynamiques d'échange entre les copolymères triblocs P104 et les membranes lipidiques pour essayer de mieux comprendre les mécanismes d'échange dans la vétorisation des médicaments hydrophobes. Notre système d'étude est composé par des liposomes, représentant cellules, des micelles de copolymères tribloc, modélisant les véhicules, et le pyrène alkylée hautement hydrophobe, PyC_{18} représentant le principe actif dans le cœur des micelles. Les conditions expérimentales sélectionnées sont proches des conditions physiologiques moyennes, pH=6.5 et température contrôlée de 37 °C, afin de faciliter la compréhension des interactions pendant la libération des médicaments par des vecteurs micellaires avec des membranes de phospholipides.

Le rayon hydrodynamique des micelles sphériques reste constant dans la gamme de température de 30 à 54 ° C, avec moyenne de 11.4 ± 1 nm. La charge nette de micelles P104 a été évaluée avec des mesures de potentiel ζ à une température de 37 °C et à un pH de 6.5, pour lesquelles on obtient une valeur de -5.8 ± 0.4 mV, ce qui révèle une légère charge négative due vraissemblablement aux traces d'hydroxyde de potassium ou de sodium utilisé comme catalyseur lors de l'étape de synthèse du copolymère tribloc P104.

Des vésicules de L-α phosphatidylcholine, GUVs et des LUVs ont été préparées avec des tailles moyennes de 12 μm et de 160 ± 20 nm, respectivement. Les LUVs ont été préparées à partir de la solution initiale de GUVs afin d'obtenir une suspension à la même composition lipidique; elles ont été utilisées pour effectuer des mesures de diffusion dynamique de la lumière de dans des conditions convenables. Le potentiel ζ est une mesure de la charge électrique d'un liposome, qui est un paramètre important, car la charge de particules affecte à la fois la stabilité et la pharmacologie liposomale (dont les interactions électrostatiques). A un pH de 6.5, correspondant au pH de la préparation des liposomes (GUVs et LUVs) le potentiel ζ est négatif et a une valeur d'environ -22 mV. Dans cette étude, la valeur du pH des GUVs et des LUVs est maintenue à pH=6.5, où la membrane est chargée négativement et est stable.

Les interactions électrostatiques entre les liposomes hautement chargés négativement et les micelles de copolymères triblocs ont été étudiées par des mesures de potentiel ζ. La *Figure 13* montre la dépendance du potentiel ζ avec le rapport de la concentration de micelles de P104 et la concentration en lipides, correspondante à la moitié des têtes polaires qui sont sur la face externe de la vésicule et qui contribuent aux interactions avec le milieu extérieur, soit [P104] / [Lipid out], à un pH constant de 6.5 et une température de 37 °C. Différentes quantités de solution de micelles de P104 avec une concentration de 10 mg/mL ont été mélangés avec une suspension de GUVs 25 mg/mL, résultant sur différents rapports [P104]/ [Lipid out]. On observe que le potentiel ζ diminue légèrement avec l'augmentation de la quantité de micelles de P104, suggérant la présence d'interactions électrostatiques entre les micelles et la membrane lipidique.
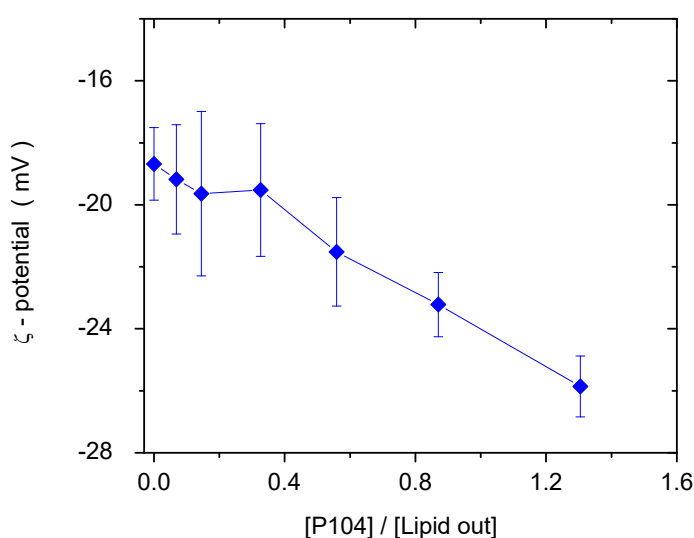
Figure 13. *Variation du potentiel ζ avec le rapport [P104]/[Lipid out], à une température constante de 37 ° C et à pH = 6.5.*

La dynamique entre les micelles de P104, choisis comme vecteurs, et les GUVs préparés avec L-α-phosphatidylcholine sont étudiées par fluorescence en insérant des molécules du dérivé fluorescent hydrophobe du pyrène, PyC_{18}, dans le cœur des micelles. Les spectres de fluorescence des micelles de copolymère contenant plus d'une molécule de PyC_{18} présentent une bande d'émission d'excimère à 480 nm et une bande d'émission à 376 nm pour le monomère.

Les *Figures 14 a* et *b* montrent les spectres d'émission d'une suspension de GUVs à une concentration de 25 mg/mL et le spectres d'émission du PyC_{18} dans une solution aqueuse de P104 avec une concentration de 10 mg/mL mélangée avec une suspension de liposomes 17.5 mg/mL et le spectre d'émission de la suspension de liposomes, respectivement, mesurés à une température de 37 °C. L'intensité de signal des liposomes est presque négligeable par rapport à l'intensité de signal obtenu

pour les micelles de P104 avec inclusion de PyC$_{18}$, et sera soustraite des spectres d'émission du PyC$_{18}$ dans les mélanges liposomes-micelles de P104.
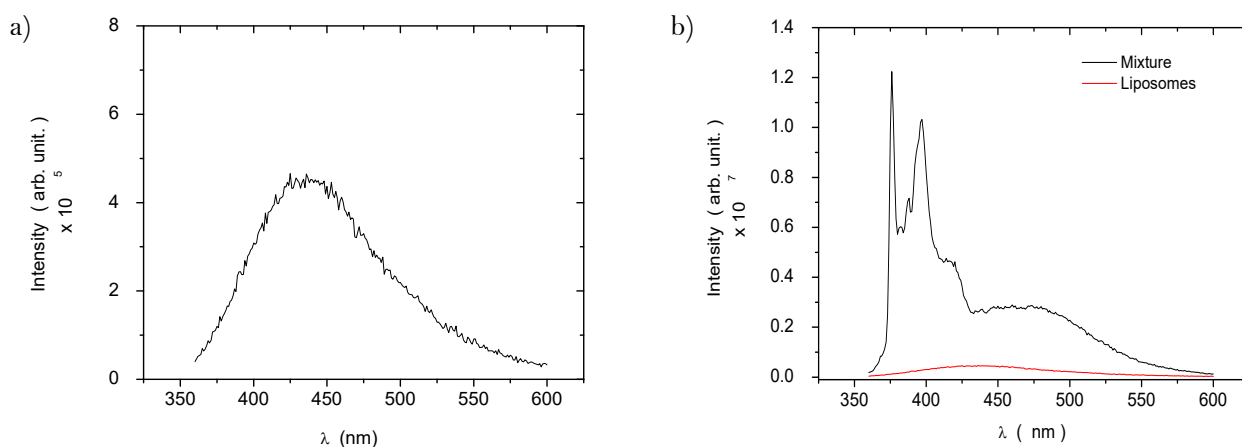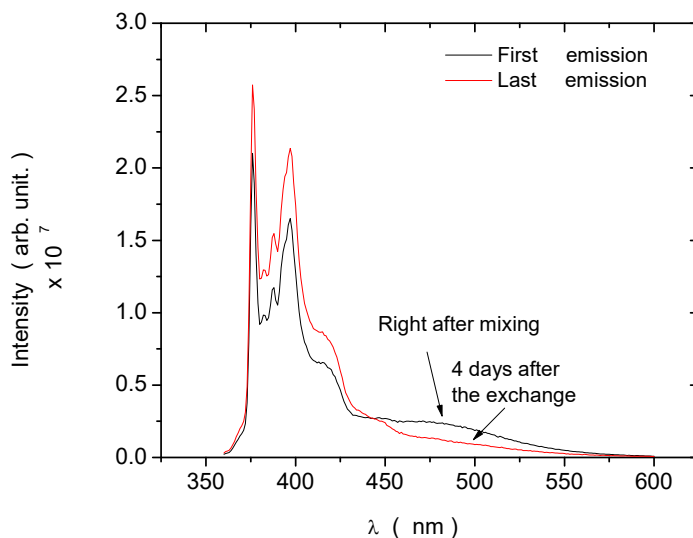

Figure 14 *Spectres d'émission a) d'une suspension de GUVs à une concentration de 25 mg/mL et b) du PyC$_{18}$ dans des micelles de P104 avec une concentration de 10 mg/mL mélangés avec une suspension de liposomes 17.5mg/mL et l'émission de la suspension de GUVs. Les mesures ont été faites à une température de 37 °C et à un pH = 6.5.*

La CMC du copolymère tribloc P104 a été vérifiée en présence d'eau et d'une solution de GUVs par des mesures de fluorescence. Dans les deux cas on a d'identifié des changement d'intensités I$_{mon}$/I$_{ex}$ en fonction de la concentration de P104 localisés à des concentrations de P104 de 0.67 mg/mL (dans l'eau) et de 0.53 mg/mL (dans les suspensions de liposomes), valeurs liées à la CMC du copolymère tribloc P104, en bon accord avec résultats précédents. Le contrôle de la stabilité des structures de vecteurs de libération de principes actifs avec la variation de l'environnement joue un rôle important dans l'efficacité de libération contrôlée de médicaments. La faible CMC est considérée comme un indicateur qui montre que l'administration après dilution ne conduira pas à la rupture des micelles, leur permettant de circuler dans l'environnement dans lequel ils sont libérés et de s'accumuler sur leur cible spécifique.

La *Figure 15* montre le spectre d'émission du PyC$_{18}$ dans une solution aqueuse de P104 avec une concentration de 3 mg/mL avec une suspension à une concentration de GUVs 17.5 mg/mL juste après le mélange et le spectre d'émission 4 jours après l'échange. De la même façon que pour la dynamique d'échange entre des micelles de copolymère tribloc amphiphile suivie avec les spectres d'émission du PyC$_{18}$, le spectre obtenu pour les micelles-liposomes présente deux grands pics dans les émissions de l'excimère, à 480 nm et du monomère, entre 376-400 nm. De l'existence de l'émission de l'excimère à 480 nm on déduit la présence de micelles de P104 portant deux ou plusieurs molécules PyC$_{18}$. L'augmentation du monomère représente l'interaction du PyC$_{18}$ avec la membrane lipidique hydrophobe des GUVs. La réponse de l'émission 4 jours après le mélange de micelles de P104 et des GUVs montre une diminution considérable de l'excimère et une augmentation de l'intensité du monomère. Cependant,

il est possible de constater que la dynamique d'échanges entre les micelles de P104 et les suspensions des GUVS sont beaucoup plus lentes que les dynamiques entre micelles.

Figure 15. *Spectres d'émission du PyC₁₈ dans une solution de P104 3 mg/mL mélangée avec une suspension de GUVs 17.5 mg/mL juste après le mélange et après 4 jours, les deux mesurés à une température de 37 ° C.*

L'évolution des spectres d'émission en fonction du temps est traitée en termes du rapport de la valeur obtenu à partir de l'intégration du pic d'intensité de l'excimère (440 nm $<l_{ex}<$550 nm) et l'intégration du pic d'intensité du monomère (366 nm $<I_{mon}<$425 nm); chaque déclin est analisé (I_{mon}, l_{ex} et I_{ex}/I_{mon}).
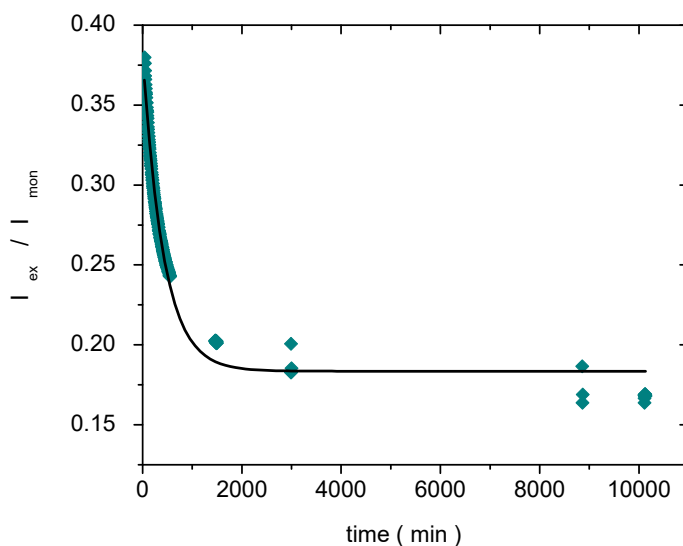
Figure 16. *Déclins du rapport I_{ex}/I_{mon} en fonction du temps obtenus pendant l'échange de micelles de P104 3 mg/mL contenant du PyC₁₈ avec des suspensions de GUVs à des concentrations de 17.5 mg/mL. La température*

de mesure est de 37 ° C. La ligne continue correspond à la fonction mono-exponentielle qui simule le déclin de l'excimère.

La *Figure 16* présente le déclins de I_{ex} en fonction du temps après les mélanges d'une solution de micelles de P104 à la concentration de 3 mg/mL avec une suspensions de GUVs 17.5 mg/mL. La décroissance cinétique peut être simulée par une fonction mono-exponentielle avec un temps de relaxation apparent (τ).

La *Figure 17* montre la dépendance de la constante cinétique (k_{decay}) avec la concentration de liposomes après le mélange avec une solution des micelles de P104 remplis avec du PyC_{18} à une concentration de 3 mg/mL. Nous pouvons observer une augmentation des valeurs de k_{decay} avec l'augmentation de la concentration des liposomes dans le mélange et une dépendance linéaire dans la gamme de concentration de 8 à 17.5 mg / ml selon l'équation suivante:

$$k_{decay} = k_1 + k_2 \, [liposomes] \tag{3}$$

Ensuite, il est possible de déterminer que le mécanisme d'échange est composé par les deux processus suivants: un mécanisme de premier ordre avec une vitesse linéaire indépendante de la concentration en liposomes et avec une constante cinétique appelé k_1, liée au processus d'échange-séparation, et un mécanisme de deuxième ordre, avec une dépendance linéaire du k_{decay} en fonction de la concentration liposomes, avec une constante cinétique de fusion-adhésion appelée k_2. Nous pouvons conclure que la dynamique d'échange entre des micelles de copolymère amphiphiles P104 et des liposomes est un mécanisme collectif qui peut être contrôlée avec la variation de la quantité de liposomes dans la suspension.
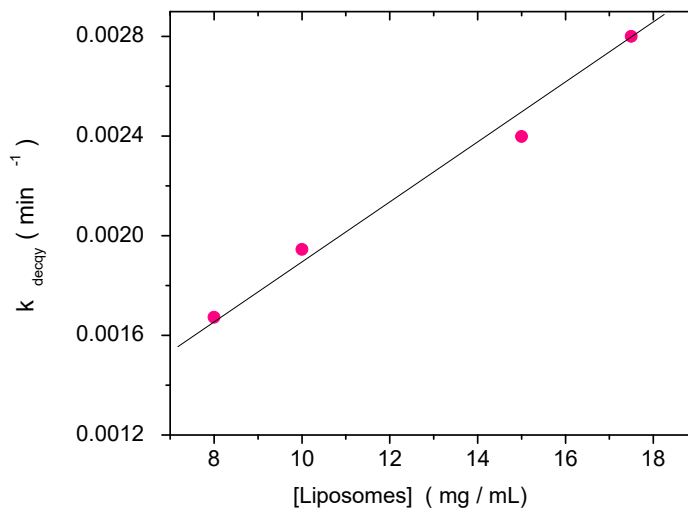
Figure 17. *Constante cinétique (k_{decay}) en fonction de la concentration en liposomes. La température de mesure est de 37 °C.*

Nous proposons un mécanisme d'interaction entre les micelles de copolymères P104 et des suspensions de GUVs obtenues avec la L-α-phosphatidylcholine dominé par des dynamiques collectives qui pourraient impliquer les étapes suivantes: collision d'une micelle et d'une GUV, adhérence des micelles sur la membrane lipidique, le transfert de la molécule hydrophobe à l'intérieur de la membrane lipidique et une séparation possible. La réponse observée après l'échange montre la présence de du pyrène hautement hydrophobe (PyC$_{18}$) dans la membrane lipidique et est représenté par la diminution de la valeur de l'intensité de l'excimère et l'augmentation de la valeur d'intensité du monomère. Les dynamiques de vectorisation des médicaments hydrophobes par des vecteurs tels que les copolymères triblocs amphiphiles peuvent être suivis, étudiés et quantifiés en utilisant la technique de fluorescence.

Finalement, dans les applications des liposomes, le recouvrement avec un polymère peut améliorer et augmenter la stabilité de la structure des membranes, la biocompatibilité et l'efficacité de la délivrance des médicaments. Pour cela, le chitosane a été récemment utilisée pour améliorer la biocompatibilité, la biodégradabilité et la mucoadhésivité des liposomes. Dans ce travail, on étudie aussi l'influence de l'adsorption du chitosane sur des liposomes dans les interactions entre les micelles de P104 et les liposomes. Dans un premier temps, le rôle de l'adsorption du chitosane sur les LUVs a été déterminé à l'aide de mesures de DLS, de mesures du potentiel ζ, et ensuite, en utilisant la microscopie confocale de fluorescence pour les GUVs. Le pH initial de la solution de chitosane et des suspensions de LUVs et de GUVs, qui est égal à 6.5, a été contrôlé afin de maintenir la charge nette de chaque composante constante pendant le processus d'adsorption. Le revêtement des GUVs avec du chitosane cationique à différents potentiels ζ, dans lequel les liposomes présentent des comportements différents (d'isolement ou d'agrégation), ont été utilisés pour étudier les interactions avec les micelles de P104.

Après avoir étudié le rôle de l'adsorption du chitosane sur les LUVs et les GUVs, on a étudié l'adsorption du chitosane sur des micelles de copolymères triblocs P104. Les suivants changements ont été identifiés dans la structure des micelles de P104 lors de l'ajout du chitosane cationique: agrégation des micelles de P104 lors de l'addition du chitosane au point isoélectrique, ζ= 0 mV, et des micelles de P104 revêtues de chitosane isolées et en excès de chitosane. Ces modifications de caractéristiques des micelles de P104 pourraient améliorer la stabilité de stockage des médicaments hydrophiles dans le cœur des micelles et pourrait empêcher leur libération avant d'atteindre la cible spécifique et la réception des stimuli adéquats pour parvenir à une libération de médicament efficace et contrôlée.

Les échanges entre micelles de P104 et GUVs revêtues de chitosane ont été étudiés par des mesures de potentiel ζ et de fluorescence, en utilisant le PyC$_{18}$ hautement hydrophobe pour la simulation du médicament hydrophobe. L'influence du chitosane adsorbé sur des liposomes et/ou sur des micelles a été examinée pour mettre en évidence son rôle sur le transfert de pyrène. Dans la *Figure 18 a*, des micelles de P104 chargés négativement ont été progressivement ajoutées à des liposomes revêtus de chitosane avec un potentiel ζ de 0 mV (formation des agrégats, *Figure 18 b*). Le potentiel ζ devient négatif comme une preuve des interactions de micelles P104. Après 9 heures, une faible modification du spectre de

fluorescence est observée (*Figure 18 c*). Lorsque des liposomes sont fortement chargés positivement, ils sont stables et isolés, comme on le voit dans la *Figure 18 b*. Dans ce cas, le potentiel ζ montre une légère modification et le spectre de fluorescence est légèrement modifié. Une hypothèse est que les micelles adsorbent l'excès de chitosane présent dans le milieu et que ces deux types de particules se repoussent mutuellement, les deux étant chargées positivement.

a)

b)

c)
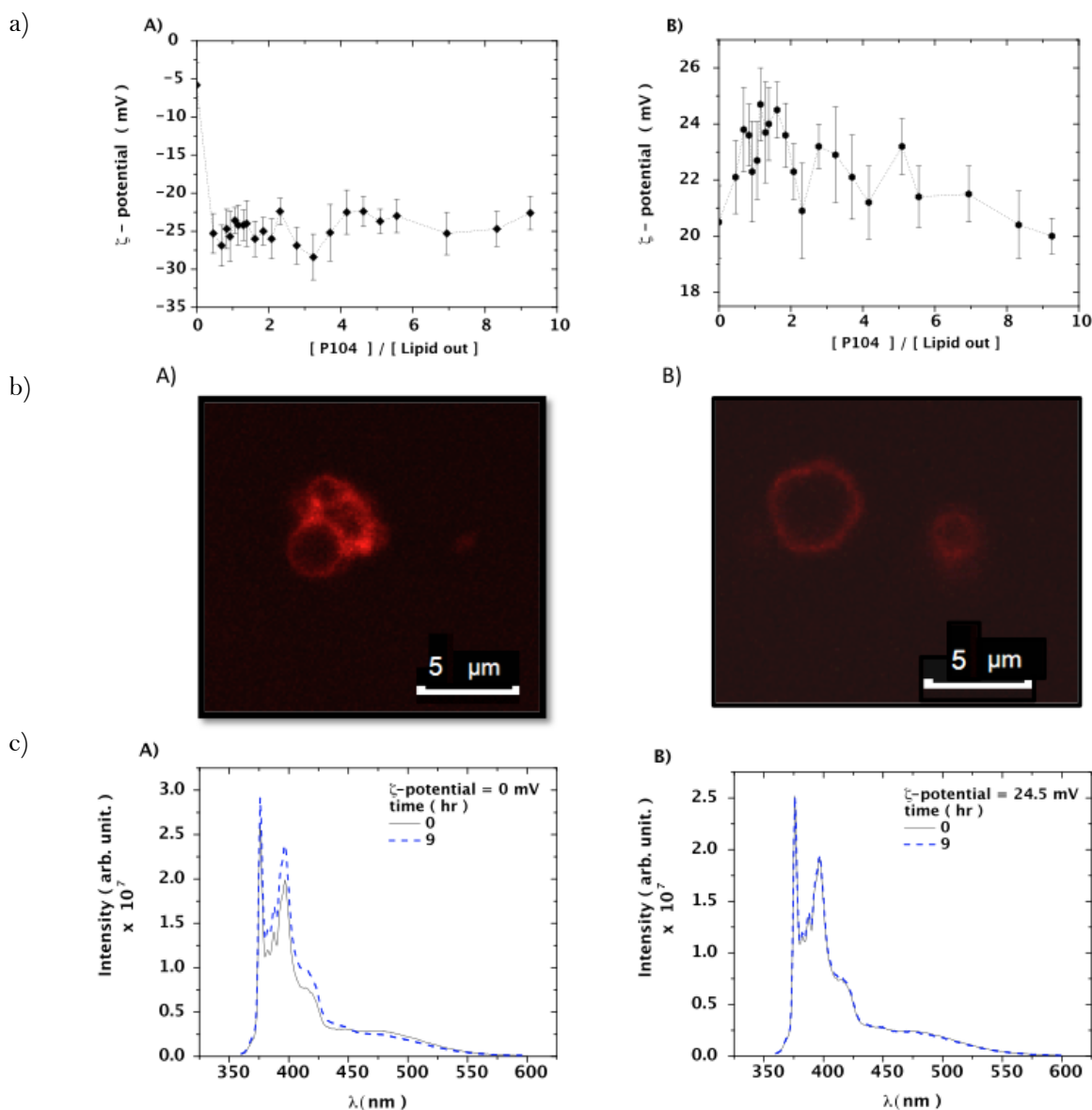
Figure 18. *a) Variation du potentiel ζ avec l'addition de micelles de P104 à des liposomes 10 mg/mL revêtus de chitosane à: A) potentiel ζ=0 mV et B) potentiel ζ= 24.5 mV, b) Visualisations du liposome initiale en A) état d'agrégation état pour des GUVs revêtues de chitosane au point isoélectrique et B) GUVs revêtues de chitosane isolés observés par microscopie confocale de fluorescence et c) Première et dernière émission du PyC₁₈ (P) dans des solutions de P104 10 mg/mL mélangées avec des GUVs revêtues de chitosane: A) potentiel ζ=0 mV et B) potentiel ζ= 24.5 mV. La temperature es toujours de 37 °C.*

2.5. Conclusions

Le comportement structurel du système P104 /eau a été analysée à détail, permettant la détermination de la température critique micellaire (CMT), la température de croissance micellaire (MGT) et la température de point de trouble (CPT) en fonction de la concentration P104. Les structures micellaires déterminées pour P104 copolymère amphiphile dans la gamme de température comprise entre 25 et 55 °C, peuvent être utilisés comme nanosupports micellaires pour la libération contrôlée de médicaments. Les propriétés rhéologiques du P104 en solution ont été étudiées dans une gamme de concentration en P104 de 50 à 600 mg/mL et sont fortement dépendantes de la température et de la concentration.

Le processus de croissance de micelles sphériques à micelles allongées de P104 a été étudié par DLS. L'intensité de lumiére diffusé, le rayon hydrodynamique et l'évolution du facteur de forme en fonction du temps ont été analysés en utilisant une fonction mono-exponentielle avec un temps de relaxation apparent. La dépendance linéaire de la vitesse de croissance avec la concentration en P104 montre que la croissance structurale est dominée par un mécanisme de fusion-fission.

La dynamique d'échange entre copolymères amphiphiles tribloque et les liposomes a été suivie avec succès à l'aide d'une molécule fluorescente hydrophobe qui peut être échangé via mécanismes différents. La cinétique du rapport excimère/monomère, I_{ex}/I_{mon}, suit une décroissance exponentielle après le mélange des copolymères et liposomes, à partir de laquelle il est possible de quantifier la constante cinétique d'échange. On a montré que la dynamique d'échange entre copolymères triblocs et liposomes est une dynamique collective.

Results of this thesis

1) Awards:

1) First place *"Best Poster Prize 2012"*

XVIth *International Congress on Rheology 2012*, Lisboa, Portugal (August 2012).

"Characterization of DNA/Buffer/H2O system by densimetry, rheometry and electrochemical impedance spectroscopy (EIS)"

<u>Lourdes Mónica Bravo Anaya</u>, Francisco Carvajal Ramos, V. Vladimir Fernández Escamilla, Emma Rebeca Macías Balleza, Norberto Casillas Santana, Erika Roxana Larios Durán, J.F. Armando Soltero Martínez.

2) *"Best Poster Award EIS 2013"*

9th *International Symposium on Electrochemical Impedance Spectroscopy* 2013, Okinawa, Japan (June 2013).

"Structural behavior of Au-Calf-thymus DNA Interface Estimated Through an EIS and SPR Study".

<u>Lourdes Mónica Bravo Anaya</u>, Emma Rebeca Macías, José Luis Hernández-López, V.Vladimir Fernández Escamilla, M. Alejandra Carreón Alvarez, J. F. Armando Soltero, Erika Roxana Larios-Durán.

3) Best Poster Award *"Biotechnology"*

XXXV Congreso Nacional de la AMIDIQ, Puerto Vallarta, México (May 2014).

"Efecto del reacomodo estructural de moléculas de ADN de timo de ternera en el proceso de oxidación de la guanina en electrodos de Au"

<u>Lourdes Mónica Bravo Anaya</u>, Maite Rentería Urquiza, María Alejandra Carreón Álvarez, Erika Roxana Larios-Durán.

4) Poster award *"Journée des Doctorants"*

Journée des Doctorants Ecole doctorale I MEP², Grenoble, France (June 2015).

"Chitosan/DNA Nanoparticles Development for Gene Therapy"

<u>Lourdes Mónica Bravo Anaya</u>, J.F. Armando Soltero, Yahya Rharbi, Marguerite Rinaudo.

2) Publications:

1) DNA Conformational Transitions at Different Concentrations and Temperatures Monitored by EIS.

L. M. Bravo-Anaya, E. R. Macías, F. Carvajal Ramos, V. V. A. Fernández, N. Casillas, J. F. A. Soltero and E. R. Larios-Durán .

ECS Electrochem. Lett. 2012, Volume 1, Issue 2, Pages G1-G3. doi: 10.1149/2.014202eel.

2) DNA Transitions by an Adsorption Impedance Study.

L. M. Bravo-Anaya, E. R. Macías, F. Carvajal Ramos, J.G. Álvarez-Ramírez, N. Casillas, J. F. A. Soltero and E. R. Larios-Durán.

J. Electrochem. Soc. 2013, Volume 160, Issue 4, Pages G69-G74, doi: 10.1149/2.029306jes.

3) Structural Behavior of Au-Calf-Thymus DNA Interface Estimated Through an Electrochemical Impedance Spectroscopy and Surface Plasmon Resonance Study

L. M. Bravo-Anaya, E.R. Macías Balleza, J.L. Hernández-López, V.V. Fernández-Escamilla, A. Carreón-Álvarez, J.R. Rodríguez, J. F. A. Soltero and E.R. Larios-Durán.

Electrochimica Acta 2014, Volume 131, Pages 60-70.

4) Characterization of DNA/Buffer/H₂O System Through Electrochemical Impedance Spectroscopy.

L. M. Bravo-Anaya, E.R. Larios-Durán, N. Casillas, V.V. Fernández-Escamilla, E.R. Macías Balleza and J. F. A. Soltero

ECS Transactions 2013, Volume 47(1), Pages 109-121. doi:10.1149/04701.0109ecst © The Electrochemical Society.

5) The Scaling of Electrochemical Parameters of DNA Aqueous Solutions with Concentration and Temperature Through an Electrochemical Impedance Spectroscopy Study.

L. M. Bravo-Anaya, E.R. Macías Balleza, N. Casillas, F. Carvajal Ramos, V.V. Fernández-Escamilla, J. F. A. Soltero and E.R. Larios-Durán.

Electrochimica Acta 2015, Volume 167, Pages 311-320.

6) Triblock copolymer P104 detailed behavior through a density, sound velocity and DLS study

L. M. Bravo-Anaya, C. Fierro-Castro, Y. Rharbi and J. F. A. Soltero Martínez.

AIP Conference Proceedings 2014, Volume 1599, Pages 480-484.

7) Conformation and rheological properties of calf-thymus DNA in solution

L. M. Bravo-Anaya, M. Rinaudo and J. F. A. Soltero Martínez.

In press: Polymers, 2016.

Poster presentations in national and international conferences:

1) *XXXIII Congreso de la AMIDIQ* (May 01-04 2012, San José del Cabo, BCS, México).

« Evaluación de propiedades reológicas de soluciones de ADN/Buffer/H₂O»

Lourdes Mónica Bravo Anaya, Emma Rebeca Macías Balleza, Erika Roxana Larios-Durán, Francisco Carvajal Ramos, V. Vladimir Fernández Escamilla, Norberto Casillas, J.F. Armando Soltero Martínez.

2) *XVIth International Congress on Rheology*, ICR 2012 (August 05-10 2012, Lisboa, Portugal).

« Characterization of DNA/Buffer/H_2O system by densimetry, rheometry and electrochemical impedance spectroscopy (EIS)»

Lourdes Mónica Bravo Anaya, Francisco Carvajal Ramos, V. Vladimir Fernández Escamilla, Emma Rebeca Macías Balleza, Norberto Casillas Santana, Erika Roxana Larios Durán, J.F. Armando Soltero Martínez.

3) 63 *Annual Meeting of the International Society of Electrochemistry* (August 19-24 2012, Praga, Czech Republic).

« Study of the interface Platinum-DNA/Buffer/H2O at different concentrations and temperatures by EIS »

Lourdes Mónica Bravo Anaya, Francisco Carvajal Ramos, Emma Rebeca Macías Balleza, Norberto Casillas Santana, Erika Roxana Larios Durán, J.F. Armando Soltero Martínez.

4) *XXXIV Congreso de la AMIDIQ* (May 07-10 2013, Mazatlán, Sinaloa, México).

«Determinación y análisis de la hidratación de moléculas de ADN en soluciones acuosas mediante densidad y velocidad del sonido»

Lourdes Mónica Bravo-Anaya, Emma Rebeca Macías-Balleza, Erika Roxana Larios-Durán, Francisco Carvajal Ramos, María Guadalupe Pérez García, Norberto Casillas, V. Vladimir Fernández Escamilla, J.F. Armando Soltero Martínez.

5) *9th International Symposium on Electrochemical Impedance Spectroscopy* (June 16-21 2013, Okinawa, Japón).
 «Structural Behavior of Au-Calf Thymus DNA Interface Estimated Through an EIS and SPR Study»

Lourdes Mónica Bravo Anaya, Emma Rebeca Macías, José Luis Hernández-López, V.Vladimir Fernández Escamilla, M. Alejandra Carreón Alvarez, J. F. Armando Soltero, Erika Roxana Larios-Durán.

6) *64th Annual Meeting of the International Society of Electrochemistry* (September 08-13 2013, Querétaro, México)

«Polarization Potential Effect on DNA Molecules Adsorption onto Platinum Electrodes»

Lourdes Mónica Bravo Anaya, J.F.Armando Soltero, Norberto Casillas, M.Alejandra Carreón Alvarez, Erika Roxana Larios Durán.

7) *XXXV Congreso de la AMIDIQ* (May 06-09 2014, Puerto Vallarta, Jalisco, México).

«Efecto del reacomodo estructural de moléculas de ADN de timo de ternera en el proceso de oxidación de la guanina en electrodos de Au»

<u>Lourdes Mónica Bravo Anaya</u>, Maite Rentería Urquiza, María Alejandra Carreón Álvarez, Erika Roxana Larios-Durán.

«Evaluación de propiedades fisicoquímicas de soluciones acuosas de Pluronic P104 mediante viscosimetría y densimetría»

<u>Carolina Fierro Castro</u>, Lourdes Mónica Bravo Anaya, Emma Rebeca Macías Balleza, Edgar Figueroa Ochoa, Francisco Carvajal Ramos, J.F. Armando Soltero Martínez.

8) *15ª Feria de posgrados de calidad 2014* (04-05 april, Distrito Federal, 07 april, Mazatlán, 09 april, Puebla, 11 april, Oaxaca, México).

Poster presentation representing the PhD in Science in Chemical Engineering from the Universidad de Guadalajara.

«Determinación de cambios conformacionales de moléculas de ADN en solución mediante densimetría, reometría y técnicas electroquímicas»

<u>Lourdes Mónica Bravo Anaya</u>, Erika Roxana Larios-Durán, J.F. Armando Soltero Martínez.

9) *15th Topical Meeting of the International Society of Electrochemistry* (April 27-30 2014, Niagara Falls, Canada).

«Impedance Transfer Function Designed to Simulate a Capacitve Behavior for DNA-Au and DNA-Pt Interfaces»

<u>Lourdes Mónica Bravo Anaya</u>, J.F.Armando Soltero, Emma Rebeca Macías, Jesús Gómez Guzmán, V.Vladimir Fernández Escamilla, M.Alejandra Carreón Alvarez, Erika Roxana Larios Durán.

10) *VII International Conference Times of Polymers (TOP) & Composites* (June 22-26 2014, Ischia, Italy).

«Triblock copolymer P104 detailed behavior through a density, sound velocity and DLS study»

<u>Lourdes Mónica Bravo Anaya</u>, Carolina Fierro-Castro, Yahya Rharbi, J.F.Armando Soltero Martínez.

11) *Condensed matter in Paris 2015* (August 24-29 2014, Paris, France)

«Linear and Non-linear Flow Properties of Entangled Calf-Thymus DNA Solutions»

<u>Lourdes Mónica Bravo Anaya</u>, Emma Rebeca Macías Balleza, Juan Humberto Pérez-López, Erika Roxana Larios Durán, Francisco Carvajal Ramos, Yahya Rharbi, J.F. Armando Soltero Martínez.

12) *Journée des Doctorants Ecole doctorale I MEP²* (June 2015, Grenoble, France).

«Chitosan/DNA Nanoparticles Development for Gene Therapy»

<u>Lourdes Mónica Bravo Anaya</u>, J.F. Armando Soltero, Yahya Rharbi, Marguerite Rinaudo.

13) *10ᵗʰ Annual European Rheology Conference* (April 14-17, Nantes, France)

« Fusion and fission dynamics are identified as the dominant processes in changing the shape of block copolymer micelles »

<u>Lourdes Mónica Bravo Anaya</u>, Gabriel Landazuri, J.F. Armando Soltero, Y. Rharbi.

« Exchange dynamics between amphiphilic block copolymers and lipid membranes for vectorization of hydrophobic molecules»

<u>Lourdes Mónica Bravo Anaya</u>, Gabriel Landazuri, J.F. Armando Soltero, Y. Rharbi.

14) *ECIS 2015, 29ᵗʰ Conference of the European Colloid and Interface Society* (September 06-11, Bordeaux, France)

« Chitosan Influence in the Vectorization Dynamics Between Amphiphilic Block Copolymer Micelles and Liposomes»

<u>Lourdes Mónica Bravo Anaya</u> , Marguerite Rinaudo, J.F.Armando Soltero, Yahya Rharbi.

Oral presentations in national and international conferences:

1) *XXXIII Congreso de la AMIDIQ (*May 01-04 2012, San José del Cabo, BCS, México).

« Evaluación des propiedades fisicoquímicas de soluciones de ADN/Buffer/H_2O por densimetría, velocidad del sonido et viscosimetría»

<u>Lourdes Mónica Bravo Anaya</u>, Emma Rebeca Macías Balleza, Erika Roxana Larios-Durán, Francisco Carvajal Ramos, V. Vladimir Fernández Escamilla, Norberto Casillas, J.F. Armando Soltero Martínez.

2) *XXVII Congreso de la Sociedad Mexicana de electroquímica* (June 11-15 2012, Toluca, México).

« Caracterización del sistema ADN/Buffer/H_2O por espectroscopía de impedancia electroquímica (EIS)»

<u>Lourdes Mónica Bravo-Anaya</u>, Erika Roxana Larios-Durán, Norberto Casillas, Francisco Carvajal, V. Vladimir Fernández Escamilla, Emma Rebeca Macías-Balleza, and J. F. Armando Soltero.

3) *XXXIV Congreso de la AMIDIQ* (May 07-10 2013, Mazatlán, Sinaloa, México).

« Estudio y caracterización del sistema ADN/Buffer mediante la técnica de resonancia de plasmones superficiales»

Lourdes Mónica Bravo-Anaya, Emma Rebeca Macías-Balleza, Erika Roxana Larios-Durán, Francisco Carvajal Ramos, Norberto Casillas, J.F. Armando Soltero Martínez, José Luis Hernández López.

4) *9th International Symposium on Electrochemical Impedance Spectroscopy* (June 16-21 2013, Okinawa, Japón).

« DNA transitions by an adsorption impedance study»

Lourdes Mónica Bravo Anaya, Emma Rebeca Macías, Francisco Carvajal Ramos, J. G. Álvarez-Ramírez, Norberto Casillas, J. F. Armando Soltero, Erika Roxana Larios-Durán.

5) *64th Annual Meeting of the International Society of Electrochemistry* (September 08-13 2013, Querétaro, México).

« The Scaling of Electrochemical Parameters of DNA Aqueous Solutions with Concentration and Temperature Through an EIS Study»

Lourdes Mónica Bravo Anaya, J.F.Armando Soltero, Emma Rebeca Macías, Norberto Casillas, V.Vladimir Fernández Escamilla, Francisco Carvajal Ramos, Erika Roxana Larios-Durán.

6) *49ème Congrès Annuel du Groupe Français de Rhéologie* (October 27-29, 2014, Grenoble, France)

«La dynamique de fusion et fission dans les micelles de copolymères amphiphiles à l'équilibre et leurs effets sur la rhéologie»

Lourdes Mónica Bravo Anaya, Gabriel Landazuri, J.F. Armando Soltero, Y. Rharbi.

7) *IV Simposio Becarios CONACyT en Europa* (November 05-07, Strasbourg 2015, France)

«Evaluación del comportamiento estructural de moléculas de ADN en solución mediante técnicas electroquímicas, ópticas y reología»

Lourdes Mónica Bravo Anaya, Emma Rebeca Macías Balleza, Juan Humberto Pérez López, Noberto Casillas, Yahya Rharbi, José Luis Hernández-López, Erika Roxana Larios Durán, J.F.Armando Soltero.

8) *10th Annual European Rheology Conference* (April 14-17, Nantes, France)

«Dynamics of Entangled Calf-Thymus DNA Solutions»

Lourdes Mónica Bravo Anaya, Emma Rebeca Macías Balleza, Juan Humberto Pérez López, Frédéric Pignon, Yahya Rharbi, J.F. Armando Soltero.

9) *17th Topical Meeting of the International Society of Electrochemistry* (May 31- June 03 2015, Saint-Malo, France)

« Thermodynamic Study of the Adsorption of Calf Thymus DNA at the Platinum/Buffer Electrolyte Interface»

Lourdes Mónica Bravo Anaya, Yahya Rharbi, Norberto Casillas, J.F. Armando Soltero, Erika Roxana Larios Durán.

10) *ISPAC 2015. 28ᵗʰ International Symposium on Polymer Analysis and Characterization* (June 8-10 2015, Houston, Texas).

« DNA-Chitosan Electrostatic Complex Formation: Stoichiometry and Conformation»

Lourdes Mónica Bravo Anaya, Yahya Rharbi, J.F.Armando Soltero, <u>Marguerite Rinaudo.</u>

11) *Sofun School 2015* (September 02-05, Carcans, France)

« Vectorization Dynamics Between Amphiphilic Block Copolymer Micelles and Liposomes»

<u>Lourdes Mónica Bravo Anaya</u>, J.F. Armando Soltero, Yahya Rharbi.